



HAL
open science

Flows at soft interfaces : the roles of elasticity, capillarity & fluctuations

Vincent Bertin

► **To cite this version:**

Vincent Bertin. Flows at soft interfaces : the roles of elasticity, capillarity & fluctuations. Physics [physics]. Université de Bordeaux, 2021. English. NNT : 2021BORD0206 . tel-03370619

HAL Id: tel-03370619

<https://theses.hal.science/tel-03370619>

Submitted on 8 Oct 2021

HAL is a multi-disciplinary open access archive for the deposit and dissemination of scientific research documents, whether they are published or not. The documents may come from teaching and research institutions in France or abroad, or from public or private research centers.

L'archive ouverte pluridisciplinaire **HAL**, est destinée au dépôt et à la diffusion de documents scientifiques de niveau recherche, publiés ou non, émanant des établissements d'enseignement et de recherche français ou étrangers, des laboratoires publics ou privés.

THÈSE PRÉSENTÉE
POUR OBTENIR LE GRADE DE
DOCTEUR
DE L'UNIVERSITÉ DE BORDEAUX

ECOLE DOCTORALE SCIENCES ET PHYSIQUE DE L'INGÉNIEUR

LASERS, MATIÈRE, NANOSCIENCES

Par **Vincent Bertin**[†]

Écoulements au voisinage d'interfaces molles : les rôles de l'élasticité, la
capillarité & les fluctuations

Flows at soft interfaces: the roles of elasticity, capillarity & fluctuations

Sous la direction de : **Thomas Salez**
Co-directeur : **Elie Raphaël**

Soutenue le 09 septembre 2021

Membres du jury :

Mme. Isabelle Cantat	Professeure	Université de Rennes 1	Rapporteure
M. Dominic Vella	Professor	University of Oxford	Rapporteur
Mme. Elisabeth Charlaix	Professeure	Université Grenoble Alpes	Examinatrice
M. David Dean	Professeur	Université de Bordeaux	Président du jury
Mme. Joelle Frechette	Professor	UC Berkeley	Examinatrice
M. Howard A. Stone	Professor	Princeton University	Examineur
M. Thomas Salez	Chargé de Recherche	CNRS	Directeur
M. Élie Raphaël	Directeur de Recherche	CNRS	Co-Directeur

[†] E-mail : vincent.bertinn@gmail.com

Écoulements au voisinage d'interfaces molles : les rôles de l'élasticité, la capillarité & les fluctuations

Résumé : Dans ce manuscrit, nous étudions des écoulements au voisinage d'interfaces molles au travers de systèmes divers. Dans une première partie, nous nous intéressons à la lubrification élastohydrodynamique, et analysons le mouvement confiné d'une sphère rigide se déplaçant à proximité d'une surface déformable. Les interactions hydrodynamiques entre une sphère oscillante et la déformation de la surface permettent de caractériser sans contact la réponse mécanique complexe des matériaux, comme la viscoélasticité, la poroélasticité ou la capillarité. Les résultats théoriques sont confrontés à des expériences de microscopie à force atomique avec une sonde colloïdale, permettant de mesurer la rhéologie d'élastomères et la tension de surface d'interfaces liquide-air en présence d'impuretés. Ensuite, nous calculons les forces et couples qui s'appliquent sur des sphères ayant la liberté de se déplacer et de tourner dans toutes les directions. La force de portance élastohydrodynamique, mesurée expérimentalement, est en accord avec les prédictions théoriques pour des faibles déformations de la surface. Dans une deuxième partie, nous nous intéressons à la dynamique de films visqueux mince. Au travers de travaux théoriques et expérimentaux sur le nivellement capillaire de films de polymères, nous analysons la dynamique de films reposant sur un substrat élastique, de films bicouches et de films suspendus. Une dernière partie est dédiée à la diffusion de sphères dans des écoulements cisailés et au voisinage d'une paroi. Nous analysons l'augmentation du coefficient de diffusion effectif induit par le couplage entre diffusion et advection. Un intérêt particulier est porté sur la dynamique aux temps courts devant le temps de diffusion et sur les interactions des particules avec le mur.

Mots-clés : Rhéologie, élasticité, capillarité, lubrification, films minces, diffusion.

Flows at soft interfaces: the roles of elasticity, capillarity & fluctuations

Abstract: In this manuscript, we study flows in the vicinity of soft interfaces through various systems. In a first part, we focus on elastohydrodynamic lubrication, and analyze the confined motion of a rigid sphere moving close to a soft surface. The hydrodynamic interactions between an oscillating sphere and the deformation of the surface allow us to characterize without contact the complex mechanical response of materials, such as viscoelasticity, poroelasticity or capillarity. Theoretical results are confronted with colloidal-probe atomic force microscopy experiments, allowing us to measure the rheology of elastomers and the surface tension of liquid-air interfaces in the presence of impurities. Then, we calculate the forces and torques that apply on spheres that are free to move and rotate in all directions. The elastohydrodynamic lift force, measured experimentally, is in agreement with theoretical predictions for small surface deformations. In a second part, we focus on the dynamics of thin films. Through theoretical and experimental work on the capillary leveling of thin polymer films, we analyze the dynamics of films resting on an elastic substrate, bilayer films and freestanding films. A last part is dedicated to the diffusion of spheres in shear flows and near a wall. We analyze the enhancement of the effective diffusion coefficient induced by the coupling between diffusion and advection. Particular interest is given to the dynamics at short times compared with the diffusion time and to the interactions of the particles with the wall.

Keywords: Rheology, elasticity, capillarity, lubrication, thin films, diffusion.

Remerciements

Wouah, la thèse s'achève ici. La recherche académique ressemble à un sport collectif. On retient le nom des chercheurs (voir du premier ou dernier auteur d'un article), mais le travail de recherche fait intervenir beaucoup plus de personnes à différents niveaux que je souhaite remercier ici.

I would first like to thank my thesis committee for the time they spent reading my work, in particular the referees Isabelle Cantat and Dominic Vella. I would also like to thank Elisabeth Charlaix, David Dean, Joelle Frechette and Howard Stone for agreeing to be members of the jury. I am honoured by your presence and I'm very grateful for our discussions that will trigger new thoughts for sure.

Je tiens tout particulièrement à remercier mes deux directeurs de thèse Thomas Salez et Elie Raphaël. Nous nous sommes rencontrés il y a maintenant 4 ans à l'occasion de mon stage de master à la suite duquel, c'était une évidence que je voulais travailler avec vous. Je ne vous remercierais jamais assez de m'avoir laissé une si grande liberté, et surtout de m'avoir très rapidement considéré comme un collègue. J'espère emporter avec moi votre rigueur, votre intégrité, votre générosité et bien sûr vos nombreuses qualités humaines qui font de vous d'excellents chercheurs.

J'ai eu la chance pendant cette thèse de travailler sur plusieurs projets qui m'ont amené à collaborer avec de nombreux chercheurs partout dans le monde et que je voudrais remercier ici. Many thanks to Kari Dalnoki-Veress for hosting me at McMaster for a few months in 2018. It was a great pleasure to work with such an enthusiastic person and even to try some experiments. I would also like to thank also Carmen, John, Clementine, Raffi, J-C and Adam for the time spent there. I would like to thank Oliver Bäumchen and Herbert Hui for the great discussions on the soft leveling project, it was an honour to join the team. I also thanks Anand Jagota, Andreas Carlson, Fred Restagno, Pascal Damman among others for the numerous discussions along with my PhD.

Je remercie également tous les collègues du LOMA. Yacine, c'était toujours un grand plaisir de discuter avec toi à chacune de mes visites Bordelaises, merci pour l'accueil. Un grand merci aussi à Abdelhamid pour nos multiples projets d'Elastohydrodynamique. C'est toujours très enrichissant de discuter et de comprendre les mystères des expériences AFM. C'était un grand plaisir de travailler avec la jeune équipe EMetBrown. Je vous souhaite à tous le meilleur, Christian, Elodie, Julien, Louis, Maxime, Nicolas, Yann, et Zaicheng.

Je tiens à remercier vivement tout le laboratoire Gulliver ! C'est avec grand plaisir que je monte les trois étages du bâtiment F (puis G) depuis trois ans pour venir travailler. Cette thèse doit beaucoup à ce cadre de travail exceptionnel et cette atmosphère chaleureuse qui permettent aux étudiants de s'épanouir, de rencontrer des chercheurs, de poser des questions et de présenter leurs travaux aux multiples réunions et ateliers. Pour cela, je remercie les directeurs Elie puis Olivier Dauchot, les gestionnaires Solange, Fée (grand merci), mais aussi Stéphanie, Hyo-Jin, David, Elisa et tous les chercheurs qui impulsent cette qualité de travail, David, Ludwik, Josh, Mathilde, Matthieu, Michael,

Paddy, Teresa, Vincent, Yanick, Zorana, ect.. Un grand merci à Charlotte, Mathilde et Olivier de m'avoir proposé de travailler sur le projet des gouttes nageuses, c'était un grand plaisir ! Et merci à Josh et Alex de m'avoir inclus à l'équipe afin de comprendre le mystère du TIRFM.

Ensuite, je souhaiterais remercier l'ESPCI dans son ensemble qui offre un très bon cadre de travail (à part les travaux). Je remercie Vincent Demery, Elie et Christophe Gissinger de m'avoir accepté dans leur équipe d'enseignement et les étudiants de l'ESPCI et l'ENS pour leurs questions pertinentes et leur intérêt. Enfin, merci à Alice Romiti pour l'organisation de la fête de la science, c'était super de pouvoir monter un stand.

Enfin arrivent les amis ! Merci à tous les doctorants, postdocs, stagiaires de Gulliver que j'ai eu la chance de rencontrer ces dernières années. Une mention spéciale à Pierre Soulard, mon co-bureau, co-thésard, coloc de chambre en conférence, co-Picard fan, un très grand plaisir d'avoir partagé cette aventure avec toi ! Merci aux biologistes : notre bébé Antoine, Thibault mon babos préféré et ses bières hautes qualités, VAS the best Russian I know, ... Après 3 ans, j'ai enfin compris ce qu'était une protéine ! Un grand merci également à Martyna (et David) pour les soirées jeux, concerts, rando calanque, à Paul et ses metamatériaux actif, toujours au top pour une petite grotte, ou un café, ou discuter science, mais aussi Alex, Alice, Charles, Coline, Guillaume, Haggai, Jérémy, Juliane, Rocio, ...

Merci aux amis de Marseille, Baptiste, Marina, Massad, Val (et une petite pensée pour notre André-Pierre national que je remercie), toujours un grand plaisir de se voir quand on rentre à la maison ou lors des week-end parisiens ! Merci aux potes de prépa : Andréa (bis), Cauchy, Charles, Charlotte Demonsant, Elsie, Hanto, Loris, Lucas pour ces belles soirées et après-midi contrée. Merci à tous les potes de Montreuil et à tous ces foots aux Guillands. Et enfin, je remercie toute la team ENS, les vacances en Ardèche, à Celles-sur-Ource, à Chavon, en Corse, à Lacanau, à Hossegor, aux festivals, la team vélo, la team rando Pyrénées/Alpes, les mois confinés au Poyet, la Bretagne. Je ne me risque pas à une liste exhaustive et je vais simplement vous remercier tous d'être là. Pour finir, je remercie ma famille et le soutien inconditionnel depuis 26 ans, je suis honoré de vous avoir vu pour la soutenance. Et mes dernières pensées pour Margo.

Contents

Introduction (French)	11
Introduction	19
I Elasto-hydrodynamic	23
1 Contactless rheology of soft interfaces	25
1.1 Introduction	25
1.1.1 Context: mechanical response of a soft interface	25
1.1.2 Scientific instruments for contactless measurements	29
1.1.3 Contactless experimental setup	31
1.1.4 Linear elasto-hydrodynamic response to a vertical oscillation . . .	32
1.2 Characterization of the complex properties of the solid	38
1.2.1 Viscoelastic substrate	38
1.2.2 Viscoelastic measurements of PDMS layer	40
1.2.3 Poroelasticity	43
1.2.4 Capillarity of soft solids	47
1.3 Viscocapillary response of a model liquid-air interface	49
1.3.1 Introduction	49
1.3.2 Experimental setup	49
1.3.3 Model	50
1.3.4 Asymptotic-matching method	51
1.3.5 Experimental results	56
1.3.6 Tensiometry measurements	59
1.4 Inertial effects	60
1.4.1 Introduction	60
1.4.2 Lubrication approximation	62
1.4.3 Generalized Lorentz reciprocal theorem	64
1.4.4 Low-Reynolds number expansion	65
1.5 Conclusion	68

2	Soft-lubrication interactions between a rigid sphere and an elastic wall	71
2.1	Introduction	71
2.1.1	Context: interactions between flow and solids	71
2.1.2	Surfaces near contact: lubrication	71
2.1.3	Particle dynamics near soft surfaces	74
2.2	Elastohydrodynamic model	77
2.3	Perturbation theory	79
2.3.1	Zeroth-order solution	79
2.3.2	First-order solution	80
2.3.3	Resulting force	82
2.4	Reciprocal theorem	84
2.4.1	Introduction	84
2.4.2	Normal force	85
2.4.3	Lateral force	87
2.5	Rotation of the sphere	87
2.6	Response of thin-elastic layers	89
2.6.1	Compressible elastic material	89
2.6.2	The incompressible limit	91
2.7	Experimental measurement of the EHD lift force	93
2.7.1	AFM setup	93
2.7.2	Experimental results	94
2.7.3	Numerical results at large deformation for a steady sliding	98
2.8	Conclusion	101
II	Thin-film dynamics near soft interfaces	103
3	Elastocapillary levelling of thin viscous films on soft substrates.	111
4	Capillary Levelling of Immiscible Bilayer Films	135
5	Symmetrization of Thin Free-Standing Liquid Films via Capillary-Driven Flow	161
III	Dispersion	169
6	Taylor-Aris dispersion	171
6.1	Introduction	171
6.1.1	Context: transport of microscopic particles	171
6.1.2	Advection-diffusion coupling: Taylor-Aris dispersion	174
6.2	Experimental results	179
6.2.1	Setup	180
6.2.2	Signal intensity distribution	181
6.2.3	Velocity fields	183

6.2.4	Local distributions of particle displacement	185
6.2.5	Time- and space-dependent dispersion	187
6.3	Theoretical models for tracer particles	189
6.3.1	Short-time asymptotics: Chatwin theory	190
6.3.2	Moment theory	191
6.3.3	Langevin simulations	194
6.3.4	Results	194
6.3.5	Comparison with experiments	195
6.3.6	Absorbing boundary condition at the top wall	197
6.4	Finite-size particles	199
6.4.1	Dynamics of a colloid	199
6.4.2	Moment theory for finite-size charged colloids	203
6.4.3	Long-time dispersion coefficient	205
6.4.4	Comparison with experiments	206
6.5	Conclusion	207
	Conclusion & Perspectives	211
	Conclusion & Perspectives (French)	215
	A Elastohydrodynamic forces computed with the Lorentz reciprocal theorem	217
	B Taylor-dispersion in a rectangular channel in the presence of a gravity field	221
	C Enhanced Dip-Coating on a Soft Substrate.	223
	D Swimming droplet in 1D geometries, an active Bretherton problem.	229
	Bibliography	245

Introduction (French)

Cette thèse de doctorat est l'aboutissement de mes recherches, que j'ai effectuées à la fois au *Laboratoire Ondes et Matière d'Aquitaine* (Université de Bordeaux) et au laboratoire *Gulliver*, sous la direction de Thomas Salez et Élie Raphaël. Nos travaux ont donné lieu à la rédaction de huit articles [1, 2, 3, 4, 5, 6, 7, 8].

Contexte général

La *matière molle* est un terme popularisé par le physicien français Pierre Gilles de Gennes, prix Nobel de physique 1991 [9]. Il désigne un domaine de recherche interdisciplinaire, entre la physique, la chimie, la biologie, la mécanique et dans lequel s'inscrit ce travail doctoral. En particulier, la caractéristique principale de la matière molle, qui lui sert parfois de définition, est que les énergies d'interaction entre ses éléments constitutifs mésoscopiques sont du même ordre de grandeur que l'énergie thermique. Les principales conséquences sont que la matière molle réagit fortement à de faibles sollicitations et que les fluctuations thermiques sont importantes. Par exemple, on observe de nombreux réarrangements et transitions de phases en matière molle qui résultent de changements infimes de la température ou la composition du système. Ce qui nous intéresse dans cette thèse, est que la matière molle réagit fortement à des contraintes mécaniques, ce qui lui confère une faible rigidité, et des propriétés complexes entre celles des fluides et des solides. On retrouve la matière molle dans une large variété d'exemples, dans les objets du quotidien (plastiques, bulles de savon, gels, cosmétiques, etc...), dans la nature (boues, sable, etc...), en biologie (cellules, vésicules, membranes, etc...).

Dans cette thèse, nous nous intéressons à divers problèmes mêlant mécanique des fluides et *élasticité*. En particulier, nous étudions des *écoulements au voisinage d'interfaces molles*, qui sont intéressants et complexes du fait de la capacité des interfaces de la matière molle à se déformer sous l'effet des contraintes mécaniques de l'écoulement. Ainsi, la modification des interfaces induit une rétroaction sur l'écoulement. En outre, au voisinage d'interfaces molles, les forces de surface (par exemple la *capillarité*) et les *fluctuations thermiques* ont souvent un rôle important et seront également abordées. Les outils développés ici sont principalement théoriques et numériques. Néanmoins, la quasi-totalité des sujets traités accompagne des expériences réalisées par des collaborateurs, ou est motivée par de potentielles futures expériences. Enfin, comme souvent en physique, notre approche consiste à réduire la complexité au travers de systèmes modèles. L'objectif est d'en dégager des principes simples et fondamentaux afin de comprendre en profondeur les phénomènes en question.

Presentation et résumé du manuscrit

Ce manuscrit est articulé autour de trois parties indépendantes. La partie I est constituée de deux chapitres traitant des interactions elasto-hydrodynamiques entre une

sphère rigide et une surface molle.

Chapitre 1 : Rhéologie sans contact d'interfaces molles.

À des échelles micrométriques et nanométriques, la caractérisation des propriétés mécaniques est un défi de taille car les forces de surface jouent souvent un rôle dominant. Pour accomplir cette tâche, nous présentons dans ce chapitre une méthode expérimentale sans contact direct entre la sonde et la surface, et basée sur les interactions élastohydrodynamiques. Une sphère est mise en mouvement et oscille dans la direction normale à une surface molle. En mesurant la force nécessaire pour entretenir le mouvement, la réponse mécanique de la surface peut être inférée. Nous développons un modèle pour prendre en compte les propriétés viscoélastiques et poroélastiques du substrat, ainsi que la capillarité de la surface du solide. Des expériences avec un microscope à force atomique confirment la robustesse de la méthode et permettent de mesurer la viscoélasticité de couches d'élastomères. Ensuite, nous utilisons la technique sans contact pour mesurer la réponse mécanique d'une bulle déposée sur une surface. La taille de la bulle modifie la réponse mécanique, et nous développons un modèle, basé sur un raccordement asymptotique, pour prendre en compte les effets de taille finie. Cette méthode permet de mesurer la tension de surface d'une interface liquide-air en présence d'impuretés. Enfin, nous étudions l'influence de l'inertie du fluide, généralement négligée dans les modèles.

Chapitre 2 : Interactions de lubrification entre une sphère rigide et un mur élastique.

Dans ce deuxième chapitre, nous nous intéressons aussi aux interactions hydrodynamiques entre une sphère rigide et une surface molle. Nous développons un modèle général, dans lequel une sphère est libre de se déplacer et dans les directions normales et tangentielles à la surface, et de tourner. Les forces et couples élastohydrodynamiques sont calculés par une méthode directe, en caractérisant l'écoulement, et par une méthode indirecte en exploitant le théorème réciproque de Lorentz. Les calculs analytiques sont réalisés dans la limite de faible déformation de la surface molle par rapport à la distance entre la sphère et la surface. La réponse mécanique de la surface est calculée dans le cadre de l'élasticité linéaire, pour des substrats élastiques plats et dans les cas-limites de couches épaisses et minces. Une partie de ces résultats théoriques est confrontée avec succès à des mesures expérimentales de la force de portance élastohydrodynamique.

La partie II de ce manuscrit discute de films minces de polymères autour de trois chapitres. Nous étudions l'écoulement de films minces déposés sur des surfaces molles. Une courte introduction présente le contexte de ce travail et résume les résultats obtenus dans le groupe sur la dynamique des films minces en amont de cette thèse. Chaque chapitre est constitué de la reproduction d'un article publié dans une revue scientifique.

Chapitre 3 : Elastocapillary levelling of thin viscous films on soft substrates.

Dans ce chapitre, nous étudions la dynamique de nivellement d'un film mince placé au-dessus d'une couche d'élastomère. Plus précisément, un film de polystyrène est préparé à l'état vitreux dans une condition initiale en forme de marche d'escalier en superposant deux films. En chauffant l'échantillon, le film s'écoule et nous nous intéressons à la dynamique de relaxation de cette perturbation. Notons toutefois que les plus grandes tailles caractéristiques en jeu sont micrométriques, de telle sorte que les forces capillaires dominant devant la gravité et pilotent l'écoulement. De manière surprenante, la dynamique de nivellement est très différente sur un substrat rigide ou sur la couche d'élastomère. Aux premiers instants, la relaxation est plus rapide sur l'élastomère, comme si celui-ci amortissait le choc initial. En revanche, aux temps longs, la dynamique est plus lente, et le profil de l'interface suit une loi de diffusion qui diffère de celle sur substrat rigide. Plusieurs modèles sont développés, un dans l'approximation de lubrification et l'autre en résolvant les équations de Stokes. Les modèles reproduisent certaines caractéristiques aux temps courts de la relaxation, mais la dynamique lente au temps long n'est pas expliquée à ce jour.

Chapitre 4 : Capillary Levelling of Immiscible Bilayer Films.

Ce chapitre suit une méthode très similaire à celle du chapitre 3. Des films minces de polymères sont préparés dans la configuration marche comme précédemment et placés au dessus d'un autre type de substrat déformable : un autre film de polymère, liquide, et non-miscible. Ce système bi-couche est un modèle simplifié de matériaux multicouches que l'on retrouve dans des objets du quotidien et dans les processus industriels de coextrusion multicouche de polymères. Nous nous intéressons en particulier à des systèmes dans lesquels le film du dessous est le moins visqueux, jouant le rôle d'un lubrifiant effectif. Là aussi, le nivellement est modifié par la présence de la sous-couche car celle-ci réagit à l'écoulement et se déforme. Contrairement au nivellement sur un substrat rigide, nous n'observons pas de dynamique de relaxation de type diffusive unique mais plutôt des transitions entre différents régimes. Un modèle asymptotique est développé, en supposant des longues perturbations par rapport à l'épaisseur du film, et ce dernier retrouve qualitativement les transitions entre différents régimes. En étudiant la variation de l'énergie du système, nous interprétons ces transitions comme des transitions entre les différents mécanismes de dissipation visqueuse du fait des divers écoulements dans les deux films.

Chapitre 5 : Symmetrization of Thin Free-Standing Liquid Films via Capillary-Driven Flow.

Dans le dernier chapitre de la partie, nous étudions des films minces de polymère suspendus. Ces membranes liquides ont des applications dans des processus industrielles (fabrication de verre flotté), mais aussi en géophysique (tectonique des plaques). Nous observons la dynamique de relaxation d'une perturbation cylindrique nanométrique à l'une des deux interfaces du film. Nous observons que la perturbation se symétrise dans un premier temps, avant de s'élargir et disparaître. Un modèle qui prend en compte tous les termes des équations de Stokes est développé. La dynamique peut être

décomposée en deux modes indépendants qui diffèrent par leur symétrie miroir. Le mode antisymétrique, qui est analogue au mode de flexion visqueux dans les membranes liquides, relaxe exponentiellement, confirmant les observations expérimentales.

La dernière partie de ce manuscrit comporte un chapitre et discute de la dispersion de Taylor.

Chapitre 6 : Taylor-Aris dispersion.

A l'échelle microscopique, les particules diffusent sous l'effet du mouvement Brownien. Le transport de particules dans un canal est induit à la fois par l'écoulement du fluide et la diffusion. Le couplage entre ces deux modes de transport engendre une augmentation de la dispersion des particules dans le sens de l'écoulement par rapport à la diffusion moléculaire. Le chapitre discute du phénomène associé appelé dispersion de Taylor. Nous analysons des données expérimentales obtenues en utilisant une technique de microscopie en onde évanescente. Nous suivons les trajectoires de nanoparticules dans un microcanal au voisinage de la paroi afin d'en extraire la dispersion. Dans un premier temps, nous nous concentrons sur la dispersion de Taylor aux temps courts, c'est-à-dire pour des temps plus faibles que le temps de diffusion sur la largeur du canal. Nous constatons que le coefficient de dispersion augmente avec le temps et sature vers la loi de Taylor-Aris aux temps longs. De plus, la dispersion aux temps courts dépend de la distribution initiale des particules, et croît linéairement en temps pour une distribution des particules initialement étalée, et quadratiquement en temps pour des particules ayant une position initiale identique. Nous discutons de la condition au bords à employer théoriquement pour modéliser les expériences de microscopie à ondes évanescentes, dans lesquelles les particules peuvent sortir de la zone d'observation au cours de leur mouvement. Dans un second temps, nous nous intéressons aux interactions entre les nanoparticules et la surface en verre qui délimite le canal. D'une part, du fait de la répulsion électrostatique des particules par le mur, les particules explorent une zone plus restreinte du canal ce qui réduit le coefficient de dispersion. D'autre part, les interactions hydrodynamiques réduisent le coefficient de diffusion car la friction augmente près du mur et les effets stériques interdisent les premières couches de fluide proche de la surface. Combinant ces deux effets, la dispersion diminue à mesure que la taille des particules augmente.

Les deux annexes A et B apportent des résultats complémentaires aux chapitres 2 et 6. L'annexe C décrit un projet toujours en cours. Nous nous intéressons à une technique expérimentale, *l'enduction par trempage* (dip coating), largement répandue pour déposer un film liquide sur une surface. En particulier, nous étudions l'influence de la rigidité de la surface sur l'épaisseur du film déposé. L'annexe D de ce mémoire est

dédié à un projet annexe à ma thèse que j'ai effectué avec d'autres chercheurs du laboratoire *Gulliver*. Nous étudions expérimentalement et théoriquement le mouvement de gouttes auto-propulsées dans des capillaires de différentes sections.

Introduction

This doctoral dissertation is the outcome of my research, performed both in the *Laboratoire Ondes et Matière d'Aquitaine* (Université de Bordeaux) and in the laboratory *Gulliver*, under the supervision of Thomas Salez and Elie Raphaël. Our work led to the writing of eight articles [1, 2, 3, 4, 5, 6, 7, 8], some of which are reproduced in the manuscript.

Context

Soft matter is a term popularized by the French physicist Pierre Gilles de Gennes [9], winner of the 1991 Nobel Prize in Physics. It designates a field of research at the interface between physics, chemistry, biology, and mechanics and in which this thesis is inscribed. In particular, the common feature that is shared by soft matter, which is sometimes used as a definition, is that the interaction energies between its mesoscopic constitutive elements is on the same order of magnitude as the thermal energy. The main consequence is that soft matter reacts strongly to weak solicitations, and that thermal fluctuations are significant. For example, we observe many rearrangements and phase transitions in soft matter that result from minute changes in the temperature or composition of the system. What is interesting to us in this thesis, is that soft matter reacts strongly to mechanical constraints, which gives it a low rigidity, and exhibits complex properties between those of fluids and solids. Soft matter is found in a wide variety of examples, in everyday life (plastics, soap bubbles, gels, cosmetics, etc.), in nature (muds, sand, etc.), in biology (cells, vesicles, membranes, etc.).

In this thesis, we are interested in various problems mixing fluid mechanics and *elasticity*. In particular, we study *flows near soft interfaces*, which are interesting and complex because of the ability of the soft matter interfaces to deform under the mechanical stress induced by the flow. Thus, the modification of the interfaces induces a feedback on the flow. In addition, near soft interfaces, surface forces (*e.g.* capillarity) and thermal fluctuations often play an important role and will also be discussed. The tools developed here are mainly theoretical and numerical. Nevertheless, almost all of the topics treated are related to experiments performed by collaborators, or are motivated by potential future experiments. Finally, as is often the case in physics, our approach consists in reducing the complexity through the use of model systems. The objective is to derive simple and fundamental principles in order to understand in depth the phenomena in question.

Presentation of the manuscript

This manuscript is articulated around three independent parts. Part I consists of two chapters dealing with elastohydrodynamic interactions between a rigid sphere and a soft surface.

Chapter 1 : Contactless rheology of soft interfaces.

At micro- and nanoscale scales, the characterization of mechanical properties is a major challenge because surface forces often play a dominant role. To address this challenge, we present an experimental method without direct contact between the probe and the surface, and based on elasto-hydrodynamic interactions. A sphere is driven to oscillate in the direction normal to a soft surface. By measuring the force required to maintain the motion, the mechanical response of the surface can be inferred. We develop a model to account for the viscoelastic and poroelastic properties of the substrate, as well as the capillarity of the solid surface. Experiments with an atomic force microscope confirm the robustness of the method and allow us to measure the rheology of elastomeric layers. Then, we use the contactless technique to measure the mechanical response of an air bubble deposited on a surface. The size of the bubble modifies the mechanical response, and we develop a model, based on asymptotic matching, to take into account the finite size effects. This method allows us to robustly measure the surface tension of an interface in presence of impurities. Finally, we study influence of fluid inertia, usually neglected.

Chapter 2 : Soft-lubrication interactions between a rigid sphere and an elastic wall.

In this second chapter, we are also interested in hydrodynamic interactions between a rigid sphere and a soft surface. We develop a general model, in which a sphere is free to move in directions normal and tangential to the surface, and to rotate. The elasto-hydrodynamic forces and torques are computed from a direct method, by characterizing the flow, and from an indirect method by exploiting the Lorentz reciprocal theorem. The analytical calculations are performed in the limit of small deformation of the soft surface with respect to the distance between the sphere and the surface. The mechanical response of the surface is calculated in the linear-elasticity framework, for flat elastic substrates and in the limiting cases of thick and thin layers. Some of these theoretical results are successfully compared with experimental measurements of the elasto-hydrodynamic lift force.

The part II of this manuscript discusses polymer thin films around three chapters. We study the flow of thin films deposited on soft surfaces. A short introduction presents the context of this work and summarizes the results obtained in the group on thin film dynamics prior to this thesis. Each chapter is a reproduction of a published article.

Chapter 3 : Elastocapillary levelling of thin viscous films on soft substrates.

In this chapter, we study the leveling dynamics of a thin film placed on top of an elastomeric layer. Specifically, a polystyrene film is prepared in the glassy state in a stepped initial condition by superimposing two films. By annealing the sample, the film flows and we are interested in the relaxation dynamics of the perturbation. Note however that the largest characteristic length scales of the system are micrometric, so that capillary forces dominate over gravity and drive the flow. Surprisingly, the leveling dynam-

ics is very different on a rigid substrate compared to the elastomeric layer. At the first instants, the relaxation is faster on the elastomer, as if the substrate would absorb the initial “shock”. On the other hand, at long times, the dynamics is slower, and the profile of the interface follows a diffusion law which differs from that on a rigid substrate. Several models are developed, one in the lubrication approximation and the other solving the Stokes equations. The models reproduce some characteristics at short times of the relaxation, but the slow dynamics at long time is not explained at this time.

Chapter 4 : Capillary Levelling of Immiscible Bilayer Films.

This chapter follows a very similar method to that of chapter 3. Thin films of polymers are prepared in the same stepped configuration as before and placed on top of another type of deformable substrate: another immiscible liquid polymer film. This bilayer system is a simplified model of multilayer materials found in everyday objects and in industrial multilayer coextrusion processes. We are particularly interested in systems in which the bottom film is the least viscous, playing the role of an effective lubricant. Here too, the leveling is modified by the presence of the underlying layer because it reacts to the flow and deforms. Unlike the leveling on a rigid substrate, we do not observe a single diffusive type of relaxation dynamics but rather transitions between different regimes. An asymptotic model is developed, assuming long perturbations with respect to the film thickness, and it qualitatively reproduces the transitions between different regimes. By studying the energy variation in the system, we interpret these transitions as transitions between the different viscous dissipation mechanisms of the system due to the different flows in the two films.

Chapter 5 : Symmetrization of Thin Free-Standing Liquid Films via Capillary-Driven Flow.

In the last chapter of the section, we study freestanding polymer thin films. These liquid membranes have applications in industrial processes (fracturing of floating glass), but also in geophysics (plate tectonics). We observe the relaxation dynamics of a nanometric cylindrical perturbation at one of the two interfaces of the film. At first, the perturbation symmetrizes, before widening and disappearing. A model that takes into account all the terms of the Stokes equations is developed. The dynamics can be decomposed into two independent modes which differ by their symmetries. The antisymmetric mode, which is analogous to the viscous bending mode in liquid membranes, relaxes exponentially, confirming experimental observations.

The last part of this manuscript consists of a single chapter and discusses Taylor dispersion.

Chapter 6 : Taylor-Aris dispersion.

At the microscopic scale, particles diffuse because of Brownian motion. The transport

of particles in a channel is induced by both flow and diffusion. The coupling between these two modes of transport results in an increase in the dispersion of particles in the direction of flow compared to simple molecular diffusion. The chapter discusses the associated phenomenon called Taylor dispersion. We analyze experimental data obtained using an evanescent-wave microscopy technique. We follow the trajectories of nanoparticles in a microchannel near the surface in order to extract the dispersion. First, we focus on Taylor dispersion at short times, *i.e.* for times smaller than the diffusion time over the channel width. We find that the dispersion coefficient increases with time and saturates towards the Taylor-Aris law at long times. Moreover, the dispersion at short times depends on the initial particle distribution, and grows linearly in time for an initially wide distribution of particles, and quadratically in time for particles with identical initial position. We discuss the boundary condition to be used theoretically to model evanescent-wave microscopy experiments, in which the particles may leave the observation area during their motion. In a second step, we are interested in the interactions between the nanoparticles and the glass surface that delimits the channel. On the one hand, due to the electrostatic repulsion of the particles by the wall, the particles explore a smaller area of the channel which reduces the dispersion coefficient. On the other hand, hydrodynamic interactions reduce the diffusion coefficient because friction increases near the wall and steric effects prohibit the first layers of fluid near the surface from being accessible. Combining these two effects, the dispersion decreases as the particle size increases.

The two appendices A and B provide complementary results to chapters 2 and 6 respectively. The appendix C presents an ongoing project. We are interested in an experimental technique, dip coating (dip coating), widely used to deposit a liquid film on a surface. In particular, we study the influence of the surface stiffness on the thickness of the deposited film. The appendix D of this thesis is dedicated to a project that I carried out with other researchers of the laboratory *Gulliver*. We study experimentally and theoretically the motion of self-propelled droplets in capillaries of different sections.

Part I

Elastohydrodynamic

Chapter 1

Contactless rheology of soft interfaces

1.1 Introduction

1.1.1 Context: mechanical response of a soft interface

Elasticity

Finding the deformation of an object in response to a force is the paradigm of mechanics. How much can I deform a material? What shape this material will adopt? Why are some structures mechanically stable, and others not? These questions have been addressed for centuries and have been resolved using theoretical tools in mechanics such as elasticity theories and many experimental techniques. Let us first describe one of the simplest examples and probably the most emblematic one: the tensile test. Imagine an elongated object like a rod of cross-sectional area A and of length L_0 , on which we apply a traction force F . In response, the rod is extended and has a new length $L_0 + \Delta L$. If the deformation is small, its deformation is linearly proportional to the force. To be more quantitative, we define the strain ϵ , the dimensionless ratio $\Delta L/L_0$ and the stress σ , as the force per unit area F/A , such that the mechanical law reads:

$$\sigma = \frac{F}{A} = E \frac{\Delta L}{L_0} = E\epsilon, \quad (1.1)$$

where E denotes the Young's modulus of the material, with the unit of a pressure. The Young's modulus is an elastic parameter, that characterizes the rigidity of the material, ranging from ~ 100 GPa for stiff materials such as metals, to ~ 1 kPa for very soft materials such as gels. Equation (1.1) is known as *Hooke's law*, and was first enunciated by Robert Hooke in 1678 [10]. It is very useful to illustrate the theory of elasticity but it is quite useless in practice given that it is restricted to a 1d geometry.

A local generalization of Hooke's law in 3d was first derived by Augustin-Louis Cauchy in the early nineteenth century, yielding to modern continuum mechanics. In

this continuum theory, strain and stress are space-dependent 2nd-rank tensor fields related via the linear relation $\sigma_{ij} = C_{ijkl}\epsilon_{ij}$, where Einstein's summation convention is used. The strain tensor ϵ is related to the displacement field \mathbf{u} of the elastic solid with respect to a reference configuration, as $\epsilon = \frac{1}{2}(\nabla\mathbf{u} + (\nabla\mathbf{u})^T)$, where ∇ is the nabla operator and T is the transpose operator. The stress tensor σ characterizes the force within the solid such that if we consider an infinitesimal surface dS oriented with a normal vector \mathbf{n} , then the force applied on the surface is given by $\mathbf{n} \cdot \sigma dS$. For a homogeneous and isotropic material, the 4th-rank tensor C_{ijkl} may be reduced to only two independent parameters using symmetry arguments: the Young modulus E (previously introduced), and a dimensionless parameter called the Poisson ratio and denoted ν here. The latter gives information about the compressibility of the material that amounts to answering the question: if we pull on a material along a given direction, how much will it shrink in the others? We note that the generalized Hooke's law can be written in the following way:

$$\sigma = \mu \left(\nabla\mathbf{u} + (\nabla\mathbf{u})^T \right) + \lambda (\nabla \cdot \mathbf{u}) \mathbf{I}, \quad (1.2)$$

where $\mu = E/(2(1 + \nu))$ and $\lambda = E\nu/((1 + \nu)(1 - 2\nu))$ are the Lamé coefficients and \mathbf{I} is the identity tensor.

Viscoelasticity

Although elasticity theories describe the mechanical response of most solid materials, it exists a class of material for which these theories fail at explaining the mechanical behavior. As an example, toothpaste appears as an elastic solid in its tube but flows once a large-enough pressure is applied on the tube. This state of matter, in between fluid and solid, is often called *viscoelastic* materials and is widely spread in biology (cells, blood, ...), in everyday life (creams, gels, foams, ...), and in nature (mug, lava, ...). A common feature of viscoelasticity is that the strain state is not only a function of the instantaneous stress state at a given time, as in linear elasticity but also depends on the "mechanical history" of the considered material. Mathematically, Hooke's law (see Eq. (1.1)) is modified to account for this property, as:

$$\sigma(t) = \int_{-\infty}^t \psi(t - t') \dot{\epsilon}(t') dt', \quad (1.3)$$

where ψ is a response function and the dot denotes a time derivative. Notably, the response of the material largely depends on the typical time scale of the excitation, or its frequency. One example is cornstarch solution, which deforms elastically like a solid for a quick excitation. However, for long-time excitation, the solution flows as a liquid. Viscolastic materials are composed of macromolecules, colloids, droplets, or bubbles of typical sizes ranging from a few nanometers to a micron, much larger than the atomic scale (~ 0.1 nm). These objects have a much larger intrinsic relaxation time, or slower dynamics, than molecules for which the relaxation time is on the order of 1 – 10 ps. Therefore, the constitutive law of viscoelastic materials (see Eq. (1.3)) emerges from

the fact that the response depends on how the typical time scale of the macroscopic excitation compares with the microscopic relaxation time of the individual compounds of the material.

Capillarity

The cohesive property of the condensed states of matter comes from the attractive interactions between the molecules. A molecule at an interface with another phase (e.g. a liquid-gas interface) has fewer neighboring identical molecules, and therefore a higher energy state than a molecule in the bulk. The direct consequence is that the creation of an extra interface area is associated with an energy cost per unit of surface, which is called surface tension and denoted γ . The physical phenomenon associated with surface tension is called *capillarity* [11, 12]. As an example of consequences, liquid jets break into droplets because the process decreases the surface and therefore the capillary energy. When comparing capillarity to gravity, a length scale $\sqrt{\gamma/(\rho g)}$ emerges, where ρ and g denote the density and gravity acceleration, respectively. This length is called the *capillary length* and is on the order of 1 mm for standard liquids. It provides the typical scale below which capillarity dominates.

Besides, a pressure difference ΔP is observed across a curved interface, which is known as the Laplace law:

$$\Delta P = \gamma\kappa, \quad (1.4)$$

where κ is the mean curvature of the interface. The sign convention is set such that curvature is positive for concave shapes. In other words, for a spherical interface like a droplet, the pressure is large inside the droplet. This law characterizes the mechanical response of capillary interfaces and is important to understand the deformation of droplets, bubbles, and the dynamics of thin films (see Part II). Even though capillarity may seem restricted to fluid-fluid interfaces, solid-fluid interfaces also have an energy cost for the same reason as the one above [13]. Interestingly, here again, a length scale emerges when comparing bulk elasticity to capillarity, γ/E , called the *elastocapillary length*. Similarly, this length scale sets the typical length below which capillarity dominates the mechanical response of a solid. For hard materials like metal this length scale is ~ 0.1 nm, on the same order as the atomic size, hence solid capillarity can be safely neglected. Nevertheless, for very soft gels, this length may reach 10 – 100 μm and have a potential impact on the mechanical response. For instance, capillarity smoothens out corners of soft gels on a typical size γ/E [14] and drives mechanical instabilities [15, 16] as it tends to minimize the surface energy.

Measurements

There are many existing methods to measure the mechanical response of a soft interface and an exhaustive list is out of the scope of the current manuscript. Here, we quickly review the main experimental techniques before introducing the methods discussed in this chapter.

As briefly discussed above, tensile testing is likely the most common technique in mechanical engineering to measure the elastic response of a material. This method also allows measuring the high-strain response of materials and the associated strain-hardening and fracture properties [17]. Indentation-based hardness tests are the other classical methods to assess the mechanical response. They consist in pressing a hard tip, of known shape and mechanical properties, on a given sample and measuring the deformation. Viscoelasticity and the associated frequency-dependent rheology of soft solids are usually measured with conventional rheometers [18]. For instance, the sample is fixed in between two rotating plates, and a rotating displacement is imposed on one plate while the applied torque is measured on the other one. Lastly, surface tension is measured by a large variety of techniques: the pendant-drop method [19] and the spinning-drop method exploit energy minimization principles while Wilhelmy plates or du Noüy rings [20] measure capillary forces.

Towards nanomechanics

All these experimental methods involve a large volume of material and require a homogeneous and isotropic matter. Nevertheless, at mesoscopic scales, the constitutive elements of soft condensed matter do not necessarily fulfill these conditions. An important example in living systems is cells which are composed of compartmentalized regions, and combine multiple sources of elasticity (*e.g.* phospholipid membrane, cytoskeleton, ...). Moreover, the mechanical behavior of cells is intrinsically coupled to the cell function [21] which raises important questions in biology.

Many progress has been made with the development in the 1980's of optical techniques in order to both manipulate and probe the mechanical response of microscopic objects. For example, optical tweezers, which consist of a highly focused laser beam, permit to trap micron-size particles like colloids and cells [22, 23]. The Surface Force Apparatus and the Atomic Force Microscope are alternative experimental systems allowing to achieve similar goals. These instruments are described in more detail in section 1.1.2. Interestingly, the down-scaling toward micro and nanometers brings a lot of questions and challenges for physicists. Notably, at such scales, the granularity/discreteness of matter questions the continuum description of mechanics. Additionally, the electronic interactions between molecules lead to forces such as electrostatic and van der Waals forces which may become dominant at such scales.

Within this context, we present in the present chapter a method to measure the mechanical response of a soft interfaces, from the micro to the nanoscale. This experimental method is based on the elastohydrodynamic interactions between a spherical probe and the soft surface. The advantages of the method are: i) it necessitates small stresses and does not damage the sample, ii) the measurements are done with no contact, allowing to get the mechanical response in the absence of possible adhesion between the probe and the sample. In particular, we investigate how contactless colloidal-probe-AFM method can be used to probe very soft elastomers in section 1.2, bubbles in section 1.3 and we explore the effect of fluid inertia in section 1.4.

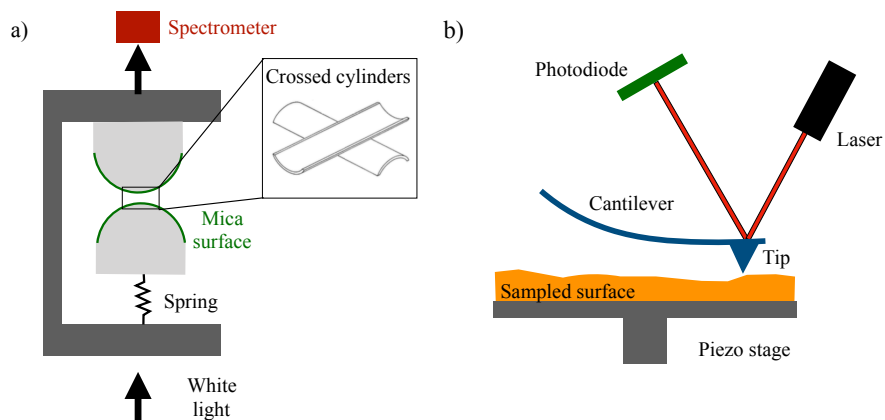


Figure 1.1: a) Simplified schematic of the Surface Force Apparatus, in its original design by J. Israelachvili. b) Simplified schematic of an Atomic Force Microscope.

1.1.2 Scientific instruments for contactless measurements

There are two main experimental tools, first developed for contact nanoscience and that were then adapted to conduct contactless elastohydrodynamic measurements. We briefly present the concept and the history of these devices and we encourage an interested reader to look at a more specific experimental review [24] or book [25] for further experimental information.

Surface Force Apparatus

The surface Force Apparatus (SFA) is a scientific instrument first conceived by D. Tabor, R. H. S. Winterton & J. Israelachvili in the 70's in order to measure the interactions between two surfaces [26, 27]. The principle is to bring almost into contact two surfaces, usually in a sphere-plan geometry, *e.g.* using two crossed cylinders of typical curvature radius in the centimeter range (see Fig. 1.1a)). Piezoelectric positioning elements are used to displace the surfaces with good accuracy and the separation distance between the surfaces is measured through optical interferometry. One of the two surfaces is connected to a spring, such that the deformation of the spring allows to have access to the interaction forces between the surfaces. In the first experiments using SFA, the interaction forces between two freshly cleaved mica surfaces were measured in vacuum, revealing the van der Waals forces. Freshly cleaved mica surfaces are atomically smooth over a wide area, which allows one to reach separation distances as small as a nanometer. Later on, the SFA has been adapted to a solvent environment such as water and has been used to measure other static interaction forces like electrostatic double-layer forces [28], adhesion and capillary forces, and even the forces due to the structural form of liquids near surfaces [29].

Additionally, the SFA also provided a method to measure hydrodynamic forces of confined liquids such as the friction forces between sheared surfaces [30] (see Chap. 2)

and the hydrodynamic forces during the drainage of a liquid film when the surfaces approach [31] to cite a few examples. More recently, a dynamic SFA apparatus [32] was developed in the group of Elisabeth Charlaix to perform the contactless rheological measurements that are discussed in this chapter. In such a setup, a sphere is driven to oscillate normally to a planar surface. The force required to maintain the oscillatory motion is measured through the displacement of a cantilever, which allows one to determine the mechanical impedance of the system. Dynamic SFA has been used to measure the slip length of water over hydrophobic surfaces [33] and bubble mattresses [34], the slip length of polyelectrolyte solutions [35], as well as the elastohydrodynamic interactions between a sphere and soft polymer layers [36] or glasses [37].

Atomic Force Microscope

The Atomic Force Microscope (AFM) is another scientific instrument developed in 1985 by the Nobel laureates Gerd Binnig & Heinrich Rohrer¹ [38]. They were working in a laboratory of the IBM company and the AFM was commercialized soon after its design in 1989 and is now widely spread in the research world.

An atomic force microscope is made of a flexible cantilever, with a sharp tip at the end (see Fig. 1.1b)). The deflection of the cantilever is usually measured by reflecting a laser beam on the tip and recording the deviation of the laser with a photodiode. The sample is placed on a *xyz* piezo stage that allows moving the sample with respect to the tip. The AFM is used in many contexts and disciplines ranging from biology to solid-state physics [25]. For instance, it allows: i) to make topography imaging of surfaces with a nanometric resolution in height and over an area $\sim 10 \times 10 \mu\text{m}^2$ (see Part II), ii) to measure the interactions between a pair of molecules [39], and iii) to manipulate and stretch a single polymer [40]. Besides, the AFM tip can be used as a nano-indenter to measure the mechanical response of the sampled surface. The AFM is usually used in three modes of operation: one static and two dynamic modes. In the *static mode* (also called contact mode), the tip is in contact with the sample and the measurement of the deflection of the cantilever allows to get the surface topography of the sample. The dynamic modes exploit the fact that the AFM cantilever is a mechanical resonator, with a certain resonance frequency. In particular, in the *tapping mode* (also called amplitude modulation or AM-AFM), the cantilever is driven to oscillate near its resonance frequency. The interactions of the AFM tip with the sampled surface induce an additional deflection of the tip that is measured. This method is very similar to the one used in dynamic SFA, and is discussed in the current manuscript. Lastly, the AFM can be used in the *frequency modulation mode* (FM-AFM), where the cantilever is always excited at its resonance frequency using a feedback loop. In that case, the modification of the resonance properties of the cantilever allows measuring the interactions with the sample.

The colloidal-probe technique, developed independently by Ducker [41] and Butt [42]

¹They obtained a Nobel price in 1986 for their design of the scanning tunneling microscope, which is an other scientific instrument to image a surface, and is based on the concept of quantum tunneling.

in 1991, was largely employed in colloidal science since then. It consists of gluing a smooth spherical probe on the tip of a cantilever, of typical radius $\sim 1 - 50 \mu\text{m}$, which amplifies the magnitude of the interaction between the tip and the surface in order to make quantitative measurements of surface forces with a higher resolution. The AFM appears as a complementary device to SFA as it permits to measure intermolecular forces (*e.g.* electrostatic or van der Waals) between colloids, or between colloids and surfaces with the advantage of being more versatile and of smaller size. The typical force resolution is of the order of 1 nN with the AFM and 1 μN in SFA. This technique has been adapted to measure hydrodynamic interactions, the slip length of water on hydrophobic surfaces [43], interactions between bubbles [44, 45] or droplets [46, 47, 48]. We also stress that other probe shapes have been employed, such as nano-fibers in order to measure wetting properties [49, 50, 51, 52, 53] and viscoelasticity [54, 55]. Lastly, recent developments of tuning fork atomic force microscopes have been used to measure the rheological and tribological measurements of gold nanojunctions [56], ionic liquids [57].

1.1.3 Contactless experimental setup

The experimental setup that is discussed in this section has been conceived by Abdelhamid Maali. The experiment results that are presented in the manuscript have been obtained by Zaicheng Zhang, Muhammad Arshad, Samir Almohamad and Abdelhamid Maali.

The experiments are performed using an AFM (Bioscope, Bruker) equipped with a liquid cell (DTFML-DD-HE). A spherical borosilicate particle (MO-Sci Corporation) with a $R_s = 54 \pm 2 \mu\text{m}$ radius is glued at the edge of a silicon nitride cantilever (ORC8-10, Bruker AFM Probes). The stiffness $k_c = 0.20 \pm 0.01 \text{ N/m}$ of the cantilever (with the sphere attached to it) is determined from the drainage method [58]. The bulk resonance frequency $\omega_0/(2\pi) = 1240 \pm 3 \text{ Hz}$ and the bulk quality factor $Q = 3.4 \pm 0.1$ are obtained from the resonance spectrum at large distance [59]. A multi-axis piezo stage (NanoT series, Mad City Labs) is used to control the distance between the sphere and the sample, by imposing a displacement to the substrate at very low velocity. The amplitude A and phase φ of the cantilever's deflection signal are measured by a lock-in amplifier (Model 7280, Signal Recovery), and are recorded versus the piezo displacement. Additionally, the DC component of the cantilever's deflection is also recorded and used to determine the average gap distance D . We stress that the amplitude of the spherical probe's oscillation is a few nanometers, and always less than 3.5 nm, which is itself smaller than D , fixed to be typically in the 10 nm - 20 μm range.

The schematic of the experimental setup is shown in Fig. 1.2a). The cantilever is excited by the base oscillation $\mathcal{R}[A_b e^{i\omega t}]$, where ω and A_b are the angular frequency and amplitude of the base vibration, respectively, where $\mathcal{R}[\cdot]$ denotes the real part and t denotes time. The system essentially behaves as a damped oscillator, where the vertical displacement $Z(t)$ of the center of mass of the sphere with respect to its rest position

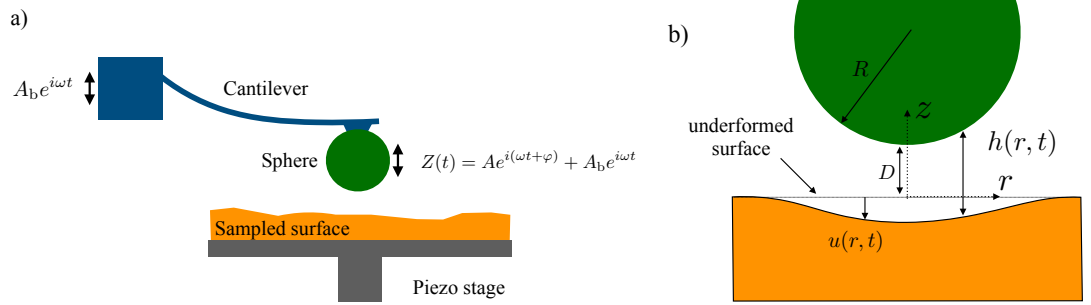


Figure 1.2: a) Simplified schematic of an Atomic Force Microscope with a colloidal probe in the tapping mode. b) Schematic of the model problem in section 1.1.4.

satisfies:

$$m_c \ddot{Z} + \Gamma_{\text{bulk}} \dot{Z} + k_c Z = F_d + F, \quad (1.5)$$

with m_c the effective mass (*i.e.* including the added fluid mass), Γ_{bulk} the damping coefficient in the bulk, k_c the stiffness of the cantilever, F_d the driving force due to the imposed oscillation of the cantilever, and $F = \mathcal{R}[F^* e^{i\omega t}]$ the hydrodynamic force resulting from the interaction between the oscillating sphere and the air-water interface. The displacement $Z(t)$ of the sphere includes the cantilever deflection $\mathcal{R}[A e^{i(\omega t + \varphi)}]$ measured by AFM and the base displacement, and thus reads $Z(t) = \mathcal{R}[A e^{i(\omega t + \varphi)} + A_b e^{i\omega t}] = \mathcal{R}[Z^* e^{i\omega t}]$, where A and $Z^* = A e^{i\varphi} + A_b$ are real and complex amplitudes respectively [59]. We further define the mechanical impedance $G^* = -F^*/Z^*$. Invoking the complex version of Eq. (1.5), the impedance reads:

$$G^* = -k_c \left[1 - \left(\frac{\omega}{\omega_0} \right)^2 + i \frac{\omega}{\omega_0 Q} \right] \frac{A e^{i\varphi} - A_\infty e^{i\varphi_\infty}}{A e^{i\varphi} + A_b}, \quad (1.6)$$

where A_∞ and φ_∞ are respectively the amplitude (A) and phase (φ) measured far from the surface (*i.e.* where F vanishes), $\omega_0 = \sqrt{k_c/m_c}$ is the bulk resonance frequency, and $Q = m_c \omega_0 / \Gamma_{\text{bulk}}$ is the bulk quality factor. Equation (1.6) provides a direct way to measure G^* experimentally from the cantilever's deflection signal and thus assess the mechanical response of the sample.

1.1.4 Linear elastohydrodynamic response to a vertical oscillation

This section is largely inspired by the work of Samuel Leroy & Elisabeth Charlaix published in Ref. [60] with the aim to model the mechanical impedance G^* in the AFM colloidal probe experiments.

Hydrodynamic

We consider the axisymmetric system composed of a rigid sphere located at an average distance D from a planar soft surface as schematized in Fig. 1.2b). The ensemble is immersed in an incompressible Newtonian fluid with a dynamical shear viscosity η . The spherical probe oscillates vertically with nanometric amplitude Z^* and frequency $\omega/(2\pi)$, and generates a drainage flow. In the experimental setup, the sphere-plan distance is smaller than the sphere radius, so that we employ the lubrication approximation. The Reynolds number is very small as the oscillation amplitude is nanometric and the viscous penetration depth $\delta = \sqrt{\eta/(\rho\omega)}$ is supposed to be larger than the sphere-plan distance, *i.e.* $\delta \gg D$, so that the flow is steady² and the liquid-gap thickness profile, denoted $h(r, t)$, obeys the Reynolds equation [61]:

$$\frac{\partial h(r, t)}{\partial t} = \frac{1}{12\eta r} \frac{\partial}{\partial r} \left[r h^3(r, t) \frac{\partial p(r, t)}{\partial r} \right], \quad (1.7)$$

where r is the radial coordinate, $p(r, t)$ is the excess hydrodynamic pressure field with respect to the rest state. The no-slip boundary condition is assumed at both the sphere and soft surfaces. Here, we are interested in hydrodynamic interactions, such that we ignore the static equilibrium forces such as van der Waals or electrostatic double-layer forces. In the regime of small sphere-plan distance with respect to the sphere radius, we use the parabolic approximation of spherical contact, such that the liquid-gap thickness reads:

$$h(r, t) = D + Z^* \cos(\omega t) + r^2/(2R) + u(r, t), \quad (1.8)$$

where $u(r, t)$ is the surface normal deflection (see Fig. 1.2b)). The oscillation amplitude is supposed to be much smaller than the sphere-plan distance as well as the surface deflection, so that the non-linear terms in Z^* of Eq. (1.7) are neglected and we focus on the linear response. The excess pressure and the surface deformation are supposed to be harmonic functions of time and reads $p(r, t) = \mathcal{R}[p^*(r)e^{i\omega t}]$ and $u(r, t) = \mathcal{R}[u^*(r)e^{i\omega t}]$. Introducing these expressions in Eq. (1.7), we find:

$$12i\eta\omega r(Z^* + u^*(r)) = \frac{d}{dr} \left[r \left(D + \frac{r^2}{2R} \right)^3 \frac{dp^*(r)}{dr} \right], \quad (1.9)$$

Surface mechanical response

The main goal of the elastohydrodynamic model is to quantify the influence of the surface mechanical response $u(r, t)$ on the mechanical impedance of the system. Because of the lubrication approximation, the viscous shear stresses in the liquid film are negligible with respect to the normal stresses (ratio of order $\sqrt{D/R}$), the latter being approximated by $\sigma_{zz} \approx -p(r, t)$, where z denotes the vertical axis. Therefore, the surface deformation can be found via the mechanical response of the sample to an axisymmetric pressure $p(r, t)$ acting on its surface. Leroy & Charlaix focused on the mechanical

²This assumption is discussed in details in section 1.4.

response of an elastic layer of thickness h_{sub} , and of infinite extent in the xy plane. The substrate is assumed to follow the linear elasticity constitutive law of Eq. (1.2). The stress tensor and displacement fields are denoted $\boldsymbol{\sigma}_{\text{sub}}$ and \mathbf{u}_{sub} respectively. The inertia of the solid is neglected, assuming that the working frequency is small enough such that the stress is instantaneously distributed, with no acoustic wave. The substrate is at mechanical equilibrium such that the stress tensor $\boldsymbol{\sigma}_{\text{sub}}$ follows the Navier stress condition:

$$\nabla \cdot \boldsymbol{\sigma}_{\text{sub}} = \mathbf{0}. \quad (1.10)$$

Furthermore, the substrate is assumed to be rigidly attached at the bottom surface $z = -h_{\text{sub}}$ leading to no displacement, *i.e.* $\mathbf{u}_{\text{sub}}(z = -h_{\text{sub}}) = \mathbf{0}$. The stress continuity at the liquid-solid surface leads to the boundary conditions:

$$\sigma_{\text{sub},zz} = -p(r, t), \quad \sigma_{\text{sub},rz} = 0, \quad \text{at } z = 0. \quad (1.11)$$

Within these assumptions, the normal surface deformation $u(r, t) = -u_{\text{sub},z}(z = 0)$ has been computed analytically in Refs. [62, 63], using the Hankel transform framework and the complex notation, and reads:

$$\hat{u}^*(k) = \frac{2}{\tilde{E}} \frac{X(kh_{\text{sub}})}{k} \hat{p}^*(k), \quad (1.12)$$

where $\tilde{E} = E/(1 - \nu^2)$ is the reduced Young's modulus, X the response function that reads:

$$X(kh_{\text{sub}}) = \frac{\xi (1 - e^{-4kh_{\text{sub}}}) - 4kh_{\text{sub}}e^{-2kh_{\text{sub}}}}{\xi (1 + e^{-4kh_{\text{sub}}}) + (\xi^2 + 1 + 4(kh_{\text{sub}})^2) e^{-2kh_{\text{sub}}}}, \quad \xi = 3 - 4\nu, \quad (1.13)$$

and where the Hankel transforms of zeroth order are defined as:

$$\hat{u}^*(k) = \int_0^\infty u^*(r) J_0(kr) r dr, \quad u^*(r) = \int_0^\infty \hat{u}^*(k) J_0(kr) k dk, \quad (1.14a)$$

$$\hat{p}^*(k) = \int_0^\infty p^*(r) J_0(kr) r dr, \quad p^*(r) = \int_0^\infty \hat{p}^*(k) J_0(kr) k dk, \quad (1.14b)$$

where J_n is the Bessel function of the first kind and of index n . The set of Eqs. (1.9) and (1.12) cannot be solved analytically but it may be written in the form of a Fredholm equation of the second kind for the pressure field in Hankel space, for convenience. We first integrate Eq. (1.9) with respect to r and replace $u^*(r)$ with its Hankel transform:

$$\frac{dp^*(r)}{dr} = \frac{6i\eta\omega Z^* r}{(D + \frac{r^2}{2R})^3} + \frac{24i}{(D + \frac{r^2}{2R})^3} \frac{\eta\omega}{\tilde{E}} \int_0^\infty \frac{X(kh_{\text{sub}})}{k} \hat{p}^*(k) J_1(kr) dk, \quad (1.15)$$

where the identity $\int_0^r J_0(kr') r' dr' = J_1(kr)r/k$ has been used. Finally, introducing the dimensionless variables:

$$x = \frac{r}{\sqrt{2RD}}, \quad q = k\sqrt{2RD}, \quad H_{\text{sub}} = \frac{h_{\text{sub}}}{\sqrt{2RD}}, \quad P^* = \frac{\eta\omega Z^* R}{D^2} p^*, \quad (1.16)$$

$$\hat{P}^* = \frac{2\eta\omega Z^* R^2}{D} \hat{p}^*, \quad D_c = 8R \left(\frac{\eta\omega}{\tilde{E}} \right)^{2/3},$$

and performing the first-order Hankel transform of Eq. (1.15), we obtain:

$$\hat{P}^*(q) = -\frac{3i}{2}qK_1(q) - 3i\left(\frac{D_c}{D}\right)^{3/2} \int_0^\infty \hat{P}^*(q')X(q'H_{\text{sub}})M(q, q') dq' \quad (1.17a)$$

$$M(q, q') = \int_0^\infty \frac{J_1(qx)J_1(q'x)}{qq'(1+x^2)^3} x dx = \begin{cases} \frac{q^2+q'^2}{8qq'}K_1(q)I_1(q') - \frac{1}{4}K_2(q)I_2(q') & \text{if } q > q', \\ \frac{q^2+q'^2}{8qq'}K_1(q')I_1(q) - \frac{1}{4}K_2(q')I_2(q) & \text{if } q < q', \end{cases} \quad (1.17b)$$

where I_j (resp. K_j) is the modified Bessel functions of the first (resp. second) kind and of index j . The typical elasto-hydrodynamic distance is denoted D_c . Lastly, the mechanical impedance can be evaluated by computing the hydrodynamic force applied on the sphere:

$$G^* = -\frac{F^*}{Z^*} = -\frac{1}{Z^*} \int_0^\infty p^*(r) 2\pi r dr = -\frac{4\pi\eta\omega R^2}{D} \hat{P}^*(k=0), \quad (1.18)$$

which can be evaluated numerically by inverting Eq. (1.17). Interestingly, the mechanical response function X of an elastic layer, which is plotted in Fig. 1.3a), exhibits three asymptotic regimes:

- For large substrate thickness, *i.e.* $h_{\text{sub}} \gg \sqrt{2RD}$, the response function does not depend on the substrate thickness and is constant: $X(kh_{\text{sub}}) = 1$. In real space, this leads to the relation:

$$u^*(\mathbf{r}) = \frac{(1-\nu^2)}{E} \int_{\mathbb{R}^2} \frac{p^*(\mathbf{r}')}{|\mathbf{r}' - \mathbf{r}|} d\mathbf{r}' = \frac{4(1-\nu^2)}{E} \int_0^\infty \frac{r'}{r+r'} \mathcal{K}\left(\frac{4rr'}{(r+r')^2}\right) p^*(r') dr', \quad (1.19)$$

where \mathbf{r} is the 2d position vector on the xy plane, with $r = |\mathbf{r}|$, and \mathcal{K} is the complete elliptic integral of the second kind [64]. The second equality may be obtained by integrating over the azimuthal angle [65]. Therefore, the EHD equation Eq. (1.17) simplifies into:

$$\hat{P}^*(q) = -\frac{3i}{2}qK_1(q) - 3i\left(\frac{D_c}{D}\right)^{3/2} \int_0^\infty \hat{P}^*(q')M(q, q') dq'. \quad (1.20)$$

- For thin compressible layers, of Poisson ratio $\nu < 1/2$ and with $h_{\text{sub}} \ll \sqrt{2RD}$, the response function is $X(kh_{\text{sub}}) = kh_{\text{sub}} \frac{1-2\nu}{2(1-\nu)^2}$, leading to the so-called Winkler foundation [66]:

$$u^*(\mathbf{r}) = \frac{h_{\text{sub}}(1-2\nu)(1+\nu)}{E(1-\nu)} p^*(\mathbf{r}), \quad (1.21)$$

which is of the same form as the Hooke's law for a spring. Therefore, the EHD equation Eq. (1.17) simplifies into:

$$\hat{P}^*(q) = -\frac{3i}{2}qK_1(q) - 3i\left(\frac{D_n}{D}\right)^2 \int_0^\infty q' \hat{P}^*(q')M(q, q') dq', \quad (1.22)$$

$$D_n = \left(\frac{8\eta\omega R h_{\text{sub}}(1-2\nu)(1+\nu)}{E(1-\nu)}\right)^{1/2},$$

where D_n is the relevant elastohydrodynamic distance scale in this limit.

- For thin incompressible layers, of Poisson ratio $\nu = 1/2$ and with $h_{\text{sub}} \ll \sqrt{2RD}$, the response function is $X(kh_{\text{sub}}) = 2/3(kh_{\text{sub}})^3$ which leads to:

$$u^*(\mathbf{r}) = -\frac{4h_{\text{sub}}^3}{3E} \nabla_{2d}^2 p^*(\mathbf{r}), \quad (1.23)$$

where ∇_{2d}^2 is the Laplacian operator on the xy plane. Here, the EHD equation Eq. (1.17) simplifies into:

$$\hat{P}^*(q) = -\frac{3i}{2} q K_1(q) - 3i \left(\frac{D_s}{D} \right)^3 \int_0^\infty q'^3 \hat{P}^*(q') M(q, q') dq', \quad D_s = h_{\text{sub}} \left(\frac{4\eta\omega}{E} \right)^{1/3} \quad (1.24)$$

where D_s is the relevant elastohydrodynamic distance scale in this regime.

Experimental results

In Figs. 1.3b-d), we show experimental results, published in Ref. [36], of the EHD mechanical impedance $G^* = G' + iG''$, measured using a dynamic surface force apparatus versus the sphere-plan distance. It illustrates the three regimes of EHD discussed previously. The sampled surfaces are: a layer of polydimethylsiloxane (PDMS) elastomer of thickness $h_{\text{sub}} = 1$ mm (resp. $4.4 \mu\text{m}$) in Fig. 1.3b) (resp. Fig. 1.3c)) and a textured hydrophobic surface covered with microbubbles in Fig. 1.3d). In each panel is plotted the corresponding asymptotic EHD model: semi-infinite (see Eq. (1.20)) in b), thin-incompressible (see Eq. (1.24)) in c) and thin-compressible (see Eq. (1.22)) in d). All EHD models are in good agreement with the experimental data and display the same qualitative features. At large distance, the viscous contribution G'' dominates and follows a D^{-1} scaling law. In this regime, the flow is not large enough for the pressure to significantly deform the substrate and can be approximated by the flow near a rigid surface. Assuming no substrate deformation, the pressure fields can be integrated from Eq. (1.15), and reads:

$$p^*(r) \simeq -\frac{3i\eta Z^* \omega R}{(D + \frac{r^2}{2R})^2}. \quad (1.25)$$

Integrating the latter expression gives an imaginary (*i.e.* damping) part of the mechanical impedance $G'' \simeq 6\pi\eta\omega R^2/D$, in good agreement with the experimental data. Nevertheless, the deformation of the substrate leads to a non-zero real (*i.e.* elastic) component G' of the mechanical impedance, that follows a D^{-n} scaling law, where the exponent n differs in the three regimes of EHD: $-5/2$, -3 , and -4 in the semi-infinite, Winkler and thin-incompressible cases respectively. Interestingly, this difference among the various models allows us to distinguish them and identify the properties of the sampled surface. The existence of this power-law regime can be proven, including the exact prefactor, by performing a perturbative expansion of the pressure field: $p^* = p_0^* + (D_i/D)^\alpha p_1^*$, where i and α should be adapted to the according regime, and p_0^* is the rigid solution

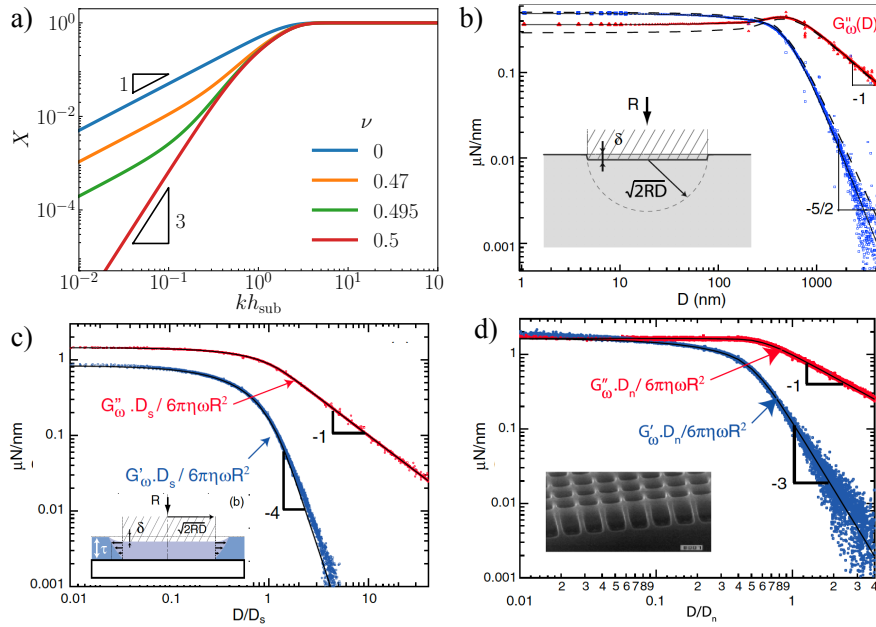


Figure 1.3: a) Response function of an elastic layer of thickness h_{sub} for different Poisson ratios ν (see Eqs. (1.12) and (1.13)) versus dimensionless Hankel variable kh_{sub} in log-log scale. Slope triangles indicate power-law behaviors. b-d) Mechanical impedance G^* (real part in blue and imaginary part in red) versus sphere-plan distance D measured in dynamic surface force apparatus experiments with a PDMS slab as a sample in b)-c) and a textured hydrophobic surface covered with microbubbles in d). In b) the PDMS thickness is 1 mm and larger than the hydrodynamic radius $\sqrt{2RD}$ in most of the distance range of the experiment. The model which accounts for finite thickness is displayed in black solid lines and the semi-infinite model (see Eq. (1.20)) is shown in dashed lines. In c) the PDMS thickness is $h_{\text{sub}} = 4.4 \mu\text{m}$, and smaller than the hydrodynamic radius on most of the distance range of the experiment. The distance in the x -axis is rescaled by an elasto-hydrodynamic distance $D_s = h_{\text{sub}}(4\eta\omega/E)$ and the solid lines display the model with the thin-incompressible response of Eq. (1.22). d) The surface mechanical response is well described by a Winkler model Eq. (1.22), see shown in solid lines. The panels b)-d) are adapted from Ref. [36].

of Eq. (1.25) (see [60]). At small distance, both G' and G'' saturate to constant values that are independent of the sphere-plan distance. As the distance decreases, the magnitude of the pressure field increases (see Eq. (1.25)), and so does the surface deformation. However, the surface deformation cannot exceed the oscillation amplitude of the spherical probe, which leads to the saturation of G^* at small distance. In this near-contact regime, the sample deformation accommodates the sphere motion, and the liquid is no longer expelled from the gap for radii smaller than $r < \sqrt{2RD_c}$, and viscous flows only occur outside this region. Here again, the precise value of the saturation mechanical

impedance at small distance directly depends on the substrate response, and the ratio between its real and imaginary part is different for each case of the EHD model, allowing one to distinguish between the models. There is no analytic prediction for the saturation mechanical impedance but it can be evaluated numerically.

The rest of the chapter is organized as follows: In section 1.2, we revisit the linear EHD model presented here for substrates with a linear *viscoelastic* response in subsection 1.2.1, to *poroelastic* response in subsection 1.2.3 and an *elastocapillary* response in subsection 1.2.4. Experimental results with a very soft PDMS surface are shown and compared to the viscoelastic model. Then in section 1.3, we derive an EHD model for the response of a bubble deposited on a surface and the model is compared to experimental data. Lastly, the influence of fluid inertia via the unsteady-term of the Navier-Stokes equation is discussed in section 1.4.

1.2 Characterization of the complex properties of the solid

As mentioned in the introduction, soft solids often exhibit a complex mechanical response beyond linear elasticity. Here, we revisit the EHD models for several classical types of soft mechanical response.

1.2.1 Viscoelastic substrate

The mechanical response of viscoelastic solids is characterized with a response function (see Eq. (1.3) in the introduction). In particular, the mechanical response of a viscoelastic material to an applied pressure field is characterized by both elastic and viscous parts. Contactless experiments, using long-needle probe and AFM in frequency modulation mode, have been introduced in the group of Penger Tong to measure the viscoelastic properties of thin polymer films [54] and allow one to perform a mapping of the viscoelastic properties of living cells [55]. Here, we assume that the substrate is an incompressible (Poisson ratio $\nu = 1/2$) linear viscoelastic material, for which the stress reads:

$$\sigma_{i,j}(\mathbf{x}, t) = \int_{-\infty}^t \Psi(t - t') \dot{\epsilon}_{i,j}(\mathbf{x}, t') dt' - p(\mathbf{x}, t) \delta_{i,j}, \quad (1.26)$$

where $\Psi(t)$ is the shear relaxation function, $\delta_{i,j}$ the Kronecker symbol and p is the pressure field, *i.e.* the isotropic part of the stress tensor. Using the complex notation introduced in the previous section, we get:

$$\sigma_{i,j}^*(\mathbf{x}) = \mu^*(\omega) \epsilon_{i,j}^*(\mathbf{x}) - p^*(\mathbf{x}) \delta_{i,j}, \quad (1.27)$$

where $\mu^*(\omega)$ is the complex shear modulus, that is related to the shear relaxation function via:

$$\mu^*(\omega) = i\omega \int_0^{\infty} \Psi(t) e^{-i\omega t} dt = \mu'(\omega) + i\mu''(\omega). \quad (1.28)$$

For an incompressible material, the complex shear modulus is related to the complex Young's modulus via $E^* = 3\mu^* = E' + iE''$ that is used in what follows. The real

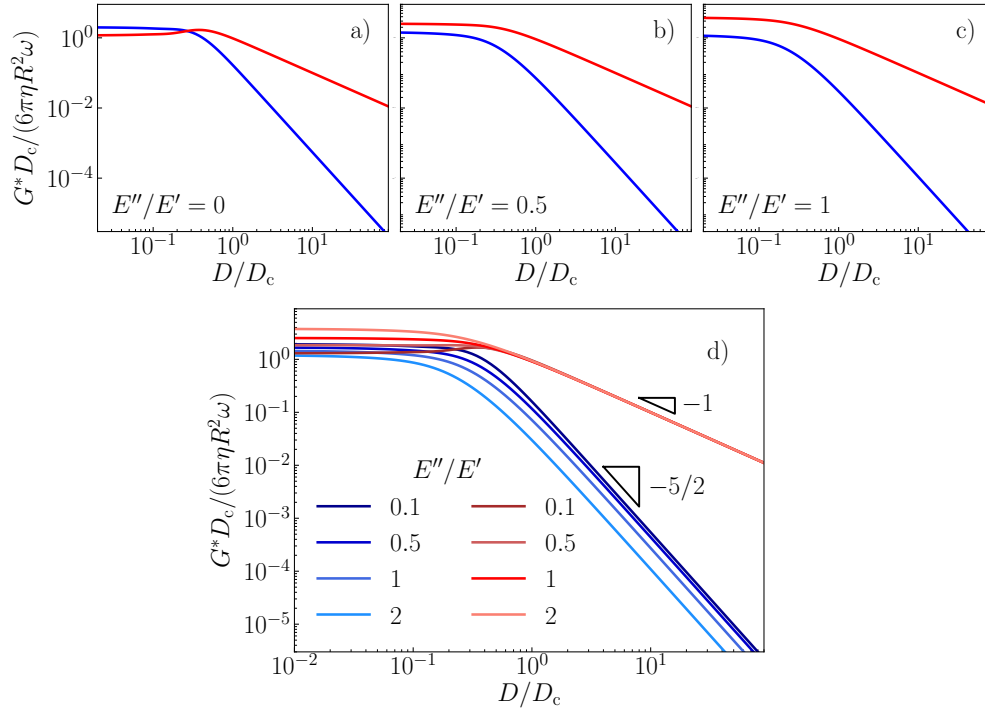


Figure 1.4: **Viscoelasticity.** Dimensionless mechanical impedance versus the dimensionless sphere-plan distance for a semi-infinite viscoelastic substrate. The real (resp. imaginary) part of the mechanical impedance is plotted in blue (resp. red). The ratio between the imaginary and real parts of the complex modulus is 0 (elastic substrate) in panel a) and 0.5 (resp. 1) in b) (resp. c)). In panel d) the dimensionless mechanical impedance for various loss moduli are superimposed.

and imaginary parts are often called *storage* and *loss* moduli respectively. With the complex notation, the constitutive law of a viscoelastic substrate is equivalent to the one of a linear homogeneous incompressible substrate. Therefore, we can directly use the results from section 1.1.4 and write the surface deformation of the substrate by replacing the Young's modulus by its complex version. This leads to:

$$\hat{u}^*(k) = \frac{2}{\tilde{E}^*} \frac{X(kh_{\text{sub}})}{k} \hat{p}^*(k). \quad (1.29)$$

where $\tilde{E}^* = \frac{4}{3}E^*$ is the complex reduced modulus for an incompressible material. Following section 1.1.4, the governing equation for the pressure field in Hankel space is:

$$\hat{P}^*(q) = -\frac{3i}{2}qK_1(q) - 3i\left(\frac{D_c}{D}\right)^{3/2} \frac{1-iB}{1+B^2} \int_0^\infty \hat{P}^*(q')X(q'H_{\text{sub}})M(q, q') dq', \quad (1.30)$$

where $B = E''/E'$ is the dimensionless ratio of imaginary to real parts of the complex modulus. The critical distance is written here as $D_c = 8R \left(3\eta\omega/(4E') \right)^{2/3}$ and involves the storage modulus only. As such, the viscoelasticity is entirely parametrized by the term in B . At the end, the mechanical impedance takes the form:

$$G^*(D) = \frac{6\pi\eta R^2\omega}{D_c} \mathcal{G}^* \left(\frac{D}{D_c}, B \right), \quad \mathcal{G}^* \left(\frac{D}{D_c}, B \right) = -\frac{4D_c}{6D} \hat{P}^*(q=0), \quad (1.31)$$

where \mathcal{G}^* is the dimensionless mechanical impedance.

In Fig. 1.4 is plotted the dimensionless mechanical impedance versus the dimensionless distance. The substrate thickness is assumed to be large with respect to the hydrodynamic radius $\sqrt{2RD}$ such that we use the semi-infinite limit $X(q'H_{\text{sub}}) = 1$. In Fig. 1.4a-c) is plotted the mechanical impedance as a function of the distance for three ratios of loss to storage moduli, respectively $E''/E' = 0, 0.5$ and 1 . We observe that the real part of the mechanical impedance decreases with increasing B while the imaginary part increases. The substrate gets effectively stiffer and the dissipation increases. In Fig. 1.4d), the mechanical impedances are superimposed on the same plot for various E''/E' . The asymptotic power-law decay at large distance is not affected by viscoelasticity. The real (resp. imaginary) part decays with a power law $D^{-5/2}$ (resp. D^{-1}). Interestingly, the prefactor of the power-law decay of the real part decreases with B as the substrate becomes effectively stiffer and reads:

$$G^* \simeq \frac{81\pi^3}{32\sqrt{2}} \frac{\eta^2\omega^2 R^{7/2}}{D^{5/2}} \frac{E'}{E'^2 + E''^2} + i \frac{6\pi\eta\omega R^2}{D}, \quad (1.32)$$

for $D_c/D \ll 1$, which is obtained following [60]. Furthermore, we observe that the limit of the mechanical impedance at small distance depends largely on the ratio E''/E' and may allow for a precise determination of the viscoelastic properties when comparing the model with experimental data. In particular, for the numerical integration, we find:

$$\begin{cases} G' \approx \frac{6\pi\eta R^2\omega}{D_c} \left(2.01 - 0.77 \frac{E''}{E'} \right) \\ G'' \approx \frac{6\pi\eta R^2\omega}{D_c} \left(1.16 + 1.34 \frac{E''}{E'} \right) \end{cases} \quad (1.33)$$

for $D_c/D \gg 1$ and $E''/E' < 1$.

1.2.2 Viscoelastic measurements of PDMS layer

Setup

In the experiments, the AFM setup described in section 1.1.3 is used. The studied samples are PDMS substrates prepared as follows. First, uncrosslinked PDMS (Sylgard 184, Dow Corning) and a curing agent are mixed with a weight ratio of 71:1. Following a degassing process in vacuum, a droplet of the mixture is spin-coated on a cover slide with a size of $24 \times 24 \text{ mm}^2$ for a minute, in order to get a sample of thickness

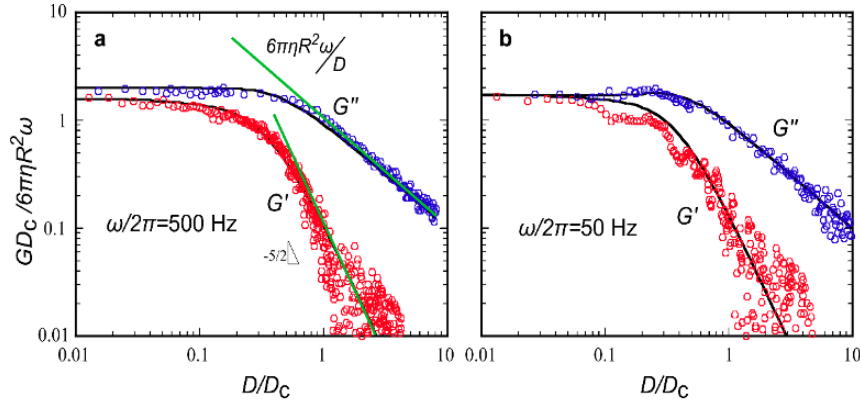


Figure 1.5: Normalized real and imaginary parts of the mechanical impedance as functions of normalized distance for two oscillation frequencies, respectively 500 and 50 Hz in a) and b). The solid lines are fitting curves using Eq. (1.31). In a), the extracted free parameters are the storage and loss moduli, $E' = 3.2 \pm 0.5$ kPa and $E'' = 2.0 \pm 0.2$ kPa respectively. b) Results for an oscillation frequency of 50 Hz. The extracted moduli are $E' = 1.6 \pm 0.4$ kPa and $E'' = 0.69 \pm 0.10$ kPa.

$h_{\text{sub}} = 26 \pm 3$ μm . The sample is then annealed in an oven at 50°C and for 24h, to promote an efficient cross-linking. Using the method described in section 1.1.3, the mechanical impedance G^* of the system is measured through Eq. (1.6). The oscillation frequency of the cantilever is varied in the experiments, ranging from 25 to 1500 Hz, which allows to measure the frequency-dependent rheology of PDMS.

Contactless measurements

Fig. 1.5 shows the dimensionless mechanical impedance $G^* D_c / (6\pi\eta R^2 \omega)$ as a function of the dimensionless distance D/D_c for two frequencies. In Fig. 1.5a, the oscillation frequency is set to $\omega/(2\pi) = 500$ Hz. The solid black lines correspond to Eq. (1.31), where the values of the storage modulus $E' = 3.2 \pm 0.3$ kPa and loss modulus $E'' = 2.1 \pm 0.2$ kPa are the fit parameters. Fig. 1.5b shows the results for the frequency $\omega/(2\pi) = 50$ Hz. Similarly, we obtain the values of the storage modulus $E' = 1.6 \pm 0.2$ kPa and loss modulus $E'' = 0.6 \pm 0.1$ kPa. The semi-infinite model is found to be in good agreement with the experimental data over the full range of distance. In particular, the different limiting behaviors, found in section 1.2.1 at large and small distance (respectively Eqs. (1.32) and (1.33)), are recovered.

The extracted storage modulus E' and loss modulus E'' for various oscillation frequencies are shown in Fig. 1.6. Both moduli increase as the frequency increases. In our experiment, the PDMS sample is a soft elastomer, and the frequency dependence of its complex Young's modulus can be modeled by the Chasset–Thirion law [67, 68, 69]:

$$E^*(\omega) = E'(\omega) + iE''(\omega) = E_0 (1 + (j\omega\tau)^n) \quad (1.34)$$

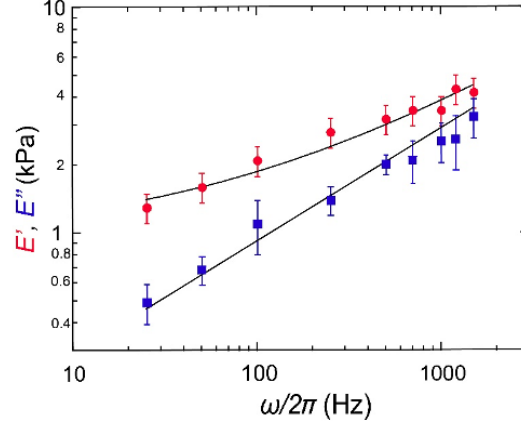


Figure 1.6: Storage modulus E' (red) and loss modulus E'' (blue) obtained from the fit in Fig. 1.5 as functions of the oscillation frequency. The solid lines are fits from Eq.(1.34) from which we get the free parameters: $E_0 = 1.0 \pm 0.1$ kPa, $n = 0.50 \pm 0.02$ and $\tau = 3.0 \pm 0.2$ ms.

where E_0 indicates the static ($\omega = 0$) Young's modulus, τ is the relaxation time and n is an exponent, which all depend on the sample preparation (i.e. curing procedure, stoichiometric ratio between the PDMS and curing agent). The empirical exponent n typically takes values between $1/2$ and $2/3$ [70]. In Fig. 1.6, the solid lines are the fitting curves from Eq. (1.34) for both the storage and loss moduli, from which we obtain the free parameters: $E_0 = 1.0 \pm 0.1$ kPa, $n = 0.50 \pm 0.02$ and $\tau = 3 \pm 0.2$ ms. The obtained relaxation time is close to the value obtained from the Kelvin-Voigt model: $\eta_s/E_0 \approx 2-3$ ms, where $\eta_s \approx 2-3$ Pa.s is the dynamic viscosity of the PDMS.

Indentation experiments

In order to check the validity of the method above for robust rheological characterization of soft materials, we have also performed an indentation experiment with the AFM. The measured DC component of the cantilever's deflection versus the piezo displacement allows us to construct the force-indentation curve. The static force F is obtained by multiplying the DC component of the deflection by the spring constant k_c of the cantilever. The indentation depth δ is obtained by subtracting the cantilever's deflection from the piezo displacement. The contact origin ($\delta = 0$) is defined as the position where the deflection increases sharply. To minimize the contributions of adhesion and elastocapillary effects [71], which are important at small indentations for such soft samples, we performed the analysis only: i) in advancing mode (i.e. increasing indentation), as it is standard to avoid adhesive contributions in JKR (Johnson Kendall Roberts) tests [71]; and ii) in the regime of large indentation depth, in order to maximize the ratio between the contact radius $\sqrt{R\delta}$ and the elastocapillary length γ/E_0 , where $\gamma \approx 3$ mN/m is the substrate-liquid surface tension. However, since for large

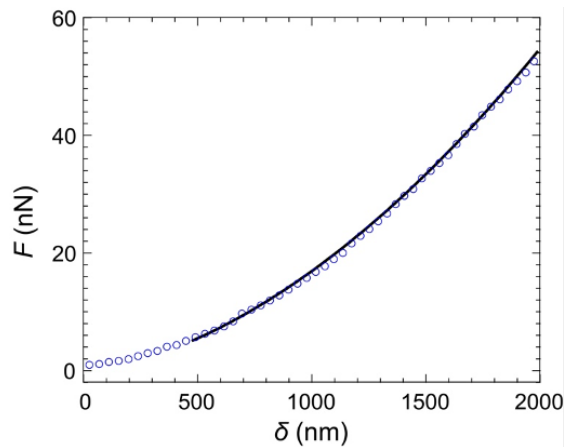


Figure 1.7: Indentation experiments. Measured static force F versus indentation depth δ . The solid line shows the best fit to Eq.(1.35) for the large- δ range, from which we obtain the static Young's modulus $E_0 = 0.9 \pm 0.1$ kPa.

indentation depths the value of the contact radius becomes comparable to the thickness h_{sub} of the soft substrate, the traditional Hertz model for elastic indentation must incorporate finite-size corrections [72]:

$$F = \frac{16}{9} E_0 R^{1/2} \delta^{3/2} \left(1 + 0.884\chi + 0.781\chi^2 + 0.386\chi^3 + 0.0046\chi^4 \right) \quad (1.35)$$

where $\chi = \sqrt{R\delta}/h_{\text{sub}}$. Fig. 1.7 shows the measured force F as a function of the indentation depth δ . The solid line represents the best fit from Eq.(1.35), for a range of indentation depths between 0.5 and 2 microns. From the fit, we obtain the static Young's modulus $E_0 = 0.9 \pm 0.1$ kPa as a single free parameter. This value is very close to the value previously obtained from the contactless method, thus showing the robustness of the latter.

We stress that the model used in Fig. 1.5 assumes an infinite thickness of the PDMS sample, which is not strictly valid here. As a matter of fact, using the response function Eq. (1.13) of finite-size layer, we obtain slightly different fitting elastic moduli (not shown here). Additional experiments, varying systematically the sample thickness, would be necessary to validate further the results presented here.

1.2.3 Poroelasticity

The work presented in this subsection has been done in close collaboration with Caroline Kopecz-Muller during her master internship that I co-supervised with Joshua McGraw and Thomas Salez, and followed during her PhD.

Context

Soft gels are widely spread in biology (tissues, bones, cartilages, ...). Synthetic gels (*e.g.* hydrogels) have a large range of applications in biology (cell culture, ...), medicine (tissue engineering, contact lenses, ...), lab-on-a-chip design (*e.g.* stimuli-responsive hydrogels to control microfluidic-channel widths *in situ*). They are made of an elastic network of cross-linked polymers swollen by a solvent. Interestingly, the mechanical response of gels implies several mechanisms at the microscopic level. First, the polymer network has a certain rigidity, leading to elastic properties. In synthetic hydrogels, the cross-link density may be varied which yields a large range of Young's moduli from 10 Pa to 1 MPa. In addition, the polymer network may exhibit some viscoelastic properties, as discussed in the previous section. Furthermore, the network is a porous medium and the solvent may flow inside, leading to an extra source of dissipation. The interplay between porous flow and matrix elasticity is usually called *poroelasticity*. One challenge is to model such complex mechanical responses [73] and to separate the different mechanisms of dissipation in hydrogels to understand their mechanical behavior [74, 75]. Several methods using indentation tests and contact mechanics have been introduced to measure the poroelasticity of gels [76, 77, 78, 79]. The question we address in this section is whether contactless EHD experiments may help to measure the poroelasticity of gels.

Poroelastic models, that combine Darcy law for porous media and Hooke law of elasticity, have first been introduced by Maurice Biot in the 1940s in order to describe soil consolidation [80], and wave propagation in porous media [81]. Such models are also suitable to describe the mechanics of tissues, bones and soft gels.

Model

Here, we follow the paper from Zhao *et al.* [82] to compute the deformation of a poroelastic layer due to an applied oscillating pressure fields. In contactless methods, the magnitude of the stress applied to the substrate is low as it results from a nanometric oscillation of the probe. Therefore we focus on the linear response. The poroelastic substrate is characterized by a displacement field \mathbf{u}_{poro} of the polymer network, a solvent concentration c and a chemical potential μ_c . The reference state is set with a given concentration c_0 of solvent with a chemical potential $\mu_{c,0}$ under no displacement. Out of equilibrium, the solvent concentration follows the conservation law:

$$\partial_t c + \nabla \cdot \mathbf{j} = 0, \quad (1.36)$$

where \mathbf{j} denotes the flux of solvent, assumed to follow the Darcy law:

$$\mathbf{j} = - \left(\frac{k_p}{\eta_s \Omega^2} \right) \nabla \mu_c, \quad (1.37)$$

where k_p denotes the permeability, η_s the solvent viscosity and Ω the molar volume of the solvent. The stress tensor $\boldsymbol{\sigma}_{\text{poro}}$ is related to the poroelastic strain tensor $\boldsymbol{\epsilon}_{\text{poro}}$ via

the poroelastic law:

$$\boldsymbol{\sigma}_{\text{poro}} = \frac{E}{1 + \nu} \left(\boldsymbol{\epsilon}_{\text{poro}} + \frac{\nu}{1 - 2\nu} \text{Tr}[\boldsymbol{\epsilon}_{\text{poro}}] \mathbf{I} \right) - \frac{\mu_c - \mu_{c,0}}{\Omega} \mathbf{I}, \quad (1.38)$$

where $\text{Tr}[\cdot]$ denotes the trace of the tensor. The solvent and polymer network are assumed to be incompressible such that the local volume variation within the network is equal to the local variation of the solvent concentration, which gives:

$$\text{Tr}[\boldsymbol{\epsilon}_{\text{poro}}] = (c - c_0)\Omega. \quad (1.39)$$

The mechanical equilibrium within the poroelastic substrate gives the Navier condition $\nabla \cdot \boldsymbol{\sigma}_{\text{poro}} = \mathbf{0}$. After combining all these equations, the solvent concentration follows a diffusive-like law:

$$\partial_t c = \mathcal{D}^* \nabla^2 c = 0, \quad \mathcal{D}^* = \frac{(1 - \nu)Ek_p}{(1 + \nu)(1 - 2\nu)\eta_s} \quad (1.40)$$

where \mathcal{D}^* is an effective diffusion constant. Assuming that the initial solvent concentration is homogeneous, the displacement fields follows:

$$\frac{E\Omega}{2(1 + \nu)} \left(\nabla^2 \mathbf{u}_{\text{poro}} + \frac{\Omega}{1 - 2\nu} \nabla c \right) = \nabla \mu_c. \quad (1.41)$$

We assume that the poroelastic surface at $z = 0$ is subjected to an applied axisymmetric and oscillating normal stress, $\sigma_{zz}^*(r, z = 0, t) = -p^*(r)$, where the complex notation is used. For the sake on simplicity, we take a semi-infinite substrate and assume that it is impermeable, $\mathbf{J} \cdot \mathbf{n} = 0$ at $z = 0$, where \mathbf{n} denotes the normal vector to the poroelastic surface, which means $\partial_z \mu_c = 0$ at $z = 0$. Following the derivation in Ref. [82], the deformation of the poroelastic surface reads:

$$\hat{u}^*(k) = \frac{1 + \nu}{Ek} \left[1 + \frac{1 - 2\nu}{1 - \nu} \frac{k^2 \mathcal{D}^*}{i\omega} \left(\frac{1}{\sqrt{1 + \frac{i\omega}{k^2 \mathcal{D}^*}}} - 1 \right) \right]^{-1} \hat{p}^*(k). \quad (1.42)$$

Using the dimensionless scales introduced before, we find:

$$\frac{\hat{u}^*(q)}{Z^*} = \frac{1}{16(1 - \nu)} \left(\frac{D_c}{D} \right)^{3/2} \frac{1}{q} \left[1 + \frac{1 - 2\nu}{1 - \nu} \frac{q^2 \omega_c}{i\omega} \frac{D}{D_c} \left(\frac{1}{\sqrt{1 + \frac{i\omega}{q^2 \omega_c} \frac{D}{D_c}}} - 1 \right) \right]^{-1} \hat{P}^*(q). \quad (1.43)$$

where $\omega_c = \mathcal{D}^*/(2RD_c)$ is a critical pulsation. Introducing this relation in the linear-response theory in section 1.1.4, we can compute the mechanical impedance. In Fig. 1.8, we display the poroelastic mechanical impedance, varying the permeability of the substrate through the ratio ω/ω_c between the pulsation and the critical pulsation. Here, the Poisson ratio is fixed to $\nu = 0.3$. All the curves are almost superimposed while the pulsation ratio is varied over 4 orders of magnitude. In the right panel, we display a zoom at large distance of the real part of the mechanical impedance. In addition, the

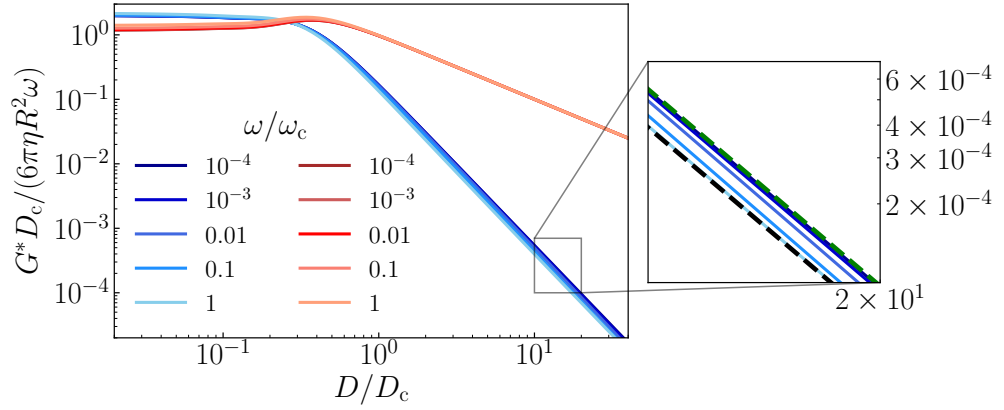


Figure 1.8: **Poroelasticity.** Dimensionless mechanical impedance versus dimensionless sphere-plan distance for a semi-infinite poroelastic substrate. The real (resp. imaginary) part of the mechanical impedance is plotted in blue (resp. red). Here, the substrate is assumed to be impermeable and of Poisson ratio $\nu = 0.3$. The inset shows a zoom. The asymptotic law for an incompressible (resp. compressible) semi-infinite elastic substrate of shear modulus $E/(2(1 + \nu))$ is displayed in dashed black (resp. dashed green).

large-distance asymptotic scaling law for G' , in the case of a semi-infinite incompressible elastic substrate of shear modulus $E/(2(1 + \nu))$, is found to be in good agreement with the mechanical response of poroelastic substrates at large frequency. Similarly, the large-distance asymptotic scaling law G' for an elastic material (Eq. (1.19)) is plotted in green dashed lines and is in good agreement with the low-frequency response of poroelastic substrates. Indeed, taking the limit of the poroelastic response at small and large frequencies, leads to:

$$u^*(k) = \begin{cases} \frac{1+\nu}{Ek} \hat{p}^*(k), & \text{if } \omega \rightarrow \infty, \\ \frac{1+\nu}{Ek} \frac{1}{1-\frac{1}{2}\frac{1-2\nu}{1-\nu}} \hat{p}^*(k) = \frac{2(1-\nu^2)}{Ek} \hat{p}^*(k), & \text{if } \omega \rightarrow 0. \end{cases} \quad (1.44)$$

We recover that the substrate deformation takes the same form as the one for semi-infinite elastic substrates with a rescaled elastic modulus in both limits [83]. At large frequency, the solvent has no time to migrate and the substrate deforms as an incompressible solid. However, at long times, the stress has relaxed and the substrate deforms as a compressible solid with no influence of the solvent.

Lastly, we note that we have done a similar study, assuming a permeable poroelastic substrate, meaning the equality of the chemical potentials in the liquid and poroelastic media, at the surface (*i.e.* $\mu_c(z = 0) = \mu_{c,0}$). This case is relevant if the gel is submerged in its own solvent. Then, the mechanical impedance shows the exact same features (not shown) as above, meaning that the affinity of the outer liquid with the gels does not change drastically the mechanical response.

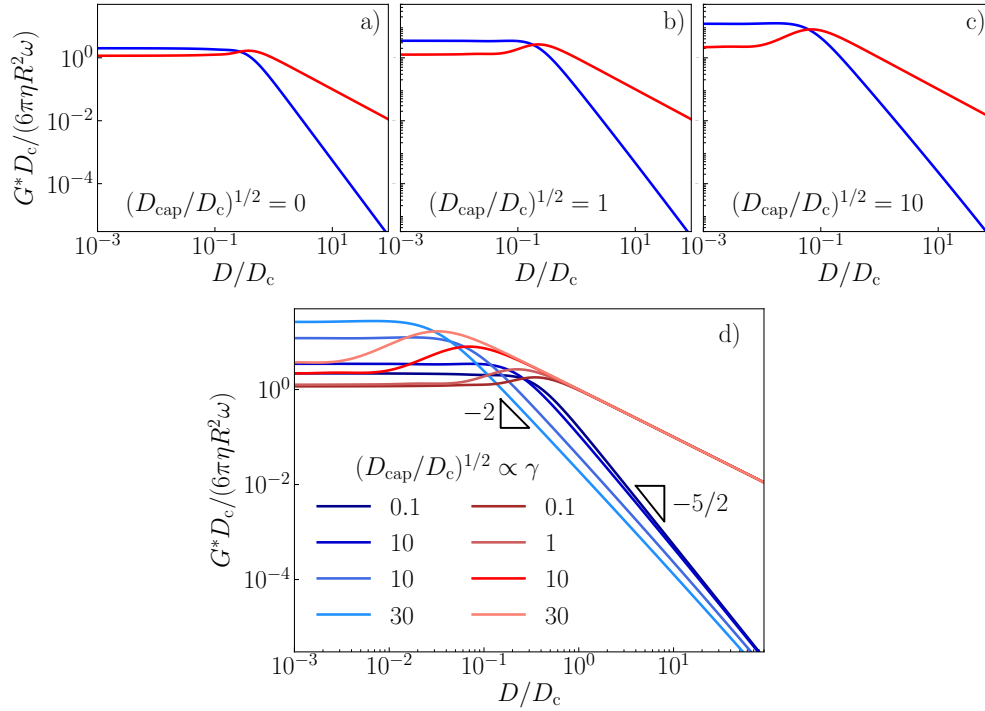


Figure 1.9: **Capillarity**. Dimensionless mechanical impedance versus dimensionless sphere-plan distance for a semi-infinite elastic substrate with a surface tension γ . The real (resp. imaginary) part of the mechanical impedance is plotted in blue (resp. red).

1.2.4 Capillarity of soft solids

As briefly mentioned in the introduction, capillarity is not a concept restricted to fluid-fluid interfaces, as solid-fluid interfaces also have an intrinsic interfacial energy. Capillarity generates surface stresses that lead to surface deformations for soft solids. The competition between elasticity and capillarity, called *elastocapilarity*, has been largely investigated in the last decade [13, 84, 85, 86]. For example, solid capillarity tends to smoothen out interfaces with high curvatures, as observed in the topography of soft gels fabricated in molds with rectangular patterns [14]. It may also trigger mechanical instabilities. One example is soft cylindrical gels that deform and adopt a complex undulated shape to reduce their surface [15, 87]. This process is very similar to the Rayleigh-Plateau instability. Additionally, a lot of interest has been devoted to the wetting properties of droplets on soft solids. Significant departure from the classical Young-Dupré law has been observed for small droplets, because surface stresses deform the solid and create a wetting ridge [88, 89].

Interestingly, a fundamental difference between solid and fluid capillarities is that the surface stress of soft solids depends on the strain via the Shuttleworth equation: $\Upsilon = \gamma + \frac{d\gamma}{d\varepsilon}$, where Υ is the surface stress [90]. Recently, several groups have tried to

measure this dependence in stretched elastomers and gels, through the wetting properties [91, 92, 93]. The absolute determination of the surface tension of stretched gels is challenging and the goal of this subsection is to investigate whether contactless method may help to achieve this task. Therefore, we compute the mechanical impedance of an EHD contact involving an elastic substrate including capillarity. To account for the capillarity of soft solids, we need to modify the stress boundary condition at the substrate surface and include the surface tension, as:

$$\boldsymbol{\sigma} \cdot \mathbf{n} = \mathbf{f} + \gamma_s \kappa \mathbf{n}, \quad (1.45)$$

where \mathbf{f} is the force distribution that is applied on the substrate, equal to the hydrodynamic stress, γ_s denotes the solid-liquid surface tension and κ the interface curvature. We further assume a linear deformation of the surface, small slopes, *i.e.* $|\nabla_{2d} u| \ll 1$, and that the dominant hydrodynamic stress is the pressure term (see section 1.1.4). Then, the stress boundary condition becomes

$$\sigma_{zz} = -p + \gamma \nabla_{2d}^2 u. \quad (1.46)$$

Here again, for the sake of simplicity, we restrict ourselves to the case of a semi-infinite material. The substrate deformation can be computed following section 1.1.4 and reads:

$$\hat{u}^* = \frac{2}{\tilde{E}k + 2\gamma_s k^2} \hat{p}^*. \quad (1.47)$$

Injecting this relation in the Eq. (1.9), we find that the pressure fields in Hankel space follows, once again, a Fredholm equation of the second kind:

$$\hat{P}^*(q) = -\frac{3i}{2} q K_1(q) - 3i \left(\frac{D_c}{D} \right)^{3/2} \frac{1}{1 + q \sqrt{D_{\text{cap}}/D}} \int_0^\infty \hat{P}^*(q') M(q, q') dq', \quad (1.48)$$

$$D_{\text{cap}} = \frac{2\gamma^2}{\tilde{E}^2 R},$$

where D_{cap} is a distance scale emerging from the model. The mechanical impedance can then be computed numerically through the inversion of Eq. (1.48). In Fig. 1.4, we plot the dimensionless mechanical impedance versus the distance ratio D/D_c , varying the surface tension to Young's modulus ratio by changing D_{cap}/D_c . In Fig. 1.4 d), we superimpose the impedances for several D_{cap}/D_c . At large distance, the real part of the mechanical impedance decreases with increasing surface tension, as if the surface gets effectively stiffer. Interestingly, for $D_{\text{cap}}/D_c \gg 1$, G' follows a D^{-2} scaling law, which differs from the elastic one, *i.e.* $D^{-5/2}$. The latter is preserved at vanishing surface tension. At small distance, the mechanical impedance increases, both for its real and imaginary parts. However, the ratio between real to imaginary parts increases with γ . Interestingly, the cross-over distance between the two regimes seems to decrease with increasing capillarity.

1.3 Viscocapillary response of a model liquid-air interface

The results presented in this section come from a collaborative work with Zaicheng Zhang and Abdelhamid Maali in the LOMA laboratory at the University of Bordeaux. All the experiments have been performed by Zaicheng Zhang.

1.3.1 Introduction

Surface active molecules – *i.e.* surfactants – are widely used to stabilize capillary interfaces on purpose, *e.g.* in emulsions or foams, but are also inevitable due to pollution. These contaminants, which are usually adsorbed at the interface between two immiscible fluids, lower the surface tension and are responsible for specific interfacial rheological properties of the interface [94]. To understand the dynamics of soft materials, the interaction between objects such as droplets and bubbles, or to quantify the amount of interfacial contamination, capillary interfacial rheology is essential. The interfacial rheology is usually measured with the Langmuir trough [95, 96, 97], oscillating-disk devices [98, 99], particle tracking techniques [100, 101, 102, 103], oscillating pendant drop [104, 105, 106, 107] or through the measurement of capillary waves [108, 109, 110, 111, 112].

The air-water interface is suitable to test EHD-like couplings, since the interface deformation has an elastic-like capillary restoring response. The interface deformation is described in the framework of the Young-Laplace equation (see Eq. (1.4)) that couples the hydrodynamic pressure and the capillary deformation of the interface. Importantly, the EHD coupling at the air-water interface has a long-range lateral extent due to the structure of the Young-Laplace equation. For large enough systems, the millimetric capillary length $\sqrt{\gamma/(\rho g)}$ characterizes the lateral extent of the capillary deformation. However, for systems with lateral extents narrower than the capillary length, the deformation depends strongly on the system size [52]. Therefore, in the case of air bubbles in water, we expect the bubble stiffness defined as the ratio between the hydrodynamic force and bubble deformation to depend not only on the surface tension but also on the bubble size.

1.3.2 Experimental setup

In the experiments, the AFM setup described in section 1.1.3 is used. The soft surface is a microbubble as schematized in Fig 1.10. Air microbubbles are deposited onto spin-coated polystyrene layers, within SDS solutions in water. The SDS concentrations C are in the 0.2 – 40 mM range. As measured with an optical microscope, the bubble radii R_b are in the 0.2 – 0.6 mm range, and the contact angles θ (see definition in Fig. 1.10) are in the 40 – 90° range, with the exact value depending on C .

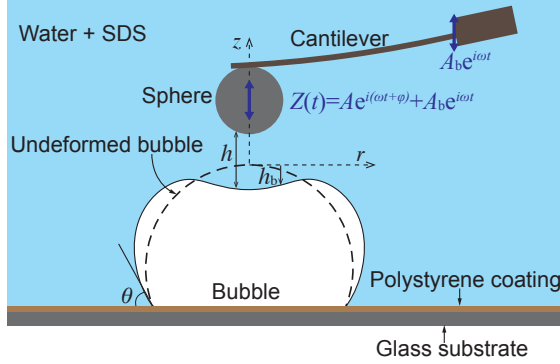


Figure 1.10: A glass sphere attached to an AFM cantilever is driven to oscillate vertically near an air bubble deposited on a polystyrene surface in a SDS solution at a frequency of $\omega/(2\pi)$. θ is the contact angle of the SDS solution on polystyrene in air. The vertical displacement of the sphere $Z(t) = A_s e^{i(\omega t + \varphi)} + A_b e^{i\omega t}$ includes the cantilever deflection $A_s e^{i(\omega t + \varphi)}$ and the base displacement $A_b e^{i\omega t}$. The motion results in an axisymmetric liquid-gap thickness profile $h(r, t)$ depending on the radial distance r and time t , that includes an axisymmetric vertical profile h_b of the deformed bubble surface.

1.3.3 Model

We consider the axisymmetric system composed of the rigid sphere located at an average distance D from the apex of the undeformed air bubble (see Fig. 1.10). In this subsection, the sphere radius is denoted with a subscript “s” to distinguish it from the bubble curvature radius, defined with a subscript “b”. Here, the undeformed surface is not flat, such that we define the effective curvature radius R_{eff} of the lubricated contact from: $R_{\text{eff}}^{-1} = R_s^{-1} + R_b^{-1}$. The experiments are done at low enough frequencies so that we can assume a no-slip boundary condition at the air-water interface [113]. Therefore, the liquid-gap thickness, denoted $h(r, t)$, obeys the Reynolds equation (1.7) as in section 1.1.4. The liquid-gap thickness is modified with respect to :

$$h(r, t) = h_s(r, t) - h_b(r, t) \simeq D + Z(t) + r^2/(2R_s) - h_b(r, t) \quad (1.49)$$

where h_s and h_b are the sphere and bubble surface profile respectively (see Fig. 1.10). The bubble surface profile follows the Young-Laplace equation (see Eq. (1.4)), which is expressed in cylindrical coordinates as:

$$\gamma \kappa = \frac{\gamma}{r} \frac{\partial}{\partial r} \left[r \frac{\frac{\partial h_b}{\partial r}}{\sqrt{1 + \left(\frac{\partial h_b}{\partial r}\right)^2}} \right] = \Delta P(t) + p(r, t), \quad (1.50)$$

where ΔP is the pressure drop across the interface. The Young-Laplace equation can be obtained by minimizing the free energy of the system [47], and the pressure difference ΔP appears as the Lagrange multiplier associated with the volume conservation of

the air bubble in this framework. At equilibrium, the pressure difference is $-2\gamma/R_b$ the bubble's surface profile follows a spherical cap. In the following, we write the pressure difference as $\Delta P(t) = -2\gamma/\bar{R}(t)$, where $\bar{R}(t)$ is the mean curvature radius in the presence of an excess hydrodynamic pressure field. In addition, we consider acute contact angles θ , as is the case for an air bubble deposited onto a PS substrate within water. Therefore, the bubble's surface profile $h_b(r, t)$ is a multivalued function of r , and Eq. (1.50) is valid only in the upper part of the bubble, corresponding to the z_+ branch in Fig. 1.11. One can integrate Eq. (1.50) with respect to r and get:

$$\frac{r\partial h_b/\partial r}{\sqrt{1 + (\partial h_b/\partial r)^2}} = -\frac{r^2}{\bar{R}(t)} + \frac{1}{\gamma} \int_0^r p(r', t) r' dr'. \quad (1.51)$$

The excess pressure field decays over a typical radial extent $\sim \sqrt{2R_{\text{eff}}D}$, that is the usual hydrodynamic radius in lubrication problems, where R_{eff} is the effective curvature radius of the liquid-gap thickness between the sphere and the bubble. We focus on the situations in which this typical hydrodynamic radius is small with respect to the bubble size, yielding the scale separation: $\sqrt{2R_{\text{eff}}D} \ll R_b$.

1.3.4 Asymptotic-matching method

Outer solution

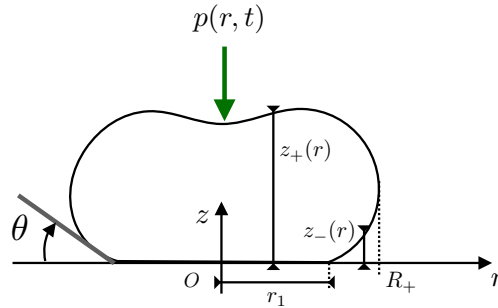


Figure 1.11: Schematic of the outer problem.

We use the method of matched asymptotic expansions [114], following specifically Refs. [47, 115]. We first describe the outer solution (denoted with the subscript “out”, which is a good approximation of the solution outside the hydrodynamic region, *i.e.* for $r \gg \sqrt{2R_{\text{eff}}D}$). In this limit, the integral $2\pi \int_0^r p(r', t) r' dr'$ does essentially not depend on r and can be approximated by the hydrodynamic force $F(t) = 2\pi \int_0^\infty p(r', t) r' dr'$. Therefore, the outer problem is equivalent to the one schematized in Fig. 1.11. The solution is derived in Ref. [115], and we recall the main steps here. We drop the time dependencies for conciseness, and the two interfacial branches are denoted z_\pm , where $+$ denotes the upper section of the bubble and $-$ the lower section (see Fig. 1.11). The functions z_\pm are related to the bubble's surface profile via the relation $h_{b,\text{out}} = z_\pm -$

$R_b(1 + \cos \theta)$. Equation (1.51) can be written conveniently for both branches as:

$$\pm \frac{r \partial z_{\pm} / \partial r}{[1 + (\partial z_{\pm} / \partial r)^2]^{1/2}} = -\frac{r^2}{\bar{R}} + \frac{F}{2\pi\gamma}. \quad (1.52)$$

The maximal lateral extent R_+ of the bubble (see Fig. 1.11) can be found by taking the limit $\partial z_{\pm} / \partial r \rightarrow \mp \infty$ in Eq. (1.52), and satisfies the polynomial equation:

$$R_+^2 / \bar{R} - R_+ = F / (2\pi\gamma). \quad (1.53)$$

Equation (1.52) can be integrated and the solution can be expressed using the elliptic integrals of the first and second kinds, \mathcal{F} and \mathcal{E} respectively, and the constant R_+ as:

$$z_{\pm}(r) = \pm \left[R_+ \mathcal{E}(K(r), q) - \frac{F}{2\pi\gamma} \frac{\bar{R}}{R_+} \mathcal{F}(K(r), q) \right] \\ \mp \left[R_+ \mathcal{E}(K(r_1), q) - \frac{F}{2\pi\gamma} \frac{\bar{R}}{R_+} \mathcal{F}(K(r_1), q) \right], \quad (1.54)$$

with:

$$K(r) = \arcsin \left(\sqrt{\frac{R_+^2 - r^2}{R_+^2 - (\frac{F}{2\pi\gamma})^2 \bar{R}^2 / R_+^2}} \right), \quad q^2 = 1 - \frac{(\frac{F}{2\pi\gamma})^2 \bar{R}^2}{R_+^4}, \quad (1.55)$$

and where r_1 denotes the contact radius of the bubble on the substrate (see Fig. 1.11). We focus on situations in which the deviation of the bubble's surface profile is small with respect to the equilibrium spherical cap, *i.e.* in the small-force limit where $\frac{F}{2\pi\gamma} \ll R_b$, which allows us to expand Eq. (1.54) at leading order in $F / (2\pi\gamma R_b)$. In this limit, we have $q^2 \approx 1$ and for $r \ll \bar{R}$, the elliptic integrals can be approximated by $\mathcal{E}(K(r), 1) \simeq \sin(K(r))$ and $\mathcal{F}(K(r), 1) \simeq \frac{1}{2} \log\left(\frac{1 + \sin(K(r))}{1 - \sin(K(r))}\right)$, which yields to an expression for the bubble interface profile near the apex of the bubble:

$$z_+(r) \simeq \bar{R} \left[1 - \frac{r^2}{2\bar{R}^2} + \sqrt{1 - \frac{r_1^2}{R_+^2}} \right] \\ + \frac{F}{2\pi\gamma} \left[1 + \sqrt{1 - \frac{r_1^2}{R_+^2}} + \frac{1}{2} \log\left(\frac{r^2}{4\bar{R}^2}\right) - \log\left(\frac{1 + \sqrt{1 - \frac{r_1^2}{R_+^2}}}{1 - \sqrt{1 - \frac{r_1^2}{R_+^2}}}\right) \right]. \quad (1.56)$$

To get a closed expression for the bubble's surface profile near the apex, we need to find the relations between \bar{R} , R_+ , r_1 and the force F . To do so, we expand the mean curvature radius as:

$$\bar{R} = R_b + \delta R \quad (1.57)$$

where δR is a perturbation with respect to the equilibrium value, which scales as $\sim F / (2\pi\gamma)$. Using Eq. (1.53), the maximal lateral extent of the bubble is expanded as:

$$R_+ \simeq R_b + F / (2\pi\gamma) + \delta R. \quad (1.58)$$

Here, we assume that the contact line is pinned, which amounts to fix the contact radius to a value $r_1 = R_b \sin \theta$, where θ is the equilibrium contact angle. The relation between δR and F can be found expressing the volume conservation of the bubble. The air volume inside the bubble can be evaluated at leading order in $F/(2\pi\gamma R_b)$ using Eq. (1.54) and reads:

$$\begin{aligned} V_b &= 2\pi \int_{r_1}^{R_+} z_-(r) r dr + 2\pi \int_0^{R_+} z_+(r) r dr \\ &\simeq \pi \bar{R}^3 \left[\frac{2}{3} + \frac{1}{3} \sqrt{1 - \frac{r_1^2}{R_+^2}} \left(2 + \frac{r_1^2}{\bar{R}^2} \right) + \frac{F}{2\pi\gamma \bar{R}} \left(1 + \sqrt{1 - \frac{r_1^2}{R_+^2}} \left(1 + \frac{1}{3} \frac{r_1^2}{\bar{R}^2} \right) \right) \right]. \end{aligned} \quad (1.59)$$

Introducing the expansions of Eqs. (1.57) and (1.58) in Eq. (1.59), we write the volume variation at leading order as:

$$V_b - V_{b,0} \simeq \frac{\pi R_b^2}{\cos \theta} \left[\frac{F}{2\pi\gamma} (1 + \cos \theta) + \delta R (1 + \cos \theta)^2 \right], \quad (1.60)$$

where $V_{b,0} = \pi R_b^3 [2/3 + \cos \theta - \cos^3(\theta)/3]$ is the equilibrium bubble volume. Assuming that the bubble is incompressible, we get:

$$\delta R = -\frac{F}{2\pi\gamma} \frac{1}{1 + \cos \theta}. \quad (1.61)$$

Therefore, the bubble's surface profile reads:

$$z_+(r) \simeq R_b \left(1 + \cos \theta - \frac{r^2}{2R_b^2} \right) + \frac{F}{2\pi\gamma} \left[1 + \log \left(\frac{r}{2R_b} \right) - \log \left(\frac{1 + \cos \theta}{1 - \cos \theta} \right) \right], \quad (1.62)$$

and, thus, the outer solution finally reads for $r \ll R_b$:

$$h_{b,\text{out}} \simeq -\frac{r^2}{2R_b} + \frac{F}{2\pi\gamma} \left[1 + \log \left(\frac{r}{2R_b} \right) - \log \left(\frac{1 + \cos \theta}{1 - \cos \theta} \right) \right]. \quad (1.63)$$

Inner solution

We now focus on the inner asymptotic solution (denoted with the subscript "in", in the region near the apex of the bubble, for which the radial coordinate r is of the same order as the hydrodynamic radius $\sqrt{2R_{\text{eff}}D}$). In this region, the slope $\partial_r h_{b,\text{in}}$ of the bubble's surface profile is small with respect to unity, such that Eq. (1.50) can be linearized into:

$$\frac{\gamma}{r} \frac{\partial}{\partial r} \left(r \frac{\partial h_{b,\text{in}}}{\partial r} \right) = \Delta P(t) + p(r, t). \quad (1.64)$$

Therefore, we can expand the bubble's surface profile as the sum of a parabolic equilibrium shape and a deviation $u_{\text{in}}(r, t)$, *i.e.* :

$$h_{b,\text{in}}(r, t) \simeq -\frac{r^2}{2R_b} - u_{\text{in}}(r, t). \quad (1.65)$$

Injecting the latter expression in Eq. (1.49), the liquid-gap thickness in the inner region takes the same form as in section 1.1.4:

$$h(r, t) = D + \frac{r^2}{2R_{\text{eff}}} + Z(t) + u_{\text{in}}(r, t). \quad (1.66)$$

Using the expansion of the pressure difference $\Delta P(t) = -\frac{2\gamma}{R} \simeq -2\gamma/R_b + 2\gamma\delta R(t)/R_b^2$, with Eq. (1.61) and the linear properties of Eq. (1.64), we find:

$$-\frac{\gamma}{r} \frac{\partial}{\partial r} \left(r \frac{\partial u_{\text{in}}}{\partial r} \right) = -\frac{F(t)}{\pi R_b^2} \frac{1}{1 + \cos \theta} + p(r, t). \quad (1.67)$$

The inner solution must match asymptotically the outer solution of Eq. (1.63), which imposes the following asymptotic expression at $r \gg \sqrt{2R_{\text{eff}}D}$:

$$u_{\text{in}} \sim -\frac{F(t)}{2\pi\gamma} \left[1 - \log \left(\frac{1 + \cos \theta}{1 - \cos \theta} \right) + \log \left(\frac{r}{2R_b} \right) \right], \quad (1.68)$$

which is used as a boundary condition in the model. As in section 1.1.4, the modulus $|Z^*|$ of the amplitude Z^* of the vertical displacement Z of the sphere and the deformation of the bubble are assumed to be much smaller than the average sphere-bubble distance D , so that we can neglect the contributions of Z and u_{in} in the non-linear ($\propto h^3$) factor within the Reynolds equation in Eq. (1.7). The complex version of the latter thus becomes of the same form as Eq. (1.9), and reads:

$$12\eta r i \omega \left[Z^* + u_{\text{in}}^*(r) \right] = \frac{d}{dr} \left[r \left(D + \frac{r^2}{2R_{\text{eff}}} \right)^3 \frac{dp^*(r)}{dr} \right]. \quad (1.69)$$

Similarly, Eq. (1.67) written with complex variables reads:

$$-\frac{\gamma}{r} \frac{d}{dr} \left(r \frac{du_{\text{in}}^*}{dr} \right) = \frac{G^* Z^*}{\pi R_b^2} \frac{1}{1 + \cos \theta} + p^*(r). \quad (1.70)$$

Finally, we introduce the dimensionless variables:

$$\begin{aligned} x &= \frac{r}{\sqrt{2R_{\text{eff}}D}}, & U_{\text{in}}^* &= \frac{u_{\text{in}}^*}{Z^*}, & P^* &= \frac{p^*}{\frac{\eta R_{\text{eff}} Z^* \omega}{D^2}}, \\ \mathcal{G}^* &= \frac{G^* D_c}{6\pi\eta\omega R_{\text{eff}}^2}, & D_c &= \frac{16R_{\text{eff}}^2 \eta \omega}{\gamma}, \end{aligned} \quad (1.71)$$

such that Eqs. (1.69) and (1.70) become:

$$24i \left[1 + U_{\text{in}}^*(x) \right] = \frac{1}{x} \frac{d}{dx} \left[x (1 + x^2)^3 \frac{dP^*(x)}{dx} \right], \quad (1.72)$$

$$-\frac{1}{x} \frac{d}{dx} \left(x \frac{dU_{\text{in}}^*}{dx} \right) = \frac{2R_{\text{eff}}D}{R_b^2} \frac{3}{16} \frac{1}{1 + \cos \theta} \mathcal{G}^* + \frac{D_c}{8D} P^*(x). \quad (1.73)$$

Then, Eqs. (1.72) and (1.73) are solved numerically using a standard finite-difference scheme. The boundary conditions are set to:

$$\frac{dP^*}{dx}(0) = 0, \quad P^*(x_{\max}) = 0, \quad (1.74)$$

and:

$$U_{\text{in}}^*(x_{\max}) = \frac{3}{8} \mathcal{G}^* \left[1 - \log \left(\frac{1 + \cos \theta}{1 - \cos \theta} \right) + \log \left(\frac{r_{\max}}{2R_b} \right) \right], \quad (1.75)$$

where $x_{\max} = r_{\max}/\sqrt{2R_{\text{eff}}D}$ and r_{\max} are the dimensionless boundary and corresponding real boundary of the numerical domain, respectively. The boundary condition of Eq. (1.75) is set following the asymptotic expression in Eq. (1.68), which means that r_{\max} is a typical radius that matches the two asymptotic solutions. We checked that the solution is not dependent on r_{\max} , provided that $\sqrt{2R_{\text{eff}}D} \ll r_{\max} \ll R_b$.

Large-distance asymptotic expression

Here, we perform an asymptotic calculation at large distance in the inner model. We assume that D_c/D is a small parameter, and we use the following first-order expansions of the fields U_{in}^* , P^* and of the mechanical impedance \mathcal{G}^* :

$$U_{\text{in}}^*(x) \simeq 0 + \frac{D_c}{D} U_{\text{in},1}^*(x), \quad (1.76)$$

$$P^*(x) \simeq P_0^*(x) + \frac{D_c}{D} P_1^*(x), \quad (1.77)$$

$$\mathcal{G}^* \simeq \mathcal{G}_0^* + \frac{D_c}{D} \mathcal{G}_1^*. \quad (1.78)$$

The zeroth-order term P_0^* is given by Eq. (1.25) in the undeformed-bubble limit, and reads:

$$P_0^*(x) = -\frac{3i}{(1+x^2)^2}, \quad (1.79)$$

which gives to the viscous expression:

$$\mathcal{G}_0^*(x) = i \frac{D_c}{D}. \quad (1.80)$$

Then, the first-order term $U_{\text{in},1}^*$ is found by inserting P_0^* in Eq. (1.73), and by invoking the boundary condition of Eq. (1.75). We find:

$$\begin{aligned} U_{\text{in},1}^*(x) &= \frac{2R_{\text{eff}}D}{R_b^2} \frac{3i}{32} \left(x_{\max}^2 - x^2 \right) \frac{1}{1 + \cos \theta} - \frac{3i}{32} \left[\log(1 + x_{\max}^2) - \log(1 + x^2) \right] \\ &+ \frac{3i}{16} \left[1 - \log \left(\frac{1 + \cos \theta}{1 - \cos \theta} \right) + \log \left(\frac{r_{\max}}{2R_b} \right) \right]. \end{aligned} \quad (1.81)$$

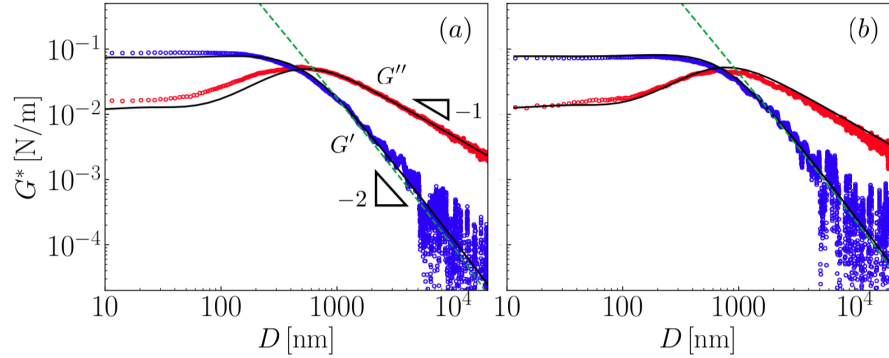


Figure 1.12: Real (blue circles) and imaginary (red circles) parts of the measured mechanical impedance $G^* = G' + iG''$ versus average sphere-bubble distance D , for a surfactant concentration $C = 1$ mM, and frequencies $\omega/(2\pi) = 200$ Hz (a), and 300 Hz (b). The bubble radius is $R_b = 346 \pm 2 \mu\text{m}$ and the contact angle is $\theta = 81 \pm 2^\circ$. The best fits to the model are displayed with solid black lines, using a single fitting parameter $\gamma = 54 \pm 4$ mN/m. The large-distance asymptotic solution for G' (see Eq. (1.85)) is also shown with green dashed lines. The slope triangles indicate power-law exponents.

In what follows, we neglect the first term of the right-hand side of Eq. (1.81) to keep the leading order in the asymptotic-matching condition r_{\max}/R_b . Then, introducing $U_{\text{in},1}^*$ in Eq. (1.72) allows us to express the first-order pressure:

$$P_1^*(x) = \frac{3}{32} \left[\frac{-3 - 6 \log\left(\frac{1+\cos\theta}{1-\cos\theta}\right) - 6x^2 + 6 \log\left(\frac{r_{\max}}{R_b}\right) - 3 \log 4 - 3 \log(1+x_{\max}^2)}{(1+x^2)^2} + \pi^2 - 6 \frac{\log(1+x^2)}{1+x^2} + 3 \log^2(1+x^2) + 6 \text{Li}_2(-x^2) \right], \quad (1.82)$$

where Li_2 denotes the dilogarithm function [64]. After some algebra, we find that:

$$\mathcal{G}_1^* = \frac{3}{32} \left(\frac{D_c}{D} \right) \left[-3 + \log(4) - 2 \log\left(\frac{1+\cos\theta}{1-\cos\theta}\right) - 2 \log\left(\frac{r_{\max}}{R_b}\right) + \log(1+x_{\max}^2) \right]. \quad (1.83)$$

Finally, assuming that the boundary coordinate x_{\max} is much larger than unity, we get:

$$\mathcal{G}_1^* \simeq \frac{3}{32} \left(\frac{D_c}{D} \right) \left[-3 + \log(4) - 2 \log\left(\frac{1+\cos\theta}{1-\cos\theta}\right) + \log\left(\frac{R_b^2}{2R_{\text{eff}}D}\right) \right]. \quad (1.84)$$

1.3.5 Experimental results

The real and imaginary parts of the measured mechanical impedance $G^* = G' + iG''$ are plotted in Fig. 1.12, as functions of the average sphere-bubble distance D , for two frequencies and a given surfactant concentration. Best fits to the model are also shown, in

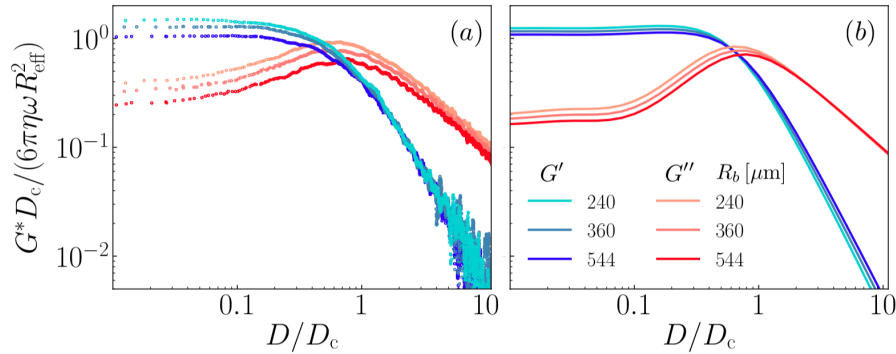


Figure 1.13: Dimensionless mechanical impedance versus dimensionless distance, for three bubble sizes as indicated, a single frequency $\omega/(2\pi) = 200$ Hz, and a single surfactant concentration $C = 1$ mM. The experimental data are shown in (a). The results of the model are plotted in (b), using the previously-obtained best-fit parameter $\gamma = 54$ mN/m.

good agreement with the data, the air-water surface tension $\gamma = 54 \pm 4$ mN/m being the only fitting parameter. Furthermore, two asymptotic regimes can be observed, at large and small distances respectively. They crossover near $D \approx 1000$ nm, which corresponds to the typical viscocapillary distance $D_c = 16R_{\text{eff}}^2 \eta \omega / \gamma$ emerging from the model, and equal to 771 and 1160 nm in Figs. 1.12(a) and (b), respectively. At large distance, the viscous contribution G'' dominates and follows a $\sim D^{-1}$ scaling law, as expected from the asymptotic expression $G'' \simeq 6\pi\eta R_{\text{eff}}^2 \omega / D$ [60]. In contrast, the restoring contribution G' due to the air-water capillary interface appears with an apparent $\sim D^{-2}$ scaling law at large distance. We stress that the latter is not an exact scaling law, due to a logarithmic correction:

$$G'(D) \simeq \frac{9\pi\eta^2 R_{\text{eff}}^4 \omega^2}{\gamma D^2} \left[-3 + \log(4) - 2 \log\left(\frac{1 + \cos\theta}{1 - \cos\theta}\right) + \log\left(\frac{R_b^2}{2R_{\text{eff}} D}\right) \right]. \quad (1.85)$$

At small distance, both G' and G'' saturate to constant values, which is reminiscent of elastohydrodynamic responses near soft substrates [36, 37, 60, 83, 116, 117], and might be related to saturations in the deformation and pressure fields. At such small distances, the capillary deformation of the bubble surface essentially accommodates the sphere's oscillation, and the liquid is no longer expelled from the gap, which further leads to a stronger capillary response than the viscous one.

In order to reveal the importance of finite-size effects in the viscocapillary response, we introduce the dimensionless mechanical impedance $\mathcal{G}^* = G^* D_c / (6\pi\eta\omega R_{\text{eff}}^2)$. In Fig. 1.13, the experimental and theoretical dimensionless mechanical impedances are plotted versus the dimensionless average sphere-bubble distance, for three bubble radii. Except for the viscous contribution in the large-distance limit, the dimensionless impedance is generally found to depend on the bubble size in a nontrivial way, which is correctly reproduced by the model. This observation highlights the importance of finite-size ef-

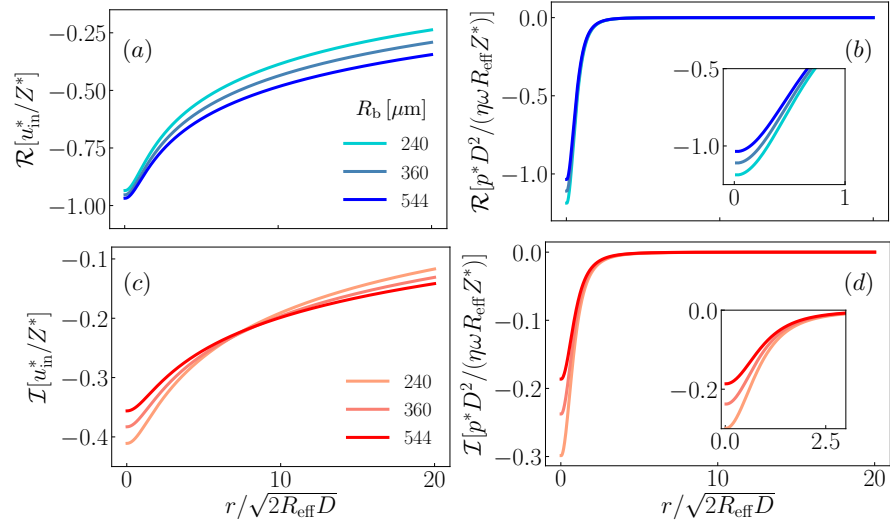


Figure 1.14: Real (a) and imaginary (c) parts of the amplitude of the dimensionless inner deformation field as functions of the dimensionless radial coordinate, at a dimensionless distance $D/D_c = 0.3$, for the three bubble radii of Fig. 1.13, as obtained from the model Eqs. (1.72) and (1.73). Similarly, the real and imaginary parts of the amplitude of the dimensionless excess pressure field are plotted in panels (b) and (d), respectively. The insets display zooms near the symmetry axis.

fects in viscocapillary interactions, resulting from the long-range capillary deformation of the air-water interface. We note that the logarithmic correction in the large-distance asymptotic expression of the capillary contribution (see Eq. (1.85)) contains a bubble-size dependence which cannot be resolved with the AFM sensitivity and the current bubble-size range. At small distance, the size dependence is more pronounced and both the real and imaginary parts of the dimensionless impedance decrease when increasing the bubble size.

Having discussed the finite-size effects on the global hydrodynamic force, we now investigate their influence on the amplitudes of the local excess pressure and deformation fields. To do so, we perform numerical integrations of Eqs. (1.72) and (1.73) using the asymptotic expression for the inner deformation field. Figure 1.14 shows the results for $D/D_c = 0.3$, with the same parameters as in Fig. 1.13. We observe that the real and imaginary parts of the dimensionless amplitude of the excess pressure field decay rapidly on a typical distance $\sim \sqrt{R_{\text{eff}} D}$, and depend weakly on the bubble radius. In sharp contrast, the real and imaginary parts of the dimensionless amplitude of the inner deformation field largely depend on the bubble radius, as well as on the contact angle (not shown).

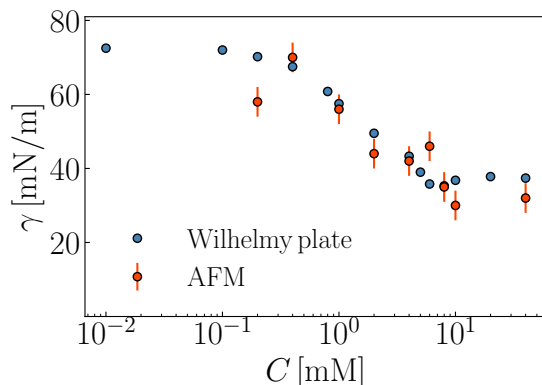


Figure 1.15: Air-water surface tension as a function of surfactant (SDS) concentration, as obtained from fits (see Fig. 1.12) of the AFM experimental data by the model (red dots). Statistical error bars associated with multiple measurements at different frequencies are indicated. For comparison, independent measurements using the Wilhelmy-plate method are provided (blue dots).

1.3.6 Tensiometry measurements

So far, the air-water surface tension was considered as a free parameter and was fixed by fitting the AFM experimental data to the model. The fitted values of the surface tension as a function of the SDS concentration in water are shown in Fig. 1.15. We observe that the surface tension globally decreases with increasing surfactant concentration, as expected. At surfactant concentrations smaller than ~ 0.5 mM, the surface tension is close to the 72 mN/m value for pure water. At concentrations larger than ~ 8 mM, the surface tension saturates to a value on the order of 30 mN/m. The critical micellar concentration (CMC) of SDS in water is estimated to be around 8 mM [118, 119], which is in agreement with the latter observation. The uncertainty on the fitted values of the surface tension is on the order of ± 4 mN/m, which mainly results from the fact that the experiments at different frequencies lead to slight variations.

Finally, we discuss the capacity of our method to be used as a robust tensiometer. To do so, we perform independent tensiometry experiments on similar air-water-SDS interfaces using the Wilhelmy-plate method [20]. The results are shown in Fig. 1.15, and agree well with the ones obtained with our method. Possible systematic deviations at the highest concentrations may result from a surfactant-induced depinning of the contact line of the bubble on the substrate [120]. In such a scenario, the hydrodynamic pressure would not only trigger a local capillary deformation (see Eq. (1.50)), but would also induce a spreading-dewetting cycle of the bubble on the substrate. In addition, the bubble resonance frequency being lower at lower surface tension, capillary waves might be excited at the air-water interface at large surfactant concentrations. Besides, at the smallest concentration (0.2 mM) used in the AFM experiment, the air-water interface may not be entirely covered with an adsorbed surfactant layer, poten-

tially resulting in slippage. In such a scenario, the surfactant advection induced by the flow would add an elastic-like component to the mechanical response [113, 121], which might explain the small deviations observed in Fig. 1.15.

1.4 Inertial effects

1.4.1 Introduction

The drag force exerted by a fluid on a moving particle is a fundamental quantity of fluid mechanics. So far, we have been interested in the previous sections of the chapter in the particular case of an inertia-less fluid, where viscous effects are dominant. The dimensionless number of fluid mechanics that measures the relative importance of inertial and viscous effects is the Reynolds number, $Re = \rho\mathcal{L}V/\eta$, where \mathcal{L} and V are the typical length and velocity scales of the flow. In the canonical case of an object of size \mathcal{L} , moving with a velocity V a bulk viscous medium, the drag force takes different scalings in the two regimes of fluid mechanics: i) in the viscous-dominated regime, *i.e.* at low Re , the drag follows the Stokes-like law $\sim \eta\mathcal{L}V$; ii) at high Re , the drag reads $\rho SC_D V^2/2$, where S is the cross-sectional area of the object, and C_D is the so-called drag coefficient. In this section, we assume a small, but finite Re number and we wonder how fluid inertia affects the flow in colloidal-probe methods.

In the small but finite Re limit, the convective term of the Navier-Stokes equation, $\rho(\mathbf{v} \cdot \nabla)\mathbf{v}$, may generate non-trivial effects. As an example, for a particle moving in a shear flow, the convective term induces a lift force normal to the velocity direction. The inertial lift force has been widely investigated [122, 123, 124, 125, 126, 127], has important applications in microfluidics for droplet-sorting purposes [128, 129], and may play a role in the migration of red blood cells in blood vessels [130]. Moreover, Cox & Brenner have investigated the drainage flow generated by a spherical particle moving toward a planar surface with a constant velocity V_\perp . They have derived the first order correction to the Reynolds force, considering inertia as a small parameter and using asymptotic-matching methods in the small sphere-wall distance limit, which gives $6\pi/5\eta RV_\perp(1 + \frac{\rho RV_\perp}{2\eta}) \ln(R/D)$ [131]. Here, we focus on the situation of a small oscillating flow normal to the surface.

Transient, and oscillatory flows are often described using the unsteady Stokes' equations, that neglect the nonlinear convective term, of the Navier-Stokes equation. The time-derivative term, $\rho\partial_t\mathbf{v}$, is significant when the typical time scale of the flow is small or comparable to the diffusion time scale of vorticity, which scales as $\sim \rho\mathcal{L}^2/\eta$. Such flows have been investigated to understand the short-time dynamics of Brownian motions [132], the effect of inertia in wave propagation [133], in free-surface transient flows [134], and in the locomotion of micro-organisms resulting from beating cilia [135] to cite a few examples. Interestingly, in the sphere-plan geometry, the unsteady Stokes' equations do not exhibit a series-expansion solution with the appropriate eigenvalues in the bi-spherical coordinates, as for the Stokes equations [136, 137]. However, the solution may be written in an integral form [138, 139], and exact results can be obtained

asymptotically using methods such as the point-particle approximation [140] and the method of reflections [141].

In contactless colloidal probe methods, fluid inertia is taken into account in the equation of motion of the cantilever, via the effective mass (see Eq. (1.5) in section 1.1.3). Indeed, a spherical particle, that moves with a time-dependent Lagrangian velocity $V(t)$ in an unbounded fluid at rest, is submitted to a force:

$$\mathbf{F} = -6\pi\eta R\mathbf{V}(t) - 6R^2\sqrt{\pi\rho\eta} \int_{-\infty}^t \frac{1}{\sqrt{t-\tau}} \frac{d\mathbf{V}(\tau)}{d\tau} d\tau - \frac{2\pi\rho R^3}{3} \frac{d\mathbf{V}}{dt}, \quad (1.86)$$

where a small Reynolds number is assumed. Considering Newton's second law for the particle, the last term of the right hand side of Eq. (1.86) is equivalent to an inertial term, where the *added mass* $\frac{2\pi\rho R^3}{3}$ is equal to half of the displaced fluid mass. The hand-waving argument used to explain the origin of this term is that the particle must move some fluid mass during its motion. The second term is called the Basset force and depends on the *history* of the particle trajectory [142]. The standard procedure in the colloidal-probe method is to calibrate the quality factor and resonance frequency of the cantilever far from the surface which gives an estimation of the effective mass of the cantilever, including the added mass. However, the fluid-inertia force varies with the sphere-plan distance, which modifies the resonance properties of the cantilever and affects the measurements [143]. Using dimensional analysis, we can write the force applied on the sphere in the following scaling form:

$$F^* = \eta R Z^* \omega f^* \left(\frac{D}{R}, \frac{R^2}{\delta^2} \right), \quad (1.87)$$

where $\delta = \sqrt{\eta/(\rho\omega)}$ denotes the viscous penetration length, and f^* is a dimensionless function. Theoretical expressions have been derived in Ref. [139] in the case of a sphere far from the substrate surface. In the joint limit where $R \ll D$ and $\delta \ll D$ we have:

$$F^* = -6i\pi\eta R Z^* \left(1 + \sqrt{i\text{Re}} + \frac{i\text{Re}^2}{9} \right) - \frac{3i\pi\eta R^4 Z^*}{2(D+R)^3} \left(1 + \sqrt{i\text{Re}} + \frac{i\text{Re}}{3} \right) \left[\frac{1}{3} + \frac{3}{2i\text{Re}} \left(1 + \sqrt{i\text{Re}} + \frac{i\text{Re}}{9} \right) \right], \quad (1.88)$$

where the Reynolds number is defined here as $\text{Re} = \rho R^2 \omega / \eta = (R/\delta)^2$. The first term of Eq. (1.88) corresponds to the Basset equation of Eq. (1.86) written in Fourier space (in infinite space). In the limit of large Reynolds numbers, the added mass takes the form $\frac{2\pi\rho R^3}{3} \left(1 + \frac{3R^3}{(R+D)^3} \right)$, and decreases with increasing sphere-plan distance. The $1/D^3$ dependence of the added mass has been observed in the shift of the resonance frequency of the AFM in Ref. [143]. Interestingly, in the limit of large viscous penetration length, where $R \ll D \ll \delta$, the hydrodynamic force follows the asymptotic expression:

$$F^* = -6i\pi\eta R Z^* \left(1 + \frac{9R}{8(R+D)} \right) + \frac{9\pi}{4} \rho \omega^2 R^2 (R+D) Z^*, \quad (1.89)$$

with a space-dependent added mass $\frac{9\pi}{4}\rho R^2(R+D)$, that here increases with increasing distance. Nevertheless, a complete description of the added mass and its dependence on the sphere-plan distance is still missing and is the subject of the subsection.

In this section, we first describe the problem. Then, we derive a lubrication model to describe the flow in the small sphere-plan distance limit. The force predicted by the lubrication model diverges and should be regularized with the outer solution. Then, we use the Lorentz reciprocal theorem to get an expression which is valid in the low-Reynolds number limit only.

Model

We focus here on the effect of fluid inertia, such that the planar surface is taken to be rigid and immobile. We consider the same settings of the section 1.1.4, and use the linear response framework. The velocity \mathbf{v} and pressure fields are harmonic and written as $\mathbf{v}(\mathbf{r}, t) = \mathbf{v}^*(\mathbf{r})e^{i\omega t}$, and $p(\mathbf{r}, t) = p^*(\mathbf{r})e^{i\omega t}$ respectively, and follows the linear unsteady Stokes equations:

$$\nabla \cdot \boldsymbol{\sigma}^* = \eta \nabla^2 \mathbf{v}^* - \nabla p^* = i\rho\omega \mathbf{v}^*, \quad \nabla \cdot \mathbf{v}^* = 0, \quad (1.90)$$

where $\boldsymbol{\sigma}^*$ is the fluid stress tensor. We assume a no-slip boundary condition at both the sphere and the plane surfaces denoted \mathcal{S}_0 and \mathcal{S}_w . The velocity is assumed to vanish at infinity, denoted as \mathcal{S}_∞ . Therefore, the boundary conditions of the flow can be written in a concise form as:

$$\mathbf{v}^* = \begin{cases} i\omega Z^* \mathbf{e}_z, & \text{if } \mathbf{r} \in \mathcal{S}_0, \\ \mathbf{0}, & \text{if } \mathbf{r} \in \mathcal{S}_\infty \cup \mathcal{S}_w, \end{cases} \quad (1.91)$$

where \mathbf{e}_z denotes the unit vector in the z direction.

1.4.2 Lubrication approximation

As a first approach, we use the lubrication approximation, assuming that the sphere-plan distance is small with respect to the sphere radius, which is the main application range of colloidal-probe methods. Therefore, there is a scale separation between the lateral length scale of the flow \sqrt{RD} , and the vertical one D , which means a larger lateral velocity than the vertical one through mass conservation. Expressing the corresponding scales, the viscous term of the Navier-Stokes equation is approximated by the dominant shear term $\eta \nabla^2 \mathbf{v}^* \approx \eta \partial_z^2 v_r^* \mathbf{e}_r$, where the lateral velocity field is directed along \mathbf{e}_r because of the axisymmetry of the problem. Thus, the unsteady Stokes equations in Eq. (1.90) become:

$$i\rho\omega v_r^* = -\frac{\partial p^*}{\partial r} + \eta \frac{\partial^2 v_r^*}{\partial z^2}, \quad (1.92a)$$

$$0 = -\partial_z p. \quad (1.92b)$$

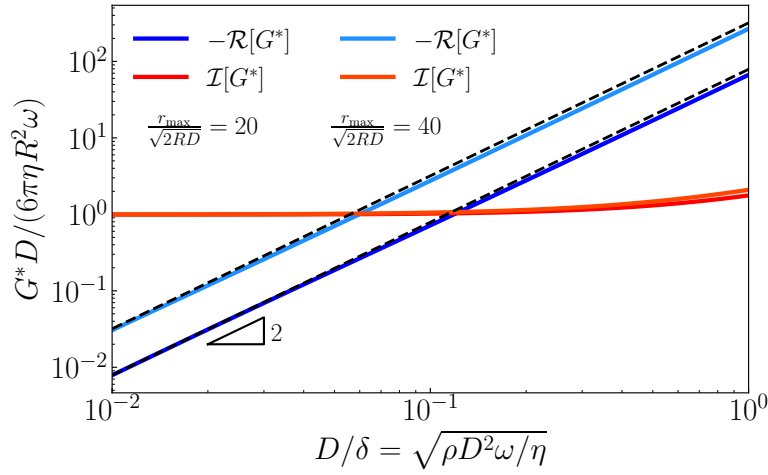


Figure 1.16: Dimensionless mechanical impedance versus sphere-plan distance to viscous penetration depth ratio resulting from the numerical integration of Eq. (1.94). Two numerical solutions are shown, with boundaries of the numerical domain at $r_{\max} = 20\sqrt{2RD}$ and $40\sqrt{2RD}$ respectively. The black dashed lines the asymptotic expression Eq. (1.96).

We solve Eq.(1.92) using the boundary condition Eq. (1.91) and find the velocity field:

$$v_r^*(z) = \frac{\delta^2}{i\eta} \frac{\partial p^*}{\partial r} \frac{\sinh(\frac{\sqrt{i}z}{\delta}) - \sinh(\frac{\sqrt{i}h}{\delta}) - \sinh(\frac{\sqrt{i}[z-h]}{\delta})}{\sinh(\frac{\sqrt{i}h}{\delta})}, \quad (1.93)$$

Expressing the mass conservation, $\frac{\partial h}{\partial t} = -\frac{1}{r} \frac{\partial}{\partial r} (r \int_0^h v_r(z, t) dz)$, and using the complex notations, we find:

$$i\omega Z^* = \frac{1}{r} \frac{d}{dr} \left(r \sqrt{i} \delta^3 \frac{2 \cosh(\frac{\sqrt{i}h}{\delta}) - 2 - \frac{\sqrt{i}h}{\delta} \sinh(\frac{\sqrt{i}h}{\delta})}{\eta \sinh(\frac{\sqrt{i}h}{\delta})} \frac{dp^*}{dr} \right). \quad (1.94)$$

First, in the viscous limit where $\delta \rightarrow \infty$, the ratio $\sqrt{i} \delta^3 \frac{2 \cosh(\frac{\sqrt{i}h}{\delta}) - 2 - \frac{\sqrt{i}h}{\delta} \sinh(\frac{\sqrt{i}h}{\delta})}{\eta \sinh(\frac{\sqrt{i}h}{\delta})}$ is equivalent to $h^3/(12\eta)$, such that we recover the viscous case of Eq. (1.9) with no surface deformation. The Eq. (1.94) does not exhibit any analytical solution, and is solved numerically using a finite-difference scheme. A uniform radial grid is introduced in the range $r \in [0, r_{\max}]$, where r_{\max} is the boundary of the numerical domain.

The real and imaginary parts of the mechanical impedance G^* , defined in section 1.1.4, rescaled by the viscous impedance, are plotted in Fig. 1.16 as functions of the dimensionless ratio between the sphere-plan distance and the viscous penetration length. At small distance, or equivalently in the viscous limit, the imaginary part of the mechanical impedance is dominant and we recover the viscous expression $G^* = 6i\pi\eta R^2\omega/D$. The real part of the mechanical impedance is negative with the sign

convention of G^* , and follows a scaling law $-G' \sim \delta^{-2}$ at small distances. The prefactor of the scaling law is found to depend on the boundary of the numerical domain, and increases with the latter.

To get further insight on this numerical result, we perform an asymptotic expansion, assuming a small but finite ratio $D/\delta \ll 1$, and assuming that the pressure field vanishes at a given radius r_{\max} . In this limit, the ratio in the bracket of Eq. (1.94) can be expanded as $\sqrt{i}\delta^3 \frac{2 \cosh(\frac{\sqrt{ih}}{\delta}) - 2 - \frac{\sqrt{ih}}{\delta} \sinh(\frac{\sqrt{ih}}{\delta})}{\eta \sinh(\frac{\sqrt{ih}}{\delta})} \simeq \frac{h^3}{12\eta} (1 - i \frac{h^2}{10\delta^2})$. Expanding the pressure field as $p^* = p_0^* + (D/\delta)^2 p_1^*$, and keeping the first-order term in D/δ , we find:

$$p^* \simeq -\frac{3i\eta R\omega Z^*}{(D + \frac{r^2}{2R})^2} + \frac{3\eta R\omega Z^*}{5D^2} \left(\frac{D}{\delta}\right)^2 \ln\left(\frac{1 + r_{\max}^2/(2RD)}{1 + r^2/(2RD)}\right), \quad (1.95)$$

leading to the asymptotic expression of the mechanical impedance:

$$\begin{aligned} G^* &\simeq \frac{6i\pi\eta R^2\omega}{D} - \frac{6\pi\eta R^2\omega}{5D} \left(\frac{D}{\delta}\right)^2 \left[\frac{r_{\max}^2}{2RD} - \ln\left(1 + \frac{r_{\max}^2}{2aD}\right) \right] \\ &\simeq \frac{6i\pi\eta R^2\omega}{D} - \frac{6\pi\rho R^2\omega^2 D}{5} \left[\frac{r_{\max}^2}{2RD} - \ln\left(1 + \frac{r_{\max}^2}{2RD}\right) \right]. \end{aligned} \quad (1.96)$$

The asymptotic expression in Eq. (1.96) is plotted in Fig. 1.16 and is in agreement with the numerical integration in the small D/δ limit.

Here, the flow in the lubrication model depends on the boundary r_{\max} and diverges as $r_{\max} \rightarrow \infty$. Therefore it cannot be used *per se*. One way to circumvent this problem would be to write a correct asymptotic matching method in the small D/R limit, where the lubrication solution would correspond to the inner problem that should be matched to the outer solution, following Ref. [131]. This has not been done in the framework of my thesis and is left for future work. In the following section, we use the Lorentz reciprocal theorem to go beyond the lubrication model.

1.4.3 Generalized Lorentz reciprocal theorem

We refer to the section 2.4 for an introduction on the reciprocal theorem in fluid mechanics. The Lorentz reciprocal theorem is written in Eq. (2.38) for viscous problems, governed by the Stokes equation [144]. It can be generalized in the presence of a body force \mathbf{b}^* , including the unsteady term of Navier-Stokes equations by choosing $\mathbf{b}^* = -i\omega\rho\mathbf{v}^*$. With this notation, the Eq. (1.90) becomes $\nabla \cdot \hat{\boldsymbol{\sigma}}^* + \hat{\mathbf{b}}^* = \mathbf{0}$. The generalized Lorentz reciprocal theorem states that for any model problem (denoted with a hat $\hat{\cdot}$) of the Stokes equations on the same fluid domain with a body force $\hat{\mathbf{b}}$:

$$\nabla \cdot \hat{\boldsymbol{\sigma}} + \hat{\mathbf{b}} = \mathbf{0}, \quad \nabla \cdot \hat{\mathbf{v}} = 0, \quad (1.97)$$

then, the stress tensors and velocity fields of both problems follow the identity:

$$\int_S \mathbf{n} \cdot \boldsymbol{\sigma}^* \cdot \hat{\mathbf{v}} dS - \int_S \mathbf{n} \cdot \hat{\boldsymbol{\sigma}} \cdot \mathbf{v}^* dS = \int_V \hat{\mathbf{v}} \cdot \mathbf{b}^* dV - \int_V \mathbf{v}^* \cdot \hat{\mathbf{b}} dV \quad (1.98)$$

where $\mathcal{S} = \mathcal{S}_0 + \mathcal{S}_w + \mathcal{S}_\infty$ denotes the surface integral over all the bounding surfaces, with \mathbf{n} being the normal unit vector directed toward the fluid, and \mathcal{V} being the total fluid volume. The great advantage of the reciprocal theorem is to compute surface integrals such as the force applied on a sphere without the precise knowledge of the complete fields. Here, we choose the problem of a sphere oscillating normally to plane wall with a velocity $\hat{\mathbf{v}}_s = -\omega Z^* e^{i\omega t} \mathbf{e}_z$, with no external force or inertia, *i.e.* $\hat{\mathbf{b}} = 0$. Therefore the boundary conditions for the model problem, written with the complex notations, are:

$$\hat{\mathbf{v}}^* = \begin{cases} -\omega Z^* \mathbf{e}_z, & \text{if } \mathbf{r} \in \mathcal{S}_0, \\ \mathbf{0}, & \text{if } \mathbf{r} \in \mathcal{S}_\infty \cup \mathcal{S}_w. \end{cases} \quad (1.99)$$

Applying the Lorentz reciprocal theorem yields:

$$-\omega Z^* F_z^* - i\omega Z^* \hat{F}_z = -i\omega\rho \int_{\mathcal{V}} \hat{\mathbf{v}}^* \cdot \mathbf{v}^* dV, \quad (1.100)$$

where $F_z^* = \mathbf{e}_z \cdot \int_{\mathcal{S}_0} \mathbf{n} \cdot \boldsymbol{\sigma}^* dS$ is the vertical force that applies on the sphere, and \hat{F}_z the one in the model problem. The drag force in the model problem has been computed exactly in Ref. [136] for all distances using a spectral decomposition with the bi-spherical coordinates and reads:

$$\frac{\hat{F}_z}{6\pi\eta R Z^* \omega} = \frac{4}{3} \sinh \alpha \sum_{n=1}^{\infty} \frac{n(n+1)}{(2n-1)(2n+3)} \left[\frac{2 \sinh(2n+1)\alpha + (2n+1) \sinh 2\alpha}{4 \sinh^2(n+\frac{1}{2})\alpha - (2n+1)^2 \sinh^2 \alpha} - 1 \right], \quad (1.101)$$

where $\cosh \alpha = 1 + D/R$. Here, the Lorentz reciprocal theorem does not leads to an expression for F_z^* in a closed form, as the r.h.s. of Eq. (1.100) depends on \mathbf{v}^* , which is unknown so far. Nevertheless, we can obtain an expression in the small-Reynolds-number limit, as derived in the following section.

1.4.4 Low-Reynolds number expansion

In the rest of the section, we use dimensionless variables (unless explicitly written), using ωZ^* , R , $\eta\omega Z^*/R$ and $\eta\omega Z^* R$ as velocity, length, pressure and force scales, and we drop the $*$ for clarity. The unsteady Stokes equations of Eq. (1.90) become:

$$\nabla \cdot \boldsymbol{\sigma} + \mathbf{b} = \nabla^2 \mathbf{v} - \nabla p - i\text{Re } \mathbf{v} = \mathbf{0}, \quad \nabla \cdot \mathbf{v} = 0. \quad (1.102)$$

The Reynolds number is assumed to be small, *i.e.* $\text{Re} \ll 1$, and the fields are expanded as: $\boldsymbol{\sigma} = \boldsymbol{\sigma}_0 + \text{Re } \boldsymbol{\sigma}_1$ and $\mathbf{v} = \mathbf{v}_0 + \text{Re } \mathbf{v}_1$ such that the linear Stokes equations becomes:

$$\nabla \cdot \boldsymbol{\sigma}_0 = \mathbf{0}, \quad \nabla \cdot \mathbf{v}_0 = 0, \quad (1.103a)$$

$$\nabla \cdot \boldsymbol{\sigma}_1 - i\mathbf{v}_0 = \mathbf{0}, \quad \nabla \cdot \mathbf{v}_1 = 0. \quad (1.103b)$$

Besides, the boundary conditions are:

$$\mathbf{v}_0 = \begin{cases} i \mathbf{e}_z, & \mathbf{r} \in \mathcal{S}_0 \\ \mathbf{0}, & \mathbf{r} \in \mathcal{S}_\infty \cup \mathcal{S}_w \end{cases} \quad (1.104a)$$

$$\mathbf{v}_1 = \mathbf{0}, \quad \mathbf{r} \in \mathcal{S}_0 \cup \mathcal{S}_\infty \cup \mathcal{S}_w. \quad (1.104b)$$

The vertical force applied on the sphere is also expanded as $F_z = F_{z,0} + \text{Re } F_{z,1}$, such that the Eq. (1.100) at leading order $\mathcal{O}(\text{Re}^0)$, we get:

$$F_{z,0} = -i\hat{F}_z, \quad (1.105)$$

which is expected from the linearity of the Stokes equations, as we also have $\mathbf{v}_0 = -i\hat{\mathbf{v}}$. At first order $\mathcal{O}(\text{Re}^1)$, the inertial correction reads:

$$F_{z,1} = i \int_{\mathcal{V}} \hat{\mathbf{v}} \cdot \mathbf{v}_0 \, dV = \int_{\mathcal{V}} \hat{\mathbf{v}} \cdot \hat{\mathbf{v}} \, dV. \quad (1.106)$$

We compute the integral Eq. (1.106) numerically using the exact solution with the bi-spherical coordinates for the velocity field $\hat{\mathbf{v}}$ [136]. In cylindrical coordinates (r, θ, z) , the dimensionless integral reads:

$$\int_{\mathcal{V}} \hat{\mathbf{v}} \cdot \hat{\mathbf{v}} \, dV = \int_{\mathcal{V}} (\hat{v}_r^2 + \hat{v}_z^2) r \, dr \, dz \, d\theta. \quad (1.107)$$

Introducing the stream function of the flow:

$$\hat{v}_r = \frac{1}{r} \frac{\partial \psi}{\partial z}, \quad \hat{v}_z = -\frac{1}{r} \frac{\partial \psi}{\partial r}, \quad (1.108)$$

and using the bi-spherical coordinates $(\xi, \tilde{\eta}^3, \theta)$:

$$r = \sinh(\alpha) \frac{\sin \tilde{\eta}}{\cosh \xi - \cos \tilde{\eta}}, \quad z = \sinh(\alpha) \frac{\sinh \xi}{\cosh \xi - \cos \tilde{\eta}}. \quad (1.109)$$

The fluid domain is defined by $0 < \xi < \alpha$, and $0 < \tilde{\eta} < \pi$. By using the chain rule of a composite function, we find:

$$\frac{\partial \psi}{\partial \tilde{\eta}} = \frac{\partial z}{\partial \tilde{\eta}} \frac{\partial \psi}{\partial z} + \frac{\partial r}{\partial \tilde{\eta}} \frac{\partial \psi}{\partial r} = r \hat{v}_r \frac{\partial z}{\partial \tilde{\eta}} - r \hat{v}_z \frac{\partial r}{\partial \tilde{\eta}}, \quad (1.110)$$

$$\frac{\partial \psi}{\partial \xi} = \frac{\partial z}{\partial \xi} \frac{\partial \psi}{\partial z} + \frac{\partial r}{\partial \xi} \frac{\partial \psi}{\partial r} = r \hat{v}_r \frac{\partial z}{\partial \xi} - r \hat{v}_z \frac{\partial r}{\partial \xi}. \quad (1.111)$$

We can find a relation between the norm of the velocity field and the stream function as follows:

$$\left(\frac{\partial \psi}{\partial \tilde{\eta}} \right)^2 + \left(\frac{\partial \psi}{\partial \xi} \right)^2 = \frac{r^2 (\hat{v}_r^2 + \hat{v}_z^2) \sinh^2 \alpha}{(\cosh \xi - \cos \tilde{\eta})^2} = \frac{(\hat{v}_r^2 + \hat{v}_z^2) \sinh^4 \alpha \sin^2 \tilde{\eta}}{(\cosh \xi - \cos \tilde{\eta})^4} \quad (1.112)$$

such that the Eq.(1.107) becomes:

$$\int_{\mathcal{V}} (\hat{v}_r^2 + \hat{v}_z^2) \, dV = \int_{\mathcal{V}} \left[\left(\frac{\partial \psi}{\partial \xi} \right)^2 + \left(\frac{\partial \psi}{\partial \tilde{\eta}} \right)^2 \right] \frac{(\cosh \xi - \cos \tilde{\eta})^4}{\sinh^4 \alpha \sin^2 \tilde{\eta}} \, dV. \quad (1.113)$$

³Here, $\tilde{\eta}$ denotes the bi-spherical coordinates and should not be confused with the viscosity.

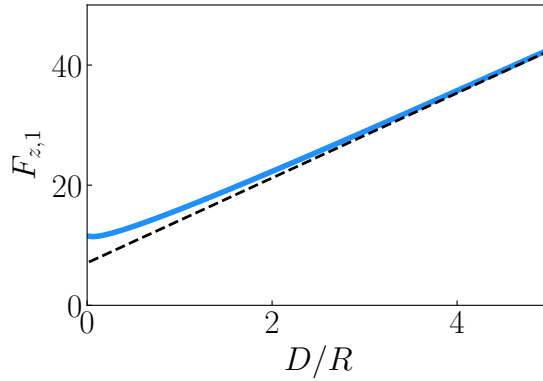


Figure 1.17: Dimensionless inertial correction to the Reynolds force, obtained by integrating numerically Eq. (1.106) (see Appendix A). The black dashed line displays the asymptotic result at large distance, see Eq. (1.120), as derived in Ref. [139].

Evaluating the Jacobian of the bi-spherical change of variable, we find that the infinitesimal volume element is $dV = \sinh^3 \alpha \sin \tilde{\eta} / (\cosh \xi - \cos \tilde{\eta})^3 d\xi d\tilde{\eta} d\theta$, which yields:

$$\int_{\mathcal{V}} \hat{\mathbf{v}} \cdot \hat{\mathbf{v}} dV = \int_{\mathcal{V}} \left[\left(\frac{\partial \psi}{\partial \xi} \right)^2 + \left(\frac{\partial \psi}{\partial \tilde{\eta}} \right)^2 \right] \frac{(\cosh \xi - \cos \tilde{\eta})}{\sinh \alpha \sin \tilde{\eta}} d\xi d\tilde{\eta} d\theta. \quad (1.114)$$

In bi-spherical coordinates, the stream function can be expanded on a spectral basis as:

$$\psi(\xi, \tilde{\eta}) = \frac{1}{(\cosh \xi - \cos \tilde{\eta})^{3/2}} \sum_{n \in \mathbb{N}} U_n(\xi) C_{n+1}^{-1/2}(\cos \tilde{\eta}), \quad (1.115)$$

$$U_n(\xi) = a_n \cosh\left(n - \frac{1}{2}\right)\xi + b_n \sinh\left(n - \frac{1}{2}\right)\xi + c_n \cosh\left(n + \frac{3}{2}\right)\xi + d_n \sinh\left(n + \frac{3}{2}\right)\xi, \quad (1.116)$$

and $C_{n+1}^{-1/2}$ is the Gegenbauer polynomial of order $n + 1$ and degree $-1/2$. Using the boundary conditions of the velocity field, written in Eq. (1.99), one can find the coefficients a_n, b_n, c_n, d_n as:

$$c_n = -a_n = \frac{n(n+1)(2n+1) \sinh^4 \alpha}{\sqrt{2} [4 \sinh^2(n + \frac{1}{2}) \alpha - (2n+1)^2 \sinh^2 \alpha]}, \quad (1.117)$$

$$d_n = -\frac{(2n-1)}{(2n+3)} b_n = -\frac{n(n+1) \sinh^2 \alpha}{\sqrt{2}(2n+3)} \left[\frac{2 \sinh(2n+1)\alpha + (2n+1) \sinh 2\alpha}{4 \sinh^2(n + \frac{1}{2}) \alpha - (2n+1)^2 \sinh^2 \alpha} - 1 \right]. \quad (1.118)$$

The integral Eq. (1.106) is then computed numerically, by evaluating the stream function on an uniform two-dimensional grid and using a Riemann summation. The dimensionless inertial force is then plotted in Fig. 1.17 versus the sphere-plan-distance-to-sphere-radius ratio. We observe that the dimensionless force has a finite limit as

$D/R \rightarrow 0$, leading to a mechanical impedance:

$$G^* \approx i \frac{6\pi\eta R^2 \omega}{D} - 11.5\rho R^3 \omega^2. \quad (1.119)$$

The prefactor 11.5 is found numerically. Furthermore, the force increases with the distance to the wall, following a linear function with D/R at large distance. In Ref. [139], using the method of reflections, the inertial force at large sphere-plan distance is found to be:

$$F = \frac{9\pi}{4} \rho R^2 \omega^2 Z^*(R + D), \quad (1.120)$$

which is in agreement with the numerical result in Fig. 1.17.

1.5 Conclusion

In the last fifteen years or so, contactless methods have been designed to measure the mechanical response of soft interfaces and successfully applied to elastic layers. Specifically, a spherical colloidal probe attached to the AFM cantilever is vibrated in a liquid environment close and normally to a sample (*e.g.* a soft surface) in order to generate a nanoscale lubrication flow. This viscous flow generates hydrodynamic stresses that may deform the soft surface, leading to an elasto-hydrodynamic coupling. Measurements of the mechanical impedance of the system permit to access the specific response of the sample. We question in this chapter extensions of contactless methods to soft interfaces that have a complex response.

Soft elastic materials often display dissipation within the material, resulting in a viscoelastic response. We investigate how the viscous character of elastic layers affects the mechanical impedance. The global shape of the impedance-distance curve, including the scaling with the probe-sample distance, is not modified by the presence of viscoelasticity, but the prefactors of the scaling laws are, showing a non-trivial dependence with the loss to storage modulus ratio. Such a model is then applied to experiments using PDMS elastomers as a sample. The frequency dependencies of the measured elastic moduli were found to be in good agreement with the Chasset–Thirion law for viscoelastic elastomers.

Soft gels are made of cross-linked networks, swollen by a solvent. Such materials are considered as porous, as the solvent may flow within the network. Using a linear poroelastic model for infinite-thickness substrate, we find that the mechanical impedance is a function of the oscillation frequency relative to a typical frequency scale that implies the permeability of the network, the solvent viscosity and the elastic modulus. Contactless methods are not suitable for the precise determination of the permeability of semi-infinite poroelastic materials, because of the similarity of the response in the full range of frequencies. The mechanical response of the poroelastic is very closed to the response of an elastic layer, with a rescaled elastic modulus: incompressible at large frequency and compressible at small frequency. As a perspective, it would

be interesting to extend the analysis for substrates of finite thicknesses which display different compressible and incompressible responses.

We then investigate the influence of the capillarity of the liquid-solid interface in elastic layers of infinite thicknesses. The mechanical impedance of the sphere is found to be largely affected by the capillarity of the soft substrate and via a specific dependence in a typical distance scale ℓ_{ec}^2/R , where $\ell_{ec} = \gamma/E$ is the elastocapillary length. A new scaling regime of the elastic part of the mechanical impedance at large distance ($\sim D^{-2}$) is found when the capillary response is dominant. Interestingly, the typical distance that emerges in the model, and that quantifies the magnitude of capillarity, scales increases with decreasing probe radius. Therefore, using small probes might be a good strategy to amplify capillary effects. Contactless methods appear as good candidate for an absolute determination of the capillarity of elastomers, and is a promising tool to measure the strain dependence of surface stresses in such materials.

Motivated by our findings on the capillarity of soft elastic layers, we turn to fluid-fluid interfaces. We have performed contactless experiments of the mechanical response of an air bubble pinned on a surface, and immersed within a surfactant solution in water. The mechanical impedance is found to depend on the bubble size. We also developed a model, coupling axisymmetric lubrication flow and capillary deformations, and accounting for finite-size effects through an asymptotic-matching method. The experimental results were found to be in good agreement with the model, the air-water surface tension being the single free parameter. Finally, from a comparison with independent tensiometry measurements using the Wilhelmy-plate method, we discussed the capacity of contactless methods to measure surface tensions robustly. The volume of the liquid required in our method can be as small as tens of microliters. All together, this work paves the way to contactless capillary rheology, with fundamental perspectives in confined soft matter, and practical applications towards micro-monitoring of water contamination.

In the low-Reynolds number limit, fluid inertia is known to induce a force on a moving sphere that is proportional to the acceleration of the sphere, analogous to extra inertia, and termed added mass. In the last section of the chapter, we focus on rigid surfaces, and compute the drag for applied on an oscillating sphere normally to a planar surface as in contactless methods. Using the Lorentz reciprocal theorem, we compute the added mass in the limit of a small Reynolds number, and find that the added mass depends on the sphere-plan distance. In particular, near the contact, and counterintuitively perhaps when considering the restricted volume of flowing matter, the added mass saturates to a value of $11.5\rho R^3$, larger than its value $2\pi\rho R^3/3$ for a sphere in an unbounded fluid domain. Furthermore, the added mass exhibits a non-monotonic dependence with the sphere-plan distance, as it increases linearly with the distance for $R \ll D \ll \delta$, but decreases at much larger distances to reach the unbounded value. In contactless experiments, the effective mass of the driven sphere probe (including the added mass) is calibrated far from the surface. Nevertheless, in a typical contactless experiments, when the sphere is bring close to the sampled surface, we can estimate the variation of added mass for a sphere to be on the order of $\Delta m \approx (11.5 - 2\pi/3)\rho R^3$. As a

result, it induces a variation of impedance on the cantilever on the order of $\sim 10\rho R^3\omega^2$. Using the numbers of the AFM experiments shown here, $\omega \simeq 200$ Hz, $R \simeq 50$ μm , and $\rho \simeq 10^3$ kg/m³, we find a variation of the impedance on the order of 2×10^{-3} N/m. However, we stress that if one works at a higher frequencies, typically the resonance frequency of the AFM probe ($\simeq 1.2$ kHz), we find an impedance ~ 0.07 N/m, which is not much smaller than the stiffness of the spring $\simeq 0.2$ N/m. This indicates that the added-mass dependence on the sphere-plan distance may perturb the contactless measurements. Lastly, in this work, we only computed the unsteady force in the *small Reynolds number* regime. Further work, *e.g.* solving the full unsteady Stokes equations numerically, would be necessary to have a complete description of the added mass and a more accurate prediction for its influence on contactless measurements.

Chapter 2

Soft-lubrication interactions between a rigid sphere and an elastic wall

2.1 Introduction

2.1.1 Context: interactions between flow and solids

An object or an interface moving in a fluid drags the molecules of the surrounding fluid along with it which induces a flow. As a result, any deformation of a solid drives a flow, and respectively, a flow may deform significantly a material. The so-called fluid-structure interaction between flows and solids is a central question in continuum mechanics, encountered at many length and velocity scales. To give a few examples, birds and fish deform their body and the resulting flow induces a propelling force, allowing them to fly or swim. Also, many objects are subjected to flows, either natural flows driven by wind and ocean currents, or man-made flows in the industry. It is of importance to understand the effects of flows on these objects in many situations, for instance to extract energy from the wind in wind power plants, but also to avoid the damaging of materials during extreme climate events or the wear of industrial devices.

Within the context of fluid-structure interactions, we focus in this chapter on the interaction between flows and solid deformations of *confined* objects. We consider all along the chapter the respective motion of two objects almost in contact, separated by a liquid film.

2.1.2 Surfaces near contact: lubrication

Friction

Before discussing the effects of the flowing liquid film in this system, let us briefly introduce the friction force between two surfaces in contact in a dry case. The classical sketch of such a system is drawn on the top right corner of Fig. 2.1a) and can be found

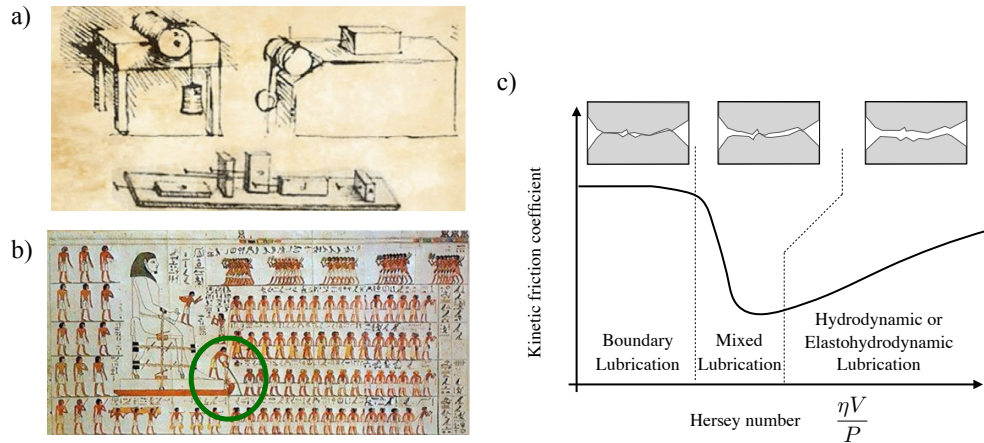


Figure 2.1: a) Drawing by Leonardo da Vinci in 1493 found in the Codex Madrid I. b) Wall painting from Ancient Egypt found in the tomb of Djehutihotep dated in 1880 B.C. The man circled in green is pouring liquid in front of the sliding support. c) Schematic of a Striebeck curve (Adapted from Ref. [145]). The kinetic friction coefficient is plotted versus the Hersey number $He = \eta V/P$. Three regimes : Boundary, Mixed, and Hydrodynamic are usually found and schematized. In my PhD thesis, I focus on the hydrodynamic and elastohydrodynamic regimes of lubrication.

in most general physics textbooks. An object, here in a form of a rectangular cuboid, is standing on a table, in contact with the latter via a normal load equal to its gravitational weight. The observation that one can make is that there is a certain minimal lateral force that must be applied to the object for it to be displaced laterally. Otherwise, it “sticks” to the surface. In addition, the minimal force is proportional to the normal force, which is known as the Amontons-Coulomb law in tribute to the French scientists *Guillaume Amontons* & *Charles-Augustin de Coulomb* [146, 147, 148]. The drawing in Fig. 2.1a) was made by Leonardo da Vinci in 1493 who is likely to be the actual pioneer of modern tribology¹. The proportionality factor between the normal load and the minimal lateral force is called the static friction coefficient and usually denoted μ_s . In addition, the friction coefficient does not depend on the apparent area of contact.

If the force applied to the object is exceeding the minimal force, the object moves with a given velocity and is subjected to a frictional force that resists the motion. The *kinetic* friction force is again proportional to the normal load, and the proportionality factor is called the kinetic friction coefficient μ_k which is generally smaller than the static one. Friction is an important quantity in contact mechanics, and designing surfaces with a well-controlled friction coefficient is a great challenge in material science. Usually, for industrial purposes, the goal is to minimize friction as it causes heating and

¹Tribology is the name for the science of interacting surfaces in contact, that includes friction, lubrication and wear.

damaging of the object².

The main way of reducing friction is the addition of a liquid film, called a lubricant, in between the two contacting objects. This strategy is known at least since the Ancient Egypt civilization as seen in Fig. 2.1b). On this wall painting dated 1880 B.C. and found in the tomb of Djehutihotep, a man is pouring liquid on the sand to lubricate the contact in order to facilitate the sliding of a giant statue. We notice that there is still a open debate on the precise reason of the use of the liquid, and some archaeologists have interpreted it as being purely ceremonial [150]. Later on in history, the discovery of oil in the 1860s in Pennsylvania (US) had a major impact on society. Besides the amazing features of oil as an energy source, its use as a lubricant is argued as being one of the most important technological outbreak of history, replacing animal grease, and allowing the development of modern industry in the late 19th century [151]. Lubricants are now widely spread in industry and used in roller bearings, pistons, and gears [152]. Lubrication is also encountered in various natural contexts such as in faults [153], and landslides [154].

Regimes of friction

The effect of a lubricant on the kinetic friction coefficient is usually explained through Stribeck curves, as schematized in Fig. 2.1c). The kinetic friction coefficient is plotted versus the so-called Hersey number $He = \eta V/P$, where η denotes the lubricant viscosity, V the sliding velocity, and P is the normal force per unit length. Three regimes are found in the friction coefficient. At small velocities, or high loading, the two solid surfaces are in direct contact at few points given by the asperities of the surfaces. This regime is called boundary lubrication and the friction coefficient is independent of the velocity and is equal to the dry kinetic friction discussed above. At the other limit, at high velocity or moderate loading, there is no direct contact between the solids that are separated by a continuous liquid film. The effective friction coefficient is smaller than in the boundary lubrication and increases with the velocity³. This regime is called hydrodynamic lubrication. Moreover, in some cases, the hydrodynamic pressure generated by the flow may be sufficient to deform the surfaces elastically in a so-called elastohydrodynamic (EHD) lubrication regime [152, 155], which is the main concern of this chapter. Lastly, in between these two regimes is a mixed lubrication regime where regions of continuous liquid film and regions of direct contact co-exist along the contact area.

Frictional properties are central to interfacial soft condensed matter, at very different pressure and velocity scales with respect to industrial lubricants. Notably, several biomaterials such as eyelids [156], cartilaginous joints [157, 158], as well as biomimetic gels [159] are found to have a remarkably low friction coefficient (down to 10^{-6}), which triggers a lot of questions at the frontier between biology and materials science. Indus-

²The amount of energy lost via friction and wear is estimated to be about 20 – 30% of the total energy consumption [149].

³It may eventually become larger than the dry-friction coefficient at very large velocity.

trial soft materials such as rubbers [160, 161, 162, 163] are also studied.

2.1.3 Particle dynamics near soft surfaces

Elastohydrodynamic interactions

Besides the lubricated sliding of surfaces in contact, the motion of particles in the vicinity of soft boundaries leads to other types of elastohydrodynamic lubrication interactions. We highlight some examples here. First, the approach of two surfaces, that occurs *e.g.* in the front collision between two soft spheres or the rebound of a sphere on a planar surface, requires the drainage flow of a thin lubrication film which is affected by the softness of the surfaces [65, 164, 165]. Similarly, the separation of two surfaces leads to a so-called viscous adhesion altered by the elastic properties of the solid [166, 167]. Secondly, dense suspensions, composed of colloidal particles immersed in a solvent, are widely spread in nature and industry (*e.g.* mug, cream, ...). The flow of such complex fluids implies at the microscopic level the relative motion of neighboring particles. A better understanding of the resulting hydrodynamic interactions between particles, including the role of the elastic properties of the latter, will help to understand the macroscopic rheology of suspensions [160, 168]. Thirdly, EHD interactions have a potential impact on the transport of biological entities. Indeed, the *in vivo* world is full of examples of particles that move in a confined environment, such as red blood cells in blood capillaries or vesicles inside cells [169, 170]. Lastly, contactless rheological methods have been recently introduced to measure the mechanical properties of confined liquids and soft surfaces using Atomic Force Microscopy or Surface Force Apparatus. These methods are based on the EHD interactions between a probe and a surface of interest and are discussed in Chapter 1.

Elastohydrodynamic lift force

Perhaps the most emblematic example of soft-lubrication interaction is the non-inertial lift force predicted for a particle sliding near a soft boundary [160, 171, 173, 174, 175, 176]. The origin of such a lift force is highlighted in Fig. 2.2a). A symmetric object sliding along and near a rigid boundary experiences no vertical force. This can be explained by the time-reversal symmetry of the Stokes equations. The object generates an antisymmetric pressure field in its direction of motion. However, for a soft interface, the hydrodynamic pressure field deforms the surface, breaking the fore-aft contact symmetry and inducing a lift force. The associated dynamical repulsion from an immersed soft interface has been studied experimentally only recently. A preliminary qualitative observation was reported in the context of smart lubricants and elastic polyelectrolytes [177]. Then, a study involving the sliding of an immersed macroscopic cylinder along an inclined plane pre-coated with a thin layer of gel, showed quantitatively an effective reduction of friction induced by the EHD lift force [116]. Subsequently, the same effect was observed in the trajectories of micrometric spherical beads within a microfluidic channel coated with a biomimetic polymer layer [178], and

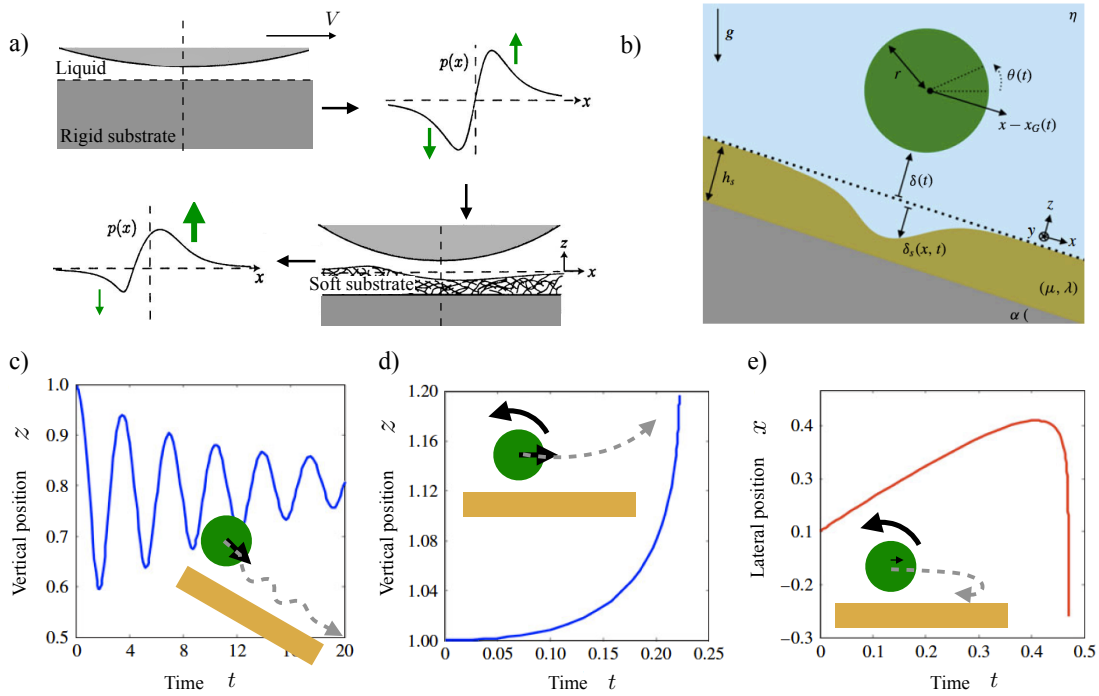


Figure 2.2: a) Principle of the Elastohydrodynamic lift force. The pressure field $p(x)$ induced by the sliding (velocity V) of a symmetric object (e.g. cylinder or sphere) near a rigid surface (top left) is antisymmetric with respect to direction of motion, as drawn in the top right panel. Thus, the normal force applied on the object is null, as the pressure field pushes and pulls with the same magnitude. However, if the substrate is soft, it gets deformed as in the bottom right panel. The deformation of the boundary modifies the resulting pressure field that is no-longer antisymmetric (bottom left), resulting in a net lift force. Adapted from Ref. [171]. b) The free dynamics of a rigid cylinder sliding and sedimenting near a soft wall is studied in Ref. [172]. Some resulting trajectories are reproduced in panels c)-e) with different slopes (45° in c) and 0° in d)-e) as shown in the inset) and initial conditions. The initial velocity and angular velocity are drawn with black arrows, the magnitude indicated through the linewidth. The trajectories are shown in grey.

through the sedimentation of a macroscopic sphere near a pre-tensed suspended elastic membrane [179]. Finally, measurements of the stresses between two sheared mica surfaces coated with a microgel surface revealed an out-of-equilibrium shear contribution attributed to elastohydrodynamic [180].

Inertia-like dynamic at zero Reynolds number

In a recent theoretical study by Salez & Mahadevan [172], the dynamics of an immersed free cylinder sliding over a soft inclined plane has been investigated [172] (see Fig. 2.2b)). By assuming: i) small liquid gap with respect to the cylinder radius, ii) small deformation of the planar surface with respect to the gap distance, iii) that the soft surface response follows the Winkler foundation (see section 2.6.1), they derived the equations of motion for the cylinder's trajectories including rotation. A numerical integration of the equations leads to intriguing particle trajectories, that depend on the slope of the plane and the initial conditions. As an illustration, we reproduce some of these trajectories in Fig. 2.2c)-e): a cylinder sedimenting on a 45° angle plane oscillates before reaching its steady position where the elastohydrodynamic lift force balances buoyancy [116]. A cylinder sliding and rotating over a flat surface may lift up (see Fig. 2.2d)), following a Magnus-like effect that is usually found in ball sports [181], or may follow a so-called spin-induced reversal for large initial rotational speed and change the direction of its lateral motion (see Fig 2.2e)). These features are widely spread in high Reynolds-number flows, *e.g.* in aeronautics, and may be recovered analogously here for viscous fluids due the action of soft boundaries.

Despite the increasing number of EHD studies involving spherical probes, and their relevance in colloidal science, the soft-lubrication interactions of a free spherical object immersed in a viscous fluid and moving near an elastic substrate still have to be calculated. In this chapter, we aim at filling this gap by deriving a soft-lubrication perturbation theory.

The present chapter is organized as follows. First, we introduce the soft-lubrication framework for a sphere translating near a soft planar surface, both in the normal and tangential directions. As a first step, the substrate deformation is assumed to follow the constitutive response of a linear elastic semi-infinite material. We then use a perturbative approach, assuming the substrate deformation to be small with respect to the fluid-gap thickness, which allows us to find the normal and tangential forces as well as the torque experienced by the sphere, at first order in dimensionless compliance. In complement, the EHD forces and torques are computed using the Lorentz reciprocal theorem, allowing for analytical results. We discuss the effect of the rotation of the sphere. In a second step, we focus on the compressible and incompressible responses of thin materials and compute the corresponding EHD forces. Lastly, we present some experimental measurements of the elastohydrodynamic lift force acting on a sphere moving within a viscous liquid and along a soft substrate, under nanometric confinement, showing good agreement with the aforementioned theory in the small-deformation limit. Some numerical calculations are introduced to discuss the large-deformation regime observed experimentally.

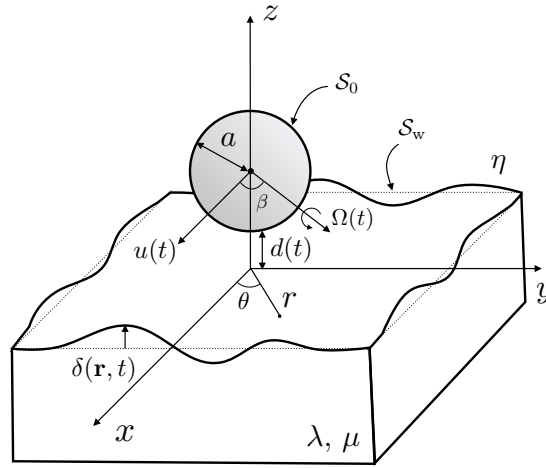


Figure 2.3: Schematic of the system. A rigid sphere of surface S_0 is freely moving in a viscous fluid, near a soft wall of surface S_w in the flat undeformed state. The lubrication pressure field deforms the latter which induces an elastohydrodynamic coupling, with forces and torque exerted on the sphere.

2.2 Elastohydrodynamic model

The system is depicted in Fig. 2.3. We consider a sphere of radius a , immersed in a Newtonian fluid of dynamic shear viscosity η and density ρ . The sphere is moving with a tangential velocity $\mathbf{u}(t) = u(t) \mathbf{e}_x$ directed along the x -axis (by definition of the latter axis), where \mathbf{e}_j denotes the unit vector along j . In this first section, we assume that the sphere does not rotate, *i.e.* the angular velocity reads $\boldsymbol{\Omega} = \mathbf{0}$. The sphere is placed at a time-dependent distance $d(t)$ (thus a $\dot{d} \mathbf{e}_z$ vertical velocity of the sphere) of an isotropic and homogeneous elastic substrate of Lamé coefficients λ and μ , with a reference undeformed flat surface in the xy plan at $z = 0$. We suppose that the sphere-wall distance is small with respect to the sphere radius, such that the lubrication approximation is valid. Fluid inertia is neglected here as we assume $\text{Re}(d/a) \ll 1$, where the Reynolds number is $\text{Re} = \rho a u / \eta$. Furthermore, we suppose that the typical time scale of variation of the sphere velocity is much larger than the diffusion time scale of vorticity that scales as $d^2 / (\eta / \rho)$, such that the fluid follows the steady Stokes equations. This amounts to assume $|\rho \dot{u} / u| \ll \eta / d^2$ and $|\rho \dot{d} / \dot{d}| \ll \eta / d^2$. No-slip boundary conditions are assumed at both the sphere and wall surfaces. Finally, the system is equivalent to a sphere at rest near a wall translating with a $-(d(t) \mathbf{e}_z + \mathbf{u}(t))$ velocity. In such a framework, the fluid velocity field can be written as:

$$\mathbf{v}(\mathbf{r}, z, t) = \frac{\nabla p(\mathbf{r}, t)}{2\eta} (z - h_0(r, t))(z - \delta(\mathbf{r}, t)) - \mathbf{u}(t) \frac{h_0(r, t) - z}{h_0(r, t) - \delta(\mathbf{r}, t)}, \quad (2.1)$$

where $\mathbf{r} = (r, \theta)$ is the position in the tangential plane xy , ∇ is the 2d gradient operator on xy , $\delta(\mathbf{r}, t)$ is the substrate deformation, and $z = h_0(r, t)$ is the sphere surface. Near

contact, the latter can be approximated by its parabolic expansion $h_0(r, t) \simeq d(t) + r^2/(2a)$. Volume conservation further leads to the Reynolds equation:

$$\partial_t h(\mathbf{r}, t) = \nabla \cdot \left(\frac{h^3(\mathbf{r}, t)}{12\eta} \nabla p(\mathbf{r}, t) + \frac{h(\mathbf{r}, t)}{2} \mathbf{u}(t) \right), \quad (2.2)$$

where $h(\mathbf{r}, t) = h_0(r, t) - \delta(\mathbf{r}, t)$ is the fluid-gap thickness. In the sections 2.2 to 2.5 of the chapter, we assume that the constitutive elastic response is linear and instantaneous, and that the substrate is a semi-infinite medium, such that the deformation reads:

$$\delta(\mathbf{r}, t) = -\frac{(\lambda + 2\mu)}{4\pi\mu(\lambda + \mu)} \int_{\mathbb{R}^2} d^2 \mathbf{x} \frac{p(\mathbf{x}, t)}{|\mathbf{r} - \mathbf{x}|}. \quad (2.3)$$

We non-dimensionalize the problem through:

$$h(\mathbf{r}, t) = d^* H(\mathbf{R}, T), \quad \mathbf{r} = \sqrt{2ad^*} \mathbf{R}, \quad d(t) = d^* D(T), \quad \delta(\mathbf{r}, t) = d^* \Delta(\mathbf{R}, T), \quad (2.4)$$

$$p(\mathbf{r}, t) = \frac{\eta c \sqrt{2ad^*}}{d^{*2}} P(\mathbf{R}, T), \quad \mathbf{u}(t) = c U(T) \mathbf{e}_x, \quad \mathbf{v} = c \mathbf{V}, \quad t = \frac{\sqrt{2ad^*}}{c} T. \quad (2.5)$$

where d^* and c are characteristic fluid-gap distance and lateral velocity, respectively. The governing equations are then:

$$12\partial_T H(\mathbf{R}, T) = \nabla \cdot \left(H^3(\mathbf{R}, T) \nabla P(\mathbf{R}, T) + 6H(\mathbf{R}, T) U(T) \right), \quad (2.6)$$

$$H(\mathbf{R}, T) = D(T) + R^2 - \Delta(\mathbf{R}, T), \quad (2.7)$$

and:

$$\Delta(\mathbf{R}, T) = -\kappa \int_{\mathbb{R}^2} d^2 \mathbf{X} \frac{P(\mathbf{X}, T)}{4\pi|\mathbf{R} - \mathbf{X}|}, \quad (2.8)$$

where we introduced the dimensionless compliance:

$$\kappa = \frac{2\eta ca(\lambda + 2\mu)}{d^{*2}\mu(\lambda + \mu)}. \quad (2.9)$$

The latter is the only dimensionless parameter in the problem. When κ is small with respect to unity, it corresponds to the ratio between two length scales: the typical substrate deformation $\delta \sim \frac{2\eta ca(\lambda + 2\mu)}{d^* \mu(\lambda + \mu)}$ induced by a lateral velocity c , and the typical fluid-gap thickness d^* . In most of the present chapter, we focus on the small-deformation regime of soft-lubrication where $\kappa \ll 1$ [182]. Some discussions on the intermediate-to-large-deformation regime are provided in section 2.7.3 with numerical solutions of Eqs. (2.2) and (2.3).

2.3 Perturbation theory

We perform a perturbation analysis at small κ [160, 171, 172, 173, 174, 175, 176, 183, 184, 185], as follows:

$$H(\mathbf{R}, T) = H_0(\mathbf{R}, T) + \kappa H_1(\mathbf{R}, T) + O(\kappa^2), \quad (2.10)$$

$$P(\mathbf{R}, T) = P_0(\mathbf{R}, T) + \kappa P_1(\mathbf{R}, T) + O(\kappa^2), \quad (2.11)$$

where the subscript 0 corresponds to the solution for a rigid wall, with $H_0(\mathbf{R}, T) = D(T) + R^2$.

2.3.1 Zeroth-order solution

Equation (2.6) reads at zeroth order $O(\kappa^0)$:

$$12\dot{D} = \nabla \cdot \left(H_0^3 \nabla P_0 + 6H_0 \mathbf{U} \right). \quad (2.12)$$

In polar coordinates, Eq. (2.12) can be rewritten as:

$$\mathcal{L}.P_0 = R^2 \partial_R^2 P_0 + \left(R + \frac{6R^3}{D + R^2} \right) \partial_R P_0 + \partial_\theta^2 P_0 = \frac{R^2}{(D + R^2)^3} \left(12\dot{D} - 12R \cos \theta U \right), \quad (2.13)$$

where \mathcal{L} is a linear operator. We solve this equation, using an angular-mode decomposition:

$$P_0(\mathbf{R}, T) = P_0^{(0)}(R, T) + P_0^{(1)}(R, T) \cos \theta, \quad (2.14)$$

where the two coefficients are solutions of the ordinary differential equations:

$$R^2 \frac{d^2 P_0^{(0)}}{dR^2} + \left(R + \frac{6R^3}{D + R^2} \right) \frac{dP_0^{(0)}}{dR} = 12 \frac{R^2 \dot{D}}{(D + R^2)^3}, \quad (2.15)$$

$$R^2 \frac{d^2 P_0^{(1)}}{dR^2} + \left(R + \frac{6R^3}{D + R^2} \right) \frac{dP_0^{(1)}}{dR} - P_0^{(1)} = -12 \frac{R^3 U}{(D + R^2)^3}. \quad (2.16)$$

In accordance with the boundary conditions, $P(R \rightarrow \infty) = 0$ and $P(R = 0) < \infty$, the solution is thus:

$$P_0(\mathbf{R}, T) = -\frac{3\dot{D}}{2(D + R^2)^2} + \frac{6RU \cos \theta}{5(D + R^2)^2}. \quad (2.17)$$

The substrate deformation H_1 can then be computed from Eq. (2.8) at order $O(\kappa)$:

$$H_1(\mathbf{R}, T) = \int_{\mathbb{R}^2} d^2 \mathbf{X} \frac{P_0(\mathbf{X}, T)}{4\pi |\mathbf{R} - \mathbf{X}|}. \quad (2.18)$$

Using *e.g.* the spatial Fourier transform $\tilde{H}_1(\mathbf{K}) = \int_{\mathbb{R}^2} H_1(\mathbf{R}) e^{-i\mathbf{R} \cdot \mathbf{K}} d^2 \mathbf{R}$, and the convolution theorem, we find:

$$H_1(\mathbf{R}, T) = -\frac{3\dot{D}}{8\sqrt{D}} \frac{\mathcal{E}(-R^2/D)}{D + R^2} + \frac{3U}{10R\sqrt{D}} \left(-\frac{D \mathcal{E}(-R^2/D)}{D + R^2} + \mathcal{K}(-R^2/D) \right) \cos \theta, \quad (2.19)$$

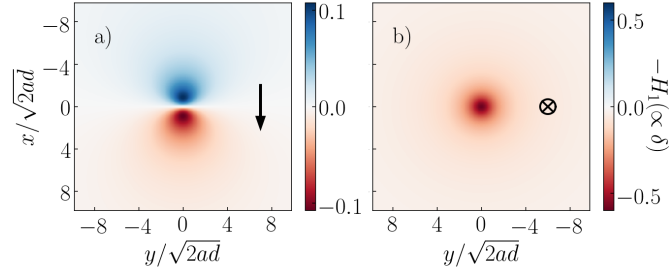


Figure 2.4: Dimensionless deformation field on the xy plane, for a sphere at a unit distance $D = 1$. In a), the sphere velocity is directed tangentially to the plane, along the x -axis, with $U = 1$, as indicated by the black arrow. In b) the sphere is approaching the plane with a unit velocity $\dot{D} = -1$.

where \mathcal{K} and \mathcal{E} are complete elliptic integrals of the first and second kinds [186]. The dimensionless hydrodynamically-induced substrate deformations are plotted in Fig 2.4. In Fig 2.4a), the sphere is moving tangentially to the plane only with a unit velocity $U = 1$. The deformation exhibits a “dipolar” symmetry with a negative component at the front of the sphere. The isotropic term generated by a sphere moving perpendicularly to the plane is shown in Fig. 2.4b). In particular, for a sphere approaching a soft substrate, the deformation is negative, *i.e.* an indentation of the substrate.

2.3.2 First-order solution

We can now compute the pressure field P_1 , from Eq. (2.6) at order $O(\kappa)$:

$$12\partial_T H_1 = \nabla \cdot \left(H_0^3 \nabla P_1 + 3H_0^2 H_1 \nabla P_0 + 6H_1 \mathbf{U} \right). \quad (2.20)$$

Invoking the same linear operator \mathcal{L} as in Eq. (2.13), we can rewrite Eq. (2.20) as:

$$\mathcal{L}.P_1 = \frac{R^2}{H_0^3} \left(12\partial_T H_1 - \nabla \cdot \left[3H_0^2 H_1 \nabla P_0 + 6H_1 \mathbf{U} \right] \right). \quad (2.21)$$

We then expand all the terms in the right-hand side of Eq. (2.21), and we perform once again the angular-mode decomposition:

$$\mathcal{L}.P_1 = F_0(R, T) + F_1(R, T) \cos \theta + F_2(R, T) \cos 2\theta, \quad (2.22)$$

where we have introduced the auxiliary functions:

$$\begin{aligned}
F_0(R, T) = & \frac{18R^2U^2}{25D^{1/2}(D+R^2)^6} \left[(-10D^2 + 2DR^2) \mathcal{E} \left(-\frac{R^2}{D} \right) \right. \\
& \left. + (8D^2 + 7DR^2 - R^4) \mathcal{K} \left(-\frac{R^2}{D} \right) \right] \\
& + \frac{9R^2\dot{D}^2}{4D^{3/2}(D+R^2)^6} \left[(13D^2 + 3R^2D + 2R^4) \mathcal{E} \left(-\frac{R^2}{D} \right) \right. \\
& \left. + (-4D^2 - 5R^2D - R^4) \mathcal{K} \left(-\frac{R^2}{D} \right) \right] \\
& - \frac{9R^2\ddot{D} \mathcal{E} \left(-\frac{R^2}{D} \right)}{2D^{1/2}(D+R^2)^4},
\end{aligned} \tag{2.23}$$

and:

$$\begin{aligned}
F_1(R, T) = & -\frac{27RU\dot{D}}{5D^{1/2}(D+R^2)^6} \left[(-2D^2 + 7DR^2 + R^4) \mathcal{E} \left(-\frac{R^2}{D} \right) \right. \\
& \left. + 2(D+R^2)(D-R^2) \mathcal{K} \left(-\frac{R^2}{D} \right) \right] \\
& - \frac{18R\dot{U}}{5D^{1/2}(D+R^2)^4} \left[-D \mathcal{E} \left(-\frac{R^2}{D} \right) + (D+R^2) \mathcal{K} \left(-\frac{R^2}{D} \right) \right].
\end{aligned} \tag{2.24}$$

Note that we have not provided the full expression of F_2 as it does not contribute in the forces and torque. Invoking the angular-mode decomposition $P_1(\mathbf{R}, T) = P_1^{(0)}(R, T) + P_1^{(1)}(R, T) \cos \theta + P_1^{(2)}(R, T) \cos 2\theta$, we get in particular:

$$R^2 \frac{d^2 P_1^{(0)}}{dR^2} + \left(R + \frac{6R^3}{D+R^2} \right) \frac{dP_1^{(0)}}{dR} = F_0(R, T), \tag{2.25}$$

$$R^2 \frac{d^2 P_1^{(1)}}{dR^2} + \left(R + \frac{6R^3}{D+R^2} \right) \frac{dP_1^{(1)}}{dR} - P_1^{(1)} = F_1(R, T). \tag{2.26}$$

Using scaling arguments, we can write the two relevant first-order pressure components $P_1^{(i)}$ as:

$$P_1^{(0)} = \frac{U^2}{D^{7/2}} \phi_{U^2}(R/\sqrt{D}) + \frac{\dot{D}^2}{D^{9/2}} \phi_{\dot{D}^2}(R/\sqrt{D}) + \frac{\ddot{D}}{D^{7/2}} \phi_{\ddot{D}}(R/\sqrt{D}), \tag{2.27}$$

and:

$$P_1^{(1)} = \frac{U\dot{D}}{D^4} \phi_{U\dot{D}}(R/\sqrt{D}) + \frac{\dot{U}}{D^3} \phi_{\dot{U}}(R/\sqrt{D}), \tag{2.28}$$

where the ϕ_i are five dimensionless scaling functions that depend on the self-similar variable R/\sqrt{D} only. Equations (2.27) and (2.28) can be solved numerically with a

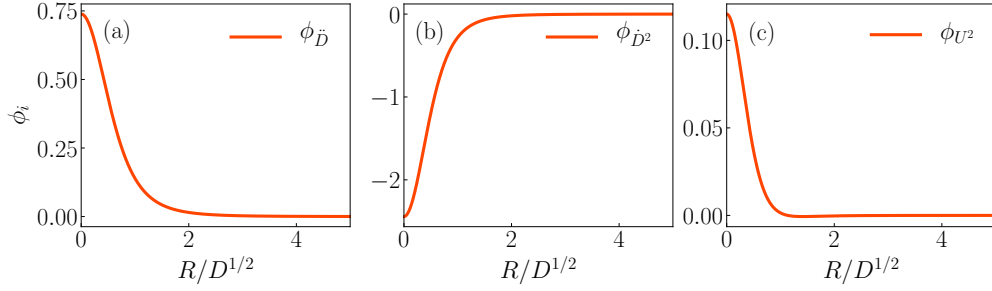


Figure 2.5: Scaling functions for $P_1^{(0)}$ (see Eq. (2.27)), obtained from numerical integration of Eq. (2.25), with the boundary conditions $\partial_R P_1^{(0)}(R = 0, T) = 0$ and $P_1^{(0)}(R \rightarrow \infty, T) = 0$.

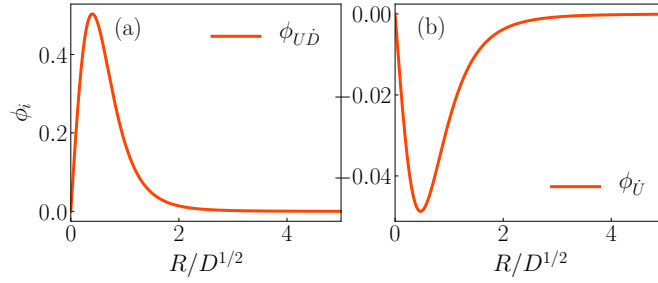


Figure 2.6: Scaling functions for $P_1^{(1)}$ (see Eq. (2.28)), obtained from numerical integration of Eq. (2.26), with the boundary conditions $P_1^{(1)}(R = 0, T) = 0$ and $P_1^{(1)}(R \rightarrow \infty, T) = 0$.

Runge-Kutta algorithm, and a shooting parameter in order to ensure the boundary condition $P_1(R \rightarrow \infty, \theta, T) = 0$. All the scaling functions are plotted in Figs. 2.5 and 2.6.

As a remark, we recall that the surface deformation is induced by the flow, and is linear in the velocity field (see Eq. (2.17)). Volume conservation equation involves the time derivative of the fluid-layer thickness and therefore the time derivative $\partial_t \delta$ of the surface deformation (see Eq. (2.2)). Thus, solving for the first-order EHD pressure field, we find terms proportional to the acceleration components of the sphere \ddot{D} and \ddot{U} , despite considering a steady Stokes flow.

2.3.3 Resulting force

The force \mathbf{F} exerted by the fluid on the sphere is given by:

$$\mathbf{F} = \int_{S_0} \mathbf{n} \cdot \boldsymbol{\sigma} \, ds, \quad (2.29)$$

where $\boldsymbol{\sigma} = -p\mathbf{I} + \eta(\nabla\mathbf{v} + \nabla\mathbf{v}^T)$ is the fluid stress tensor, \mathbf{n} is the unit vector normal to the sphere surface and pointing towards the fluid, and \mathbf{I} is the identity tensor. Within the lubrication approximation, the fluid stress tensor reads $\boldsymbol{\sigma} \simeq -p\mathbf{I} + \eta\mathbf{e}_z\partial_z\mathbf{v}$. One can then evaluate the vertical force as:

$$F_z = \int_{\mathbb{R}^2} p(\mathbf{r}) d^2\mathbf{r} = -\frac{6\pi\eta a^2 \dot{d}}{d} + 0.41623 \frac{\eta^2 u^2 (\lambda + 2\mu)}{\mu(\lambda + \mu)} \left(\frac{a}{d}\right)^{5/2} - 41.912 \frac{\eta^2 \dot{d}^2 (\lambda + 2\mu)}{\mu(\lambda + \mu)} \left(\frac{a}{d}\right)^{7/2} + 18.499 \frac{\eta^2 \ddot{d} a (\lambda + 2\mu)}{\mu(\lambda + \mu)} \left(\frac{a}{d}\right)^{5/2}, \quad (2.30)$$

where the prefactors have been found numerically using Eq. (2.27). We recover the classical Reynolds force $-6\pi\eta a^2 \dot{d}/d$ at zeroth order. Tangential motions do not induce any vertical force at zeroth order in κ , as the corresponding pressure field is antisymmetric in x (see Eq. (2.13)), but induce a lift force at first order in κ . Interestingly, vertical velocities generate a viscous adhesive force at first order in compliance [167]. Furthermore, a EHD force proportional to the sphere vertical acceleration is also found as discussed previously.

Similarly, at leading order in the lubrication parameter d/a , the tangential force reads:

$$\mathbf{F}_{\parallel} = \int_{\mathbb{R}^2} \left(-p(\mathbf{r}, t) \frac{\mathbf{r}}{a} - \eta \partial_z \mathbf{v} \right)_{z=h_0(\mathbf{r}, t)} d^2\mathbf{r}. \quad (2.31)$$

Using symmetry arguments, we can show that the tangential force is directed along x , *i.e.* $\mathbf{F}_{\parallel} = F_x \mathbf{e}_x$. At small κ , we further expand it as $F_x \simeq F_{x,0} + \kappa F_{x,1}$, where $F_{x,0}$ is the viscous drag force applied on a sphere near a rigid plane wall, and $\kappa F_{x,1}$ is the first-order EHD correction. The zeroth-order term cannot be evaluated using the lubrication model introduced in the previous section, because the integral in Eq. (2.31) diverges, as the shear term $\eta \partial_z \mathbf{v}$ scales as $\sim r^{-2}$ at large r . An exact calculation has been performed in Ref. [137] using bispherical coordinates and provides a solution in the form of a series expansion. Asymptotic-matching methods have also been employed in order to get the asymptotic behavior at small d/a [187, 188], which reads $F_{x,0} \approx 6\pi\eta a u \left(\frac{8}{15} \log\left(\frac{d}{a}\right) - 0.95429 \right)$ (see [189] for high-precision expansion). We notice that the sphere vertical velocity does not contribute to the zeroth-order lateral force by symmetry. Nevertheless, the first-order EHD correction can be computed with the present model, as the correction pressure field and shear stress scale as $\sim r^{-5}$, at large r . It reads:

$$F_{x,1} = 2\pi\eta c a \int_0^\infty \left[-2RP_1^{(1)} - \frac{H_0}{2} \left(\partial_R P_1^{(1)} + \frac{P_1^{(1)}}{R} \right) - \frac{H_1^{(1)}}{2} \partial_R P_0^{(0)} - \frac{H_1^{(0)}}{2} \left(\partial_R P_0^{(1)} + \frac{P_0^{(1)}}{R} \right) + 2 \frac{UH_1^{(0)}}{H_0^2} \right] R dR, \quad (2.32)$$

where $H_1^{(i)}$, with $i = 0, 1$, is the amplitude of the i^{th} mode in the angular-mode decomposition of H_1 . Evaluating the latter integral numerically, we find:

$$F_x \approx 6\pi\eta a u \left(\frac{8}{15} \log \left(\frac{d}{a} \right) - 0.95429 \right) - 10.884 \frac{\eta^2 u \dot{a} (\lambda + 2\mu)}{\mu(\lambda + \mu)} \left(\frac{a}{\bar{d}} \right)^{5/2} + 0.98661 \frac{\eta^2 \dot{a} a (\lambda + 2\mu)}{\mu(\lambda + \mu)} \left(\frac{a}{\bar{d}} \right)^{3/2}. \quad (2.33)$$

The torque exerted by the fluid on the sphere, with respect to its center of mass, is given by:

$$\mathbf{T} = \int_{S_0} a \mathbf{n} \times (\mathbf{n} \cdot \boldsymbol{\sigma}) ds. \quad (2.34)$$

The latter is directed along the y direction for symmetry reasons, *i.e.* $\mathbf{T} = T_y \mathbf{e}_y$. At small κ , we further expand it as $T_y \simeq T_{y,0} + \kappa T_{y,1}$. For the same reason as with the viscous drag force near a rigid wall, the viscous torque near a rigid wall cannot be computed within the lubrication model. Using asymptotic-matching methods [187], it is found to be $T_{y,0} \approx 8\pi\eta u a^2 \left(-\frac{1}{10} \log \left(\frac{d}{a} \right) - 0.19296 \right)$. However, the leading-order EHD correction can be computed with the present model, and reads:

$$T_{y,1} = -2\eta c a^2 \pi \int_0^\infty \left[\frac{H_0}{2} \left(\partial_R P_1^{(1)} + \frac{P_1^{(1)}}{R} \right) + \frac{H_1^{(1)}}{2} \partial_R P_0^{(0)} + \frac{H_1^{(0)}}{2} \left(\partial_R P_0^{(1)} + \frac{P_0^{(1)}}{R} \right) + 2 \frac{U H_1^{(0)}}{H_0^2} \right] R dR. \quad (2.35)$$

Evaluating the latter integral numerically, we find:

$$T_y \approx 8\pi\eta u a^2 \left(-\frac{1}{10} \log \left(\frac{d}{a} \right) - 0.19296 \right) + 10.884 \frac{\eta^2 u \dot{a} (\lambda + 2\mu)}{\mu(\lambda + \mu)} \left(\frac{a}{\bar{d}} \right)^{5/2} - 0.98661 \frac{\eta^2 \dot{a} a^2 (\lambda + 2\mu)}{\mu(\lambda + \mu)} \left(\frac{a}{\bar{d}} \right)^{3/2}. \quad (2.36)$$

So far, a numerical solution of the EHD flow has been obtained leading to a numerical calculation of the force and torque applied on the sphere. However, recently, an additional method has been introduced in the purpose of computing the force and torque only, using the Lorentz reciprocal theorem [144, 179, 184, 190]. In the next section, we introduce the Lorentz reciprocal theorem and show how it may be used in order to get the prefactors of Eqs. (2.30), (2.33) and (2.36) analytically.

2.4 Reciprocal theorem

2.4.1 Introduction

Reciprocity is a general concept in physics. To give an idea of its meaning, we start with a famous example in acoustic. The acoustic reciprocity principle states that the

sound received by a receptor B from a source in A is identical to the one of the situation where the source and receptor are interchanged [191]. Said in a trivial way, “if you can hear me, I can hear you”. The same principle holds in optics. However, reciprocity is not restricted to the wave propagating problems cited above, and one can find reciprocal theorems in other fields of physics and engineering such as : i) in electromagnetism via the Rayleigh-Carson reciprocity theorem [192, 193], ii) in elasticity via the Maxwell-Betti reciprocal work theorem [194], iii) in heat and mass transport [144]. It is usually written as a relation between the fields of any couple of solutions of the problem (*e.g.* Maxwell equations in electromagnetism) that share the same geometry. In general, a reciprocal theorem applies in equilibrium systems, when the fields are related through linear Hermitian operators.

A reciprocal theorem appeared in fluid mechanics in the late nineteenth century, and is attributed to the Dutch physicist Hendrik Lorentz [195]. In particular, two theorems exist in both low-Reynolds and high-Reynolds number flows and has been used in many contexts. To give a few examples, the reciprocal theorem allowed to set the basis for and develop the Boundary Element Methods to solve numerically the Stokes equation [138], and is a fantastic tool to compute the force applied on a particle in a flow including the effects of inertia, geometry, porosity, slip, self-propulsion, *etc...* See the recent review by Masoud & Stone [144] for a complete description. The great advantage of the so-called Lorentz reciprocal theorem is the simplicity of the resulting equation that consists of surface integrals on the boundary of the fluid domain. The fluid mechanics equations are generally a boundary value problem, with well-defined boundary conditions. Therefore, the Lorentz reciprocal theorem allows getting information about surface integrals such as the force and torques that are exerted by the fluid on an object, without the precise knowledge of the entire flow field. In particular, such methods have been introduced recently in soft lubrication to compute the EHD forces and torque on a cylinder and a sphere near a soft surface [179, 184, 190].

In the following subsections, we make use of the Lorentz reciprocal theorem for Stokes flows to compute the leading-order EHD forces that apply to the sphere. In the section 1.4.3, the Lorentz reciprocal theorem is used to investigate the influence of fluid inertia on a sphere oscillating perpendicularly to a planar surface.

2.4.2 Normal force

In this first part, we focus on the normal force exerted on the particle, and the lateral force is computed in section 2.4.3. To do so, we introduce the model problem of a sphere moving in a viscous fluid and towards an immobile, rigid, planar surface. We note $\hat{\mathbf{V}}_{\perp} = -\hat{V}_{\perp} \mathbf{e}_z$ the velocity at the particle surface S_0 , and we assume a no-slip boundary condition at the undeformed wall surface S_w located at $z = 0$ (see Fig. 2.3). The viscous stress and velocity fields of the model problem follow the steady, incompressible Stokes equations $\nabla \cdot \hat{\boldsymbol{\sigma}}_{\perp} = \mathbf{0}$ and $\nabla \cdot \hat{\mathbf{v}}_{\perp} = 0$, and we use the lubrication approximation. In

this framework, the stress tensor is $\hat{\boldsymbol{\sigma}}_{\perp} \simeq -\hat{p}_{\perp} \mathbf{I} + \eta \mathbf{e}_z \partial_z \hat{\mathbf{v}}_{\perp}$, with:

$$\hat{p}_{\perp}(\mathbf{r}) = \frac{3\eta \hat{V}_{\perp} a}{\hat{h}^2(\mathbf{r})}, \quad \hat{\mathbf{v}}_{\perp}(\mathbf{r}, z) = \frac{\nabla \hat{p}_{\perp}(\mathbf{r})}{2\eta} z(z - \hat{h}(\mathbf{r})), \quad \hat{h}(\mathbf{r}) = d + \frac{r^2}{2a}. \quad (2.37)$$

The Lorentz reciprocal theorem states that:

$$\int_{\mathcal{S}} \mathbf{n} \cdot \boldsymbol{\sigma} \cdot \hat{\mathbf{v}}_{\perp} \, ds = \int_{\mathcal{S}} \mathbf{n} \cdot \hat{\boldsymbol{\sigma}}_{\perp} \cdot \mathbf{v} \, ds, \quad (2.38)$$

where $\mathcal{S} = \mathcal{S}_0 + \mathcal{S}_w + \mathcal{S}_{\infty}$ is the total surface bounding the flow, and \mathcal{S}_{∞} is the surface located at $\mathbf{r} \rightarrow \infty$. The latter does not contribute here. Using the boundary conditions for the model problem, we get:

$$\hat{V}_{\perp} \cdot \mathbf{F} = -\hat{V}_{\perp} F_z = \int_{\mathcal{S}} \mathbf{n} \cdot \hat{\boldsymbol{\sigma}}_{\perp} \cdot \mathbf{v} \, ds. \quad (2.39)$$

To find the force exerted on the sphere in the real problem, one needs to specify the boundary conditions for the velocity field \mathbf{v} which is the only unknown here. We assume that the sphere does not rotate, as in section 2.3, and we recall that the flow is given in the translating frame of the particle. The no-slip boundary condition thus reads $\mathbf{v} = \mathbf{0}$ on \mathcal{S}_0 . To perform the calculation here, we further assume a small deformation of the wall, so that the velocity field at the undeformed wall surface can be obtained using the Taylor expansion:

$$\begin{aligned} \mathbf{v}|_{z=0} &\simeq \mathbf{v}|_{z=\delta} - \delta \partial_z \mathbf{v}|_{z=0} \\ &\simeq -u \mathbf{e}_x - \dot{d} \mathbf{e}_z + (\partial_t - u \partial_x) \delta \mathbf{e}_z - \delta \partial_z \mathbf{v}|_{z=0}, \end{aligned} \quad (2.40)$$

where \mathbf{v}_0 is the zeroth-order velocity field near a rigid surface and where the kinematic condition is used. The Taylor expansion performed above is equivalent to the perturbation theory introduced in section 2.3. Using the zeroth-order flow computed in section 2.3.1, we find:

$$\partial_z \mathbf{v}_0|_{z=0} = -\frac{3\dot{d}r}{(d + \frac{r^2}{2a})^2} \mathbf{e}_r + \frac{2u}{5(d + \frac{r^2}{2a})} \left(\left(7 - \frac{6d}{d + \frac{r^2}{2a}} \right) \cos \theta \mathbf{e}_r - \sin \theta \mathbf{e}_{\theta} \right). \quad (2.41)$$

Combining Eqs. (2.37) and (2.39), we find the vertical force:

$$F_z = \frac{1}{\hat{V}_{\perp}} \int_{\mathbb{R}^2} \left(\hat{p}_{\perp}(-\dot{d} + \partial_t \delta - u \partial_x \delta) + \eta \partial_z \hat{\mathbf{v}}_{\perp}|_{z=0} \cdot \partial_z \mathbf{v}_0|_{z=0} \delta \right) d\mathbf{r}. \quad (2.42)$$

The integrals are computed in Fourier space, using the Parseval's theorem, $\int_{\mathbb{R}^2} f(\mathbf{R})g(\mathbf{R})d^2\mathbf{R} = \int_{\mathbb{R}^2} \tilde{f}(\mathbf{K})\tilde{g}^*(\mathbf{K})d^2\mathbf{K}/(2\pi)^2$, and we recover the same expression as in Eq. (2.30), that reads:

$$\begin{aligned} F_z &= -\frac{6\pi\eta a^2 \dot{d}}{d} + \frac{243\pi^3}{12800\sqrt{2}} \frac{\eta^2 u^2 (\lambda + 2\mu)}{\mu(\lambda + \mu)} \left(\frac{a}{\bar{d}} \right)^{5/2} \\ &\quad - \frac{3915\pi^3}{2048\sqrt{2}} \frac{\eta^2 \dot{d}^2 (\lambda + 2\mu)}{\mu(\lambda + \mu)} \left(\frac{a}{\bar{d}} \right)^{7/2} + \frac{27\pi^3}{32\sqrt{2}} \frac{\eta^2 \ddot{d} a (\lambda + 2\mu)}{\mu(\lambda + \mu)} \left(\frac{a}{\bar{d}} \right)^{5/2}. \end{aligned} \quad (2.43)$$

Details of the calculations are provided in Appendix A. The prefactors found here are in very good agreement with the numerical integration in section 2.3.3, confirming both methods.

2.4.3 Lateral force

In order to compute the lateral force acting on the particle, we apply the Lorentz reciprocal theorem, but introducing a different model problem with respect to the latter section. We consider a sphere translating parallel to a rigid immobile plane, with a velocity \hat{V}_{\parallel} along the x-axis, with no-slip boundary conditions at both the sphere and plane surfaces. The velocity and stress fields are denoted $\hat{\sigma}_{\parallel}$ and \hat{v}_{\parallel} respectively and are solutions of the Stokes equations. The lubrication approximation is used here, and the solution reads:

$$\hat{p}_{\parallel}(\mathbf{r}) = \frac{6\eta\hat{V}_{\parallel}r\cos\theta}{5\hat{h}^2(\mathbf{r})}, \quad \hat{v}_{\parallel}(\mathbf{r}, z) = \frac{\nabla\hat{p}_{\parallel}(\mathbf{r})}{2\eta}z(z - \hat{h}(\mathbf{r})) + \hat{V}_{\parallel}\frac{z}{\hat{h}(\mathbf{r})}, \quad (2.44)$$

as shown in the section 2.3.1, for the same problem written in the reference frame of the sphere. The Lorentz reciprocal theorem leads to:

$$\hat{V}_{\parallel} \cdot \mathbf{F} = \hat{V}_{\parallel} F_x = \int_S \mathbf{n} \cdot \hat{\sigma}_{\parallel} \cdot \mathbf{v} \, ds. \quad (2.45)$$

Using the lubrication expression of the stress tensor of the model problem, $\hat{\sigma}_{\parallel} \simeq -\hat{p}_{\parallel}\mathbf{I} + \eta\mathbf{e}_z\partial_z\hat{v}_{\parallel}$, we get an expression for the lateral force as:

$$F_x = \frac{1}{\hat{V}_{\parallel}} \int_{\mathbb{R}^2} \left[-\eta\partial_z\hat{v}_{\parallel} \cdot u(t)\mathbf{e}_x - \hat{p}_{\parallel}(\partial_t - u(t)\partial_x)\delta - \eta(\partial_z\hat{v}_{\parallel} \cdot \partial_z\mathbf{v}_0)\delta \right] d\mathbf{r}. \quad (2.46)$$

For the same reason as the one invoked in section 2.3.3, the zeroth-order tangential drag force (term in $-\eta\partial_z\hat{v}_{\parallel} \cdot u(t)\mathbf{e}_x$ in Eq. (2.46)) cannot be computed here as the integral diverges within the lubrication approximation. However, the first-order EHD force, denoted $F_{x,1}$, converges and is computed in Fourier space using Parseval's theorem.

$$\kappa F_{x,1} = -\frac{3177\pi^3}{6400\sqrt{2}} \frac{\eta^2 u \dot{d}(\lambda + 2\mu)}{\mu(\lambda + \mu)} \left(\frac{a}{d}\right)^{5/2} + \frac{9\pi^3}{200\sqrt{2}} \frac{\eta^2 \dot{u} a(\lambda + 2\mu)}{\mu(\lambda + \mu)} \left(\frac{a}{d}\right)^{3/2}. \quad (2.47)$$

The details of the calculation are provided in Appendix A, and the prefactors are in very good agreement with the numerical calculations in section 2.3.3.

2.5 Rotation of the sphere

We now add the rotation of the sphere, with angular velocity $\mathbf{\Omega}(t)$ in the xy plane (see Fig. 2.3), to the previous translational motion. We define β as the angle between $\mathbf{\Omega}$ and the x -axis. We stress that $\mathbf{\Omega}$ is not necessarily orthogonal (*i.e.* $\beta = \pi/2$) to the translation

velocity. We discard the rotation along the z -axis (e.g. for a spinner), because it does not induce any soft-lubrication coupling. Finally, the system is equivalent to a purely rotating sphere with angular velocity $\boldsymbol{\Omega}(t)$, near a wall translating with a $-\mathbf{u}(t)$ velocity. In such a framework, the fluid velocity field at the sphere surface is $\mathbf{v} = -\boldsymbol{\Omega} \times a\mathbf{n}$, and thus $\mathbf{v} \simeq \boldsymbol{\Omega} \times a\mathbf{e}_z$ at leading order in the lubrication parameter. All together, the fluid velocity field is modified as:

$$\begin{aligned} \mathbf{v}(\mathbf{r}, z, t) = & \frac{\nabla p(\mathbf{r}, t)}{2\eta} (z - h_0(r, t))(z - \delta(\mathbf{r}, t)) - \mathbf{u}(t) \frac{h_0(r, t) - z}{h_0(r, t) - \delta(\mathbf{r}, t)} \\ & + a\boldsymbol{\Omega}(t) \times \mathbf{e}_z \frac{z - \delta(\mathbf{r}, t)}{h_0(r, t) - \delta(\mathbf{r}, t)}, \end{aligned} \quad (2.48)$$

and the Reynolds equation becomes:

$$\partial_t h(\mathbf{r}, t) = \nabla \cdot \left(\frac{h^3(\mathbf{r}, t)}{12\eta} \nabla p(\mathbf{r}, t) + \frac{h(\mathbf{r}, t)}{2} \underbrace{\left[\mathbf{u}(t) - a\boldsymbol{\Omega}(t) \times \mathbf{e}_z \right]}_{\tilde{\mathbf{u}}} \right). \quad (2.49)$$

The problem is thus formally equivalent to the one of a sphere that is purely translating with effective velocity $\tilde{\mathbf{u}}(t) = \mathbf{u}(t) - a\boldsymbol{\Omega}(t) \times \mathbf{e}_z$. Therefore, we can directly apply the results from the previous sections, and write all the forces and torque exerted on the sphere, as:

$$\begin{aligned} F_z = & -\frac{6\pi\eta a^2 \dot{d}}{d} + \frac{243\pi^3}{12800\sqrt{2}} \frac{\eta^2 |\mathbf{u} - a\boldsymbol{\Omega} \times \mathbf{e}_z|^2}{\mu} \left(\frac{a}{d}\right)^{5/2} \\ & - \frac{3915\pi^3}{2048\sqrt{2}} \frac{\eta^2 \dot{d}^2}{\mu} \left(\frac{a}{d}\right)^{7/2} + \frac{27\pi^3}{32\sqrt{2}} \frac{\eta^2 \ddot{d}a}{\mu} \left(\frac{a}{d}\right)^{5/2}, \end{aligned} \quad (2.50)$$

$$\begin{aligned} \mathbf{F}_{\parallel} = & 6\pi\eta a \mathbf{u} \left[\frac{8}{15} \log\left(\frac{d}{a}\right) - 0.95429 \right] + 6\pi\eta a^2 \mathbf{e}_z \times \boldsymbol{\Omega} \left[\frac{2}{15} \log\left(\frac{d}{a}\right) + 0.25725 \right] \\ & - \frac{3177\pi^3}{6400\sqrt{2}} \frac{\eta^2 (\mathbf{u} - a\boldsymbol{\Omega} \times \mathbf{e}_z) \dot{d}}{\mu} \left(\frac{a}{d}\right)^{5/2} + \frac{9\pi^3}{200\sqrt{2}} \frac{\eta^2 (\dot{\mathbf{u}} - a\dot{\boldsymbol{\Omega}} \times \mathbf{e}_z) a}{\mu} \left(\frac{a}{d}\right)^{3/2}, \end{aligned} \quad (2.51)$$

and:

$$\begin{aligned} \mathbf{T}_{\parallel} = & 8\pi\eta a^2 \mathbf{e}_z \times \mathbf{u} \left[-\frac{1}{10} \log\left(\frac{d}{a}\right) - 0.19296 \right] + 8\pi\eta a^3 \boldsymbol{\Omega} \left[\frac{2}{5} \log\left(\frac{d}{a}\right) - 0.37085 \right] \\ & + \frac{3177\pi^3}{6400\sqrt{2}} \frac{\eta^2 (\mathbf{u} - a\boldsymbol{\Omega} \times \mathbf{e}_z) a \dot{d}}{\mu} \left(\frac{a}{d}\right)^{5/2} - \frac{9\pi^3}{200\sqrt{2}} \frac{\eta^2 (\dot{\mathbf{u}} - a\dot{\boldsymbol{\Omega}} \times \mathbf{e}_z) a^2}{\mu} \left(\frac{a}{d}\right)^{3/2}, \end{aligned} \quad (2.52)$$

where we have invoked the force and torque induced by the rotation of a sphere near a rigid wall [176, 188].

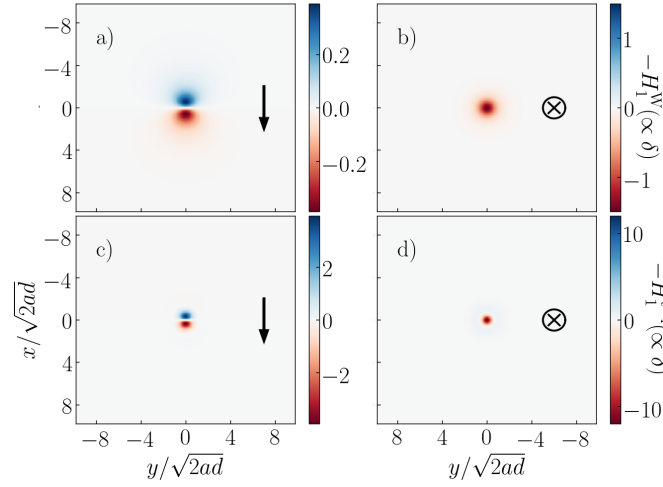


Figure 2.7: Dimensionless deformation field on the xy plane for a thin substrate, using the same representation as in Fig. 2.4. In a) and b) the soft surface mechanical response follows the Winkler foundation of Eq. (2.53), while in c) and d) the surface mechanical response is the one of a thin incompressible layer, see Eq. (2.64).

2.6 Response of thin-elastic layers

So far, we have focused on the situation where the mechanical response of the surface is the one of a thick elastic material, modeled as a semi-infinite elastic medium. However, thin elastic materials such as polymer thin films (see Part II) are widely spread in material sciences and biology. As a result, we investigate the EHD interactions exerted on a sphere immersed in a viscous fluid and near a thin compressible substrate in section 2.6.1 and a thin incompressible substrate in section 2.6.2 (see section 1.1.4).

2.6.1 Compressible elastic material

In this section, we derive the EHD interactions exerted on a sphere immersed in a viscous fluid and near a thin compressible substrate of thickness h_{sub} . The deformation field follows the Winkler foundation [66]:

$$\delta(\mathbf{r}, t) = -\frac{h_{\text{sub}}}{(2\mu + \lambda)} p(\mathbf{r}, t), \quad (2.53)$$

which is valid for substrates of thickness smaller than the typical lateral extent of the pressure field, namely the hydrodynamic radius $\sqrt{2ad}$ [60, 196, 197]. We perform the same asymptotic expansion as the one in section 2.3, defining the Winkler dimensionless compliance as [172]:

$$\kappa^{\text{W}} = \frac{\sqrt{2}h_{\text{sub}}\eta ca^{1/2}}{d^{*5/2}(2\mu + \lambda)}. \quad (2.54)$$

The substrate deformation, or equivalently here the zeroth-order pressure, reads:

$$H_1^W(\mathbf{R}, T) = P_0(\mathbf{R}, T) = \frac{3\dot{D}}{2(D + R^2)^2} + \frac{6RU \cos \theta}{5(D + R^2)^2}. \quad (2.55)$$

The deformation field is plotted in Fig. 2.7a) and b) for lateral and vertical motions of the sphere respectively. The deformation exhibits the same structure as the one in Fig. 2.4 for semi-infinite substrates, but the lateral extent of the deformation is narrower. This is expected as the deformation field induced by an applied load for a thin-compressible layer is local (see Eq. (2.53)), while a semi-infinite substrate displays non-local effects via its Green's function (see Eq. (2.3)). The first-order pressure correction follows the same type of equation as in section 2.3:

$$\mathcal{L}.P_1^W = F_0^W(R, T) + F_1^W(R, T) \cos \theta + F_2^W(R, T) \cos 2\theta, \quad (2.56)$$

with:

$$F_0^W(R, T) = -\frac{144R^2U^2}{25(D + R^2)^7} \left[D^2 - 6DR^2 + R^4 \right] + \frac{18R^2\dot{D}^2}{(D + R^2)^7} \left[5D - 4R^2 \right] - \frac{18R^2\ddot{D}}{(D + R^2)^5}, \quad (2.57)$$

and:

$$F_1^W(R, T) = \frac{216R^3U\dot{D}}{5(D + R^2)^7} \left[-5D + R^2 \right] + \frac{72R\dot{U}}{5(D + R^2)^5}. \quad (2.58)$$

We note that F_2^W does not contribute for the forces and torque, as in section 2.3. The isotropic component of the pressure can be found analytically, using polynomial fractions, as:

$$P_1^{W,(0)}(R, T) = \frac{9}{125} \frac{7 - 5Y^2}{(1 + Y^2)^5} \frac{U^2}{D^4} - \frac{3}{40} \frac{71 + 55Y^2 + 30Y^4}{(1 + Y^2)^5} \frac{\dot{D}^2}{D^5} + \frac{3}{2} \frac{1}{(1 + Y^2)^3} \frac{\ddot{D}}{D^4}, \quad (2.59)$$

where $Y = R/D^{1/2}$ is the self-similar variable. However, the first angular component of the pressure does not exhibit such an analytical solution, and is thus found as in section 2.3 by numerical integration of two scaling functions:

$$P_1^{W,(1)}(R, T) = \frac{U\dot{D}}{D^{9/2}} \phi_{UD}^W \left(\frac{R}{D^{1/2}} \right) + \frac{\dot{U}}{D^{7/2}} \phi_U^W \left(\frac{R}{D^{1/2}} \right). \quad (2.60)$$

Following the same calculation as in section 2.3, we find the vertical force as:

$$F_z^W = -\frac{6\pi\eta a^2 \dot{d}}{d} + \frac{48\pi}{125} \frac{\eta^2 u^2 h_{\text{sub}}}{a(2\mu + \lambda)} \left(\frac{a}{d} \right)^3 - \frac{72\pi}{5} \frac{\eta^2 \dot{d}^2 h_{\text{sub}}}{a(2\mu + \lambda)} \left(\frac{a}{d} \right)^4 + \frac{6\pi\eta^2 \ddot{d} h_{\text{sub}}}{(2\mu + \lambda)} \left(\frac{a}{d} \right)^3. \quad (2.61)$$

We stress that the prefactors $48\pi/125$ and 6π are in agreement with the results obtained in Refs. [175] and [60], respectively. Similarly, the force along x reads:

$$F_x^W = 6\pi\eta a u \left(\frac{8}{15} \log \left(\frac{d}{a} \right) - 0.95429 \right) - \frac{484\pi}{125} \frac{\eta^2 u \dot{d} h_{\text{sub}}}{a(2\mu + \lambda)} \left(\frac{a}{d} \right)^3 + \frac{12\pi}{25} \frac{\eta^2 \dot{u} h_{\text{sub}}}{(2\mu + \lambda)} \left(\frac{a}{d} \right)^2, \quad (2.62)$$

which has been computed using the Lorentz reciprocal theorem following the section 2.4.3. The torque can be evaluated as well, and reads:

$$T_y^W = 8\pi\eta u a^2 \left(-\frac{1}{10} \log\left(\frac{d}{a}\right) - 0.19296 \right) + \frac{484\pi\eta^2 u d h_{\text{sub}}}{125(2\mu + \lambda)} \left(\frac{a}{d}\right)^3 - \frac{12\pi\eta^2 u a h_{\text{sub}}}{25(2\mu + \lambda)} \left(\frac{a}{d}\right)^2. \quad (2.63)$$

Finally, following section 2.5, it is straightforward to generalize Eqs. (2.61), (2.62) and (2.63) in order to incorporate rotation.

2.6.2 The incompressible limit

Here, we suppose that the substrate of thickness h_{sub} is incompressible, *i.e.* of Poisson ratio $\nu = \frac{\lambda}{2(\lambda + \mu)} = 1/2$, which means that the first Lamé coefficient λ is infinite. In this situation, the Winkler foundation is not valid. Instead, the mechanical response of a thin substrate follows the relation ([60, 196]):

$$\delta(\mathbf{r}, t) = \frac{h_{\text{sub}}^3}{3\mu} \nabla^2 p(\mathbf{r}, t), \quad (2.64)$$

where ∇^2 denotes the 2d Laplacian operator. We perform the same asymptotic expansion as the one in section 2.3, defining the thin-incompressible dimensionless compliance as:

$$\kappa^{\text{t-i}} = \frac{\eta c h_{\text{sub}}^3}{3\sqrt{2}\mu d^{*7/2} a^{1/2}}. \quad (2.65)$$

The substrate deformation reads:

$$H_1^{\text{t-i}}(\mathbf{R}, T) = -\nabla^2 P_0(\mathbf{R}, T) = -\frac{12\dot{D}(D - 2R^2)}{(D + R^2)^4} + \frac{48RU(2D - R^2)\cos\theta}{5(D + R^2)^4}. \quad (2.66)$$

The deformation fields is plotted in Figs. 2.7c) and d). The first-order pressure correction follows the same type of equation as in section 2.3:

$$\mathcal{L}.P_1^{\text{t-i}} = F_0^{\text{t-i}}(R, T) + F_1^{\text{t-i}}(R, T)\cos\theta + F_2^{\text{t-i}}(R, T)\cos 2\theta, \quad (2.67)$$

with:

$$F_0^{\text{t-i}}(R, T) = \frac{1152R^2U^2(R^2 - 2D)(+2D^2 - 11R^2D + 2R^4)}{25(D + R^2)^9} + \frac{432R^2(2D(D - 5R^2) + 3R^4)\dot{D}^2}{(D + R^2)^9} + \frac{144R^2(2R^2 - D)\ddot{D}}{(D + R^2)^7}, \quad (2.68)$$

and:

$$F_1^{\text{t-i}}(R, T) = -\frac{2592R^3\dot{D}U(7D^2 - 12R^2D + R^4)}{5(D + R^2)^9} - \frac{576R^3\dot{U}(-2D + R^2)}{5(D + R^2)^7}. \quad (2.69)$$

We note that $F_2^{\text{t-i}}$ does not contribute for the forces and torque, as in section 2.3. The isotropic component of the pressure can be found analytically, using polynomial fractions, as:

$$P_1^{\text{t-i},(0)}(R, T) = \frac{288(7Y^4 - 21Y^2 + 17)}{875(1 + Y^2)^7} \frac{U^2}{D^5} + \frac{126Y^2 - 198}{7(1 + Y^2)^7} \frac{\dot{D}^2}{D^6} + \frac{36}{5(1 + Y^2)^5} \frac{\ddot{D}}{D^5}, \quad (2.70)$$

where $Y = R/D^{1/2}$ is the self-similar variable. However, the first angular component of the pressure does not exhibit such an analytical solution, and is thus found as in section 2.3 by numerical integration of two scaling functions:

$$P_1^{\text{t-i},(1)}(R, T) = \frac{U\dot{D}}{D^{11/2}} \phi_{U\dot{D}}^{\text{t-i}}\left(\frac{R}{D^{1/2}}\right) + \frac{\dot{U}}{D^{9/2}} \phi_{\dot{U}}^{\text{t-i}}\left(\frac{R}{D^{1/2}}\right). \quad (2.71)$$

Following the same calculation as in section 2.3, we find the vertical force as:

$$F_z^{\text{t-i}} = -\frac{6\pi\eta a^2 \dot{d}}{d} + \frac{432\pi}{875} \frac{\eta^2 u^2 h_{\text{sub}}^3}{a^3 \mu} \left(\frac{a}{\bar{d}}\right)^4 - \frac{192\pi}{35} \frac{\eta^2 d^2 h_{\text{sub}}^3}{a^3 \mu} \left(\frac{a}{\bar{d}}\right)^5 + \frac{12\pi}{5} \frac{\eta^2 \dot{d} h_{\text{sub}}^3}{a^2 \mu} \left(\frac{a}{\bar{d}}\right)^4. \quad (2.72)$$

We stress that the prefactor $12\pi/5$ is consistent with the linear-response theory in [60]. Similarly, the force along x reads:

$$F_x^{\text{t-i}} = 6\pi\eta a u \left(\frac{8}{15} \log\left(\frac{d}{a}\right) - 0.95429\right) - \frac{64\pi}{35} \frac{\eta^2 u d h_{\text{sub}}^3}{a^3 \mu} \left(\frac{a}{\bar{d}}\right)^4 + \frac{32\pi}{125} \frac{\eta^2 \dot{u} h_{\text{sub}}^3}{a^2 \mu} \left(\frac{a}{\bar{d}}\right)^3. \quad (2.73)$$

The torque can be evaluated as well, and reads:

$$T_y^{\text{t-i}} = 8\pi\eta u a^2 \left(-\frac{1}{10} \log\left(\frac{d}{a}\right) - 0.19296\right) + \frac{64\pi}{35} \frac{\eta^2 u d h_{\text{sub}}^3}{a^2 \mu} \left(\frac{a}{\bar{d}}\right)^4 - \frac{32\pi}{125} \frac{\eta^2 \dot{u} h_{\text{sub}}^3}{a \mu} \left(\frac{a}{\bar{d}}\right)^3. \quad (2.74)$$

Here again, the prefactors of the lateral force and torque are found using the Lorentz reciprocal theorem as discussed in section 2.4. We shall notice that the thin-incompressible limit is valid mathematically for purely incompressible substrates, but its range of application is limited in practice. Usual elastomers or gels, that are considered as almost incompressible, have a Poisson ratio of order $\nu \simeq 0.49$, and thus a tiny compressibility. In recent articles, it has been shown that the mechanical response of thin elastic substrates is better described by the Winkler foundation derived in section 2.6.1 than the thin-incompressible limit discussed here [196]. An empirical scaling, based on the full numerical solution of the EHD lift coefficient has been derived and suggests that the thin-incompressible model is valid for thicknesses that are comprised in the range $\frac{\sqrt{7}}{3}(1/2 - \nu)^{1/2} \ll h_{\text{sub}}/\sqrt{2ad} \leq 0.12$ [197]. For $\nu = 0.49$, the lower bound of the latter window is 0.088, which confirms that the validity range of such models is quite limited.

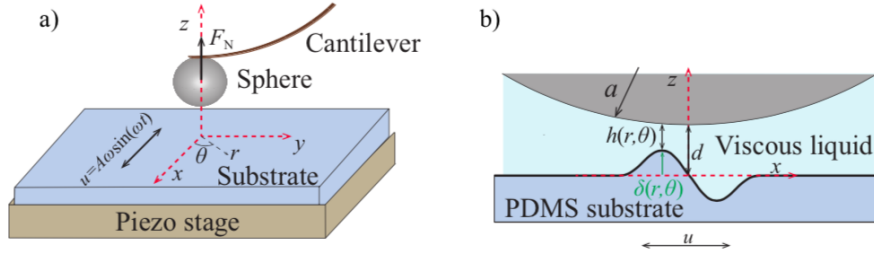


Figure 2.8: Schematic of the experimental setup. The soft PDMS sample is fixed to a rigid piezo stage that is transversally oscillated along time t , at angular frequency ω , and with amplitude A . A rigid borosilicate sphere is glued to an AFM cantilever and placed near the substrate, with silicone oil or 1-decanol as a viscous liquid lubricant. The normal force F_N exerted on the sphere, at a gap distance d from the surface, is directly measured from the deflection of the cantilever.

2.7 Experimental measurement of the EHD lift force

The experiments presented in this section have been performed by Zaicheng Zhang and Muhammad Arshad under the supervision of Abdelhamid Maali in the LOMA laboratory at the University of Bordeaux.

2.7.1 AFM setup

A schematic of the experimental setup is shown in Fig. 2.8. The experiment is performed using an AFM (Bruker, Bioscope) equipped with a cantilever holder (DTFMLDD-HE) that allows working in a liquid environment. We use a spherical borosilicate particle (MO-Sci Corporation) with a radius $a = 60 \pm 1 \mu\text{m}$ and a roughness of 0.9 nm measured over a $1 \mu\text{m}^2$ surface area. That sphere is glued at the end of a silicon nitride triangular shaped cantilever (DNP, Brukerafmprobes) using epoxy glue (Araldite, Bostik, Coubert). The soft samples are fixed on a multiaxis piezo-system (NanoT series, Mad City Labs), which allows (i) to control and scan the gap distance d between the sphere and the sample by displacing the sample vertically; and (ii) to vibrate the sample transversally at a frequency $f = \omega/(2\pi) = 25$ or 50 Hz, and with an amplitude A ranging from 3.6 to 36 μm . Note that, the normal displacement speed 20 nm/s being much smaller than the smallest transversal velocity amplitude $A\omega = 0.36 \text{ mm/s}$, the former can be neglected and a quasistatic description with respect to the normal motion is valid. Using the drainage method [58], the effective stiffness $k_c = 0.21 \pm 0.02 \text{ N/m}$ of the cantilever when the sphere is attached to it is determined using a rigid silicon wafer as a substrate, and for large-enough gap distances ($d = 200 - 20000 \text{ nm}$). The studied polydimethylsiloxane (PDMS) substrates are prepared as follows. First, uncross-linked PDMS (Sylgard 184, Dow Corning) and its curing agent are mixed into three different solutions, with different mixing ratios (10:1, 20:1, 30:1). Following a preliminary degassing process, a few droplets of each solution are spin-coated on a glass substrate

during a minute to get a sample of thickness in the 25–30 μm range. This is followed by an annealing step, in an oven at 50°C and during 24 h, in order to promote an efficient cross-linking. The measured Young’s moduli E of the samples (10:1), (20:1), and (30:1) are, respectively, (1455 ± 100 kPa.s), (600 ± 50 kPa.s), and (293 ± 20 kPa.s), where the Poisson ratio is fixed to $\nu = 0.5$ since crosslinked PDMS is an incompressible material to a very good approximation. At the Young’s moduli and low frequencies studied here, the loss modulus of PDMS is negligible [198]. We note that the viscoelastic properties of the PDMS is be discussed in section 1.2.1. The viscous liquids employed are silicone oil and 1-decanol with dynamic viscosities $\eta = 96$ mPa.s and 14.1 mPa.s, respectively.

2.7.2 Experimental results

Using the asymptotic theory derived in section 2.3, the lift force acting on a sphere immersed in a viscous fluid and moving at time-dependent velocity $u(t)$, near and parallel to a semi-infinite incompressible elastic substrate of shear modulus $\mu = E/[2(1 + \nu)]$ placed at a given distance d is:

$$F_{\text{N}} = \frac{243\pi^3}{12800\sqrt{2}} \frac{\eta^2 V^2}{\mu} \left(\frac{a}{d}\right)^{5/2} \approx 0.416 \frac{\eta^2 V^2}{\mu} \left(\frac{a}{d}\right)^{5/2}, \quad (2.75)$$

in the limit of small dimensionless compliance, *i.e.* $\kappa = 2\eta Va/(\mu d^2) \ll 1$. We recall that, in this limit, κ corresponds to the ratio between substrate’s deformation and gap distance, V being the velocity scale. Note also that, due to Galilean invariance, moving the substrate at given velocity instead of the sphere leads to the same lift force which justifies the use of the model of section 2.3. In view of the low frequencies at which the substrate is oscillating, and since inertial effects are negligible for such a confined viscous flow, this invariance and the expression of the lift force above remain excellent approximations in our case - with the substitution $u(t) = A\omega \sin(\omega t)$ in Eq. (2.75). In addition, in all experiments, the hydrodynamic radius $\sqrt{2ad}$ being much smaller than the thickness of the soft substrate, the latter can indeed be described as semi-infinite. Interestingly, with such a periodic driving, and since the lift force depends on the squared velocity, it can be expressed as two additive components: (i) a time-independent one $\sim \eta^2 A^2 \omega^2 a^{5/2}/(2\mu d^{5/2})$; and (ii) a component oscillating at double frequency $2f$. Focusing only on the former, it is measured though a temporal average $F = \langle F_{\text{N}} \rangle$ of the instantaneous normal force F_{N} recorded by AFM (see Fig. 2.8).

Figure 2.9 shows the force F as a function of the gap distance d , for rigid (silicon wafer) and soft (PDMS 20:1) substrates. To determine the gap distance, we take into account the cantilever’s deflection induced by the normal force, by solving the equation: $d = D + Z$, where D is the raw gap distance imposed by the piezo, and Z is the measured DC cantilever’s deflection. As a remark, in most cases studied here, the typical substrate’s deformation $\sim F/(\mu\sqrt{2ad})$ remains much smaller than the cantilever’s deflection. For the rigid case, no finite force is detected above the current nanonewton resolution, at all distances. This is expected, since for such a hard surface (Young’s modulus in the 100 GPa range), the elastohydrodynamic effects occur at gap distances

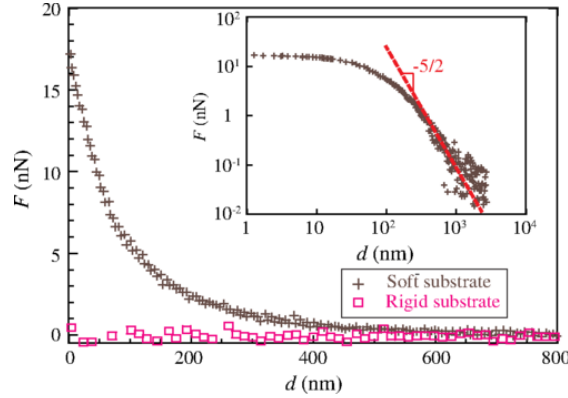


Figure 2.9: Temporal average F of the normal force F_N (see Fig. 2.8) as a function of the gap distance d to the substrate, for both rigid (silicon wafer) and soft (PDMS 20:1) substrates. The liquid used is silicone oil with viscosity $\eta = 96$ mPa.s. The amplitude of the velocity is $A\omega = 0.57$ mm/s. The inset shows a log-log representation of the data for the soft substrate, and the solid line therein indicates a $-5/2$ power law.

much smaller than the ones typically probed here [37]. As a remark, the fact that no force - even purely hydrodynamic - is measured in this case is a direct confirmation for the validity of the quasistatic description with respect to the imposed normal motion of the sphere. In sharp contrast, for the soft case, a systematic nonzero force is measured, and observed to increase as the gap distance is reduced. Furthermore, as shown in the inset, the force asymptotically scales as $F \sim d^{-5/2}$ at large gap distances, in agreement with the prediction of Eq. (2.75). Interestingly, at smaller gap distances, a saturation of the lift effect is observed, as reported previously [174].

Having tested the asymptotic dependence of the force with the main geometrical parameter, *i.e.*, the gap distance, which showed a first evidence of the lift, we now turn to the other key elastohydrodynamic parameters appearing in Eq. (2.75): the velocity amplitude $A\omega$, the viscosity η of the liquid, and the shear modulus μ of the substrate. To test the dependences of the force with these three parameters, we introduce two dimensionless variables: the dimensionless compliance κ , and the dimensionless force F/F^* with $F^* = \eta VR^{3/2}/d^{1/2}$, where V is systematically replaced by its root-mean-squared value $A\omega/\sqrt{2}$ due to the temporal averaging introduced above. In such a representation, Eq. (2.75) becomes $F/F^* = \frac{243\pi^3}{12800\sqrt{2}}\kappa \approx 0.416\kappa$. In Fig. 2.10, we thus plot F as a function of d , and in the rescaled form, F/F^* as a function of κ , for various sets of parameters: two different oscillation amplitudes (Fig. 2.10(a)), two different oscillation frequencies (Fig. 2.10(b)), two different viscosities (Fig. 2.10(c)), and three different shear moduli (Fig. 2.10(d)). In the inset of each of these panels, we first observe at small κ that F/F^* is linear in κ , and that the curves for various values of the varied parameter collapse with one another, which validates further Eq. (2.75). Moreover, around $\kappa \sim 1$, a deviation from the previous asymptotic behavior is observed, leading to a maximum prior to an interesting decay at large κ . In addition, the collapse for various values of

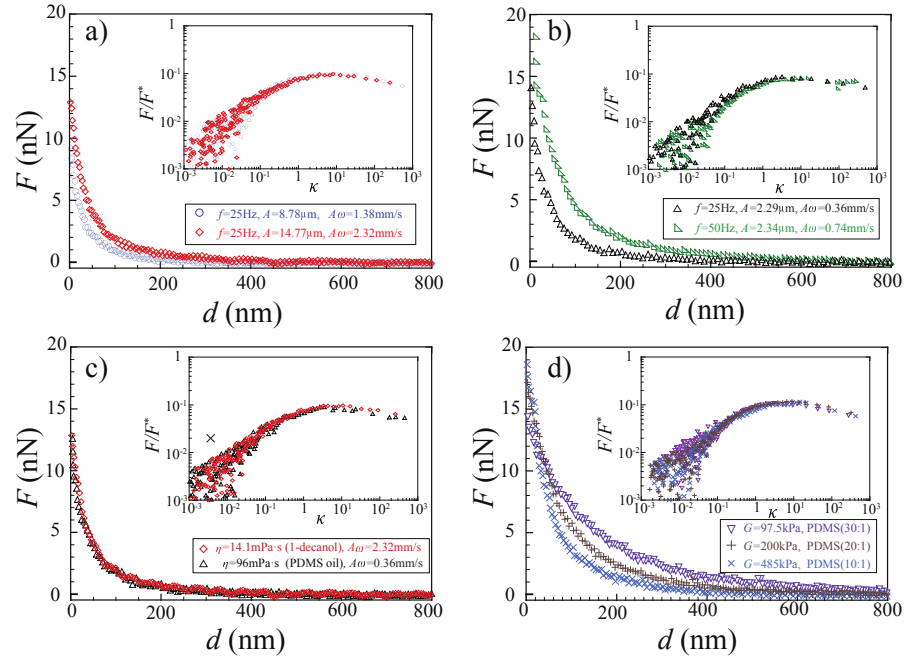


Figure 2.10: Measured temporal-averaged force F as a function of gap distance d to the soft PDMS substrates, and (insets) dimensionless force F/F^* as a function of dimensionless compliance κ in logarithmic scales, for various sets of parameters. (a) Two different velocity amplitudes (as indicated) obtained with different oscillation amplitudes are investigated. The substrate is cross-linked PDMS (10:1), and the liquid is 1-decanol with viscosity $\eta = 14.1$ mPa.s; (b) two different velocity amplitudes (as indicated) obtained with two different working frequencies are investigated. The substrate is cross-linked PDMS (10:1), and the liquid is silicone oil with viscosity $\eta = 96$ mPa.s; (c) two different liquids with different associated viscosities (as indicated) are investigated. The substrate is cross-linked PDMS (10:1), and the velocity amplitudes are $A\omega = 0.36$ mm/s and $A\omega = 2.32$ mm/s for silicone oil ($\eta = 96$ mPa.s) and 1-decanol ($\eta = 14.1$ mPa.s) respectively; (d) three different shear moduli (as indicated) of the substrate are investigated. The liquid is silicone oil with viscosity $\eta = 96$ mPa.s, and the velocity amplitude is $A\omega = 0.36$ mm/s.

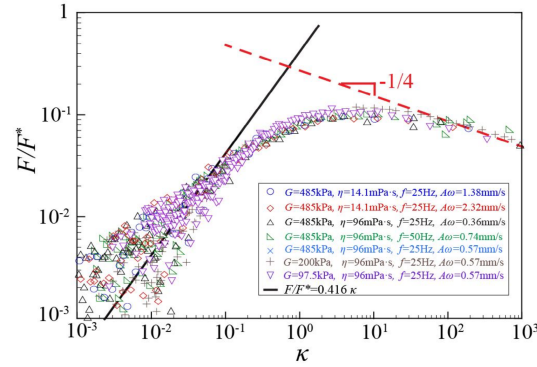


Figure 2.11: Dimensionless force F/F^* as a function of dimensionless compliance κ (see definitions in text) in logarithmic scales, as measured from force-distance data (see Figs. 2.9 and 2.10), for all the experiments performed in this study (see Fig. 2.10). The solid line corresponds to the theoretical prediction for F at low κ , obtained from Eq. (2.75) where V is replaced by $A\omega/\sqrt{2}$ due to the temporal averaging step. The dashed lined indicates a $-1/4$ power law.

the varied parameter is maintained, indicating that even at large dimensionless compliance κ , the dimensionless force F/F^* remains a function of κ only. This suggests that the same physics, coupling lubrication flow and linear elasticity, is at play at large κ .

In order to test this prediction, we plot F/F^* as a function of κ in Fig. 2.11, for all the experiments performed in this study. First, all the experimental data collapses on a single nonmonotonic master curve, confirming further the results of Fig. 2.10. Second, Eq. (2.75) is found to be in excellent agreement with the low- κ part of the data, with no adjustable parameter. Finally, the behavior at large κ reveals the possible existence of a power law: $F/F^* \sim \kappa^{-1/4}$, equivalent to $F \sim \eta^{3/4}V^{3/4}\mu^{1/4}a^{5/4}$. This gap-independent empirical scaling suggests that the lift force saturates at small enough distances, in agreement with the observation made in Fig. 2.9. Such a result might tentatively be attributed to a competition between the increase of the elastohydrodynamic symmetry breaking and the decrease of the pressure magnitude due to the substrate's deformation, but further work is needed to quantify this hypothetical mechanism, and to disentangle it from potential nonstationary effects [199].

The large- κ regime of soft lubrication corresponds to a situation where the substrate deformation is typically larger than the liquid-film thickness. This physical situation is relevant in many applications in engineering and geological settings, as discussed in the introduction of the chapter. We note that elastohydrodynamic models in such settings are usually written in a slightly different formalism than in section 2.2. A given normal load, typically the weight of the object, is generally imposed at the contact and the exact position of the base of the sphere is unknown [200]. The main interest in EHD lubrication is the steady solution, where the velocity is constant, *i.e.* $u(t) = V$, which is simpler to handle theoretically and relevant in most applications. In this context and

in the large-deformation limit, the base of the sphere altitude can reach negative values $d < 0$ with the definition of the z -axis in section 2.2.

In the absence of liquid, the deformation of an elastic material indented by a sphere at a given load is well described by the Hertz contact theory [201, 202]. It predicts a relation between the force and the substrate deformation: $F = \frac{\mu(\lambda+\mu)}{(\lambda+2\mu)} \frac{16}{3} E a^{1/2} \delta^{3/2}$. In lubricated contact at large load and relatively small velocity, or equivalently small shear stress with respect the normal one, the deformation of the material is close to the one predicted by Hertz theory, which justifies that this regime of EHD lubrication is usually called the Hertz limit. The liquid-film thickness for spherical contact has been computed using a boundary-layer theory, that describes the flow at the inlet and outlet of the contact, and that allows for a determination of the liquid-gap thickness and the lateral friction force [162, 200]. In particular, a scaling relation between the lift force and the velocity $F \sim (\eta V)^{3/4} \mu^{1/4}$ is predicted, which is in good agreement with the dashed line in Fig. 2.11, suggesting that the signature of the Hertz-limit of EHD lubrication may be observed in the experiments [182].

2.7.3 Numerical results at large deformation for a steady sliding

To get further insights on the experimentally observed saturation if the lift force at large κ (see Fig. 2.11), and its possible relation with the Hertz limit of EHD lubrication, we turn to numerical methods to solve the EHD model of section 2.2 defined by the Eqs. (2.2) and (2.3) for arbitrary values of κ . Numerical methods are largely employed in the EHD lubrication community to access the variety of regimes of soft lubrication [203], and to model realistic lubricated contact. As an example, numerical models can investigate the rheological piezoviscous and thermoviscous properties of industrial lubricants, namely the pressure dependence of viscosity and density that is important at high load. In addition, one can use numerical models to verify the asymptotic calculations in section 2.3. We present here some preliminary unpublished numerical results to get the full non-linear curve $F/F^* = f(\kappa)$, where f is a function, that is shown in Fig. 2.11.

As a first attempt, we consider a steady flow $u(t) = V$, leaving aside the non-stationary effects in the flow induced by the lateral oscillation of the spherical probe. Written in dimensionless Cartesian coordinates, denoted with the capital letters (X, Y) , the stationary versions of Eqs. (2.2) and (2.3) give:

$$\partial_X \left(H^3 \partial_X P \right) + \partial_Y \left(H^3 \partial_Y P \right) = 6 \partial_X H, \quad (2.76)$$

$$H(X, Y) = 1 + X^2 + Y^2 - \Delta(X, Y), \quad \Delta(X, Y) = \kappa \int_{\mathbb{R}^2} \mathcal{G}(X - X', Y - Y') P(X', Y') dX' dY', \quad (2.77)$$

where $\mathcal{G}(X, Y) = 1/(4\pi\sqrt{X^2 + Y^2})$ is the dimensionless Green's function of the elastic response. The X and Y dimensionless spatial coordinates are discretized on a uniform grid, with i and j being the respective spatial indices and $DX = DY$ the increments of

the spatial grid. The differential operators are also discretized using a centered finite-difference scheme, leading to:

$$\begin{aligned} \frac{1}{DX^2} \left[H_{i+\frac{1}{2},j}^3 P_{i+1,j} - \left(H_{i+\frac{1}{2},j}^3 + H_{i-\frac{1}{2},j}^3 \right) P_{i,j} + H_{i-\frac{1}{2},j}^3 P_{i-1,j}, \right. \\ \left. + H_{i,j+\frac{1}{2}}^3 P_{i,j+1} - \left(H_{i,j+\frac{1}{2}}^3 + H_{i,j-\frac{1}{2}}^3 \right) P_{i,j} + H_{i,j-\frac{1}{2}}^3 P_{i,j-1} \right] = 12X_i - 6 \frac{\Delta_{i+1,j} - \Delta_{i,j}}{DX}, \end{aligned} \quad (2.78)$$

$$\Delta_{i,j} = \kappa \sum_{i',j'} \mathcal{G}(X_i - X_{i'}, Y_i - Y_{i'}) P_{i',j'}, \quad (2.79)$$

where we introduced the auxiliary function $H_{i+1/2,j} = (H_{i+1,j} + H_{i,j})/2$. We then use the same iterative technique as the one invoked by Ref. [174]: we first guess a displacement field and compute the corresponding pressure field by solving Eq. (2.78). Then, that pressure field is used to compute a new displacement field via Eq. (2.79). This procedure is iterated further until a difference of less than 1 ppm in the fields, between two successive iterations, is reached.

A typical numerical pressure field P_{num} for $\kappa = 0.2$ is plotted in Fig. 2.12(a), and is found to be very close to the analytical prediction for a rigid wall ($\kappa = 0$, see Fig. 2.12(b)), as expected. In Fig. 2.12(c) is plotted the difference between these two solutions, showing a quasi-isotropic excess pressure field. In Fig. 2.12(d), we plot the asymptotic analytical expression for the isotropic part of the first-order pressure term (see Eq. (2.27)), and we see similar spatial extent and features as in Fig. 2.12(c). The numerical deformation of the soft substrate Δ_{num} is shown in Fig. 2.12(e), and agrees quantitatively with the analytical prediction computed from our asymptotic soft-lubrication theory at first order in κ (see Fig. 2.12(f)). All together, the proximity of numerical and asymptotic expressions gives a good confidence in the numerical methods presented here.

In Fig. 2.13, we plot the resulting numerical lift force as a function of κ and add for comparison the experimental data and the asymptotic soft-lubrication theory of Fig. 2.11. The asymptotic prediction agrees well with the numerical result at small κ , which again gives confidence to both the analytical asymptotic solution and the new numerical method. Interestingly, at finite κ values, we find a larger numerical lift force as compared to the experimental data. This suggests that transient terms associated with the non-steady character of the oscillatory driving, are crucial at large compliances and/or small gap thicknesses. Nevertheless, it is not the case in the small-deformation regime, *i.e.* at small κ , as shown in section 2.3. The steady expression is still valid at order 1 in κ , provided that one simply replaces the steady velocity by the transient one, in a quasi-steady fashion.

We point out that the iterative algorithm described above does not converge within reasonable time for values of κ larger than 16. As a sanity check, we have thus implemented another, non-linear local relaxation method, based on the Gauss-Seidel scheme, see Chap 2.10 in Ref. [203], and it self-consistently produces the same results. But again, while the algorithm converges at intermediate κ values (up to 10), results at larger κ

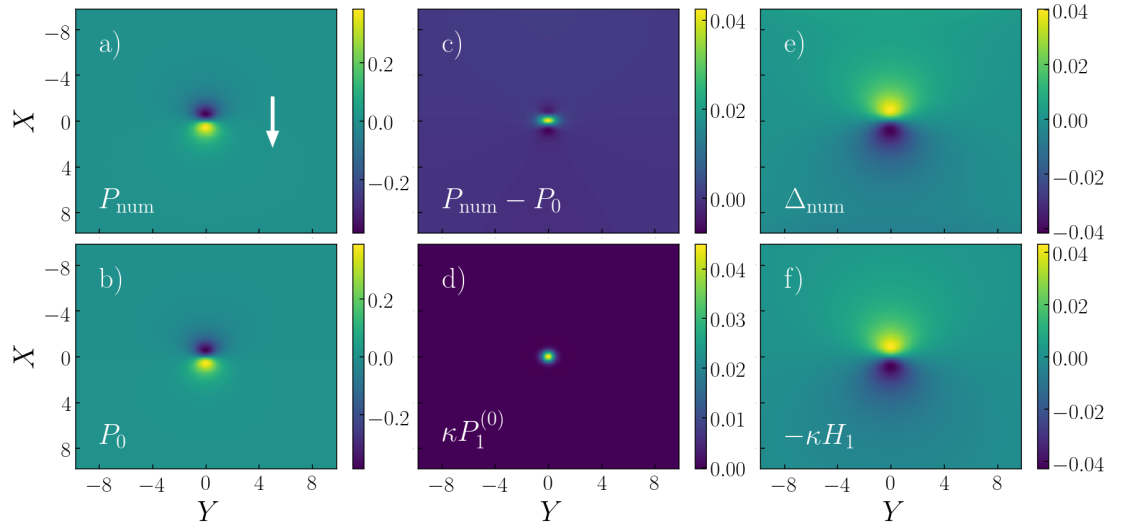


Figure 2.12: a) Pressure field P_{num} resulting from the numerical integration of Eq. (2.78) and (2.79) at $\kappa = 0.2$. The white arrow recalls the direction of the sphere motion. b) Zeroth-order pressure from the analytical lubrication model Eq. (2.17), that corresponds to the case of an immersed sphere sliding near and along a rigid wall. c) Difference between the numerical pressure field and the zeroth-order analytical pressure field. d) Isotropic part of the asymptotic analytic expression of the first-order pressure Eq. (2.27). e) Deformation of the soft substrate Δ_{num} resulting from the numerical integration. f) First-order substrate deformation field from the analytical soft-lubrication model Eq. (2.19).

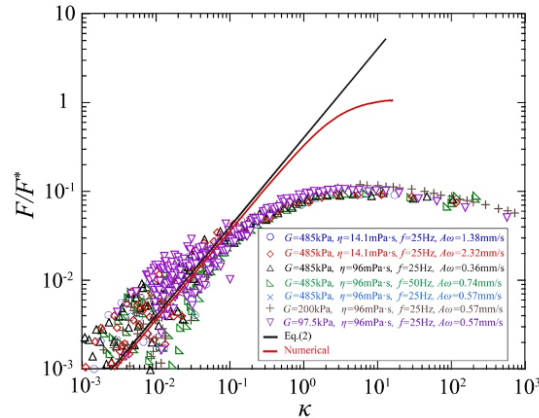


Figure 2.13: Rescaled lift force as a function of dimensionless compliance, as computed from the numerical solutions (“Numerical”) of the discretized soft-lubrication equations (see Eqs. (2.78) and (2.79)). The asymptotic solution Eq. (2.75) is plotted for comparison, as well as all the experimental data of Fig. 2.11.

values are not accessible within reasonable time. Therefore, it was not possible to verify the validity of the experimentally observed $-1/4$ power law in Fig. 2.11 at large κ and its connection with the Hertz limit of steady lubrication. New numerical schemes, as the ones described in Ref. [162], would be necessary to understand the role of transient EHD lubrication and the Hertz limit.

2.8 Conclusion

We developed a soft-lubrication model in order to compute the EHD interactions exerted on an immersed sphere undergoing both translational and rotational motions near various types of elastic walls. The deformation of the surface was assumed to be small, which allowed us to employ a perturbation analysis in order to obtain the leading-order EHD forces and torque. The obtained interaction matrix exhibits a qualitatively similar form as the one found for a two-dimensional cylinder moving near a thin compressible substrate [172]. In both cases, the EHD coupling is nonlinear and generates quadratic terms in the sphere velocity, thus breaking the time-reversal symmetry of the Stokes equations. In addition, original inertial-like terms proportional to the acceleration of the sphere are found – despite the assumption of steady flows. Therefore, while the quantitative details such as numerical prefactors and exponents differ in 3d and when using more realistic constitutive elastic responses, we expect that the typical zoology of trajectories identified previously [172] will also hold for spherical objects – and will even be extended with the added degree of freedom. As such, the asymptotic predictions obtained here may open new perspectives in colloidal science and biophysics, through the understanding and control of the emerging interactions within soft confinement or assemblies.

Among these EHD interactions, we report experimental results demonstrating the existence of the elastohydrodynamic lift force at the nanoscale. For the first time, the force is directly measured using colloidal-probe atomic force microscopy. We observe a collapse of all the data with amplitudes, frequencies, viscosities, shear moduli on a single master curve, that is in good agreement with the asymptotic calculation in the framework of soft lubrication. For large compliances, or equivalently at small confinement length scales, a saturation of the lift force is observed and an empirical scaling law is found and agrees with the Hertz model. A numerical finite-difference model is developed, assuming stationary sliding, and predict a force about ten times larger than the one measured with oscillating shear flow. In the future, focusing the efforts on the resolution of the non linear problem at any dimensionless compliance, and including non stationary terms associated with the driving oscillation, might help to explore further the saturation regime. We anticipate important implications of the existence of the elastohydrodynamic lift force at the nanoscale for nano-science and biology.

Part II

Thin-film dynamics near soft interfaces

In this third part of the thesis, I present my work on the levelling dynamics of thin liquid films. This work is the follow-up of a 10-year collaborative project involving numerous researchers in Canada, France and Germany: Matilda Backholm, Oliver Bäumchen, Michael Benzaquen, Yu Chai, Kari Dalnoki-Veress, James Forrest, Paul Fowler, Mark Ilton, Carmen Lee, Joshua McGraw, John Niven, Élie Raphaël, Marco Rivetti and Thomas Salez (in alphabetical order). The part is structured as follows. I first give a brief introduction on thin liquid films and I review the main results obtained in the collaborative network over the years. Then, each of the three following chapters contains an article that I co-author. A preface sums up the main results and explains my contribution to the project.

Context

Thin liquid films refer to a large variety of systems of various thicknesses from the kilometer to the nanometer, and are encountered in many fields of science beyond soft-matter physics such as geophysics, biophysics or engineering. As a result, the dynamics of thin films is a rich field involving diverse physical processes. For instance, geological films are driven by gravity, and examples are the continental ice-sheet dynamics important within the context of climate change and the rise of sea level [204], but also lava flows [205] and landslides [154]. In biology, micro-organisms (*e.g.* bacteria) often aggregate at solid-air interfaces to form biofilms [206], and liquid films are also found in vivo in lung airways [207], or in the eye [208]. In terms of engineering applications, thin-liquid films enter in the fabrication process of various surface treatments [209]. Those are encountered in many contexts for their specific properties such as mechanical (soft, brittle, malleable), optical (reflective, transparent), chemical (hydrophobic, antioxidant), electronic (conductor, insulator) to cite a few. They have been involved in a lot of technological outbreaks in the last century, like semiconductor devices, thin-film solar cells, optical coatings. Lastly, thin films are also found in soft matter systems such as soap films, Langmuir–Blodgett films, or through the wetting dynamics [210].

The dynamics of thin-liquid films is fascinating for applied mathematicians and physicists. By exploiting the large aspect ratio of thin films, researchers have developed asymptotic theories, performing long-wave expansion of the fluid dynamics equations [211]. This allows to reduce the complexity of the governing equations and boundary conditions of the flow to a single conservative equation (or set of equations) for the film thickness. This is done at the price of dealing with non-linear partial differential equations that are, in most cases, not solvable. Nevertheless, these theories are used to study wave propagation, stability, pattern formation, dewetting dynamics, etc... [212]

In the general context of my thesis, *i.e.* flows at soft interfaces, I investigated the dynamics of thin viscous films that are deposited on soft substrates. In particular, we wondered how the deformation of the underlying interface modifies the thin-film dynamics.

Capillary levelling as a rheological probe

We briefly present the spirit of the capillary-leveling method in the canonical case of a thin liquid film supported on a rigid substrate.

Thin-film equation and full-Stokes models

In thin-viscous films, a perturbation of the liquid-air interface relaxes toward the flat equilibrium state. We assume the lateral extent ℓ_0 of the perturbation of the interface to be smaller than the capillary length ℓ_{cap} so that capillary forces dominate over gravity. The curvature of the interface induces an excess Laplace pressure p with respect to the ambient one that drives the flow. In this introduction, we suppose that the film is supported on an immobile substrate at $z = 0$, with a no-slip boundary condition. However, through the following chapters, this condition is relaxed and we investigate the cases of thin films supported on a soft elastic layer in chapter 3, an immiscible thin-liquid film in chapter 4 and finally thin films in freestanding configurations in chapter 5. The liquid-air interface is defined by $z = h(\mathbf{r}, t)$, where \mathbf{r} denotes the position in the xy plane in the tangential direction, t being the time. A no-stress boundary condition is assumed at the liquid-air interface. The typical film thickness h_0 (e.g. thickness at rest) is supposed to be much smaller than the typical lateral extent ℓ_0 of the interface perturbation. We use the standard long-wave expansion of the Stokes equations, assuming the ratio $\varepsilon = h_0/\ell_0$ to be small with respect to unity [211], leading to the thin-film equation:

$$\frac{\partial h}{\partial t} = \nabla \cdot \left(\frac{h^3}{3\eta} \nabla p \right) = -\nabla \cdot \left(\frac{\gamma h^3}{3\eta} \nabla (\nabla^2 h) \right) \quad (2.80)$$

where ∇ is here the gradient in the tangential direction, and where we have used the expression of the Laplace pressure $p \simeq -\gamma \nabla^2 h$ in the small-slope limit. In chapter 3, we provide a more detailed derivation of a long-wave expansion of the Stokes equations for bilayer films. In the case considered here, the long-wave expansion is often called lubrication approximation (see Part I).

In my thesis, I developed an additional method, termed *full-Stokes* model, to derive the evolution equations of the film thickness without asymptotic long-wave expansions. Precisely, for symmetric film, the velocity can be expressed with the stream function $\psi(\mathbf{r}, z)$, as $\mathbf{v} = \nabla \times (\psi \mathbf{e}_j)$, where $j = y$ for films invariant in the y direction, and $j = \theta$ for axially invariant film (using the polar coordinates). The stream function verifies the biharmonic equation: $\left(\nabla^2 + \frac{\partial^2}{\partial z^2} \right)^2 \psi = 0$. By introducing the Fourier transform of the tangential variables, the general solution of the biharmonic equation can be expressed with four parameters that are determined with the boundary conditions of the flow. The evolution equation for the film thickness can be solved analytically only for linearized liquid-air interface profiles. We stress that similar methods have already been employed, e.g. to perform linear-stability analysis of thin films [213].

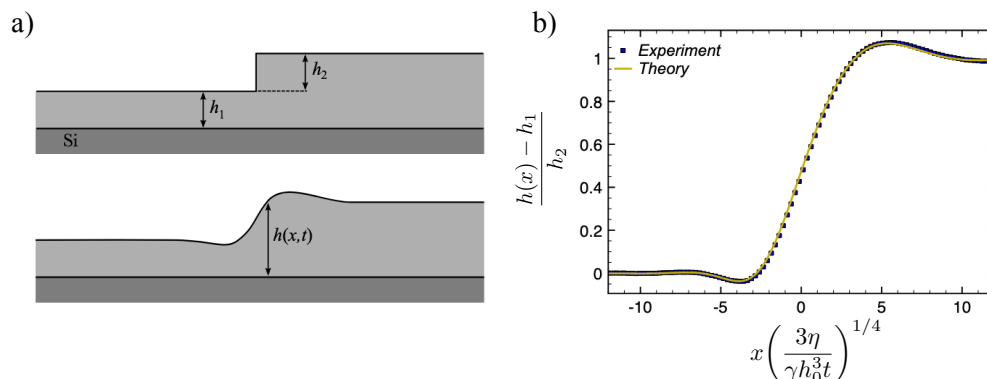


Figure 2.14: a) Schematic of the initial stepped state of the polymer films. b) The rescaled interface profile is plotted versus dimensionless self-similar variable that involves the horizontal position x , rescaled by time with a $1/4$ power, where γ , η , $h_0 = h_1 + h_2/2$ denote the surface tension, viscosity and equilibrium thickness. The solid lines show a fit of the numerical solution of Eq. (2.80). The system is a polystyrene (PS) stepped film, with a molecular weight $M_w = 118$ kg/mol and $h_1 = h_2 = 89$ nm, leveling on a silicon substrate. The annealing temperature is 140°C . The figure is adapted from Ref. [214]

Experimental system

Experimentally, thin polymer films are used, with thicknesses on the order of 100 nm. We recall that polymers are macromolecules composed of many repeating subunits, up to $\sim 10^5$ units for synthetic polymers and up to $\sim 10^9$ units for DNA. In particular, typical polymer conformations take the form of a random coil, whose radius of gyration varies from few angströms to tens of nanometers. The polymers used here are typically one million to one billion times more viscous than water, which justifies that inertia is neglected here. Furthermore, polymer exhibit some viscoelastic properties and are glassy [215]. Thin polymer films can be obtained in the glassy state by spin-coating a polymer solution on a silicon wafer. The perturbation of the initial polymer interface is done by superimposing two polymer films in the glassy state, resulting in films in a stepped configuration, invariant along one direction. In this way, the initial profile can be described by a Heavyside function \mathcal{H} , as $h(\mathbf{r}, t = 0) = h_1 + h_2\mathcal{H}(x)$ (see Fig. 2.14a)). Then the sample is annealed above the glass-transition temperature for a certain amount of time and the levelling process occurs, before the sample is quenched back to the glassy state [216, 217]. Atomic force microscopy (see chapter 1) is used to scan the topography of the polymer interface in the glassy state, and to obtain interface profiles, as shown in Fig. 2.14b). Interestingly, along the levelling dynamics, the interface profile displays self-similar properties [218], through the self-similar variable $x \left(\frac{3\eta}{\gamma h_0^3 t} \right)^{1/4}$, where $h_0 = h_1 + h_2/2$ is the average thickness. As shown in Ref. [217], the

interface profiles at several annealing times collapse on a master curve when plotting them versus the self-similar variables, and are in good agreement with numerical solutions of Eq. (2.80) [214]. The capillary velocity γ/η being the only adjustable parameter, the capillary-levelling method appears as a probe of the rheological properties of thin viscous polymer films.

Apart from the stepped geometry, the capillary-levelling method has been used to describe the relaxation dynamics of finite-size perturbations such as trenches [219], and cylindrical holes [220]. In these examples, the relaxation dynamics also involves self-similar solutions resulting from the structure of the thin-film equation [221, 222]. Lastly, an extension of the method to freestanding films has also been developed, and the resulting dynamics is also in good agreement with long-wave asymptotic models [223], that differ from the thin-film equation. In the rest of the introduction, we illustrate the capacity of the capillary-levelling method to measure interfacial properties of polymers.

Surface mobility of glassy polymer

Unlike the liquid-crystal phase transition, the glass transition is not defined based on thermodynamical principles and depends on kinetic quantities such as the cooling rate. It describes the drastic slowing down of the relaxation dynamics of amorphous materials near a given temperature T_g , called the glass-transition temperature. The behaviour is empirically described by the Vogel-Fulcher-Tammann (VFT) law, where the viscosity follows:

$$\eta(T) = \eta_0 \exp\left(\frac{A}{T - T_g}\right), \quad (2.81)$$

where T is the temperature and η_0 , A being constant factors. The capillary-levelling method is used here above and below the glass-transition temperature of PS [224]. Surprisingly, PS thin films flow, down to tens of degrees below the glass-transition temperature. The levelling dynamics is consistent with the existence of a liquid mobile layer (see Fig. 2.15a)) over which the flow is localized. Furthermore, the technique permits to extract the mobility of the fluid layer (see Fig. 2.15b)), which is inversely proportional to the viscosity. The latter seems to follow an Arrhenius-like law $\eta \sim \exp(B/T)$, where B is a constant below T_g as for simple liquids, in contrast with Eq. (2.81) recovered above T_g .

Interfacial slip

So far, we have been using a no-slip boundary condition at the solid-liquid surface, meaning that the velocity fields vanish at the solid boundary. However, there are no fundamental principles supporting that, and, as pointed out by Navier in 1823, the boundary condition at solid surfaces may imply a non-zero tangential velocity [227]. By expressing the boundary condition as a stress balance between viscous shear and the friction between fluid molecules and the wall, the boundary conditions is postulated to be $k v_{\parallel} = \eta \frac{\partial v_{\parallel}}{\partial z}$, where v_{\parallel} denotes the tangential velocity of the fluid at the wall,

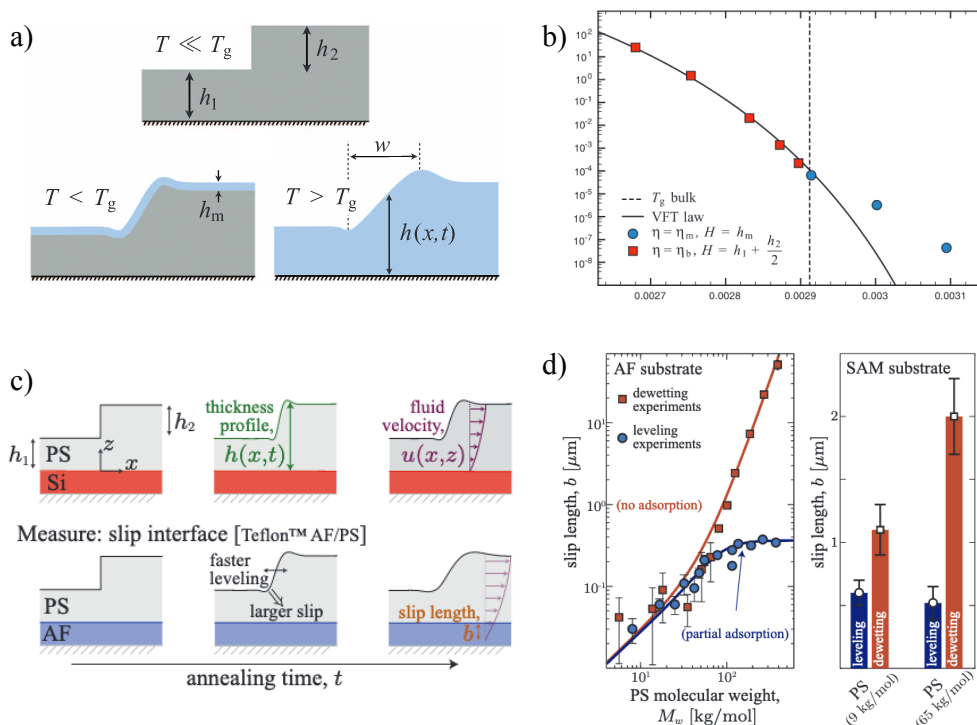


Figure 2.15: a) Schematic of the experiments in Ref. [224]. For a temperature range below T_g , capillary levelling is observed in a surface layer. b) Liquid mobility $H^3/(3\eta)$ versus inverse temperature. Above T_g (squares), the mobility follows the Vogel-Fulcher-Tammann (VFT) law for supercooled liquids, H being the average film thickness. Below T_g (circles), the flow is localized in a near-surface region, with $H = h_m$, and seems to follow an Arrhenius-like law, which is characteristic of simple liquids. c) Schematic of the experiment in Ref. [225]. The interfacial slip causes a faster levelling. d) (left) Slip length as a function of molecular weight, from capillary-levelling experiments (blue circles) of polystyrene (PS) on Teflon (AF) substrates. For comparison, results from PS dewetting experiments (orange squares, data from Ref. [226]) on AF substrates are also shown. Two equations with one free parameter (solid lines) describe both sets of experiments: they assume adsorption of chains in the low-shear-rate levelling experiments and no chain adsorption in the high-shear-rate dewetting experiments. d) (right) The difference in the measured slip length between levelling (blue) and dewetting (orange) experiments is confirmed using a different substrate, a self-assembled monolayer (SAM).

and k being a friction coefficient. By rewriting this expression as $v_{\parallel} = b \frac{\partial v_{\parallel}}{\partial z}$, we introduce the slip length $b = \eta/k$ that scales as a ratio between viscosity (bulk-dependent quantity) and a friction coefficient (surface-dependent quantity). If the no-slip assumption has been proven to be valid at macroscopic scales, the emergence of micro and

nanofluidics has shown the existence of slip lengths on the order of few nanometers at most solid-liquid interfaces for simple fluids, in agreement with the order of magnitude expected [228]. In polymer melts, the viscosity is largely dependent on the size of the macromolecules and increases by orders of magnitude with respect to simple fluid. Therefore, as pointed out by P.G. de Gennes, the slip length is expected to increase by the same amount, when considering polymer melts [229].

In Ref. [225], the capillary-levelling method has been employed to measure the slip lengths of PS on both Teflon (AF) and self-assembled monolayer (SAM) surfaces as shown in Figs. 2.15c-d). The slip lengths are found to be much larger than for simple fluids and to depend on the molecular weight of PS (hence, the viscosity). More interestingly, the slip lengths measured through the levelling dynamics are found to be significantly smaller than the ones measured in Ref. [226] using dewetting experiments of PS thin films over the same surface. The experiments using dewetting methods recover the molecular weight dependence of the slip length predicted by de Gennes. The major difference between the two sets of experiments is the magnitude of the stress involved. The difference in slip lengths measured in the two methods may be rationalized by considering adsorbed polymer chains at the surface [225].

Chapter 3

Elastocapillary levelling of thin viscous films on soft substrates.

This chapter describes some of the work that I have done during my master internship in the spring 2017. The experiments shown here have been carried out by Marco Rivetti, with the help from Christine Linne and under the supervision of Oliver Bäumchen at the Max Planck Institute in Göttingen, Germany.

We investigate the levelling dynamics of thin polystyrene films deposited on soft PDMS layers. The initial state of the polystyrene films is a step configuration and the interface topographies are scanned with an atomic force microscope. The flow is driven by the Laplace pressure gradient and is mediated by viscosity. The Laplace pressure also deforms the soft PDMS surface, and the latter alters the flow, leading to “elasto-capillary-hydrodynamics” interactions. The relaxation dynamics of the initial perturbation towards the flat equilibrium state follows diffusive-like law, where the width w of the perturbation grows in time with a power law, $w \sim t^{1/6}$. Interestingly, the associated $1/6$ exponent differs from the classical one, $1/4$, found in the thin-film equation and in experiments with rigid substrates. Prior my internship, a first model, based on linear elasticity to described the substrate deformation and the lubrication approximation for the liquid phase, has been derived by Thomas Salez, Maxence Arutkin with inputs from Herbert Hui and Haibin Wu (Cornell University). My contribution to the project was to derive the full Stokes model, in complement to the lubrication one. I reproduce here an article, published in *Physical Review Fluids* [1], that I co-author.

Elastocapillary levelling of thin viscous films on soft substrates

Marco Rivetti,¹ Vincent Bertin,² Thomas Salez,^{2,3} Chung-Yuen Hui,⁴ Christine Linne,¹
 Maxence Arutkin,² Haibin Wu,⁴ Elie Raphaël,² and Oliver Bäumchen^{1,*}

¹*Max Planck Institute for Dynamics and Self-Organization (MPIDS), Am Faßberg 17,
 37077 Göttingen, Germany*

²*Laboratoire de Physico-Chimie Théorique, UMR CNRS 7083 Gulliver, ESPCI Paris,
 PSL Research University, 10 rue Vauquelin, 75005 Paris, France*

³*Global Station for Soft Matter, Global Institution for Collaborative Research and Education,
 Hokkaido University, Sapporo, Hokkaido 060-0808, Japan*

⁴*Department of Mechanical & Aerospace Engineering, Cornell University, Ithaca, New York 14853, USA*

(Received 31 March 2017; published 1 September 2017)

A thin liquid film with nonzero curvature at its free surface spontaneously flows to reach a flat configuration, a process driven by Laplace pressure gradients and resisted by the liquid's viscosity. Inspired by recent progresses on the dynamics of liquid droplets on soft substrates, we here study the relaxation of a viscous film supported by an elastic foundation. Experiments involve thin polymer films on elastomeric substrates, where the dynamics of the liquid-air interface is monitored using atomic force microscopy. A theoretical model that describes the coupled evolution of the solid-liquid and the liquid-air interfaces is also provided. In this soft-levelling configuration, Laplace pressure gradients not only drive the flow, but they also induce elastic deformations on the substrate that affect the flow and the shape of the liquid-air interface itself. This process represents an original example of elastocapillarity that is not mediated by the presence of a contact line. We discuss the impact of the elastic contribution on the levelling dynamics and show the departure from the classical self-similarities and power laws observed for capillary levelling on rigid substrates.

DOI: [10.1103/PhysRevFluids.2.094001](https://doi.org/10.1103/PhysRevFluids.2.094001)

I. INTRODUCTION

Interactions of solids and fluids are often pictured by the flapping of a flag in the wind, the oscillating motion of an open hosepipe, or that of a fish fin in water, a set of examples in which the inertia of the fluid plays an essential role. In contrast, at small scales, and more generally for low-Reynolds-number (Re) flows, fluid-solid interactions involve viscous forces rather than inertia. Of particular interest are the configurations where a liquid flows along a soft wall, i.e., an elastic layer that can deform under the action of pressure and viscous stresses. For instance, when a solid object moves in a viscous liquid close to an elastic wall, the intrinsic symmetry of the Stokes equations that govern low- Re flows breaks down. This gives rise to a qualitatively different—elastohydrodynamical—behavior of the system in which the moving object may experience lift or oscillating motion [1–3], and a swimmer can produce a net thrust even by applying a time-reversible stroke [4], in apparent violation of the so-called scallop theorem [5]. This coupling of viscous dynamics and elastic deformations is particularly significant in lubrication problems, such as the aging of mammalian joints and their soft cartilaginous layers [6], or roll-coating processes involving rubber-covered rolls [7], among others.

When adding a liquid-vapor interface, capillary forces may come into play, thus allowing for elastocapillary interactions. The latter have attracted a lot of interest in the past decade [8–10]. In order to enhance the effect of capillary forces, the elastic object has to be either slender or soft. The

*oliver.baumchen@ds.mpg.de

first case, in which the elastic structure is mainly bent by surface tension, has been explored to explain and predict features like deformation and folding of plates, wrapping of plates (capillary origami) or fibers around droplets, and liquid imbibition between fibers [11–18]. The second case involves rather thick substrates, where capillary forces are opposed by bulk elasticity. A common example is that of a small droplet sitting on a soft solid. Lester [19] has been the first to recognize that the three-phase contact line can deform the substrate by creating a ridge. Despite the apparent simplicity of this configuration, the substrate deformation close to the contact line represents a challenging problem because of the violation of the classical Young’s construction for the contact angle, the singularity of the displacement field at the contact line, and the difficulty to predict the exact shape of the capillary ridge. In the last few years, several theoretical and experimental works have contributed to a better fundamental understanding of this static problem [20–25], recently extended by the dynamical case of droplets moving along a soft substrate [26–28].

Besides, another class of problems—the capillary levelling of thin liquid films on rigid substrates, or in freestanding configurations—has been studied in the last few years using thin polymer films featuring different initial profiles, such as steps, trenches, and holes [29–34]. From the experimental point of view, this has been proven to be a reliable system due to systematic reproducibility of the results and the possibility to extract rheological properties of the liquid [35,36]. A theoretical framework, based on Stokes flow and the lubrication approximation, results in the so-called thin-film equation [37], which describes the temporal evolution of the thickness profile. From this model, characteristic self-similarities of the levelling profiles, as well as numerical [38] and analytical [39,40] solutions have been derived, which were found in excellent agreement with the experimental results. Furthermore, coarse-grained molecular dynamics models allowed us to extend the framework of capillary levelling by offering local dynamical insights and probing viscoelasticity [41].

In this article, by combining the two classes of problems above—elastocapillarity and capillary levelling—we design a dynamical elastocapillary situation free of any three-phase contact line. Specifically, we consider a setting in which a thin layer of viscous liquid with a nonflat thickness profile is supported onto a soft foundation. The liquid-air interface has a spatially varying curvature that leads to gradients in Laplace pressure, which drive flow coupled to substrate deformation. The resulting elastocapillary levelling might have practical implications in biological settings and nanotechnology.

II. EXPERIMENTAL SETUP

First, polydimethylsiloxane (PDMS, Sylgard 184, Dow Corning) is mixed with its curing agent in ratios varying from 10:1 to 40:1. In order to decrease its viscosity, liquid PDMS is diluted in toluene (Sigma-Aldrich, Chromasolv, purity >99.9%) to obtain a 1:1 solution in weight. The solution is then poured on a 15×15 mm Si wafer (Si-Mat, Germany) and spin-coated for 45 s at 12.000 RPM. The sample is then immediately transferred to an oven and kept at 75°C for 2 h. The resulting elastic layer has a thickness $s_0 = 1.5 \pm 0.2 \mu\text{m}$, as obtained from atomic force microscopy (AFM, Multimode, Bruker) data. The Young’s modulus of PDMS strongly depends on the ratio of base to cross linker, with typical values of $E = 1.7 \pm 0.2$ MPa for 10:1 ratio, $E = 600 \pm 100$ kPa for 20:1, and $E = 50 \pm 20$ kPa for 40:1 [42,43].

In order to prepare polystyrene (PS) films exhibiting nonconstant curvatures, we employ a technique similar to that described in [29]. Solutions of 34 kg/mol PS (PSS, Germany, polydispersity <1.05) in toluene with typical concentrations varying between 2% and 6% are made. A solution is then spin-cast on a freshly cleaved mica sheet (Ted Pella, USA) for about 10 s, with typical spinning velocities on the order of a few thousands RPM. After the rapid evaporation of the solvent during the spin-coating process, a thin (glassy) film of PS is obtained, with a typical thickness of 200–400 nm.

To create the geometry required for the levelling experiment, a first PS film is floated onto a bath of ultrapure (MilliQ) water. Due to the relatively low molecular weight of the PS employed here, the glassy film spontaneously ruptures into several pieces. A second (uniform) PS film on

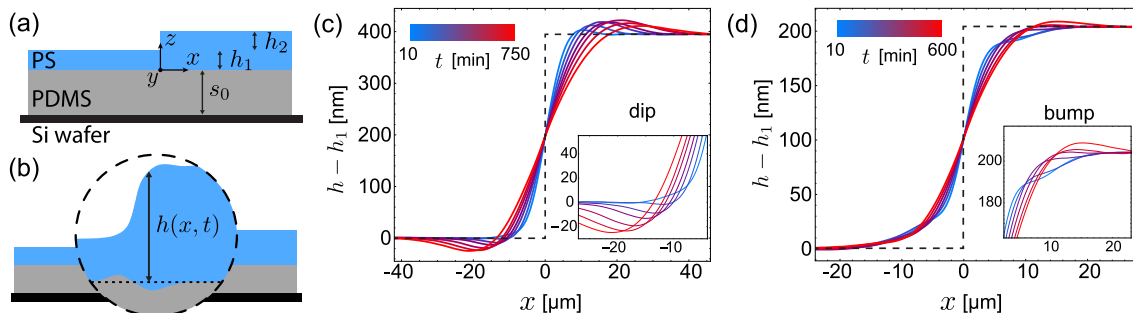


FIG. 1. (a) Schematics of the initial geometry: a stepped liquid polystyrene (PS) film is supported by an elastic layer of polydimethylsiloxane (PDMS). (b) Schematics of the levelling dynamics: the liquid height h depends on the horizontal position x and the time t . The elastic layer deforms due to the interaction with the liquid. (c) Experimental profiles of the liquid-air interface during levelling at $T_a = 140^\circ\text{C}$ on 10:1 PDMS. The initial step has $h_1 = h_2 = 395$ nm. The inset shows a closeup of the dip region. (d) Experimental profiles during levelling at $T_a = 140^\circ\text{C}$ on the softer 40:1 PDMS. The initial step has $h_1 = h_2 = 200$ nm. The inset shows a magnification of the bump region. Dashed lines in (c) and (d) indicate the initial condition.

mica is approached to the surface of water, put into contact with the floating PS pieces and rapidly released as soon as the mica touches the water. That way a collection of PS pieces is transferred onto the second PS film, forming a discontinuous double layer that is then floated again onto a clean water surface. At this stage, a sample with the elastic layer of PDMS is put into the water and gently approached to the floating PS from underneath. As soon as contact between the PS film and the PDMS substrate is established, the sample is slowly released from the bath. Finally, the initial configuration depicted in Fig. 1(a) is obtained. For a direct comparison with capillary levelling on rigid substrates, we also prepared stepped PS films of the same molecular weight 600 on freshly cleaned Si wafers (Si-Mat, Germany) using the same transfer procedure.

Using an optical microscope we identify spots where isolated pieces of PS on the uniform PS layer display a clean and straight interfacial front. A vertical cross section of these spots corresponds to a stepped PS-air interface, which is invariant in the y dimension [see Fig. 1(a) for a sketch of this geometry]. Using AFM, the 3D shape of the interface is scanned and a 2D profile is obtained by averaging along y . From this profile the initial height of the step h_2 is measured. The sample is then annealed at an elevated temperature $T_a = 120\text{--}160^\circ\text{C}$ (above the glass-transition temperature of PS) using a high-precision heating stage (Linkam, UK). During this annealing period the liquid PS flows. Note that on the experimental time scales and for the typical flow velocities studied here the PS is well described by a Newtonian viscous fluid [29,31–34] (viscoelastic and non-Newtonian effects are absent since the Weissenberg number $Wi \ll 1$ and the Deborah number $De \ll 1$). After a given annealing time t , the sample is removed from the heating stage and quenched at room temperature (below the glass-transition temperature of PS). The three-dimensional (3D) PS-air interface in the zone of interest is scanned with the AFM and a 2D profile is again obtained by averaging along y . This procedure is repeated several times in order to monitor the temporal evolution of the height $h(x,t)$ of the PS-air interface [defined with respect to the undeformed elastic-liquid interface; see Fig. 1(b)]. At the end of each experiment, the thickness h_1 of the uniform PS layer is measured by AFM.

III. EXPERIMENTAL RESULTS AND DISCUSSION

A. Profile evolution

The temporal evolutions of two typical profiles are reported in Figs. 1(c) and 1(d), corresponding to films that are supported by elastic foundations made of 10:1 PDMS and 40:1 PDMS, respectively. As expected, the levelling process manifests itself in a broadening of the initial step over time.

In all profiles, three main regions can be identified (from left to right): a region with positive curvature (negative Laplace pressure in the liquid), an almost linear region around $x = 0$ (zero Laplace pressure), and a region of negative curvature (positive Laplace pressure in the liquid). These regions are surrounded by two unperturbed flat interfaces exhibiting $h = h_1$ and $h = h_1 + h_2$. In analogy with earlier works on rigid substrates [31], we refer to the positive-curvature region of the profile as the *dip*, and the negative-curvature region as the *bump*. Close-up views of those are given in the insets of Figs. 1(c) and 1(d).

The decrease of the slope of the linear region is a direct consequence of levelling. A less intuitive evolution is observed in the bump and dip regions. For instance, in the first profile of Fig. 1(c), recorded after 10 min of annealing, a bump has already emerged while a signature of a dip cannot be identified yet. As the interface evolves in time, a dip appears and both the bump and the dip grow substantially. At a later stage of the evolution, the height of the bump and the depth of the dip eventually saturate. This vertical evolution of the bump and the dip is at variance with what has been observed in the rigid-substrate case [29,31], where the values of the maximum and the minimum are purely dictated by h_1 and h_2 and stay fixed during the experimentally accessible evolution. That specific signature of the soft foundation is even amplified for PS levelling on the softer (40:1 PDMS) foundation; see Fig. 1(d). The evolution of the bump and dip results from the interaction between the liquid and the soft foundation. Indeed, the curvature gradients of the liquid-air interface give rise to Laplace pressure gradients that drive the flow. The pressure and flow fields both induce elastic deformations in the substrate. Intuitively, the negative Laplace pressure below the dip results in a traction that pulls upwards on the PDMS substrate, while the positive Laplace pressure below the bump induces a displacement in the opposite direction. In addition, a no-slip condition at the solid-liquid interface coupled to the flow induces an horizontal displacement field in the PDMS substrate. These displacements of the foundation act back on the liquid-air interface by volume conservation. According to this picture, the displacement of the solid-liquid interface is expected to tend to zero over time, since the curvature gradients of the liquid-air interface and the associated flow decrease.

B. Temporal evolution of the profile width

The capillary levelling on a rigid substrate possesses an exact self-similar behavior in the variable $x/t^{1/4}$, leading to a perfect collapse of the rescaled height profiles of a given evolution [31]. In contrast, for a soft foundation, no collapse of the profiles is observed (not shown) when the horizontal axis x is divided by $t^{1/4}$.

To determine whether another self-similarity exists or not, we first quantify the horizontal evolution of the profile by introducing a definition of its width [see Fig. 2(a), inset]: $w(t) = x(h = h_1 + 0.6 h_2) - x(h = h_1 + 0.4 h_2)$. With this definition, only the linear region of the profile matters and the peculiar shapes of the dip and bump do not affect the value of w . The temporal evolution of w was measured in several experiments, featuring different values of h_1 , h_2 as well as three stiffnesses of the soft foundation. First, the absolute value of w at a given time is larger for thicker liquid films, as expected since more liquid can flow. Second, the data plotted in Fig. 2(a) clearly show that in all these experiments the width increases as $w \sim t^{1/6}$. Equivalently, dividing the horizontal axis x by $t^{1/6}$ leads to a collapse of all the linear regions of the profiles, as shown in Figs. 2(b) and 2(c). However, while allowing for the appreciation of the vertical evolution of the bump and dip, the noncollapse of the full profiles indicates the absence of true self-similarity in the problem. Nevertheless, we retain that for practical purposes associated with elastocapillary levelling, the $w \sim t^{1/6}$ scaling encompasses most of the evolution in terms of flowing material.

C. Role of viscosity

The impact of the soft foundation on the levelling dynamics depends on two essential aspects: the stiffness of the foundation and how strongly the liquid acts on it. The first aspect is constant, and

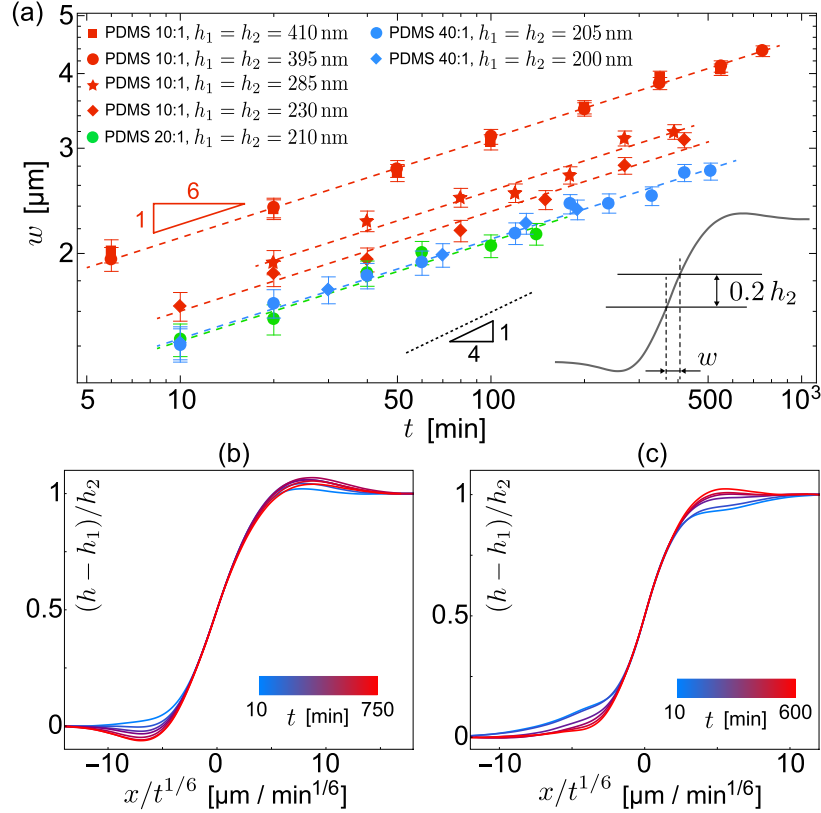


FIG. 2. (a) Experimental evolution of the profile width w (proportional to the lateral extent of the linear region as displayed in the inset) as a function of time t , in log-log scale, for samples involving different liquid-film thicknesses and substrate elasticities. All datasets seem to exhibit a $t^{1/6}$ power law. The slope corresponding to a $t^{1/4}$ evolution (rigid-substrate case) is displayed for comparison. (b) Experimental levelling profiles on 10:1 PDMS from Fig. 1(c) with the horizontal axis rescaled by $t^{-1/6}$. (c) Same rescaling applied for the levelling profiles on 40:1 PDMS shown in Fig. 1(d).

controlled by both the Young's modulus E and the thickness s_0 of the (incompressible) PDMS layer, the former being fixed by the base-to-cross-linker ratio. The second aspect is ultimately controlled by the Laplace pressure, which is directly related to the curvature of the liquid-air interface. Even for a single experiment, the amplitude of the curvature field associated with the profile evolves along time, from large values at early times, to small ones at long times when the profile becomes almost flat. Thus, we expect the relative impact of the soft foundation to change over time.

This time dependence can be explored by adjusting the PS viscosity. Indeed, the latter strongly decreases for increasing annealing temperature, while the other quantities remain mostly unaffected by this change. Hence, the levelling dynamics can be slowed down by performing experiments at lower annealing temperature, in order to investigate the dynamics close to the initial condition, and accelerated at higher annealing temperature in order to access the late-stage dynamics. Here, we report on experiments at 120°C (high viscosity) and 160°C (low viscosity) and compare the results to our previous experiments at 140°C .

Following lubrication theory [37], the typical time scale of a levelling experiment is directly fixed by the capillary velocity γ/η , where γ denotes the PS-air surface tension and η the PS viscosity, as well as the thickness $h_0 = h_1 + h_2/2$ of the PS film. In Fig. 3, the experimental profile width is plotted as a function of $\gamma h_0^3 t / \eta$ [31], for experiments involving different liquid film thicknesses, substrate elasticities, and annealing temperatures. Samples with PS stepped films on bare (rigid) Si wafers were used to measure the capillary velocity γ/η at different annealing temperatures [36]. In these calibration measurements, the profile width follows a $t^{1/4}$ power law, as expected [31]. In

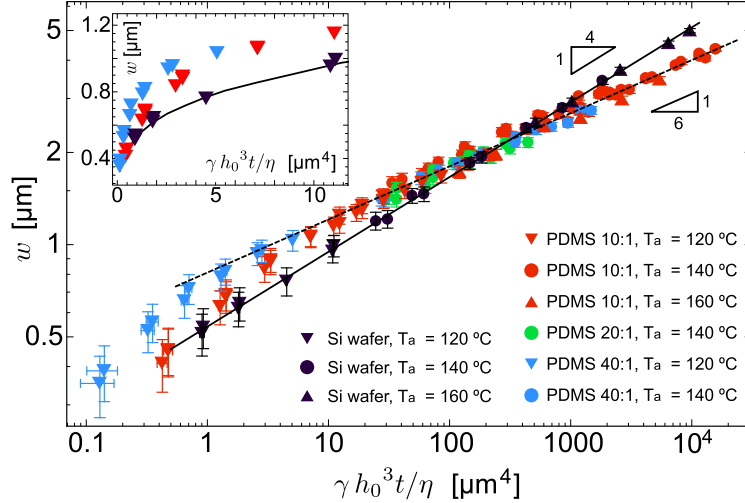


FIG. 3. Experimental profile width w [see Fig. 2(a), inset] as a function of $\gamma h_0^3 t / \eta$ (see definitions in text), in log-log scale, for all the different samples and temperatures. Experiments for 10:1 (red), 20:1 (green), and 40:1 (blue) PDMS substrates, as well as annealing temperatures $T_a = 120^\circ\text{C}$ (down triangle), 140°C (circle), 160°C (up triangle) are displayed. Most of the data collapses on a single curve of slope $1/6$ (dashed line). The data for capillary levelling on rigid substrates (black symbols) are shown for comparison and collapse on a single curve of slope $1/4$ (solid line). The inset displays a closeup of the early-time regime in linear representation.

contrast, for the experiments on elastic foundations, two different regimes might be distinguished: for $\gamma h_0^3 t / \eta$ larger than $\sim 5 \mu\text{m}^4$, the width follows a $t^{1/6}$ power law and all datasets collapse onto a single master curve over three to four orders of magnitude on the horizontal scale; for values of $\gamma h_0^3 t / \eta$ smaller than $\sim 5 \mu\text{m}^4$, the evolution depends on the elastic modulus and it appears that the softer the foundation the faster the evolution (see inset of Fig. 3).

D. Vertical evolution of the dip and bump

Guided by the previous discussion, we now divide the horizontal axis x of all the height profiles in different experiments by the quantity $(\gamma h_0^3 t / \eta)^{1/6}$. As shown in Fig. 4, this rescaling leads to a collapse in the linear region of the profiles, while the dip and the bump regions display significant deviations from a universal collapse.

In order to characterize these deviations, we introduce the Maxwell-like viscoelastic time η/E and define the dimensionless time $\tau = Et/\eta$. This dimensionless parameter quantifies the role of the deformable substrate: experiments on softer foundations (lower E) or evolving slower (larger η) correspond to smaller values of τ , and are therefore expected to show more pronounced elastic behaviors. As seen in Fig. 4, we find a systematic trend when plotting the experimental levelling profiles using the parameter τ . Profiles with large τ (dark green and black) display clear bumps and dips, comparable in their vertical extents to the corresponding features observed on rigid substrates (not shown). In contrast, profiles with small τ (yellow and bright green) feature large deviations with respect to this limit.

The previous observation can be quantified by tracking the temporal evolution of the height of the liquid-air interface $h_d(t) = h(x_d, t)$ at the dip position x_d , which we define as the (time-independent) position at which the global minimum is located at the latest time of the levelling dynamics (see arrow in Fig. 4). The inset of Fig. 4 displays the normalized difference between h_d and the corresponding value for a rigid substrate $h_{d,\text{rig}}$, plotted as a function of τ . We find that the parameter τ allows for a reasonable rescaling of the data. As anticipated, the difference between levelling on rigid and soft substrates decreases monotonically as a function of this dimensionless time. For small τ , the

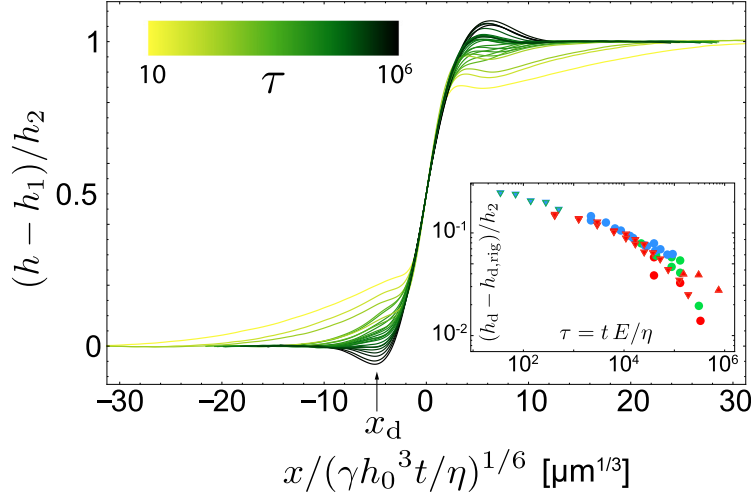


FIG. 4. Rescaled experimental profiles for all data displayed in Fig. 3, color coded according to the dimensionless time $\tau = tE/\eta$. Inset: Evolution with τ of the normalized distance between the height h_d of the liquid-air interface at the dip position x_d and the corresponding value $h_{d,\text{rig}}$ for the rigid case. Note that in all the experiments $h_1 = h_2$. Symbols are chosen to be consistent with Fig. 3.

difference can be larger than 20% of the liquid film thickness, while for large τ it drops to less than 1%, which corresponds to the vertical resolution of the AFM.

IV. THEORETICAL MODELLING

A. Model and solutions

We consider an incompressible elastic slab atop which a viscous liquid film with an initial stepped liquid-air interface profile is placed. The following hypotheses are retained: (i) the height h_2 of the step is small as compared to the thickness $h_0 = h_1 + h_2/2$ of the (flat) equilibrium liquid profile; (ii) the slopes at the liquid-air interface are small, such that the curvature of the interface can be approximated by $\partial_x^2 h$; (iii) the lubrication approximation applies in the liquid, i.e., typical vertical length scales are much smaller than horizontal ones; (iv) the components of the displacement field in the elastic material are small compared to the thickness of the elastic layer (linear elastic behavior); (v) the elastic layer is incompressible (valid assumption for PDMS). Note that the hypotheses (i)–(iii) have been successfully applied in previous work on the levelling dynamics of a stepped perturbation of a liquid film placed on a rigid substrate [39].

Below, we summarize the model, the complete details of which are provided in the Supplemental Material [44]. The main difference with previous work [39] is the coupling of fluid flow and pressure to elastic deformations of the substrate. The Laplace pressure is transmitted by the fluid and gives rise to a vertical displacement $\delta(x, t)$ of the solid-liquid interface, and thus a horizontal displacement $u_s(x, t)$ of the latter by incompressibility. Consequently, the no-slip condition at the solid-liquid interface implies that a fluid element in contact with the elastic surface will have a nonzero horizontal velocity $\partial_t u_s$. In addition, we assume no shear at the liquid-air interface. After linearization, the modified thin-film equation reads

$$\frac{\partial \Delta}{\partial t} + \frac{\partial}{\partial x} \left[-\frac{h_0^3}{3\eta} \frac{\partial p}{\partial x} + h_0 \frac{\partial u_s}{\partial t} \right] = 0, \quad (1)$$

where $\Delta(x, t) = h(x, t) - \delta(x, t) - h_0$ is the excess thickness of the liquid layer with respect to the equilibrium value h_0 . The excess pressure $p(x, t)$ in the film, with respect to the atmospheric value,

is given by the (small-slope) Laplace pressure:

$$p \simeq -\gamma \frac{\partial^2(\Delta + \delta)}{\partial x^2}. \quad (2)$$

Furthermore, the surface elastic displacements are related to the pressure field through

$$\delta = -\frac{1}{\sqrt{2\pi\mu}} \int_{-\infty}^{\infty} k(x-x')p(x',t) dx', \quad (3)$$

$$u_s = -\frac{1}{\sqrt{2\pi\mu}} \int_{-\infty}^{\infty} k_s(x-x')p(x',t) dx', \quad (4)$$

where $\mu = E/3$ is the shear modulus of the incompressible substrate, and where $k(x)$ and $k_s(x)$ are the Green's functions (see Supplemental Material [44]) for the vertical and horizontal surface displacements, i.e., the fundamental responses due to a linelike pressure source of magnitude $-\sqrt{2\pi\mu}$ acting on the surface of the infinitely long elastic layer.

Equations (1)–(4) can be solved analytically using Fourier transforms (see Supplemental Material [44]), and we obtain

$$\tilde{\Delta}(\lambda, t) = -\frac{h_2}{2i\lambda} \sqrt{\frac{2}{\pi}} \exp \left[-\left(\frac{\gamma\lambda^4 h_0^3}{3\eta} \right) \frac{t}{1 + (\gamma\lambda^2/\mu)(\tilde{k} + i\lambda h_0 \tilde{k}_s)} \right], \quad (5)$$

$$\tilde{\delta} = \frac{-\tilde{k}}{\mu} \frac{\gamma\lambda^2 \tilde{\Delta}}{[1 + (\gamma\lambda^2/\mu)\tilde{k}]}, \quad (6)$$

where $\tilde{\cdot}$ denotes the Fourier transform of a function and λ is the conjugated Fourier variable, i.e., $\tilde{f}(\lambda) = \frac{1}{\sqrt{2\pi}} \int_{-\infty}^{\infty} f(x)e^{i\lambda x} dx$. The vertical displacement $h(x, t) - h_0$ of the liquid-air interface with respect to its final state is then determined by summing the inverse Fourier transforms of Eqs. (5) and (6).

Figure 5(a) displays the theoretical profiles of both the liquid-air interface $z = h(x, t)$ and the solid-liquid interface $z = \delta(x, t)$, for a stepped liquid film with thicknesses $h_1 = h_2 = 2h_0/3 = 120$ nm, supported by a substrate of stiffness $\mu = 25$ kPa and thickness $s_0 = 2$ μ m. The viscosity $\eta = 2.5 \times 10^6$ Pa s is adapted to the PS viscosity at the annealing temperature $T_a = 120^\circ\text{C}$ in the experiment. The PS-air surface tension is fixed to $\gamma = 30$ mN/m [45]. We find that the profiles predicted by this model reproduce some of the key features observed in our experiments. In particular, the evolutions of the bump and dip regions in the theoretical profiles (see Fig. 5 inset) qualitatively capture the characteristic behaviors recorded in the experiment [see Fig. 1(c) inset].

An advantage of this theoretical approach is the possibility to extract information about the deformation of the solid-liquid interface. As shown in Fig. 5, the substrate deforms mainly in the bump and dip regions, as a result of their large curvatures. The maximal vertical displacement of the solid-liquid interface in this example is ~ 25 nm, and it reduces over time, due to the levelling of the profile and the associated lower curvatures.

B. Evolution of the profile width

The temporal evolution of the width w [see Fig. 2(a), inset] of the profiles was extracted from our theoretical model for a series of different parameters. Figure 6 shows the theoretical width w as a function of the quantity $\gamma h_0^3 t / \eta$ for all cases studied. With this rescaling, it is evident that the width of the theoretical profile depends strongly on elasticity at early times, while all datasets collapse onto a single curve at long times. Moreover, this master curve exhibits a slope of 1/4, and thus inherits a characteristic signature of capillary levelling on a rigid substrate. The early-time data show that the width is larger than on a rigid substrate, but with a slower evolution and thus a lower effective exponent. These observations are in qualitative agreement with our experimental data. However,

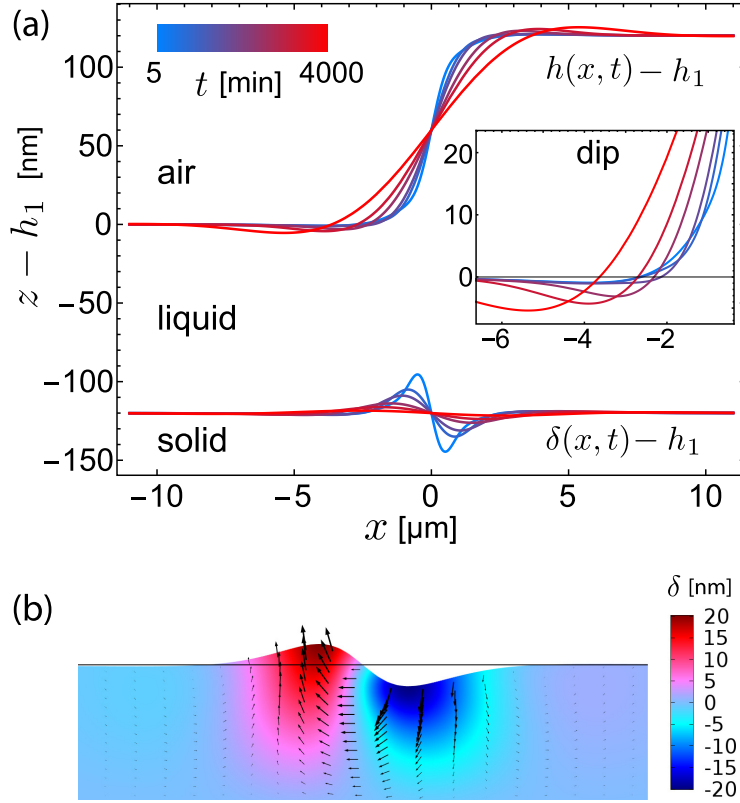


FIG. 5. (a) Theoretical profiles for the liquid-air interface $z = h(x, t)$ and the solid-liquid interface $z = \delta(x, t)$, both shifted vertically by $-h_1$. Here, we employ $s_0 = 2 \mu\text{m}$, $h_1 = h_2 = 2h_0/3 = 120 \text{ nm}$, $\mu = 25 \text{ kPa}$, $\gamma = 30 \text{ mN/m}$, $\eta = 2.5 \times 10^6 \text{ Pa s}$. The inset displays a close-up of the dip region. (b) Finite-element simulation (COMSOL) of the solid's total displacement (black arrows) and its vertical component δ (color code). The result has been obtained by imposing the Laplace pressure field corresponding to the first profile in (a) to a slab of elastic material exhibiting comparable geometrical and mechanical properties as in (a). The maximal displacement of 22 nm is in good agreement with the theoretical prediction shown in (a).

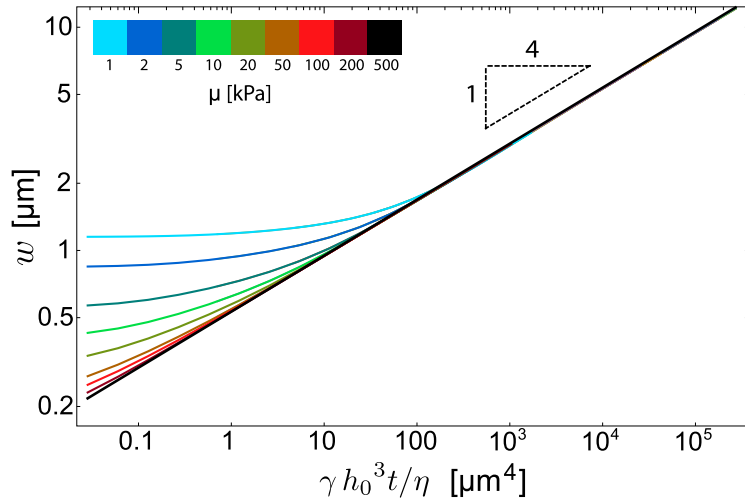


FIG. 6. Temporal evolution of the profile width [see definition in Fig. 2(a), inset], in log-log scale, as predicted by the theoretical model, for different shear moduli, viscosities, and liquid-film thicknesses. The $1/4$ power law corresponding to a rigid substrate is indicated.

interestingly, we do not recover in the experiments the predicted transition to a long-term rigidlike 1/4 exponent, but instead keep a 1/6 exponent (see Fig. 3).

It thus appears that we do not achieve a full quantitative agreement between the theoretical and experimental profiles. The initially sharp stepped profile could possibly introduce an important limitation on the validity of the lubrication hypothesis. Indeed, while this is not a problem for the rigid case since the initial condition is rapidly forgotten [40], it is not *a priori* clear if and how elasticity affects this statement. We thus checked (see Supplemental Material [44]) that replacing the lubrication approximation by the full Stokes equations for the liquid part does not change notably the theoretical results. We also checked that the linearization of the thin-film equation is not the origin of the aforementioned discrepancy: in a test experiment with $h_2 \ll h_1$ on a soft substrate we observed the same characteristic features—and especially the 1/6 temporal exponent absent of the theoretical solutions—as the ones reported for the $h_1 \approx h_2$ geometry (see Supplemental Material [44]). Besides, we note that while the vertical deformations of the elastic material (see Fig. 5) are small compared to the thickness s_0 of the elastic layer in the experimentally accessible temporal range, the assumption of small deformations could be violated at earlier times without affecting the long-term behavior at stake.

Finally, we propose a simplified argument to qualitatively explain the smaller transient exponent in Fig. 6. We assume that the vertical displacement $\delta(x, t)$ of the solid-liquid interface mostly translates the liquid above, such that the liquid-air interface displaces vertically by the same amount, following

$$h(x, t) = h_r(x, t) + \delta(x, t), \quad (7)$$

where h_r is the profile of the liquid-air interface that would be observed on a rigid substrate. Note that this simplified mechanism does not violate conservation of volume in the liquid layer. By deriving the previous equation with respect to x , and evaluating it at the center of the profile ($x = 0$), we obtain an expression for the central slope of the interface:

$$\partial_x h(0, t) = \partial_x h_r(0, t) + \partial_x \delta(0, t). \quad (8)$$

Due to the positive (negative) displacement of the solid-liquid interface in the region $x < 0$ ($x > 0$), $\partial_x \delta(0, t)$ is always negative, as seen in Fig. 5. Therefore, we expect a reduced slope of the liquid-air interface in the linear region, which is in agreement with the increased width observed on soft substrates. Moreover, taking the second derivative of Eq. (7) with respect to x leads to

$$\partial_x^2 h(x, t) = \partial_x^2 h_r(x, t) + \partial_x^2 \delta(x, t). \quad (9)$$

In the dip region, $h_r(x, t)$ is convex in space (positive second derivative with respect to x), while $\delta(x, t)$ is assumed to be concave in space (negative second derivative with respect to x) up to some distance from the center (see Fig. 5). Therefore, the resulting curvature is expected to be reduced. A similar argument leads to the same conclusion in the bump region. This effect corresponds to a reduction of the Laplace pressure and, hence, of the driving force for the levelling process: the evolution is slower which translates into a smaller effective exponent.

C. Finite-element simulations

To check the validity of the predicted shape of the solid-liquid interface, we performed finite-element simulations using COMSOL Multiphysics. Starting from an experimental profile of the liquid-air interface at a given time t , the curvature and the resulting pressure field $p(x, t)$ were extracted. This pressure field was used as a top boundary condition for the stress in a 2D slab of an incompressible elastic material exhibiting a comparable thickness and stiffness as in the corresponding experiment. The slab size in the x direction was chosen to be 20 μm , which is large enough compared to the typical horizontal extent of the elastic deformation [see Fig. 5(a)]. The bottom boundary of the slab was fixed (zero displacement), while the left and right boundaries were let free (zero stress). The deformation field predicted by these finite-element simulations is shown in Fig. 5(b) and found to be in quantitative agreement with our theoretical prediction.

V. CONCLUSION

We report on the elastocapillary levelling of a thin viscous film flowing above a soft foundation. The experiments involve different liquid film thicknesses, viscosities, and substrate elasticities. We observe that the levelling dynamics on a soft substrate is qualitatively and quantitatively different with respect to that on a rigid substrate. At the earliest times, the lateral evolution of the profiles is faster on soft substrates than on rigid ones, as a possible result of the “instantaneous” substrate deformation caused by the capillary pressure in the liquid. Immediately after, this trend reverses: the lateral evolution of the profiles on soft substrates becomes slower than on rigid ones, which might be related to a reduction of the capillary driving force associated with the elastic deformation. Interestingly, we find that the width of the liquid-air interface follows a $t^{1/6}$ power law over several orders of magnitude on the relevant scale, in sharp contrast with the classical $t^{1/4}$ law observed on rigid substrates.

To the best of our knowledge, this system is a unique example of dynamical elastocapillarity that is not mediated by the presence of a contact line, but only by the Laplace pressure inside the liquid. Notwithstanding, this process is not trivial, since the coupled evolutions of both the liquid-air and solid-liquid interfaces lead to an intricate dynamics. Our theoretical approach, based on linear elasticity and lubrication approximation, is able to reproduce some observations, such as the typical shapes of the height profiles and the dynamics at short times.

While some characteristic experimental features are captured by the model, a full quantitative agreement is still lacking to date. Given the careful validation of all the basic assumptions underlying our theoretical approach (i.e., lubrication approximation, linearization of the thin-film equation, and linear elasticity), we hypothesize that additional effects are present in the materials or experiments. For instance, it remains unclear whether the physicochemical and rheological properties at the surface of PDMS films, which were prepared using conventional recipes, are correctly described by bulk-measured quantities [9]. We believe that further investigations of the elastocapillary levelling on soft foundations, using different elastic materials and preparation schemes, could significantly advance the understanding of such effects and dynamic elastocapillarity in general.

Finally, we would like to stress that the signatures of elasticity in the elastocapillary levelling dynamics are prominent even on substrates that are not very soft (bulk Young’s moduli of the PDMS in the \sim MPa range) and for small Laplace pressures. In light of applications such as traction-force microscopy, where localized displacements of a soft surface are translated into the corresponding forces acting on the material, the elastocapillary levelling on soft substrates might be an ideal model system to quantitatively study surface deformations in soft materials with precisely controlled pressure fields.

ACKNOWLEDGMENTS

The authors acknowledge S. Herminghaus, J. Snoeijer, A. Pandey, H. Stone, M. Brinkmann, C. Mailliet, P. Damman, K. Dalnoki-Veress, A. Jagota, and J. McGraw for interesting discussions. The German Research Foundation (DFG) is acknowledged for financial support under Grant No. BA 3406/2. V.B. acknowledges financial support from École Normale Supérieure. T.S. acknowledges financial support from the Global Station for Soft Matter, a project of Global Institution for Collaborative Research and Education at Hokkaido University. C.-Y.H. (elasticity modelling) acknowledges financial support from the U.S. Department of Energy, Office of Basic Energy Sciences, Division of Materials Sciences and Engineering under Award No. DE-FG02-07ER46463, and from the Michelin-ESPCI Paris Chair. O.B. acknowledges financial support from the Joliot ESPCI Paris Chair and the Total-ESPCI Paris Chair.

-
- [1] J. M. Skotheim and L. Mahadevan, Soft Lubrication, *Phys. Rev. Lett.* **92**, 245509 (2004).
 [2] T. Salez and L. Mahadevan, Elastohydrodynamics of a sliding, spinning and sedimenting cylinder near a soft wall, *J. Fluid Mech.* **779**, 181 (2015).

- [3] B. Saintyves, T. Jules, T. Salez, and L. Mahadevan, Self-sustained lift and low friction via soft lubrication, [Proc. Natl. Acad. Sci. USA **113**, 5847 \(2016\)](#).
- [4] R. Trouilloud, T. S. Yu, A. E. Hosoi, and E. Lauga, Soft Swimming: Exploiting Deformable Interfaces for Low Reynolds Number Locomotion, [Phys. Rev. Lett. **101**, 048102 \(2008\)](#).
- [5] E. M. Purcell, Life at low reynolds number, [Am. J. Phys **45**, 3 \(1977\)](#).
- [6] C. W. McCutchen, Lubrication of and by articular cartilage, in *Cartilage: Biomedical Aspects*, Vol. 3 (Academic Press, New York, 1983), pp. 87–107.
- [7] D. J. Coyle, Forward roll coating with deformable rolls: a simple one-dimensional elastohydrodynamic model, [Chem. Eng. Sci. **43**, 2673 \(1988\)](#).
- [8] B Roman and J Bico, Elasto-capillarity: deforming an elastic structure with a liquid droplet, [J. Phys.: Condens. Matter **22** 493101 \(2010\)](#).
- [9] B. Andreotti, O. Bäümchen, F. Boulogne, K. E. Daniels, E. R. Dufresne, H. Perrin, T. Salez, J. H. Snoeijer, and R. W. Style, Solid capillarity: when and how does surface tension deform soft solids? [Soft Matter **12**, 2993 \(2016\)](#).
- [10] R. W. Style, A. Jagota, C.-Y. Hui, and E. R. Dufresne, Elastocapillarity: Surface tension and the mechanics of soft solids, [Annu. Rev. Condens. Matter Phys. **8**, 99 \(2016\)](#).
- [11] C. Py, P. Reverdy, L. Doppler, J. Bico, B. Roman, and C. N. Baroud, Capillary Origami: Spontaneous Wrapping of a Droplet with an Elastic Sheet, [Phys. Rev. Lett. **98**, 156103 \(2007\)](#).
- [12] A. Antkowiak, B. Audoly, C. Jossierand, S. Neukirch, and M. Rivetti, Instant fabrication and selection of folded structures using drop impact, [Proc. Natl. Acad. Sci. USA **108**, 10400 \(2011\)](#).
- [13] C. Duprat, S. Protiere, A. Y. Beebe, and H. A. Stone, Wetting of flexible fibre arrays, [Nature \(London\) **482**, 510 \(2012\)](#).
- [14] N. Nadermann, C.-Y. Hui, and A. Jagota, Solid surface tension measured by a liquid drop under a solid film, [Proc. Natl. Acad. Sci. USA **110**, 10541 \(2013\)](#).
- [15] R. D. Schulman and K. Dalnoki-Veress, Liquid Droplets on a Highly Deformable Membrane, [Phys. Rev. Lett. **115**, 206101 \(2015\)](#).
- [16] J. D. Paulsen, V. Demery, C. D. Santangelo, T. P. Russell, B. Davidovitch, and N. Menon, Optimal wrapping of liquid droplets with ultrathin sheets, [Nat. Mater. **14**, 1206 \(2015\)](#).
- [17] H. Elettro, S. Neukirch, F. Vollrath, and A. Antkowiak, In-drop capillary spooling of spider capture thread inspires hybrid fibers with mixed solid-liquid mechanical properties, [Proc. Natl. Acad. Sci. USA **113**, 6143 \(2016\)](#).
- [18] R. D. Schulman, A. Porat, K. Charlesworth, A. Fortais, T. Salez, E. Raphaël, and K. Dalnoki-Veress, Elastocapillary bending of microfibers around liquid droplets, [Soft Matter **13**, 720 \(2017\)](#).
- [19] G. R. Lester, Contact angles of liquids at deformable solid surfaces, [J. Colloid Sci. **16**, 315 \(1961\)](#).
- [20] R. Pericet-Cámara, A. Best, H.-J. Butt, and E. Bonaccorso, Effect of capillary pressure and surface tension on the deformation of elastic surfaces by sessile liquid microdrops: An experimental investigation, [Langmuir **24**, 10565 \(2008\)](#).
- [21] E. R. Jerison, Y. Xu, L. A. Wilen, and E. R. Dufresne, Deformation of an Elastic Substrate by a Three-Phase Contact Line, [Phys. Rev. Lett. **106**, 186103 \(2011\)](#).
- [22] A. Marchand, S. Das, J. H. Snoeijer, and B. Andreotti, Contact Angles on a Soft Solid: from Young’s Law to Neumann’s Law, [Phys. Rev. Lett. **109**, 236101 \(2012\)](#).
- [23] L. Limat, Straight contact lines on a soft, incompressible solid, [Eur. Phys. J. E **35**, 1 \(2012\)](#).
- [24] R. W. Style, R. Boltyskiy, Y. Che, J. S. Wettlaufer, L. A. Wilen, and E. R. Dufresne, Universal Deformation of Soft Substrates Near a Contact Line and the Direct Measurement of Solid Surface Stresses, [Phys. Rev. Lett. **110**, 066103 \(2013\)](#).
- [25] L. A. Lubbers, J. H. Weijs, L. Botto, S. Das, B. Andreotti, and J. H. Snoeijer, Drops on soft solids: free energy and double transition of contact angles, [J. Fluid Mech. **747**, R1 \(2014\)](#).
- [26] R. W. Style, Y. Che, S. J. Park, B. M. Weon, J. H. Je, C. Hyland, G. K. German, M. P. Power, L. A. Wilen, J. S. Wettlaufer, and E. R. Dufresne, Patterning droplets with durotaxis, [Proc. Natl. Acad. Sci. USA **110**, 12541 \(2013\)](#).
- [27] S. Karpitschka, S. Das, M. van Gorcum, H. Perrin, B. Andreotti, and J. H. Snoeijer, Droplets move over viscoelastic substrates by surfing a ridge, [Nat. Commun. **6** 7891 \(2015\)](#).

- [28] S. Karpitschka, A. Pandey, L. A. Lubbers, J. H. Weijss, L. Botto, S. Das, B. Andreotti, and J. H. Snoeijer, Liquid drops attract or repel by the inverted cheerios effect, *Proc. Natl. Acad. Sci. USA* **113**, 7403 (2016).
- [29] J. D. McGraw, N. M. Jago, and K. Dalnoki-Veress, Capillary levelling as a probe of thin film polymer rheology, *Soft Matter* **7**, 7832 (2011).
- [30] J. Teisseire, A. Revaux, M. Foresti, and E. Barthel, Confinement and flow dynamics in thin polymer films for nanoimprint lithography, *Appl. Phys. Lett.* **98**, 013106 (2011).
- [31] J. D. McGraw, T. Salez, O. Bäumchen, E. Raphaël, and K. Dalnoki-Veress, Self-Similarity and Energy Dissipation in Stepped Polymer Films, *Phys. Rev. Lett.* **109**, 128303 (2012).
- [32] O. Bäumchen, M. Benzaquen, T. Salez, J. D. McGraw, M. Backholm, P. Fowler, E. Raphaël, and K. Dalnoki-Veress, Relaxation and intermediate asymptotics of a rectangular trench in a viscous film, *Phys. Rev. E* **88**, 035001 (2013).
- [33] M. Backholm, M. Benzaquen, T. Salez, E. Raphaël, and K. Dalnoki-Veress, Capillary levelling of a cylindrical hole in a viscous film, *Soft Matter* **10**, 2550 (2014).
- [34] M. Ilton, M. M. P. Couchman, C. Gerbelot, M. Benzaquen, P. D. Fowler, H. A. Stone, E. Raphaël, K. Dalnoki-Veress, and T. Salez, Capillary Levelling of Freestanding Liquid Nanofilms, *Phys. Rev. Lett.* **117**, 167801 (2016).
- [35] E. Rognin, S. Landis, and L. Davoust, Viscosity measurements of thin polymer films from reflow of spatially modulated nanoimprinted patterns, *Phys. Rev. E* **84**, 041805 (2011).
- [36] J. D. McGraw, T. Salez, O. Bäumchen, E. Raphaël, and K. Dalnoki-Veress, Capillary leveling of stepped films with inhomogeneous molecular mobility, *Soft Matter* **9**, 8297 (2013).
- [37] A. Oron, S. H. Davis, and S. G. Bankoff, Long-scale evolution of thin liquid films, *Rev. Mod. Phys.* **69**, 931 (1997).
- [38] T. Salez, J. D. McGraw, S. L. Cormier, O. Bäumchen, K. Dalnoki-Veress, and E. Raphaël, Numerical solutions of thin-film equations for polymer flows, *Eur. Phys. J. E* **35**, 114 (2012).
- [39] T. Salez, J. D. McGraw, O. Bäumchen, K. Dalnoki-Veress, and E. Raphaël, Capillary-driven flow induced by a stepped perturbation atop a viscous film, *Phys. Fluids* **24**, 102111 (2012).
- [40] M. Benzaquen, T. Salez, and E. Raphaël, Intermediate asymptotics of the capillary-driven thin film equation, *Eur. Phys. J. E* **36**, 82 (2013).
- [41] I. Tanis, H. Meyer, T. Salez, E. Raphaël, A. C. Maggs, and J. Baschnagel, Molecular dynamics simulation of the capillary leveling of viscoelastic polymer films, *J. Chem. Phys.* **146**, 203327 (2017).
- [42] X. Q. Brown, K. Ookawa, and J. Y. Wong, Evaluation of polydimethylsiloxane scaffolds with physiologically-relevant elastic moduli: interplay of substrate mechanics and surface chemistry effects on vascular smooth muscle cell response, *Biomaterials* **26**, 3123 (2005).
- [43] A. Hemmerle, M. Schröter, and L. Goehring, A cohesive granular material with tunable elasticity, *Sci. Rep.* **6**, 35650 (2016).
- [44] See Supplemental Material at <http://link.aps.org/supplemental/10.1103/PhysRevFluids.2.094001> for further details on the theoretical model, a comparison between lubrication and full-Stokes models for the liquid part, and an additional experiment with a small step atop a thick liquid base film (the ensemble being placed on the soft foundation).
- [45] J. Brandrup, E. H. Immergut, E. A. Grulke, A. Abe, and D. R. Bloch, *Polymer Handbook* (Wiley, New York, 1989), Vol. 7.

Elastocapillary Levelling of Thin Viscous Films on Soft Substrates – Supplementary Material –

Marco Rivetti¹, Vincent Bertin², Thomas Salez^{2,3}, Chung-Yuen Hui⁴, Christine Linne¹, Maxence Arutkin², Haibin Wu⁴, Elie Raphaël², and Oliver Bäumchen^{1,*}

¹ *Max Planck Institute for Dynamics and Self-Organization (MPIDS), Am Faßberg 17, 37077 Göttingen, Germany.* ² *Laboratoire de Physico-Chimie Théorique, UMR CNRS 7083 Gulliver, ESPCI Paris, PSL Research University, 10 rue Vauquelin, 75005 Paris, France.* ³ *Global Station for Soft Matter, Global Institution for Collaborative Research and Education, Hokkaido University, Sapporo, Hokkaido 060-0808, Japan.* ⁴ *Dept. of Mechanical & Aerospace Engineering, Cornell University, Ithaca, NY 14853, USA.*
(Dated: June 25, 2017)

I. INTRODUCTION

As a reference state, we consider a thin viscous film of height h_0 sitting on an incompressible elastic layer of thickness s_0 (see Fig. S1). The elastic layer is itself placed atop a rigid substrate. We use a Cartesian coordinate system (x, y, z) , with z being the vertical coordinate. We assume the system to be infinite in the x and y directions. The surface tension of the air-liquid interface is denoted γ , the viscosity of the fluid (assumed to be Newtonian) η , and the shear modulus of the elastic material (assumed incompressible, *i.e.* with a Poisson ratio of $1/2$) μ . At initial time, $t = 0$, we perturb the air-liquid interface by adding a step function $h(x) = h_2 H(x)$ with $H(x < 0) = -1/2$ and $H(x > 0) = 1/2$. We assume invariance in the y direction, and that the step height h_2 is small compared with the reference height h_0 .

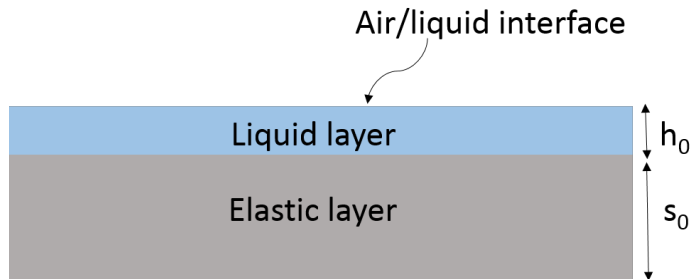


FIG. S1: Cross-sectional view of the reference equilibrium state, to which will be superimposed a deformation of the air-liquid interface at initial time ($t = 0$).

II. CONTROL EXPERIMENT WITH A STEPPED PERTURBATION

The previous $h_2 \ll h_0$ condition is not verified in our experiments (where $h_2 = h_1 = 2h_0/3$). However, we checked that this simplification in the model does not affect our general conclusions and is not the source of some discrepancy observed with the experiments. Indeed, in a test experiment with $h_2 \ll h_0$, we find that the profile width follows a $t^{1/6}$ power law with time t (see Fig. S2), consistently with the $h_1 = h_2$ experimental case (see Figs. 2 and 3), and in contrast to the theoretical prediction (see Fig. 6).

*E-mail: oliver.baeumchen@ds.mpg.de

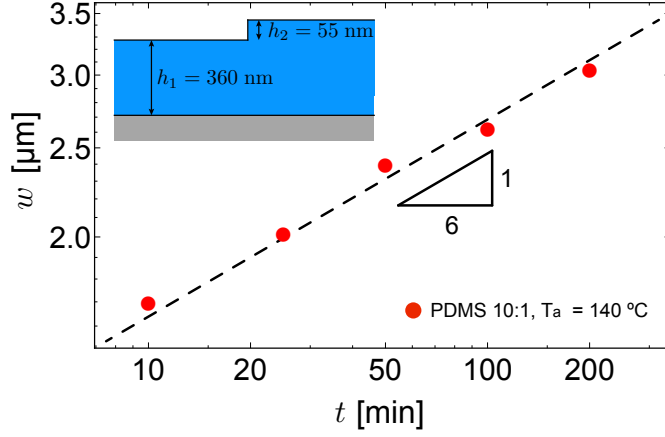


FIG. S2: Temporal evolution of the profile width w (defined in the inset of Fig. 2(a)), in log-log scale, for an experiment with $h_2 \ll h_1$ (see inset). We used the same annealing temperature T_a and PDMS substrate (in grey in the inset) as in the experiments reported in Figs. 1 and 2.

III. LUBRICATION-ELASTIC MODEL

A. Lubrication description of the liquid layer

As for the capillary levelling of a thin liquid film, of viscosity η , on a rigid substrate [39], we invoke the lubrication approximation which assumes that the typical horizontal length scale of the flow is much larger than the vertical one. As a result, at leading order, the vertical flow is neglected and the excess pressure field p (with respect to the atmospheric pressure) does not depend on z . The incompressible Stokes' equations thus reduce to:

$$\frac{\partial p}{\partial x} = \eta \frac{\partial^2 v_x}{\partial z^2}, \quad (\text{S1})$$

which can be integrated in z to get the horizontal velocity v_x . The main difference here with the previous model [39] is that the pressure acts on the elastic layer, giving rise to vertical and horizontal displacements of the liquid-elastic interface, $\delta(x, t)$ and $u_s(x, t)$ respectively. In addition, the no-slip condition at the liquid-elastic interface implies that a fluid particle in contact with the elastic surface will have a non-zero horizontal velocity $\partial u_s / \partial t$. Using this condition, the vanishing shear stress at the air-liquid interface, and invoking volume conservation, allow one to derive the following equation:

$$\frac{\partial \Delta}{\partial t} + \frac{\partial}{\partial x} \left[-\frac{(h_0 + \Delta)^3}{3\eta} \frac{\partial p}{\partial x} + (h_0 + \Delta) \frac{\partial u_s}{\partial t} \right] = 0, \quad (\text{S2})$$

where $\Delta(x, t) = h(x, t) - \delta(x, t) - h_0$ is the excess thickness of the liquid layer with respect to the equilibrium value h_0 , and $h(x, t)$ is defined in Fig. 1(b). Since the pressure is independent of z , it is fixed by the proper boundary condition, *i.e.* the Laplace pressure at the air-liquid interface (we neglect the non-linear term of the curvature at small slopes):

$$p(x, t) = -\gamma \frac{\partial^2 h}{\partial x^2} = -\gamma \frac{\partial^2 (\Delta + \delta)}{\partial x^2}. \quad (\text{S3})$$

Finally, as the perturbation is assumed to be small ($\Delta \ll h_0$), one can linearize Eq. (S2) and get the governing equation:

$$\frac{\partial \Delta}{\partial t} + \frac{\partial}{\partial x} \left[-\frac{h_0^3}{3\eta} \frac{\partial p}{\partial x} + h_0 \frac{\partial u_s}{\partial t} \right] = 0. \quad (\text{S4})$$

B. Coupling with the elastic layer

The surface displacements of the liquid-elastic interface are given by:

$$\delta(x, t) = -\frac{1}{\sqrt{2\pi\mu}} \int_{-\infty}^{\infty} dx' k(x-x')p(x', t) , \quad (\text{S5a})$$

$$u_s(x, t) = -\frac{1}{\sqrt{2\pi\mu}} \int_{-\infty}^{\infty} dx' k_s(x-x')p(x', t) , \quad (\text{S5b})$$

where k and k_s are the Green's functions of the elastic problem (see Section III C), corresponding to the vertical and horizontal displacements induced by a normal line load of magnitude $-\sqrt{2\pi}\mu$. We introduce the Fourier transform \tilde{f} of a function f with respect to its variable x as:

$$\tilde{f}(\lambda) = \frac{1}{\sqrt{2\pi}} \int_{-\infty}^{\infty} dx f(x)e^{i\lambda x} , \quad (\text{S6})$$

where λ is the Fourier variable (*i.e.* the angular wavenumber). Taking the Fourier transform of Eqs. (S3), (S4), and (S5), we obtain:

$$\tilde{\delta} = -\frac{\tilde{p}\tilde{k}}{\mu} = \frac{-\tilde{k}\gamma\lambda^2}{\mu(1 + \tilde{k}\gamma\lambda^2/\mu)} \tilde{\Delta} , \quad (\text{S7})$$

$$\tilde{u}_s = -\frac{\tilde{p}\tilde{k}_s}{\mu} = \frac{-\tilde{k}_s\gamma\lambda^2}{\mu(1 + \tilde{k}\gamma\lambda^2/\mu)} \tilde{\Delta} , \quad (\text{S8})$$

$$\frac{\partial \tilde{\Delta}}{\partial t} = -\Omega(\lambda)\tilde{\Delta} , \quad (\text{S9})$$

and:

$$\Omega(\lambda) = \frac{\gamma\lambda^4 h_0^3}{3\eta} \frac{1}{1 + (\gamma\lambda^2/\mu) (\tilde{k} + i\lambda h_0 \tilde{k}_s)} . \quad (\text{S10})$$

The solution of Eq. (S9) is:

$$\tilde{\Delta}(\lambda, t) = \tilde{\Delta}(\lambda, 0) \exp[-\Omega(\lambda)t] = -\frac{h_2}{2i\lambda} \sqrt{\frac{2}{\pi}} \exp[-\Omega(\lambda)t] , \quad (\text{S11})$$

where we have used the initial conditions $\Delta(x, 0) = h_2 H(x)$ (see section I) and $\delta(x, 0) = 0$. Finally, using Eq. (S7), one has:

$$\tilde{\Delta}(\lambda, t) + \tilde{\delta}(\lambda, t) = \frac{\tilde{\Delta}(\lambda, t)}{1 + \tilde{k}\gamma\lambda^2/\mu} . \quad (\text{S12})$$

Therefore, once the Green's functions \tilde{k} and \tilde{k}_s are determined (see Section III C), the displacement $h(x, t) - h_0 = \Delta(x, t) + \delta(x, t)$ of the air-liquid interface with respect to its equilibrium position can be obtained by taking the inverse Fourier transform of Eq. (S12).

C. Green's functions for the elastic layer

We consider an incompressible and linear elastic layer of thickness s_0 supported on a rigid substrate (the latter is located at $z = -s_0$, see Fig. 1(a)). The deformation state of the elastic layer is that of plane strain, where the out-of-plane (*i.e.* along y , see Fig. 1(a)) displacement is identically zero. The horizontal and vertical displacement fields, $u_x(x, z, t)$ and $u_z(x, z, t)$ respectively, are both fixed to zero at the rigid substrate:

$$u_x(x, -s_0, t) = 0 , \quad (\text{S13a})$$

$$u_z(x, -s_0, t) = 0 . \quad (\text{S13b})$$

On the other side of the layer, the liquid-elastic interface (located at $z = 0$ at zeroth order in the perturbation, see Fig. 1(a)) is subjected to the lubrication pressure field $p(x, t)$, but we assume no shear which is valid at leading lubrication order. Therefore, one has:

$$\sigma_{zz}(x, 0, t) = -p(x, t) , \quad (\text{S14a})$$

$$\sigma_{xz}(x, 0, t) = 0 . \quad (\text{S14b})$$

In plane strain, the stresses are given by the Airy stress function $\phi(x, z, t)$ which satisfies the spatial biharmonic equation. Specifically:

$$\sigma_{xx} = \frac{\partial^2 \phi}{\partial z^2} , \quad \sigma_{zz} = \frac{\partial^2 \phi}{\partial x^2} \quad \text{and} \quad \sigma_{xz} = -\frac{\partial^2 \phi}{\partial x \partial z} . \quad (\text{S15})$$

The generalized Hooke's law for an incompressible material in plane strain reads:

$$2\mu \partial_z u_z = \sigma_{zz} - \Gamma , \quad (\text{S16a})$$

$$2\mu \partial_x u_x = \sigma_{xx} - \Gamma , \quad (\text{S16b})$$

$$\mu(\partial_x u_z + \partial_z u_x) = \sigma_{xz} , \quad (\text{S16c})$$

where $\Gamma(x, z, t)$ is the pressure needed to enforce incompressibility, that can be found using the incompressibility condition:

$$\partial_x u_x + \partial_z u_z = 0 \quad \Rightarrow \quad \Gamma = \frac{\sigma_{xx} + \sigma_{zz}}{2} . \quad (\text{S17})$$

Combining the above, and using the same Fourier-transform convention as in the previous section, we find the following relations:

$$\tilde{\sigma}_{xx} = \tilde{\phi}'' , \quad \tilde{\sigma}_{zz} = -\lambda^2 \tilde{\phi} \quad \text{and} \quad \tilde{\sigma}_{xz} = i\lambda \tilde{\phi}' , \quad (\text{S18})$$

$$2\mu \tilde{u}'_z = -\frac{\tilde{\phi}'' + \lambda^2 \tilde{\phi}}{2} , \quad (\text{S19a})$$

$$-2i\lambda \mu \tilde{u}_x = \frac{\tilde{\phi}'' + \lambda^2 \tilde{\phi}}{2} , \quad (\text{S19b})$$

$$\mu(-i\lambda \tilde{u}_z + \tilde{u}'_x) = i\lambda \tilde{\phi}' , \quad (\text{S19c})$$

where the prime denotes the partial derivative with respect to z . Taking the Fourier transform of the spatial biharmonic equation results in a fourth-order ordinary differential equation:

$$\lambda^4 \tilde{\phi} - 2\lambda^2 \tilde{\phi}'' + \tilde{\phi}'''' = 0 , \quad (\text{S20})$$

whose general solution is:

$$\tilde{\phi}(\lambda, z, t) = A(\lambda, t) \cosh(\lambda z) + B(\lambda, t) \sinh(\lambda z) + C(\lambda, t) z \cosh(\lambda z) + D(\lambda, t) z \sinh(\lambda z) . \quad (\text{S21})$$

The parameters A, B, C, D are determined using the boundary conditions (Eqs. (S13a), (S13b), (S14a), and (S14b)) and the relations between the Airy stress function and the stresses/displacements (Eqs. (S18) and (S19)). After some algebra, we find:

$$A = \frac{\tilde{p}}{\lambda^2} , \quad B = \frac{\tilde{p}}{\lambda^2} \frac{\sinh(\lambda s_0) \cosh(\lambda s_0) - \lambda s_0}{\cosh^2(\lambda s_0) + (\lambda s_0)^2} , \quad C = -\lambda B \quad \text{and} \quad D = -\frac{\tilde{p}}{\lambda} \frac{\cosh^2(\lambda s_0)}{\cosh^2(\lambda s_0) + (\lambda s_0)^2} . \quad (\text{S22})$$

Then, invoking Eqs. (S19b), (S19c), (S21) and (S22) the vertical displacement $\delta(x, t) = u_z(x, 0, t)$ of the liquid-elastic interface reads in Fourier space:

$$\tilde{\delta}(\lambda, t) = \frac{1}{i\lambda} \left(\tilde{u}'_x - \frac{i\lambda\tilde{\phi}'}{\mu} \right) (\lambda, 0, t) = -\frac{\tilde{p}}{2\mu\lambda} \frac{\sinh(\lambda s_0) \cosh(\lambda s_0) - \lambda s_0}{\cosh^2(\lambda s_0) + (\lambda s_0)^2}. \quad (\text{S23})$$

Using Eqs. (S7) and (S23), we find:

$$\tilde{k}(\lambda) = \frac{1}{2\lambda} \frac{\sinh(\lambda s_0) \cosh(\lambda s_0) - \lambda s_0}{\cosh^2(\lambda s_0) + (\lambda s_0)^2}. \quad (\text{S24})$$

In exactly the same way, the horizontal displacement $u_s(x, t) = u_x(x, 0, t)$ of the liquid-elastic interface reads in Fourier space:

$$\tilde{u}_s(\lambda, t) = i \frac{\lambda^2 \tilde{\phi} + \tilde{\phi}''}{4\mu\lambda} (\lambda, 0, t) = \frac{i\tilde{p}}{2\mu} \frac{\lambda s_0^2}{\cosh^2(\lambda s_0) + (\lambda s_0)^2}, \quad (\text{S25})$$

which gives:

$$\tilde{k}_s(\lambda) = \frac{1}{2i} \frac{\lambda s_0^2}{\cosh^2(\lambda s_0) + (\lambda s_0)^2}. \quad (\text{S26})$$

IV. STOKES-ELASTIC MODEL

The previous lubrication-elastic model assumes that the typical vertical length scale of the flow is much smaller than the horizontal one. However, the initial stepped interface and thus the early-time profiles are not compatible with this criterion. Therefore, we now instead solve the incompressible Stokes' equations for the liquid layer, in order to go beyond the lubrication approximation.

A. Hydrodynamic description of the liquid layer

We introduce the 2D stream function ψ that is related to the velocity field \vec{v} via the relation $\vec{v} = \vec{\nabla} \times (\psi \vec{e}_y)$ with \vec{e}_y the out-of-plane unit vector and $\vec{\nabla} \times \cdot$ the curl operator. Similarly to the Airy stress function, the stream function verifies a biharmonic equation. The kinematic and no-slip conditions at the liquid-elastic interface (located at $z = 0$ at zeroth order in the perturbation, see Fig. 1(a)) imply, respectively:

$$v_z(x, 0, t) = \partial_x \psi(x, 0, t) = \partial_t u_z(x, 0, t) = \partial_t \delta(x, t), \quad (\text{S27a})$$

$$v_x(x, 0, t) = -\partial_z \psi(x, 0, t) = \partial_t u_x(x, 0, t) = \partial_t u_s(x, t). \quad (\text{S27b})$$

In addition, at the air-liquid interface (located at $z = h_0$ at zeroth order in the perturbation, see Figs. 1(a) and S1), we assume no shear and the pressure is set by the Laplace pressure. The continuity of stress thus gives:

$$\sigma_{xz}(x, h_0, t) = \eta(\partial_{xx}\psi - \partial_{zz}\psi)(x, h_0, t) = 0, \quad (\text{S28a})$$

$$\sigma_{zz}(x, h_0, t) = -\mathcal{P}(x, h_0, t) + 2\eta\partial_z(\partial_x\psi)(x, h_0, t) = -p(x, t). \quad (\text{S28b})$$

with $\mathcal{P}(x, z, t)$ the excess pressure (with respect to the atmospheric pressure) in the liquid, and $p(x, t) = -\gamma\partial_{xx}h$ the Laplace pressure. Note that we neglect all nonlinear terms in $\partial_x h$ that come from the curvature in the Laplace pressure and the projection of the normal and tangential vectors onto the x and z axes. Now, we employ a similar method as the one developed in the previous lubrication-elastic model, and first take the Fourier transform of the biharmonic equation satisfied by the stream function:

$$\lambda^4 \tilde{\psi} - 2\lambda^2 \tilde{\psi}'' + \tilde{\psi}'''' = 0, \quad (\text{S29})$$

whose general solution is:

$$\tilde{\psi}(\lambda, z, t) = A_2(\lambda, t) \cosh(\lambda z) + B_2(\lambda, t) \sinh(\lambda z) + C_2(\lambda, t) z \cosh(\lambda z) + D_2(\lambda, t) z \sinh(\lambda z) . \quad (\text{S30})$$

Taking the Fourier transforms of the boundary conditions (Eqs. (S27) and (S28)), we find:

$$-i\lambda A_2 = \partial_t \tilde{\delta} . \quad (\text{S31a})$$

$$\lambda B_2 = -\frac{i\tilde{p}}{2\eta\lambda} \frac{\sinh(\lambda h_0)\lambda h_0 + \cosh(\lambda h_0)}{\cosh^2(\lambda h_0) + (\lambda h_0)^2} - i\partial_t \tilde{\delta} \frac{\sinh(\lambda h_0) \cosh(\lambda h_0) - \lambda h_0}{\cosh^2(\lambda h_0) + (\lambda h_0)^2} - \partial_t \tilde{u}_s \frac{(\lambda h_0)^2}{\cosh^2(\lambda h_0) + (\lambda h_0)^2} , \quad (\text{S31b})$$

$$C_2 = \frac{i\tilde{p}}{2\eta\lambda} \frac{\sinh(\lambda h_0)\lambda h_0 + \cosh(\lambda h_0)}{\cosh^2(\lambda h_0) + (\lambda h_0)^2} + i\partial_t \tilde{\delta} \frac{\sinh(\lambda h_0) \cosh(\lambda h_0) - \lambda h_0}{\cosh^2(\lambda h_0) + (\lambda h_0)^2} - \partial_t \tilde{u}_s \frac{\cosh^2(\lambda h_0)}{\cosh^2(\lambda h_0) + (\lambda h_0)^2} , \quad (\text{S31c})$$

$$D_2 = \frac{-ih_0\tilde{p}}{2\eta} \frac{\cosh(\lambda h_0)}{\cosh^2(\lambda h_0) + (\lambda h_0)^2} - i\partial_t \tilde{\delta} \frac{\cosh^2(\lambda h_0)}{\cosh^2(\lambda h_0) + (\lambda h_0)^2} + \partial_t \tilde{u}_s \frac{\lambda h_0 + \sinh(\lambda h_0) \cosh(\lambda h_0)}{\cosh^2(\lambda h_0) + (\lambda h_0)^2} . \quad (\text{S31d})$$

Finally, we note that the pressure $\mathcal{P}(x, z, t)$ is entirely determined by the stream function. Indeed, in Fourier space, and invoking the stream function, the x -projection of the Stokes' equation reads:

$$i\lambda \tilde{\mathcal{P}} = \eta \left(\tilde{\psi}''' - \lambda^2 \tilde{\psi}' \right) . \quad (\text{S32})$$

B. Coupling with the elastic layer

As in the previous lubrication-elastic model, we solve the elastic part of the problem by introducing the Airy stress function ϕ given by Eq. (S21) in Fourier space. Assuming no displacement at the interface between the elastic layer and the rigid substrate (located at $z = -s_0$, see Fig. 1(a)), one has:

$$u_x(x, -s_0, t) = 0 , \quad (\text{S33a})$$

$$u_z(x, -s_0, t) = 0 . \quad (\text{S33b})$$

Equation (S19) can be used to relate the boundary conditions (Eq. (S33)) to the parameters A, B, C, D (Eq. (S21)). After some algebra, one finds:

$$\lambda A = 2\mu \frac{i\tilde{u}_s(\lambda s_0)^2 - \tilde{\delta}[\cosh(\lambda s_0) \sinh(\lambda s_0) + \lambda s_0]}{\sinh^2(\lambda s_0) - (\lambda s_0)^2} , \quad (\text{S34a})$$

$$\lambda B = -2\mu \tilde{\delta} , \quad (\text{S34b})$$

$$C = 2\mu \frac{-i\tilde{u}_s[\cosh(\lambda s_0) \sinh(\lambda s_0) - \lambda s_0] + \sinh^2(\lambda s_0)\tilde{\delta}}{\sinh^2(\lambda s_0) - (\lambda s_0)^2} , \quad (\text{S34c})$$

$$D = 2\mu \frac{-i\tilde{u}_s \sinh^2(\lambda s_0) + \tilde{\delta}[\cosh(\lambda s_0) \sinh(\lambda s_0) + \lambda s_0]}{\sinh^2(\lambda s_0) - (\lambda s_0)^2} . \quad (\text{S34d})$$

At the liquid-elastic interface (located at $z = 0$ at zeroth order in the perturbation, see Fig. 1(a)), the normal-stress continuity reads:

$$-\mathcal{P}(x, 0, t) + 2\eta \partial_z (\partial_x \psi)(x, 0, t) = \partial_{xx} \phi(x, 0, t) , \quad (\text{S35})$$

or, equivalently, in Fourier space:

$$\tilde{\mathcal{P}}(\lambda, 0, t) + 2i\lambda\eta\tilde{\psi}'(\lambda, 0, t) = \lambda^2\tilde{\phi}(\lambda, 0, t) . \quad (\text{S36})$$

Then, by taking the $z \rightarrow 0$ limit of Eq. (S32) and by combining it with Eqs. (S21), (S30), and (S36), one obtains:

$$-2i\eta\lambda^2 B_2 = -\lambda^2 A . \quad (\text{S37})$$

Invoking Eqs. (S22) and (S31), Eq. (S37) becomes:

$$\begin{aligned} & -\tilde{p} \frac{\cosh(\lambda h_0) + \lambda h_0 \sinh(\lambda h_0)}{\cosh^2(\lambda h_0) + (\lambda h_0)^2} - 2\eta\lambda\partial_t\tilde{\delta} \frac{\cosh(\lambda h_0) \sinh(\lambda h_0) - \lambda h_0}{\cosh^2(\lambda h_0) + (\lambda h_0)^2} + 2i\eta\lambda\partial_t\tilde{u}_s \frac{(\lambda h_0)^2}{\cosh^2(\lambda h_0) + (\lambda h_0)^2} \\ & = 2\lambda\mu \frac{-i\tilde{u}_s(\lambda s_0)^2 + \tilde{\delta}[\cosh(\lambda s_0) \sinh(\lambda s_0) + \lambda s_0]}{\sinh^2(\lambda s_0) - (\lambda s_0)^2} . \end{aligned} \quad (\text{S38})$$

For simplicity, we neglect the terms of order $T\partial_t\tilde{\delta}$ or $T\partial_t\tilde{u}_s$ with respect to the terms of order $\tilde{\delta}$ or \tilde{u}_s , where $T = \eta/\mu$ is a composite Maxwell-like viscoelastic time. This assumption essentially means that the elastic layer has an instantaneous response to the applied stress, or that we decouple the fast and slow dynamics and focus on the latter. This is relevant in our case since T is much smaller than the experimental time scale (see inset of Fig. 4). Doing so, we get in Fourier space:

$$-\tilde{p} \frac{\cosh(\lambda h_0) + \lambda h_0 \sinh(\lambda h_0)}{\cosh^2(\lambda h_0) + (\lambda h_0)^2} = 2\lambda\mu \frac{-i\tilde{u}_s(\lambda s_0)^2 + \tilde{\delta}[\cosh(\lambda s_0) \sinh(\lambda s_0) + \lambda s_0]}{\sinh^2(\lambda s_0) - (\lambda s_0)^2} . \quad (\text{S39})$$

Besides, the tangential-stress continuity reads:

$$\eta(\partial_{xx}\psi - \partial_{zz}\psi)(x, 0, t) = -\partial_{xz}\phi(x, 0, t) , \quad (\text{S40})$$

and thus, with a similar treatment, one gets in Fourier space:

$$\tilde{p} \frac{\lambda h_0 \cosh(\lambda h_0)}{\cosh^2(\lambda h_0) + (\lambda h_0)^2} = 2\lambda\mu \frac{-i\tilde{u}_s(\cosh(\lambda s_0) \sinh(\lambda s_0) - \lambda s_0) + \tilde{\delta}(\lambda s_0)^2}{\sinh^2(\lambda s_0) - (\lambda s_0)^2} . \quad (\text{S41})$$

By analogy with Eqs. (S5a) and (S5b) of the previous lubrication-elastic model, we introduce two new Green's functions $k_2(x)$ and $k_{s2}(x)$. Equations (S39) and (S41) thus lead to:

$$\tilde{\delta} = -\frac{\tilde{p}\tilde{k}_2}{\mu} = \frac{-\tilde{p}}{2\mu\lambda} \frac{(\lambda s_0)^2(\lambda h_0) \cosh(\lambda h_0) + [\sinh(\lambda h_0)\lambda h_0 + \cosh(\lambda h_0)][\cosh(\lambda s_0) \sinh(\lambda s_0) - \lambda s_0]}{[\cosh^2(\lambda h_0) + (\lambda h_0)^2][\cosh^2(\lambda s_0) + (\lambda s_0)^2]} , \quad (\text{S42})$$

$$\tilde{u}_s = -\frac{\tilde{p}\tilde{k}_{s2}}{\mu} = \frac{i\tilde{p}}{2\mu\lambda} \frac{\lambda h_0 \cosh(\lambda h_0)[\cosh(\lambda s_0) \sinh(\lambda s_0) + \lambda s_0] + [\cosh(\lambda h_0) + \sinh(\lambda h_0)\lambda h_0](\lambda s_0)^2}{[\cosh^2(\lambda h_0) + (\lambda h_0)^2][\cosh^2(\lambda s_0) + (\lambda s_0)^2]} , \quad (\text{S43})$$

with:

$$\tilde{k}_2(\lambda) = \frac{1}{2\lambda} \frac{(\lambda s_0)^2(\lambda h_0) \cosh(\lambda h_0) + [\sinh(\lambda h_0)\lambda h_0 + \cosh(\lambda h_0)][\cosh(\lambda s_0) \sinh(\lambda s_0) - \lambda s_0]}{[\cosh^2(\lambda h_0) + (\lambda h_0)^2][\cosh^2(\lambda s_0) + (\lambda s_0)^2]} , \quad (\text{S44})$$

$$\tilde{k}_{s2}(\lambda) = \frac{1}{2i\lambda} \frac{\lambda h_0 \cosh(\lambda h_0)[\cosh(\lambda s_0) \sinh(\lambda s_0) + \lambda s_0] + [\cosh(\lambda h_0) + \sinh(\lambda h_0)\lambda h_0](\lambda s_0)^2}{[\cosh^2(\lambda h_0) + (\lambda h_0)^2][\cosh^2(\lambda s_0) + (\lambda s_0)^2]} . \quad (\text{S45})$$

The two Green's functions k_2 and k_{s2} have forms that are quite similar to the ones of the previous lubrication-elastic model, k and k_s (see Eqs. (S24) and (S26)). Moreover, in the lubrication limit where $\lambda h_0 \rightarrow 0$, k_2 and k_{s2} tend towards k and k_s , respectively.

C. Temporal evolution of the air-liquid interface

Let us write the mass conservation for the liquid layer:

$$\partial_t \Delta = -\partial_x \int_{\delta(x,t)}^{h(x,t)} dz v_x(x, z, t) = \partial_x \int_{\delta(x,t)}^{h(x,t)} dz \partial_z \psi(x, z, t) = \partial_x \psi[x, h(x, t), t] - \partial_x \psi[x, \delta(x, t), t], \quad (\text{S46})$$

with $\Delta(x, t) = h(x, t) - \delta(x, t) - h_0$ as in the previous lubrication-elastic model. At the lowest order in the perturbation, this general expression becomes:

$$\partial_t \Delta = \partial_x \psi(x, h_0, t) - \partial_x \psi(x, 0, t), \quad (\text{S47})$$

or, equivalently, in Fourier space:

$$\partial_t \tilde{\Delta} + i\lambda[\tilde{\psi}(\lambda, h_0, t) - \tilde{\psi}(\lambda, 0, t)] = 0. \quad (\text{S48})$$

Using Eqs. (S3), (S42), and (S43), one gets:

$$\tilde{\delta} = \frac{-\tilde{k}_2 \gamma \lambda^2}{\mu(1 + \tilde{k}_2 \gamma \lambda^2 / \mu)} \tilde{\Delta}, \quad (\text{S49})$$

$$\tilde{u}_s = \frac{-\tilde{k}_{s2} \gamma \lambda^2}{\mu(1 + \tilde{k}_2 \gamma \lambda^2 / \mu)} \tilde{\Delta}. \quad (\text{S50})$$

By injecting Eqs. (S30) and (S31) in Eq. (S48), one obtains the ordinary differential equation:

$$\partial_t \tilde{\Delta} = -\Omega_2(\lambda) \tilde{\Delta}, \quad (\text{S51})$$

with:

$$\Omega_2(\lambda) = \frac{\gamma \lambda}{2\eta} \frac{\mathcal{A}(\lambda h_0)}{\mathcal{B}(\lambda h_0) + \frac{\gamma \lambda^2}{\mu} \mathcal{C}(\lambda h_0)}, \quad (\text{S52})$$

and:

$$\mathcal{A}(\lambda h_0) = \cosh(\lambda h_0) \sinh(\lambda h_0) - \lambda h_0, \quad (\text{S53a})$$

$$\mathcal{B}(\lambda h_0) = \cosh^2(\lambda h_0) + (\lambda h_0)^2, \quad (\text{S53b})$$

$$\mathcal{C}(\lambda h_0) = \tilde{k}_2 [\cosh(\lambda h_0) + (\lambda h_0) \sinh(\lambda h_0)] + i\tilde{k}_{s2} \lambda h_0 \cosh(\lambda h_0). \quad (\text{S53c})$$

This differential equation can be solved with the initial condition (step of height h_2 , see Fig. 1(a)):

$$\tilde{\Delta}(\lambda, 0) = -\frac{h_2}{2i\lambda} \sqrt{\frac{2}{\pi}}, \quad (\text{S54})$$

thus leading to:

$$\tilde{\Delta}(\lambda, t) = -\frac{h_2}{2i\lambda} \sqrt{\frac{2}{\pi}} \exp[-\Omega_2(\lambda)t]. \quad (\text{S55})$$

Then, using Eq. (S49), one has:

$$\tilde{\Delta} + \tilde{\delta} = \frac{\tilde{\Delta}}{1 + \gamma \lambda^2 \tilde{k}_2 / \mu}. \quad (\text{S56})$$

Finally, the displacement $h(x, t) - h_0 = \Delta(x, t) + \delta(x, t)$ of the air-liquid interface with respect to its equilibrium position can be obtained by taking the inverse Fourier transform of Eq. (S56). Figure S3 displays the temporal evolutions of the profile width ω (see definition in the inset of Fig.2(a)), as derived from the two models presented in this supplementary material. The Stokes-elastic model exhibits the same qualitative features as the lubrication-elastic one. In particular, the width of the profile depends on elasticity only at early times, and rapidly tends to a 1/4 power law – characteristic of the rigid-substrate case. This result suggests that the lubrication approximation, which is not valid at early times, is not responsible for the discrepancy between the lubrication-elastic model and the experiments reported in the main text.

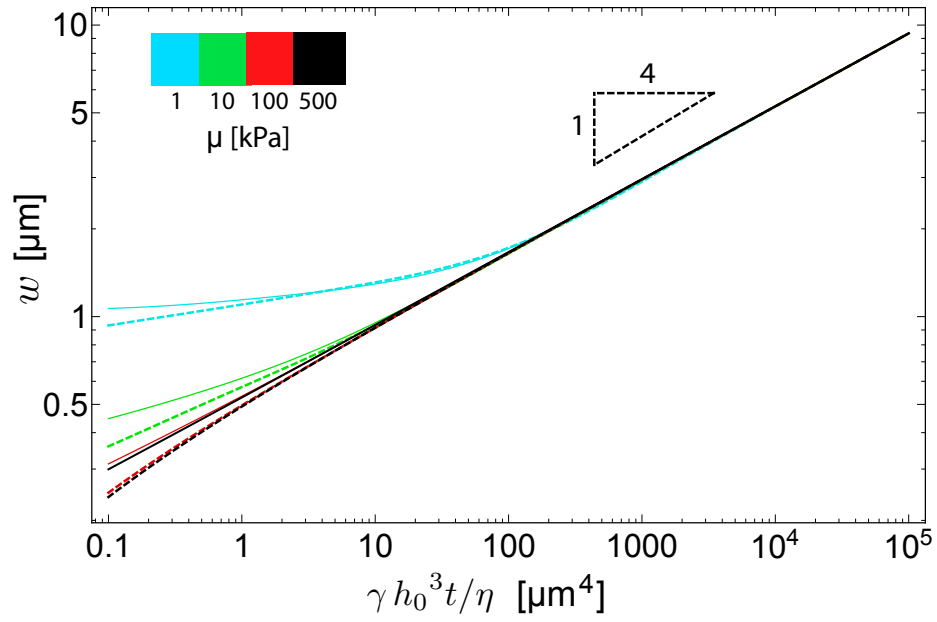


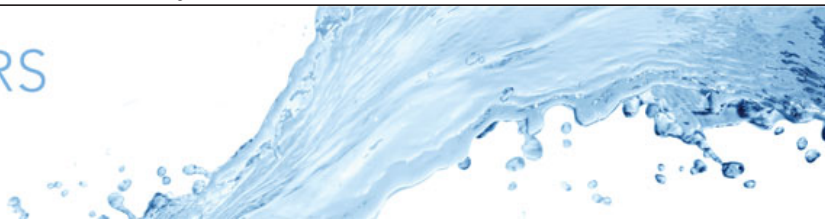
FIG. S3: Temporal evolution of the profile width (defined in the inset of Fig. 2(a)), in log-log scale, as predicted by both theoretical models, for different shear moduli, viscosities and liquid-film thicknesses. The $1/4$ power law corresponding to a rigid substrate is indicated. The solid lines represent the lubrication-elastic model, and the dashed lines represent the Stokes-elastic model. The shear moduli are given by the color code, which is identical to the one in Fig. 6. All the other parameters are identical to the ones used in Fig. 6.

Chapter 4

Capillary Levelling of Immiscible Bilayer Films

The experiments presented here have been designed by Carmen Lee and Kari Dalnoki-Veress at McMaster University, Canada. I have contributed to some experiments during my stay in Canada in the spring 2018 and I lead the theoretical model.

In the same vein as in the previous chapter, we study the levelling dynamics of stepped polymer thin films placed atop of other kind of “soft substrates”, namely immiscible polymer layers. Such a bilayer system can be seen as a minimal model of multilayer thin films that are encountered in materials science. The levelling largely depends on the viscosity ratio between the two liquids. In the bottom film is more viscous than the top one, the levelling of the top film is similar to the classical levelling on a rigid substrate. In the opposite case, when the bottom film is less viscous, the dynamics is more complex and does not exhibit clear self-similar properties. The excess surface (proportional to the excess energy) decays to zero following a apparent power-law regimes with time $t^{-1/2}$ and $t^{-1/4}$. We perform a long-wave expansion of the Stokes equations to model the system and we find a good agreement with the experimental results. The model reveals a double cross-over in time, from Poiseuille flow, to plug flow and finally Couette flow as the main source of dissipation. A full Stokes model is also provided to support the asymptotic long-wave model. I include here an article, published in Journal of Fluid Mechanics, that I co-wrote with Carmen Lee [4].



Capillary levelling of immiscible bilayer films

Vincent Bertin^{1,2}, Carmen L. Lee³, Thomas Salez^{1,4}, Elie Raphaël² and Kari Dalnoki-Veress^{1,3,†}

¹Univ. Bordeaux, CNRS, LOMA, UMR 5798, 33405 Talence, France

²UMR CNRS Gulliver 7083, ESPCI Paris, PSL Research University, 75005 Paris, France

³Department of Physics and Astronomy, McMaster University, 1280 Main Street West, Hamilton, ON L8S 4M1, Canada

⁴Global Station for Soft Matter, Global Institution for Collaborative Research and Education, Hokkaido University, Sapporo, Japan

(Received 1 May 2020; revised 21 September 2020; accepted 18 November 2020)

Flow in thin films is highly dependent on the boundary conditions. Here, we study the capillary levelling of thin bilayer films composed of two immiscible liquids. Specifically, a stepped polymer layer is placed atop another, flat polymer layer. The Laplace pressure gradient resulting from the curvature of the step induces flow in both layers, which dissipates the excess capillary energy stored in the stepped interface. The effect of different viscosity ratios between the bottom and top layers is investigated. We invoke a long-wave expansion of the low-Reynolds-number hydrodynamics to model the energy dissipation due to the coupled viscous flows in the two layers. Good agreement is found between the experiments and the model. Analysis of the latter further reveals an interesting double cross-over in time, from Poiseuille flow, to plug flow and finally to Couette flow. The cross-over time scales depend on the viscosity ratio between the two liquids, allowing for the dissipation mechanisms to be selected and finely tuned by varying this ratio.

Key words: capillary flows, thin films

1. Introduction

Flow in a thin film is affected by the boundary conditions of the film, especially when the thickness of the film approaches that of the interfacial layer (Oron, Davis & Bankoff 1997; Bocquet & Charlaix 2010). As an example, the presence of slippage at a solid–liquid interface affects flows in thin films as observed in the dewetting dynamics of thin polymer films (Kargupta, Sharma & Khanna 2004; Fetzer *et al.* 2005; Münch, Wagner & Witelski 2005; Bäumchen & Jacobs 2009). The dynamics is more complex in bilayer or stratified films, because the flow depends on the relative viscosities and

† Email address for correspondence: dalnoki@mcmaster.ca

interfacial energies of the two layers in addition to the interfacial boundary conditions (Brochard-Wyart, Martin & Redon 1993; Pototsky *et al.* 2004; Merabia & Bonet Avalos 2008; Jachalski *et al.* 2014). Liquid–liquid interfaces, in particular those between two polymers, often exhibit apparent slip (de Gennes 1989; Brochard-Wyart & de Gennes 1990; de Gennes & Brochard-Wyart 1990), and have been studied with molecular dynamics simulations (Koplik & Banavar 2006; Razavi, Koplik & Kretzschmar 2014; Poesio, Damone & Matar 2017) and experiments (Lee *et al.* 2009; Xu, Zhang & Shi 2016). Such an effective reduction of friction has important practical implications, e.g. for smart liquid-impregnated surfaces (Howell 2015; Keiser *et al.* 2017). The stability and dewetting of thin multilayer polymer films is also a subject of interest for physicists (Lambooy *et al.* 1996; Segalman & Green 1999; Lal *et al.* 2017; Peschka *et al.* 2018), and finds applications in industry e.g. materials manufactured from coextrusion processes (Zhao & Macosko 2002; Ponting, Hiltner & Baer 2010; Bironeau *et al.* 2017; Chebil *et al.* 2018).

Capillary-driven levelling occurs when an excess of interfacial area is relaxed by smoothing topographical perturbations, such as a thin film with a surface feature: a bump, a valley, a hole, etc. Typically, the levelling is driven by the surface tension γ of the liquid–vapour interface. The curvature of the free interface results in a Laplace pressure, and a gradient in the curvature induces flow, thereby reducing the surface energy of the system. The flow is mediated by the viscosity η of the liquid. Capillary-driven levelling is a useful tool for studying fluid flow in nanofilms and can be used to investigate the boundary conditions (de Gennes, Brochard-Wyart & Quéré 2003). With well-known initial conditions, capillary-driven levelling has been used to study various interfacial polymeric properties, such as glass transition anomalies, confinement effects and nanorheology in thin polymers films (Buck *et al.* 2004; Fakhraai & Forrest 2008; Yang *et al.* 2010; Rognin, Landis & Davoust 2011; Teisseire *et al.* 2011; Chai *et al.* 2014). Previous work on nanorheology in thin films has shown that, in addition to the importance of surface tension and viscosity, the flow is sensitive to the boundary conditions (Münch *et al.* 2005; Xu *et al.* 2011; Jachalski *et al.* 2014). The capillary-levelling technique was applied to a variety of geometries and configurations, which range from imprinted nano-patterns (Stillwagon & Larson 1988; Buck *et al.* 2004; Rognin *et al.* 2011; Teisseire *et al.* 2011), to steps (McGraw, Jago & Dalnoki-Veress 2011), trenches (Bäumchen *et al.* 2013), holes (Backholm *et al.* 2014; Bertin *et al.* 2020) and inhomogeneous mixtures (McGraw *et al.* 2013).

In the present work, we focus on the influence of a deformable liquid–liquid interface between two immiscible polymers by studying the capillary-driven levelling of a stepped bilayer film. The latter is depicted schematically in figure 1(a). A stepped polymer film is placed on a flat film of another, immiscible polymer supported on a rigid substrate. The initial surface perturbation can be described as a Heaviside function, where the vertical height profile varies abruptly from one thickness to another as the horizontal x -direction is varied. The system is invariant in the other horizontal direction. During the subsequent evolution, the height profile $h(x, t)$ can be described as a function of both the horizontal position x and time t . Furthermore, the dynamics is expected to depend on the relative viscosities of the bilayer. Indeed, one can expect that, if the viscosity of the bottom flat film is much higher than that of the top stepped film, then the former is much like a rigid substrate: the top film can flow like a liquid film on a solid substrate. In contrast, if the bottom film has a relatively negligible viscosity, then the top film can flow with little hindrance at the bottom, akin to a freestanding liquid film. For these reasons, it is of value to consider the two extreme cases of a single film on a solid substrate and a freestanding film.

Capillary levelling of immiscible bilayer films

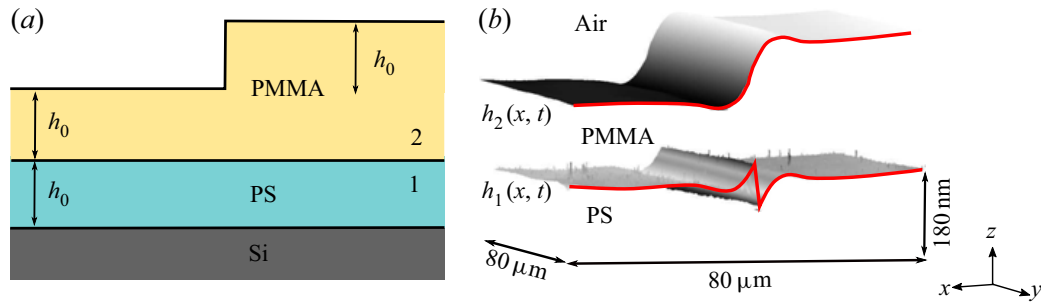


Figure 1. (a) Schematic of the as-prepared sample, with the indicated materials. The upper portion of the stepped film, the lower portion of the stepped film and the bottom film all have the same thickness h_0 . (b) Atomic force microscopy profiles of the liquid–air interface and the liquid–liquid interface. The two scans are shifted in the vertical direction to reconstruct the actual profile of the sample.

In the case of a thin liquid film on a solid substrate (McGraw *et al.* 2011, 2012; Salez *et al.* 2012a), there is typically a no-slip boundary condition at the solid–liquid interface and a no-shear-stress boundary condition at the liquid–air interface. Using the lubrication approximation for Stokes flow, the interface profile follows the thin-film equation (Oron *et al.* 1997) with a parabolic Poiseuille velocity profile. In earlier works on stepped films, it was found that the thin-film equation admits a self-similar solution in the rescaled variable $x/t^{1/4}$ (McGraw *et al.* 2012; Salez *et al.* 2012a).

In contrast, for a freestanding film, there are no-shear-stress boundary conditions at each of the two interfaces. As a consequence, the excess surface energy of a symmetric topographical perturbation must be dissipated through elongational flow, instead of shear flow, as was found in soap films (Acheson 1990). Within a long-wave approximation, the flow profile is consistent with plug flow. The interface profile $h(x, t)$ follows a system of coupled partial differential equations (Erneux & Davis 1993) which admits a self-similar solution in the rescaled variable $x/t^{1/2}$ (Ilton *et al.* 2016). We note that freestanding films are described by the same equations as that for supported films on slippery substrates with an infinite slip length, since the absence of friction at the solid–liquid interface implies the absence of any shear stress at that interface (Münch *et al.* 2005).

For a thin liquid film placed onto another, immiscible thin liquid film, the flow profile depends on the viscosity ratio between the two films, as well as on the ratio between the two relevant interfacial tensions. While the levelling of a liquid film atop a more viscous liquid is expected to be similar to that of a liquid film atop a solid substrate, the opposite case of liquid film atop a lower-viscosity liquid is non-trivial and is the primary focus of the present article. Here, we use experiments and low-Reynolds-number hydrodynamics in order to investigate the flow in such a geometry. Based on previous works on supported and freestanding films, we expect the widths of the interfacial perturbations to follow some combinations of the limiting $\sim t^{1/4}$ and $\sim t^{1/2}$ relaxation laws. We demonstrate that the main viscous dissipative mechanism cross-overs in time from being Poiseuille like, to elongational and then to Couette like, and that this double cross-over is tuneable with the viscosity ratio.

2. Methods

2.1. Experiments

The sample preparation and experimental protocol follow modified versions of the ones described in previous works (McGraw *et al.* 2011; Peschka *et al.* 2018). Figure 1(a) shows

a schematic of the sample, with a stepped film of poly(methyl methacrylate) (PMMA) atop a polystyrene (PS) film supported on a silicon (Si) substrate. PS and PMMA are an immiscible pair (Tanaka, Takahara & Kajiyama 1996). The thin polymer films are prepared by spin coating PS or PMMA from solutions in toluene (Fisher Chemical, Optima), onto 1 cm × 1 cm Si wafers (University Wafer) and freshly cleaved mica sheets (Ted Pella, Inc.), respectively. The PMMA molecular weight is $M_w = 56 \text{ kg mol}^{-1}$ (Polymer Source, Inc., polydispersity index ≤ 1.08). The PS molecular weights are $M_w = 53.3, 183$ and $758.9 \text{ kg mol}^{-1}$ (Polymer Source, Inc. and Scientific Polymer Products, Inc., polydispersity index ≤ 1.06). After spin coating, all films are annealed at 150°C , i.e. above the glass transition temperatures of both polymers, for 10 minutes to remove any residual solvent and to relax the polymer chains. The films of PMMA are then floated from the mica surface onto a bath of ultra-pure water ($18.2 \text{ M}\Omega \text{ cm}$). A floating film of PMMA is transferred off the water surface onto the PS-coated Si substrate to create a flat bilayer film supported on Si. The molecular weight of the PMMA is low enough such that the polymer chains are not highly entangled: a thin film of this polymer easily fractures upon perturbation on the surface of water, which results in portions with straight edges (Bäumchen *et al.* 2013). A second film of PMMA is fractured and transferred onto the flat bilayer, the sharp, fractured edge thus creating the step (see figure 1a). For each sample studied here, the upper portion of the PMMA stepped film, the lower portion of the PMMA stepped film, and the bottom PS film all have the same thickness, h_0 , within 10 % of each other, as confirmed with ellipsometry (Accurion, EP3). The thicknesses used in this work are $h_0 = 100, 180$ and 240 nm .

To examine the evolution of the step with time, the samples are annealed above the glass transition temperature of both polymers ($\sim 100^\circ\text{C}$), with a temperature controlled stage (Linkam). The samples are held at the elevated temperature for a given period of time, during which flow and levelling occur, before being quenched back into the glassy state at room temperature. Surface profiles of the liquid–air interface are obtained with atomic force microscopy (AFM, Bruker). For some experiments, the liquid–liquid interface is exposed by dissolving of the top PMMA layer with a selective solvent ($\sim 67\%$ acetic acid and $\sim 33\%$ ultra-pure water). This procedure allows for AFM profiles of the liquid–liquid interface to be measured. Figure 1(b) shows typical AFM profiles of the liquid–air and liquid–liquid interfaces taken at the same location on the sample. The actual profile of the whole sample is reconstructed by vertically shifting the AFM profiles according to the original layer thickness.

The dynamics of capillary-driven levelling depends on two dimensionless numbers: the viscosity ratio $\mu = \eta_1/\eta_2$ between the bottom (PS, 1) and top (PMMA, 2) layers, and the interfacial tension ratio $\Gamma = \gamma_1/\gamma_2$ between the liquid–liquid and liquid–air interfaces. The viscosity ratio is varied by changing the molecular weight of the bottom layer, as well as by changing the annealing temperature; this results in the viscosity ratio varying over 6 orders of magnitude, from $\mu \approx 5.3 \times 10^{-5}$ to $\mu \approx 1.4 \times 10^1$. The range of viscosity ratios μ was fixed by the accessible experimental time scales, such that levelling was slow enough to be monitored with AFM but fast enough to have reasonable experimental times. The individual viscosities were measured independently through the capillary levelling of simple stepped films of each single polymer, using the method described previously (McGraw *et al.* 2011)(see table 1). Variations of the interfacial tension ratio over the experimental temperature range are negligible, so that the ratio is taken to be $\Gamma = 0.053$ (Wu 1970); thus the liquid–air surface tension largely dominates that of the liquid–liquid interface.

M_w (PS) (kg mol ⁻¹)	T (°C)	μ (best fit)	μ (independent)
53.3	150	1.1×10^{-4}	5.3×10^{-5}
53.3	165	1.5×10^{-3}	3.0×10^{-4}
53.3	180	7.1×10^{-3}	7.1×10^{-4}
183	150	8.5×10^{-3}	4.2×10^{-3}
183	165	7.4×10^{-3}	2.0×10^{-2}
183	180	4.6×10^{-2}	4.6×10^{-2}
758.9	150	1.7×10^{-1}	6.9×10^{-1}
758.9	165	1.2×10^0	5.8×10^0
758.9	180	1.5×10^0	1.4×10^1

Table 1. The viscosity ratios μ , between the bottom (PS) and top (PMMA) layers, for various PS molecular weights M_w (PS), and annealing temperatures T . The viscosity ratios are obtained from: (i) a best fit of the theory to the experimental excess capillary energy ('best fit'); and (ii) the capillary levelling of simple stepped films of each single polymer ('independent').

2.2. Theory

The system is modelled as two thin liquid layers atop each other, the ensemble being placed on a rigid substrate, as sketched in figure 1(a), and Cartesian coordinates (x, y, z) are used, as shown in figure 1(b). The system is assumed to be infinite in both the x -direction and y -direction, and invariant by translation in the latter. The typical length scales of the experiment are well below the capillary length, thus gravitational effects can be neglected. In thin, highly viscous polymer films, with Reynolds and Mach numbers are much smaller than 1, relaxation is driven by capillarity, and inertial and compressibility effects can be neglected. Furthermore, the polymer melts may be treated as Newtonian liquids (McGraw *et al.* 2012), since the typical viscoelastic times, under the present experimental conditions, are of the order of a few seconds (Hirai *et al.* 2003) whereas the levelling time scales are much larger (minutes to hours). Finally, the film thicknesses are chosen to be large enough such that disjoining forces are weak in comparison with the Laplace pressure (Seemann, Herminghaus & Jacobs 2001; Sharma & Verma 2004).

The velocity fields and excess pressure fields with respect to the atmospheric pressure are denoted as $\mathbf{u}_i = (u_i, 0, w_i)$ and p_i , respectively. In the small-slope limit, the tangential stress balance at the liquid–liquid interface reads $\eta_1(\partial u_1/\partial z) = \eta_2(\partial u_2/\partial z)$ (Jachalski *et al.* 2014). In the regime where $\mu \ll 1$, this relation further leads to $\partial u_2/\partial z = 0$ to leading order. Together with a no-shear-stress boundary condition at the liquid–air interface, these are consistent with plug flow in the top layer: much like in the freestanding case discussed above. Within the lubrication approximation, the bottom layer is expected to display a horizontal Poiseuille-like flow. Furthermore, we assume continuity of the velocity field across the liquid–liquid interface, i.e. we impose a no-slip boundary condition. As a result, we expect an additional linear term in z (like Couette flow for a simple shear geometry) in the horizontal velocity field of the bottom layer.

Within this framework, and invoking the lubrication-like scale separation, the heights $h_i(x, t)$ of both interfaces (see figure 1b) follow a set of nonlinear partial differential equations (see appendix A for more details). We refer to this first model as the asymptotic model. We note that a similar derivation was made for the non-Newtonian case for the upper liquid using the Jeffreys model (Jachalski, Münch & Wagner 2015). The governing

equations are

$$\partial_t(h_2 - h_1) = -[(h_2 - h_1)u_2]', \quad (2.1a)$$

$$\partial_t h_1 = - \left[(\gamma_2 h_2'' + \gamma_1 h_1'') \frac{h_1^3}{12\eta_1} + \frac{h_1 u_2}{2} \right]' = - \left[-p_1' \frac{h_1^3}{12\eta_1} + \frac{h_1 u_2}{2} \right]', \quad (2.1b)$$

$$\gamma_2 h_2''' (h_2 - h_1) + (\gamma_2 h_2'' + \gamma_1 h_1'') \frac{h_1}{2} + 4\eta_2 [u_2' (h_2 - h_1)]' - \eta_1 \frac{u_2}{h_1} = 0, \quad (2.1c)$$

where the prime indicates a derivative with respect to x . The excess pressure field $p_1 = -\gamma_1 h_1''(x) - \gamma_2 h_2''(x)$ in the bottom film corresponds to the sum of the two interfacial Laplace pressure jumps in the small-slope limit. Notably, (2.1c) has the same form as the tangential stress balance for a single liquid film on a solid substrate with a large slip length (Münch *et al.* 2005). The associated apparent slip length in our configuration is $b \sim h_1/\mu$ (Jachalski *et al.* 2015), which is large if $\mu \ll 1$, i.e. if the bottom layer is much less viscous than the top one. We note that a similar analogy with flow over a slippery substrate has been proposed to describe the flow of nanobubbles on hydrophobic surfaces (Lauga & Brenner 2004).

The heights of the two interfaces can be further expressed as perturbations from the equilibrium configuration: $h_1(x, t) = \bar{h}_1 + \delta h_1(x, t)$ and $h_2(x, t) = \bar{h}_2 + \delta h_2(x, t)$, where \bar{h}_i denote the mean heights of the two interfaces: $\bar{h}_1 = h_0$ and $\bar{h}_2 = 5h_0/2$ in our specific geometry. We then assume that $\delta h_i \ll \bar{h}_i$, and keep only the leading-order linear terms. We stress that this condition is not strictly valid at the liquid–air interface, but: (i) the linearization allows us to obtain an analytical solution; and (ii) in both limiting cases of freestanding and supported films, the linearization does preserve the self-similar structure of the nonlinear problem (Salez *et al.* 2012a,b; Ilton *et al.* 2016). Therefore, our approach is still expected to provide some relevant features for the experimental system.

Using the Fourier transform $\tilde{f}(k)$ of a function $f(x)$, defined as $\tilde{f}(k) = (1/\sqrt{2\pi}) \int dx f(x) \exp(ikx)$, we find from the linearization of the governing equations above, that

$$\frac{\partial \tilde{\delta h}_i}{\partial t} = s_{i,j}(k) \tilde{\delta h}_j, \quad (2.2)$$

with $s_{i,j}$ representing the elements of the decay-rate matrix s associated with the mode k (see appendix A). The Einstein summation convention is used in (2.2). The general solution to this set of equations is

$$\tilde{\delta h}_1 = \alpha \exp(\lambda_1 t) + \beta \exp(\lambda_2 t), \quad (2.3a)$$

$$\tilde{\delta h}_2 = \alpha K_1 \exp(\lambda_1 t) + \beta K_2 \exp(\lambda_2 t), \quad (2.3b)$$

where (λ_1, λ_2) and $(1, K_1), (1, K_2)$ are the eigenvalues and eigenvectors of s , respectively. The two coefficients α and β can be found using the initial conditions: $\delta h_1(x, t = 0) = 0$, and $\delta h_2(x, t = 0) = h_0[\Theta(x) - 1/2]$, where Θ denotes the Heaviside function (i.e. $\Theta(x > 0) = 1, \Theta(x < 0) = 0$).

We stress that the main assumption in the asymptotic model is the small-slope approximation. However, the initial profile is sharp in the experiments, with large slopes. Therefore, the early-time dynamics cannot be fully captured. To evaluate and extend the validity of the asymptotic model described so far, a second model was developed that does not assume any specific leading-order flow profiles in the two layers, and that takes into account all the terms of the Stokes equations. Thus, this model includes the

Capillary levelling of immiscible bilayer films

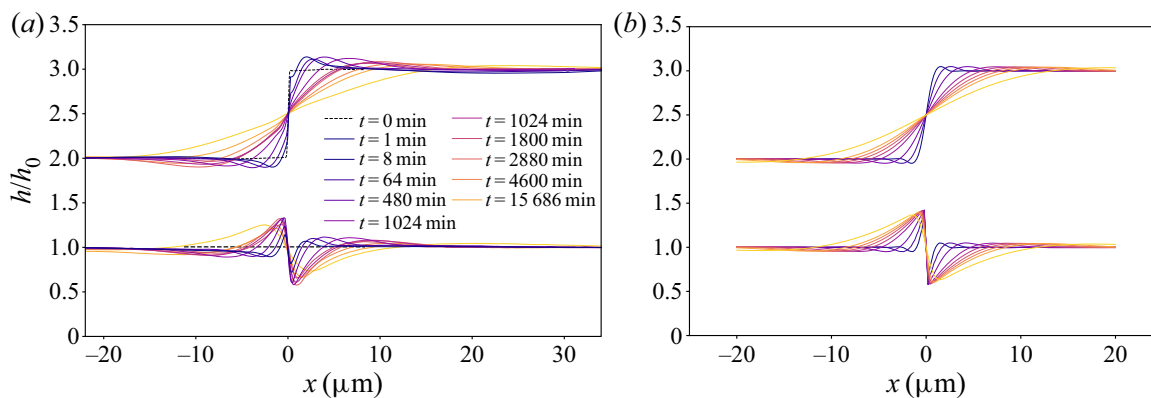


Figure 2. (a) Experimental profiles $h(x, t) = h_i(x, t)$ of the liquid–liquid ($i = 1$, bottom) and liquid–air ($i = 2$, top) interfaces of a PMMA ($M_w = 56 \text{ kg mol}^{-1}$) stepped layer on a PS ($M_w = 53.3 \text{ kg mol}^{-1}$) layer (see figure 1), during levelling at $T = 150^\circ\text{C}$. The viscosity ratio for these samples is $\mu = 1.1 \times 10^{-4}$ (see table 1). The samples were fabricated with $h_0 = 180 \text{ nm}$. (b) Theoretical profiles calculated using the asymptotic model. The times, rheological properties and geometry have been chosen to match the experimental conditions of the data shown in (a).

contribution of vertical flow in the leading-order momentum balance, in contrast with the asymptotic model. We refer to this second model as the full-Stokes model (see details in appendix B). The stress boundary conditions are linearized in the profiles' perturbations, in order to get an analytical solution that can be compared with the asymptotic model. As a result, the full-Stokes model exhibits governing equations similar to (2.2), with the exception of the matrix elements $s_{i,j}^{Stokes}$, which are more complicated functions of k than $s_{i,j}$. Excellent self-consistent agreement between the solutions of the two models is found in the small-slope limit at small wavenumber (see appendix B).

3. Results and discussion

3.1. Interface profiles

In figure 2(a), we show the experimental profiles of the liquid–air and liquid–liquid interfaces at different stages of evolution for the case of PMMA with $M_w = 56 \text{ kg mol}^{-1}$, PS with $M_w = 53 \text{ kg mol}^{-1}$ and an annealing temperature of 150°C . We note that each pair of interface profiles at a given annealing time corresponds to a different sample, as the top layer must be removed in order to image the buried liquid–liquid interface. Thus, a series of equivalent samples was prepared in order to reconstruct the entire evolution. Each sample was annealed for a given time, its liquid–air interface was imaged, the PMMA layer removed, and finally the profile of the bottom layer at the same location was imaged. The liquid–air interface develops a ‘bump’ on the upper side of the step with positive curvature (i.e. negative second derivative of the profile), and a ‘dip’ on the lower side with negative curvature. With increasing annealing time, the bump and dip spread apart horizontally as the step levels. Furthermore, at late times, the bump and dip decrease in height. As discussed previously (Salez *et al.* 2012a), the bump and dip develop to alleviate the large gradients in Laplace pressure due to the highly curved corners of the original stepped geometry. At early annealing times ($t < 8 \text{ min}$), there is a sharp feature near the centre of the step that seems to be a remnant of the initial corner of the step.

The liquid–liquid interface deforms significantly in response to the Laplace pressure due to the stepped liquid–air interface. Remarkably, the deformation of the liquid–liquid

interface initially grows vertically, before levelling out, which implies that while the surface energy associated with the liquid–air interface decreases, it partially does so at the cost of an increasing surface energy of the liquid–liquid interface. On either side of the step one can observe features in the liquid–liquid interface which mimic that of the bump and dip of the liquid–air interface. The deformation of the liquid–liquid interface can be qualitatively understood by considering the interfacial tension ratio $\Gamma = \gamma_1/\gamma_2$, as well as the viscosity ratio $\mu = \eta_1/\eta_2$ (see § 3.2 for a detailed study of the latter) introduced above. Since $\Gamma \ll 1$, the liquid–liquid interface is much more compliant than the liquid–air interface, and hence the liquid–liquid interface adapts and follows the liquid–air interface. Moreover, the total interfacial energy of the system is dominated by the liquid–air contribution, as demonstrated quantitatively below (see § 3.3).

Figure 2(b) shows the theoretical profiles generated from the asymptotic model, with all the physical parameters matching the experimental conditions of the data in figure 2(a). The model captures the essential features observed in the experiments, with the exception of a few early-time features (e.g. initial vertical growth of the liquid–liquid interface and sharp feature near the step corner). In fact, at early times, the small-slope approximation is violated since $\partial h_2/\partial x|_{x=0}$ is of order one. We thus suspect vertical flows, which were neglected in the leading-order momentum balance of the asymptotic model, to be responsible for such features. The full-Stokes model, which accounts for vertical flow, does capture these early-time details (see appendix B), which supports our suggestion.

3.2. Effect of the viscosity ratio

Figure 3(a) shows the experimental liquid–air (i.e. PMMA–air) interface profiles, at an annealing temperature of 165 °C, for various annealing times and PS molecular weights. For the experimental profiles in figures 2(a) and 3, μ is always much smaller than 1 – except in the case of $M_w(PS) = 758.9 \text{ kg mol}^{-1}$ at 165 °C, for which μ is of order unity (see table 1). As explained in § 3.1, the evolution of the system is mostly driven by the gradients in Laplace pressure along the liquid–air interface. The resulting pressure field in the top PMMA layer is transferred to the underlying PS layer, thereby inducing flow in the latter and thus deformation of the liquid–liquid interface. Finally, it is immediately clear from figure 3(a) that for samples having identical annealing temperatures, annealing times and geometry, the lower the viscosity of the underlying PS layer, the faster the levelling of the liquid–air interface. This highlights the importance of the bottom layer in the relaxation of the top layer, and is in line with the discussion in § 2.2 about the apparent slip length $b \sim h_1/\mu$ in our configuration (Jachalski *et al.* 2015).

As discussed in the introduction, the capillary levelling of thin liquid films can exhibit self-similar regimes. For films supported on no-slip substrates and with the associated Poiseuille flow, the self-similar variable is $x/t^{1/4}$, while for freestanding films and plug flow, $x/t^{1/2}$ provides the appropriate rescaling. Figure 3(b) shows the same data as in figure 3(a) with the horizontal axis rescaled as expected for a Poiseuille flow. For the largest viscosity ratio, obtained with $M_w(PS) = 758.9 \text{ kg mol}^{-1}$, the rescaled profiles collapse well with one another. This is consistent with the physical intuition that a high enough viscosity in the bottom layer renders the situation analogous to capillary levelling on a solid substrate. However, for the two smaller viscosity ratios, there is no such collapse, which suggests that there is no $\sim t^{1/4}$ self-similar behaviour within the experimental temporal range. Similarly, rescaling the x -axis by $t^{1/2}$ (not shown) does not allow us to collapse the experimental profiles either. Therefore, in order to investigate the temporal evolution in more detail, we consider in § 3.3 the evolution of the surface

Capillary levelling of immiscible bilayer films

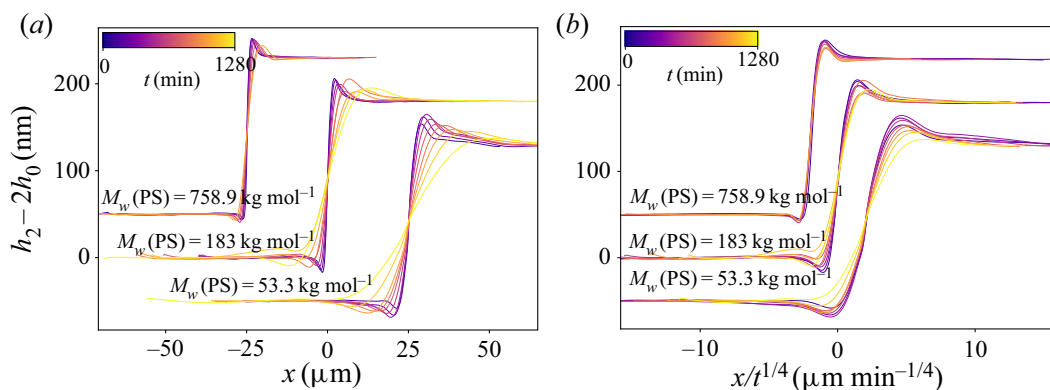


Figure 3. (a) Experimental liquid–air (i.e. PMMA–air) interface profiles, at an annealing temperature of 165 °C, for various annealing times and PS molecular weights, as indicated. (b) Same experimental data as in (a), but with a rescaled horizontal axis. For both panels, the 53.3 and 758.9 kg mol⁻¹ data have been shifted horizontally and vertically for clarity.

energy of the system – i.e. a global observable linked to capillary levelling (McGraw *et al.* 2012).

3.3. Energetic considerations

The excess capillary energy \mathcal{E}_i of interface i is proportional to the interfacial tension γ_i , as well as to the difference between the interfacial area S_i and the interfacial area S_i^0 of the flat equilibrium state: $\mathcal{E}_i = \gamma_i(S_i - S_i^0)$. Given the invariance of the system with respect to the y -direction, and relating the interfacial lengths to the local profiles $h_i(x)$, we consider the excess capillary energies per unit length defined as: $E_i = \gamma_i \int dx (\sqrt{1 + h_i'(x)^2} - 1)$.

In order to account for the different initial liquid–liquid interfacial lengths, resulting from the different h_0 values and thus step heights, the excess capillary energies per unit length can be normalized by the corresponding initial values $\gamma_2 h_0$ for the liquid–air interface. In figure 4 the normalized excess capillary energy per unit length is plotted versus dimensionless time for both the liquid–liquid ($i = 1$) and liquid–air ($i = 2$) interfaces, from the data shown in figure 2(a), as well as from data obtained with two other thicknesses h_0 . At dimensionless times $t\gamma_2/(h_0\eta)$ larger than ~ 10 , one observes that the excess capillary energies of both interfaces seem to decrease as $t^{-1/2}$ power laws. In addition, as expected and discussed in § 3.1, the contribution of the liquid–liquid interface is ~ 7 times smaller than that of the liquid–air interface. This dominance of the liquid–air excess interfacial energy to the total interfacial energy confirms the intuitive remark made previously that the liquid–liquid interface deforms with a relatively little cost since $\Gamma \ll 1$. In the following, we thus focus on the liquid–air interface alone. Conveniently, one can then prepare a single sample and follow the evolution of the liquid–air interface through repeated annealing, rather than having to sacrifice the sample by dissolving the top PMMA layer. The excess capillary energies per unit length can be computed from the asymptotic model, i.e. in the small-slope limit, with the approximation $E_i \simeq \gamma_i \int dx h_i'(x)^2/2$. We note that, under this approximation, if the profile of a given interface is self-similar, such that $h_i(x, t) = f_i(x/t^\alpha)$ with f_i a function of a single variable, then $E_i \sim t^{-\alpha}$. Therefore, $E_i \sim t^{-1/4}$ or $E_i \sim t^{-1/2}$ indicate the dominance of Poiseuille or plug flows, respectively, as discussed in § 3.2.

Figure 5(a–c) shows the normalized excess capillary energy per unit length E_2 of the liquid–air interface as a function of time t , for different annealing temperatures and PS

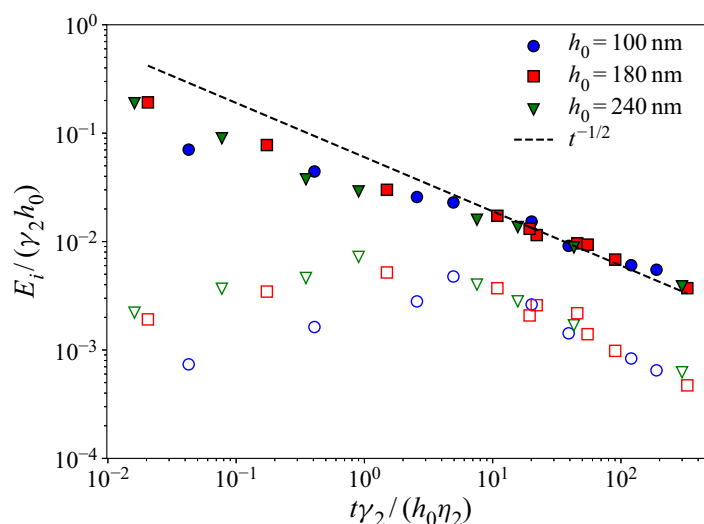


Figure 4. Normalized excess capillary energy per unit length of the liquid–liquid ($i = 1$, unfilled) and liquid–air ($i = 2$, filled) interfaces, for PMMA ($M_w = 56 \text{ kg mol}^{-1}$) stepped films on PS ($M_w = 53.3 \text{ kg mol}^{-1}$) films, with three different values of the nominal thickness h_0 (see figure 1) as indicated, and an annealing temperature of $150 \text{ }^\circ\text{C}$. The excess capillary energies per unit length have been normalized by the corresponding initial values for the liquid–air interface. Long-term $\sim t^{-1/2}$ behaviours are indicated with dashed lines.

molecular weights. For each panel, three identical samples were prepared and annealed at different temperatures. The experimental data are overlaid with best fits to the excess capillary energy per unit length E_2 of the liquid–air interface obtained from the asymptotic model, using the PS viscosity as the single free parameter. We note an excellent agreement between experiments and theory, except at the earliest times for the sample made with a 53.3 kg mol^{-1} PS molecular weight and annealed at $150 \text{ }^\circ\text{C}$. In that case, the experimental values are substantially higher than predicted by the model, which is likely due to the sharp feature observed at early times (see figure 2a), as noted in § 3.1. Indeed, this feature cannot be captured by the asymptotic model (see figure 2b) which neglects any vertical flow in the leading-order momentum balance (see appendix B), and it would elevate the capillary energy compared to a profile without that feature. Finally, the viscosity ratios obtained from the fits are in good agreement with independent measurements (see table 1) – both approaches being within an order of magnitude of each other. We note that the viscosities are highly dependent on temperature and that small temperature differences between samples can have large effects on the measured viscosity ratio. Furthermore, as the driving force for flow is surface energy, there is a possibility of trace contaminants reducing the surface energy from what is assumed, thus modifying the capillary velocity of the system (Hourlier-Fargette *et al.* 2017; Peaudcerf *et al.* 2017). However, this contribution to any error in the capillary velocity is small in comparison to that related to the temperature variation on the viscosity.

While the experimental data in figures 4 and 5(a) seem consistent with a $E_2 \sim t^{-1/2}$ trend, the asymptotic model does not predict a well-defined regime with such a scaling law. Instead, the model seems to exhibit a double cross-over, with a transient exponent that changes smoothly from a value near $-1/4$, to a value near $-1/2$, before increasing again towards $-1/4$, as seen in figure 5(a–c). The latter seems to correspond to a proper long-term self-similar regime, valid for all viscosity ratios. Thus, the energy eventually becomes independent of the viscosity η_2 of the top film, which indicates that most of the dissipation occurs in the bottom film at late times. This long-term self-similar

Capillary levelling of immiscible bilayer films

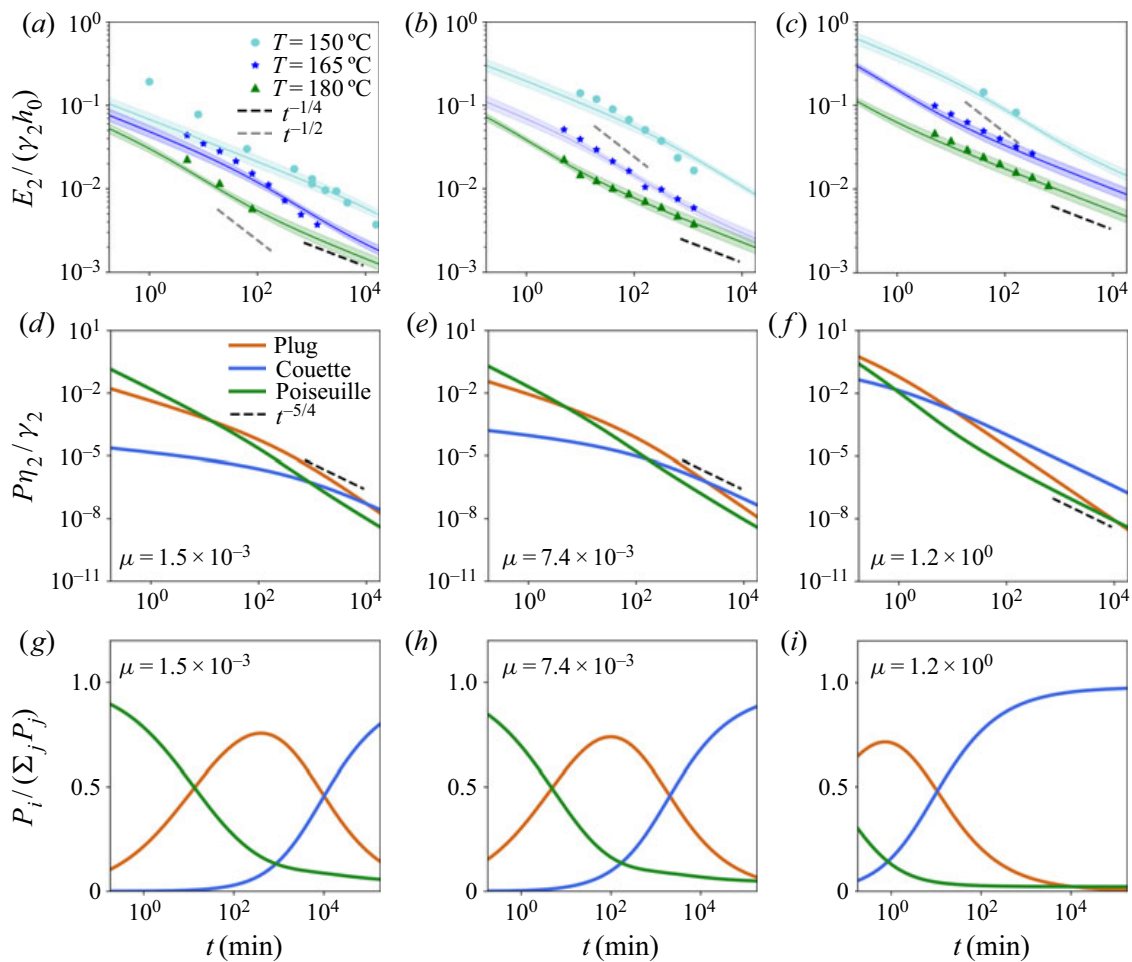


Figure 5. (a–c) Normalized excess capillary energy per unit length $E_2/(\gamma_2 h_0)$ of the liquid–air interface as a function of time t , for PMMA ($M_w = 56 \text{ kg mol}^{-1}$) stepped layers on PS layers, annealed at 150°C (\circ), 165°C (\star) and 180°C (\triangle). The PS molecular weights are: (a) $M_w = 53.3 \text{ kg mol}^{-1}$, (b) $M_w = 183 \text{ kg mol}^{-1}$ and (c) $M_w = 758.9 \text{ kg mol}^{-1}$. The solid lines of corresponding colours indicate the normalized excess capillary energy per unit length $E_2/(\gamma_2 h_0)$ of the top interface calculated from the asymptotic model, with the PS viscosity as a single fitting parameter. The bands span a variation in viscosity ratio from half of the best fit to double of the best fit. The excess capillary energies per unit length have been normalized by the corresponding initial values for the liquid–air interface. The $t^{-1/2}$ and $t^{-1/4}$ trends are indicated with dashed lines. (d–f) Normalized viscous dissipation power per unit length $P\eta_2/\gamma_2$ as a function of time t , calculated from the asymptotic model, for the three viscous mechanisms of (3.1): plug ($P = P_{\text{plug}}$), Poiseuille ($P = P_{\text{Poiseuille}}$) and Couette ($P = P_{\text{Couette}}$). For each panel, the viscosity ratio μ corresponds to the 165°C (\star) experimental data in the panel above. The $t^{-5/4}$ trend is indicated with dashed lines. (g–i) The fractional composition of the total viscous dissipation displayed in the panel above.

regime is reached experimentally in some cases (see figure 5b,c), but is not accessible for the smallest viscosity ratios due to the large experimental time scales involved. The apparent $E_2 \sim t^{-1/2}$ regime observed in figures 4 and 5(a) is thus a transient, intermediate behaviour.

The asymptotic model can be used to gain further insight into the effect of the viscosity ratio, by expressing the conservation of energy. As the films are thin, body forces may be neglected. The capillary energy decreases primarily through viscous dissipation. The rate of change of the total capillary energy per unit length can be written as the sum of the three contributions to the viscous dissipation power induced by the characteristic flows

highlighted in § 2.2

$$\partial_t E = - \underbrace{\int dx 4\eta_2 (h_2 - h_1) u_2^2}_{P_{\text{plug}}} - \underbrace{\int dx \frac{p_1^2 h_1^3}{12\eta_1}}_{P_{\text{Poiseuille}}} - \underbrace{\int dx \eta_1 \frac{u_2^2}{h_1}}_{P_{\text{Couette}}}. \quad (3.1)$$

An explicit derivation of (3.1) is provided in [appendix C](#). The first term (P_{plug}) is related to a velocity profile that is invariant vertically through the top layer's thickness, corresponding to plug flow. The second term ($P_{\text{Poiseuille}}$) is related to a parabolic velocity profile, i.e. Poiseuille flow, caused by the horizontal Laplace pressure gradient in the bottom layer. The third term (P_{Couette}) corresponds to a linear variation in the velocity profile of the bottom layer, as seen in a simple shear geometry or Couette flow.

Figure 5(d–f) displays the normalized viscous dissipation power per unit length as a function of the rescaled time, calculated from the asymptotic model, for the three viscous mechanisms of (3.1). The normalized viscous dissipation power per unit length has been calculated for the three experimentally relevant viscosity ratios, which correspond to the experimental results from [figure 5\(a–c\)](#), respectively. Three main regimes can be identified from the respective fractions of the total viscous dissipation power shown in [figure 5\(g–i\)](#). At early times, the Poiseuille contribution dominates, which is associated with a $E \sim t^{-1/4}$ behaviour (McGraw *et al.* 2012) and thus $\partial_t E \sim t^{-5/4}$. At late times, the Couette contribution dominates, but since the Couette flow in the bottom layer is indirectly induced by the Laplace pressure gradient from the liquid–air interface, it also exhibits a $E \sim t^{-1/4}$ power law like the Poiseuille flow. Therefore, at late times, we also expect a $\partial_t E \sim t^{-5/4}$ behaviour. Furthermore, we recover the result stated above that the dissipation occurs mostly in the bottom film in this regime. Finally, at intermediate times, in between these two extreme regimes, the plug contribution seems to dominate. This is associated with a transient temporal exponent for the energy, passing by the $-1/2$ value (Ilton *et al.* 2016). Taking into account the early, intermediate and late times discussed above, we recover the non-monotonic trend for the temporal exponent from the theoretical predictions (lines) in [figure 5\(a–c\)](#). The non-monotonic trend can be further characterized as a Poiseuille-to-plug-to-Couette double cross-over.

In the case where $\mu \sim 1$, valid for PS with a molecular weight of $758.9 \text{ kg mol}^{-1}$, the shear stress at the liquid–liquid interface does not vanish and therefore shear terms must be taken into account in the top layer. The asymptotic model should thus be refined for bilayer films with such material properties (see the lubrication model in [appendix B.3](#)). However, according to the asymptotic model, the late-time dissipation is mainly dominated by the Couette contribution in the bottom layer (see [figure 5f](#)), and this model reproduces qualitatively the data and in particular the $x/t^{1/4}$ self-similarity of the profiles (see [figure 3b](#)). Nevertheless, we stress that the prefactor of the late-time scaling law $E_2 \sim t^{-1/4}$ from the asymptotic model is larger than the one from the lubrication model, as observed in [figure 8](#) (see [appendix B.3](#)). As a result, the fitting procedure leads to a systematic underestimation of the viscosity of the bottom layer, as confirmed in [table 1](#).

Finally, as stated in § 2.2, the set of equations (see (2.1a), (2.1b) and (2.1c)) that forms the asymptotic model is reminiscent of the equations that describe capillary levelling on a substrate with slip (Münch *et al.* 2005). For a nearly constant bottom layer thickness h_1 , the Couette dissipation power per unit length $P_{\text{plug}} = \eta_1 \int dx u_2^2 / h_1$ (see (3.1)) is indeed similar to the power per unit length $k \int dx u_2^2$ dissipated on a solid substrate through friction, provided that the friction coefficient k is identified to η_1 / h_1 and the slip velocity to u_2 . As a consequence, the bottom film acts as a lubrication layer below the top stepped

film, which leads to an apparent slip length given by $b \sim h_1 \eta_2 / \eta_1$. As such, our first (i.e. Poiseuille-to-plug) cross-over mimics the one expected for a single film supported on a rigid substrate with varying slip boundary condition (Münch *et al.* 2005; McGraw *et al.* 2016).

4. Conclusion

In this article, we examined the effect of a thin liquid substrate on the capillary levelling of a thin liquid film placed atop. Specifically, we prepared stepped polymer layers that were placed onto other, immiscible and flat polymer layers supported on solid substrates. The bilayer films were observed to flow and relax towards a flat equilibrium configuration. We showed that the liquid–liquid interface deforms substantially. In the samples studied, the viscosity ratio between the two layers was varied over a large range, with the bottom layer being less viscous, or as viscous as the top layer. We have shown that the viscosity ratio has a major impact on the resulting dynamics. Unlike the capillary levelling of simple stepped films on solid substrates, or freestanding films, the interfacial profiles do not exhibit any clear, unique and stable self-similar behaviour. We have developed and validated a thin-film model in which the governing flow in the top layer is plug like, and flow in the bottom layer is a with a combination of Poiseuille and Couette flows. Using an energetic treatment, we have shown that the excess capillary energy introduced by the step, with respect to the flat equilibrium state, is dissipated by those three coupled viscous mechanisms, thus leading to a novel Poiseuille-to-plug-to-Couette double cross-over. The time scales in the process depend on the viscosity ratio between the bottom and top layers. We have found that the bottom, less viscous layer is analogous to a solid substrate with a certain finite slip length. The experimentally measured energy dissipation is in agreement with that obtained from the model. The results presented illuminate the intricate dynamics of viscous bilayer assemblies, and might find applications through friction control by lubrication, self-assembly and stability of multilayer processes.

Acknowledgements. The authors are grateful to J. Niven for valuable insight and discussions.

Funding. We gratefully acknowledge financial support by the Natural Science and Engineering Research Council (NSERC) of Canada. V.B. and C.L.L. contributed equally to this work.

Declaration of interests. The authors report no conflict of interest.

Author ORCID*s*.

- ① Vincent Bertin <https://orcid.org/0000-0002-3139-8846>;
- ① Carmen L. Lee <https://orcid.org/0000-0002-4397-6332>;
- ① Thomas Salez <https://orcid.org/0000-0001-6111-8721>;
- ① Elie Raphaël <https://orcid.org/0000-0003-0007-4790>;
- ① Kari Dalnoki-Veress <https://orcid.org/0000-0002-0885-6634>.

Appendix A. Asymptotic model

A.1. Model

This appendix expands upon the asymptotic model discussed in § 2.2. Dimensionless variables are denoted by capital letters

$$\left. \begin{aligned} u_i &= uU_i, & w_i &= wW_i = u\epsilon W_i, & x &= lX, & z &= h_0Z, \\ p_i &= pP_i, & t &= \frac{l}{u}T, & h_i &= h_0H_i, & \epsilon &= \frac{h_0}{l}, \end{aligned} \right\} \quad (\text{A1})$$

where ϵ is the ratio between the typical vertical scale h_0 (see figure 1) and a horizontal length scale l , $P = \gamma_2 h_0 / l^2$ is the typical pressure scale set by the Laplace pressure and $u = \gamma_2 h_0 / \eta_2 l$ is the characteristic velocity which is chosen such that the leading-order equation for the top layer is compatible with plug flow. We note that there is no intrinsic horizontal length scale in our configuration. Therefore, the length scale l is the typical extent of the non-zero Laplace pressure, which can be estimated as the width of the levelling profile (McGraw *et al.* 2011). Thus, the asymptotic model is valid when this length scale is much larger than the typical height h_0 . Experimentally, this condition is not valid at early times ($t < 10$ min in figure 2a). We rescale the viscosity ratio as $M = \epsilon^{-2} \mu$ for appropriate governing equations in the bottom layer (Jachalski *et al.* 2015). Non-dimensionalization yields the governing Stokes equations for both viscous layers

$$0 = -\epsilon^2 \partial_X P_2 + \epsilon^2 \partial_X^2 U_2 + \partial_Z^2 U_2, \tag{A2a}$$

$$0 = -\partial_Z P_2 + \epsilon^2 \partial_X^2 W_2 + \partial_Z^2 W_2, \tag{A2b}$$

$$\partial_X U_2 + \partial_Z W_2 = 0, \tag{A2c}$$

$$0 = -\partial_X P_1 + M(\epsilon^2 \partial_X^2 U_2 + \partial_Z^2 U_1), \tag{A2d}$$

$$0 = -\partial_Z P_1 + M(\epsilon^4 \partial_X^2 W_1 + \epsilon^2 \partial_Z^2 W_1), \tag{A2e}$$

$$\partial_X U_1 + \partial_Z W_1 = 0. \tag{A2f}$$

At the free interface, the boundary conditions are the stress balance and the kinematic condition (Jachalski *et al.* 2014)

$$P_2 + \frac{\partial_X^2 H_2}{[1 + \epsilon^2 (\partial_X H_2)^2]^{3/2}} = 2 \frac{\partial_Z W_2 [1 - \epsilon^2 (\partial_X H_2)^2] - (\partial_Z U_2 + \epsilon^2 \partial_X W_2) \partial_X H_2}{1 + \epsilon^2 (\partial_X H_2)^2}, \quad Z = H_2, \tag{A3a}$$

$$(\partial_Z U_2 + \epsilon^2 \partial_X W_2) [1 - \epsilon^2 (\partial_X H_2)^2] = 4\epsilon^2 \partial_X U_2 \partial_X H_2, \quad Z = H_2, \tag{A3b}$$

$$\partial_T H_2 = W_2 - U_2 \partial_X H_2, \quad Z = H_2. \tag{A3c}$$

The boundary conditions at the liquid–liquid interface are the stress balance and the kinematic condition. Furthermore, we assume that there is no slip at the interface. All together, these read

$$P_1 - P_2 + \Gamma \frac{\partial_X^2 H_1}{[1 + \epsilon^2 (\partial_X H_1)^2]^{3/2}} = 2 \frac{\partial_Z (M\epsilon^2 W_1 - W_2) [1 - \epsilon^2 (\partial_X H_1)^2]}{1 + \epsilon^2 (\partial_X H_1)^2} - 2 \frac{[\partial_Z (M\epsilon^2 U_1 - U_2) + \epsilon^2 \partial_X (M\epsilon^2 W_1 - W_2)] \partial_X H_1}{1 + \epsilon^2 (\partial_X H_1)^2}, \quad Z = H_1 \tag{A4a}$$

$$[\partial_Z (M\epsilon^2 U_1 - U_2) + \epsilon^2 \partial_X (M\epsilon^2 W_1 - W_2)] [1 - \epsilon^2 (\partial_X H_1)^2] = 4\epsilon^2 \partial_X (M\epsilon^2 U_1 - U_2) \partial_X H_1, \quad Z = H_1 \tag{A4b}$$

$$\partial_T H_1 = W_1 - \partial_X H_1, \quad Z = H_1 \tag{A4c}$$

$$W_2 - W_1 = (U_2 - U_1) \partial_X H_1, \quad Z = H_1 \tag{A4d}$$

$$U_2 - U_1 + \epsilon^2 (W_2 - W_1) \partial_X H_1 = 0, \quad Z = H_1. \tag{A4e}$$

Capillary levelling of immiscible bilayer films

At the solid–liquid interface, we assume no-slip and impermeability boundary conditions

$$U_1 = W_1 = 0, \quad Z = 0. \quad (\text{A5a,b})$$

We consider the flow in the top layer as a perturbation

$$(U_2, W_2, P_2) = (U_2^{(0)}, W_2^{(0)}, P_2^{(0)}) + \epsilon^2(U_2^{(1)}, W_2^{(1)}, P_2^{(1)}). \quad (\text{A6})$$

The leading order can be described as

$$\partial_Z U_2^{(0)}(X, Z, T) = 0 \quad \rightarrow \quad U_2^{(0)}(X, Z, T) = U_2(X, T), \quad (\text{A7a})$$

$$W_2^{(0)}(X, Z, T) = -(Z - H_1)\partial_X U_2 + W_1(Z = H_1), \quad (\text{A7b})$$

$$P_2^{(0)}(X, T) = -2\partial_X U_2 - \partial_X^2 H_2, \quad (\text{A7c})$$

$$\partial_Z P_1(X, Z, T) = 0 \quad \rightarrow \quad P_1(X, T) = -\partial_X^2 H_2(X, T) - \Gamma \partial_X^2 H_1(X, T) \quad (\text{A7d})$$

$$U_1(X, Z, T) = -\frac{1}{2M} \partial_X P_1(Z^2 - ZH_1) + U_2(X, T) \frac{Z}{H_1}. \quad (\text{A7e})$$

The in-plane component of the flow is described by a set of coupled nonlinear equations. Invoking further the kinematic condition results in (2.1a)

$$\partial_t(H_2 - H_1) = -[(H_2 - H_1)U_2]', \quad (\text{A8})$$

where the prime denotes the derivative with respect to X . The volume conservation of the bottom layer gives (2.1b)

$$\partial_t H_1 = -\left(-P_1' \frac{H_1^3}{12M} + \frac{H_1 U_2}{2}\right)' = -\left[(H_2''' + \Gamma H_1''') \frac{H_1^3}{12M} + \frac{H_1 U_2}{2}\right]'. \quad (\text{A9})$$

The final equation that relates U_2 to the other variables can be found by integrating the horizontal component of the Stokes equation with respect to Z at the next leading order

$$\begin{aligned} \partial_Z^2 U_2^{(1)} + \partial_X^2 U_2^{(0)} &= \partial_X P_2^{(0)} \quad \rightarrow \quad \partial_Z U_2^{(1)}(Z = H_2) - \partial_Z U_2^{(1)}(Z = H_1) \\ &= (\partial_X P_2^{(0)} - \partial_X^2 U_2)(H_2 - H_1). \end{aligned} \quad (\text{A10})$$

We find the last governing equation, (2.1c), by inserting the two tangential stress balances, (A3b) and (A4b), at leading order into the previous equation

$$H_2'''(H_2 - H_1) + (H_2''' + \Gamma H_1''')H_1/2 + 4[U_2'(H_2 - H_1)]' - M \frac{U_2}{H_1} = 0. \quad (\text{A11})$$

A.2. Decay rates

The elements $s_{i,j}$ of the decay-rate matrix s are found by taking the Fourier transforms of the linearized governing equations

$$\left. \begin{aligned} s_{1,1}(k) &= -\gamma_1 k^4 \left[\frac{\bar{h}_1^3}{12\eta_1} + \frac{\bar{h}_1^3}{4(\eta_1 + 4\eta_2 k^2 \bar{h}_1 \bar{h}_2)} \right], \\ s_{1,2}(k) &= -\gamma_2 k^4 \left[\frac{\bar{h}_1^3}{12\eta_1} + \frac{\bar{h}_1^2 \bar{h}_2 \left(1 - \frac{\bar{h}_1}{2\bar{h}_2}\right)}{2(\eta_1 + 4\eta_2 k^2 \bar{h}_1 \bar{h}_2)} \right], \end{aligned} \right\} \quad (\text{A12a})$$

$$\left. \begin{aligned} s_{2,1}(k) &= -\gamma_1 k^4 \left[\frac{\bar{h}_1^3}{12\eta_1} + \frac{\bar{h}_1^2 \bar{h}_2 \left(1 - \frac{\bar{h}_1}{2\bar{h}_2}\right)}{2(\eta_1 + 4\eta_2 k^2 \bar{h}_1 \bar{h}_2)} \right], \\ s_{2,2}(k) &= -\gamma_2 k^4 \left[\frac{\bar{h}_1^3}{12\eta_1} + \frac{\bar{h}_1 \bar{h}_2^2 \left(1 - \frac{\bar{h}_1}{2\bar{h}_2}\right)^2}{(\eta_1 + 4\eta_2 k^2 \bar{h}_1 \bar{h}_2)} \right]. \end{aligned} \right\} \quad (\text{A12b})$$

The eigenvalues are the decay rates, and are given by

$$\lambda_i = \frac{\text{Tr}(s) \pm \sqrt{\text{Tr}(s)^2 - 4 \text{Det}(s)}}{2}. \quad (\text{A13})$$

The eigenvectors of s take the form $(1, K_i)$ with

$$K_i = \frac{\lambda_i - s_{1,1}}{s_{1,2}}. \quad (\text{A14})$$

Appendix B. Full-Stokes model

B.1. Model

To remove any assumption associated with pre-supposed flow types and the temporal scalings of the capillary energies, we derive a model from the Stokes equations (Huang & Suo 2002; Rivetti *et al.* 2017). The stream functions ψ_i of each layer ($i = 1, 2$) are defined as

$$u_i = -\partial_z \psi_i, \quad (\text{B1a})$$

$$w_i = \partial_x \psi_i. \quad (\text{B1b})$$

The velocity fields satisfy the Stokes equations. This in turn implies that the stream functions are solutions of biharmonic equations

$$(\partial_x^4 + 2\partial_x^2 \partial_z^2 + \partial_z^4) \psi_i = 0. \quad (\text{B2})$$

We take the Fourier transforms (defined in the main text) with respect to the variable x , of the biharmonic equations, through the Fourier transforms $\tilde{\psi}_i$ of the stream functions,

Capillary levelling of immiscible bilayer films

which results in fourth-order ordinary differential equations

$$\left(\frac{d}{dz}\right)^4 \tilde{\psi}_i - \left(\frac{d}{dz}\right)^2 k^2 \tilde{\psi}_i + k^4 \tilde{\psi}_i = 0. \quad (\text{B3})$$

The general solutions are

$$\tilde{\psi}_i(k, z) = A_i(k) \cosh(kz) + B_i(k) \sinh(kz) + C_i(k)z \cosh(kz) + D_i(k)z \sinh(kz). \quad (\text{B4})$$

The eight coefficients A_i, B_i, C_i, D_i can be found using the boundary conditions: vanishing velocity at the solid–liquid interface, continuity of velocity (including no slip) and stress across the liquid–liquid interface and continuity of stress (including no shear stress) at the liquid–air interface. The nonlinear terms of the curvature in the Laplace pressure are neglected, as well as the nonlinear terms of the normal and tangential vectors to the interfaces. This means that this model would be valid in the limit of small perturbation of the interface. The boundary condition are listed below

$$w_1 = 0 \quad \rightarrow \quad \tilde{\psi}_1 = 0, \quad z = 0, \quad (\text{B5a})$$

$$u_1 = 0 \quad \rightarrow \quad \left(\frac{d}{dz}\right) \tilde{\psi}_1 = 0, \quad z = 0, \quad (\text{B5b})$$

$$w_2 = w_1 \quad \rightarrow \quad -ik\tilde{\psi}_2 = -ik\tilde{\psi}_1, \quad z = h_1, \quad (\text{B5c})$$

$$u_2 = u_1 \quad \rightarrow \quad -\left(\frac{d}{dz}\right) \tilde{\psi}_1 = -\left(\frac{d}{dz}\right) \tilde{\psi}_2, \quad z = h_1, \quad (\text{B5d})$$

$$\begin{aligned} \eta_2(\partial_z u_2 + \partial_x w_2) &= \eta_1(\partial_z u_1 + \partial_x w_1) \quad \rightarrow \quad \eta_1 \left[\left(\frac{d}{dz}\right)^2 \psi_1 + k^2 \psi_1 \right] \\ &= \eta_2 \left[\left(\frac{d}{dz}\right)^2 \psi_2 + k^2 \psi_2 \right], \quad z = h_1. \end{aligned} \quad (\text{B5e})$$

$$\begin{aligned} \eta_1 \left[3k^2 \left(\frac{d}{dz}\right) \tilde{\psi}_1 - \left(\frac{d}{dz}\right)^3 \tilde{\psi}_1 \right] - \eta_2 \left[3k^2 \left(\frac{d}{dz}\right) \tilde{\psi}_2 - \left(\frac{d}{dz}\right)^3 \tilde{\psi}_2 \right] &= ik^3 \gamma_1 \tilde{h}_1, \quad z = h_1. \\ &\rightarrow \quad -(p_1 - p_2) + 2\partial_z(\eta_1 w_1 - \eta_2 w_2) = -\gamma_1 \partial_x^2 h_1 \end{aligned} \quad (\text{B5f})$$

$$\eta_2(\partial_z u_2 + \partial_x w_2) = 0 \quad \rightarrow \quad \left(\frac{d}{dz}\right)^2 \psi_2 + k^2 \psi_2 = 0, \quad z = h_2. \quad (\text{B5g})$$

$$\begin{aligned} -p_2 + 2\eta_2 \partial_z w_2 &= -\gamma_2 \partial_x^2 h_2 \quad \rightarrow \quad \eta_2 \left[3k^2 \left(\frac{d}{dz}\right) \tilde{\psi}_2 - \left(\frac{d}{dz}\right)^3 \tilde{\psi}_2 \right] \\ &= ik^3 \gamma_2 \tilde{h}_2, \quad z = h_2. \end{aligned} \quad (\text{B5h})$$

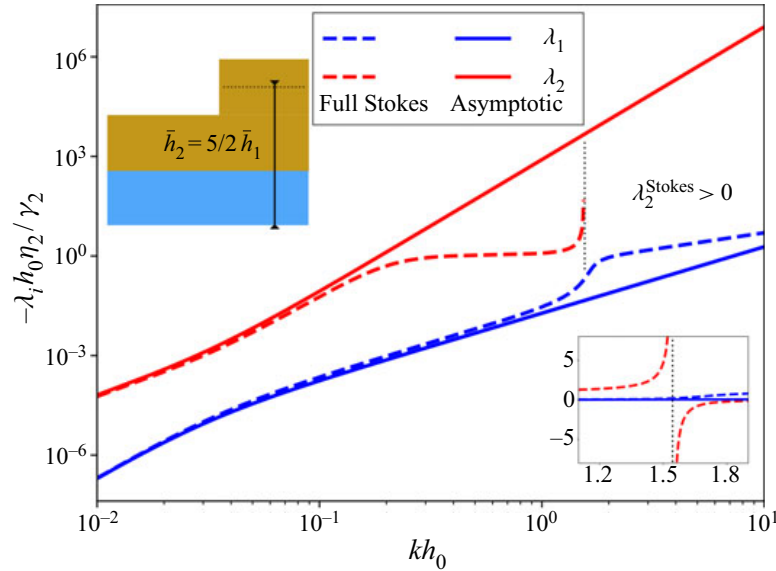


Figure 6. Dimensionless decay rates for the full-Stokes model ($\lambda_i^{\text{Stokes}}$) and asymptotic model (λ_i) versus the dimensionless wavenumber kh_0 , in the experimental configuration where $\bar{h}_2 = 5/2\bar{h}_1 = 5/2h_0$ (see schematic in the top left inset). The bottom right inset displays a zoom of the same curves near $kh_0 = 1.5$, and is plotted with linear scales.

The Stokes equations in the x -direction read

$$\partial_x p_i = \eta_i (\partial_x^2 u_i + \partial_z^2 u_i) \quad \rightarrow \quad -ik\tilde{p}_i = \eta_i \left[k^2 \frac{d}{dz} \tilde{\psi}_i - \left(\frac{d}{dz} \right) \tilde{\psi}_i''' \right]. \quad (\text{B6})$$

The governing equations for the temporal evolutions of the thickness profiles can be found using the kinematic conditions

$$\partial_t h_i + u_i \partial_x h_i = w_i, \quad (\text{B7})$$

where u_i and w_i are evaluated at $z = h_i$. We further invoke small interfacial perturbations and proceed to linearization as in the asymptotic model

$$\partial_t \tilde{h}_1 = \tilde{w}_1(z = \bar{h}_1) = s_{11}^{\text{Stokes}} \tilde{\delta h}_1 + s_{12}^{\text{Stokes}} \tilde{\delta h}_2, \quad (\text{B8a})$$

$$\partial_t \tilde{h}_2 = \tilde{w}_2(z = \bar{h}_1 + \bar{h}_2) = s_{21}^{\text{Stokes}} \tilde{\delta h}_1 + s_{22}^{\text{Stokes}} \tilde{\delta h}_2. \quad (\text{B8b})$$

These equations have the same general solutions as in the asymptotic model developed in § 2.2. The elements $s_{i,j}^{\text{Stokes}}$ of the decay-rate matrix are not written here but can be found using a formal calculation software. It is then straightforward to write the solutions as in (2.3) with the corresponding eigenvalues $\lambda_i^{\text{Stokes}}$ and eigenvectors $(1, K_i^{\text{Stokes}})$. Figure 6 displays the normalized decay rates as functions of the normalized wavenumber in both the full-Stokes model and the asymptotic model, with the same dimensionless parameters as in figure 2, i.e. $\mu = 1.1 \times 10^{-4}$ and $\Gamma = 0.053$. The two models agree in the small-wavenumber limit, $kh_0 \rightarrow 0$. At an intermediate wavenumber $kh_0 \sim 1.544$, the determinant of the matrix s^{Stokes} changes sign and therefore one of the two eigenvalues, $\lambda_2^{\text{Stokes}}$, becomes positive at larger wavenumbers (see bottom right inset of figure 6). Thus, in the full-Stokes model, the large wavenumbers are unstable and grow with time: the interface perturbation diverges as time increases. This is not physical as capillarity is the only driving force and acts to stabilize the interface. We suspect that nonlinear terms in the stress balances at interfaces – neglected so far – will regularize this behaviour.

Capillary levelling of immiscible bilayer films

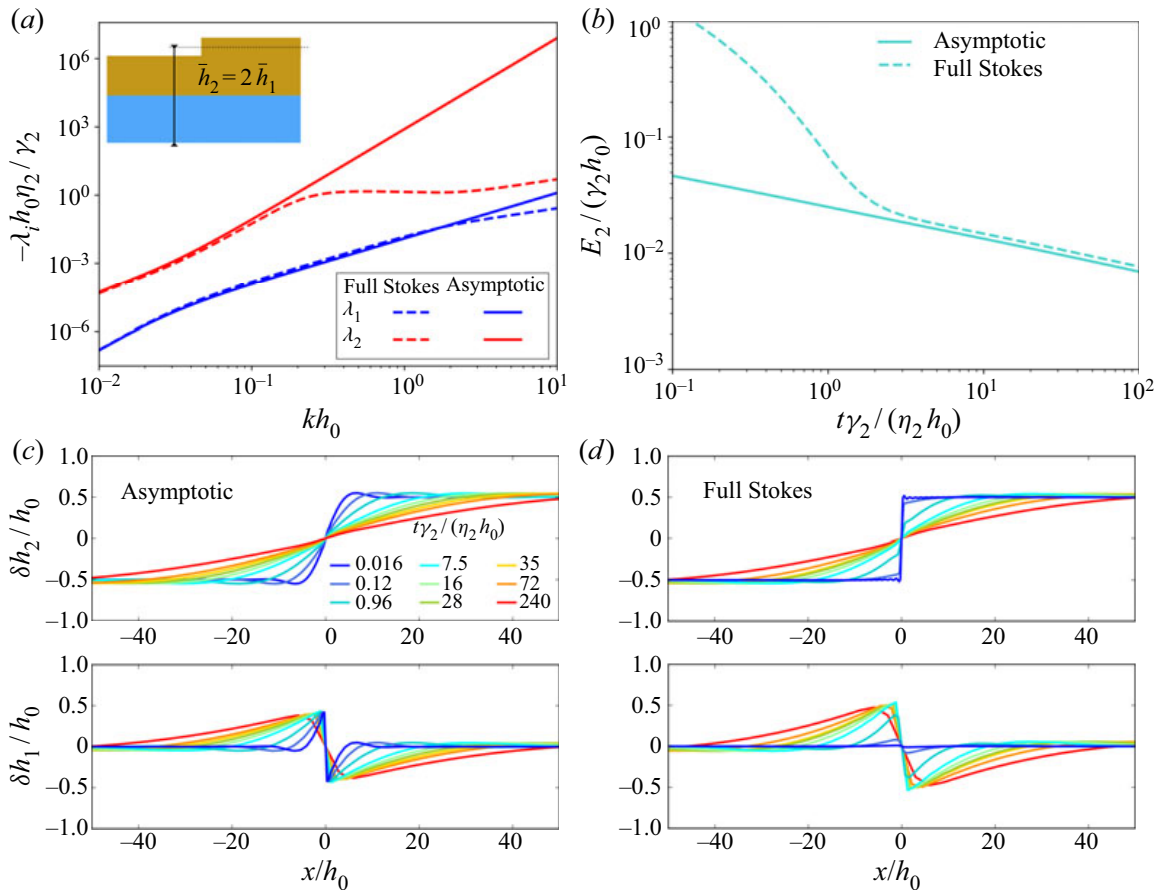


Figure 7. Comparison of the full-Stokes model and the asymptotic model in the specific case where $\bar{h}_2 = 2\bar{h}_1$. (a) Dimensionless decay rates for the full-Stokes model ($\lambda_i^{\text{Stokes}}$, dashed lines) and asymptotic model (λ_i , solid lines) versus the dimensionless wavenumber kh_0 . (b) Normalized excess capillary energies per unit length $E_2 / (\gamma_2 h_0)$ of the liquid–air interface, as functions of dimensionless time, as evaluated from the small-slope expression $E_2 \simeq \gamma_2 \int dx \delta h_2^2 / 2$, for both models and for the same parameters as in figure 5(a) at 150 °C. (c) (respectively (d)) Interface perturbation profiles δh_i in the asymptotic model (respectively full-Stokes model). The colours indicate the same experimental times as in figure 2.

B.2. Particular case: equal average layer thicknesses

We found empirically that the instability described in the previous section is not present when the mean thicknesses of the two layers are equal, which amounts to $\bar{h}_2 = 2\bar{h}_1$. Therefore, we can compare in a more complete manner the two models in this case. Figure 7(a) displays the normalized decay rates as functions of the normalized wavenumber in both the full-Stokes model and the asymptotic model. We no longer observe any positive decay rate in the full-Stokes model. At small wavenumber, which means in the small-slope limit, we recover the previous statement which is that both models are consistent with each other. In figure 7(b), the normalized excess capillary energies per unit length of the liquid–air interface for both models are plotted as functions of dimensionless time. In the long-time limit, when the step has levelled sufficiently such that the typical slopes of the interfaces are much smaller than unity, we find an excellent agreement between both models. However, at short times, the profile slopes are close to unity and thus vertical flows and nonlinear terms play a significant role. Therefore, at short times the full-Stokes model, which accounts for vertical flows, differs from the asymptotic model. We point out that the excess capillary energies per unit length E_2 of the

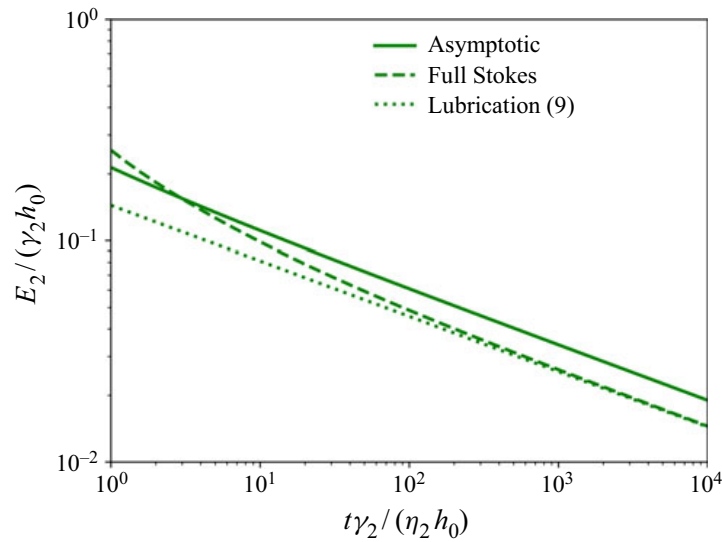


Figure 8. Normalized excess capillary energies per unit length E_2 of the liquid–air interface as functions of dimensionless time, as evaluated from the small-slope expression $E_2 \simeq \gamma_2 \int dx \delta h_2^2 / 2$, for the three models indicated, and for $\mu = 14$, $\gamma = 0.053$, with equal mean thicknesses $\bar{h}_1 = \bar{h}_2$.

liquid–air interface, from both models, are systematically computed with the small-slope expression $E_2 \simeq \gamma_2 \int dx \delta h_2^2 / 2$ which is not necessarily valid at short times. The exact expression should be used instead to make direct comparisons with experiments at short times. The discrepancy between the two models at short times is illustrated on the interface perturbation profiles in figures 7(c) and 7(d), that would correspond to an experiment with the same material properties as in figure 2 but with equal mean thicknesses. Interestingly, we observe similar short-term characteristics in the full-Stokes model as the one observed experimentally: a small sharp feature near the step and the deformation growth of the liquid–liquid interface.

B.3. Case of a large viscosity ratio

We consider the $\mu \gg 1$ case. In figure 8, the normalized total excess capillary energies per unit length as functions of dimensionless time are plotted for the two models described above. We also add for comparison the perturbative solution of a two-layer lubrication model (see Jachalski *et al.* (2014) for a complete derivation in a more general case with weak slip)

$$\frac{\partial h_1}{\partial t} = \left[-\gamma_2 \frac{h_1^2 (3h_2 - h_1)}{6\eta_1} h_2''' - \gamma_1 \frac{h_1^3}{3\eta_1} h_1''' \right]', \tag{B9a}$$

$$\frac{\partial (h_2 - h_1)}{\partial t} = \left\{ -\gamma_2 \left[\frac{(h_2 - h_1)^3}{3\eta_2} + \frac{h_1 (h_2 - h_1) (h_2 - h_1/2)}{\eta_1} \right] h_2''' - \gamma_1 \frac{h_1^2 (h_2 - h_1)}{2\eta_1} h_1''' \right\}'. \tag{B9b}$$

We observe that the asymptotic model is no longer in accordance with the full-Stokes model in the large-time limit, while the lubrication model is. Indeed, when the viscosity of the bottom layer is comparable to or larger than the one of the top layer, i.e. $\mu \gtrsim 1$, the

asymptotic model is no more valid as it neglects shear terms in the top layer with respect to elongational ones.

Appendix C. Energy balance

In this section, we derive the energy balance in (3.1) from the asymptotic model. In the limit of small slopes, the excess capillary energies per unit length of the two interfaces are

$$E_2 = \frac{\gamma_2}{2} \int dx h_2'(x)^2, \tag{C1a}$$

$$E_1 = \frac{\gamma_1}{2} \int dx h_1'(x)^2. \tag{C1b}$$

We can derive these quantities with respect to time and get

$$\partial_t E_2 = \gamma_2 \int dx h_2' \partial_t h_2' = -\gamma_2 \int dx h_2'' \partial_t h_2, \tag{C2a}$$

$$\partial_t E_1 = \gamma_1 \int dx h_1' \partial_t h_1' = -\gamma_1 \int dx h_1'' \partial_t h_1. \tag{C2b}$$

The second equalities are obtained after integrating by parts. We can then use (2.1a) and (2.1b), which leads to

$$\begin{aligned} \partial_t E_2 &= -\gamma_2 \int dx h_2'' \{ \partial_t h_1 - [(h_2 - h_1)u_2]' \} \\ &= -\gamma_2 \int dx h_2'' \left\{ - \left(-p_1' \frac{h_1^3}{12\eta_1} + \frac{h_1 u_2}{2} \right)' - [(h_2 - h_1)u_2]' \right\}, \end{aligned} \tag{C3a}$$

$$\partial_t E_1 = \gamma_1 \int dx h_1'' \left(-p_1' \frac{h_1^3}{12\eta_1} + \frac{h_1 u_2}{2} \right)'. \tag{C3b}$$

We then integrate by parts

$$\partial_t E_2 = \gamma_2 \int dx h_2''' \left\{ - \left(-p_1' \frac{h_1^3}{12\eta_1} + \frac{h_1 u_2}{2} \right) - [(h_2 - h_1)u_2] \right\}, \tag{C4a}$$

$$\partial_t E_1 = -\gamma_1 \int dx h_1''' \left(-p_1' \frac{h_1^3}{12\eta_1} + \frac{h_1 u_2}{2} \right). \tag{C4b}$$

Introducing the total excess capillary energy per unit length $E = E_1 + E_2$, one gets

$$\partial_t E = - \int dx [\gamma_2 h_2''' (h_2 - h_1)] u_2 + \int dx p_1' \left(-p_1' \frac{h_1^3}{12\eta_1} + \frac{h_1 u_2}{2} \right). \tag{C5}$$

We can then use (2.1c) to replace the term in square brackets

$$\begin{aligned} \partial_t E &= - \int dx \left\{ - \frac{p_1' h_1}{2} - 4\eta_2 [u_2' (h_2 - h_1)]' + \eta_1 \frac{u_2}{h_1} \right\} u_2 \\ &\quad + \int dx p_1' \left(-p_1' \frac{h_1^3}{12\eta_1} + \frac{h_1 u_2}{2} \right). \end{aligned} \tag{C6}$$

This can be further simplified and after another integration by parts of the term in $[u_2'(h_2 - h_1)]'u_2$, one gets

$$\partial_t E = - \int dx 4\eta_2 (h_2 - h_1) u_2'^2 - \int dx \eta_1 \frac{u_2^2}{h_1} - \int dx \frac{p_1^2 h_1^3}{12\eta_1}. \quad (\text{C7})$$

REFERENCES

- ACHESON, D.J. 1990 *Elementary Fluid Dynamics*. Oxford University Press.
- BACKHOLM, M., BENZAQUEN, M., SALEZ, T., RAPHAËL, E. & DALNOKI-VERESS, K. 2014 Capillary levelling of a cylindrical hole in a viscous film. *Soft Matter* **10**, 2550–2558.
- BÄUMCHEN, O., BENZAQUEN, M., SALEZ, T., MCGRAW, J., BACKHOLM, M., FOWLER, P., RAPHAËL, E. & DALNOKI-VERESS, K. 2013 Relaxation and intermediate asymptotics of a rectangular trench in a viscous film. *Phys. Rev. E* **88**, 035001.
- BÄUMCHEN, O. & JACOBS, K. 2009 Slip effects in polymer thin films. *J. Phys.: Condens. Matter* **22** (3), 033102.
- BERTIN, V., NIVEN, J., STONE, H.A., SALEZ, T., RAPHAËL, E. & DALNOKI-VERESS, K. 2020 Symmetrization of thin free-standing liquid films via capillary-driven flow. *Phys. Rev. Lett.* **124**, 184502.
- BIRONEAU, A., SALEZ, T., MIQUELARD-GARNIER, G. & SOLLOGOUB, C. 2017 Existence of a critical layer thickness in PS/PMMA nanolayered films. *Macromolecules* **50** (10), 4064–4073.
- BOCQUET, L. & CHARLAIX, E. 2010 Nanofluidics, from bulk to interfaces. *Chem. Soc. Rev.* **39**, 1073–1095.
- BROCHARD-WYART, F. & DE GENNES, P.-G. 1990 Molécules coulissantes à une interface polymère-polymère. *C.R. Acad. Sci.* **317**, 13–17.
- BROCHARD-WYART, F., MARTIN, P. & REDON, C. 1993 Liquid/liquid dewetting. *Langmuir* **9** (12), 3682–3690.
- BUCK, E., PETERSEN, K., HUND, M., KRAUSCH, G. & JOHANNSMANN, D. 2004 Decay kinetics of nanoscale corrugation gratings on polymer surface: evidence for polymer flow below the glass temperature. *Macromolecules* **37** (23), 8647–8652.
- CHAI, Y., SALEZ, T., MCGRAW, J., BENZAQUEN, M., DALNOKI-VERESS, K., RAPHAËL, E. & FORREST, J.A. 2014 A direct quantitative measure of surface mobility in a glassy polymer. *Science* **343** (6174), 994–999.
- CHEBIL, M.S., MCGRAW, J.D., SALEZ, T., SOLLOGOUB, C. & MIQUELARD-GARNIER, G. 2018 Influence of outer-layer finite-size effects on the dewetting dynamics of a thin polymer film embedded in an immiscible matrix. *Soft Matter* **14** (30), 6256–6263.
- ERNEUX, T. & DAVIS, S.H. 1993 Nonlinear rupture of free films. *Phys. Fluids A* **5** (5), 1117–1122.
- FAKHRAAI, Z. & FORREST, J.A. 2008 Measuring the surface dynamics of glassy polymers. *Science* **319** (5863), 600–604.
- FETZER, R., JACOBS, K., MÜNCH, A., WAGNER, B. & WITELSKI, T.P. 2005 New slip regimes and the shape of dewetting thin liquid films. *Phys. Rev. Lett.* **95** (12), 127801.
- DE GENNES, P.-G. 1989 Adhésion de polymères légèrement incompatibles. *CR Acad Sci* **308**, 1401–1403.
- DE GENNES, P.-G. & BROCHARD-WYART, F. 1990 Glissement à l'interface de deux polymères légèrement incompatibles. *C.R. Acad. Sci.* **310**, 1169–1173.
- DE GENNES, P.-G., BROCHARD-WYART, F. & QUÉRÉ, D. 2003 *Capillarity and Wetting Phenomena: Drops, Bubbles, Pearls, Waves*. Springer.
- HIRAI, Y., YOSHIKAWA, T., TAKAGI, N., YOSHIDA, S. & YAMAMOTO, K. 2003 Mechanical properties of poly-methyl methacrylate (PMMA) for nano imprint lithography. *J. Photopolym. Sci. Technol.* **16** (4), 615–620.
- HOURLIER-FARGETTE, A., ANTKOWIAK, A., CHATEAUMINOIS, A. & NEUKIRCH, S. 2017 Role of uncrosslinked chains in droplets dynamics on silicone elastomers. *Soft Matter* **13**, 3484–3491.
- HOWELL, C., *et al.* 2015 Stability of surface-immobilized lubricant interfaces under flow. *Chem. Mater.* **27** (5), 1792–1800.
- HUANG, R. & SUO, Z. 2002 Instability of a compressed elastic film on a viscous layer. *Intl J. Solids Struct.* **39** (7), 1791–1802.
- ILTON, M., COUCHMAN, M., GERBELOT, C., BENZAQUEN, M., FOWLER, P., STONE, H., RAPHAËL, E., DALNOKI-VERESS, K. & SALEZ, T. 2016 Capillary leveling of freestanding liquid nanofilms. *Phys. Rev. Lett.* **117**, 167801.
- JACHALSKI, S., MÜNCH, A. & WAGNER, B. 2015 Thin-film models for viscoelastic liquid bi-layers. WIAS Preprint 2187.

Capillary levelling of immiscible bilayer films

- JACHALSKI, S., PESCHKA, D., MÜNCH, A. & WAGNER, B. 2014 Impact of interfacial slip on the stability of liquid two-layer polymer films. *J. Engng Maths* **86** (1), 9–29.
- KARGUPTA, K., SHARMA, A. & KHANNA, R. 2004 Instability, dynamics, and morphology of thin slipping films. *Langmuir* **20** (1), 244–253.
- KEISER, A., KEISER, L., CLANET, C. & QUÉRÉ, D. 2017 Drop friction on liquid-infused materials. *Soft Matter* **13**, 6981–6987.
- KOPLIK, J. & BANAVAR, J. 2006 Slip, immiscibility, and boundary conditions at the liquid-liquid interface. *Phys. Rev. Lett.* **96**, 044505.
- LAL, J., MALKOVA, S., MUKHOPADHYAY, M.K., NARAYANAN, S., FLUERASU, A., DARLING, S.B., LURIO, L.B. & SUTTON, M. 2017 Dewetting in immiscible polymer bilayer films. *Phys. Rev. Mater.* **1** (1), 015601.
- LAMBOOY, P., PHELAN, K.C., HAUGG, O. & KRAUSCH, G. 1996 Dewetting at the liquid-liquid interface. *Phys. Rev. Lett.* **76** (7), 1110.
- LAUGA, E. & BRENNER, M.P. 2004 Dynamic mechanisms for apparent slip on hydrophobic surfaces. *Phys. Rev. E* **70**, 026311.
- LEE, P.C., PARK, H.E., MORSE, D.C. & MACOSKO, C.W. 2009 Polymer-polymer interfacial slip in multilayered films. *J. Rheol.* **53** (4), 893–915.
- MCGRAW, J., SALEZ, T., BÄUMCHEN, O., RAPHAËL, E. & DALNOKI-VERESS, K. 2012 Self-similarity and energy dissipation in stepped polymer films. *Phys. Rev. Lett.* **109**, 128303.
- MCGRAW, J.D., CHAN, T.S., MAURER, S., SALEZ, T., BENZAQUEN, M., RAPHAËL, E., BRINKMANN, M. & JACOBS, K. 2016 Slip-mediated dewetting of polymer microdroplets. *Proc. Natl Acad. Sci. USA* **113** (5), 1168.
- MCGRAW, J.D., JAGO, N. & DALNOKI-VERESS, K. 2011 Capillary levelling as a probe of thin film polymer rheology. *Soft Matter* **7**, 7832–7838.
- MCGRAW, J.D., SALEZ, T., BÄUMCHEN, O., RAPHAËL, E. & DALNOKI-VERESS, K. 2013 Capillary leveling of stepped films with inhomogeneous molecular mobility. *Soft Matter* **9**, 8297–8305.
- MERABIA, S. & BONET AVALOS, J. 2008 Dewetting of a stratified two-component liquid film on a solid substrate. *Phys. Rev. Lett.* **101**, 208304.
- MÜNCH, A., WAGNER, B.A. & WITELSKI, T.P. 2005 Lubrication models with small to large slip lengths. *J. Engng Maths* **53** (3–4), 359–383.
- ORON, A., DAVIS, S. & BANKOFF, S. 1997 Long-scale evolution of thin liquid films. *Rev. Mod. Phys.* **69** (3), 931–980.
- PEAUDECERF, F.J., LANDEL, J.R., GOLDSTEIN, R.E. & LUZZATTO-FEGIZ, P. 2017 Traces of surfactants can severely limit the drag reduction of superhydrophobic surfaces. *Proc. Natl Acad. Sci. USA* **114** (28), 7254–7259.
- PESCHKA, D., BOMMER, S., JACHALSKI, S., SEEMANN, R. & WAGNER, B. 2018 Impact of energy dissipation on interface shapes and on rates for dewetting from liquid substrates. *Sci. Rep.* **8** (1), 13295.
- POESIO, P., DAMONE, A. & MATAR, O.K. 2017 Slip at liquid-liquid interfaces. *Phys. Rev. Fluids* **2** (4), 044004.
- PONTING, M., HILTNER, A. & BAER, E. 2010 Polymer nanostructures by forced assembly: process, structure, and properties. In *Macromolecular Symposia*, vol. 294, pp. 19–32. Wiley Online Library.
- POTOTSKY, A., BESTEHORN, M., MERKT, D. & THIELE, U. 2004 Alternative pathways of dewetting for a thin liquid two-layer film. *Phys. Rev. E* **70** (2), 025201.
- RAZAVI, S., KOPLIK, J. & KRETZSCHMAR, I. 2014 Molecular dynamics simulations: insight into molecular phenomena at interfaces. *Langmuir* **30** (38), 11272–11283.
- RIVETTI, M., BERTIN, V., SALEZ, T., HUI, C.-Y., LINNE, C., ARUTKIN, M., WU, H., RAPHAËL, E. & BÄUMCHEN, O. 2017 Elastocapillary levelling of thin viscous films on soft substrates. *Phys. Rev. Fluids* **2**, 094001.
- ROGNIN, E., LANDIS, S. & DAVOUST, L. 2011 Viscosity measurements of thin polymer films from reflow of spatially modulated nanoimprinted patterns. *Phys. Rev. E* **84**, 041805.
- SALEZ, T., MCGRAW, J., BÄUMCHEN, O., DALNOKI-VERESS, K. & RAPHAËL, E. 2012a Capillary-driven flow induced by a stepped perturbation atop a viscous film. *Phys. Fluids* **24**, 102111.
- SALEZ, T., MCGRAW, J.D., CORMIER, S.L., BÄUMCHEN, O., DALNOKI-VERESS, K. & RAPHAËL, E. 2012b Numerical solutions of thin-film equations for polymer flows. *Eur. Phys. J. E* **35** (11), 114.
- SEEMANN, R., HERMINGHAUS, S. & JACOBS, K. 2001 Dewetting patterns and molecular forces: a reconciliation. *Phys. Rev. Lett.* **86** (24), 5534–5537.
- SEGALMAN, R.A. & GREEN, P.F. 1999 Dynamics of rims and the onset of spinodal dewetting at liquid/liquid interfaces. *Macromolecules* **32** (3), 801–807.

V. Bertin and others

- SHARMA, A. & VERMA, R. 2004 Pattern formation and dewetting in thin films of liquids showing complete macroscale wetting: from “pancakes” to “swiss cheese”. *Langmuir* **20**, 10337–10345.
- STILLWAGON, L.E. & LARSON, R.G. 1988 Fundamentals of topographic substrate leveling. *J. Appl. Phys.* **63** (11), 5251–5258.
- TANAKA, K., TAKAHARA, A. & KAJIYAMA, T. 1996 Film thickness dependence of the surface structure of immiscible polystyrene/poly(methyl methacrylate) blends. *Macromolecules* **29**, 3232–3239.
- TEISSEIRE, J., REVAUX, A., FORESTI, M & BARTHEL, E. 2011 Confinement and flow dynamics in thin polymer films for nanoimprint lithography. *Appl. Phys. Lett.* **98**, 013106.
- WU, S. 1970 Surface and interfacial tensions of polymer melts. II. Poly(methyl methacrylate), poly(n-butyl methacrylate) and polystyrene. *J. Phys. Chem.* **74**, 632–638.
- XU, L., BANDYOPADHYAY, D, SHI, T., AN, L., SHARMA, A. & JOO, S.W. 2011 Dewetting kinetics of thin polymer bilayers: role of under layer. *Polymer* **52**, 4345–4354.
- XU, L., ZHANG, H. & SHI, T. 2016 Liquid-liquid interfacial slip induced layer instability in a thin polymer bilayer. *Polymer* **99**, 185–192.
- YANG, Z., FUJII, Y.K., LEE, Y., LAM, C.-H. & TSUI, O.K.C. 2010 Glass transition dynamics and surface layer mobility in unentangled polystyrene films. *Science* **328**, 1676–1679.
- ZHAO, R. & MACOSKO, C. 2002 Slip at polymer–polymer interfaces: rheological measurements on coextruded multilayers. *J. Rheol.* **46**, 145–167.

Chapter 5

Symmetrization of Thin Free-Standing Liquid Films via Capillary-Driven Flow

We present here experiments that have been designed and performed by John Niven, under the supervision of Kari Dalnoki Veress in McMaster University, Canada. I developed the theoretical model used in the article after some discussions with John Niven during my stay in Canada.

In this chapter, we examine the relaxation dynamics of a cylindrical perturbations at one of the two interfaces of freestanding films. Interestingly, the films are observed to undergo a rapid symmetrization of the perturbation to become mirror symmetric. We derive a full Stokes model, revealing that the dynamics can be decomposed in two independent modes that differ by their mirror symmetry. The antisymmetric mode, that is analogous to the viscous bending mode in liquid sheets, relaxes exponentially on a time scale $h_0\eta/\gamma$, where h_0 is the average film thickness, which agrees with the experimental observations. The article reproduced here has been published in Physical Review Letters [3].

Symmetrization of Thin Freestanding Liquid Films via a Capillary-Driven Flow

Vincent Bertin,^{1,2,†} John Niven,^{3,†} Howard A. Stone,⁴ Thomas Salez^{1,5}, Elie Raphaël², and Kari Dalnoki-Veress^{2,3,*}


¹Univ. Bordeaux, CNRS, LOMA, UMR 5798, 33405 Talence, France

²UMR CNRS Gulliver 7083, ESPCI Paris, PSL Research University, 75005 Paris, France

³Department of Physics and Astronomy, McMaster University, Hamilton, Ontario L8S 4M1, Canada

⁴Department of Mechanical and Aerospace Engineering, Princeton University, Princeton, New Jersey 08544, USA

⁵Global Station for Soft Matter, Global Institution for Collaborative Research and Education, Hokkaido University, Sapporo, Hokkaido 060-0808, Japan

 (Received 16 December 2019; revised manuscript received 2 March 2020; accepted 21 April 2020; published 8 May 2020)

We present experiments to study the relaxation of a nanoscale cylindrical perturbation at one of the two interfaces of a thin viscous freestanding polymeric film. Driven by capillarity, the film flows and evolves toward equilibrium by first symmetrizing the perturbation between the two interfaces and eventually broadening the perturbation. A full-Stokes hydrodynamic model is presented, which accounts for both the vertical and lateral flows and which highlights the symmetry in the system. The symmetrization time is found to depend on the membrane thickness, surface tension, and viscosity.

DOI: [10.1103/PhysRevLett.124.184502](https://doi.org/10.1103/PhysRevLett.124.184502)

Surface tension will smoothen interfacial perturbations on a thin liquid film, since the curvature of the perturbation profile induces a Laplace pressure that drives flow. This capillary-driven leveling causes the brush strokes on paint to flatten, or the spray of small droplets to form a uniform film. Such flows have been studied in detail and much of the framework is provided by the lubrication theory (a simplified version of the Navier-Stokes equations appropriate for laminar thin-film flow), where one can assume that flow in the plane of the film dominates and that the velocity vanishes at the solid-liquid interface [1,2]. Freestanding liquid films do not support a shear-stress at *both* liquid-air interfaces, which modifies the boundary conditions and results in a different phenomenology [1]. These boundary conditions arise in biological membranes [3], soap films [4–9], liquid-crystal films [10–12], fragmentation processes [13], or energy-harvesting technologies [14].

The dynamics of liquid sheets has been studied extensively [15,16] and shows similarities with the mechanics of elastic plates. The evolution can be described with two dominant modes, which are the stretching and bending modes associated with linear momentum and torque balances. At macroscopic scales, a viscous sheet experiences bending instabilities such as wrinkling [17–20] and folding [21] when submitted to compression. Such viscous buckling phenomena occur in tectonic-plate dynamics [22,23] and industrial float-glass processes [24–27].

In thin freestanding films, surface tension is dominant and stabilizes the interfaces against buckling [15]. Most theoretical models in this context assume that the interfaces are mirror symmetric and thus focus on the stretching mode, also called the symmetric mode. This approach is

employed to study the rupture dynamics of films in the presence of disjoining forces that destabilize long waves in thin films [28–35]. Using nanometric freestanding polystyrene (PS) films, Ilton *et al.* observed that a film with initially asymmetric interfaces symmetrized over short timescales [36]. This symmetrization was attributed to flow perpendicular to the film, but the dynamics was not accessible experimentally.

Here we study the viscocapillary relaxation of a nanoscale cylindrical perturbation initially present at one interface of a thin freestanding PS film. Both the symmetric (viscous stretching) and antisymmetric (viscous bending) modes are probed with experiments (Fig. 1). Atomic force microscopy (AFM) is used to obtain the profiles of the top and bottom interfaces [Fig. 1(a)]. A full-Stokes flow linear hydrodynamic model is developed to characterize the dynamics of the two modes. To provide intuition for the energy dissipation, we turn to the schematic excess surface energy as a function of time, shown in Fig. 1(d). Initially, the top interfacial profile, denoted h_+ , has a high excess energy due to the additional interface that forms the perturbation, while the bottom interfacial profile h_- is flat and has no excess surface energy. The excess energy resulting from the perturbation drives flow that is mediated by viscosity η . As the film evolves, the total energy dissipates as the excess interface decreases. With decreasing global energy, the symmetrization process requires energy transfer from the top interface to the bottom, dominated by vertical flow. Once both interfaces are symmetric, they relax in tandem, dominated by lateral flow. Remarkably, the temporal evolution of the interfacial profiles, when appropriately decomposed into their symmetric and antisymmetric components, obey power laws.

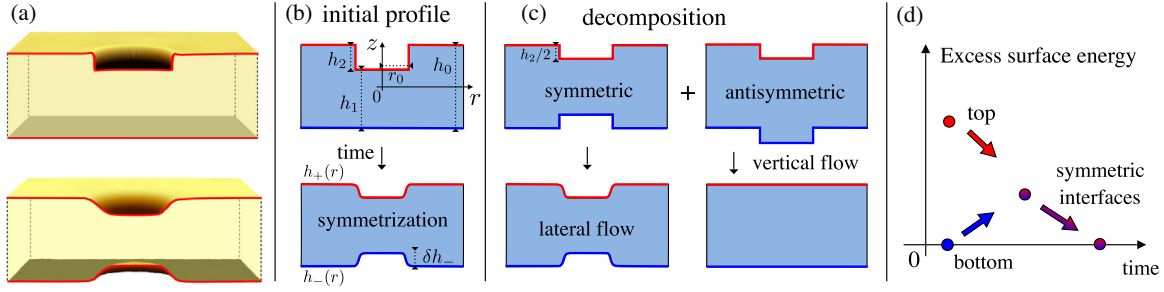


FIG. 1. (a) AFM images of sample with surface perturbation with initial radius $r_0 \approx 6.2 \mu\text{m}$ and depth $h_2 \approx 80 \text{ nm}$ (top) and after 500 min of annealing (bottom). (b) Schematic of an initial cylindrical hole of depth h_2 and radius r_0 , on one side of a polystyrene freestanding film, which evolves toward symmetric. (c) Symmetric-asymmetric decomposition of the interfacial profiles. A symmetric profile leads to lateral flow, while an antisymmetric one leads to vertical flow. (d) Schematic of the evolution of the excess surface energy. The top and bottom surface energies equalize before vanishing in tandem on larger timescales.

We construct freestanding films with a nanometric perturbation by stacking a film with small cylindrical pores on a second thicker film that is intact, following a method similar to that previously described [36,37]. This process results in a film with a cylindrical hole at one interface. PS with molecular weight $M_w = 183 \text{ kg/mol}$ (Polymer Source, polydispersity index = 1.06) is dissolved in toluene (Fisher Scientific, Optima) with concentrations of 2% and 7.5% by weight. Films are prepared by spin coating from solution onto freshly cleaved mica (Ted Pella) and annealed at 130°C in vacuum ($1 \times 10^{-5} \text{ mbar}$) for 24 h. The films have thicknesses $h_1 = 530$ and $h_2 = 80 \text{ nm}$, as measured using ellipsometry (Accurion, EP3). The freestanding films are prepared in a two-step process inspired by Backholm *et al.* [37]. Films are floated from mica substrates onto the surface of ultrapure water ($18.2 \text{ M}\Omega \text{ cm}$) and picked up on a thin circular steel washer (thickness = 0.1 mm, AccuGroup), creating a freestanding film supported only at the edges of the washer. The thicker film, with $h_1 = 530 \text{ nm}$, is picked up on a washer with an internal diameter of 3 mm and briefly heated above the glass-transition temperature $T_g \approx 100^\circ\text{C}$ on a hot stage (Linkam, UK), resulting in a smooth, taught film. Similarly, the thinner film with $h_2 = 80 \text{ nm}$ is transferred from the water to a washer with an internal diameter of 5 mm. This film is heated ($100^\circ\text{C}/\text{min}$) to 125°C under a microscope for several seconds and holes are nucleated on small defects in the film, which grow with time [34,38–40]. When the holes become visible, the film is quenched to room temperature, resulting in a freestanding film with randomly distributed holes of diameter 1–10 μm . The two films are then placed in contact and adhere through van der Waals forces, and the larger diameter washer can be removed. This process results in a freestanding film of thickness $h_0 = h_1 + h_2$, with cylindrical holes of depth h_2 [Figs. 1(a) and (b)].

The films are annealed on the hot stage at $T = 130^\circ\text{C}$ and covered with a coverslip to ensure a uniform temperature with $\eta \approx 1.1 \times 10^8 \text{ Pa s}$ and surface tension $\gamma \approx 30 \text{ mJ/m}^2$ [41]. After some annealing time, the film is

quenched to room temperature, thus returning to the glassy state where flow becomes arrested. The surface profiles of three holes in the same film are then measured after each annealing step using AFM (Bruker, Multimode). Since the film is freestanding and has two polymer-air interfaces, both the top and bottom profiles are measured. The angular-averaged profiles are extracted at each time and provide a cross section of the film as it evolves (Fig. 2).

Initially, the film has different curvature gradients at the top and bottom interfaces, resulting in pressure gradients in vertical and lateral directions. The initial response of the film in the vicinity of the hole is for the bottom interface to buckle downward, forming a small ($\sim 10 \text{ nm}$) elastic bump. This feature is not a result of a viscoelastic response to interfacial forces [42], as this would generate an opposite displacement. We speculate that this feature is the result of residual stresses associated with sample preparation: it is known that during hole formation the shear-strain rate near the rim of the hole perturbs polymer chains from equilibrium [39,40]. Upon adhering the two films, the nonequilibrium chains in the rim can impart a tension along the rim

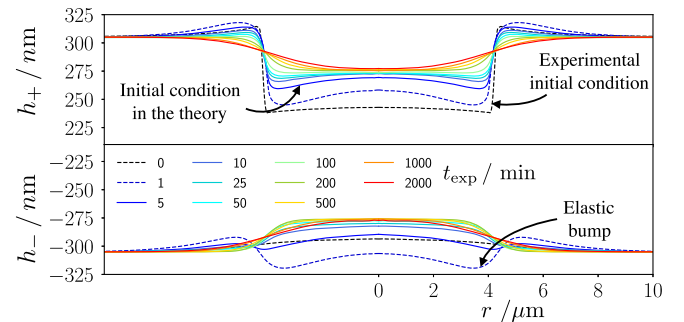


FIG. 2. AFM profiles of the top and bottom interfaces of a freestanding hole with $h_2 = 80 \text{ nm}$, $h_0 = 610 \text{ nm}$, and $r_0 = 4.2 \mu\text{m}$ (Fig. 1), at various annealing times t_{exp} as indicated. An “elastic bump” is seen at $t_{\text{exp}} = 1 \text{ min}$ due to the residual stresses in the film from the sample preparation. The viscous model takes the profiles at 5 min as initial profiles, in order to ignore any prior elastic effect.

acting to compress and buckle the sample. As the film is annealed, the elastic bump relaxes on a timescale ~ 5 min, which is similar to the macromolecular relaxation time for PS (the reptation time at $T = 130^\circ\text{C}$ is ~ 13 min [43]).

After relaxation of the bump, the flow depends on capillarity and viscosity. First, there is vertical flow to equilibrate the Laplace pressures and symmetrize the top and bottom interfaces. Indeed, two symmetric interfacial profiles are observed at times larger than ~ 200 min. Subsequently, the symmetric interfaces evolve in tandem through lateral flow and dissipate the excess surface energy [30]. The film is annealed for ~ 2000 min before rupturing.

We now turn to a theoretical description. The polymer is assumed to be a Newtonian fluid with viscosity η . We introduce cylindrical coordinates (r, z) , as well as the Hankel transforms [44] of the velocity field $\tilde{u}(r, z, t) = (u_r, u_z)$ and of the interfacial profiles $h_\pm(r, t)$: $\tilde{u}_r(k, z, t) = \int_0^\infty dr r u_r(r, z, t) J_1(kr)$, $\tilde{u}_z(k, z, t) = \int_0^\infty dr r u_z(r, z, t) J_0(kr)$, and $\tilde{h}_\pm(k, t) = \int_0^\infty dr r h_\pm(r, t) J_0(kr)$, where t is time, and the J_i are the Bessel functions of the first kind with indices $i = 0, 1$. Injecting these into the steady Stokes equations, we find $\partial_z^3 \tilde{u}_r + k \partial_z^2 \tilde{u}_z - k^2 \partial_z \tilde{u}_r - k^3 \tilde{u}_z = 0$ and $\partial_z \tilde{u}_z + k \tilde{u}_r = 0$, which gives

$$\tilde{u}_r = -\frac{1}{k}(kA + kzC + D) \sinh(kz) - \frac{1}{k}(kB + kzD + C) \cosh(kz), \quad (1a)$$

$$\tilde{u}_z = (A + zC) \cosh(kz) + (B + zD) \sinh(kz), \quad (1b)$$

where $A(t)$, $B(t)$, $C(t)$, and $D(t)$ are integration constants. The depth of the hole is assumed to be small in comparison with the thickness of the film, which is valid for the experiments, and we linearize the problem by writing the profiles as $h_\pm = \pm h_0/2 + \delta h_\pm$, where the perturbations δh_\pm are small compared to the film thickness h_0 . We assume no-shear-stress boundary conditions at both fluid-air interfaces and neglect nonlinearities from the scalar projections of the normal and tangential vectors to the interface, which gives

$$\left(\pm kA + C \frac{kh_0}{2} \right) \sinh\left(\frac{kh_0}{2}\right) + \left(kB \pm D \frac{kh_0}{2} \right) \cosh\left(\frac{kh_0}{2}\right) = \pm \frac{\gamma k^2}{2\eta} \delta \tilde{h}_\pm, \quad (2a)$$

$$\left(kA \pm C \frac{kh_0}{2} + D \right) \cosh\left(\frac{kh_0}{2}\right) + \left(\pm kB + D \frac{kh_0}{2} \pm C \right) \sinh\left(\frac{kh_0}{2}\right) = 0. \quad (2b)$$

Finally, we invoke the linearized kinematic conditions $\partial_t \tilde{h}_\pm = \tilde{u}_z(k, z = \pm h_0/2, t)$ and obtain a set of coupled linear differential equations. The symmetric-antisymmetric

decomposition, through $\tilde{h}_{\text{sym}} = \delta \tilde{h}_+ - \delta \tilde{h}_-$ and $\tilde{h}_{\text{anti}} = \delta \tilde{h}_+ + \delta \tilde{h}_-$ [see Fig. 1(c)], appears as the natural modal decomposition for this system. These two modes relax independently to equilibrium, with distinct decay rates λ_{sym} and λ_{anti} , since

$$\partial_t \tilde{h}_{\text{sym}} = -\frac{\gamma k}{\eta} \frac{\sinh^2(\frac{kh_0}{2})}{\sinh(kh_0) + kh_0} \tilde{h}_{\text{sym}} = -\lambda_{\text{sym}} \tilde{h}_{\text{sym}}, \quad (3a)$$

$$\partial_t \tilde{h}_{\text{anti}} = -\frac{\gamma k}{\eta} \frac{\cosh^2(\frac{kh_0}{2})}{\sinh(kh_0) - kh_0} \tilde{h}_{\text{anti}} = -\lambda_{\text{anti}} \tilde{h}_{\text{anti}}. \quad (3b)$$

The dimensionless decay rates are plotted in Fig. 3 as a function of the dimensionless wave number kh_0 . For each rate, two asymptotic behaviors can be distinguished. At large kh_0 , both rates exhibit the same asymptotic behavior: $\lambda(k) \sim \gamma k/\eta$. At small kh_0 , the symmetric rate becomes identical to the one in the symmetric long-wave freestanding film model: $\lambda_{\text{sym}} \sim \gamma h_0 k^2/(8\eta)$ [30,36], and thus Eq. (3) reduces to a heatlike equation in Hankel space, with a diffusion coefficient $\gamma h_0/(8\eta)$. In the same limit, the antisymmetric rate has a different scaling law: $\lambda_{\text{anti}} \sim 6\gamma/(\eta h_0^3 k^2)$. Therefore, long waves are quickly damped for the antisymmetric mode. We note that λ_{anti} has a minimum at $k \simeq 3.28/h_0$, corresponding to a slowest mode, which sets the relaxation dynamics.

The model assumes a Newtonian fluid and must be compared to experimental profiles corresponding to annealing times longer than the polymeric relaxation time. Thus, we take the experimental profiles at $t_{\text{exp}} = 5$ min as the initial conditions for the model (Fig. 2). Equations (3a) and (3b) are solved, yielding

$$\tilde{h}_{\text{sym/anti}}(k, t) = \tilde{h}_{\text{sym/anti}}(k, 0) \exp[-\lambda_{\text{sym/anti}}(k)t], \quad (4)$$

where $t = t_{\text{exp}} - 5$ min. The symmetric and antisymmetric modes are shown in Fig. 4 and reveal a qualitative

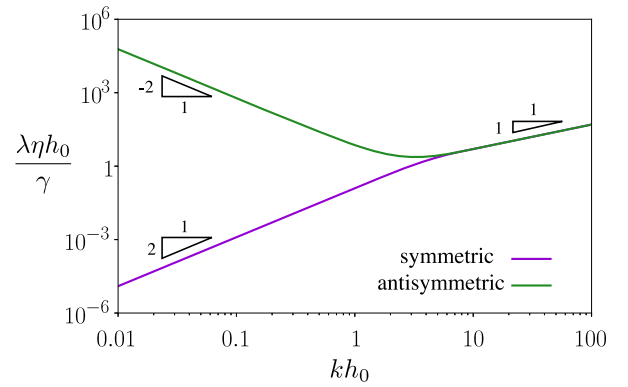


FIG. 3. Dimensionless decay rates of the symmetric and antisymmetric modes [Eqs. (3a) and (3b)] as a function of the dimensionless wave number. The slope triangles indicate power-law exponents.

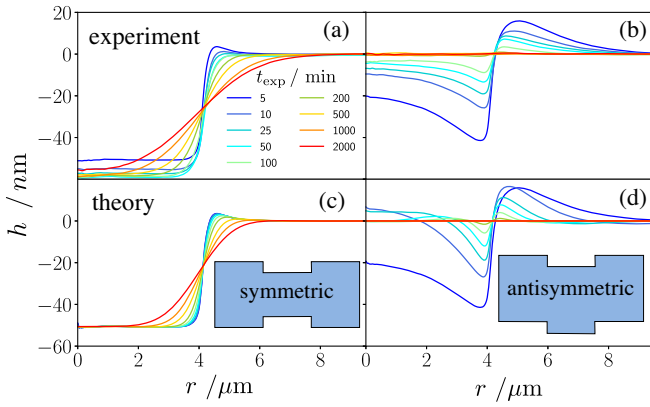


FIG. 4. (a) Symmetric and (b) antisymmetric modes of the experimental (angular-averaged) profiles for various times. The colors correspond to the same times as in Fig. 2. (c) Symmetric and (d) antisymmetric modes of the theoretical profiles, according to Eq. (4), for various times, and with the experimental profiles at $t_{\text{exp}} = 5$ min as the initial conditions ($t = 0$).

agreement between theory and experiment. Notably, the symmetric mode exhibits a self-similar behavior when plotted (not shown) as a function of the variable $(r - r_0)/t^{1/2}$. This result for freestanding films is to be compared to the capillary leveling of a cylindrical hole in a film supported on a substrate, which is self-similar in $(r - r_0)/t^{1/4}$ [37]. In contrast, the antisymmetric mode vanishes, on a timescale on the order of ~ 200 min, resulting in top and bottom interfacial profiles that are mirror symmetric, as observed in Fig. 2. The long waves are damped more quickly than the short ones, in agreement with the limiting scaling behaviors of $\lambda_{\text{anti}}(k)$ (Fig. 3).

A measure of proximity to equilibrium lies in the excess capillary energy, which is proportional to the excess surface area S with respect to a flat film $S_i = 2\pi \int_0^\infty dr r (\sqrt{1 + (\partial_r h_i)^2} - 1)$, where i can refer to +, -, sym, or anti, depending on the profile or mode in question. In the small-slope limit (valid at $t_{\text{exp}} > 5$ min), $S_i \approx \pi \int_0^\infty dr r (\partial_r h_i)^2$. Figure 5(a) shows the excess surface areas of the top and bottom, normalized by the initial value, as a function of dimensionless time $\gamma t / (h_0 \eta)$ for three holes of different initial radii, $r_0 = 2.3, 4.2,$ and $6.2 \mu\text{m}$ on the same film. The trends are consistent with the intuition provided by Fig. 1(d), and the theoretical curves are in excellent agreement with the experimental data, which validates the hydrodynamic model. We further see that the top interface, which has an initially high excess surface area, exchanges energy with the bottom one, causing the excess surface area of the latter to initially increase. This happens through vertical flow, a process that continues until the top and bottom interfaces are mirror symmetric at $\gamma t / (h_0 \eta) \sim 0.5$, after which the excess surface areas of both interfaces are equal. At later times, the surface areas decrease as $S \propto t^{-1/2}$ because of the self-similar

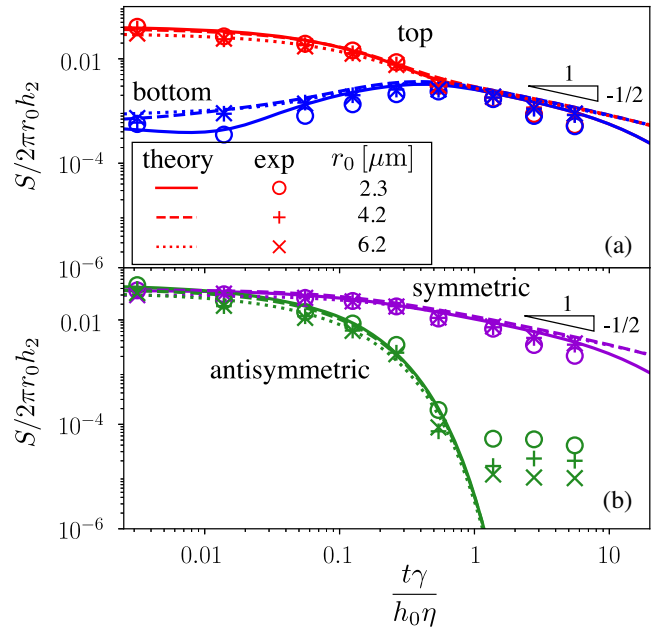


FIG. 5. Dimensionless excess surface area as a function of dimensionless time. The experimental data for three different holes are shown with different marker symbols, as indicated. The corresponding theoretical data are shown with different line styles, as indicated (fit parameter $\gamma/\eta \approx 4.6 \times 10^{-5} \mu\text{m/s}$ [45]). (a) The top and bottom interfacial profiles. (b) The symmetric and antisymmetric modes. The slope triangles indicate power-law exponents.

properties of the heatlike equation that governs the symmetric mode.

One can define and plot the symmetric and antisymmetric surface areas S_{sym} and S_{anti} as functions of the dimensionless time [Fig. 5(b)]. The symmetric mode exhibits a long term $S_{\text{sym}} \propto t^{-1/2}$ scaling, as a result of lateral flow. In contrast, the vertical flow in the antisymmetric mode dissipates energy more quickly, with a timescale $\sim \eta h_0 / \gamma$ corresponding to the symmetrization time. The experiments reveal that this symmetrization time does not depend on the initial radius of the hole and is set by the dynamics of the slowest relaxation mode, i.e., the Fourier-Bessel mode k at which $\lambda_{\text{anti}}(k)$ is minimal (Fig. 3) (the data at long times for the antisymmetric mode deviate from theory because of limitations in measuring a vanishing excess surface area).

We note that the governing equation of the antisymmetric mode is $\frac{1}{6} \eta h_0^3 \partial_t \nabla^2 h_{\text{anti}} = \gamma h_{\text{anti}}$ in the long-wave limit. Upon taking the Laplacian of this expression, we recover on the right-hand side the Laplace pressure $\delta P = \gamma \nabla^2 h_{\text{anti}}$ across the film. Then, the midplane line $H = h_{\text{anti}}/2$ follows the equation $\frac{1}{3} \eta h_0^3 \nabla^4 \partial_t H = \delta P$. This equation corresponds to the torque balance in the liquid film [15,26,27] and is the viscous analog of the Föppl-von Kármán equation for an elastic membrane in pure bending, where the bending modulus is replaced by $\eta h_0^3/3$

and the deflection field is replaced by the deflection rate $\partial_t H$.

In conclusion, we have reported on the symmetrization dynamics of cylindrical holes in freestanding polymer films. The topographies of both interfaces of the films were measured using AFM at various times, to track the evolution while they were annealed above the glass-transition temperature. The films were found to undergo a rapid symmetrization process in order to equilibrate the Laplace pressures of the two liquid-air interfaces. This process transfers excess surface energy between the two interfaces and eventually results in mirror-symmetric profiles on both sides of the film. A full-Stokes flow linear hydrodynamic model was developed and shown to be consistent with the observations. The model revealed the important roles of two modes, which differ by their symmetry with respect to the midplane of the film. The antisymmetric mode is associated with vertical flow, driven by the pressure gradient across the film, and exhibits faster dynamics than the symmetric mode, associated with lateral flow. The vertical symmetrization was found to occur on a universal timescale $\eta h_0/\gamma$, while the symmetric mode dominates at later times. Surprisingly, the evolutions of the interfacial profiles, when decomposed into the symmetric and antisymmetric components, are found to obey power laws, with the decrease in surface area of the symmetric mode scaling as $t^{-1/2}$, analogous to the heat equation.

We gratefully acknowledge financial support by the Natural Science and Engineering Research Council of Canada. We thank Hendrik Meyer for valuable discussions and Paul Fowler for help with preliminary experiments.

* dalnoki@mcmaster.ca

† V. B. and J. N. contributed equally.

- [1] A. Oron, S. H. Davis, and S. G. Bankoff, *Rev. Mod. Phys.* **69**, 931 (1997).
- [2] R. V. Craster and O. K. Matar, *Rev. Mod. Phys.* **81**, 1131 (2009).
- [3] M. Tanaka and E. Sackmann, *Nature (London)* **437**, 656 (2005).
- [4] Y. Couder, J. Chomaz, and M. Rabaud, *Physica (Amsterdam)* **37D**, 384 (1989).
- [5] M. A. Rutgers, X. Wu, R. Bhagavatula, A. A. Petersen, and W. Goldburg, *Phys. Fluids* **8**, 2847 (1996).
- [6] A. Aradian, E. Raphaël, and P.-G. de Gennes, *Europhys. Lett.* **55**, 834 (2001).
- [7] D. Georgiev and P. Vorobieff, *Rev. Sci. Instrum.* **73**, 1177 (2002).
- [8] M.-J. Huang, C.-Y. Wen, I.-C. Lee, and C.-H. Tsai, *Phys. Fluids* **16**, 3975 (2004).
- [9] J. Seiwert, M. Monloubou, B. Dollet, and I. Cantat, *Phys. Rev. Lett.* **111**, 094501 (2013).
- [10] R. Stannarius, C. Bohley, and A. Eremin, *Phys. Rev. Lett.* **97**, 097802 (2006).
- [11] K. Harth, A. Eremin, and R. Stannarius, *Soft Matter* **7**, 2858 (2011).
- [12] A. Eremin, S. Baumgarten, K. Harth, R. Stannarius, Z. H. Nguyen, A. Goldfain, C. S. Park, J. E. MacLennan, M. A. Glaser, and N. A. Clark, *Phys. Rev. Lett.* **107**, 268301 (2011).
- [13] E. Villermaux, *Annu. Rev. Fluid Mech.* **39**, 419 (2007).
- [14] J. Nie, Z. Wang, Z. Ren, S. Li, X. Chen, and Z. L. Wang, *Nat. Commun.* **10**, 2264 (2019).
- [15] P. D. Howell, *Eur. J. Appl. Math.* **7**, 321 (1996).
- [16] N. M. Ribe, *J. Fluid Mech.* **457**, 255 (2002).
- [17] G. I. Taylor, in *Applied Mechanics* (Springer, New York, 1969), pp. 382–388.
- [18] G. Debrégeas, P.-G. de Gennes, and F. Brochard-Wyart, *Science* **279**, 1704 (1998).
- [19] R. da Silveira, S. Chaïeb, and L. Mahadevan, *Science* **287**, 1468 (2000).
- [20] A. Boudaoud and S. Chaïeb, *Phys. Rev. E* **64**, 050601(R) (2001).
- [21] N. M. Ribe, *Phys. Rev. E* **68**, 036305 (2003).
- [22] M. A. Biot, *Geol. Soc. Am. Bull.* **72**, 1595 (1961).
- [23] L. Guillou-Frottier, J. Buttles, and P. Olson, *Earth Planet. Sci. Lett.* **133**, 19 (1995).
- [24] J. R. Pearson, *Mechanics of Polymer Processing* (Springer, New York, 1985).
- [25] B. Scheid, S. Quiligotti, B. Tran, R. Gy, and H. A. Stone, *J. Fluid Mech.* **636**, 155 (2009).
- [26] G. Pfingsttag, B. Audoly, and A. Boudaoud, *J. Fluid Mech.* **683**, 112 (2011).
- [27] S. Srinivasan, Z. Wei, and L. Mahadevan, *Phys. Rev. Fluids* **2**, 074103 (2017).
- [28] E. Ruckenstein and R. K. Jain, *J. Chem. Soc., Faraday Trans. 2* **70**, 132 (1974).
- [29] M. Prévost and D. Gallez, *J. Chem. Phys.* **84**, 4043 (1986).
- [30] T. Erneux and S. H. Davis, *Phys. Fluid A* **5**, 1117 (1993).
- [31] D. Vaynblat, J. R. Lister, and T. P. Witelski, *Phys. Fluids* **13**, 1130 (2001).
- [32] O. K. Matar, *Phys. Fluids* **14**, 4216 (2002).
- [33] S. S. Thete, C. Anthony, P. Doshi, M. T. Harris, and O. A. Basaran, *Phys. Fluids* **28**, 092101 (2016).
- [34] M. Ilton, C. DiMaria, and K. Dalnoki-Veress, *Phys. Rev. Lett.* **117**, 257801 (2016).
- [35] A. Choudhury, V. K. Paidi, S. K. Kalpathy, and H. N. Dixit, *arXiv:1902.11018*.
- [36] M. Ilton, M. M. P. Couchman, C. Gerbelot, M. Benzaquen, P. D. Fowler, H. A. Stone, E. Raphaël, K. Dalnoki-Veress, and T. Salez, *Phys. Rev. Lett.* **117**, 167801 (2016).
- [37] M. Backholm, M. Benzaquen, T. Salez, E. Raphaël, and K. Dalnoki-Veress, *Soft Matter* **10**, 2550 (2014).
- [38] G. Debrégeas, P. Martin, and F. Brochard-Wyart, *Phys. Rev. Lett.* **75**, 3886 (1995).
- [39] K. Dalnoki-Veress, B. G. Nickel, C. Roth, and J. R. Dutcher, *Phys. Rev. E* **59**, 2153 (1999).
- [40] C. B. Roth and J. R. Dutcher, *J. Polym. Sci. B* **44**, 3011 (2006).
- [41] J. D. McGraw, T. Salez, O. Bäümchen, E. Raphaël, and K. Dalnoki-Veress, *Soft Matter* **9**, 8297 (2013).
- [42] M. Benzaquen, T. Salez, and E. Raphaël, *Europhys. Lett.* **106**, 36003 (2014).

- [43] A. Bach, K. Almdal, H. K. Rasmussed, and O. Hassager, *Macromolecules* **36**, 5174 (2003).
- [44] J.D. Gaskill, *Linear Systems, Fourier Transforms, and Optics* (Wiley, New York, 1978), Vol. 576.
- [45] The fit value of $\gamma/\eta \approx 4.6 \times 10^{-5} \mu\text{m/s}$ differs from experimental $\gamma/\eta \approx 2.8 \times 10^{-4} \mu\text{m/s}$. This is within experimental error given strong dependence of viscosities on temperature.

Part III

Dispersion

Chapter 6

Taylor-Aris dispersion

6.1 Introduction

6.1.1 Context: transport of microscopic particles

Diffusion and Brownian motion

The concept of diffusion has been first introduced in physics, by the French physicist and mathematician Joseph Fourier in 1822 to explain heat transfer, where he postulated that the heat flux is proportional to the temperature gradient, the proportionality factor being the heat conductivity [230]. In this way, he discovered the diffusion (or heat) equation. A few decades later, by analogy with the work of Fourier on heat, Albert Fick established in 1855 the diffusion law for particles, where the flux of particles \mathbf{j} is assumed to be proportional to the gradient of the concentration, *i.e.* $\mathbf{j} = -D_0 \nabla c$, where c denotes the concentration field and D_0 the so-called diffusion constant [231]. Injecting the flux in the conservation equation $\frac{\partial c}{\partial t} = -\nabla \cdot \mathbf{j}$, we can derive the diffusion equation:

$$\frac{\partial c}{\partial t} = D_0 \nabla^2 c. \quad (6.1)$$

Interestingly, diffusion tends to homogenize the considered spatial distribution whatever the perturbation in the concentration field is, as the flux points toward the region of low density. Furthermore, we point out that the Navier-Stokes equations, describing the transport of a fluid, is also a type of diffusion equation for linear momentum, where diffusion comes from the viscosity. As far as the dynamics is concerned, a common and specific feature of diffusive processes is that spatial perturbations propagate in a non-linear fashion with time. More specifically, if we imagine an initial and point-like perturbation, that can be a concentration source (*e.g.* ink droplet in a glass of water), the latter will propagate on a distance r following the diffusive law $r = \sqrt{2Dt}$ ¹. This holds

¹More specifically, one can show that the solution of this problem is the Green's function of the diffusion equation, which reads $c(\mathbf{r}) = 1/(4\pi Dt)^{3/2} \exp(-r^2/(4Dt))$ that exhibits self-similarity in the variable $r/\sqrt{2Dt}$.

at the macroscopic level, looking at fields in space, coarse-graining the microscopic dynamics.

Brownian motion describes the random motion of a particle in a fluid (liquid or gas). This motion results from the collisions between the molecules of the fluid and the particle itself. It was first observed under a microscope by the Scottish botanist Robert Brown in 1827, revealing the endless and random motion of pollen grains at the surface of water. The link between the Brownian dynamics at the microscopic level and diffusion at the macroscopic level has been suggested much later, in the early twentieth century, by the physicists Albert Einstein, Marian Smoluchowski and Paul Langevin [232, 233, 234]. They showed that the probability density function of the position of a Brownian particle indeed follows the diffusion equation. The nature of the collisions between the fluid molecules and a particle is isotropic, unpredictable, and it is modeled by a force acting to the particle that has random direction and magnitude. In response to this force, the particle experiences a random motion. To give a brief flavor of the link between Brownian motion and diffusion, let us consider a simple example which consists in a random walker in one dimension, *e.g.* on a line. At each time step i , it performs a spatial step of length ℓ_i , that is either in the $+$ or $-$ direction. After N time steps, the walker has been displaced by $\Delta X_N = \sum_{i=1}^N \ell_i$, where ℓ_i is a random variable that can take two values $\pm\ell$ with equal probabilities. On average, the displacement of the walker is zero: $\langle \Delta X_N \rangle = \langle \sum_{i=1}^N \ell_i \rangle = \sum_{i=1}^N \langle \ell_i \rangle = 0$. However, after N time steps, the so-called mean square displacement is given by $\langle \Delta X_N^2 \rangle = \langle (\sum_{i=1}^N \ell_i)^2 \rangle = \sum_{i=1}^N \langle \ell_i^2 \rangle + 2 \sum_{i \neq j} \underbrace{\langle \ell_i \ell_j \rangle}_0 = \sum_{i=1}^N \ell^2 = N\ell^2$, where the cross term $\langle \ell_i \ell_j \rangle$ vanishes because

the steps are uncorrelated. As the number of steps N is proportional to time t , we recover with this example a propagation of the form $r^2 \sim D_0 t$, r^2 being the the mean square displacement, which is characteristic of diffusive processes.

Advection

Diffusive processes are included in the wider class of transport phenomena, that concern the spatial exchange of quantities such as mass, energy, momentum, etc... The motion of fluids is another major source of transport. One example is thermal convection, which consists in the transport of energy by a fluid flow and that is ubiquitous in geophysical systems (*e.g.* mantle, ocean, atmosphere, etc...) among others. In the same way, the concentration fields tends to follow the streamlines of the flow, resulting in a flux $\mathbf{j} = c\mathbf{v}$. Injecting the latter in the conservation law, we find the advection law:

$$\frac{\partial c}{\partial t} = -\nabla \cdot (c\mathbf{v}). \quad (6.2)$$

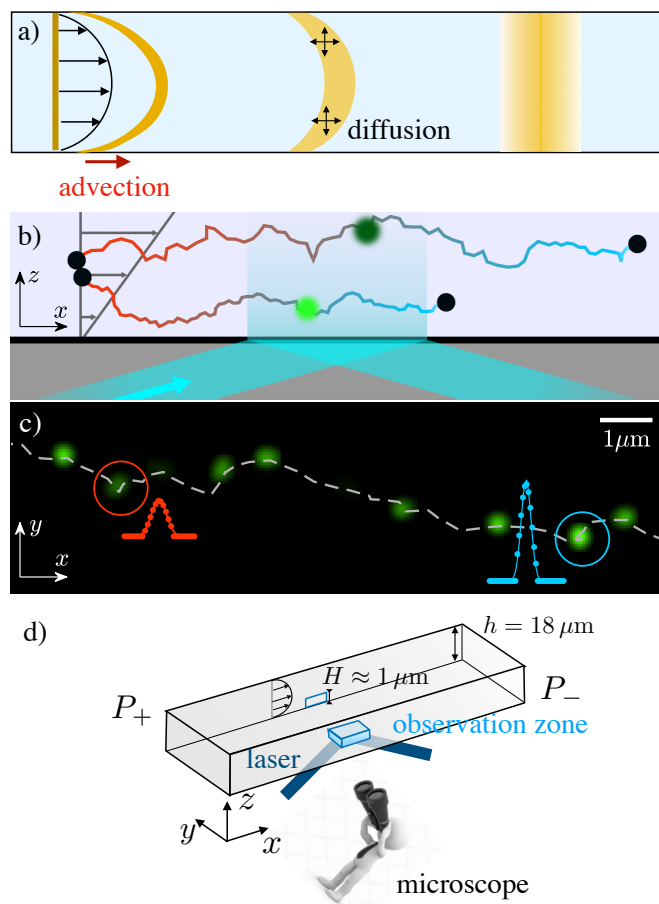


Figure 6.1: a) Schematic of the Taylor-dispersion in a channel. It may represent either a two-dimensional channel (*i.e.* in microfluidics) or the cross-section of a cylindrical tube. A solute is initially dispersed uniformly on a band and both is advected by a parabolic flow while diffusing too. b) Schematic of two Brownian colloids transported by a near-surface shear flow in a microchannel illuminated by an evanescent wave. c) Superposition of experimental images with lag time $\tau = 12.5$ ms, showing successive positions of a fluorescent 55 nm-radius nanoparticle. Two intensity profiles are shown (arbitrary units) with the red and blue dots fitted by Gaussian profiles. The dashed grey line is a guide to the eye. d) Schematic of the microfluidic channel used in the experiment in section 6.2, highlighting the geometry and scales. P_+ (resp. P_-) are the pressure at the entrance (resp. exit) of the channel, $\Delta P = P_+ - P_-$ being the pressure drop.

6.1.2 Advection-diffusion coupling: Taylor-Aris dispersion

Diffusion in a shear flow

Most hydrodynamic theories assume a no-slip condition at solid-liquid interfaces, as already encountered in the manuscript. Mathematically, this means that the fluid has a zero velocity relative to the solid because of the friction associated with the interactions between fluid and solid particles. As a result, hydrodynamic flows typically exhibit spatially varying velocity profiles. As an example, the flow in a rectangular channel takes the form of a parabolic profile, as depicted in Fig. 6.1a), which is a solution of the Stokes equations called *Poiseuille flow*.

The transport of microscopic particles can be induced by both the advection of the flow and molecular diffusion. Interestingly, in a closed environment, *e.g.* in a channel, diffusion and advection result in a non-linear coupling that enhances the dispersion. This coupling is the main topic of the present chapter. The associated phenomenon is usually called *Taylor-Aris dispersion* or *Taylor dispersion*. We briefly explain the underlying mechanism using hand-waving arguments. Let us imagine that a certain amount of solute, colored in yellow in Fig. 6.1a), is dispersed uniformly in a band across the channel height at the initial time. In the absence of diffusion, the band of solute would have been stretched by the flow, in an increasingly deep paraboloid shape. Alternatively, in the absence of flow, the band of solute would have spread, following the diffusive law. Here, diffusion acting to homogenize the solute concentration, it induces transverse transports of the solute across the channel, thus enhancing the spreading of the solute along the flow.

One other way of explaining Taylor Aris dispersion can be at the molecular level, as depicted in Fig. 6.1b). Let us imagine two particles, leaving at the same instant from the same position. The particles are advected in a linear shear flow and experience Brownian motion. The two particles experience their own trajectories in the perpendicular direction to the flow, such that even if they have started at the same position, they may not have spent the same amount of time in the high-velocity region of the channel. Therefore, they may not have been transported by the flow over the same distance, resulting in a shear-induced dispersion. Brownian motions in the streamwise direction is not necessary to observe this enhancement. The minimal ingredients to observe Taylor-Aris dispersion are: i) a shear flow and ii) transverse diffusion along the velocity gradients.

G.I. Taylor's theory: long-time dispersion in a tube

Quantitatively, the enhancement of dispersion in a shear flow was first described by G.I. Taylor in 1953 [235]. We summarize here his original derivation that can be found in many textbooks on fluid dynamics and transport phenomena [236, 237]. Taylor's theory considers a cylindrical tube of radius a , where a Poiseuille velocity profile is established:

$$u(r) = 2u_0 \left(1 - \frac{r^2}{a^2} \right), \quad (6.3)$$

along the main axis of the tube (denoted x), where u_0 denotes the mean velocity, r being the radial coordinate. We assume that a given solute is initially dispersed at a given position of the tube $x = 0$, and is described by its concentration field $c(r, x, t)$. For simplicity, the initial concentration is assumed to be uniform across the channel (see Fig. 6.1a), such that the solute concentration is axisymmetric at all times. The solute diffuses and is advected by the flow, and thus follows the advection-diffusion equation, obtained by combining Eqs. (6.1) and (6.2), as:

$$\frac{\partial c}{\partial t} + u(r) \frac{\partial c}{\partial x} = D_0 \left(\frac{1}{r} \frac{\partial}{\partial r} \left[r \frac{\partial c}{\partial r} \right] + \frac{\partial^2 c}{\partial x^2} \right), \quad (6.4)$$

with no flux at the boundary, *i.e.* $\frac{\partial c}{\partial r}(r = a, x, t) = 0$. We introduce the cross-sectional average operator of a radial function f , defined as $\langle f \rangle_S = \frac{1}{\pi a^2} \int_0^a f(r) 2\pi r dr$, and we decompose the concentration field as a sum of the average concentration and its deviation \tilde{c} , *i.e.* $c(r, x, t) = \langle c \rangle_S(x, t) + \tilde{c}(r, x, t)$, such that the advection-diffusion equation becomes:

$$\frac{\partial \langle c \rangle_S}{\partial t} + \frac{\partial \tilde{c}}{\partial t} + u(r) \frac{\partial \langle c \rangle_S}{\partial x} + u(r) \frac{\partial \tilde{c}}{\partial x} = D_0 \left(\frac{1}{r} \frac{\partial}{\partial r} \left[r \frac{\partial \tilde{c}}{\partial r} \right] + \frac{\partial^2 \langle c \rangle_S}{\partial x^2} + \frac{\partial^2 \tilde{c}}{\partial x^2} \right). \quad (6.5)$$

Taking the cross-sectional averaging of the latter and using the no-flux boundary condition, we find:

$$\frac{\partial \langle c \rangle_S}{\partial t} + u_0 \frac{\partial \langle c \rangle_S}{\partial x} + \left\langle u(r) \frac{\partial \tilde{c}}{\partial x} \right\rangle_S = D_0 \frac{\partial^2 \langle c \rangle_S}{\partial x^2}. \quad (6.6)$$

Taylor theory focuses on the long-time transport of the average concentration field, that is characterized by $\langle c \rangle_S$. However, Eq. (6.6) is not written in a closed form as it depends on the deviation \tilde{c} via the term $\left\langle u(r) \frac{\partial \tilde{c}}{\partial x} \right\rangle_S$. The challenge is to estimate the latter, which requires some assumptions. First, by subtracting Eq. (6.6) from Eq. (6.5), we get:

$$\frac{\partial \tilde{c}}{\partial t} + \left(u(r) - u_0 \right) \frac{\partial \langle c \rangle_S}{\partial x} + \left(u(r) \frac{\partial \tilde{c}}{\partial x} - \left\langle u(r) \frac{\partial \tilde{c}}{\partial x} \right\rangle_S \right) = D_0 \left(\frac{1}{r} \frac{\partial}{\partial r} \left[r \frac{\partial \tilde{c}}{\partial r} \right] + \frac{\partial^2 \tilde{c}}{\partial x^2} \right). \quad (6.7)$$

We consider the limit of long times with respect to the typical diffusion time of a solute particle across the channel which scales as a^2/D_0 . On such time scales, solute particles have explored all radii of the tube, such that the initial paraboloid concentration front generated by advection (see Fig. 6.1a) has diffused transversely and became homogeneous. We thus expect the deviation to be small with respect to the average concentration, *i.e.* $\tilde{c} \ll \langle c \rangle_S$, so that we may neglect $\left(u(r) \frac{\partial \tilde{c}}{\partial x} - \left\langle u(r) \frac{\partial \tilde{c}}{\partial x} \right\rangle_S \right)$ with respect to $\left(u(r) - u_0 \right) \frac{\partial \langle c \rangle_S}{\partial x}$. Furthermore, on such long times, the system has reached a steady state so that the time derivative term $\frac{\partial \tilde{c}}{\partial t}$ can be neglected. Lastly, we assume the cylinder to be of large aspect ratio, such that the gradient $\partial \tilde{c} / \partial x$ in the x direction of the deviation concentration is much smaller than the one in the radial direction, *i.e.* $\partial \tilde{c} / \partial r$.

With such assumptions, Eq. (6.7) reduces to:

$$\left(u(r) - u_0\right) \frac{\partial \langle c \rangle_S}{\partial x} = \frac{D_0}{r} \frac{\partial}{\partial r} \left[r \frac{\partial \tilde{c}}{\partial r} \right]. \quad (6.8)$$

Integrating the latter equation with Eq. (6.3), we find:

$$\tilde{c}(r, x, t) = \frac{a^2 u_0}{24 D_0} \frac{\partial \langle c \rangle_S}{\partial x} \left(6 \frac{r^2}{a^2} - 3 \frac{r^4}{a^4} - 2 \right), \quad (6.9)$$

where we have used the fact that \tilde{c} is finite at $r = 0$ and of zero cross-sectional average. Lastly, injecting the cross-sectional average $\langle u(r) \frac{\partial \tilde{c}}{\partial x} \rangle_S$ in Eq. (6.6), we find:

$$\frac{\partial \langle c \rangle_S}{\partial t} + u_0 \frac{\partial \langle c \rangle_S}{\partial x} = \left(D_0 + \frac{u_0^2 a^2}{48 D_0} \right) \frac{\partial^2 \langle c \rangle_S}{\partial x^2}. \quad (6.10)$$

Equation (6.10) is known as the Taylor-Aris law. Written in the translated frame $\tilde{x} = x - u_0 t$, it takes the form of a diffusion equation with an effective diffusion coefficient $D_{\text{eff}} = D_0 + \frac{u_0^2 a^2}{48 D_0} = D_0 \left(1 + \frac{\text{Pe}^2}{48} \right)$, where $\text{Pe} = u_0 a / D_0$ is the Péclet number that measures the ratio between advection and diffusion. Since Taylor's article, the validity of this asymptotic calculation has been proven more rigorously using the center-manifold description [238, 239, 240, 241].

Aris' theory

In 1956, Rutherford Aris developed a theoretical framework to compute the moments of the solute distribution [242]. This framework has been extended further, notably to get the full time dependence of the first three moments [243], and has been adapted for time-dependent flows [244, 245]. The idea of the method is to introduce the moments in x of the distribution and to compute them recursively. Here again, we focus on the case of the transport inside a cylindrical tube, with an initial condition that is uniformly distributed over localized line at $x = 0$, such that $c(r, x, t = 0) = \delta(x)$, where a unit mass is used, and δ denotes the Dirac distribution. The p^{th} moment c_p in x of the concentration and its cross-sectional average m_p are defined as:

$$c_p(r, t) = \int_{\mathbb{R}} x^p c(r, x, t) dx \quad \text{and} \quad m_p(t) = \int_0^a c_p(r, t) \frac{2\pi r}{\pi a^2} dr. \quad (6.11)$$

We assume that the solute concentration vanishes at infinity in x , sufficiently rapidly for the concentration field to verify the condition: $\lim_{x \rightarrow \pm\infty} x^\mu \partial_x^\nu c = 0$ for arbitrary integers μ and ν , such that all the moments exist and are finite. Multiplying Eq. (6.4) by x^p and integrating it with respect to x on \mathbb{R} , we have:

$$\frac{\partial c_p}{\partial t} - \frac{D_0}{r} \frac{\partial}{\partial r} \left[r \frac{\partial c_p}{\partial r} \right] = D_0 p(p-1) c_{p-2} + u(r) p c_{p-1}. \quad (6.12)$$

Then, taking the cross-sectional average and using the no-flux boundary condition $\frac{\partial c_p}{\partial r}(r = a, t) = 0$, which applies to each moment, we find:

$$\frac{dm_p}{dt} = p(p-1)D_0\langle c_{p-2} \rangle_S + p\langle uc_{p-1} \rangle_S. \quad (6.13)$$

For $p = 0$, Eq. (6.13) yields $\frac{dm_0}{dt} = 0$, meaning that the zeroth moment is constant and equal to the number of solute particles, *i.e.* $m_0(t) = 1$. This condition expresses the global conservation of matter in the tube. Eq. (6.12) for $p = 0$ reduces to the axisymmetric heat equation that can be solved for any initial condition by expanding on the spectral basis of the Laplacian (see section 6.3.2). Here, for the specific case of a uniform initial condition, the solution of the heat equation is trivial, and reads: $c_0(r, t) = 1$. Then, for $p = 1$, Eq. (6.13) reads:

$$\frac{dm_1}{dt} = \int_0^a u(r)c_0(r, t) \frac{2\pi r}{\pi a^2} dr = \int_0^a 2u_0 \left(1 - \frac{r^2}{a^2}\right) \frac{2\pi r}{\pi a^2} dr = u_0. \quad (6.14)$$

This means that the average concentration moves with the mean speed of the flow. The first moment c_1 follows the equation:

$$\frac{\partial c_1}{\partial t} - \frac{D_0}{r} \frac{\partial}{\partial r} \left[r \frac{\partial c_1}{\partial r} \right] = u(r)c_0(r, t) = 2u_0 \left(1 - \frac{r^2}{a^2}\right). \quad (6.15)$$

Given the form of the cross-sectional average moment m_1 in Eq. (6.14), we search for solution of the type: $c_1(r, t) = u_0 t + \delta c_1(r, t)$, δc_1 being a function. Introducing this ansatz in Eq. (6.15), we find that the steady-state solution for δc_1 follows a similar equation as the leading-order equation in Taylor's theory (6.8) for the deviation to the average concentration field. Then, we can write the general solution as:

$$c_1(r, t) = u_0 t + \frac{u_0 a^2}{24D_0} \left(6 \frac{r^2}{a^2} - 3 \frac{r^4}{a^4} - 2\right) + \sum_{n=1}^{\infty} A_n J_0 \left(\frac{\alpha_n r}{a} \right) \exp \left(- \frac{\alpha_n^2 D_0 t}{a^2} \right), \quad (6.16)$$

where J_0 is the Bessel function of the first kind and of order 0, α_n is the n^{th} zero of $\frac{dJ_0}{dx}(x)$, and A_n is a coefficient that can be found through the initial condition $c_1(r, t = 0) = 0$, and reads:

$$A_n = - \frac{8u_0 a^2}{D_0} \frac{1}{\alpha_n^4 J_0(\alpha_n)}. \quad (6.17)$$

Aris was interested in the long-time asymptotic regime of the solute concentration distribution. From Eq. (6.16), the first moment follows: $c_1(r, t) = m_1(t) + \frac{u_0 a^2}{24D_0} \left(6 \frac{r^2}{a^2} - 3 \frac{r^4}{a^4} - 2\right) + O(\exp(-\alpha_1^2 D_0 t / a^2))$, where $\alpha_1 \approx 3.8317$. Inserting the long-time asymptotic

expression for c_1 in Eq. (6.13) for $p = 2$, we find:

$$\begin{aligned} \frac{dm_2(t)}{dt} &= 2D_0\langle c_0 \rangle_S + 2\langle uc_1 \rangle_S \\ &\simeq 2D_0 + 2 \int_0^a u(r) \left[u_0 t + \frac{u_0 a^2}{24D_0} \left(6\frac{r^2}{a^2} - 3\frac{r^4}{a^4} - 2 \right) \right] \frac{2\pi r}{\pi a^2} dr \\ &\quad + O(\exp(-\alpha_1^2 D_0 t/a^2)). \end{aligned} \quad (6.18)$$

Then, for times much larger than the time for a solute molecule to diffuse across the tube $t \gg a^2/D_0$, we find:

$$\frac{dm_2(t)}{dt} \simeq 2D_0 + \frac{u_0^2 a^2}{24D_0} + 2u_0^2 t. \quad (6.19)$$

The long-time effective diffusion coefficient, defined as $D_{\text{eff}} = \lim_{t \rightarrow \infty} \frac{1}{2} \frac{d}{dt} \left[m_2(t) - m_1^2(t) \right]$, can be computed and reads:

$$D_{\text{eff}} = D_0 + \frac{u_0^2 a^2}{48D_0} = D_0 \left(1 + \frac{\text{Pe}^2}{48} \right), \quad (6.20)$$

where we recover the result from Taylor's theory.

The theory of Taylor & Aris has been extended by Howard Brenner among others to a more general framework called *generalized Taylor dispersion*, as reviewed in Ref. [246]. Lastly, the Taylor-Aris equation has been also recovered by using methods from non-equilibrium statistical physics such as large-deviation theory [247, 248], or Green-Kubo formulas [249, 250, 251, 252].

Applications

There are several applications of Taylor dispersion in various fields of science², as the combination of flow, confined space and transport is a generic feature to many systems. We give a brief overview here. In Earth sciences, Taylor dispersion influences the spreading of pollutants in rivers and estuaries [253], and is significant in the transport in porous and heterogeneous media [246, 254, 255]. Taylor dispersion enhances diffusion and mixing which is important in "lab-on-a-chip" devices which often involve the mixing of chemical reactants [256, 257]. It is also encountered in chromatography for the separation of a mixture. Besides, Taylor dispersion is found in biological transports such as in pulmonary circulation [258, 259], cerebrospinal-fluid mixing [260], DNA and bacterial mobility [261, 262, 263], as well as in other contexts at micro- and nano-scales [240, 264].

²The seminal article from G.I. Taylor [235] is the most cited one from the British professor (~ 6300 , Google Scholar), which emphasizes the importance of Taylor dispersion in sciences and its numerous applications.

In this chapter, we address several problems related to Taylor dispersion. My interest in this topic started from a collaborative work with the experimentalists Alexandre Vilquin and Joshua McGraw as well as another theoretician PhD student Pierre Soulard. The idea of the project is to observe the Brownian trajectories of nanoparticles near surfaces using a specific microscopy technique called *total internal reflection fluorescence microscopy* (TIRFM), which is described later in the chapter. In a first part, we focus on Taylor dispersion at short times, meaning for times shorter than the diffusion time over the channel width such that the Taylor-Aris law is not valid. This problem has already been addressed theoretically [265] and the moment theory introduced by Aris has also been generalized to access the full dynamics of Taylor dispersion [243]. The dispersion coefficient is found to increase with time and saturates toward the Taylor-Aris law at long times. Furthermore, the short-time regime of Taylor dispersion is found to crucially depend on the particle concentration, and displays a quadratic dependence in time for an initial point-like concentration (or a single particle), whereas an extended initial spatial distribution leads to an additional contribution that is linear in time. Some of the applications of Taylor dispersion in micro and nanoscience, such as drug delivery from a suddenly ruptured cargo [266, 267] or the kinetics of nanoconfined chemical reactions [268, 269], should critically depend on the initial distribution of solutes [270]. In a second part, we discuss the consequences of the interactions of the nanoparticles with the surface of the channel in Taylor dispersion. Here, some specificity of the TIRFM detection method are also discussed.

Organization

The rest of the chapter is structured as follows: section 6.2 is devoted to the experimental work, mostly performed by our collaborators. We explain the TIRFM setup and some of its limitations, before showing how it allows us to measure velocity profiles, as well as dispersion. Then, in section 6.3, we review several existing theories to describe Taylor dispersion for tracer-like particles in the full temporal range before comparing them to the experiments. A discussion on the specific boundary condition in TIRFM is also provided. Lastly, we discuss in section 6.4 the interactions between the nanoparticles in TIRFM and the surface.

6.2 Experimental results

The experiments presented in this manuscript have been designed by Alexandre Vilquin & Joshua McGraw with the help of Gabriel Guyard from the laboratory Gulliver at ESPCI Paris.

6.2.1 Setup

Microfluidic channel

In the experiments, fluorescent nanoparticles with radius $a = 55$ or 100 nm are advected along the x -direction of a pressure-driven flow (Fluigent MFCS-4C pressure controller) in microchannels with a rectangular section (see Fig. 6.1(d)). The carboxylate-modified fluorescent nanoparticles used are 55 nm-radius (Invitrogen F8803, Thermofisher) and 100 nm-radius (Invitrogen F8888 Thermofisher) latex microspheres used without further modification besides dilution by a factor of 10^3 using ultra-pure water. Microfluidic chips are fabricated by soft lithography of poly(dimethyl siloxane) (Dow Chemical, Sylgard 184) on a plasma-cleaned glass coverslip with $145 \mu\text{m}$ thickness constituting the bottom surface. In the first section, the liquids used are ultra-pure water ($18.2 \text{ M}\Omega \text{ cm}$, MilliQ) and water-glycerol mixtures with Newtonian viscosities of $\eta = 1 \text{ mPa s}$ for pure water, 2.1 and 7.6 mPa s for water-glycerol mixture, measured with a Couette-cell rheometer (Anton Paar MCR 302) up to a shear rate of 1000 s^{-1} . In section 6.4, sodium chloride (NaCl) solutions of concentrations 5.4 and 54 mg/L are also used. The particle volume fractions used are typically 10^{-5} , providing sufficient statistics while avoiding hydrodynamic interactions between the nanoparticles. Pressure drops ΔP in the range 5 - 400 mbar are applied across the microchannels with height $h = 18 \mu\text{m}$, width $w = 180 \mu\text{m}$, and length $L = 8.8 \text{ cm}$.

Optical detection

Total internal reflection fluorescence microscopy (TIRFM) measurements [271, 272], are realized by illuminating the near-surface shear flow with a laser source (Coherent Sapphire, wavelength $\lambda = 488 \text{ nm}$, power in the range 15 to 150 mW) focused off the central axis of, and on the back focal plane of a $100\times$ microscope objective with a large numerical aperture ($\text{NA} = 1.46$, Leica HCX PL APO), as depicted in Figs. 6.1b)-d). Thus, incident angles θ larger than the critical angle, $\theta_c = \arcsin(n_l/n_g)$, are reached, enabling total reflection of the laser beam at the glass-liquid interface. Here, $n_g = 1.518$ is the refractive index of the glass coverslip, $n_l = \{1.33, 1.33, 1.36, 1.40\}$ is the refractive index of the fluids for the water, NaCl solutions and the two water-glycerol mixtures, respectively; the refractive indices of the four liquids are measured using a refractometer (Atago PAL-RI). An evanescent wave propagates through the sample with an exponential decay lengths $\Pi = \lambda/(4\pi) (n_g^2 \sin^2 \theta - n_l^2)^{-1/2}$, with the angle measured *in situ* as in Ref. [273]. The penetration depth is thus $\Pi \approx 100 \text{ nm}$. The images of 528×512 pixels (px), with a resolution of $22.9 \text{ px}/\mu\text{m}$, are recorded in 16-bit format (Andor Neo sCMOS) with a frame rate of 400 Hz for a duration of 5 s . For each set of parameters, typically five videos of 2000 frames each are recorded. After a centroid detection, the intensity profile is fitted by a radially-symmetric Gaussian model for each frame as shown in Fig. 6.1c). Thus the x and y coordinates give the particle position in the plane parallel to the glass-water interface.

Given the exponentially decaying evanescent field, we call the apparent altitude of

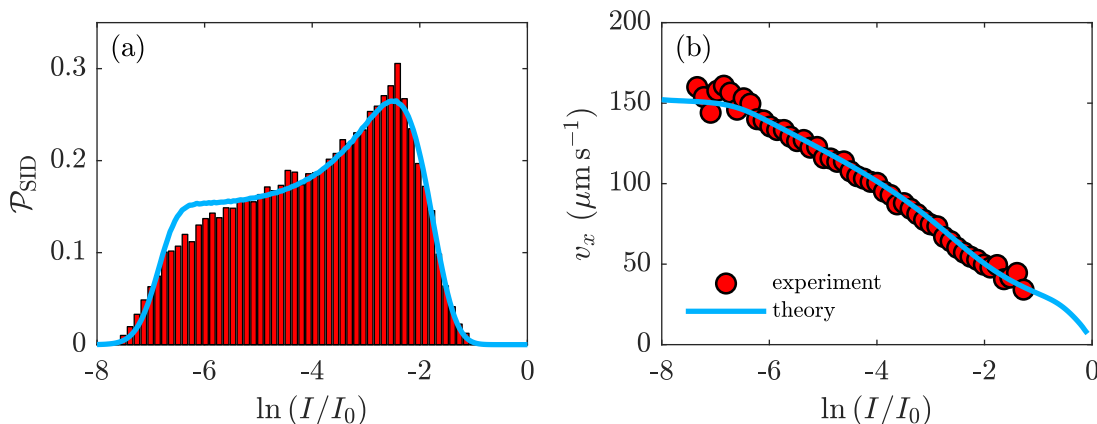


Figure 6.2: (a) Comparison between experimental and theoretical signal intensity distributions (SIDs). (b) Comparison between experimental and theoretical streamwise mean velocity profiles. The experimental data is for 55 nm-radius particles for a pressure drop of 30 mbar across the microchannel.

the center of mass of the particles $z = a + \Pi \ln(I_0/I)$, I is the measured particle intensity, as shown in Fig. 6.1c), and I_0 is the fluorescence intensity of a particle with radius a in contact with the solid-liquid boundary, the latter being defined as $z = 0$. Optical aberrations lead to small deviations from an exact exponential decay for the fluorescence intensity (see section 6.2.2). Comparing subsequent images, sample trajectories as in Fig. 6.1c) are constructed using home-built Matlab routines.

The experimental setup allows the observation of particles in a range of altitudes $a \lesssim z \lesssim 1 \mu\text{m}$ from the solid-liquid interface. In practice, for water and water-glycerol mixture we do not observe particles for $z \lesssim 200 \text{ nm}$ as a result of electrostatic and steric interactions [274, 275, 276]. The experiments in section 6.4 with NaCl solutions allows us to observe particles closer to the wall. The camera sensitivity determines the upper z -limit. In particular, we stress that the particle intensity must overcome a certain threshold for it to be detected. Therefore, for particles moving away from the wall, their intensity decreases, eventually below the threshold, so that the particles effectively leave the observation area.

6.2.2 Signal intensity distribution

This section provides additional information about how the observed signal intensity distributions (SID) [277], denoted \mathcal{P}_{SID} , and the corresponding velocity profiles can be quantitatively described simultaneously. As also described in Ref. [272], fluorescent nanoparticles detected display a range of intensities affected by several factors, the most important ones being: *i*) electrostatic interactions which determine the probability that a particle of a given radius is found at a certain distance from the wall according

to a Boltzmann-like distribution; *ii*) particle size distribution; and *iii*) the optical setup which, given the position and size of the particle, finally determines the associated collected intensity. We now discuss each of these elements in detail.

i) The glass surface exerts an electrostatic repulsion on the particles according to the fact that both surfaces are negatively charged. The details of such a repulsion are understood within the Debye–Hückel theory [274, 275] and are discussed further in section 6.4.1. The electrostatic interaction energy, ϕ_{el} , describing the electric double-layer repulsion between a particle with radius R and a flat wall [276], is given by:

$$\phi_{\text{el}}(z) = 16\epsilon R \left(\frac{k_{\text{B}}\Theta}{e} \right)^2 \tanh \left(\frac{e\psi_{\text{p}}}{4k_{\text{B}}\Theta} \right) \tanh \left(\frac{e\psi_{\text{w}}}{4k_{\text{B}}\Theta} \right) \exp \left(-\frac{z-R}{l_{\text{D}}} \right). \quad (6.21)$$

Here, z , ϵ , e , k_{B} , Θ , ψ_{p} , ψ_{w} and l_{D} are respectively the position of the center of the particle, liquid permittivity, elementary charge, Boltzmann constant, temperature, particle and wall electrostatic potentials and the Debye length. This interaction determines the particle concentration at thermal equilibrium through the Boltzmann distribution:

$$c_{\text{B}}(z) \propto \exp \left(-\frac{\phi_{\text{el}}(z)}{k_{\text{B}}\Theta} \right). \quad (6.22)$$

As already observed in TIRFM experiments, the van der Waals interaction can be neglected for pure water [272, 277]. Consequently, the typical distance between the bottom surface (located at $z = 0$) and the particles is mainly determined by the Debye length.

ii) All the particles do not have the same radius R . The radius distribution is described by a Gaussian probability function:

$$\mathcal{P}_R(R) = \frac{1}{\sqrt{2\pi\sigma_R^2}} \exp \left(-\frac{(R-a)^2}{2\sigma_R^2} \right), \quad (6.23)$$

where a is the mean radius and σ_R the standard deviation.

iii) The fluorescence intensity I of an individual particle is determined by the optical parameters of the TIRFM setup and the particle size, with $I \propto R^3$. The evanescent wave has a penetration depth Π characterizing the exponential decrease of intensity. The observed fluorescence intensity is also sensitive to the finite depth of field d_{f} of the microscope objective. In our experiments, the depth of field has a value of 415 nm, meaning that if particles are not located on the focal plane at z_{f} (typically 400–500 nm from the glass-liquid interface), they will be detected with a relatively low intensity. Putting these elements together, the observed fluorescence intensity for an individual particle is predicted [277] to be:

$$\frac{I(R, z)}{I_0} = \left(\frac{R}{a} \right)^3 \exp \left(-\frac{z-a}{\Pi} \right) \left[1 + \left(\frac{z-a-z_{\text{f}}}{d_{\text{f}}} \right)^2 \right]^{-1}, \quad (6.24)$$

where I_0 is the intensity for a particle with radius $R = a$ located at the bottom surface $z = a$, and with the focal plane at $z_f = a$.

Using a home-made MATLAB interface, we combine Eqs. (6.21)-(6.24) to generate numerical SIDs. Practically, we determine the fraction of particles having an altitude z and a radius R given by the weight $W(z, R) = C(z)\mathcal{P}_R(R)$, and compute the associated intensity given by Eq. (6.24). This procedure gives a list of weighted intensities shown in Fig. 6.2(a), using a prefactor $16a\epsilon(k_B\Theta/e)^2 \tanh(e\psi_p/(4k_B\Theta)) \tanh(e\psi_w/(4k_B\Theta)) = 2.9 \times 10^{-21}$ J, as well as $l_D = 60$ nm, $\sigma_R = 5.5$ nm, $a = 55$ nm and the optical parameters as described above, along with the experimental histogram.

6.2.3 Velocity fields

Velocity versus apparent altitude

As schematically indicated in Fig. 6.1b), Taylor dispersion crucially depends on the local shear rate for particles diffusing in a shear flow. In order to obtain mean velocity profiles along the flow direction over a given lag time τ displacements $\Delta x(z(t), \tau) = x(z(t+\tau)) - x(z(t))$ taking t as the initial observation time, are measured for each pair of frames in which identical particles are detected. Figure. 6.1(c) shows an example of particle trajectories. Since the particle intensity encodes the altitude, we first sort the particles into a series of intensity bins, each bin corresponding to a range of approximately 15 nm in the z -direction. Then, the streamwise mean velocity $v_x(\bar{z}) = \langle \Delta x(\bar{z}, \tau) \rangle_t / \tau$ is determined. Here, $\langle \cdot \rangle_t$ denotes ensemble averaging over *ca.* 10^5 particles. The notation $\bar{\cdot}$ denotes averaging over all frames during the lag time.

Figure 6.3(a) shows the streamwise velocity profiles for 55 nm-radius particles in water and several pressure drops. The solid lines show that the profiles are well approximated by linear functions. The spread of v_x intercept values arises from the spread of values for I_0 at each pressure, $z = 0$ corresponding to the mean of $a + \Pi \ln I_0$ over the different ΔP . The origin $z = 0$ is thus resolved within 20 nm of the solid-liquid interface assuming no slip [272]. The low Reynolds number indicates a viscosity-dominated flow for which $v_x(\bar{z}) = \Delta P (\bar{z}^2 - h\bar{z}) / (2\eta L)$, *i.e.* a Poiseuille flow. In the region $z \lesssim 1 \mu\text{m}$, and given the channel height $h = 18 \mu\text{m}$, the deviation of the Poiseuille profile from linearity is expected to be less than 5%. Therefore, at first order in \bar{z}/h , we have $v_x(\bar{z}) \simeq \dot{\gamma}\bar{z}$, with the shear rate defined by $\dot{\gamma} = \partial_{\bar{z}}v_x|_0 = h|\Delta P| / (2\eta L)$ and $\partial_{\bar{z}}$ denoting the partial derivative with respect to \bar{z} . In Fig. 6.3(b) are shown the shear rate values as functions of the pressure drop extracted from the velocity profiles in part (a). As highlighted by the dashed black line, the shear rate increases linearly with the pressure drop. The slope, given by $h / (2\eta L)$, provides a water viscosity $\eta = 0.9 \pm 0.1$ mPa s at 24 °C in agreement with the expected value [278], also measured with a Couette-cell rheometer independently. We stress that a good agreement is also found for the water-glycerol mixtures used here.

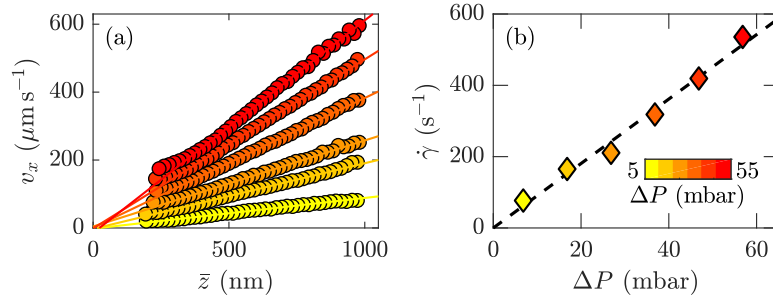


Figure 6.3: (a) Velocity profiles $v_x = \langle \Delta x \rangle_\tau / \tau$ for 55 nm-radius particles with a lag time $\tau = 2.5$ ms at several pressure drops. The plain lines indicate linear regressions, providing the shear rate value $\dot{\gamma}$. (b) Shear rate as a function of pressure drop across the microfluidic channel. The dashed black line is a linear regression and the color code applies also to (a).

Discussion on the optical aberrations

However, the mean streamwise velocity profile is not perfectly linear when using the apparent altitude $z = a + \Pi \ln(I_0/I)$ [272], particularly near the surface at $\bar{z} \approx 200$ nm in Fig. 6.3a). First, possible deviations may come from the hydrodynamic interactions between the finite-size colloids and the wall. Indeed, a spherical particle located at an altitude z from a planar wall in a shear flow rotates and has a mean streamwise velocity that differs from the one of the flow and reads $v_x(z) = f_B \dot{\gamma} z$, where f_B is the so-called ‘‘Brenner factor’’ [279]. For large z/a , the Brenner factor can be expressed as $f_B \simeq 1 - (5/16) (z/a)^{-3}$. For 55 nm-radius particles typically located at distances larger than 200 nm due to electrostatic repulsion, the deviation from the linear velocity profile is less than 1%.

Additionally, deviations from the linear velocity profile are induced by the optical methods. Using a linear shear flow in conjunction with the intensity-altitude-probability relations described in the previous section (Eqs. (6.21)-(6.24)), we follow Zheng *et al.* [277] and predict the particle’s mean streamwise velocity as a function of $\ln(I_0/I)$. Such a prediction is made with $\dot{\gamma}$ adjusted simultaneously to the physical and optical parameters of Eqs. (6.21)-(6.24). The result is shown together with the experimental results in Fig. 6.2(b), showing good agreement and capturing the main nonlinear features of the experimental data. The shear-rate values obtained with this SID method are approximately 15% smaller than the ones directly obtained using a linear regression of the velocity profiles of Fig. 6.3a) using the apparent altitude. This discrepancy is mainly due to the particle polydispersity and to the finite depth of field of the microscope objective.

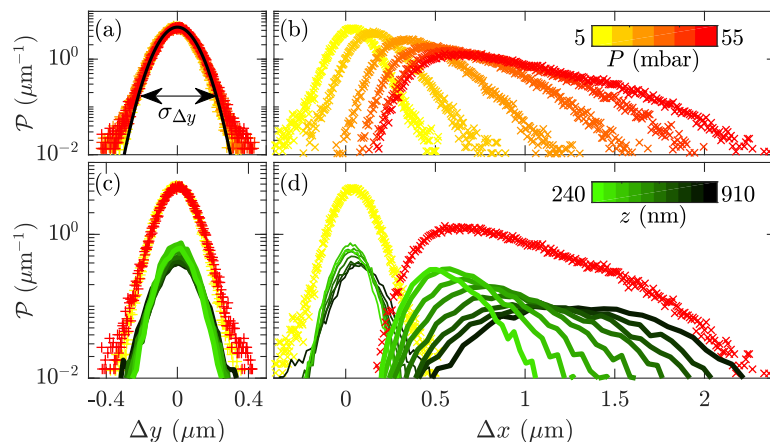


Figure 6.4: Probability density functions (PDFs) of particle displacements. (a) Transverse and (b) streamwise displacement PDFs for several pressure drops indicated in the yellow-red color bar. The black line in (a) indicates a Gaussian model $\mathcal{P}(\Delta y) = \exp\left(-\Delta y^2 / \left(2\sigma_{\Delta y}^2\right)\right) / \sqrt{2\pi\sigma_{\Delta y}^2}$. In (c) the Δy -PDF for the largest pressure drop is decomposed into PDFs for several z . Each green-black PDF corresponds to a z -range of *ca.* 30 nm (some curves omitted for clarity), and the mean value of z is indicated by the color scale of (d). The decomposed Δx -PDFs for the smallest pressure drop (thinnest green-black lines) and the largest pressure drop (thickest green-black lines), weighted by the particle number for each z -range in proportion to the total particle number, are shown in (d). All the displacements are measured for a time lag $\tau = 2.5$ ms and concern 100 nm-radius particles in water.

6.2.4 Local distributions of particle displacement

Having discussed the mean velocity of the particles, we turn our attention to the displacement distributions. Figures 6.4(a) and (b) show the probability density functions (PDFs, here called \mathcal{P}) of the transverse (Δy) and streamwise (Δx) displacements of 100 nm-radius particles in water over a duration $\tau = 2.5$ ms and several pressure drops. For Fig. 6.4 and in the following, we systematically take $z = z(t)$, the altitude at the initial observation time. This initial altitude $z(t)$ should be distinguished from the average altitude \bar{z} over the lag time τ used in Fig. 6.3(a). The uncertainties on the initial altitude are mainly determined by the average distance covered due to diffusion during the frame-capture time τ_{capt} , approximately equal to $\sqrt{D_0\tau_{\text{capt}}}$ where D_0 is the bulk diffusion coefficient. This average distance varies from 100 nm for the 55 nm-radius particles in water to 30 nm for 100 nm-radius particles in the 50% water-glycerol mixture.

In Fig. 6.4(a), it is shown that the transverse displacement PDFs do not depend on the pressure drop and are well described as Gaussian over two decades. The global standard deviation provides an approximation for the unidimensional Brownian diffusion coefficient $\sigma_{\Delta y}^2(\tau)/(2\tau) \approx 2.0 \pm 0.3 \mu\text{m}^2 \text{ s}^{-1}$, where $\sigma_{\Delta y}^2(\tau) = \langle \Delta y^2 \rangle - \langle \Delta y \rangle^2$ is the standard deviation of the displacements along y over the lag time τ . This estimate

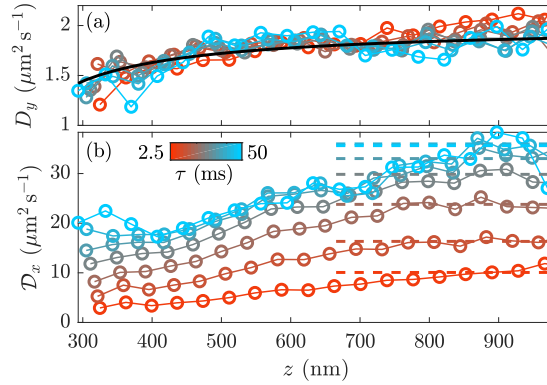


Figure 6.5: Spatio-temporal diffusion and dispersion coefficients. (a) Transverse diffusion coefficients D_y and (b) streamwise dispersion coefficient D_x as functions of the apparent altitude z and lag time τ for 100 nm-radius particles in pure water, and a pressure drop corresponding to a shear rate $\dot{\gamma} = 243 \text{ s}^{-1}$. The z -range is typically 30 nm for each initial altitude z . In (a), the plain black line corresponds to the theoretical prediction $D_y = D_0 \left(1 - (9/16) Z^{-1} + (3/8) Z^{-3} - (45/256) Z^{-4} - (1/16) Z^{-5} \right)$ with $Z = z/a$ [136]. In (b) the dashed lines indicate the streamwise dispersion coefficient averaged in the range 650-1000 nm.

is close to the value predicted by the Stokes-Einstein relation, $D_0 = k_B \Theta / (6\pi\eta a) \approx 2.2 \pm 0.2 \text{ } \mu\text{m}^2 \text{ s}^{-1}$ [232], for particles with $a = 100 \text{ nm}$ advected in water, where η is taken from bulk rheology as *ca.* 0.9 mPa s at room temperature. Contrasting with the transverse displacement PDFs, those for the streamwise direction in Fig. 6.4(b) are not Gaussian, become broadened with the pressure drop, and exhibit some asymmetry as reported in Refs. [280, 281].

The TIRFM setup provides the particle distance from the glass-liquid interface through the detected intensity, allowing us to distinguish the contributions of particles at different altitudes to the global PDFs. In the transverse direction, the local PDFs are shown for the largest pressure drop in Fig. 6.4(c) and they are all Gaussian regardless of z . In Fig. 6.4(d) are shown similar decompositions for the smallest and largest pressure drops for streamwise displacements. These decompositions demonstrate that the asymmetry of the global distributions is mainly due to the superposition of different mean displacements at different altitudes. For the smallest pressure drop the local PDFs are only slightly shifted with increasing z due to the relatively low mean velocities, *cf.* Fig. 6.3(c). For the largest pressure drop, the mean values are shifted more strongly with increasing z as a result of the higher shear rate. More importantly, the local PDFs thus provide access to the transverse diffusion along y and streamwise dispersion along x for different altitudes.

6.2.5 Time- and space-dependent dispersion

A detailed study of the local Taylor dispersion as function of time and the various physical parameters at stake is now described. In Figs. 6.5(a) and (b) are shown local transverse diffusion coefficients:

$$D_y(z, \tau) = \frac{\sigma_{\Delta y(z)}^2}{2\tau}, \quad (6.25)$$

and streamwise dispersion coefficients:

$$\mathcal{D}_x(z, \tau) = \frac{\sigma_{\Delta x(z)}^2}{2\tau}. \quad (6.26)$$

The latter comprise pure diffusive and advection effects, and are remarkably larger (up to an order of magnitude) than the former. These data are obtained from altitude decompositions as in Fig. 6.4 for several lag times τ . Figures 6.5(a) and (b) show that there is a general increase with z of D_y and \mathcal{D}_x until reaching a plateau at large z . The variation with z in both directions is due to hydrodynamic interactions between particles and the solid-liquid interface, leading to a hindered diffusion, as discussed in detail elsewhere [136, 282, 283, 284, 285] (see section 6.4). Indeed, the z -dependence of D_y is in agreement with the prediction resulting from the effective viscosity near a flat, rigid wall [136]. As expected, the transverse diffusion is not dependent on the lag time τ . In contrast, the dispersion coefficients, \mathcal{D}_x , increase significantly with τ , as shown in Fig. 6.5(b).

In Fig. 6.6(a), we show the lag-time dependence of the streamwise dispersion coefficient. To do so, we define $\overline{\mathcal{D}}_x(\tau)$ as the average value of $\mathcal{D}_x(z(t), \tau)$ in the large- z plateau for $z(t) \gtrsim H/2$ where H is the size of the observation zone, typically $1 \mu\text{m}$. That is, $\overline{\mathcal{D}}_x(\tau)$ is a conditional averaging for particles beginning their trajectories in the top half of the observation zone, thus limiting the aforementioned lubrication effects. In this figure, the bulk diffusion coefficient D_0 is varied by changing the particle size and the liquid viscosity. For the lowest values of D_0 , $\overline{\mathcal{D}}_x$ continuously increases with time and the temporal slope increases. By contrast, $\overline{\mathcal{D}}_x$ saturates to a plateau for the largest D_0 . As explained by Taylor [235], the time needed to reach the dispersion plateau corresponds approximately to the time needed to diffuse across the channel height. Here the Taylor time is defined as:

$$\tau_z = \frac{H^2}{D_0}. \quad (6.27)$$

In a rectangular channel, the exact calculation [235] gives a characteristic diffusion time τ_z/π^2 . For the 55 nm-radius particles in water, assuming a length scale $H \approx 700 \text{ nm}$, one has $\tau_z/\pi^2 \approx 13 \text{ ms}$, in reasonable agreement with the corresponding data of Fig. 6.6(a), with $D_0 = 3.9 \pm 0.4 \mu\text{m}^2 \text{ s}^{-1}$. For smaller values of D_0 , the dispersion remains mainly in the short-time, increasing-slope regime. Nevertheless, taking the longest-time data (the data of Fig. 6.6(a) at $\tau = 50 \text{ ms}$, denoted $\mathcal{D}_{\tau_{\text{max}}}$) for each D_0 value, we now examine the shear-rate dependence of the dispersion.

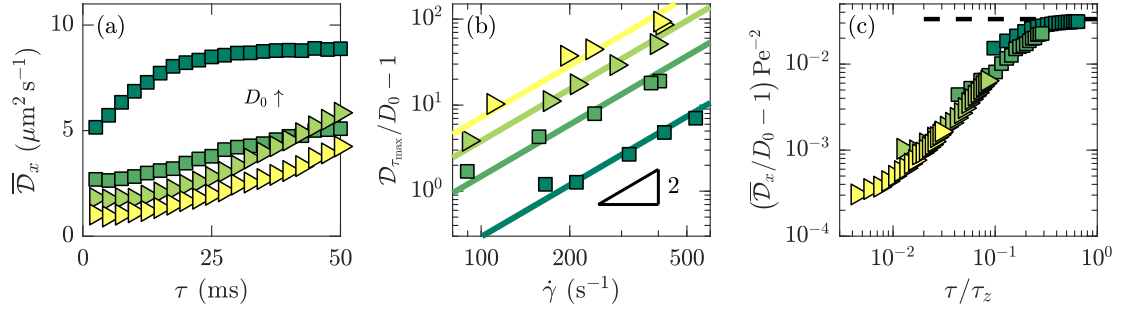


Figure 6.6: Shear rate and time dependences of the dispersion coefficients. (a) Streamwise dispersion coefficient \overline{D}_x extracted from the dashed lines in Fig. 6.5(b) as a function of lag time. From yellow to dark green, the bulk diffusion coefficient increases. In particular —from bottom to top— the shear rates, particle radii and viscosities are $\{\dot{\gamma}, a, \eta\} = \{110, 100, 7.6\}$, $\{91, 100, 2.1\}$, $\{90, 100, 1\}$, $\{165, 55, 1\}$ in units $\{\text{s}^{-1}, \text{nm}, \text{mPa s}\}$; giving $D_0 = \{0.28, 0.89, 2.1, 3.9\} \mu\text{m}^2 \text{s}^{-1}$ determined from the Stokes-Einstein relation. Marker shape indicates the liquid as water (\square) or glycerol-water mixtures (\blacktriangleright). (b) Reduced late-time dispersion coefficient versus shear rate. Solid lines have a slope 2 in this log-log representation. (c) Same data as in (a), with time rescaled using $\tau_z = H^2/D_0$, and reduced dispersion coefficient rescaled with Pe^2 . The dashed line shows the long-time limit with a prefactor predicted by Eq. (6.28).

In Fig. 6.6(b) is shown the dependence of the reduced late-time dispersion coefficient, $\mathcal{D}_{\tau_{\max}}/D_0 - 1$, for four D_0 as functions of the shear rate. The solid lines (with slope 2 in log-log representation) show that the reduced $\mathcal{D}_{\tau_{\max}}$ increases quadratically with the shear rate $\dot{\gamma}$ for all D_0 studied. To understand this result, we use the classical Taylor-Aris calculation for a plane Couette flow [246] in a rectangular channel, that can be derived using the Taylor model in section 6.1.2 for a velocity field $v_x(z) = \dot{\gamma}z$, and reads:

$$\mathcal{D}_x = D_0 \left(1 + \frac{1}{30} \text{Pe}^2 \right) \quad \tau \gg \tau_z, \quad (6.28)$$

for the infinite-time dispersion coefficient, with the Péclet number defined as:

$$\text{Pe} = \frac{\dot{\gamma}H^2}{2D_0} = \frac{\dot{\gamma}\tau_z}{2}, \quad (6.29)$$

where we have identified the mean velocity of the flow to $u = \dot{\gamma}H/2$. Equations (6.28) and (6.29) highlight the key role of velocity gradients in enhanced dispersion, and justify the quadratic shear-rate dependance of the data in Fig. 6.6(b) for the 55 nm-radius particles in water. Applying Eq. (6.28) to this latter data, we extract a length scale $H \approx 500$ nm, consistent with the range of z observed in Fig. 6.3(a). Because the lower- D_0 data does not reach the infinite-time plateau, the prefactor for the linear regressions does not reveal the corresponding size of the flow region H . However, as we show in

the following, the quadratic shear rate dependence is preserved for all time regimes, explaining the scaling of all the data in Fig. 6.6(b).

We now examine the detailed time dependence of the dispersion coefficient for all the experimentally accessed times. Partly inspired by previous theoretical works [243, 244, 245, 286] and by the shear-rate dependence of Fig. 6.6(b), we show in Fig. 6.6(c) the reduced \overline{D}_x normalized by Pe^2 as a function of the dimensionless lag time, τ/τ_z . Remarkably, the data in Fig. 6.6(a) collapse onto a single master curve, suggesting the existence of a universal function describing the reduced dispersion coefficient.

In Fig. 6.6, we considered particles beginning their trajectories in the top half of the channel. However, this fraction can be generalized, with n representing the fraction of the observation zone from which particles leave, and with $0 \leq n \leq 1$. The reduced dispersion is thus expected to follow a relation of the form

$$\left(\frac{\mathcal{D}_{\langle n \rangle}}{D_0} - 1\right) \text{Pe}^{-2} = \mathcal{F}_{\langle n \rangle} \left(\frac{\tau}{\tau_z}\right). \quad (6.30)$$

Examining Fig. 6.6(c), we note that the reduced \overline{D}_x increases with time until a plateau. According to Eq. (6.28), in the $\tau/\tau_z \rightarrow \infty$ limit, $\mathcal{F}_{\langle n \rangle}$ should reach $1/30$. This value is shown with the horizontal black dashed line and is in quantitative agreement with the late-time data. We note furthermore that the crossover to this late-time regime occurs when $\tau/\tau_z \approx 1$. Concerning the data at the shortest dimensionless lag times in Fig. 6.6(c), we find that they do not follow the typically predicted [287, 288, 289, 290, 291] and measured [292, 293, 294] early-time τ^2 dependence. A key foundation of this τ^2 dependence is the assumption that each particle begins its trajectory at the same initial altitude. In general, however, particles may leave from a non-peaked distribution of initial altitudes. This distribution is particularly relevant for Fig. 6.6(c), since the plotted quantity is related to an average of particles leaving mainly from the top half of the observation zone (indicated by the dashed lines in Fig. 6.5(b)).

6.3 Theoretical models for tracer particles

In the case of a non-peaked initial distribution, Chatwin [265] theoretically predicted that dispersion coefficients are modified by an additional term linear in time affecting the short-time regime. After, Barton, Vedel *et al.* [243, 244, 245] produced a moment theory for all times that verifies this initial-concentration dependence and show plateaus at long times when particles encounter the boundaries. In the following subsections, we outline the results from these theories that allow us to recover the main experimental observations we have described in the previous sections, and to justify the form of Eq. (6.30). We stress two limitations of this approach to describe the TIRFM experiments. First, the classical Taylor dispersion theory suppose no-flux boundary conditions at the solid-liquid interfaces. Nevertheless, in the experiments, the upper wall position is determined by the resolution of the optical setup and is not a rigid planar surface (see section 6.2.1), and particles may leave the observation zone. We discuss the choice of boundary conditions at the *fictive* wall, located at $z = H$ in section 6.3.6.

Second, the particles are considered as tracers, neglecting the electrostatic and hydrodynamic interactions with the walls [295], which are found to alter both the distribution of altitude (see Fig. 6.2(a)) and the diffusion constant (see Fig. 6.5).

6.3.1 Short-time asymptotics: Chatwin theory

We first focus on the short-time regime of dispersion and the effect of initial conditions. While several works predicted [287, 288, 289, 290, 291] and measured [292, 293, 294] a quadratic time dependence for a sharply peaked initial spatial distribution, Chatwin [265], recalling Saffmann [296], showed that for particles having an initial PDF $\mathcal{P}_i(y_i, z_i)$ and advected with a steady flow velocity $v_x(y_i, z_i)$, the dispersion coefficient at short times is given by:

$$\begin{aligned} \frac{\mathcal{D}_x}{D_0} - 1 &= \frac{1}{2} \frac{\tau}{D_0} \left[\iint v_x^2 \mathcal{P}_i dy_i dz_i - \left(\iint v_x \mathcal{P}_i dy_i dz_i \right)^2 \right] + \\ &\frac{1}{6} \tau^2 \left[\iint [\nabla^2 v_x^2 + v_x \nabla^2 v_x] \mathcal{P}_i dy_i dz_i - 3 \left(\iint v_x \mathcal{P}_i dy_i dz_i \right) \left(\iint v_x \nabla^2 \mathcal{P}_i dy_i dz_i \right) \right], \end{aligned} \quad (6.31)$$

where y_i and z_i are the coordinates for the initial distribution. The linear terms in time originate from the initial variability of the particles velocity. Assuming a 2d problem in the Oxz plane with an initial particle distribution $\mathcal{P}_{z,i} = \int \mathcal{P}_i dy_i$ and a linear shear flow $v_x(z) = \dot{\gamma}z$ as justified by our experiments, Eq. (6.31) simplifies to:

$$\frac{\mathcal{D}_x}{D_0} - 1 = \dot{\gamma}^2 \tau \frac{\langle z_i^2 \rangle - \langle z_i \rangle^2}{2D_0} + \frac{1}{3} \dot{\gamma}^2 \tau^2 \left[1 - \frac{3}{2} \langle z_i \rangle \left(\int z_i \partial_{z_i}^2 \mathcal{P}_{z,i} dz_i \right) \right]. \quad (6.32)$$

This form for the dispersion coefficient clearly shows a quadratic shear-rate dependence, as observed in Fig. 6.6(b). Furthermore, Eq. (6.32) shows that the linear temporal term is weighted here by the variance of the initial spatial distribution of the particles.

Next, we make a further simplifying assumption that particles are uniformly distributed at the initial time. The particles are thus distributed over a vertical segment of length nH and centered at altitude $\langle z_i \rangle$. The initial PDF is therefore:

$$\mathcal{P}_{z,i}(z_i) = \begin{cases} 0 & \text{if } |z_i - \langle z_i \rangle| > nH/2 \\ 1/nH & \text{if } |z_i - \langle z_i \rangle| \leq nH/2 \end{cases}. \quad (6.33)$$

Injecting this distribution into Eq. (6.32), using the Péclet number of Eq. (6.29) and with $\tau_z = H^2/D_0$, the reduced dispersion coefficient of Eq. (6.30) for short times becomes:

$$\mathcal{F}_{\langle n \rangle} \left(\frac{\tau}{\tau_z} \right) = \frac{n^2}{6} \left(\frac{\tau}{\tau_z} \right) + \frac{4}{3} \left(\frac{\tau}{\tau_z} \right)^2, \quad \tau \ll \tau_z. \quad (6.34)$$

This relation is valid for all n , and in particular, we name the $n = \{0, 1/2, 1\}$ cases as “dot”, “half-line”, and “line”. Before discussing the results of this early-time theory, we first describe a general theory valid at all times.

6.3.2 Moment theory

Given the asymptotic behaviors for both short and long times, we now use the framework of Aris, Barton and Vedel *et al.* [242, 243, 244, 245] based on concentration moments to obtain the dispersion coefficient at all times for a linear shear flow, following section 6.1.2. We consider the 2d problem of tracers with an initial concentration $c_i(z)$ advected along x with a mean velocity $U = \langle v_x \rangle_z$. We nondimensionalize the variables through $C = c / \langle c_i \rangle_z$, $X = x/H$, $Z = z/H$, $T = tD_0/H^2$, $V(Z) = v_x(z)/U$ and the Péclet number $Pe = UH/D_0$. The 2d advection-diffusion equation therefore becomes:

$$\frac{\partial C}{\partial T} + PeV(Z) \frac{\partial C}{\partial X} = \frac{\partial^2 C}{\partial X^2} + \frac{\partial^2 C}{\partial Z^2}, \quad (6.35)$$

with the initial conditions $C(X, Z, 0) = C_i(Z)\delta(X)$. The p^{th} concentration moment $C_p(Z, T)$ and the corresponding vertical-average moment $M_p(T)$ are defined as:

$$C_p(Z, T) = \int_{\mathbb{R}} X^p C(X, Z, T) dX \quad \text{and} \quad M_p(T) = \int_0^1 C_p(Z, T) dZ. \quad (6.36)$$

These definitions can be introduced into the advection-diffusion equation after multiplication by X^p and integration. Then, assuming no flux at the boundaries and that $\lim_{X \rightarrow \pm\infty} X^\mu \partial_X^\nu C = 0$ for arbitrary integers μ, ν , we recover the recursive equations of section 6.1.2:

$$\left(\frac{\partial}{\partial T} - \frac{\partial^2}{\partial Z^2} \right) C_p(Z, T) = p(p-1)C_{p-2} + PeV(Z)pC_{p-1}, \quad (6.37)$$

$$\frac{dM_p}{dT} = p(p-1)\langle 1, C_{p-2} \rangle_Z + Pe p \langle V, C_{p-1} \rangle_Z, \quad (6.38)$$

where the notation $\langle F, G \rangle_Z$ stands for the scalar product $\langle F, G \rangle_Z = \int_0^1 F(Z)G(Z)dZ$. These equations can be recursively solved to get the first moments and then, the dimensionless dispersion coefficient. For our purposes, this time-dependent dispersion coefficient is defined as $\mathcal{D}_x/D_0 = (M_2 - M_1^2)/(2T)$. We stress that this definition is used to be consistent with the Chatwin theory described in Section 6.3.1 and our experiments, even while the definition used in the work by Vedel *et al.* [244, 245] is $\mathcal{D}_x/D_0 = (1/2)\partial_T(M_2 - M_1^2)$.

As in section 6.1.2, the zeroth moment M_0 is constant and equal to unity with the normalization choice. The zeroth moment C_0 follows the 1d heat equation:

$$\frac{\partial C_0}{\partial T} - \frac{\partial^2 C_0}{\partial Z^2} = 0, \quad C_0(Z, 0) = C_i(Z) \quad (6.39)$$

that can be solved analytically by introducing the spectral basis of the 1d Laplacian operator $f_{k \in \mathbb{N}}(Z)$, which is itself solution of the eigenvalue problem:

$$\left(\lambda_k + \frac{d^2}{dZ^2} \right) f_k(Z) = 0, \quad f'_k(0) = f'_k(1) = 0. \quad (6.40)$$

The solutions are given by $f_{k \geq 1}(Z) = \sqrt{2} \cos(k\pi Z)$, $\lambda_k = k^2\pi^2$, $f_0(Z) = 1$ and $\lambda_0 = 0$. The basis f_k is orthonormal with respect to the scalar product, meaning that $\langle f_k, f_j \rangle_Z = \delta_{k,j}$, where $\delta_{k,j}$ is the Kronecker symbol. The solution for C_0 is:

$$C_0(Z, T) = \sum_{k \in \mathbb{N}} a_{0,k} f_k(Z) \exp(-\lambda_k T), \quad a_{0,k} = \langle f_k, C_0 \rangle_Z. \quad (6.41)$$

The first moment can be solved in the same manner, and follows the Eq.(6.37) for $p = 1$:

$$\frac{\partial C_1}{\partial T} - \frac{\partial^2 C_1}{\partial Z^2} = \text{Pe} V(Z) C_0(Z, T), \quad C_1(Z, 0) = 0. \quad (6.42)$$

Following Ref. [243], we seek solutions of the form:

$$C_1(z, t) = \text{Pe} \sum_{k \in \mathbb{N}} \left[\left(\gamma_{1,k} a_{0,k} T + a_{1,k} \right) f_k(Z) + a_{0,k} \phi_k(Z) \right] \exp(-\lambda_k T), \quad (6.43)$$

where $\phi_k(Z)$ are solutions of the eigenvalue problem :

$$-\left(\lambda_k + \frac{d^2}{dZ^2} \right) \phi_k(Z) = (V(z) - \gamma_{1,k}) f_k(Z), \quad \phi_k'(0) = \phi_k'(1) = 0. \quad (6.44)$$

One possibility to find ϕ_k is to project it on the basis $(f_j)_{j \in \mathbb{N}}$ as $\phi_k(Z) = \sum_{j \in \mathbb{N}} \beta_{j,k} f_j(Z)$. After multiplying Eq. (6.44) by $\langle f_j, \cdot \rangle_Z$, in the bra-ket framework, we can express the matrix elements $\beta_{j,k}$ and $\gamma_{1,k}$ as:

$$\beta_{j,k} = (1 - \delta_{j,k}) \frac{\langle f_j, u, f_k \rangle_Z}{\lambda_j - \lambda_k}, \quad \gamma_{1,k} = \langle f_k, u, f_k \rangle_Z. \quad (6.45)$$

Any values of the diagonal terms $\beta_{k,k}$ are allowed, such that they are set to zero without loss of generality. Lastly, the coefficients $a_{1,k}$ can be found using the initial condition, as $a_{1,k} = -\sum_{j \in \mathbb{N}} a_{0,j} \beta_{k,j}$. At the end, we can factorize C_1 and write it with a double sum as:

$$C_1(Z, T) = \text{Pe} \sum_{k,j \in \mathbb{N}^2} \left[\left(\gamma_{1,k} a_{0,k} T + a_{1,k} \right) \delta_{k,j} + a_{0,k} \beta_{j,k} \right] f_j(Z) \exp(-\lambda_k T). \quad (6.46)$$

The knowledge of the first two moments is sufficient to compute the dispersion coefficient. Integrating Eq. (6.38) to get $M_1(T)$ and $M_2(T)$, we can express the time-dependent dispersion coefficient as:

$$\begin{aligned} \left(\frac{D_x}{D_0} - 1 \right) \text{Pe}^{-2} = T^{-1} \sum_{k,j \in \mathbb{N}^2} & \left[\left(\gamma_{1,k} a_{0,k} T + a_{1,k} \right) \delta_{j,k} + a_{0,k} \beta_{j,k} \right] \langle V, f_j \rangle_Z g_1(k, T) \\ & - \gamma_{1,k} a_{0,k} \delta_{j,k} \langle V, f_j \rangle_Z g_2(k, T) \\ & - \frac{1}{2} a_{0,k} a_{0,j} \langle V, f_k \rangle_Z \langle V, f_j \rangle_Z g_1(k, T) g_1(j, T), \end{aligned} \quad (6.47)$$

where the auxiliary functions $g_1(k, T)$ and $g_2(k, T)$ are defined as:

$$g_1(k, T) = \begin{cases} T & \text{if } k = 0 \\ \frac{1 - \exp(-\lambda_k T)}{\lambda_k} & \text{if } k > 0 \end{cases}, \quad (6.48)$$

$$g_2(k, T) = \begin{cases} \frac{1}{2}T^2 & \text{if } k = 0 \\ \frac{T}{\lambda_k} + \frac{\exp(-\lambda_k T) - 1}{\lambda_k^2} & \text{if } k > 0 \end{cases}. \quad (6.49)$$

The solution given by Eq. (6.47) is valid for any flow profile and any initial concentration profile in 1d. To calculate the particular solutions for a linear shear flow $V(Z) = 2Z$ and uniform distributions defined in Eq. (6.33) for the dot, half-line, and line conditions, we inject $V(Z) = 2Z$, and find:

$$\gamma_{1,0} = 1, \quad \text{and} \quad \gamma_{1,k \geq 1} = \int_0^1 2 \cos^2(\pi k Z) 2Z \, dZ = 1, \quad (6.50)$$

$$\psi_0 = \langle V, f_0 \rangle_Z = 1, \quad (6.51)$$

$$\psi_{k \geq 1} = \langle V, f_k \rangle_Z = \int_0^1 \sqrt{2} \cos(\pi k Z) 2Z \, dZ = -\frac{2\sqrt{2} \left(1 - (-1)^k\right)}{\pi^2 k^2}, \quad (6.52)$$

$$\beta_{0,k} = \frac{\int_0^1 \sqrt{2} \cos(\pi k Z) 2Z \, dZ}{\lambda_0 - \lambda_k} = -\frac{\psi_k}{\lambda_k} = -\beta_{k,0}, \quad (6.53)$$

$$\begin{aligned} \beta_{j \geq 1, k \geq 1} &= \frac{\int_0^1 2 \cos(\pi k Z) \cos(\pi j Z) 2Z \, dZ}{\lambda_j - \lambda_k} \\ &= -\frac{2}{\pi^2(j^2 - k^2)} \left[\frac{1 - (-1)^{j-k}}{\pi^2(j-k)^2} + \frac{1 - (-1)^{j+k}}{\pi^2(j+k)^2} \right]. \end{aligned} \quad (6.54)$$

Then, we can evaluate the coefficients $a_{0,k}$ and $a_{1,k}$ that depend on the initial concentration field $C_i(Z)$. Considering uniform distributions, we find:

$$a_{0,0} = 1, \quad a_{0,k > 0} = \sqrt{2} \cos(k\pi \langle Z_i \rangle_Z) \operatorname{sinc}\left(\frac{k\pi n}{2}\right), \quad a_{1,k} = -\sum_{j \in \mathbb{N}} a_{0,j} \beta_{k,j}, \quad (6.55)$$

where $\langle Z_i \rangle_Z$ and n are defined as in Eq. (6.33) and $\operatorname{sinc}(x) = \sin(x)/x$. Inserting Eqs. (6.50), (6.53), and (6.55) in Eq. (6.47) allows us to calculate the dispersion coefficients at all times.

6.3.3 Langevin simulations

The advection-diffusion equation (see Eq. (6.35)) corresponds to the Fokker-Planck equation associated with the stochastic differential equations for the position of the center of mass of a particle, described with its coordinates X and Z . The stochastic differential equations are:

$$\frac{dX}{dt} = \text{Pe}V(Z(T)) + \sqrt{2}\xi_X(T) \quad (6.56a)$$

$$\frac{dZ}{dt} = \sqrt{2}\xi_Z(T) \quad (6.56b)$$

where ξ_X and ξ_Z are Gaussian white noises, such that $\langle \xi_i(T) \rangle = 0$ and $\langle \xi_i(T)\xi_j(T') \rangle = \delta_{i,j}\delta(T - T')$, where $(i, j) = (X, Z)$. Here, we perform numerical integrations of overdamped Langevin equations Eq. (6.56) as an alternative method to the short-time and moment theories. The Langevin equations are first written in the Itô sense [297], and we use the following discrete Euler scheme:

$$X(T + \delta T) = X(T) + \text{Pe}V(Z(T))\delta T + \sqrt{2\delta T}S(0, 1) \quad (6.57a)$$

$$Z(T + \delta T) = Z(T) + \sqrt{2\delta T}S(0, 1) , \quad (6.57b)$$

where $S(0, 1)$ is a random variable drawn from a Gaussian distribution with zero mean and unit variance, and δt is the numerical time step [298]. Reflective conditions are used at the boundaries of the domain, *i.e.* $Z = 0$ and $Z = 1$. Typically, 10^4 trajectories are generated to get large enough statistics, with a time step $\delta T = 10^{-4}$, and the dispersion coefficient is defined as $\mathcal{D}_x(\tau) = \text{var}[X_k]/(2\tau)$, where var is the variance of the particle positions X_k , and τ is the simulation time. The insets in each panel of Fig. 6.7 illustrate the Langevin simulations with initial conditions, trajectories and snapshots for several particles, along with the reflecting boundaries.

6.3.4 Results

Figure 6.7 summarises the theoretical and computational results described above. First, symbols show the reduced dispersion coefficients obtained from the Langevin simulations for the (a) dot, (b) half-line and (c) line conditions. These results show an initial increase with time, and a plateau reached at long times. This observation is consistent with the general trends observed in the experimental results of Fig. 6.6(c). Horizontal, black dashed lines show the asymptotic long-time limit for a linear shear flow, the prefactor value of $1/30$ shown in Eq. (6.28), also consistent with the experimental data.

The solid black lines show our implementations of the Chatwin theory expressed by Eq. (6.34) for the values of n indicated in the insets. A null variance, the dot condition, of the initial distribution arises if all particles start at the same altitude. For this condition, the classical τ^2 dependence [287, 288, 289, 290, 291, 292, 293, 294] for the reduced short-time dispersion coefficient is recovered. This quadratic dependence reflects a steadily increasing diversity of newly sampled velocities contributing to the enhanced dispersion. For non-vanishing initial variance, the early-time reduced dispersion coefficient

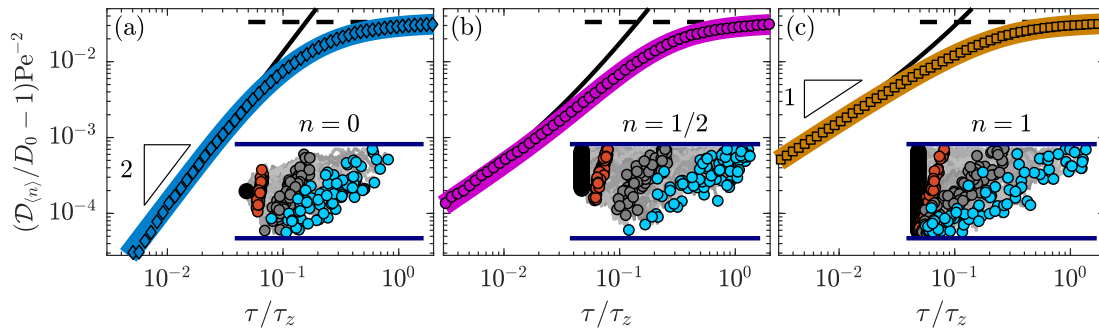


Figure 6.7: Dispersion from theory and simulations. Reduced dispersion coefficients as functions of dimensionless time obtained from the Langevin simulations, Eqs. (6.57a) and (6.57b) studied for fractions (a) $n = 0$, (b) $n = 1/2$, and (c) $n = 1$ of the channel height. The black dashed and solid lines respectively correspond to the asymptotic behaviors for the long- and short-time regimes predicted by Eqs. (6.28) and (6.34). The solid colored lines show the dispersion coefficients predicted by Eq. (6.47) from the moment theory for the corresponding initial conditions. The insets schematically show three instants of particle trajectories advected from the associated observation zone in a linear shear flow and with diffusion in z . The slope triangles in (a) and (c) respectively denote power-law exponents 2 and 1.

has a linear temporal evolution. This linear behavior for extended distributions results from particles at different altitudes transported over different distances by the linear shear flow. At times longer than the crossover time $\tau_C = 3(\langle z_i^2 \rangle - \langle z_i \rangle^2)/(2D_0)$ — obtained by setting the linear and quadratic terms of Eq. (6.34) to be equal — a quadratic time dependence is recovered. When the initial variance is small with respect to H^2 , this crossover occurs before the Taylor plateau is reached.

Lastly, colored solid lines show the full dynamic using the moment theory, expressed in Eq. (6.47). For all initial conditions depicted in Fig. 6.7, the moment solution captures the full dynamics of the dispersion accessed by the Langevin simulations and is consistent with the two asymptotic behaviors described by the long-time Taylor description and the short-time Chatwin theory. While the moment theory has the advantage to describe the dispersion for all time scales, we note that the asymptotic solution based on Chatwin’s work [265] provides a simpler picture concerning the effect of the initial conditions in the short-time regime.

6.3.5 Comparison with experiments

Having reported the theoretical predictions in the particular case of a linear shear flow, we now compare them with our experimental measurements. In Fig. 6.8(a), we show the reduced dispersion coefficient \overline{D}_x normalized by the squared Péclet number Pe^2 as a function of the dimensionless lag time, τ/τ_z . Remarkably, the data of Fig. 6.6(c), along

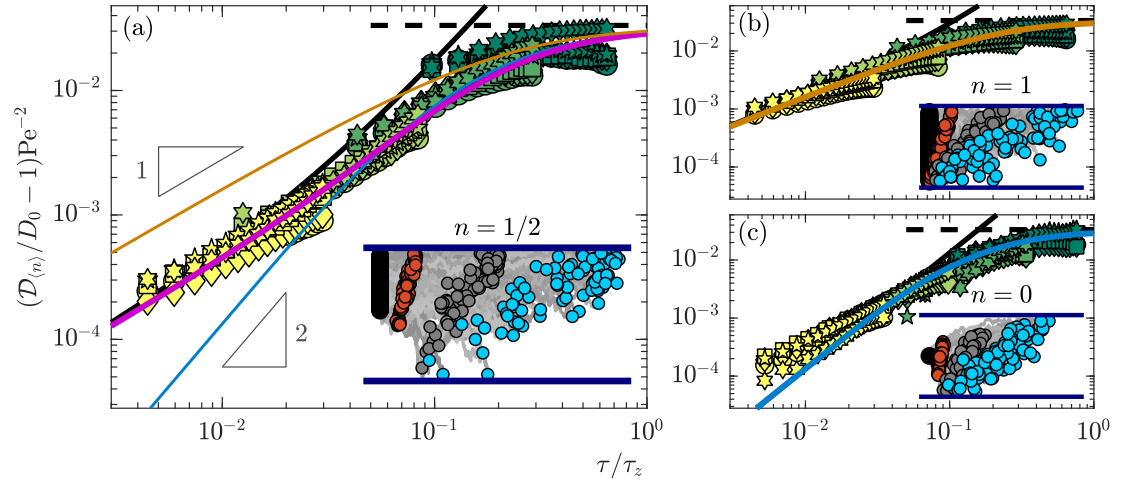


Figure 6.8: Reduced dispersion coefficients as functions of dimensionless time for all shear rates and D_0 studied, and for fractions (a) $n = 1/2$, (b) $n = 1$, and (c) $n = 0$ of the observation zone. The bulk diffusion coefficients, D_0 , for the data from dark green to yellow are identical to those in Figs. 6.4(c) and (d). The black dashed and solid lines respectively correspond to the asymptotic behaviors for the long- and short-time regimes predicted by Eqs. (6.28) and (6.34). The colored wide lines show the dispersion coefficients predicted by Eq. (6.47) from the moment theory for the $n = 1/2$, $n = 1$ and $n = 0$ conditions. (a) contains the three cases (b) and (c) only contain the corresponding solution. The insets schematically show three instants of particle trajectories advected from the associated observation zone in a linear shear flow and with diffusion in z . The slope triangles in (a) denote power-law exponents 1 and 2.

with that for experiments implementing four other shear rates per D_0 , still collapse onto a single master curve. As can be seen, there is a remarkable agreement between the experimentally measured dispersion coefficient and the moment theory given by Eq. (6.47) for the half-line condition, with $n = 1/2$. As explained in Section 6.2.5, the average dispersion \overline{D}_x is built with small z -ranges of 30 nm for a total z -range of approximately 700 nm. Thus, it is perhaps surprising to find an agreement between a nominal value of $n = 30/700 \approx 0.043$ and the half-line condition. However, we recall that a range of *apparent* altitudes defined by $z = a + \Pi \ln(I_0/I)$ is selected, which are not precisely the *real* altitudes. As detailed in section 6.2.2, the particle intensity is a function of the altitude, depth of field and position of the objective, as well as the particle size. With such ingredients, we can show numerically that a narrow distribution of apparent altitudes actually corresponds to a larger and non-uniform distribution of real altitudes. For the case selected here, $n = 1/2$ gives the best description of the data, in particular showing the power-law transition at early times and the long-time saturation.

In order to test the analytical models, we again leverage the depth resolution of the TIRFM method to select different initial distributions. First, we choose the line condition illustrated in the inset of Fig. 6.8(b). We thus study the dispersion coefficients for all observed particles, meaning that we consider the global distributions of Fig. 6.4(b). The reduced dispersions measured for this condition, as shown in Fig. 6.8(b), are systematically above the previous half-line condition shown in Fig. 6.8(a). This confirms the theoretical prediction that the short-time regime is modified because particles initially leave from an extended region of space. Moreover, the results are in quantitative agreement with the full-time moment theory, and in particular demonstrates the early-time, linear-power predicted by Chatwin [265]. Similarly, we consider particles leaving from a narrow altitude range, thus approaching the dot condition (inset of Fig. 6.8(c)). In Fig. 6.8(c) is shown the corresponding temporal evolution of the reduced dispersion coefficient for particles leaving from $z_1/H = 0.21 \pm 0.02$. While the data does not reach exactly the theoretical prediction at early times for the dot condition due to the polydispersity of the particles (and thus non-unique altitudes for a given intensity [277], as described above for the half-line condition), it is systematically below the one for the half-line condition and approaches the τ^2 asymptotic behavior predicted by Eq. (6.34) and the moment theory with $n = 0$ in Eq. (6.55). The data analysis and analytical theory, for three different initial particle distributions using the same measurement data, demonstrate the crucial role of the initial particle distribution for the short-time dispersion.

6.3.6 Absorbing boundary condition at the top wall

So far, all the modeling was done under the assumption of reflecting boundary conditions at both boundaries, *i.e.* $z = 0, H$, as if the particles were in a closed channel of size H . This is an oversimplified view of the experiment as the trajectories that are captured by the TIRFM method only involve the particles that stay in the observation zone within the observation time (see Fig. 6.1d)). Here, we discuss this simplification and we study why the model captures the data so accurately. To do so, we perform Langevin simulations using Eqs. (6.57), but modifying the boundary conditions. As a first attempt, we run a simulation with N_{part} particles, and at each time step, all particles that diffuse above the upper boundary, *i.e.* $z(t + \delta t) > H$, are removed. In this framework, the number of particles is not conserved over time. The dispersion coefficient is then computed with the particles that remain in the observation zone. The boundary condition at the top interface is therefore analogous to an absorbing condition.

Figure 6.9 compares the dispersion in the setting described in the latter paragraph with the results from section 6.3.4 in a channel with reflecting boundary conditions at both walls. The gray symbols show the reduced dispersion coefficients obtained from the Langevin simulations with initial conditions identical to the ones in Figs. 6.7a)-c) respectively, but with an absorbing condition at the boundary $z = H$. The solid lines display the results from the moment theory of section 6.3.2, as in Fig. 6.7. The dispersion coefficients with absorbing and reflecting conditions exhibit similar time

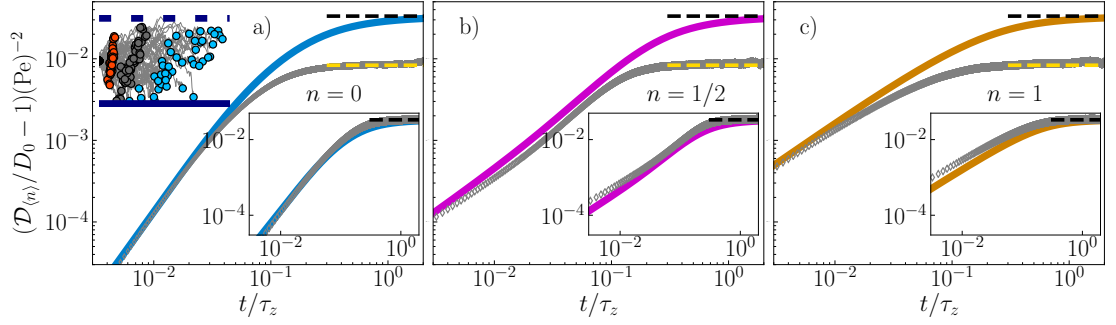


Figure 6.9: Reduced dispersion coefficients as functions of dimensionless time obtained from the Langevin simulations (gray dots), from Eqs. (6.57a) and (6.57b), for fractions (a) $n = 0$, (b) $n = 1/2$, and (c) $n = 1$ of the channel height. Here, the particles that leave the observation zone at $z = H$ are systematically removed and the dispersion coefficient are computed with the particles that remain in $[0, H]$. The black dashed lines correspond to the asymptotic behaviors for the long-time regime predicted by Eqs. (6.28). The yellow dashed lines display a coefficient $1/120$ that is found empirically to fit the long-time regime of the absorbing condition. The solid colored lines show the dispersion coefficients predicted by Eq. (6.47) from the moment theory with reflecting boundary conditions at both boundaries and for the corresponding initial conditions, as in Fig. 6.7. The inset in the top left corner of a) schematically shows three instants of particle trajectories advected in a linear shear flow and with diffusion in z . The blue solid (resp. dashed) lines represent reflecting (resp. absorbing) boundary conditions. The insets in the bottom right corner display the same Langevin simulation data, where the x and y axes are rescaled with an effective channel height $H/\sqrt{2}$.

dependencies. At short times, they follow a quadratic dependence with time for a dot condition $n = 0$ in a), and a linear dependence for initial conditions with a non-zero variance as in b) and c). At long times, the dispersion coefficients reach constant values that do not depend on the initial condition and which are significantly smaller than for the theoretical Taylor-Aris results, *i.e.* $1/30$, that is shown with black dashed lines. The yellow dashed lines display a $1/120 \approx 0.008333$ coefficient that is in fair agreement with the long-time dispersion coefficients. We note that an exact calculation has been performed by David Dean from Univ. Bordeaux (private communication) and predicts a dispersion coefficient $\mathcal{D}_x^{\text{abs}}$ with an absorbing boundary condition, which reads:

$$\left(\frac{\mathcal{D}_x^{\text{abs}}}{D_0} - 1\right)(\text{Pe})^{-2} = \frac{240 - 12\pi^2 - \pi^4}{3\pi^6} \approx 0.00837526, \quad (6.58)$$

where the superscript abs stands for absorbing. Equation. (6.58) is in agreement with the numerical simulations.

We recall that both the Péclet number Pe and the diffusion time τ_z scale with H^2 , such that the long-time dispersion coefficient actually scales with H^4 . Therefore, the

long-time dispersion coefficient with absorbing conditions is roughly equivalent to the one of a closed channel that has an effective height \tilde{H} that follows $H^4/4 \approx \tilde{H}^4$, or equivalently $\tilde{H} = H/\sqrt{2} \approx 0.7H$. In the bottom right insets of Figs. 6.9a-c), we display the same Langevin simulation data but with the x and y axes rescaled by the effective height \tilde{H} equal to 70% of the actual height. The theoretical solid lines are unchanged. By construction, the long-time dispersion plateaus of the dispersion match in both reflecting and absorbing conditions. Furthermore, with this rescaled axis, the agreement between both models on the full dynamics is fair. A small difference is observed in the small-time asymptotic limit for the $n = 1/2$ and $n = 1$ initial conditions.

As a partial conclusion, the resemblance of the dispersion curves for the two possible boundary conditions at the top wall justifies that the model with an unphysical reflecting boundary condition at $z = H$ is acceptable to describe the experimental data extracted from the TIRFM measurements. As a matter of fact, the channel height which is fitted in Fig. 6.8 to rescale the experimental data is $H \approx 500$ nm, which is smaller than the actual size of the observation zone that is $H \approx 700$ nm. This comforts the statement that a closed channel with an effectively smaller height could describe the TIRFM experiments.

6.4 Finite-size particles

In the previous section, the particles were considered as tracer particles that both diffuse and are advected in a shear flow. However, as discussed previously in the chapter, the dynamics of nanoparticles in the perpendicular directions to the wall is affected by their interactions with the walls. In this section, we refine the theoretical description to account for these interactions.

6.4.1 Dynamics of a colloid

In colloidal physics, electrostatic interactions often play a key role as colloidal particles often carry electrical charges. We consider that both the colloidal particles and the glass surfaces are negatively charged in the TIRFM experiment. Notably, the electrostatic repulsion is important in suspensions for the stabilization as it prevents the aggregation of colloids. The standard way to describe electrostatic interactions in a solvent is through the double-layer theory, in which the surface of interest is assumed to carry a uniform surface charge and attracts the counter-ions surrounding the surface, leading to a screening of the surface charge. The interaction between a charged spherical colloid and a planar surface can be described through Debye–Hückel theory via the potential given in Eq. (6.21). The main feature is that the interaction potential takes the form of an exponentially decaying function $\phi_{\text{el}}(z) \propto \exp(-(z-R)/l_{\text{D}})$, where the decay length $l_{\text{D}} = \sqrt{\epsilon k_{\text{B}} \Theta / (2c_{\text{s}} e^2)}$ is the Debye length, and c_{s} is the salt concentration. Thus, at a large salt concentration, the Debye length is small and the electrostatic repulsion is effectively weak because of the large screening of the surface charges. As an example, the addition of salt destabilizes colloidal suspensions, in which the particles make

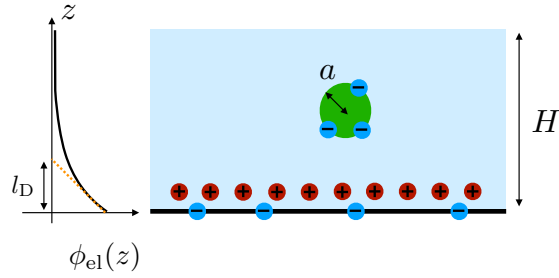


Figure 6.10: Schematic of a spherical colloid in a channel of apparent height H . In the experimental system, both the nanoparticle and the glass surfaces are negatively charged as indicated with blue circles, which results in electrostatic interactions between the surfaces. The interaction potential is described with the double layer theory, in which counter ions (red circles) are adsorbed at the surface and screen the surface charge. The shape of the interaction potential is shown in left and decays on a typical length scale l_D .

aggregates (a popular illustration of this phenomenon is e.g. the precipitation-induced formation of fresh-water river deltas near salted seas and oceans). We stress that van der Waals interactions between the surfaces may also play a role. These are attractive in most practical cases and take the form of an additional interaction potential $-AR/(6z)$, where A is the Hamaker constant. However, van der Waals interactions are important at small distances (typically few tens of nanometers). As a first step, we ignore them.

Besides, the Brownian dynamics of a colloidal particle is affected by the presence of a boundary due to hydrodynamic interactions. As discussed in Chapter 2, in an infinite space, a spherical particle that moves in a fluid with a velocity U is submitted to the Stokes drag force $-6\pi\eta RU$. Thus, a Brownian particle, that is displaced in an unbounded fluid via thermal motion, dissipates thermal energy via friction. The diffusion constant, which characterizes the intensity of the Brownian motion, follows the Stokes-Einstein law $D_0 = k_B\Theta/(6\pi\eta R)$, reflecting the balance between thermal energy and friction in the system. Close to a boundary, e.g. for a sphere near a plane wall, the friction force: i) depends on the sphere-wall distance relative to the sphere radius and increases as the sphere gets closer to the wall; ii) is anisotropic as it is more favorable for a sphere to move tangentially to the wall instead of normally to the wall. Therefore, the Brownian dynamics of a sphere near a wall can be described with two space-dependent diffusion coefficients [285], that reads:

$$\frac{D_x(z)}{D_0} \simeq 1 - \frac{9}{16} \frac{R}{z} + \frac{1}{8} \left(\frac{R}{z}\right)^3 - \frac{45}{256} \left(\frac{R}{z}\right)^4 - \frac{1}{16} \left(\frac{R}{z}\right)^5, \quad (6.59a)$$

$$\frac{D_z(z)}{D_0} \simeq \frac{6(z-R)^2 + 2(z-R)R}{6(z-R)^2 + 9(z-R)R + 2R^2}, \quad (6.59b)$$

where z denotes the altitude of the center of the sphere with respect to the wall defined by $z = 0$, and R is the sphere radius. In fact, there is no simple analytical expression for

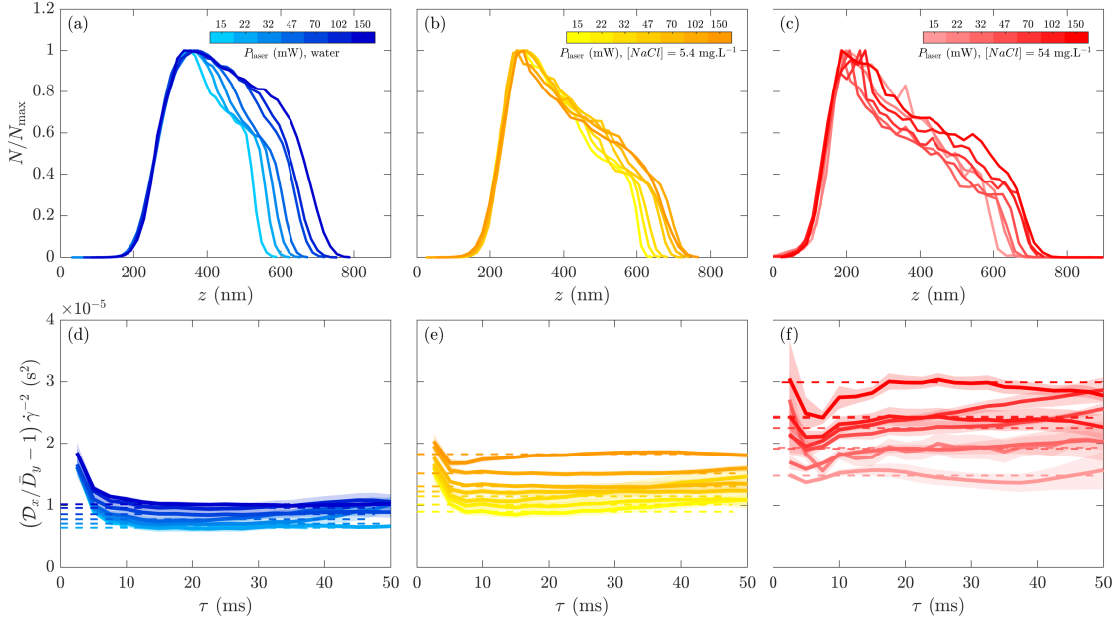


Figure 6.11: a) - c) Distributions of apparent altitudes of the particles in TIRFM experiments. The distributions are not normalized and we plot the number of particles detected in bins of size 15 nm, rescaled by the maximum number of particles in a bin. The power of the laser is varied and indicated with the colorscale. The used fluids are ultra-pure water in a) and sodium chloride (NaCl) solutions of concentration 5.4 and 54 mg/L in b) and c) respectively. d) - f) Reduced dispersion coefficients versus rescaled time. The solid lines display the average dispersion coefficient over experiments with 5 shear-rates, and the shades indicate the spreading of the data.

the space-dependent diffusion coefficient, and exact solutions are only known in the form of infinite series [136, 137]. Equations (6.59) are Padé approximants of the actual expression.

Altogether, the Taylor dispersion coefficient for finite-size charged solutes in a channel is a function of three length scales as schematized in Fig. 6.10, namely the radius of the colloids, the Debye length and the channel height. A last parameter is the surface electrical charges of the particles and the wall via the prefactor of the electrostatic potential. By rewriting Eq. (6.21) as:

$$\frac{\phi_{\text{el}}(z)}{k_{\text{B}}\Theta} = \frac{a}{r_{\text{el}}} \exp\left(-\frac{z-a}{l_{\text{D}}}\right), \quad (6.60)$$

with:

$$r_{\text{el}} = k_{\text{B}}\Theta \left[16\epsilon \left(\frac{k_{\text{B}}\Theta}{e} \right)^2 \tanh\left(\frac{e\psi_{\text{p}}}{4k_{\text{B}}\Theta}\right) \tanh\left(\frac{e\psi_{\text{w}}}{4k_{\text{B}}\Theta}\right) \right]^{-1}. \quad (6.61)$$

We find another length scale r_{el} in the system. As such, the Taylor dispersion coefficient in a channel is a function of $R, l_{\text{D}}, r_{\text{el}}$, which adds a lot of complexity with respect to the simple picture in section 6.3.

We performed additional experiments to investigate the interactions of the particle with the wall, through the modification of some of these length scales. In Fig. 6.11, we display some results of TIRFM experiments in both ultra-pure water (18.2 M Ω cm, MilliQ) in panels a) and d) and in sodium chloride (NaCl) solutions of concentrations 5.4 and 54 mg/L in panels b), e) and c), f) respectively. The average nanoparticle radius is 55 nm. In Figs. 6.11a)-c), we show the distribution of the apparent altitude z of the particles, as obtained by varying the power of the laser (which is indicated with the color scale). We proceed as in Fig. 6.2: we first sort the particles into a series of intensity bins, each bin corresponding to a spatial range of approximately 15 nm in the z -direction, and we then plot the number of particles in each bin normalized by the maximum number of particles in one bin. In this way, the distributions are not normalized but we can observe a collapse of all distributions for all laser powers near the wall, highlighting the electrostatic repulsion. As expected, the modification of the laser intensity only affects the particle distribution near the upper limit of the channel. Interestingly, the distributions near the wall are altered by the salt concentration, in such a way that particles closer to the wall are observed in concentrated solutions. Using the method described in section 6.2.2, we can fit a potential Eq. (6.21) and find Debye lengths that are 60, 31.6 and 10 nm in a)-c) respectively. As expected, the Debye length decreases with increasing salt concentration, and we find a good agreement with the law $l_{\text{D}} = 0.304/\sqrt{[\text{NaCl}]}$, where l_{D} and $[\text{NaCl}]$ are expressed in nm and mol/L respectively, which is valid for monovalent ions at room temperature [299]. Furthermore, the laser power modifies the effective height of the observation zone. Indeed, a particle is detected under the microscope if its fluorescence intensity exceeds a certain threshold that is limited by the background noise and the sensitivity of the microscope. The fluorescence intensity is proportional to the intensity of the laser, and thus decreases as the laser power decreases, which limits the observation zone.

In Figs. 6.11d)-f), we display the reduced dispersion coefficient versus time with the same color code as in Figs. 6.11a)-c). In contrast with Fig. 6.8, the dispersion coefficient is not rescaled by a channel size H , but is rescaled by the squared shear rate of the flow. In most of the time range of the experiments presented here, the dispersion coefficient has reached the long-time plateau value and does not depend on time. We observe that the dispersion coefficient systematically increases with the laser power. Indeed, the size of the observation zone increases with the laser power, which results in a larger range of accessible velocities for the particles and thus larger dispersion. Moreover, the dispersion also increases with the salt concentration. Again, the strength of the electrostatic repulsion between the particle and the wall decreases with the salt concentration, such that the particles access a larger range of altitudes and velocities.

6.4.2 Moment theory for finite-size charged colloids

The moment theory has been very successful at describing the Taylor dispersion, including the intermediate times. The advection-diffusion equation (see Eq. (6.4)) for the solute concentration field is equivalent to the Fokker-Planck equation that describes the dynamics of the probability density function of a particle. Here, we suppose that the particles are spheres of radius a placed in a 2d closed channel. We assume that the particle is advected in a shear flow of velocity field $v_x(z) = \dot{\gamma}z$, with an external potential $\phi(z)$ (e.g. electrostatic interactions) and with a space and orientation dependent diffusion coefficient. The Fokker-Planck equation describing such a process, written in terms of solute concentration, reads [252, 295]:

$$\frac{\partial c}{\partial t} + v_x(z) \frac{\partial c}{\partial x} = D_x(z) \frac{\partial^2 c}{\partial x^2} + \frac{\partial}{\partial z} \left(D_z(z) \left[\frac{\partial c}{\partial z} + \frac{\phi'(z)}{k_B \Theta} c \right] \right), \quad (6.62)$$

To mimic the experimental system, we assume a rigid wall at $z = 0$, such that the diffusion coefficients can be described with Eqs. (6.59). The impermeability condition at the wall imposes that the flux vanishes, which reads:

$$D_z(z) \left[\frac{\partial c}{\partial z} + \frac{\phi'(z)}{k_B \Theta} c \right] = 0, \quad (6.63)$$

at $z = a$, where the sphere is in contact with the bottom wall. At the top boundary, that is defined by $z = H$ we also assume no-flux for the sake of simplicity (see section 6.3.6). We note that, at equilibrium, the steady state solution of the Fokker-Planck equation is given by the Boltzmann distribution, which gives for the 1d concentration:

$$c_B(z) = \frac{\exp\left(-\frac{\phi(z)}{k_B \Theta}\right)}{\int_a^H \exp\left(-\frac{\phi(z)}{k_B \Theta}\right) dz}. \quad (6.64)$$

We assume that the initial distribution is localized at a given x position, through $c(x, z, t = 0) = c_i(z) \delta(x)$, and that the concentration vanishes at $|x| \rightarrow \infty$ such that $\lim_{x \rightarrow \pm\infty} x^\mu \partial_x^\nu c = 0$ for arbitrary integers μ, ν . The moments of the distribution are defined in the same way as in section. 6.3.2:

$$c_p(z, t) = \int_{\mathbb{R}} x^p c(x, z, t) dx \quad \text{and} \quad m_p(t) = \int_a^H c_p(z, t) dz. \quad (6.65)$$

The recursive equations satisfied by c_p and m_p can be obtained from Eq. (6.62) and are:

$$\left(\frac{\partial}{\partial t} - \frac{\partial}{\partial z} \left(D_z(z) \left[\frac{\partial}{\partial z} + \frac{\phi'(z)}{k_B \Theta} \right] \right) \right) c_p(z, t) = p(p-1) D_x(z) c_{p-2}(z, t) + p v_x(z) c_{p-1}(z, t), \quad (6.66)$$

$$\frac{dm_p(t)}{dt} = p(p-1) \langle D_x, c_{p-2} \rangle_z + p \langle v_x, c_{p-1} \rangle_z. \quad (6.67)$$

Here again, the zeroth moment is constant. Without loss of generality, we assume the initial concentration to be normalized such that $m_0(t) = 1$, and c_0 verifies the following partial differential equation and initial condition:

$$\left(\frac{\partial}{\partial t} - \frac{\partial}{\partial z} \left(D_z(z) \left[\frac{\partial}{\partial z} + \frac{\phi'(z)}{k_B \Theta} \right] \right) \right) c_0(z, t) = 0, \quad c_0(z, t = 0) = c_i(z). \quad (6.68)$$

We search for a separable solution, and inject the ansatz $c_0(z, t) = f(z) \exp(-\lambda t)$ and get:

$$\left[\lambda + \frac{d}{dz} \left(D_z(z) \left[\frac{d}{dz} + \frac{\phi'(z)}{k_B \Theta} \right] \right) \right] f(z) = 0, \quad (6.69)$$

together with the boundary conditions:

$$D_z(z) \left[\frac{d}{dz} + \frac{\phi'(z)}{k_B \Theta} \right] f(z) = 0, \quad z = a, H. \quad (6.70)$$

The eigenvalue problem of Eqs. (6.69) and (6.70) form a Sturm-Liouville problem which has a countable ensemble of solutions $(\lambda_{\phi,k}, f_{\phi,k}(z))_{k \in \mathbb{N}}$, where the trivial solution $\lambda_{\phi,0} = 0$ is the Boltzmann distribution $f_{\phi,0}(z) = c_B(z)$, and where $0 < \lambda_{\phi,1} < \lambda_{\phi,2} < \dots < \infty$. The eigenvalues are orthonormal under the definition of the scalar product $\langle f, g \rangle_\phi = \int_a^H f(z)g(z)c_B^{-1}(z) dz$. Following the calculation in section 6.3.2, we get:

$$c_0(z, t) = \sum_{k \in \mathbb{N}} a_{0,k} f_{\phi,k}(z) \exp(-\lambda_{\phi,k} t), \quad a_{0,k} = \langle f_{\phi,k}, c_i \rangle_\phi. \quad (6.71)$$

Then, the governing equation for the first moment c_1 is:

$$\left(\frac{\partial}{\partial t} - \frac{\partial}{\partial z} \left(D_z(z) \left[\frac{\partial}{\partial z} + \frac{\phi'(z)}{k_B \Theta} \right] \right) \right) c_1(z, t) = v_x(z) c_0(z, t), \quad c_1(z, t = 0) = 0. \quad (6.72)$$

Following section 6.3.2, the latter equation can be solved using the same method and reads:

$$c_1(z, t) = \sum_{k,j \in \mathbb{N}^2} \left[\left(\gamma_{1,k} a_{0,k} t + a_{1,k} \right) \delta_{k,j} + a_{0,k} \beta_{j,k} \right] f_{\phi,j}(z) \exp(-\lambda_{\phi,k} t), \quad (6.73)$$

with:

$$\beta_{j,k} = (1 - \delta_{j,k}) \frac{\langle f_{\phi,j}, v_x, f_{\phi,k} \rangle_\phi}{\lambda_{\phi,j} - \lambda_{\phi,k}}, \quad \gamma_{1,k} = \langle f_{\phi,k}, v_x, f_{\phi,k} \rangle_\phi, \quad a_{1,k} = - \sum_{j \in \mathbb{N}} a_{0,j} \beta_{k,j}. \quad (6.74)$$

Finally, integrating Eq. (6.67) for $p = 1$ and $p = 2$, we can compute the dispersion coefficient $\mathcal{D}_x(t) = \frac{m_2(t) - m_1^2(t)}{2t}$, and we get:

$$\begin{aligned}
\mathcal{D}_x = & \frac{1}{t} \sum_{k \in \mathbb{N}} a_{0,k} \langle c_B D_x, f_{\phi,k} \rangle_{\phi} g_1(k, t) \\
& + \frac{1}{t} \sum_{k,j \in \mathbb{N}^2} \left[\left(\gamma_{1,k} a_{0,k} t + a_{1,k} \right) \delta_{j,k} + a_{0,k} \beta_{j,k} \right] \langle c_B v_z, f_{\phi,j} \rangle_{\phi} g_1(k, t) \\
& - \gamma_{1,k} a_{0,k} \delta_{j,k} \langle c_B v_x, f_{\phi,j} \rangle_{\phi} g_2(k, t) \\
& - \frac{1}{2} a_{0,k} a_{0,j} \langle c_B v_x, f_{\phi,k} \rangle_{\phi} \langle c_B v_x, f_{\phi,j} \rangle_{\phi} g_1(k, t) g_1(j, t).
\end{aligned} \tag{6.75}$$

6.4.3 Long-time dispersion coefficient

In the same way as for tracer particles, the dispersion coefficient reaches a constant value at long times, when the particle have sampled all the positions of the channel. Here, we use the generalized Taylor dispersion theory, following Ref. [295], to compute an analytical expression for the long-time dispersion coefficient.

We can rewrite the zeroth moment of the concentration by extracting the steady-state term, $c_0(z, t) = a_{0,k} c_B(z) + \sum_{k \in \mathbb{N}^*} a_{0,k} f_{\phi,k}(Z) \exp(-\lambda_{\phi,k} T)$. In the long-time limit, which means here times larger than the slowest relaxing mode, *i.e.* $t \gg \frac{1}{\lambda_{\phi,1}}$, the concentration can be approximated as:

$$c_0(z, t) \simeq c_B(z) + O[\exp(-\lambda_{\phi,1} t)], \tag{6.76}$$

where we used $a_{0,k} = 1$ so that it is consistent with the choice $m_0(t) = 1$. Introducing the approximate long-time expression in Eq. (6.72), we find:

$$\left(\frac{\partial}{\partial t} - \frac{\partial}{\partial z} \left(D_z(z) \left[\frac{\partial}{\partial z} + \frac{\phi'(z)}{k_B \Theta} \right] \right) \right) c_1(z, t) \simeq c_B(z) v_x(z) + O[\exp(-\lambda_{\phi,1} t)]. \tag{6.77}$$

We search for solutions with a linear term in time, in the form $c_1(z, t) \simeq c_B(z) \left(At + B(z) \right) + O[\exp(-\lambda_{\phi,1} t)]$, and after some algebra, we find:

$$\begin{aligned}
c_1(z, t) \simeq & c_B(z) \left(\bar{v}_x t + \int_a^z \frac{dz''}{c_B(z'') D_z(z'')} \int_a^{z''} [v_x(z') - \bar{v}_x] c_B(z') dz' + \text{Const.} \right) \\
& + O[\exp(-\lambda_{\phi,1} t)],
\end{aligned} \tag{6.78}$$

where Const. is a numerical constant that is not relevant here, and $\bar{v}_x = \int_a^H v_x(z) c_B(z) dz$ is the average speed in the channel for particles distributed with the Boltzmann weight. Now, we can inject this steady solution in Eq. (6.67) for $p = 1, 2$ to get $m_1(t)$ and $m_2(t)$ and find the long-term dispersion coefficient:

$$\mathcal{D}_x = \bar{D}_x + \int_a^H dz \frac{1}{D_z(z) c_B(z)} \left(\int_0^z (v_x(z') - \bar{v}_x) c_B(z') dz' \right)^2, \tag{6.79}$$

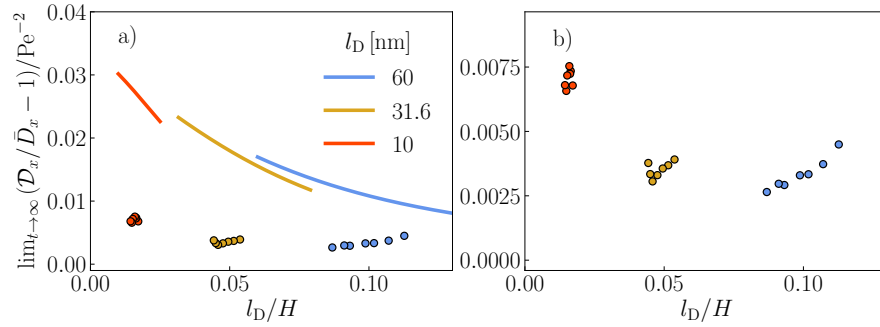


Figure 6.12: a) Long-time reduced dispersion coefficients versus the Debye length to channel height ratio for spherical particles of radius $a = 55$ nm, with a Debye–Hückel potential (see Eq. (6.21)) and hydrodynamic interactions with the wall (see Eqs. (6.59)). The colors indicate the values of the Debye length corresponding to the experiment in Fig. 6.11 where the salt concentration is varied. The solid lines show the generalized Taylor dispersion results of Eq. (6.79), where the channel size is varied in the typical range of the experiments. Circles shows the long-time reduced dispersion coefficient in the experiments. b) Zoom of the experimental data.

where $\bar{D}_x = \int_a^H D_x(z) c_B(z) dz$ is the average longitudinal diffusion coefficient. Equation. (6.79) agrees with the calculation in Ref. [252]. For tracer particles, *i.e.* $a \rightarrow 0$, and in the absence of external potential, one has $D_x(z) = D_z(z) = D_0$, and $c_B(z) = 1$. Therefore, in a linear shear flow, *i.e.* $v_x(z) = \dot{\gamma}z$, we recover the Taylor-Aris result of Eq. (6.28). Furthermore, Eq. (6.79) highlights that Taylor dispersion is not sensitive to the mean flow as a transformation $v_x \rightarrow v_x + \text{Const.}$ does not modify the dispersion. Lastly, in a linear shear flow, we find again that the reduced dispersion coefficient, that is now defined as $\mathcal{D}_x / \bar{D}_x - 1$, scales with the squared shear rate $\dot{\gamma}$.

In Appendix B, we illustrate the different methods to compute the dispersion coefficient with an example. We consider a problem simpler than the one at stake here to be analytically tractable. We consider point-like particles with a given mass and in a gravitational field. The moment theory is found to be in very good agreement with Langevin simulations in the full temporal range, as in section 6.3. The dispersion coefficient is found to reach the generalized Taylor theory expression in the long-time limit, as expected. Overall, the gravity tends reduce the Taylor dispersion, as the particles sediment and explore a smaller range of velocities.

6.4.4 Comparison with experiments

Here, we compare the dispersion coefficient obtained with the TIRFM experiments in Fig. 6.11 with the model that includes the interactions between the particles and the wall. The short-time regime and the influence of the initial conditions have already been explored in section 6.3, so that we now focus on the long-time regime, for which the initial condition is irrelevant. Thus, we take all the particles in the

channel and assume an initial concentration distributed with a Boltzmann weight. In Fig. 6.12a), we show the long-time reduced dispersion coefficient extracted from the data in Figs 6.11d)-f) versus the ratio between the Debye length and the channel height. Experimentally, the reduced dispersion coefficient is defined as $(D_x/D_y - 1)Pe^{-2}$, where D_y is the effective transverse diffusion constant (see Fig. 6.5) in order to account for the reduction of the effective diffusion constant in the channel resulting from the hydrodynamic interactions with the wall (see Eq. (6.79)), as we should have $D_y = \bar{D}_x$. The experimental channel height is estimated through the apparent altitude of the minimal detected intensity with the TIRFM, and the corresponding value is used in the definition of the Péclet number $Pe = \dot{\gamma}H^2/(2D_0)$. The particle radius a and the electrostatic radius r_{el} are fixed to 55 and 7.6 nm respectively. At a given l_D/H ratio, the theoretical curves do not collapse, as the dispersion also depends on the ratios l_D/a and l_D/r_{el} in a non-trivial way.

Qualitatively, we observe a good agreement between the experiments and the generalized Taylor theory. The long-time reduced dispersion globally decreases with increasing l_D/H . Nevertheless, for the experiments in ultra-pure water, *i.e.* $l_D = 60$ nm, the reduced dispersion coefficient seems to increase as the channel height decreases in contrast with the theoretical results. We make several remarks that might explain such deviations. First, the model assumes a reflecting boundary condition at the upper boundary, which is an unphysical assumption with respect to the actual condition for the TIRFM to detect a particle, as discussed in section 6.3.6. As a matter of fact, for tracer particles with no interactions with the wall, the ratio between the long-time dispersion coefficient in channels with absorbing and reflecting boundary conditions at the upper boundary is on the order of a factor 4 (see section 6.3.6). Here, quantitatively, we find roughly a factor 3-4 between the experiments and the generalized Taylor dispersion model with a reflecting upper boundary. Thus a model with absorbing boundary condition may give a more quantitative agreement. Second, the effective channel height is constructed via the apparent altitude of the minimal detected intensity. However, the latter might depend on the optical parameters (*e.g.* finite depth of field of the microscope) of the TIRFM, which gives some significant uncertainties on the channel height.

6.5 Conclusion

We report on an experimental, theoretical, and numerical study of advection-enhanced dispersion in 2d channels. By using evanescent wave microscopy, we make time-dependent nanometrically resolved particle dispersion measurements varying nanoparticle size, velocity gradient, salt concentration and viscosity in submicrometric near-surface flows. The experiments provide the first experimental validation of analytical models predicting the full time dynamics of Taylor dispersion. Our study particularly highlights the crucial role of the initial condition in the short time regime, for times shorter than the diffusion time. First, we experimentally demonstrate that the two regimes share the same shear-rate dependence, the shear rate being particularly large for near-surface transport. Furthermore, we reveal and characterize how the initial par-

ticle distribution affects the short-time dispersion. Specifically, we observe for the first time, the short-time, mixed-power-law behavior for the general case before reaching a crossover to the well-known long-time saturation regime for linear shear flows. In the extremal cases of *i*) full-channel observations, a linear approach in time of the dispersion coefficient to the long-time value is observed, while for *ii*) fine near-surface resolutions a quadratic temporal tendency is approached. Altogether, the experimental data are in agreement with the analytical predictions using the moment theory and results from Langevin numerical simulations for tracer particles, fitting the channel height.

The nanoparticles and the channel surfaces being negatively charged and of particles being of finite size, it results in an electrostatic repulsion and an hindered diffusion near the surface. The addition of salt in the channel screens the electrostatic interactions, so that the particles access the very near-surface in concentrated solutions. The increase of the accessible velocity-gradient region enhances the dispersion in qualitative agreement with the generalized Taylor theory. In the rich context of particle transport, such concepts should prove pertinent in quantitative prediction and observation of time-dependent, near-surface nanoparticle and solute dispersion, with applications related to microscopic biology and nanoscale technologies. This work thus sets the basis for truly nanoscale investigations of Taylor dispersion.

Conclusion & Perspectives

In this thesis, we have studied several soft matter problems by analyzing flows in the vicinity of soft and fluctuating interfaces. Here, we summarize the main conclusions and expand the perspectives of this work.

In chapter 1, we demonstrated that contactless rheological methods are efficient and robust to probe soft interfaces at micro and nanometric scales. These new tools offer great perspectives for both the modeling and the understanding of surface phenomena at small scales. In particular, the surface tension of a liquid-air interface can be determined with the bubble method described in section 1.3. In this work, we assumed that the interface response was only the result of surface tension. On the other hand, it is known that in the presence of surfactants or impurities adsorbed on the surface, fluid-fluid interfaces have a surface rheology [94, 300], which modifies multiphase flows (*e.g.* in foams). It would be interesting to pursue this and investigate whether contactless rheological methods are able to measure the interfacial rheology. Similarly, we have shown that the capillarity of solids can be measured, offering new perspectives to characterize the mechanical response of the surface of elastomers or gels and for example to understand the surprising results of chapter 3 on the leveling of thin films. Moreover, one could exploit these surface-stress measurements on a stretched elastomer to better characterize the associated Shuttleworth effect.

Chapter 2 studied the hydrodynamic forces acting on a sphere moving in the vicinity of a deformable surface. An experimental method, using colloidal-probe atomic force microscopy, was introduced to directly measure the elastohydrodynamic lift force. In viscous flows, such a lift force is allowed due to symmetry breaking of the lubricated contact between the sphere and the surface. On the other hand, a symmetry breaking can be induced by other phenomena such as slip inhomogeneity [301], or the charge distribution in electrolytes [302]. Thus potential new nanoscale lift forces generated by flows could be revealed with atomic force microscopy. From an experimental point of view, with the blooming of active matter, many designs of artificial microswimmers [303] have emerged in physics laboratories (see Appendix D for an example). The elastohydrodynamic interactions may be studied experimentally, by analyzing the dynamics of such objects in the vicinity of deformable surfaces [304].

The part II of the manuscript has been devoted to the study of the dynamics of polymer thin films and more particularly of capillary leveling in the vicinity of soft interfaces. Many questions related to polymer physics are still open and have not been addressed in this thesis. For example, we can mention the dynamics of *confined* thin films for which the film thickness is on the same order of magnitude as, or smaller than, the radius of gyration of polymers [305], glass transition temperature anomalies in nanoscale films [306] or the destabilization of films by van der Waals interactions [212]. Furthermore, at the nanoscale, thermal fluctuations (see chapter 6) are expected to dominate capillarity. Notably, fluctuations accelerate the fracture dynamics of thin films [307]. A stochastic version of the thin film equation has been recently

proposed, integrating the random constraints of the fluctuating hydrodynamics equations [308] with the lubrication approximation. Similarly, an interesting project could be to establish a stochastic version of the model describing the liquid membranes studied in chapter 5.

In the last chapter of this manuscript, we looked at the Taylor dispersion and in particular the dynamics at short times and the effect of particle-wall interactions. By exploiting the results of part I of this thesis, we could complete our study on hydrodynamic interactions by adding the possible deformation of a soft wall in the Taylor dispersion. Note however that in the presence of such interactions, the classical tools of statistical physics may not be adapted anymore (for example the Fokker-Planck equation), and thus this prospective project would be a major theoretical challenge. Moreover, the Taylor dispersion has many applications and is involved in many soft matter systems. For example, in binary mixtures, it has been shown that the dispersion of solutes influences the dynamics of a drop that evaporates [309] or spreads [310] due to buoyancy currents or Marangoni stresses, respectively.

Conclusion & Perspectives (French)

Dans cette thèse, nous avons étudié plusieurs problèmes de matière molle en analysant des écoulements au voisinage d'interfaces molles et fluctuantes. Nous résumons les principales conclusions et développons les perspectives de ce travail.

Dans le chapitre 1, nous avons démontré que les méthodes de rhéologie sans contact étaient très efficaces et robustes pour venir sonder les interfaces molles à des échelles micrométriques et nanométriques. Ces nouveaux outils offrent des perspectives intéressantes, à la fois pour la modélisation et pour la compréhension des phénomènes de surface à de petites échelles. En particulier, la tension de surface d'une interface liquide-air peut être déterminée avec la méthode des bulles décrite à la partie 1.3. Dans cette partie, nous avons supposé que la réponse de l'interface était seulement le résultat de la tension de surface. En revanche, il est connu qu'en présence de surfactants ou d'impuretés adsorbées à la surface, les interfaces fluide-fluide ont une rhéologie de surface [94, 300], ce qui modifie les écoulements multiphasiques (par exemple dans les mousses). Il serait intéressant de poursuivre dans cette voie et de regarder si les méthodes de rhéologie sans contact peuvent mesurer la rhéologie interfaciale. De même, nous avons montré que la capillarité des solides peut être mesurée, offrant de nouvelles perspectives pour caractériser la réponse mécanique de la surface d'élastomères ou de gels et par exemple comprendre les résultats surprenant du chapitre 3 sur le nivellement des films minces. En outre, on pourrait exploiter ces mesures de contraintes de surface sur un élastomère étiré, afin de mieux caractériser l'effet Shuttleworth associé.

Le chapitre 2 a étudié les forces hydrodynamiques qui s'appliquent sur une sphère se déplaçant au voisinage d'une surface déformable. Une méthode expérimentale utilisant la microscopie à force atomique avec une sonde colloïdale a été introduite pour mesurer directement la force de portance élastohydrodynamique. Dans des écoulements visqueux, une telle force de portance est permise suite à la brisure de symétrie du contact lubrifié entre la sphère et la surface. Par ailleurs, une brisure de symétrie peut être induite par d'autres phénomènes comme une inhomogénéité du glissement [301], ou la distribution de charge dans les électrolytes [302]. Ainsi de potentielles nouvelles forces de portance à l'échelle nanométrique engendrées par des écoulements pourraient être révélées avec la microscopie à force atomique. D'un point de vue expérimental, avec l'avènement de la matière active, de nombreux désigns de micronageurs artificiels [303] ont vu le jour dans les laboratoires de physique (voir Annexe D pour un exemple). Nous pouvons espérer étudier expérimentalement les interactions élastohydrodynamiques actives en analysant la dynamique de tels objets au voisinage de surface déformable [304].

La partie II du manuscrit a été consacrée à l'étude de la dynamique de films minces de polymère et plus particulièrement du nivellement capillaire au voisinage d'interfaces molles. De nombreuses questions relatives à la physique des polymères restent toujours ouvertes et n'ont pas été abordées dans cette thèse. Par exemple, nous pouvons citer la dynamique de films minces *confinés* pour lesquels l'épaisseur du film est du même ordre de grandeur ou plus petit que le rayon de giration des polymères [305], les

anomalies de la température de transition vitreuse dans les films nanométriques [306] ou encore la déstabilisation des films par les interactions de van der Waals [212]. Par ailleurs, à l'échelle nanométrique, on s'attend à ce que les fluctuations thermiques (voir chapitre 6) dominent la capillarité. En particulier, les fluctuations accélèrent la dynamique de rupture des films minces [307]. Une version stochastique de l'équation des films minces a été récemment proposée, en intégrant les contraintes aléatoires des équations de l'hydrodynamique fluctuante [308] avec l'approximation de lubrification. De la même manière, un projet intéressant pourrait être d'établir une version stochastique des membranes liquides étudiées au chapitre 5.

Dans le dernier chapitre de ce manuscrit, nous avons regardé la dispersion de Taylor et en particulier la dynamique aux temps courts et l'effet des interactions entre les particules et le mur. En exploitant les résultats de la partie I de cette thèse, on pourrait compléter notre étude sur les interactions hydrodynamiques et y ajouter la possible déformation d'un mur souple dans la dispersion de Taylor. Notons toutefois qu'en présence de telles interactions, les outils classiques de la physique statistique ne sont plus adaptés en l'état (par exemple l'équation de Fokker-Planck), et donc ce possible projet représente un défi théorique de taille. De surcroît, la dispersion de Taylor a de nombreuses applications et intervient dans plusieurs systèmes de matière molle. Par exemple, dans des mélanges binaires, il a été démontré que la dispersion des solutés influençait la dynamique d'une goutte qui s'évapore [309] ou s'étale [310], respectivement à cause des courants de flottabilité ou des contraintes de Marangoni.

Appendix A

Elastohydrodynamic forces computed with the Lorentz reciprocal theorem

Normal force

In this Appendix, we use Parseval's theorem to compute the integrals of Eqs. (2.42) and (2.46). We first write the Fourier transform of the fields that are useful in the calculation. We define $\ell = \sqrt{2ad}$ that denotes the hydrodynamic radius, which is the radial scale in section 2.2 and the 2d dimensionless Fourier variable \mathbf{k} is expressed in polar variables, where k denotes the dimensionless radial coordinate and θ its angle. First, we recall the expression:

$$\int_0^\infty \frac{r^\alpha J_\alpha(kr)}{(1+r^2)^{\beta+1}} r dr = \frac{k^\beta K_{\alpha-\beta}(k)}{2^\beta \Gamma(\beta+1)} \quad (\text{A.1})$$

for $(\alpha, \beta) \in \mathbb{N}^2$ with $2\beta + 3/2 > \alpha$, where Γ denotes the Gamma function, and where K_i is the modified Bessel function of the second kind of order i [186] that is used in what follows.

Using results from section 2.3.1, the deformation field can be written in Fourier space as:

$$\tilde{\delta}(\mathbf{k}) = 2\pi \frac{3\eta \dot{d} \ell^4}{2d^3} \frac{\ell(\lambda+2\mu)}{2\mu(\lambda+\mu)} \frac{1}{k} \frac{k K_1(k)}{2} - (-2i\pi) \frac{6\eta u(t) \ell^3}{5d^2} \frac{\ell(\lambda+2\mu)}{2\mu(\lambda+\mu)} \frac{1}{k} \frac{k K_0(k)}{2} \cos \theta. \quad (\text{A.2})$$

Similarly, its time-derivative yields:

$$\begin{aligned} \partial_t \tilde{\delta}(\mathbf{k}) = & 2\pi \frac{3\eta \ddot{d} \ell^4}{2d^3} \frac{\ell(\lambda+2\mu)}{2\mu(\lambda+\mu)} \frac{1}{k} \frac{k K_1(k)}{2} - 2\pi \frac{3\eta \dot{d}^2 \ell^4}{d^4} \frac{\ell(\lambda+2\mu)}{2\mu(\lambda+\mu)} \frac{1}{k} \frac{k^2 K_2(k)}{8} \\ & - (-2i\pi) \frac{6\eta \dot{u}(t) \ell^3}{5d^2} \frac{\ell(\lambda+2\mu)}{2\mu(\lambda+\mu)} \frac{1}{k} \frac{k K_0(k)}{2} \cos \theta \\ & + (-2i\pi) \frac{12\eta \dot{d} u(t) \ell^3}{5d^3} \frac{\ell(\lambda+2\mu)}{2\mu(\lambda+\mu)} \frac{1}{k} \frac{k^2 K_1(k)}{8} \cos \theta. \end{aligned} \quad (\text{A.3})$$

Here, we write the Fourier transform of the transverse model problem given in Eq. (2.37):

$$\tilde{p}_\perp(\mathbf{k}) = 2\pi \frac{3\eta\hat{V}_\perp\ell^4}{2d^3} \frac{kK_1(k)}{2}, \quad (\text{A.4})$$

and then the scalar product in Eq. (2.42) is:

$$\eta\partial_z\hat{\mathbf{v}}_\perp \cdot \partial_z\mathbf{v}_0|_{z=0}(\mathbf{r}) = \frac{-3\eta\hat{V}_\perp r}{(d+r^2/(2a))^2} \frac{3\dot{d}r}{(d+r^2/(2a))^2} + \frac{6\eta\hat{V}_\perp u(t)}{5(d+r^2/(2a))^3} \left(7 - \frac{6d}{d+\frac{r^2}{2a}}\right) \cos\theta, \quad (\text{A.5})$$

such that the Fourier transform of the latter yields to:

$$\begin{aligned} \eta\partial_z\widetilde{\hat{\mathbf{v}}_\perp \cdot \partial_z\mathbf{v}_0|_{z=0}}(\mathbf{k}) = & 2\pi \frac{-3\eta\hat{V}_\perp\ell}{d^2} \frac{3\dot{d}\ell^3}{d^2} \left(\frac{k^2 K_2(k)}{8} - \frac{k^3 K_3(k)}{48} \right) \\ & + (-2i\pi) \frac{3\eta\hat{V}_\perp\ell}{d^2} \frac{2u(t)\ell^2}{5d} \left(\frac{7k^2 K_1(k)}{8} - \frac{k^3 K_2(k)}{8} \right) \cos\theta \end{aligned} \quad (\text{A.6})$$

Introducing all these expressions into Eq. (2.42) and using Parseval's theorem, we find the vertical force in the form:

$$\begin{aligned} F_z = & -\frac{6\pi\eta a^2 \dot{d}}{d} + A \frac{\eta^2 u^2 (\lambda + 2\mu)}{\mu(\lambda + \mu)} \left(\frac{a}{d}\right)^{5/2} \\ & - B \frac{\eta^2 \dot{d}^2 (\lambda + 2\mu)}{\mu(\lambda + \mu)} \left(\frac{a}{d}\right)^{7/2} + C \frac{\eta^2 \ddot{d} a (\lambda + 2\mu)}{\mu(\lambda + \mu)} \left(\frac{a}{d}\right)^{5/2}, \end{aligned} \quad (\text{A.7})$$

where the numerical coefficients A, B, C can be found analytically (using Mathematica software) as:

$$\begin{aligned} A = & \frac{18\sqrt{2}\pi}{5} \int_0^\infty \left(\frac{kK_0(k)}{2}\right) \left(\frac{kK_1(k)}{2}\right) k dk \\ & - \frac{72\sqrt{2}\pi}{25} \int_0^\infty \frac{1}{k} \left(\frac{kK_0(k)}{2}\right) \left(\frac{7k^2 K_1(k)}{8} - \frac{k^3 K_2(k)}{8}\right) k dk = \frac{837\pi^3}{12800\sqrt{2}}, \end{aligned} \quad (\text{A.8})$$

$$\begin{aligned} B = & 36\sqrt{2}\pi \int_0^\infty \frac{1}{k} \left(\frac{k^2 K_2(k)}{8}\right) \left(\frac{kK_1(k)}{2}\right) k dk \\ & + 108\sqrt{2}\pi \int_0^\infty \frac{1}{k} \left(\frac{kK_1(k)}{2}\right) \left(\frac{k^2 K_2(k)}{8} - \frac{k^3 K_3(k)}{48}\right) k dk = \frac{3915\pi^3}{2048\sqrt{2}}, \end{aligned} \quad (\text{A.9})$$

$$C = 18\sqrt{2}\pi \int_0^\infty \frac{1}{k} \left(\frac{kK_1(k)}{2}\right)^2 k dk = \frac{27\pi^3}{32\sqrt{2}}, \quad (\text{A.10})$$

which correspond to Eq. (2.43).

Lateral force

We now write the pressure fields and the scalar product in Eq. (2.46) of the lateral model problem in Fourier space as:

$$\tilde{p}_{\parallel}(\mathbf{k}) = (-2i\pi) \frac{6\eta\hat{V}_{\parallel}\ell^3}{5d^2} \frac{kK_0(k)}{2} \cos\theta, \quad (\text{A.11})$$

$$\begin{aligned} \eta\partial_z\hat{\mathbf{v}}_{\parallel} \cdot \partial_z\mathbf{v}_0|_{z=0}(\mathbf{r}) &= -\frac{6\eta\hat{V}_{\parallel}\dot{d}r}{5(d+r^2/(2a))^3} \left(7 - \frac{6d}{d+\frac{r^2}{2a}}\right) \cos\theta \\ &+ \frac{4\eta\hat{V}_{\parallel}u(t)}{25(d+r^2/(2a))^2} \left[\left(7 - \frac{6d}{d+\frac{r^2}{2a}}\right)^2 \cos^2\theta + \sin^2\theta \right], \end{aligned} \quad (\text{A.12})$$

$$\begin{aligned} \eta\partial_z\hat{\mathbf{v}}_{\parallel} \cdot \partial_z\mathbf{v}_0|_{z=0}(\mathbf{k}) &= (-2i\pi) \frac{-6\eta\hat{V}_{\parallel}\dot{d}\ell^3}{5d^3} \left(\frac{7k^2K_1(k)}{8} - \frac{k^3K_2(k)}{8} \right) \cos\theta \\ &+ 2\pi \frac{4\eta\hat{V}_{\parallel}u(t)\ell^2}{25d^2} \frac{1}{2} \left(25kK_1(k) - \frac{21k^2K_2(k)}{2} + \frac{3k^3K_3(k)}{4} \right) \\ &- (2\pi) \frac{4\eta\hat{V}_{\parallel}u(t)\ell^2}{25d^2} \frac{1}{2} \cos 2\theta \int_0^{\infty} \left[\left(7 - \frac{6}{1+R^2}\right)^2 - 1 \right] J_2(kR) R dR, \end{aligned} \quad (\text{A.13})$$

where the term in $\cos 2\theta$ does not contribute to the integral Eq. (2.46) by symmetry. Injecting all these expressions in Eq. (2.46), the EHD lateral force is found to be:

$$\kappa F_{x,1} = -\alpha \frac{\eta^2 u \dot{d} (\lambda + 2\mu)}{\mu (\lambda + \mu)} \left(\frac{a}{d} \right)^{5/2} + \beta \frac{\eta^2 \dot{u} a (\lambda + 2\mu)}{\mu (\lambda + \mu)} \left(\frac{a}{d} \right)^{3/2}. \quad (\text{A.14})$$

$$\begin{aligned} \alpha &= \frac{18\sqrt{2}\pi}{5} \int_0^{\infty} \left(\frac{kK_1(k)}{2} \right) \left(\frac{kK_0(k)}{2} \right) k dk + \frac{144\sqrt{2}\pi}{25} \int_0^{\infty} \frac{1}{k} \left(\frac{kK_0(k)}{2} \right) \left(\frac{k^2K_1(k)}{8} \right) k dk \\ &+ \frac{12\sqrt{2}\pi}{25} \int_0^{\infty} \frac{1}{k} \left(\frac{kK_1(k)}{2} \right) \left(25kK_1(k) - \frac{21k^2K_2(k)}{2} + \frac{3k^3K_3(k)}{4} \right) k dk \\ &+ \frac{72\sqrt{2}\pi}{25} \int_0^{\infty} \frac{1}{k} \left(\frac{kK_0(k)}{2} \right) \left(\frac{7k^2K_1(k)}{8} - \frac{k^3K_2(k)}{8} \right) k dk = \frac{3177\pi^3}{6400\sqrt{2}}, \end{aligned} \quad (\text{A.15})$$

$$\beta = \frac{72\sqrt{2}\pi}{25} \int_0^{\infty} \frac{1}{k} \left(\frac{kK_0(k)}{2} \right)^2 k dk = \frac{9\pi^3}{200\sqrt{2}}, \quad (\text{A.16})$$

which corresponds to Eq. (2.47).

Appendix B

Taylor-dispersion in a rectangular channel in the presence of a gravity field

In this Appendix, we illustrate the capacity of the moment theory of section 6.4.2 and the generalized Taylor dispersion of section 6.4.3 to describe the Taylor dispersion with an external potential. We consider point-like particles with an isotropic diffusion, advected in a simple shear flow and in a gravity field in a 2d microchannel of height H . The dimensionless gravity potential is taken as:

$$\frac{\phi(z)}{k_B\Theta} = \frac{mgz}{k_B\Theta} = \frac{z}{l_B}, \quad (\text{B.1})$$

where m and g are the mass and the gravitational acceleration respectively, and l_B denotes the Boltzmann length, which dictates the typical length over which gravity modifies the concentration of particles. In this example, the dispersion only depends on the ratio between l_B and the channel height. In Fig. B.1, we display the Boltzmann distribution versus the altitude for three l_B/H ratios. To use the moment theory, one needs to find the solution of Eqs. (6.69) and (6.70). After some algebra, we find:

$$\lambda_{\phi, k \geq 1} = \frac{D_0(k\pi)^2}{H^2} + \frac{D_0}{4l_B^2}, \quad (\text{B.2})$$

$$f_{\phi, k \geq 1}(z) = \frac{1}{\sqrt{\frac{l_B}{H}(1 - \exp(\frac{H}{l_B}))}} \sqrt{\frac{2}{1 + \frac{H^2}{(2l_B k \pi)^2}}} \times \left[\cos\left(k\pi \frac{z}{H}\right) - \frac{H}{2l_B k \pi} \sin\left(k\pi \frac{z}{H}\right) \right] \exp\left(-\frac{z}{2l_B}\right). \quad (\text{B.3})$$

Once the eigenvalues are found, the dispersion coefficients can be computed using Eq. (6.75) for each time and initial condition. Furthermore, the long-time Taylor dispersion coefficient can be computed analytically for a gravitational potential, injecting

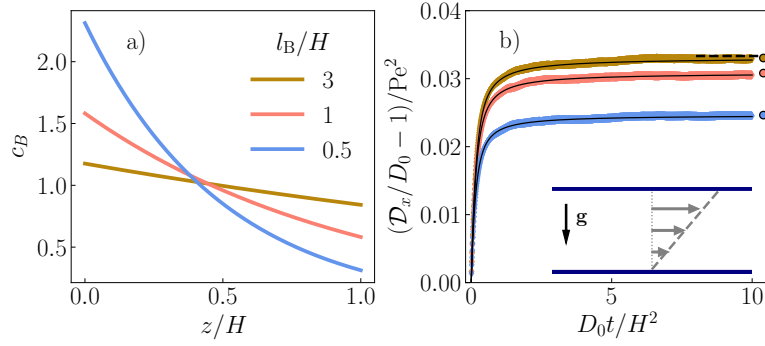


Figure B.1: a) Boltzmann distribution in a gravity field defined by the external potential Eq. (B.1). The ratio between the Boltzmann length and the channel height is indicated with a color. b) Reduced dispersion coefficient versus dimensionless time for point-like particles in a gravity field, where the colors are similar to a). The results of the Langevin simulations are shown with colored points and the moment theory is plotted with black solid lines. The black dashed lines show the Taylor-Aris limit, in the absence of gravity, see Eq. (6.28). The circles display the long-time limit obtained analytically with the generalized Taylor theory of Eq. (B.4). The inset in b) shows a schematic of the system.

Eq. (B.1) into Eq. (6.79). Doing so, we get:

$$\left(\frac{\mathcal{D}_x}{D_0} - 1\right)/\text{Pe}^2 = 8\left(\frac{l_B}{H}\right)^4 - \frac{l_B}{2H} \frac{\sinh\left(\frac{H}{l_B}\right)}{\sinh^4\left(\frac{H}{2l_B}\right)}. \quad (\text{B.4})$$

In Fig. B.1, we show the reduced dispersion coefficient versus the dimensionless time resulting from the moment theory. In the long-time limit, the dispersion coefficient converges toward the expected value from Eq. (B.4). Furthermore, we display Langevin simulations using Eqs. (6.57a) and (6.57b) with an extra gravity term $\frac{z}{l_B} \delta T$ in Eq. (6.57b). Reflecting boundary conditions are used following Ref. [298] at both $z = 0$ and $z = H$. In both the moment theory and the Langevin simulations, the initial condition is set with the Boltzmann distribution. Interestingly, the dispersion decreases with increasing gravity, or for a large channel size equivalently. For a small channel size, *i.e.* $H \ll l_B$, we recover the Taylor-Aris limit.

Besides the gravitational potential, there are few available analytical solutions of the eigenvalue problem associated with the moment theory. Nevertheless, for an arbitrary potential, numerical methods can be used. Notably, the eigenvalues can be found by using the SLEIGN2 code described in Ref. [311] that is suitable for Sturm-Liouville problems.

Appendix C

Enhanced Dip-Coating on a Soft Substrate.

In this appendix, I present a theoretical work that I initiated at the beginning of my PhD, that is not directly related to the main parts of the manuscript. I reproduce here a draft that I wrote for a future publication.

In this project, we study the so-called dip-coating problem. In a few words, an solid object withdrawn from a liquid bath entrains a thin liquid film. It is the strategy largely employed in industry to deposit a liquid layer of a given thickness on a material. Here, we study in influence of the softness of the material on the dip-coating process.

Enhanced Dip-Coating on a Soft Substrate

Vincent Bertin,^{1,2,*} Jacco H. Snoeijer,³ Elie Raphaël,² and Thomas Salez^{1,4}

¹*Univ. Bordeaux, CNRS, LOMA, UMR 5798, 33405 Talence, France.*

²*UMR CNRS Gulliver 7083, ESPCI Paris, PSL Research University, 75005 Paris, France.*

³*Physics of Fluids Group, Faculty of Science and Technology,*

and Mesa+ Institute, University of Twente, 7500AE Enschede, The Netherlands.

⁴*Global Station for Soft Matter, Global Institution for Collaborative Research and Education, Hokkaido University, Sapporo, Hokkaido 060-0808, Japan.*

(Dated: July 6, 2021)

A solid, withdrawn from a liquid bath, entrains a thin liquid film. This simple process, first discussed by Landau, Levich and Derjaguin (LLD), is observed in everyday's life and is widely used in industry. However, the liquid flux entrained can be altered by various properties of the withdrawn solid. Here, we develop a model that accounts for the additional presence of a soft solid layer atop the rigid plate. For simplicity, a Winkler's foundation is assumed as an elastic response. A new power-law regime is found for the thickness of liquid entrained $h_\infty \sim \sqrt{\ell_{ec}\ell_{cap}} \text{Ca}^{1/2}$ (where Ca denotes the capillary number, ℓ_{cap} the capillary length and ℓ_{ec} an elastocapillary length) at small Ca . At large Ca , the classical LLD scaling law $h_\infty \sim \ell_{cap} \text{Ca}^{2/3}$ is recovered. The crossover between the two regimes occurs when the substrate's deformation is comparable to the thickness of the entrained film.

Introduction. A solid object, withdrawn from a liquid bath, entrains a thin liquid film via viscous forces. Such a process is called dip-coating and is commonly used in industry to cover materials with liquid coatings and to modify the surface or optical properties [1, 2]. The fundamental quantity of interest in the process is the film thickness h_∞ that is entrained (see Fig. 1). Seminal works by Landau and Levich [3] and Derjaguin [4] (LLD) have computed the thickness, using asymptotic matching methods, where a dynamic meniscus solution matches the static meniscus. Over the last decades, many studies have extended the initial LLD description [5], by adding the effect of fluid inertia [6, 7], surfactant at the liquid-air interface [8], non-Newtonian properties [9, 10], or the rugosity of the solid [11, 12] to cite a few. Perhaps surprisingly, the effect of the softness of the withdrawn object has not been investigated so far.

Nevertheless, soft gels (Young's modulus $E \sim \text{kPa}$) exhibit rich wetting properties, as capillary forces deform such materials, creating wetting ridges of typical length scale γ/E , where γ denotes the surface tension [13, 14]. Therefore, we could expect that the Laplace pressure induces deformation of the substrate of similar magnitude in the dip-coating process.

In this letter, we study the influence of the elastic deformation of the plate on the thickness of fluid entrained in dip coating. Our theoretical approach is based on the classical LLD asymptotic matching, and the elastic deformation is model with a Winkler's foundation.

Model. We consider a two-dimensional plate (see Fig. 1), withdrawn with a velocity V from a liquid reservoir of viscosity η , density ρ . We assume the Weber number, $\text{We} = \rho V^2 \ell_{cap} / \gamma$, where $\ell_{cap} = \sqrt{\gamma / \rho g}$ is the capillary length, and capillary number, $\text{Ca} = \eta V / \gamma$, to be small with respect to unity, so that we can neglect iner-

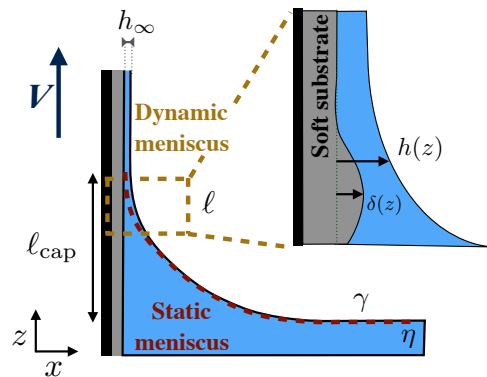


Figure 1: **Schematic of the dip-coating problem.** The inset exhibits a zoom in the dynamic meniscus zone where the flow is localized. The liquid-air interface curvature induces a negative Laplace pressure in the liquid that deforms the soft substrate.

tia and perform a LLD-like asymptotic matching [3, 15]. Therefore, the flow is described in the dynamic meniscus zone (see Fig. 1) and we use the lubrication approximation. Gravitational drainage is neglected in this regime, so that the pressure field is set by the Laplace pressure. The latter induces a normal deformation $\delta(z)$ of the solid surface. We further assume a no-slip boundary condition at the plate surface and a no-shear condition at the liquid-air interface. Assuming a steady-state interface profile, the governing equation for the liquid-air interface profile $h(z)$ is given by the following thin-film equation [16]:

$$\frac{\gamma}{3\eta} [h(z) - \delta(z)]^3 h'''(z) + V[h(z) - \delta(z)] = Vh_\infty, \quad (1)$$

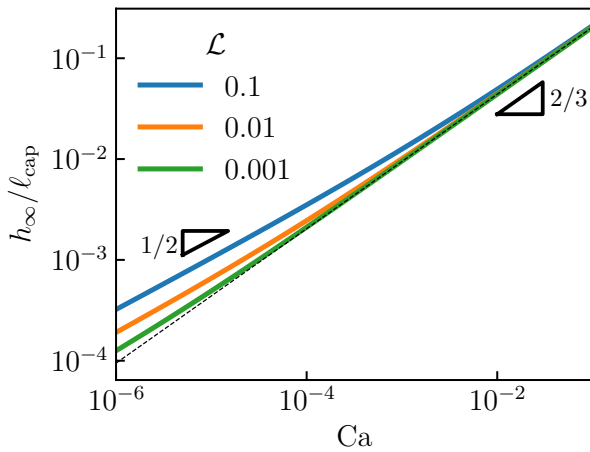


Figure 2: **Thickness.** Normalized entrained liquid thickness versus capillary number in log-log scale, for different values of the dimensionless softness parameter $\mathcal{L} = \rho g s_0 / E^*$. The black dashed line represents the LLD scaling law Eq. (6), valid at large Ca. Slope triangles indicate power-law.

where the prime denotes the spatial derivative with respect to z , $V h_\infty$ being the liquid flux, where h_∞ denotes the thickness of the entrained liquid film. The liquid is assumed to wet the solid surface (zero contact angle). Thus, the matching condition to the static meniscus solution imposes the boundary condition on the liquid-air interface profile [15]:

$$\lim_{z \rightarrow -\infty} h''(z) = \frac{\sqrt{2}}{\ell_{\text{cap}}}, \quad (2)$$

where $\sqrt{2}/\ell_{\text{cap}}$ is the curvature of the meniscus at the surface for wetting liquids [17]. The liquid-film thickness reaches the thickness h_∞ in the limit $z \rightarrow \infty$, such that the slope and curvature of the liquid-air interface profile vanishes, as:

$$h(z \rightarrow \infty) = h_\infty, \quad h'(z \rightarrow \infty) = h''(z \rightarrow \infty) = 0. \quad (3)$$

As a minimal description of the solid surface mechanical response, we use the Winkler's foundation [18]. The solid surface behaves as a mattress of independent springs – a situation relevant to thin compressible elastic materials. Thus, the normal deformation is proportional to the local Laplace pressure, which amounts to:

$$\delta(z) = \frac{s_0 \gamma}{E^*} h''(z), \quad (4)$$

where s_0 is a length scale and E^* is an elastic modulus. For thin compressible materials, s_0 represents the material thickness and $E^* = \frac{E(1-\nu)}{(1+\nu)(1-2\nu)}$, where ν denotes the Poisson ratio. The length scale, $\sqrt{s_0 \gamma / E^*} = \ell_{\text{ec}}$, ap-

pearing here is called the elastocapillary length. Therefore, a dimensionless softness parameter emerges from this model, as the ratio between elastocapillary and capillary lengths squared: $\mathcal{L} = (\ell_{\text{ec}}/\ell_{\text{cap}})^2 = \rho g s_0 / E^*$. Injecting Eq. (4) into Eq. 1, we find an ordinary differential equation:

$$h'''(z) = 3\text{Ca} \frac{h_\infty - (h - \ell_{\text{ec}}^2 h''(z))}{(h - \ell_{\text{ec}}^2 h''(z))^3}. \quad (5)$$

The Eq. (5) admits a trivial solution $h(z) = h_\infty$, corresponding to the flat film. Assuming an uniform film at $z \rightarrow \infty$, we linearize Eq. (5) as $h(z) = h_\infty + \epsilon(z)$, where $\epsilon(z) \ll h_\infty$, which gives $\epsilon'''(z) = \frac{3\text{Ca}}{h_\infty^3} [-\epsilon(z) + \ell_{\text{ec}}^2 \epsilon''(z)]$. The solution compatible with a flat film at $z \rightarrow -\infty$ takes the form $\epsilon(z) = \epsilon_0 \exp(rz)$, where r is the root of the polynomial expression: $r^3 + \frac{3\text{Ca}}{h_\infty^3} [-\ell_{\text{ec}}^2 r^2 + 1] = 0$, with a negative real part, and ϵ_0 being a numerical constant. We solve the initial value problem, defined by Eq. (5), and the initial condition at $z = 0$ being the the linearized solution of Eq. (5), with a 4th-order Runge-Kutta numerical scheme. We stress that Eq. (5) is invariant by translation along the z direction, and thus the z position of the initial condition is irrelevant here, provided that ϵ_0/h_∞ is small. The solution is found to diverge for $z \rightarrow -\infty$ with a finite second derivative, as observed in Fig. 3, whatever h_∞ . The entrained liquid thickness is found using a shooting algorithm that ensures the curvature matching condition Eq. (2).

Results. In Fig. 2, we plot the resulting entrained liquid thickness versus capillary number, varying the softness parameter. Two distinct scaling regimes can be observed. At large Ca, we recover the classical LLD law [3]:

$$h_\infty = 0.946 \ell_{\text{cap}} \text{Ca}^{2/3}, \quad (6)$$

obtained for rigid plates. Furthermore, as the soft layer rigidity increasing (decreasing \mathcal{L}), the entrained thickness tends toward the one predicted by the LLD law. At small Ca, the entrained thickness deviates from Eq. (6) and we find a novel *soft regime*, as:

$$h_\infty = 0.57 \ell_{\text{cap}} \mathcal{L}^{1/4} \text{Ca}^{1/2} = 0.57 \sqrt{\ell_{\text{cap}} \ell_{\text{ec}}} \text{Ca}^{1/2}, \quad (7)$$

where more fluid is entrained. Therefore, at small velocity, the wall softness enhances the dip-coating efficiency with respect to the classical LLD scenario. Balancing the two limiting expressions Eqs. (6) and (7) at small and large velocities, the transition between the two regimes occurs at $\text{Ca} \sim \mathcal{L}^{3/2}$.

In Fig. 3, we show the liquid-air interface profile and the normal deformation of the solid surface versus the vertical position. As discussed, the liquid-air interface profile diverges at $z \rightarrow -\infty$, matching the static meniscus Eq. (2). The normal deformation, which is proportional to the curvature of the profile in the Winkler model,

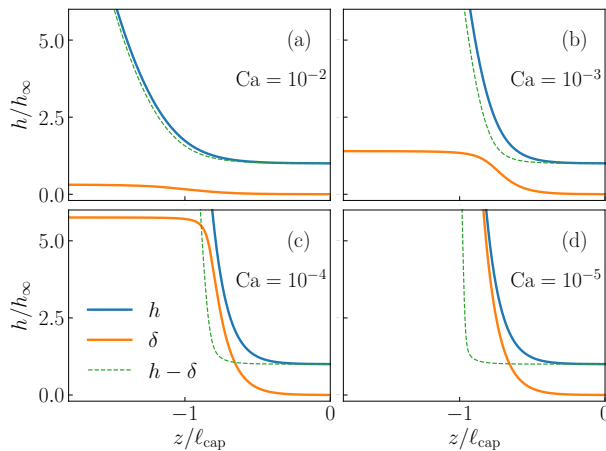


Figure 3: **Profiles.** Liquid-air interface (blue) and normal deformation (orange) normalized by the entrained thickness h_∞ versus vertical axis, rescaled by the capillary length ℓ_{cap} in the numerical integration of Eq. (5). The green dashed lines display the difference between these two quantities. The dimensionless softness parameter is set to $\mathcal{L} = 0.01$. The capillary number are $\text{Ca} = 10^{-2}, 10^{-3}, 10^{-4}$ and 10^{-5} in (a)-(d) respectively.

reaches a given value:

$$\delta(z \rightarrow -\infty) = \sqrt{2} \ell_{\text{ec}}^2 / \ell_{\text{cap}}, \quad (8)$$

which is set by the matching condition, and can be obtained by injecting Eq. (2) into Eq. (4). Interestingly, typical normal deformation Eq. (8) does not depend on the plate velocity, and increases relative to the liquid-film thickness for decreasing capillary number. Furthermore, we find that the balance between the thickness in the LLD law Eq. (6) and the limiting normal deformation Eq. (8) is equivalent to the transition between the two scaling regimes of Fig. 2, *i.e.* $\text{Ca} \sim \mathcal{L}^{3/2}$. Hence, it suggests that the condition for the soft regime to be valid is that the normal deformation is larger than the entrained film thickness.

In the soft regime, we observe that a fluid thickness $h - \delta$ is constant over a certain extent, while both the liquid-air interface profile and the normal deformation increases (see Fig. 3(c) and (d)). From this observation, we introduce the similarity ansatz $h(z) = \ell_{\text{cap}} \mathcal{L}^{1/4} \text{Ca}^{1/2} H(Z = z/\ell_{\text{ec}})$ into Eq. (5), where the z scale ℓ_{ec} is set as being the typical scale of the constant-fluid-thickness equation $h - \delta = h_\infty$, together with the Winkler law Eq. (4). The rescaling thickness is set by the soft regime Eq. (7). Hence, the Eq. (5) becomes:

$$\text{Ca}^{1/2} \mathcal{L}^{-3/4} \frac{(H - H'')^3}{3} H''' = H_\infty - H + H'' \quad (9)$$

where $H_\infty = h_\infty / (\ell_{\text{cap}} \mathcal{L}^{1/4} \text{Ca}^{1/2})$. In the soft regime,

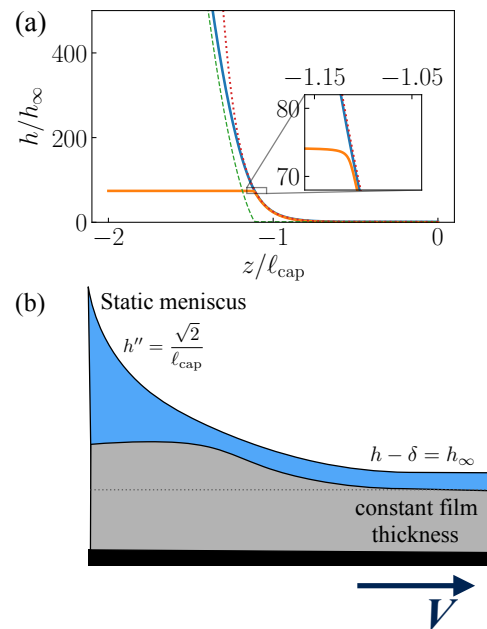


Figure 4: (a) **Profiles.** Liquid-air interface (blue) and normal deformation (orange) normalized by the entrained thickness h_∞ versus vertical axis, rescaled by the capillary length ℓ_{cap} as in Fig. 3. Here the capillary number is set to $\text{Ca} = 10^{-6}$ and the softness parameter to $\mathcal{L} = 0.01$. The dotted red line shows the soft zone solution Eq. (10) at constant fluid-thickness. The inset shows a zoom near the matching region. (b) Schematic of the profile in the soft regime. A constant fluid-thickness region matches smoothly the static meniscus. The schematic is reversed with respect to Fig. 1, and the arrow indicates the velocity.

the parameter $\text{Ca}^{1/2} \mathcal{L}^{-3/4}$ is small, such that the solution can be described by the constant-fluid-thickness equation. Solving for this equation, we find:

$$h(z) = h_\infty + \alpha \exp(-z/\ell_{\text{ec}}), \quad (10)$$

where α is an arbitrary prefactor. In Fig. 4(a), we display the liquid-air interface profile and the normal deformation in the soft regime for $\text{Ca} = 10^{-6}$ and $\mathcal{L} = 0.01$, meaning $\text{Ca}^{1/2} \mathcal{L}^{-3/4} \approx 0.0316$. The dotted red lines show the constant-fluid-thickness solution Eq. (10), which agrees with the interface profile over a large range. At a given vertical position, the normal deformation smoothly deviates from Eq. (10) and reaches its limiting value Eq. (8) (see in the inset of Fig. 4(a)). The Fig. 4(b) exhibits a schematic of the constant-fluid-thickness region that is found in the soft regime.

The soft regime scaling in Eq. (7) may be recovered using the following scaling arguments. The balance of the viscous and the pressure gradient terms of the Stokes equation, leading to $\frac{\eta V}{h_\infty^2} \sim \frac{\gamma}{\ell_{\text{cap}}} \frac{1}{\ell}$, where ℓ denotes the typical vertical scale of the dynamical meniscus (see

Fig. 1). In the classical LLD, the scaling of Eq. (6) can be obtained through the balance of curvature in the static and dynamical meniscus $\frac{h_\infty}{\ell^2} \sim \frac{1}{\ell_{\text{cap}}}$. However, for the soft regime, the appropriate normal length scale for the dynamical meniscus curvature is δ instead of h_∞ , which gives $\frac{\delta}{\ell^2} \sim \frac{1}{\ell_{\text{cap}}}$. Combining the latter scaling with the hydrodynamic scaling, we find $h_\infty \sim \delta^{1/4} \ell_{\text{cap}}^{3/4} \text{Ca}^{1/2}$. If the normal deformation follows the Winkler's foundation, and scales as $\delta \sim \frac{\ell_{\text{sc}}^2}{\ell_{\text{cap}}}$ (see Eq. (8)), then the scaling law (7) is recovered.

In the case of a plate coated with a thick elastic layer, the deformation does not depend of the layer thickness and scales as γ/E [14]. If the scenario presented in this paper is robust to different elastic response (beyond Winkler's foundation), the transition with the soft regime occurs at a critical capillary number that scales as $(\frac{\delta}{\ell_{\text{cap}}})^{3/2} \sim (\frac{\gamma}{E\ell_{\text{cap}}})^{3/2}$. Using approximate values for soft gels, *i.e.* $\ell_{\text{cap}} \approx 1$ mm and $\gamma/E \approx 10$ μm , we find a critical capillary number on the order of 10^{-3} , which is in the range accessible experimentally [5].

Conclusion. To conclude, we have studied the effect of the elasticity of the withdrawn solid in the dip-coating process. We consider a soft elastic layer placed atop of a rigid plate, and the Winkler's foundation is assumed for the substrate mechanical response. The Laplace pressure in the meniscus deforms the solid surface, and which enhances the entrained thickness. A scaling regime $h_\infty \sim \text{Ca}^{1/2}$ is found at small capillary number, a regime in which the substrate deformation is larger than the entrained thickness. As a perspective, extensions of the model to other forms of substrate mechanical responses would be interesting to verify the robustness of the new scaling regime. Viscoelastic properties of the soft solid may affect the soft regime [19].

The displacement of liquid menisci on a wet solid occurs in a other settings than the dip-coating process [20], such as the motion of a confined bubbles in a channel [21], or the spreading of a droplet on a surface [22], which also involves LLD-like solutions. It would be interesting to revisit these problems with soft boundaries with the present soft-LLD approach [23].

ACKNOWLEDGEMENTS

We thank F. Boulogne, M. Marchand, C. Poulard, F. Restagno and E. Rio for interesting discussions. This work is supported by the Agence Nationale de

la Recherche (ANR) under the EMetBrown (ANR-21-ERCC-0010-410 01) grant.

* Electronic address: vincent.bertin@u-bordeaux.fr

- [1] P. Baumeister, Optical coating technology, vol. 137 (SPIE press, 2004).
- [2] C. J. Brinker, in Chemical Solution Deposition of Functional Oxide (Springer, 2013), pp. 233–261.
- [3] B. Levich and L. Landau, Acta Physiochim **17**, 42a–54 (1942).
- [4] B. Derjaguin, in CR (Dokl.) Acad. Sci. URSS (1943), vol. 39, pp. 13–16.
- [5] E. Rio and F. Boulogne, Advances in colloid and interface science **247**, 100 (2017).
- [6] A. De Ryck and D. Quéré, Journal of colloid and interface science **203**, 278 (1998).
- [7] B. Jin, A. Acrivos, and A. Münch, Physics of Fluids **17**, 103603 (2005).
- [8] A. Q. Shen, B. Gleason, G. H. McKinley, and H. A. Stone, Physics of Fluids **14**, 4055 (2002).
- [9] R. Spiers, C. Subbaraman, and W. Wilkinson, Chemical Engineering Science **30**, 379 (1975).
- [10] W. J. Smit, C. Kusina, J.-F. Joanny, and A. Colin, Physical review letters **123**, 148002 (2019).
- [11] R. Krechetnikov and G. Homsy, Physics of Fluids **17**, 102108 (2005).
- [12] J. Seiwert, C. Clanet, and D. Quéré, Journal of Fluid Mechanics **669**, 55 (2011).
- [13] R. W. Style, A. Jagota, C.-Y. Hui, and E. R. Dufresne, Annual Review of Condensed Matter Physics **8**, 99 (2017).
- [14] B. Andreotti and J. H. Snoeijer, Annual review of fluid mechanics **52**, 285 (2020).
- [15] S. D. Wilson, Journal of Engineering Mathematics **16**, 209 (1982).
- [16] A. Oron, S. H. Davis, and S. G. Bankoff, Reviews of modern physics **69**, 931 (1997).
- [17] P.-G. De Gennes, F. Brochard-Wyart, and D. Quéré, Capillarity and wetting phenomena: drops, bubbles, pearls, waves (Springer Science & Business Media, 2013).
- [18] D. A. Dillard, B. Mukherjee, P. Karnal, R. C. Batra, and J. Frechette, Soft matter **14**, 3669 (2018).
- [19] R. Lhermerout, H. Perrin, E. Rolley, B. Andreotti, and K. Davitt, Nature communications **7**, 1 (2016).
- [20] I. Cantat, Physics of Fluids **25**, 031303 (2013).
- [21] F. P. Bretherton, Journal of Fluid Mechanics **10**, 166 (1961).
- [22] L. Tanner, Journal of Physics D: Applied Physics **12**, 1473 (1979).
- [23] V. Charitatos and S. Kumar, Soft Matter **16**, 8284 (2020).

Appendix D

Swimming droplet in 1D geometries, an active Bretherton problem.

In this appendix, I present some work that I have performed in parallel to my main PhD project under the supervision of Olivier Dauchot & Mathilde Reyssat at ESPCI Paris. The experiments have been carried out by Charlotte de Blois and Saori Suda (Kyoto University), and I lead the theoretical approach and I contributed to the writing of the initial draft of an article, published in the journal *Soft Matter* [7].

Swimming droplets are artificial microswimmers, that have been introduced about 15 years ago [312], and which self-propelled in an arbitrary direction. Such a system has been largely studied since then for many reasons: i) curiosity-driven, how can a symmetric spherical droplet self-propel, ii) it is promised to great applications in the context of drug-delivery systems, iii) it is a good model for biological microswimmers that are widely spread in organism (*e.g.* bacteria) or in the ocean (*e.g.* plankton), iv) as for many active systems, it undergoes intriguing collective properties.

Experimentally, the studied system is made of water droplets immersed in a oil-surfactant phase, where the surfactant concentration is far above the CMC. The system is out of thermodynamics equilibrium and a spontaneous transfer of water from the droplet to the micelles can be observed [313]. Furthermore, the water-oil interface is active, as gradients in solute (*i.e.* micelles) drive Marangoni flows, which induce the self-propulsion via a spontaneous symmetry-breaking instability. In this work, we investigate the swimming of droplets that are confined inside square and cylindrical capillaries. The speed of the droplet decreases in the capillaries with respect to unbounded space and saturates to a constant value for droplet larger than the capillary size. Interestingly, droplets in stretched cylindrical capillaries (*i.e.* of varying cross-sectional area) are observed to split into two droplets for large confinement. We develop a model, that is based on the Bretherton model for passive droplet, including the activity of the interfaces.



Swimming droplets in 1D geometries: an active Bretherton problem†

Cite this: DOI: 10.1039/d1sm00387a

 Charlotte de Blois, ‡*^{ab} Vincent Bertin, ‡^{ac} Saori Suda, ‡^d
 Masatoshi Ichikawa, ^d Mathilde Reyssat *^a and Olivier Dauchot ^a

We investigate experimentally the behavior of self-propelled water-in-oil droplets, confined in capillaries of different square and circular cross-sections. The droplet's activity comes from the formation of swollen micelles at its interface. In straight capillaries the velocity of the droplet decreases with increasing confinement. However, at very high confinement, the velocity converges toward a non-zero value, so that even very long droplets swim. Stretched circular capillaries are used to explore even higher confinement. The lubrication layer around the droplet then takes a non-uniform thickness which constitutes a significant difference to usual flow-driven passive droplets. A neck forms at the rear of the droplet, deepens with increasing confinement, and eventually undergoes successive spontaneous splitting events for large enough confinement. Such observations stress the critical role of the activity of the droplet interface in the droplet's behavior under confinement. We then propose an analytical formulation by integrating the interface activity and the swollen micelle transport problem into the classical Bretherton approach. The model accounts for the convergence of the droplet's velocity to a finite value for large confinement, and for the non-classical shape of the lubrication layer. We further discuss on the saturation of the micelle concentration along the interface, which would explain the divergence of the lubrication layer thickness for long enough droplets, eventually leading to spontaneous droplet division.

 Received 12th March 2021,
 Accepted 2nd June 2021

DOI: 10.1039/d1sm00387a

rsc.li/soft-matter-journal

1 Introduction

Biological micro-swimmers exhibit a number of fascinating swimming strategies, to compensate for the absence of inertia. Even more intriguing is the way such organisms manage to probe and explore their environment, probing the presence of external fields such as temperature, nutriment concentration, gravity, *etc.* In many cases, they also manage to explore narrow channel-like passages, such as in soil¹ or in the organism² of their host; or because they are placed in artificial micro-fluidic channels^{3,4} to steer their motion^{5,6} with application in drug delivery.

Euglenids⁷ are a striking example of such microorganisms, which are able to adapt their swimming strategy from flagellar propulsion to crawling. During this transition, the euglenids don't touch the wall, and are sensitive to the confinement through hydrodynamic interactions only. Another amazing example is that of paramecium,^{8,9} when they take a cylindrical shape to swim in narrow capillaries.

In the context of artificial micro-swimmers, a now classical strategy is to exploit phoretic effects^{10,11} to ensure propulsion by locally inducing gradients that generate a flow field around the swimmer, which in turn ensures its propulsion. The gradient can be induced by engineering an asymmetry in the swimming body – the so called Janus particles – and thereby obtain autophoretic swimmers (diffusio-phoresis,¹² thermo-phoresis,¹³ electro-phoresis¹⁴). More recently, it was shown that spontaneous symmetry breaking of the flow field, non-linearly coupled to the advection–diffusion of the scalar field, can also lead to self-sustained propulsion.^{15,16} Swimming droplets, generating a solute gradient around them, are the prototypical experimental realization of this mechanism.^{17–20}

The presence of walls or obstacle can alter the swimming motion in different ways. The most common and unavoidable one is the disturbance of the hydrodynamic flow field. The case of weakly confined swimmers interacting with the boundaries

^a UMR CNRS Gulliver 7083, ESPCI Paris, PSL Research University, 75005 Paris, France. E-mail: Charlotte.de-blois@espci.fr, Mathilde.Reyssat@espci.fr

^b Okinawa Institute of Science and Technology Graduate University, Onna-son, Okinawa 904-0495, Japan

^c Univ. Bordeaux, CNRS, LOMA, UMR 5798, 33405 Talence, France

^d Department of Physics, Graduate School of Science, Kyoto University, Kitashirakawa-Oiwakecho, Sakyo-ku, Kyoto 606-8502, Japan

† Electronic supplementary information (ESI) available: (1) Drp_in_Cyl.avi (1 i/s accelerated 20 times): video showing three experiments of droplets of different sizes swimming in circular capillaries of radius $h = 50 \mu\text{m}$. (2) Drp_in_Cons.avi (10 i/s accelerated 30 times): video showing two experiments inside stretched capillaries of droplets simply elongating or spontaneously dividing while swimming. See DOI: 10.1039/d1sm00387a

‡ These authors contributed equally to this work.

only *via* the far-field hydrodynamics flow has been intensively studied theoretically.^{21–28} In this situation, the flow field around the swimmer is affected through the no-slip condition at the boundaries. Theoretical studies for spherical swimmers^{23,24} demonstrated that the behavior of the swimmer (helical *vs.* straight trajectory – attraction *vs.* repulsion by the boundary) then strongly depends on its nature (pusher–puller–neutral). Experimental investigations on biological swimmers²⁹ have revealed the diversity of the flow field developing around a micro-swimmer under such confinement. In the case of the phoretic swimmers, the transport of the scalar field will also be altered and thereby modify the swimming motion. The way that a single flat boundary (a wall) alters the swimmer motion has been documented both theoretically and experimentally.^{30–34} In the case of the swimming droplets the solute is composed of micelles, the diffusion of which is way slower than molecular solutes. As a result, advection, which cannot be neglected in the transport of the solute, leads to a yet more complex situation because of the nonlinear coupling between the flow field dynamics and the advection–diffusion of the solute. The response of the swimmer motion to the proximity of the wall then depends on the relative importance of the advection and the diffusion of the scalar field. Quantitative measurements of the velocity field around a droplet swimming close to a wall could recently be analyzed and described theoretically,³⁵ but little is known about the swimming motion in more confined geometries such as micro-fluidic channels.^{36,37}

In the present work, we study experimentally the motion of a pure water swimming droplet,¹⁸ in square and cylindrical capillaries with different levels of confinement. Amazingly, the droplet keeps its ability to swim under very strong confinement $L/(2h) = 10$, where $2h$ is the width of the capillary and L is the length of the strongly elongated droplet. This is not only observed for square capillaries, but also for cylindrical ones, for which the droplet body is separated from the lateral boundaries by a lubrication film of a few microns in thickness. Furthermore, for even larger confinement, we observe the spontaneous division of the droplet at its rear part. Both observations stress the crucial role of the active stresses at the droplet interface. The main goal of the present work is to quantify these new features, qualitatively different from that of flow-driven passive droplets and unveil the Marangoni-stress driven mechanisms coupled to the interface dynamics, responsible for them.

The paper is organized as follows. After a thorough description of the experimental setting, we characterize the swimming motion of the droplet in different channel-like geometries. We then propose a theoretical description, which accounts for the main observations, despite some important simplifications. Discussion about these simplifications and perspective for future investigations conclude the paper.

2 Experimental setting

The experimental system is made of a water droplet inside a glass capillary, filled with a continuous oil–surfactant phase, a squalane solution of mono-olein at a concentration

$c = 25 \text{ mmol L}^{-1}$, that is far above the critical micellar concentration (CMC $\simeq 5 \text{ mmol L}^{-1}$).

In chambers¹⁸ of diameter and thickness much larger than the droplet size and filled with the same oil–surfactant solution, such water droplets of typical size $a = 100 \text{ }\mu\text{m}$ spontaneously start swimming. The swimming motion results from the combination of two ingredients. First, the system is far from its physico-chemical thermodynamic equilibrium, which is a micro-emulsion made of inverse micelles filled with water, in the oil phase. As a result, a flux of water takes place continuously from the droplet to the inverse micelles.³⁸ Secondly, the resulting isotropic concentration field of inverse swollen micelles happens to be unstable against an infinitesimal flow disturbance: in the presence of any tiny gradient of swollen micelles in the vicinity of the interface, Marangoni stresses and phoretic flows take place which induce the mobility of the droplet towards regions of small concentration, and therefore enhance the initial disturbance. For this instability to take place,^{15,16,18} the Péclet number $Pe = U^*a/D$ must exceed some critical value $Pe_c = O(1)$, where a is the radius of the droplet, D is the diffusion coefficient of the micelles and $U^* = \frac{A\mathcal{M}}{D}$ is the characteristic auto-phoretic velocity,¹¹ with A the activity of the droplet and \mathcal{M} the motility of the micelles. In other words, for self-propulsion to occur, the diffusion of the micelles must be slow as compared to their advection by the Marangoni flow.

Here we confine such droplets in micro-channels, of typical length $\sim 2 \text{ cm}$ much longer than the droplet size and with different cross-sectional geometries of typical inner size h in the range $40 \text{ }\mu\text{m} < h < 200 \text{ }\mu\text{m}$, comparable to or smaller than the droplet size. Three different 1D geometries are used: square glass capillaries (Fig. 1(a)), h is then defined as half the inner dimension of the capillary, circular glass capillaries (Fig. 1(c)), h is then defined as the radius of the capillary, and stretched circular capillaries (Fig. 4) whose inner radius varies continuously along their length between $h = 100 \text{ }\mu\text{m}$ (at both ends), and a constriction of radius h_{min} that ranges from $30 \text{ }\mu\text{m}$ to $80 \text{ }\mu\text{m}$, in the middle of the capillary, with a typical gradient of diameter $\frac{dh}{dx} \simeq \pm 0.02$. Then relative to the swimming of the droplet, these capillaries present a convergent region followed by a divergent one.

At the beginning of each experiment, one droplet is produced at one end of a capillary previously filled with the oil–surfactant solution. The droplet spontaneously starts swimming. Both capillary ends are left open to the air. No external flow is imposed, and we ensure that there is no global flow by checking that the oil–air interface is not moving. This will be confirmed in Section 3.2, through flow field measurements. During the experiment, the droplet swims from one end of the capillary to the other in typically one hour. Three sets of experiments are conducted. The first set focuses on the shape detection and the tracking of the droplet in square, circular and stretched capillaries (Sections 3.1 and 3.4), with an image acquisition rate of $f_{\text{acq}} = 1 \text{ Hz}$. A second set of experiments is dedicated to the study of the flow field around the droplet in circular capillaries

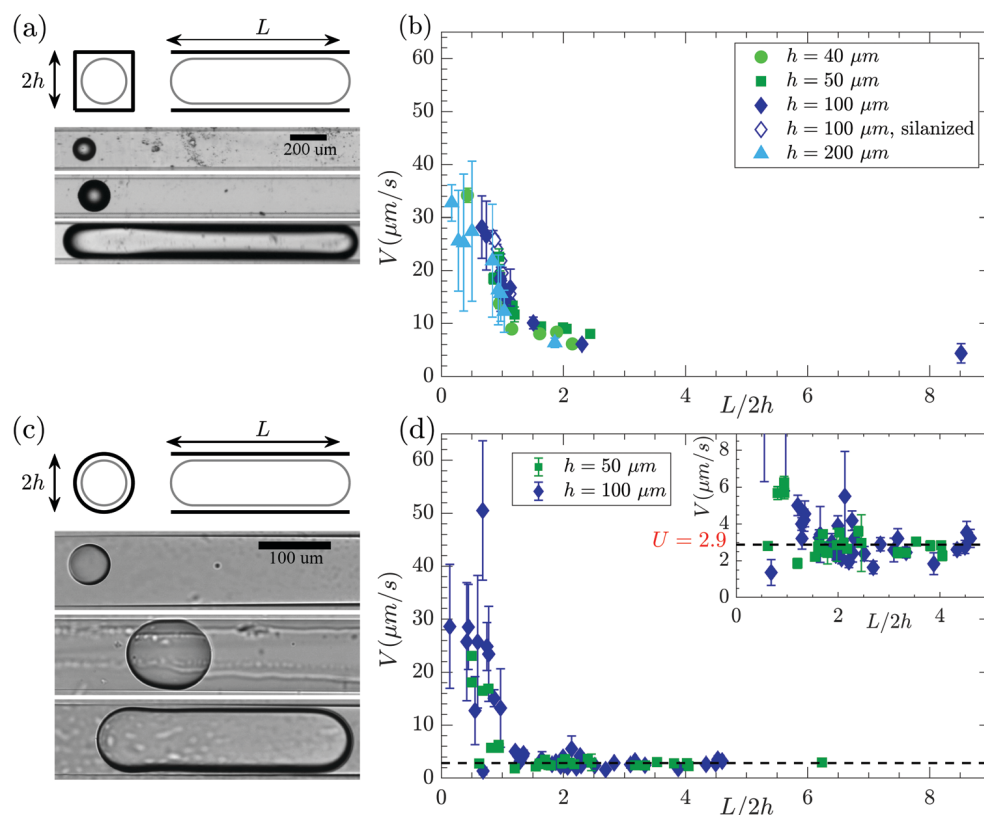


Fig. 1 Droplet velocity in square (top) and cylindrical (bottom) capillaries. (a) Sketch of a droplet in a square capillary, with snapshots of three droplets under increasing confinement $\frac{L}{2h} = 0.5$, $\frac{L}{2h} = 1$, $\frac{L}{2h} = 8.5$ in a square capillary of half-width $h = 100 \mu\text{m}$. (b) Velocity V of droplets of various lengths L swimming alone in square capillaries of different half-heights h , as a function of the confinement $\frac{L}{2h}$. (c) Sketch of a droplet in a circular capillary, and snapshots of three droplets under increasing confinement $\frac{L}{2h} = 0.5$, $\frac{L}{2h} = 1.5$, $\frac{L}{2h} = 4$ in a circular capillary of radius $h = 50 \mu\text{m}$. (d) Velocity V of droplets of various lengths L swimming alone in circular capillaries of different radii h , as a function of the confinement $\frac{L}{2h}$. The straight horizontal dotted line stresses the fact that even for the largest confinement, the droplet velocity is non-zero. The inset is a zoom of the same data on the low velocity values.

using particle image velocimetry (PIV) (Section 3.2). The image acquisition frequency is then $f_{\text{acq}} = 10 \text{ Hz}$. For the third set of experiments, a high-speed camera is used to capture the dynamics of the rear of the droplet in stretched capillaries during splitting events (Section 3.5), with an acquisition rate of $f_{\text{acq}} = 1 \text{ kHz}$ or $f_{\text{acq}} = 10 \text{ kHz}$. A complete description of the materials and methods is given in Appendix A.

3 Experimental results

We start by conducting experiments in glass capillaries of square or circular cross-sections of comparable inner size between $h = 40 \mu\text{m}$ and $h = 200 \mu\text{m}$. Upon production, in square capillaries, all the droplets start swimming. In circular ones, droplets of size up to six times the capillary diameter also swim. We observe that the droplets produced with longer sizes spontaneously divide into two droplets which each start swimming in opposite directions: the one swimming toward the closest end of the capillary immediately gets stuck on the oil–air interface, while the other swims to the other end of the capillary. After less than a minute, all swimming droplets reach a stationary state, and maintain a

persistent direction with the exception of the very small droplets, essentially unconfined ($\frac{L}{2h} < 0.2$), that sometimes change direction. In the following, we focus on droplets swimming persistently in one direction.

3.1 Droplet velocity vs. confinement

The behaviour of a swimming droplet strongly depends on the confinement, but is similar for different capillary geometries. A video of the swimming of three droplets of different sizes ($L = 50 \mu\text{m}$, $90 \mu\text{m}$ or $400 \mu\text{m}$) in circular capillaries of radius $h = 50 \mu\text{m}$ is provided in the electronic ESI.† Typical shapes of droplets in square and circular capillaries are shown in Fig. 1, together with the dependence of their velocity with the confinement $\frac{L}{2h}$. For all droplets, we measure the velocity averaged in time $\langle V \rangle$, together with its standard deviation $\sqrt{\langle V^2 \rangle - \langle V \rangle^2}$.

Droplets smaller than the capillary inner size are spherical of diameter L ($\frac{L}{2h} < 1$). Such droplets oscillate between the two sides of the channel (in the median plane perpendicular to gravity).

Because of buoyancy, they follow the bottom wall, thus performing a 2D motion on the bottom plane of a square capillary, and a 3D motion on the curved bottom surface of a circular capillary. The velocity of the droplet varies during an oscillation: it is minimum when the droplet reaches a side wall, and maximum far from the walls. The variations of the velocity during an oscillation period explain the large standard deviation of the velocity. Existing theoretical works^{23,24} on the behavior of swimmers in channels of circular section have predicted the existence of helical trajectories for neutral squirmers. Identifying precisely whether the observed oscillations pertain to this class of dynamics would require extracting the 3D trajectories of the droplets, together with their surrounding flow field, an interesting perspective for future studies.

Droplets larger than the capillary inner size take an elongated shape ended with two spherical caps. The total length of the droplet is denoted L ($\frac{L}{2h} \geq 1$). The elongated part of the droplet is separated from the glass wall by a film of oil (the droplet is never observed to wet the glass). Inside a square capillary, the gutters of the square cross-section give space for the outer fluid to flow. Inside a cylindrical capillary, the droplet is separated from the wall by a lubrication film of up to a few micro-meters in thickness only. We observe that the cross-section of the droplet has a radius that varies along its length, reaching a local minimum at the rear of the droplet. The region where the droplet radius is the thinnest is called the neck in what follows.

As expected, the velocity decreases with increasing confinement. More surprisingly, for confinement greater than 1 (elongated droplets), the droplet velocity rapidly converges toward a small

but finite value. As a matter of fact, the velocity remains constant while further increasing the confinement, up to $\frac{L}{2h} = 9$ in square capillaries and $\frac{L}{2h} = 6.5$ in circular capillaries. This is all the more intriguing in the case of the cylindrical capillaries, for which the mass conservation imposes that a significant amount of fluid must be driven through the thin lubrication film, leading to a potentially strong dissipation.

In the following, we focus on the behaviour of long droplets ($\frac{L}{2h} > 2$) in circular capillaries, the most intriguing situation and also the simplest geometry to handle theoretically.

3.2 Flow field

We start with PIV measurements of the flow field around the droplet. PIV is performed in the median plane, perpendicular to the gravity, of droplets swimming in cylindrical capillaries of radius $h = 50 \mu\text{m}$. Fig. 2 displays, from top to bottom, the component u_x and u_y of the flow field and a few selected streamlines around (a) a spherical droplet of typically the size of the capillary, $\frac{L}{2h} = 1$, and (b) a long droplet of size $\frac{L}{2h} = 3$. Note that, although the u_x velocity component, strictly at the apex of the droplet, is expected to be positive and equal to the droplet velocity, we measure a slightly negative value for u_x in front of the droplet. It is likely that we do not resolve well enough the velocity field at the interface of the droplet because of the conjugated effects of the non-zero thickness of the illumination plane, the resolution of the PIV, and the 3D recirculation flow that takes place close to the interface.

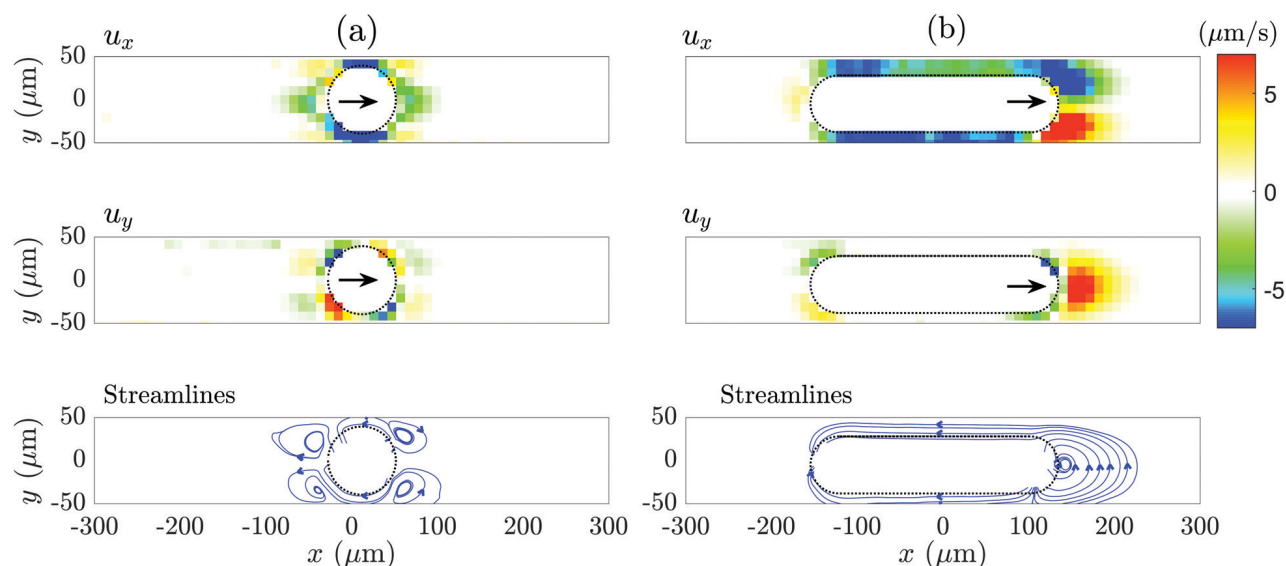


Fig. 2 PIV of the flow field around droplets swimming in circular capillaries: PIV around (a) a circular droplet ($\frac{L}{2h} = 1$) and (b) a long droplet ($\frac{L}{2h} = 3$) in a circular capillary of radius $h = 50 \mu\text{m}$. The two first rows display the color-map of the velocities u_x (direction of swimming) and u_y around the droplet in the reference frame of the lab. The black arrows point in the swimming direction of the droplet. The third row shows several streamlines around the droplet, with blue arrows that show the local direction of the flow. The inside of the droplet, masked during the PIV, is delimited by black dashed lines. x is the direction of swimming of the droplet, (xy) is the visualisation plane, orthogonal to the direction of the gravity z . The droplet's mask used for the PIV analysis is slightly smaller than the droplet size (for PIV requirement). As a result, the gap between the drop and the wall is seen larger than in reality in this representation. The flow field is to be understood as being integrated over the thickness of the PIV depth of field of a few microns.

This observation calls for a careful interpretation of our PIV observations, which should be taken as a qualitative image of the flow field, and not a quantitative 3D description as done by some of us,³⁵ when characterizing the dynamics of droplet swimming above a bottom wall. Similarly, the resolution of the PIV (10 μm per pixel), is not large enough to resolve the flux in the lubrication film on the side of the droplet, and therefore only gives a global indication of the flow direction, thanks to the depth of field of the PIV setting.

This being said, the first crucial observation is that there is no flow far from the droplet (although the two ends of the capillary are left open to the air). All flows take place close to the droplet interface, up to a distance of typically the droplet size.

In the case of spherical droplets, the flow is symmetric in y , and two recirculating regions are observed at the front and back of the droplet. The velocity of the fluid in these regions is similar in magnitude to the droplet velocity ($\sim 3 \mu\text{m s}^{-1}$). It is also worth noting that the dominant symmetry of the flow field around the droplet is quadrupolar, in contrast with the flow field around 3D unconfined squirmers, where the dipolar symmetry is dominant, and with that of swimming droplets close to a wall,³⁵ where the monopolar symmetry is dominant.

In the case of long droplets, a large recirculating region is observed at the front of the droplet, breaking the symmetry

along the y axis. The direction of the recirculation is stable during one experiment but switches between the two possible directions from one experiment to another. The physical origin of the recirculation remains unclear, but it may result from the instability of the stagnation point of the flow at the apex of the droplet. The velocity of the fluid in this region ($u_x \sim 10 \mu\text{m s}^{-1}$) is larger than the droplet velocity ($U \sim 3 \mu\text{m s}^{-1}$). Finally, we notice that the PIV at the back of the droplet is disturbed by an agglomeration of the tracers at a stagnation point located at the extremity of the back cap, which makes the precise flow profile not fully resolved in this region. One can still observe a strong asymmetry between the front and rear in the amplitude of the flow, contrasting with the case of the spherical droplets. A more advanced interpretation of the above descriptions would require a better knowledge of the flow field around a confined active droplet, which is not the purpose of this paper, and is left for future work.

3.3 Shape of the long droplets

Typical shapes for different droplet sizes are illustrated in Fig. 3(a)–(c). The shape of a droplet is stable and averaged over the duration of the experiment. Droplets smaller than the capillary diameter ($\frac{L}{2h}$) are spherical (a) while longer droplets

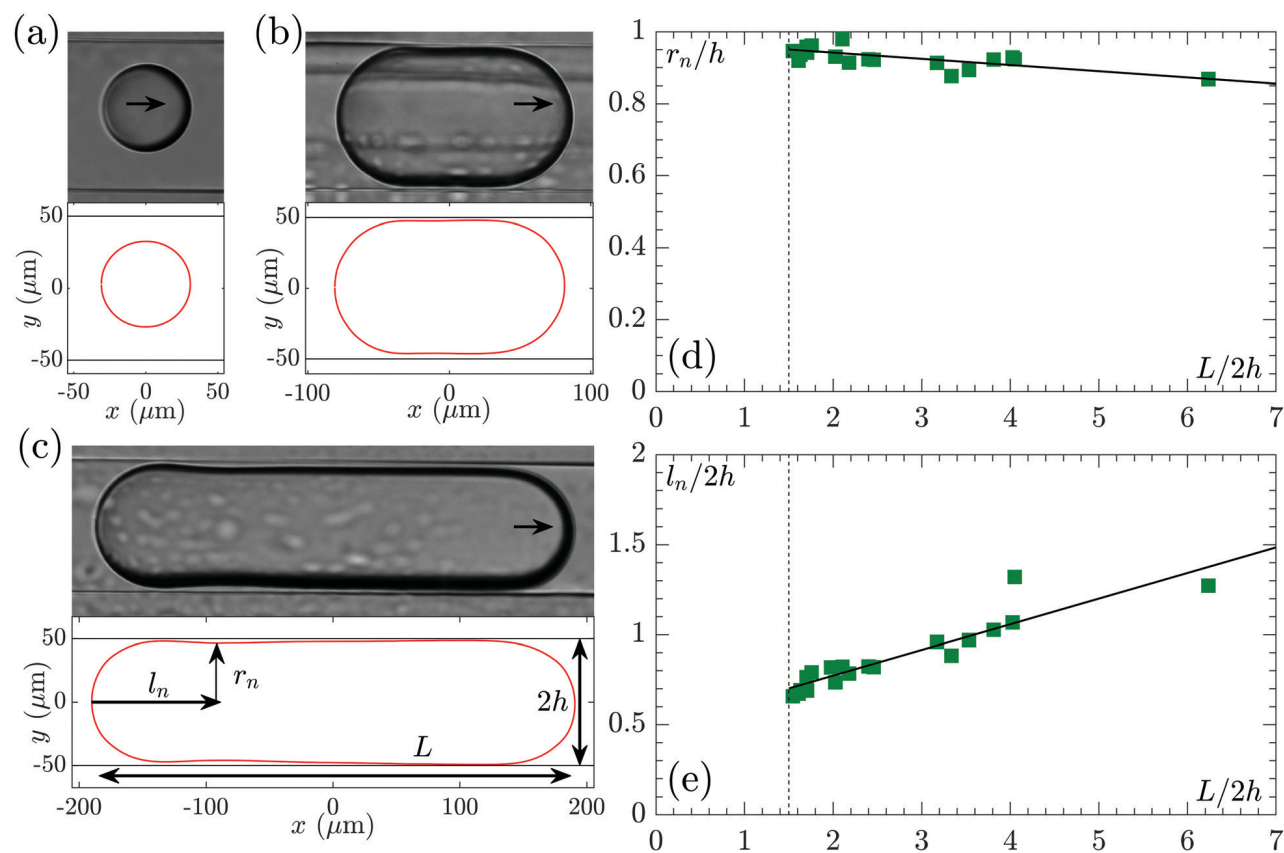


Fig. 3 Shape of an elongated droplet: (a–c), image and corresponding shape of droplets of size (a) $\frac{L}{2h} = 0.5$, (b) $\frac{L}{2h} = 1.7$, and (c) $\frac{L}{2h} = 4$. Long droplets present a neck of radius r_n located at a position l_n from the back of the droplet. (d) Evolution of the dimensionless neck radius $\frac{r_n}{h}$ with the confinement $\frac{L}{2h}$. (e) Evolution of the dimensionless neck position $\frac{l_n}{2h}$ with the confinement $\frac{L}{2h}$. The continuous black lines correspond to a linear regression of the data.

take an elongated shape ((b) and (c)). This elongated shape presents two particularities. First the thickness of the lubrication film is not constant, but increases toward the back of the droplet; this is a tiny but systematic effect. Second, for confinement larger than $\frac{L}{2h} = 1.5$, a neck appears at the rear of the droplet. Fig. 3(d) and (e) display the neck radius r_n , and its distance from the back of the droplet l_n . At the smallest confinement, the neck forms at a distance $\frac{l_n}{2h} \simeq 0.5$. The neck is then shallow, $\frac{r_n}{h} \ll 1$. As the confinement increases, the neck goes further away from the rear of the droplet, and deepens. The shape of the droplet rear hence depends on the droplet length.

The fact that the film thickens from the front to the rear of the droplet and that the neck shape depends on the droplet length contrasts with the standard Bretherton phenomenology,³⁹ which describes the shape and motion of passive droplets driven externally. This underlines the conceptual difference with the present case, where active droplets are driven by self-induced local flows and calls for investigation at even higher confinement.

3.4 Further confinement

Very long droplets ($\frac{L}{2h} > 7$) in circular capillaries are not stable at production and spontaneously divide into two or more droplets. A way to explore higher confinement and to probe continuously its effects on the droplet behavior, is to conduct experiments in stretched circular capillaries. Such devices keep the ideal circular cross-section and mimic perfectly situations where real swimmers have to experience a confinement gradient.

Upon production at one end of the capillary ($h = 50 \mu\text{m}$), the droplet (of typical length between 50 and 150 μm) starts swimming. As it swims down the convergent part of the capillary, the local radius of the capillary decreases and the length of the droplet increases per conservation of the droplet volume $\mathcal{V} \left(L \propto \frac{\mathcal{V}}{h^2} \right)$, as does the confinement $\left(\frac{L}{2h} \propto \frac{\mathcal{V}}{h^3} \right)$. Two different features are observed, a simple elongation of the droplet followed by a contraction after the constriction, or spontaneous successive divisions, presented respectively in Fig. 4 and 6. A video of the swimming of two droplets in the two cases is provided in the ESI.† For each experiment, the droplet is tracked, and its shape detected along its motion. At each time, the radius of the capillary h at the position of the droplet center of mass (b), the confinement of the droplet $\frac{L}{2h}$ (c), the velocity of the droplet V (d), the dimensionless neck radius r_n (e) and the dimensionless neck position l_n (f) are measured as a function of the position of the droplet center of mass x .

Let us first focus on the simple elongation of the droplet. Fig. 4 shows in (a) three snapshots of a droplet swimming in a stretched circular capillary, when it is in the convergent region, at the constriction, and when it is in the divergent region. Two different experiments are shown in Fig. 4, corresponding to

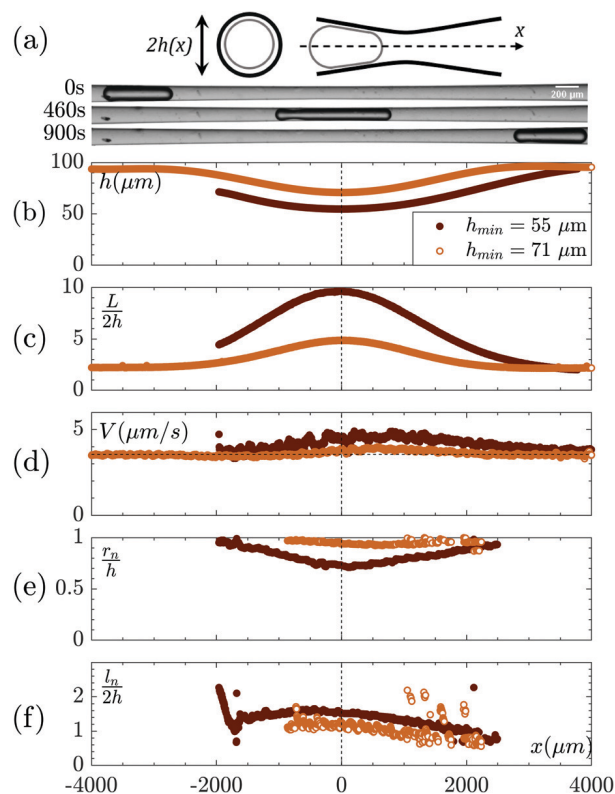


Fig. 4 Elongation of a swimming droplet in a stretched capillary: (a) sketch of the geometry and images of the droplet at three different times corresponding to three positions in the stretched capillary. At 460 s, the droplet is at the position where the confinement is the highest. (b–f) The evolution of several quantities with the position x of the droplet in the capillary. (b) Height of the capillary at the center of mass of the droplet, (c) confinement of the droplet, (d) velocity of the droplet, (e) dimensionless radius of the neck, (f) dimensionless distance of the neck from the front of the droplet. The vertical black dashed line marks the position of the minimum capillary diameter. The two colors correspond to two different experiments made with different droplet sizes and capillary shapes.

different stretched capillaries, with a minimal radius of $h_{\min} = 55 \mu\text{m}$ and $h_{\min} = 71 \mu\text{m}$ respectively. Throughout the experiment, the droplet swims from one end of the capillary to the other. We note a small variation of the droplet velocity and a more significant dependence of the neck position and radius with the confinement. More importantly, although the thickness profiles of the stretched capillary in the converging and diverging regions are symmetric, the shape and speed of the droplet are not. This is further enlightened on Fig. 5, where we compare the dependence on the confinement of (a) the velocity of the droplet, (b) the neck radius and (c) the neck position between the convergent and divergent part of the capillary for the constriction, $h_{\min} = 55 \mu\text{m}$ (brown diamonds and circles) and the straight circular capillaries (green squares).

The velocity slightly increases with the confinement, but also presents an hysteresis between the convergent (brown diamonds) and divergent (brown circles) regions of the capillary. This variation is most likely due to the gradient of capillary radius and would also exist for passive droplets: the difference of curvature between the front and back meniscus induces a

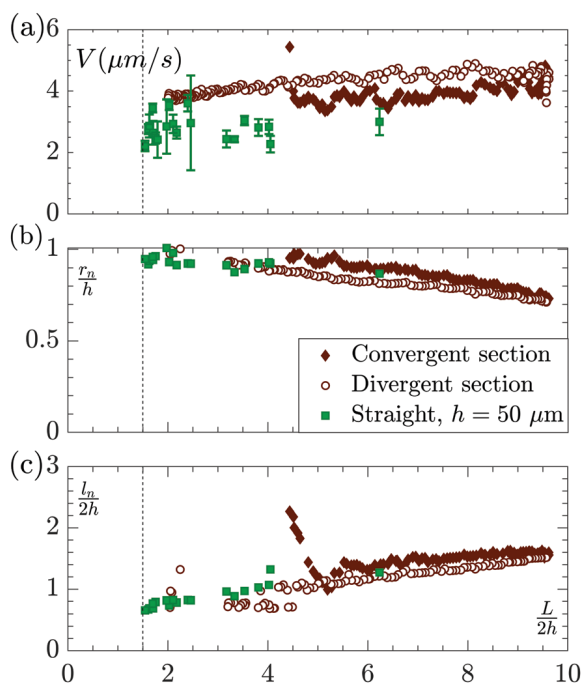


Fig. 5 Convergent vs. divergent dynamics: evolution of (a) the droplet velocity, (b) the dimensionless neck radius and (c) the dimensionless neck position with the confinement; for droplets in straight circular capillaries of half height $h = 50 \mu\text{m}$ (green squares), for one droplet in a stretched capillary, in the convergent section (dark brown filled diamond), and in the divergent section (dark brown empty circles).

capillary-induced pressure gradient inside the droplet, which, for passive droplets, makes the droplet move toward the highest radius. For an active droplet, this effect slows down the droplet in a convergent tube, while it accelerates it in a divergent one. This effect remains however weak, and comparable in magnitude to the variability of the velocity from one experiment to another (see the inset of Fig. 1d).

Fig. 5(b) and (c) exhibit the dependence of the shape of the droplet rear with the confinement: the radius of the neck decreases linearly, and its position goes further away from the back of the droplet, for increasing confinement. This evolution is reversible when the confinement is decreasing in the divergent region, indicating that the dynamics can safely be considered quasi-static, and that the influence of the capillary-induced pressure gradient is not significant here. Finally, further increasing the confinement, the neck is expected to narrow, until the droplet eventually divides spontaneously.

3.5 Spontaneous division of the droplet

The spontaneous division of droplets has been observed systematically for a dozen different experiments with a number of successive divisions ranging from one to fourteen. For the sake of conciseness, the results in this section are presented in Fig. 6 using the data from one typical experiment, but all following observations are valid for all experiments. At first the droplet swims and elongates as it moves toward the convergent region of the capillary. This behavior is similar to the one observed in the previous experiment described in Fig. 4. When the droplet

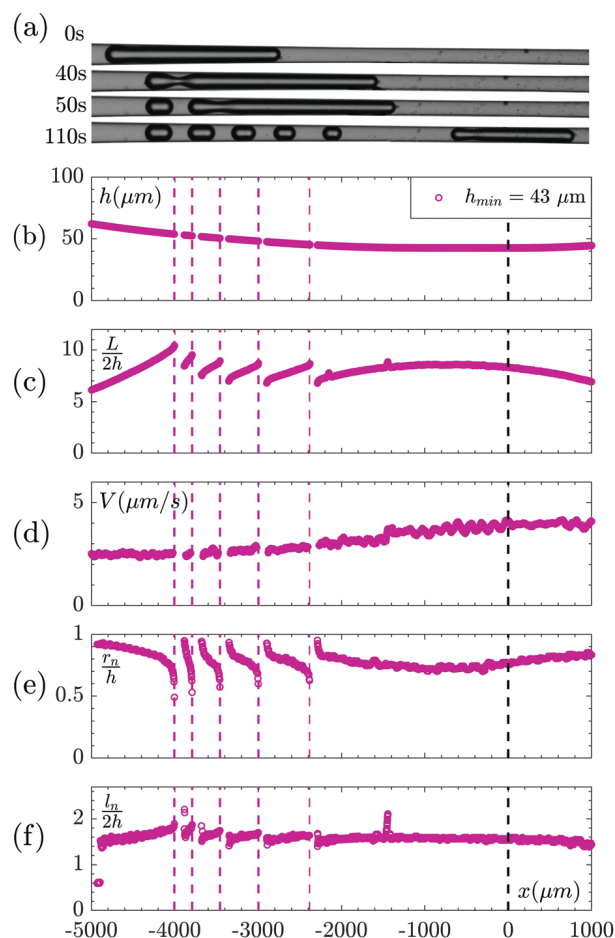


Fig. 6 Division of a droplet in a stretched capillary: (a) images of a droplet at different positions in the stretched capillary: successive divisions occur. (b)–(f) The evolution of quantities depending of the position x of the droplet in the capillary, for the corresponding experiment. (b) Height of the capillary at the center of mass of the droplet, (c) droplet confinement, (d) droplet velocity, (e) dimensionless radius of the neck, and (f) dimensionless distance of the neck from the front of the droplet. The pink dashed lines correspond to a division. The black dashed line corresponds to the position of the minimum height in the capillary.

becomes “too confined” (at time $t = 40 \text{ s}$ in the presented experiment and in the ESI⁺ video), it undergoes a spontaneous division at the position of the neck, as can be seen in Fig. 6(a). The daughter droplet (formed by the previous rear of the droplet) does not swim, which suggests that there is no fuel anymore for propulsion, namely that all micelles present in its environment have been saturated with water. The main droplet that shrunk in volume keeps swimming in the same direction. As the confinement of the droplet further increases, the droplet eventually divides a second time or more. Once the main droplet reaches the divergent region, its length decreases due to volume conservation. No division is observed in the divergent region. The behaviour of the droplet only differs from the simple elongation case at the approach of a division event ($\sim 50 \text{ s}$ before division).

Let us describe a succession of spontaneous divisions (Fig. 6(b)–(f)). Right before the division, the neck rapidly shrinks (e), until its radius reaches 0 at division. The confinement (c) at

which the division occurs, $\frac{L}{2h} \sim 10$ for the presented experiment, slightly decreases with the successive divisions. This last observation has yet to be understood. We speculate that the gradient of height of the capillary, which decreases slightly in the area of division, could play a role. More generally for all experiments, the divisions occur for a confinement level in the range $\frac{L}{2h} = [8 - 20]$, where the disparity amongst experiments can here also be attributed to variations in the imposed height gradients, from one capillary to another.

In this series of experiments, the time and spatial resolutions are not large enough to give access to the precise dynamics of a division. Another series of experiments have thus been conducted, using a microscope and a high-speed camera, and focusing on the first division of a long droplet. Because the field of view is limited, to a square of typical size $2h$, the position of the neck l_n cannot be quantitatively resolved, but the radius of the neck r_n is measured precisely. The dynamical evolution of r_n for two experiments are presented in Fig. 7, one conducted at an acquisition frequency of 1000 Hz, with a spatial resolution of $1.692 \mu\text{m}$ per pix (orange top oriented triangles), and another conducted at an acquisition frequency of 10 000 Hz, with a spatial resolution of $0.840 \mu\text{m}$ per pix (red down oriented triangles). Fig. 7 also shows the dynamical evolution of r_n for the first division of the droplet in the previous experiment conducted at a frequency of 1 Hz (pink empty circles), and the dynamical evolution of r_n during an experiment without division (dark brown full circles). In the figure, the time $t = 0$ corresponds to the division time (evaluated with the temporal resolution of each experiment). For the experiment without division, it is set such that the neck radius matches in the converging part of the capillary. Fig. 7(a) presents the data in a linear plot, while Fig. 7(b) presents the same data in a log-log plot.

The radius of the neck follows three successive regimes; the first one ($t \lesssim -10$ s) corresponds to the adaptation of the droplet shape to the confinement gradient, as discussed in Section 3.4. For droplets that do not undergo division, this regime is reversible when the confinement increases again. In this regime, the evolution of the shape of the droplet is quasi-static, and controlled by the geometry of the problem. The second and third regimes lead to the division of the droplet. Once the droplet enters these regimes, the division always takes place. The second regime is very well characterized by a power-law dependence of the neck radius with time $-t$, $\frac{r_n}{h} \approx 0.1$, $\frac{r_n}{h} \sim |t|^\beta$ with $\beta \in [1/8 - 1/6]$ over almost 3 decades in time. For $\frac{r_n}{h} \lesssim 0.1$, the radius of the neck deviates from the latter power law and deepens faster, entering a third regime that also follows an apparent power-law $\frac{r_n}{h} \sim |t|^\alpha$ with $\alpha \in [2/3 - 1]$.

Such power-law behaviours are naturally found in the ultimate fate of the break-up process for a droplet, because of the absence of characteristic length-scale but also in transient regimes.⁴⁰ The value of the exponent is dictated by which effects dominate and balance amongst surface tension, viscous and inertial forces. Here, the viscosity of the outer fluids dominates, and one expects

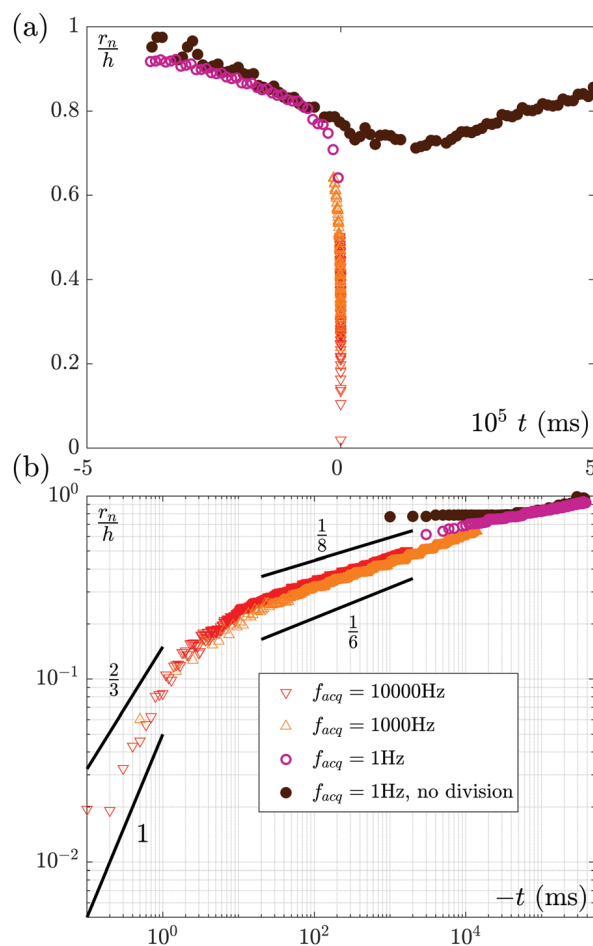


Fig. 7 Dynamic evolution of the neck: (a) linear plot and (b) logarithmic plot of the evolution of the dimensionless neck radius with time. The red and orange triangles and the pink empty circles correspond to experiments at different acquisition frequencies of droplet dividing, considering only the data up to the first division. $t = 0$ corresponds to the time of division. The brown full circles correspond to an experiment with no division, $t = 0$ is then chosen so that the convergent part of the experiment aligns with the others. The continuous black lines provide a lower and upper bound for the power law behaviors of the two fast regimes.

the simple self-similar form to be broken by the presence of logarithmic terms. Finally, the presence of active stresses is likely to alter the already numerous possible scaling regimes. Investigating such a fascinating question is beyond the scope of the present paper. It would require an even faster acquisition rate, and dedicated experiments. The exponents provided here should be seen as indicative and a source of motivation for future work.

Let us recap our main findings, which we now aim to capture theoretically, on the basis of the reformulation of the classical Bretherton problem in the realm of active droplets. Two unexpected phenomena have been observed: the convergence of the droplet velocity towards a constant value when the droplet becomes longer than the capillary height, and the spontaneous division of the droplets under high confinement. In the following section, we introduce a simple theoretical framework that will allow one to grasp the physics at play behind such observations.

4 Theoretical approach

4.1 Introduction

The motion of confined droplets or bubbles under the action of an external flow has been widely studied since its original description by F. P. Bretherton in a cylindrical tube³⁹ and is usually called the Bretherton model in tribute to the British professor. With the emergence of droplet-based microfluidics, a particular interest has been devoted to square channels.^{41,42} Pressure, or gravity driven flows are not the only way to induce droplet motions in a channel. Marangoni stresses can also induce the migration of such confined droplets as described and observed in the presence of external thermal gradients.⁴³ In our case, the motion of the droplets is not externally driven, neither by pressure nor by a temperature gradient as there is no observable flow far from the droplet ($U_\infty = 0$), but is the result of local flows induced by the spontaneous establishment of solute concentration gradients around the droplet. To the best of our knowledge, such a problem has never been considered theoretically before, and is the primary subject of the following section.

The flow around the droplet is driven by a combination of phoretic and Marangoni effects: concentration gradients of all present solute along the interface generates shear stress (denoted σ) and velocity (denoted u) jumps at the interface.¹⁰ For simplicity, we consider in the following that the velocity and stress jumps through the interface result only from the concentration gradient in swollen micelles in the outer fluid, but one should keep in mind that more complex and realistic models of the physico-chemical interactions at the interface have been proposed,⁴⁴ taking into account the surfactant concentration at the interface. Then the velocity and stress jumps can be expressed as: $\sigma_{\text{oil},\parallel} - \sigma_{\text{water},\parallel} = -K\nabla_{\parallel}c$ and $u_{\text{oil},\parallel} - u_{\text{water},\parallel} = M\nabla_{\parallel}c$, where c is the solute concentration field, ∇_{\parallel} is the gradient operator tangent to the interface, $K \approx k_B T \lambda$ and $M \approx k_B T \lambda^2 / \eta_{\text{oil}}$ where $k_B T$ is the thermal energy, λ is the typical interaction distance between the solute and the interface and η_{oil} is the oil viscosity. Under the above assumptions, the Marangoni effects dominate with respect to the phoretic ones,¹⁸ so that, in what follows, we will assume continuity of the velocity across the interface and the presence of a stress jump at the interface. We further notice that the magnitude of the viscous shear stress in the water phase $\sim \eta_{\text{water}} v / h$ is much smaller than the one in the oil phase $\sim \eta_{\text{oil}} v / e$, where v is a typical velocity in the film and e is a typical lubrication film thickness as the viscosity ratio $\eta_{\text{water}} / \eta_{\text{oil}} \approx 1/40$ and the film thickness to capillary height ratio is small with respect to unity, $e \approx 1 \mu\text{m}$ and $h \approx 100 \mu\text{m}$. Therefore, the tangential stress balance simplifies to $\sigma_{\text{oil},\parallel} = \sigma(x) = -K\nabla_{\parallel}c$. We can thus focus on the flow in the oil phase only, and we refer to the oil viscosity as η to lighten the notations. The peculiarity, and difficulty of this problem lies in that the hydrodynamic and the transport of the chemical species (surfactant molecules and swollen micelles) in the solution are non-linearly coupled *via* the Marangoni stress $\sigma(x)$, which varies along the interface.

The present theoretical description deals with highly elongated droplets, swimming in cylindrical tubes that are axially invariant, leaving aside the case of a squared channel.^{43,45}

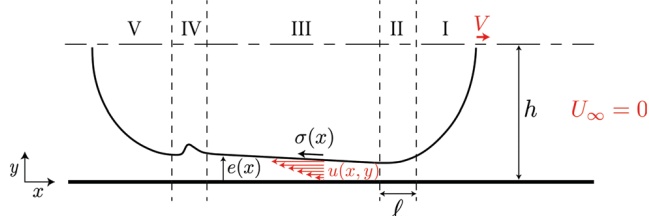


Fig. 8 Sketch of an elongated droplet in a circular capillary, in the lab frame: the droplet is divided into five regions, two spherical caps (I) and (V) of radius h , two dynamical menisci, the front dynamical meniscus (II) of typical size ℓ and the rear dynamical meniscus (IV) where a neck forms, and a lubrication film (III) of variable thickness $e(x)$, where a Marangoni stress $\sigma(x)$ at the interface induces local flows of velocity $v(x,y)$. The resulting droplet velocity is denoted V . Far from the droplet, there is no flow $U_\infty = 0$.

In such a confined environment, various lengths of different magnitude are at play: the radius of the capillary h , the length of the droplet L , the thickness of the lubrication film $e(x)$ and, at the microscopic level, the typical distance of interaction between the solute and the interface λ .¹⁰ Given the large scale separation between these lengths, $L > h \gg e \gg \lambda$, it is a standard approach to separate the problem in different regions and match the corresponding solutions asymptotically.^{39,43} Usually, five zones are distinguished, as exhibited in Fig. 8: the front (I) and rear (V) caps that are supposed spherical, the front (II) and rear (IV) dynamical menisci of variable curvature, and in between the lubrication film (III) that is defined as the limiting solution of the dynamical menisci with a uniform thickness.

We propose to use here a similar approach. In Section 4.2, we derive a lubrication model for the velocity field, coupled to the transport of solute. Then, in Section 4.3, we focus on the lubrication film dynamics (zone III) where capillary flows are negligible behind Marangoni flows and we propose a numerical resolution of the resulting system of equations. This allows us to identify the typical scales of the Marangoni stress and the film thickness in the problem. Lastly, in Section 4.4, we simplify the equation in the dynamical meniscus by assuming a uniform Marangoni stress, of typical magnitude equal to the one identified in zone III, and we find a Landau–Levich type equation. The matching of this solution to the spherical cap allows us to obtain a scaling relation of the droplet velocity, which we finally compare to the experimental data.

4.2 Lubrication model in the zone II–III–IV

We consider the steady motion of a water droplet in oil that is assumed to behave as a Newtonian fluid. The Reynolds number $Re = \rho V h / \eta$, where ρ is the oil density is much smaller than unity so that fluid inertia is neglected. The water–oil interface position, denoted $e(x)$, depends on x and is almost parallel to the direction of motion x in the regions II–III–IV so that one can use the lubrication approximation to describe the flow. Therefore the pressure field p is independent of the normal direction y and is given by the Laplace pressure, *via* the normal stress continuity:

$$p(x) = \gamma e''(x) - \gamma / h, \quad (1)$$

where γ denotes the water–oil interfacial tension. We have neglected the non-linear terms in the curvature in accordance with the lubrication approximation. We also suppose that the interfacial tension is uniform, on the basis that the surface tension difference resulting from the chemical activities is small (of the order of one tenth) with respect to the equilibrium surface tension ($\gamma_{\text{water/oil-micelles}} \simeq 2 \text{ mN m}^{-1}$ and $\Delta\gamma_{\text{activity}} \sim 0.2 \text{ mN m}^{-1}$). The momentum balance in the direction of motion reduces to $\partial_x p = \eta \partial_y^2 u_x$, where u_x is the velocity component in x . The shear-stress continuity at the water–oil interface gives $\eta \partial_y u_x|_{y=e(x)} = \sigma(x)$ at leading order in the lubrication scaling, where $\sigma(x)$ is the Marangoni stress. In the reference frame of the moving droplet, the no-slip boundary condition at the wall reads $u_x|_{y=0} = -V$. As a consequence of the global flux conservation, the flux of water must balance the oil flux, which means that the typical velocity in the film v is of the order of Vh/e , where e is the typical lubrication film thickness. Hence, the typical velocity in the film is a hundred times larger than the drop velocity and we can safely approximate the no-slip boundary condition to $u_x|_{y=0} = 0$. The resulting flow is a linear combination of a Poiseuille and Couette term and reads:

$$u_x(x, y) = \frac{p'(x)}{2\eta}(y^2 - 2ye(x)) + \frac{\sigma(x)y}{\eta}, \quad (2)$$

$$u_y(x, y) = -\frac{p''(x)}{2\eta}\left(\frac{y^3}{3} - y^2e(x)\right) + \frac{p'(x)e'(x)y^2}{2\eta} - \frac{\sigma'(x)y^2}{2\eta}. \quad (3)$$

Computing the pressure gradient from (1) and integrating the flow in y allows us to express the flux conservation. We find:

$$\frac{\gamma e^3(x)e'''(x)}{3\eta} + \frac{\sigma(x)e^2(x)}{2\eta} = -\phi, \quad (4)$$

where the oil flux per unit of orthoradial length is denoted $-\phi$, such that ϕ is a positive quantity. The first term on the left hand side of this equation corresponds to the driving by capillarity and the second one to the Marangoni ones. The global mass conservation in a plane perpendicular to the capillary axis implies that the flux of advected oil in the lubrication layer must balance the longitudinal water flux

$$\pi h^2 V = 2\pi h \phi. \quad (5)$$

The Marangoni stress originates microscopically from the gradients of swollen micelles interacting with the interface. The transport of swollen micelles obeys the stationary advection–diffusion equation

$$u_x(x, y) \frac{\partial c}{\partial x} + u_y(x, y) \frac{\partial c}{\partial y} = D \left(\frac{\partial^2 c}{\partial x^2} + \frac{\partial^2 c}{\partial y^2} \right) \approx D \frac{\partial^2 c}{\partial y^2}, \quad (6)$$

where D is the diffusion constant of swollen micelles in solution and $c(x, y)$ denotes the concentration fields of solute. In what follows, the diffusion terms in x are neglected with respect to the ones in y in agreement with the lubrication approximation. The swollen micelles are produced at the water–oil interface with a rate A , also called the droplet activity, which is assumed to be constant, and gives the boundary conditions at the water–oil interface

$$D \frac{\partial c}{\partial y} \Big|_{y=e(x)} = A. \quad (7)$$

The wall is assumed to be impermeable such that the diffusive flux vanishes at the wall, *i.e.* $-\frac{\partial c}{\partial y} \Big|_{y=0} = 0$. The Marangoni stress is induced by the concentration gradient tangent to the interface as

$$\sigma(x) = -K(\vec{t} \cdot \vec{\nabla})c \Big|_{y=e(x)} = -K(\partial_x + e'(x)\partial_y)c \Big|_{y=e(x)}. \quad (8)$$

In the following we shall not solve the general lubrication problem but focus on the dominant swimming mechanism with the aim at identifying the scaling governing the droplet velocity. In the next section, we focus on the solution in the lubrication film, which corresponds to zone III in Fig. 8.

4.3 Scaling and numerical solution in zone III

In this region, the water–oil interface is nearly flat, although we stress that the film thickness is not necessarily uniform in the lubrication film zone, which is the major difference with classical Bretherton models. The goal of this section is to provide a solution of the lubrication model in zone III.

A first step is to identify the proper length and stress scales at play. The dimensionless ratio ϕ/D is the ratio between horizontal and vertical transport scales. According to eqn (6), $u_x/D \sim x^*/e^{*2}$, where e^* and x^* denote the characteristic thickness of the film and x scales, so that $\phi/D \sim x^*/e^*$. This ratio compares advection to diffusion and is therefore analogous to a local Péclet number. In the experiments presented here, its typical magnitude is large $\text{Pe} = \phi/D \sim 100$ (see Appendix B). One finds from eqn (7) a concentration scale $c^* = \frac{A}{D}e^*$ and, from eqn (8), a stress scale $\sigma^* = \frac{KA}{\text{Pe}D} = \frac{KA}{\phi}$. The length scale e^* is chosen such that the Marangoni driving dominates in eqn (4) so that $\frac{\sigma^*e^{*2}}{\eta} = \phi$, and one obtains:

$$e^* = \phi \sqrt{\frac{\eta}{KA}}, \quad x^* = e^* \phi/D, \quad \sigma^* = \frac{KA}{\phi}, \quad c^* = \frac{\phi}{D} \sqrt{\frac{A\eta}{K}}, \quad (9)$$

Coming back to eqn (4), we then find that the Marangoni driving dominates as soon as $\sigma^*e^{*2} \gg \frac{\gamma e^{*4}}{x^{*3}}$, or, in other words when $x^* \gg \ell^*$, with $\ell^* = e^* \left(\frac{\sqrt{\eta KA}}{\gamma} \right)^{-1/3}$. One notices that the length scale ℓ^* has a similar scaling form as the dynamical meniscus length in the classical Landau–Levich–Derjaguin–Bretherton problem. A nice way to see the analogy is to understand the ratio $\text{Ca} = \frac{\sqrt{\eta KA}}{\gamma}$ as the ratio of two velocities, the Marangoni driving velocity $v^* = \sqrt{\frac{KA}{\eta}}$ and the capillary one $V_\gamma = \frac{\gamma}{\eta}$ exactly as in the classical problem where the driving velocity is externally set and $\text{Ca}_B = V/V_\gamma = \eta V/\gamma$. In the experimental system, the capillary number is estimated as $\text{Ca} \sim 10^{-3}$ (see Appendix B), which is small with respect to unity. Therefore it justifies the use of the Bretherton type scale separations in the present work.

We introduce the dimensionless variables with $\tilde{\cdot}$ as $e(x) = e^* \tilde{e}(\tilde{x})$, $y = e^* \tilde{y}$, $x = x^* \tilde{x}$, $c(x, y) = c^* \tilde{c}(\tilde{x}, \tilde{y})$, $\sigma(x) = \sigma^* \tilde{\sigma}(\tilde{x})$ and eqn (4) and (6)–(8) become:

$$-\frac{2\tilde{y}}{\tilde{e}^2} \frac{\partial \tilde{c}}{\partial \tilde{x}} + \frac{2\tilde{e}' y^2}{\tilde{e}^3} \frac{\partial \tilde{c}}{\partial \tilde{y}} = \frac{\partial^2 \tilde{c}}{\partial \tilde{y}^2}, \quad (10)$$

$$\left. \frac{\partial \tilde{c}}{\partial \tilde{y}} \right|_{\tilde{y}=\tilde{e}} = 1, \quad \left. \frac{\partial \tilde{c}}{\partial \tilde{y}} \right|_{\tilde{y}=0} = 0, \quad (11)$$

$$\tilde{\sigma}(\tilde{x}) = -\frac{2}{\tilde{e}^2(x)} = (\partial_{\tilde{x}} + \tilde{e}'(\tilde{x}) \partial_{\tilde{y}}) \tilde{c} \Big|_{\tilde{y}=\tilde{e}}. \quad (12)$$

The later equations are solved numerically using a volume-of-fluid method.⁴⁶ Eqn (10) is analogous to a 1D heat equation where $-\tilde{x}$ represents time. Therefore, we set “initial conditions” at $\tilde{x} = 0$ and solve for negative \tilde{x} . In this model, the initial conditions represent an arbitrary x position near the boundary between zone II and III in Fig. 8. There we assume that the solute has not diffused over the full lubrication film and is localized near the water/oil interface. We proceed as follows: we first choose an initial thickness $\tilde{e}(\tilde{x} = 0)$ and we take the initial concentration fields as $\tilde{c}(\tilde{x} = 0, \tilde{y}) \propto \exp\left(\frac{\tilde{e}(\tilde{x} = 0) - \tilde{y}}{\mathcal{L}}\right)$, where \mathcal{L} is a dimensionless length scale that would correspond to the length over which the solute has diffused on the region I–II in Fig. 8. The prefactor of the initial concentration is set to be consistent with the flux boundary condition eqn (11).

Fig. 9 displays the numerical solution of eqn (10). We exhibit four solutions with a subscript $i = (1, 2, 3, 4)$ that differs *via* their initial conditions, plotted in Fig. 9(a). Panel (b) shows the evolution of the lubrication film thickness along the x -axis for these four different initial conditions. The lubrication film converges toward a uniform solution, with a constant thickness $e_\infty \simeq \sqrt{2}e^* = \sqrt{2}\phi\sqrt{\eta/(KA)}$, a constant concentration gradient $\partial_x c$ and a Marangoni stress $\sigma_\infty = -\sigma^* = -KA/\phi$, whatever the initial film thickness and concentration. The exact prefactor $\sqrt{2}$ is obtained analytically in Appendix C, injecting a uniform solution ansatz in eqn (6)–(8). The concentration field of solution 1 is displayed in Fig. 9(c). As already stressed, the film thickness is not uniform; the uniform solution is obtained only for $|x| \gtrsim x^*$, that is when the solute diffusing front reaches the wall at $y = 0$. The concentration fields in this regime are in very good agreement with the uniform solution computed in Appendix C. At this stage the problem is not closed as the flux Φ is still unknown.

4.4 Scaling of the droplet velocity

In this section, we aim at deriving a scaling law for the droplet velocity using the aforementioned scales. Solving the lubrication problem in zone II, requires the full resolution of eqn (4), which has no simple or scaling solution. We therefore assume that the Marangoni stress in zone II does not change much and we give it a uniform value set by that of the uniform solution of the lubrication film $\sigma(x) = \sigma_\infty = -\sigma^*$. This is a strong assumption which will only be validated by comparison with the experimental

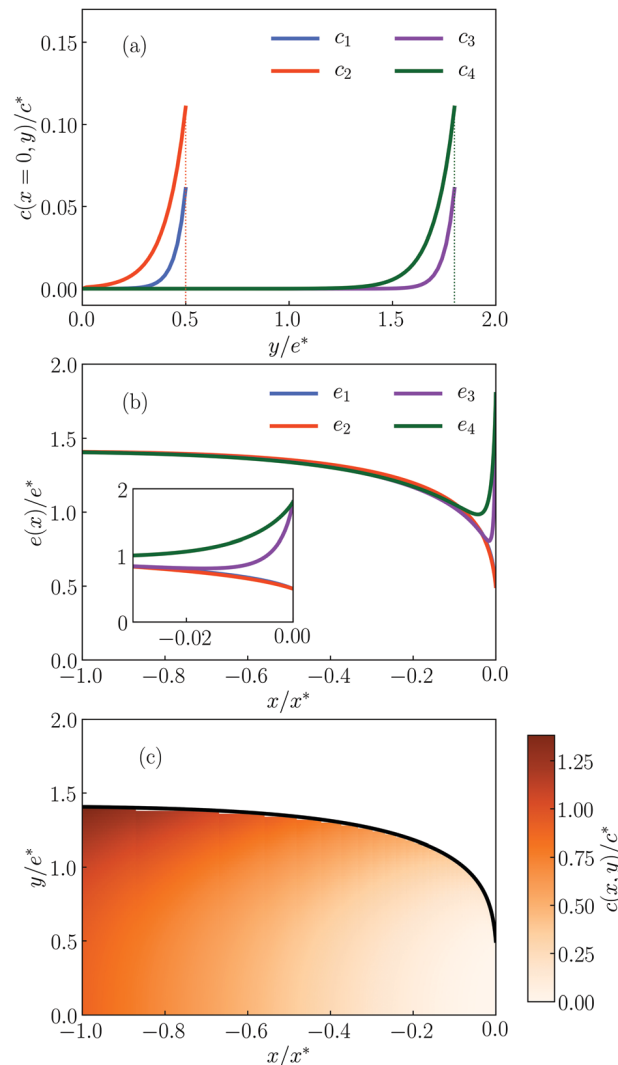


Fig. 9 (a) Initial conditions at $x/x^* = 0$ for the concentration fields given by $\tilde{c}(\tilde{x} = 0, \tilde{y}) \propto \exp\left(\frac{\tilde{e}(\tilde{x} = 0) - \tilde{y}}{\mathcal{L}}\right)$. The initial thickness is set to $\tilde{e}(\tilde{x} = 0) = 0.5$ (resp. 1.8) in the initial conditions denoted 1–2 (resp. 3–4) and the dimensionless length $\mathcal{L} = 0.05$ (resp. 0.1) in 1–3 (resp. 2–4). (b) Evolution of the non-dimensional film thicknesses along the x -axis in the numerical simulation for the different initial conditions. The inset shows a zoom near $x = 0$. (c) Colormap of the non-dimensional concentration field of solute $c(x, y)/c^*$ resulting from the numerical integration with the initial condition 1. The thickness profile is highlighted in black.

data. Having done so, eqn (4) is written in a closed form and one can then use $e_\infty = \sqrt{2}e^*$ and ℓ^* as a thickness and x scale and write the resulting flux conservation in a universal form using the dimensionless variables $E(X) = e(x)/(\sqrt{2}e^*)$, $X = x/\ell^*$:

$$\frac{2}{3} \frac{d^3 E}{dX^3} = \frac{E^2 - 1}{2E^3}. \quad (13)$$

The latter equation admits a trivial solution $E = 1$, which corresponds to the uniform film usually found in Bretherton models and which is identical to the uniform solution found at $|x| > x^*$ in the previous section. We solve eqn (13) numerically following the standard Landau–Levich approach. We assume a

uniform film at $X \rightarrow -\infty$, and linearize eqn (13) as $E = 1 + \varepsilon$, where $\varepsilon \ll 1$, which gives $\frac{2}{3}\varepsilon'''(X) = \varepsilon(X)$. The solution compatible with the flat film at $-\infty$ is $\varepsilon(X) = \varepsilon_0 \exp\left(\left(\frac{3}{2}\right)^{1/3} X\right)$, where ε_0 is an arbitrary constant. We then solve the initial value problem defined by eqn (13) using a Runge–Kutta scheme of order 4 and with the linear solution as an initial condition. The numerical solution is found to diverge at $X \rightarrow \infty$ with a finite second derivative, leading to $\lim_{x \rightarrow \infty} e''(x) = \frac{2.125}{e^*} \left(\frac{\sigma^* e^*}{\gamma}\right)^{2/3}$ for the dimensional variables. The limit curvature must be matched to the curvature of the spherical caps $\frac{1}{h}$ in order to preserve the continuity of the pressure in the region I and II, which yields the following relationship

$$\frac{e^*}{h} = 2.125 \left(\frac{\sigma^* e^*}{\gamma}\right)^{2/3}. \quad (14)$$

Note that, although the right hand side term of eqn (13) differs from the standard Landau–Levich–Derjaguin and Bretherton one, the film thickness scaling law remains of the same form, as $\sigma^* e^* / \gamma = \sqrt{\eta K A} / \gamma = \text{Ca}$. The reason is that the exponent $2/3$ results from the presence of the third order derivative in the left hand side of eqn (13) and the fact that the asymptotic matching with the spherical caps involves the curvature, hence the second derivative of $e(x)$, two aspects which are common to our problem and the classical one. The product of Marangoni stress and film thickness appears as the relevant traction force that deforms the interface, analogous to ηV in the standard Bretherton framework. Finally, recalling the global mass conservation eqn (5), one finds the swimming velocity $V = 2\phi/h = \frac{\sigma^* e^* e^*}{\eta h}$. Combining this expression with eqn (14), we find:

$$V = 2.125 \frac{\sigma^* e^*}{\eta} \left(\frac{\sigma^* e^*}{\gamma}\right)^{2/3} \sim \sqrt{\frac{K A}{\eta}} \left(\frac{\sqrt{\eta K A}}{\gamma}\right)^{2/3} \quad (15)$$

or, in a more compact form,

$$\frac{V}{v^*} \sim \text{Ca}^{2/3}. \quad (16)$$

A first validation of the present scaling relation is that it predicts a swimming velocity which does not depend on the capillary height h , as observed experimentally. Second, we can compute an estimation of the ratio between the film thickness and capillary radius $e^*/h \sim (\sigma^* e^* / \gamma)^{2/3} \sim 1/100$, that implies a film thickness of the order of 1 micron which is consistent with experimental observation. Finally, a numerical evaluation (using the numerical values given in Appendix B) leads to a droplet velocity in the micron per second range, which is consistent with what is observed in the experiments.

4.5 Saturation of the solute

The above description finds that the interface profile saturates once the solute has diffused over the film, at a position $-x \sim x^*$.

We evaluate $\frac{x^*}{2h} \sim 0.1$. This contrasts with the experimental observation of an increasingly deep neck with increasing confinement, that leads to division for $\frac{L}{2h} \gtrsim 10$. Besides, we observe experimentally that the daughter droplets that have detached themselves at the rear of the main droplet don't swim. This suggests that there is no more fuel for the propulsion – all micelles in solution have been saturated with water. We speculate that the spontaneous division of the droplet is related to this saturation of swollen micelles at the rear of the droplet, an ingredient absent so far from our theoretical description.

As a matter of fact, one expects the presence of swollen micelles near the water–oil interface to disturb the sorption kinetic of the surfactant molecules and to slow down the emission of swollen micelles.⁴⁴ In the model, the lubrication film thickness at large $-x$ is found to scale as $e_\infty \propto 1/\sqrt{A}$, and thus is expected to increase as the emission rate decreases. A precise description of the physico-chemistry that triggers the saturation is beyond the scope of this paper, but as a minimal description, the model is consistent with the scenario of a growing lubrication film, at the rear of the droplet, where the non-uniformity is now driven by the saturation of swollen micelles.

Let us simply point out a few elements of thoughts. For droplets that are not too long, we expect a continuous matching between a modest increase of the lubrication film thickness and the rear meniscus, where the active stresses have vanished. In such cases, the dynamics remains steady and the evolution of the droplet shape should be reversible when entering and escaping a constriction zone, as observed experimentally. On the contrary for very long droplets, the diverging lubrication film thickness generates strong curvatures, which will eventually trigger a Rayleigh–Plateau instability and lead to an irreversible dynamical regime, the ultimate fate of which is the division of the droplet.

5 Conclusions

In this work, we present first-of-a-kind experimental measurements of the behavior of a swimming droplet in one-dimensional capillaries of different geometries, namely square capillary, circular capillaries and stretched circular capillaries. For high enough confinement, the velocity of the droplet converges toward a small but non-zero value, while the lubrication layer, which separates the droplet from the wall, acquires non-constant thickness and a neck forms at the rear of the droplet. Under continuously increasing confinement, the deepening of the neck is observed to lead to successive spontaneous divisions of the droplet. A brief study of its dynamics shows rich behaviors that can be the ground for future work.

We introduce a simplified model for the motion of such a confined droplet following the standard Bretherton approach, with the major difference that the flow is locally driven by solute concentration gradient at the interface of the droplet. We focus on the front dynamical meniscus and the lubrication layer.

The latter is treated using the lubrication layer approximation, and we find that the solute concentration converges toward a uniform solution far from the front meniscus with a uniform thickness. The front dynamical meniscus is only treated partially, simplifying the transport equation and assuming a uniform stress at the droplet interface. The matching of these two regions, using the aforementioned uniform solution, allows us to find a scaling relation for the emerging velocity of the droplet, which, as observed experimentally, does not depend on the confinement. Finally we argue that the saturation of the swollen micelles at the rear of the droplet, decreases the solute emission flux, giving rise to increasing film thickness, which ultimately is prone to induce the spontaneous division of long enough droplets.

As the theoretical approach presented in this work was meant to be kept simple, a certain number of hypothesis have been used. Among them, the assumption of a uniform Marangoni stress in the dynamical meniscus is the strongest one. Ideally one would need to solve the advection–diffusion problem also in this region to find the precise prefactor for the droplet velocity and check the robustness of the scaling law derived here.

The experimental measurement of the flow field around a confined swimming droplet, Fig. 2(b) shows that the hydrodynamics in front of the droplet is also more complex than what we considered theoretically. More specifically, we observe a large re-circulation area, which breaks the axisymmetry of the problem. How to capture this symmetry breaking and coupling it to the above description is a completely open question. Not only does it most likely alter the droplet velocity but is also bound to have consequences on the interactions between two droplets.

Finally, the spontaneous division of the droplet under increasing confinement is an unexpected consequence of the limited amount of empty reverse micelles in solution. In this work, we kept the initial concentration of micelles constant. In a complex environment where the concentration of reverse micelles could vary with time and space, this instability would be triggered only in the region where the “food” is scarce, an amazing behavior to observe, especially in the perspective of using simple physical systems in the design of probiotic systems.

Contributions

Charlotte de Blois and Olivier Dauchot initiated the experimental project. Charlotte de Blois and Saori Suda carried out the experiments overseen by Mathilde Reyssat. Vincent Bertin initiated the theoretical part and performed the analytical calculations and the numerical simulations. All authors participated in the development of the theory, discussed the results and contributed to the final manuscript. Charlotte de Blois and Vincent Bertin wrote the manuscript under the guidance of Mathilde Reyssat and Olivier Dauchot.

Conflicts of interest

There are no conflicts to declare.

A Material and methods

The experimental system is a water droplet inside a glass capillary filled with a continuous oil–surfactant phase consisting of a surfactant mixed in squalane. The surfactant is the mono-olein, a nonionic surfactant at a concentration $c = 25 \text{ mmol L}^{-1}$, which is far above its critical micellar concentration ($\text{CMC} \approx 5 \text{ mmol L}^{-1}$). The droplets are produced using Femtojet apparatus by injecting a single droplet of controlled size in the micro-channel previously filled with the oil–surfactant solution, and left opened at both ends. The length of the droplet formed varies between 0.25 and 8 times the capillary inner size (for reference, it would correspond to equivalent spherical droplets of radius between $25 \mu\text{m}$ and $250 \mu\text{m}$.) The droplets are made from a (Milli-Q) water solution of 15 wt% NaCl. The continuous phase is a 25 mM mono-oleine surfactant (MO; 1-oleoyl-rac-glycerol, 99%, Sigma-Aldrich) solution in squalane (Sq; 99%, Sigma-Aldrich). The room temperature is kept above $25 \text{ }^\circ\text{C}$ in order to avoid mono-oleine crystallization.⁴⁷

Three different 1D geometries are used:

(1) Square glass capillaries (Fig. 3(a)) of length 5 cm, and of four different inner sizes: $2h = 400 \mu\text{m}$, $2h = 200 \mu\text{m}$, $2h = 100 \mu\text{m}$ and $2h = 80 \mu\text{m}$. The capillaries are either used native, or silanized beforehand. h is then defined as half the inner dimension of the capillary.

(2) Circular glass capillaries (Fig. 3(b)) of length 10 cm, and of two different inner sizes: $2h = 200 \mu\text{m}$ and $2h = 100 \mu\text{m}$, all silanized. h is then defined as the radius of the capillary. To make possible the imaging through the curved shape of these capillaries, the observation section is immersed into glycerol whose refractive index is close to glass.

(3) Stretched circular capillaries (Fig. 4) of length 3–5 cm, whose inner radius varies continuously along their length between $2h = 100 \mu\text{m}$ (at both ends), and a constriction of diameter $2h_{\text{min}}$, in the middle of the capillary, with a typical gradient of diameter $\frac{dh}{dx} \approx \pm 0.02$. Thus they present a convergent region followed by a divergent one. These capillaries are designed from circular glass capillaries of inner size $2h = 100 \mu\text{m}$ that are stretched by hand by locally heating and stretching a portion of the capillary of typically 0.5 cm. These stretched capillaries are silanized.

Three sets of experiments are conducted.

(i) For the first set of experiments, images of a droplet inside a square or circular capillary are acquired using a AZ100 Nikon microscope, equipped with $\times 1$ air objective. The camera is a black and white camera Dalsa Falcon II, with a resolution of 4096×3072 pixels, and an acquisition frequency of 1 Hz. The microscope has a continuous zoom between $\times 1$ and $\times 8$, and thus has a variable resolution, which is measured before each experiment by using a calibration slide. Typically, to visualize an area of 1 cm in diameter, we use the $\times 3$ zoom, which gives a resolution of 0.3 pix per μm . The droplet motion in the capillary is then tracked in the frame of reference of the laboratory, and its shape is detected using an intensity threshold algorithm.

(ii) A second set of experiments is conducted to measure the flow field around a droplet inside a circular capillary, using a

Particle Image Velocimetry (PIV) technique. Red fluorescent colloids tracers (Fluoro-Max™, 0.6 μm Red Fluorescent Polymer Microspheres, Thermo scientific) are added in the oil phase. The seeding is set to approximately 0.25 colloids per μm³, which corresponds in an illumination plane of depth 5 μm to little more than one colloid per μm², or one colloid per two pixels². The images are acquired with a CCD camera (Andor Zyla 5.5) in the median plane of the droplet using confocal microscopy with a ×10 objective, and a laser beam at 540 nm, which is the absorption wavelength of the tracers. The acquisition frequency is 10 frames per s and the exposure time is 50 ms. The spatial resolution in the plane is 0.65 μm per pixel. For each experiment, 100 images of the droplet and the surrounding flow field are acquired. The PIV analysis is performed using the PIVlab⁴⁸ code on Matlab. Pre-processing is done using a Wiener filter of window size 3 pixels. Then the PIV is performed by using cross-correlation between two successive images in two passes of respective interrogation areas of 64 pixels and 32 pixels, (which corresponds typically to a window containing ten tracer particles) and with a window overlap of 50%. The walls and the inside of the droplet are excluded from the PIV by designing a moving mask for each image. The droplet's mask is designed to be slightly smaller than the droplet size, and is moving with the droplet. Post-processing validation is not used. The final spatial resolution of the mapping of the flow field is then 16 μm per pixel. This provides us with the velocity field in Cartesian coordinates attached to the lab frame at each time step. We then average in time the instantaneous flow fields obtained from PIV, thereby reducing the experimental noise.

(iii) Finally, a third set of experiments focus on the dynamics of the rear of the droplet. Images are acquired using a Leica microscope equipped with a ×10 air objective, and a fast camera Photron Fastcam SA3 with varying acquisition frequencies between 1000 Hz and 10 000 Hz. The same image processing as for the first set of experiments is used to detect the droplet interface.

B Numerical applications

In this section, we give the numerical values used to do the numerical applications done in the main text which are based on the ones used in ref. 18.

Peclet number

Using a swollen micelle radius of $\delta = 2 \times 10^{-9}$ m, the oil viscosity $\eta = 40 \times 10^{-3}$ Pa s, the diffusion constant is evaluated as $D = \frac{kT}{6\pi\eta\delta} \sim 10^{-12}$ m² s⁻¹, $k_B = 1.38 \times 10^{-23}$ J K⁻¹ is the Boltzmann constant and $T = 300$ K is the temperature. We compute $\phi = \frac{Vh}{2} = 1.5 \times 10^{-10}$ m² s⁻¹ using the experimental parameters in Fig. 1, $V = 3$ μm s⁻¹ being the velocity of the droplet and $h = 50$ μm is the height of the channel. Then $Pe = \phi/D \sim 100$.

Capillary number

The surface tension of the water–oil interface is $\gamma = 1.7 \times 10^{-3}$ Pa m, measured using the pendant drop method.⁴⁹

The Marangoni constant K is derived from the relation $K = k_B T \lambda$, where $\lambda = 10 \times 10^{-9}$ m is the typical distance of interaction between the solute and the interface. Then $K \sim 10^{-29}$ J m. The activity, or surface flux A , is derived from the relation $A = \frac{3}{4\pi} \frac{\kappa}{\delta^3}$, where $\kappa = 5 \times 10^{-8}$ m s⁻¹ is the decrease rate of the radius of an unconfined droplet. Then $A \sim 10^{18}$ m⁻² s⁻¹. Finally, the capillary number can be evaluated as $Ca = \frac{\sqrt{\eta K A}}{\gamma} \sim 10^{-3}$.

C Uniform solution

In this section, we write the stationary solution of the solute transport equations. We make the following ansatz for the concentration field and thickness evolution

$$\tilde{c}(\tilde{x}, \tilde{y}) = A_0 + A_1 \tilde{x} + A_3 \tilde{y}^3, \quad \tilde{e}(\tilde{x}) = E. \quad (17)$$

Injecting this solution in eqn (6)–(8), one finds the following coefficient

$$A_1 = -1, \quad A_3 = \frac{1}{6}, \quad E = \sqrt{2}, \quad (18)$$

and A_0 is a free parameter.

Acknowledgements

We thank Sébastien Michelin for interesting discussions all along the duration of the present projects and other related ones. Charlotte de Blois was sponsored by a doctoral fellowship from the Ecole Doctorale Physique en Ile de France. Saori Suda was sponsored by The Kyoto University Foundation (Public Interest Incorporated Foundation) and by JSPS KAKENHI Grant Number 20J15804.

Notes and references

- 1 D. Or, B. F. Smets, J. M. Wraith, A. Dechesne and S. P. Friedman, *Adv. Water Resour.*, 2007, **30**, 1505–1527.
- 2 P. Denissenko, V. Kantsler, D. J. Smith and J. Kirkman-Brown, *Proc. Natl. Acad. Sci. U. S. A.*, 2012, **109**, 8007–8010.
- 3 J. S. Guasto, K. A. Johnson and J. P. Gollub, *Phys. Rev. Lett.*, 2010, **105**, 168102.
- 4 R. E. Pepper, M. Roper, S. Ryu, P. Matsudaira and H. A. Stone, *J. R. Soc., Interface*, 2010, **7**, 851–862.
- 5 Z. Liu, W. Chen and K. D. Papadopoulos, *Biotechnol. Bioeng.*, 1997, **53**, 238–241.
- 6 S. Das, A. Garg, A. I. Campbell, J. Howse, A. Sen, D. Velegol, R. Golestanian and S. J. Ebbens, *Nat. Commun.*, 2015, **6**, 8999.
- 7 G. Noselli, A. Beran, M. Arroyo and A. DeSimone, *Nat. Phys.*, 2019, **15**, 496–502.
- 8 J. Mannik, R. Driessen, P. Galajda, J. E. Keymer and C. Dekker, *Proc. Natl. Acad. Sci. U. S. A.*, 2009, **106**, 14861–14866.
- 9 S. Jana, S. H. Um and S. Jung, *Phys. Fluids*, 2012, **24**, 041901.
- 10 J. Anderson, *Annu. Rev. Fluid Mech.*, 1989, **21**, 61–99.

- 11 R. Golestanian, T. B. Liverpool and A. Ajdari, *New J. Phys.*, 2007, **9**, 126.
- 12 J. R. Howse, R. A. L. Jones, A. J. Ryan, T. Gough, R. Vafabakhsh and R. Golestanian, *Phys. Rev. Lett.*, 2007, **99**, 048102.
- 13 H.-R. Jiang, N. Yoshinaga and M. Sano, *Phys. Rev. Lett.*, 2010, **105**, 268302.
- 14 W. F. Paxton, K. C. Kistler, C. C. Olmeda, A. Sen, S. K. Angelo, Y. Cao, T. E. Mallouk, P. E. Lammert and V. H. Crespi, *J. Am. Chem. Soc.*, 2004, **126**, 13424–13431.
- 15 S. Michelin, E. Lauga and D. Bartolo, *Phys. Fluids*, 2013, **25**, 061701.
- 16 M. Morozov and S. Michelin, *J. Fluid Mech.*, 2019, **860**, 711–738.
- 17 S. Thutupalli, R. Seemann and S. Herminghaus, *New J. Phys.*, 2011, **13**, 073021.
- 18 Z. Izri, M. N. van der Linden, S. Michelin and O. Dauchot, *Phys. Rev. Lett.*, 2014, **113**, 248302.
- 19 C. C. Maass, C. Krüger, S. Herminghaus and C. Bahr, *Annu. Rev. Condens. Matter Phys.*, 2016, **7**, 171–193.
- 20 A. Izzet, P. G. Moerman, P. Gross, J. Groenewold, A. D. Hollingsworth, J. Bibette and J. Brujic, *Phys. Rev. X*, 2020, **10**, 021035.
- 21 E. Lauga and T. R. Powers, *Rep. Prog. Phys.*, 2009, **72**, 096601.
- 22 B. U. Felderhof, *Phys. Fluids*, 2010, **22**, 113604.
- 23 A. Zöttl and H. Stark, *Phys. Rev. Lett.*, 2012, **108**, 218104.
- 24 L. Zhu, E. Lauga and L. Brandt, *J. Fluid Mech.*, 2013, **726**, 285–311.
- 25 A. Acemoglu and S. Yesilyurt, *Biophys. J.*, 2014, **106**, 1537–1547.
- 26 B. Liu, K. S. Breuer and T. R. Powers, *Phys. Fluids*, 2014, **26**, 011701.
- 27 H. Wu, M. Thiébaud, W.-F. Hu, A. Farutin, S. Rafaï, M.-C. Lai, P. Peyla and C. Misbah, *Phys. Rev. E: Stat., Non-linear, Soft Matter Phys.*, 2015, **92**, 050701.
- 28 E. Kanso and S. Michelin, *J. Chem. Phys.*, 2019, **150**, 044902.
- 29 R. Jeanneret, D. O. Pushkin and M. Polin, *Phys. Rev. Lett.*, 2019, **123**, 248102.
- 30 M. N. Popescu, S. Dietrich and G. Oshanin, *J. Chem. Phys.*, 2009, **130**, 194702.
- 31 T.-Y. Chiang and D. Velegol, *Langmuir*, 2014, **30**, 2600–2607.
- 32 W. E. Uspal, M. N. Popescu, S. Dietrich and M. Tasinkevych, *Soft Matter*, 2015, **11**, 434–438.
- 33 Y. Ibrahim and T. Liverpool, *Eur. Phys. J.: Spec. Top.*, 2016, **225**, 1843–1874.
- 34 A. Mozaffari, N. Sharifi-Mood, J. Koplik and C. Maldarelli, *Phys. Fluids*, 2016, **28**, 053107.
- 35 C. de Blois, M. Reyssat, S. Michelin and O. Dauchot, *Phys. Rev. Fluids*, 2019, **4**, 054001.
- 36 C. Jin, C. Krüger and C. C. Maass, *Proc. Natl. Acad. Sci. U. S. A.*, 2017, **114**, 5089–5094.
- 37 P. Illien, C. de Blois, Y. Liu, M. N. van der Linden and O. Dauchot, *Phys. Rev. E*, 2020, **101**, 040602.
- 38 S. Herminghaus, C. C. Maass, C. Krüger, S. Thutupalli, L. Goehring and C. Bahr, *Soft Matter*, 2014, **10**, 7008–7022.
- 39 F. P. Bretherton, *J. Fluid Mech.*, 1961, **10**, 166.
- 40 J. Eggers and E. Villermaux, *Rep. Prog. Phys.*, 2008, **71**, 036601.
- 41 C. N. Baroud, F. Gallaire and R. Dangla, *Lab Chip*, 2010, **10**, 2032.
- 42 I. Cantat, *Phys. Fluids*, 2013, **25**, 031303.
- 43 A. Mazouchi and G. M. Homsy, *Phys. Fluids*, 2000, **12**, 542–549.
- 44 M. Morozov, *Soft Matter*, 2020, **16**, 5624–5632.
- 45 H. Wong, C. J. Radke and S. Morris, *J. Fluid Mech.*, 1995, **292**, 71–94.
- 46 G. Tryggvason, R. Scardovelli and S. Zaleski, *Direct Numerical Simulations of Gas-Liquid Multiphase Flows*, Cambridge University Press, 2001.
- 47 H. Qiu and M. Caffrey, *Biomaterials*, 2000, **21**, 223–234.
- 48 W. Thielicke and E. J. Stamhuis, *J. Open Res. Software*, 2014, **2**, e30.
- 49 J. D. Berry, M. J. Neeson, R. R. Dagastine, D. Y. Chan and R. F. Tabor, *J. Colloid Interface Sci.*, 2015, **454**, 226–237.

Bibliography

- [1] Marco Rivetti, Vincent Bertin, Thomas Salez, Chung-Yuen Hui, Christine Linne, Maxence Arutkin, Haibin Wu, Elie Raphaël, and Oliver Baumchen. Elastocapillary levelling of thin viscous films on soft substrates. *Physical Review Fluids*, 2(9):094001, 2017.
- [2] Zaicheng Zhang, Vincent Bertin, Muhammad Arshad, Elie Raphael, Thomas Salez, and Abdelhamid Maali. Direct measurement of the elastohydrodynamic lift force at the nanoscale. *Physical Review Letters*, 124(5):054502, 2020.
- [3] Vincent Bertin, John Niven, Howard A Stone, Thomas Salez, Elie Raphael, and Kari Dalnoki-Veress. Symmetrization of thin freestanding liquid films via a capillary-driven flow. *Physical review letters*, 124(18):184502, 2020.
- [4] Vincent Bertin, Carmen L Lee, Thomas Salez, Elie Raphael, and Kari Dalnoki-Veress. Capillary levelling of immiscible bilayer films. *Journal of Fluid Mechanics*, 911, 2021.
- [5] Alexandre Vilquin, Vincent Bertin, Pierre Soulard, Gabriel Guyard, Elie Raphaël, Frédéric Restagno, Thomas Salez, and Joshua D. McGraw. Time dependence of advection-diffusion coupling for nanoparticle ensembles. *Phys. Rev. Fluids*, 6:064201, Jun 2021.
- [6] Vincent Bertin, Zaicheng Zhang, Rodolphe Boisgard, Christine Grauby-Heywang, Elie Raphaël, Thomas Salez, and Abdelhamid Maali. Contactless rheology of finite-size air-water interfaces. *Phys. Rev. Research*, 3:L032007, Jul 2021.
- [7] Charlotte de Blois, Vincent Bertin, Saori Suda, Masatoshi Ichikawa, Mathilde Reyssat, and Olivier Dauchot. Swimming droplets in 1d geometries: an active bretherton problem. *Soft Matter*, 17:6646–6660, 2021.
- [8] Vincent Bertin, Yacine Amarouchene, Elie Raphael, and Thomas Salez. Soft-lubrication interactions between a rigid sphere and an elastic wall. *arXiv preprint arXiv:2104.00900*, 2021.
- [9] Pierre-Gilles De Gennes. Soft matter. *Reviews of modern physics*, 64(3):645, 1992.

- [10] Robert Hooke. De potentia restitutiva, or of spring explaining the power of springing bodies. *Sixth Cutler Lecture, published in*, 1678:331–356.
- [11] Pierre-Gilles De Gennes, Françoise Brochard-Wyart, and David Quéré. *Capillarity and wetting phenomena: drops, bubbles, pearls, waves*. Springer Science & Business Media, 2013.
- [12] Antonin Marchand, Joost H Weijs, Jacco H Snoeijer, and Bruno Andreotti. Why is surface tension a force parallel to the interface? *American Journal of Physics*, 79(10):999–1008, 2011.
- [13] Bruno Andreotti, Oliver Bäumchen, François Boulogne, Karen E Daniels, Eric R Dufresne, Hugo Perrin, Thomas Salez, Jacco H Snoeijer, and Robert W Style. Solid capillarity: when and how does surface tension deform soft solids? *Soft Matter*, 12(12):2993–2996, 2016.
- [14] Dadhichi Paretkar, Xuejuan Xu, Chung-Yuen Hui, and Anand Jagota. Flattening of a patterned compliant solid by surface stress. *Soft matter*, 10(23):4084–4090, 2014.
- [15] Serge Mora, Ty Phou, Jean-Marc Fromental, Len M Pismen, and Yves Pomeau. Capillarity driven instability of a soft solid. *Physical review letters*, 105(21):214301, 2010.
- [16] Serge Mora, Ty Phou, Jean-Marc Fromental, and Yves Pomeau. Gravity driven instability in elastic solid layers. *Physical review letters*, 113(17):178301, 2014.
- [17] Joseph R Davis. *Tensile testing*. ASM international, 2004.
- [18] Alexander Ya Malkin and Avraam I Isayev. *Rheology: concepts, methods, and applications*. Elsevier, 2017.
- [19] Joseph D Berry, Michael J Neeson, Raymond R Dagastine, Derek YC Chan, and Rico F Tabor. Measurement of surface and interfacial tension using pendant drop tensiometry. *Journal of colloid and interface science*, 454:226–237, 2015.
- [20] J Drelich, Ch Fang, and CL White. Measurement of interfacial tension in fluid-fluid systems. *Encyclopedia of surface and colloid science*, 3:3158–3163, 2002.
- [21] Daniel A Fletcher and R Dyche Mullins. Cell mechanics and the cytoskeleton. *Nature*, 463(7280):485–492, 2010.
- [22] Hu Zhang and Kuo-Kang Liu. Optical tweezers for single cells. *Journal of the Royal Society interface*, 5(24):671–690, 2008.
- [23] Philip Jones, Onofrio Maragó, and Giovanni Volpe. *Optical tweezers*. Cambridge University Press Cambridge, 2015.

- [24] Jacob Israelachvili, Younjin Min, Mustafa Akbulut, Anna Alig, Gregory Carver, Wren Greene, Kai Kristiansen, Emily Meyer, Noshir Pesika, Kenneth Rosenberg, et al. Recent advances in the surface forces apparatus (sfa) technique. *Reports on Progress in Physics*, 73(3):036601, 2010.
- [25] Peter Eaton and Paul West. *Atomic force microscopy*. Oxford university press, 2010.
- [26] David Tabor and R.H.S. Winterton. The direct measurement of normal and retarded van der Waals forces. *Proceedings of the Royal Society of London. A. Mathematical and Physical Sciences*, 312(1511):435–450, 1969.
- [27] Jacob Nissim Israelachvili and David Tabor. The measurement of van der Waals dispersion forces in the range 1.5 to 130 nm. *Proceedings of the Royal Society of London. A. Mathematical and Physical Sciences*, 331(1584):19–38, 1972.
- [28] Jacob N. Israelachvili and G.E. Adams. Direct measurement of long range forces between two mica surfaces in aqueous KNO₃ solutions. *Nature*, 262(5571):774–776, 1976.
- [29] Jacob Israelachvili. Direct measurements of forces between surfaces in liquids at the molecular level. *Proceedings of the National Academy of Sciences of the United States of America*, 84(14):4722, 1987.
- [30] Bharat Bhushan, Jacob N. Israelachvili, and Uzi Landman. Nanotribology: friction, wear and lubrication at the atomic scale. *Nature*, 374(6523):607–616, 1995.
- [31] Derek Y.C. Chan and R.G. Horn. The drainage of thin liquid films between solid surfaces. *The Journal of chemical physics*, 83(10):5311–5324, 1985.
- [32] Frédéric Restagno, Jérôme Crassous, Elisabeth Charlaix, Cécile Cottin-Bizonne, and Michel Monchanin. A new surface forces apparatus for nanorheology. *Review of scientific instruments*, 73(6):2292–2297, 2002.
- [33] C. Cottin-Bizonne, B. Cross, A. Steinberger, and E. Charlaix. Boundary slip on smooth hydrophobic surfaces: Intrinsic effects and possible artifacts. *Physical review letters*, 94(5):056102, 2005.
- [34] Audrey Steinberger, Cécile Cottin-Bizonne, Pascal Kleimann, and Elisabeth Charlaix. High friction on a bubble mattress. *Nature materials*, 6(9):665–668, 2007.
- [35] Chloé Barraud, Benjamin Cross, Cyril Picard, Frédéric Restagno, Lilianne Léger, and Elisabeth Charlaix. Large slippage and depletion layer at the polyelectrolyte/solid interface. *Soft matter*, 15(31):6308–6317, 2019.
- [36] Samuel Leroy, Audrey Steinberger, Cécile Cottin-Bizonne, Frédéric Restagno, Lilianne Léger, and Elisabeth Charlaix. Hydrodynamic interaction between a spherical particle and an elastic surface: a gentle probe for soft thin films. *Physical Review Letters*, 108(26):264501, 2012.

- [37] Richard Villey, Emmanuelle Martinot, Cécile Cottin-Bizonne, Magali Phaner-Goutorbe, Liliane Léger, Frédéric Restagno, and Elisabeth Charlaix. Effect of surface elasticity on the rheology of nanometric liquids. *Physical review letters*, 111(21):215701, 2013.
- [38] Gerd Binnig, Calvin F Quate, and Ch Gerber. Atomic force microscope. *Physical review letters*, 56(9):930, 1986.
- [39] Vincent T Moy, Ernst-Ludwig Florin, and Hermann E Gaub. Intermolecular forces and energies between ligands and receptors. *Science*, 266(5183):257–259, 1994.
- [40] Matthias Rief, Filipp Oesterhelt, Berthold Heymann, and Hermann E Gaub. Single molecule force spectroscopy on polysaccharides by atomic force microscopy. *Science*, 275(5304):1295–1297, 1997.
- [41] William A Ducker, Tim J Senden, and Richard M Pashley. Direct measurement of colloidal forces using an atomic force microscope. *Nature*, 353(6341):239–241, 1991.
- [42] Hans-Jürgen Butt. Measuring electrostatic, van der waals, and hydration forces in electrolyte solutions with an atomic force microscope. *Biophysical journal*, 60(6):1438–1444, 1991.
- [43] Elmar Bonaccorso, Michael Kappl, and Hans-Jürgen Butt. Hydrodynamic force measurements: boundary slip of water on hydrophilic surfaces and electrokinetic effects. *Physical Review Letters*, 88(7):076103, 2002.
- [44] Ivan U Vakarelski, Judy Lee, Raymond R Dagastine, Derek YC Chan, Geoffrey W Stevens, and Franz Grieser. Bubble colloidal afm probes formed from ultrasonically generated bubbles. *Langmuir*, 24(3):603–605, 2008.
- [45] Ivan U Vakarelski, Rogerio Manica, Xiaosong Tang, Sean J O’Shea, Geoffrey W Stevens, Franz Grieser, Raymond R Dagastine, and Derek YC Chan. Dynamic interactions between microbubbles in water. *Proceedings of the National Academy of Sciences*, 107(25):11177–11182, 2010.
- [46] Raymond R Dagastine, Rogério Manica, Steven L Carnie, DYC Chan, Geoffrey W Stevens, and Franz Grieser. Dynamic forces between two deformable oil droplets in water. *Science*, 313(5784):210–213, 2006.
- [47] Derek YC Chan, Evert Klaseboer, and Rogerio Manica. Film drainage and coalescence between deformable drops and bubbles. *Soft Matter*, 7(6):2235–2264, 2011.
- [48] Rico F Tabor, Franz Grieser, Raymond R Dagastine, and Derek YC Chan. Measurement and analysis of forces in bubble and droplet systems using afm. *Journal of colloid and interface science*, 371(1):1–14, 2012.

- [49] Xiaomin Xiong, Shuo Guo, Zuli Xu, Ping Sheng, and Penger Tong. Development of an atomic-force-microscope-based hanging-fiber rheometer for interfacial microrheology. *Physical Review E*, 80(6):061604, 2009.
- [50] Mathieu Delmas, Marc Monthieux, and Thierry Ondarçuhu. Contact angle hysteresis at the nanometer scale. *Physical review letters*, 106(13):136102, 2011.
- [51] Shuo Guo, Min Gao, Xiaomin Xiong, Yong Jian Wang, Xiaoping Wang, Ping Sheng, and Penger Tong. Direct measurement of friction of a fluctuating contact line. *Physical review letters*, 111(2):026101, 2013.
- [52] Julien Dupré de Baubigny, Michael Benzaquen, Laure Fabié, Mathieu Delmas, Jean-Pierre Aimé, Marc Legros, and Thierry Ondarçuhu. Shape and effective spring constant of liquid interfaces probed at the nanometer scale: Finite size effects. *Langmuir*, 31(36):9790–9798, 2015.
- [53] Caroline Mortagne, Kevin Lippera, Philippe Tordjeman, Michael Benzaquen, and Thierry Ondarçuhu. Dynamics of anchored oscillating nanomenisci. *Physical Review Fluids*, 2(10):102201, 2017.
- [54] Dongshi Guan, Elisabeth Charlaix, Robert Z Qi, and Penger Tong. Noncontact viscoelastic imaging of living cells using a long-needle atomic force microscope with dual-frequency modulation. *Physical Review Applied*, 8(4):044010, 2017.
- [55] Dongshi Guan, Elisabeth Charlaix, Robert Z Qi, and Penger Tong. Noncontact viscoelastic imaging of living cells using a long-needle atomic force microscope with dual-frequency modulation. *Physical Review Applied*, 8(4):044010, 2017.
- [56] Jean Comtet, Antoine Lainé, Antoine Nigues, Lydéric Bocquet, and Alessandro Siria. Atomic rheology of gold nanojunctions. *Nature*, 569(7756):393–397, 2019.
- [57] Antoine Lainé, Antoine Niguès, Lydéric Bocquet, and Alessandro Siria. Nanotribology of ionic liquids: transition to yielding response in nanometric confinement with metallic surfaces. *Physical Review X*, 10(1):011068, 2020.
- [58] Vincent SJ Craig and Chiara Neto. In situ calibration of colloid probe cantilevers in force microscopy: hydrodynamic drag on a sphere approaching a wall. *Langmuir*, 17(19):6018–6022, 2001.
- [59] Abdelhamid Maali and Rodolphe Boisgard. Precise damping and stiffness extraction in acoustic driven cantilever in liquid. *Journal of Applied Physics*, 114(14):144302, 2013.
- [60] Samuel Leroy and Elisabeth Charlaix. Hydrodynamic interactions for the measurement of thin film elastic properties. *Journal of Fluid Mechanics*, 674:389, 2011.
- [61] O. Reynolds. *Philos. Trans. R. Soc. Lond.*, 177:157, 1886.

- [62] Jackie Li and Tsu-Wei Chou. Elastic field of a thin-film/substrate system under an axisymmetric loading. *International Journal of Solids and Structures*, 34(35-36):4463–4478, 1997.
- [63] Takashi Nogi and Takahisa Kato. Influence of a hard surface layer on the limit of elastic contact—part i: Analysis using a real surface model. 1997.
- [64] Milton Abramowitz and Irene A Stegun. *Handbook of mathematical functions with formulas, graphs, and mathematical tables*, volume 55. US Government printing office, 1948.
- [65] Robert H Davis, Jean-Marc Serayssol, and EJ Hinch. The elasto-hydrodynamic collision of two spheres. *Journal of Fluid Mechanics*, 163:479–497, 1986.
- [66] David A Dillard, Bikramjit Mukherjee, Preetika Karnal, Romesh C Batra, and Joelle Frechette. A review of winkler’s foundation and its profound influence on adhesion and soft matter applications. *Soft matter*, 14(19):3669–3683, 2018.
- [67] R Chasset and P Thirion. Viscoelastic relaxation of rubber vulcanizates between the glass transition and equilibrium. *Rubber Chemistry and Technology*, 39(4):870–880, 1966.
- [68] Menghua Zhao, Julien Dervaux, Tetsuharu Narita, François Lequeux, Laurent Limat, and Matthieu Roché. Geometrical control of dissipation during the spreading of liquids on soft solids. *Proceedings of the National Academy of Sciences*, 115(8):1748–1753, 2018.
- [69] Etienne Rolley, Jacco H Snoeijer, and Bruno Andreotti. A flexible rheometer design to measure the visco-elastic response of soft solids over a wide range of frequency. *Review of scientific instruments*, 90(2):023906, 2019.
- [70] James C Scanlan and H Henning Winter. Composition dependence of the viscoelasticity of end-linked poly (dimethylsiloxane) at the gel point. *Macromolecules*, 24(1):47–54, 1991.
- [71] Jonathan T Pham, Frank Schellenberger, Michael Kappl, and Hans-Jürgen Butt. From elasticity to capillarity in soft materials indentation. *Physical Review Materials*, 1(1):015602, 2017.
- [72] Emiliós K Dimitriadis, Ferenc Horkay, Julia Maresca, Bechara Kachar, and Richard S Chadwick. Determination of elastic moduli of thin layers of soft material using the atomic force microscope. *Biophysical journal*, 82(5):2798–2810, 2002.
- [73] Xiao Wang and Wei Hong. A visco-poroelastic theory for polymeric gels. *Proceedings of the Royal Society A: Mathematical, Physical and Engineering Sciences*, 468(2148):3824–3841, 2012.

- [74] Daniel GT Strange, Timothy L Fletcher, Khaow Tonsomboon, Helen Brawn, Xuanhe Zhao, and Michelle L Oyen. Separating poroviscoelastic deformation mechanisms in hydrogels. *Applied Physics Letters*, 102(3):031913, 2013.
- [75] Qin Xu, Lawrence A Wilen, Katharine E Jensen, Robert W Style, and Eric R Dufresne. Viscoelastic and poroelastic relaxations of soft solid surfaces. *Physical Review Letters*, 125(23):238002, 2020.
- [76] Chung-Yuen Hui, Yu Yun Lin, Fu-Chin Chuang, Kenneth R Shull, and Wei-Chun Lin. A contact mechanics method for characterizing the elastic properties and permeability of gels. *Journal of Polymer Science Part B: Polymer Physics*, 44(2):359–370, 2006.
- [77] Yuhang Hu, Xuanhe Zhao, Joost J Vlassak, and Zhigang Suo. Using indentation to characterize the poroelasticity of gels. *Applied Physics Letters*, 96(12):121904, 2010.
- [78] Jessica Delavoipière, Yvette Tran, Emilie Verneuil, and Antoine Chateauminois. Poroelastic indentation of mechanically confined hydrogel layers. *Soft Matter*, 12(38):8049–8058, 2016.
- [79] George D Degen, Yen-Tsung Chen, Allison L Chau, Lisa K Månsson, and Angela A Pitenis. Poroelasticity of highly confined hydrogel films measured with a surface forces apparatus. *Soft Matter*, 16(35):8096–8100, 2020.
- [80] Maurice A Biot. General theory of three-dimensional consolidation. *Journal of applied physics*, 12(2):155–164, 1941.
- [81] Maurice A Biot. Theory of propagation of elastic waves in a fluid-saturated porous solid. ii. higher frequency range. *The Journal of the acoustical Society of america*, 28(2):179–191, 1956.
- [82] Menghua Zhao, François Lequeux, Tetsuharu Narita, Matthieu Roché, Laurent Limat, and Julien Dervaux. Growth and relaxation of a ridge on a soft poroelastic substrate. *Soft matter*, 14(1):61–72, 2018.
- [83] J. M. Skotheim and L. Mahadevan. Soft lubrication: The elastohydrodynamics of nonconforming and conforming contacts. *Physics of Fluids*, 17(9):092101, 2005.
- [84] Robert W Style, Anand Jagota, Chung-Yuen Hui, and Eric R Dufresne. Elastocapillarity: Surface tension and the mechanics of soft solids. *Annual Review of Condensed Matter Physics*, 8:99–118, 2017.
- [85] José Bico, Étienne Reyssat, and Benoît Roman. Elastocapillarity: when surface tension deforms elastic solids. *Annual Review of Fluid Mechanics*, 50:629–659, 2018.
- [86] Bruno Andreotti and Jacco H Snoeijer. Statics and dynamics of soft wetting. *Annual review of fluid mechanics*, 52:285–308, 2020.

- [87] Anupam Pandey, Minkush Kansal, Miguel A Herrada, Jens Eggers, and Jacco H Snoeijer. Elastic rayleigh–plateau instability: dynamical selection of nonlinear states. *Soft matter*, 17(20):5148–5161, 2021.
- [88] MER Shanahan. The influence of solid micro-deformation on contact angle equilibrium. *Journal of Physics D: Applied Physics*, 20(7):945, 1987.
- [89] Antonin Marchand, Siddhartha Das, Jacco H Snoeijer, and Bruno Andreotti. Contact angles on a soft solid: From young’s law to neumann’s law. *Physical review letters*, 109(23):236101, 2012.
- [90] Ro Shuttleworth. The surface tension of solids. *Proceedings of the physical society. Section A*, 63(5):444, 1950.
- [91] Qin Xu, Katharine E Jensen, Rostislav Boltyanskiy, Raphaël Sarfati, Robert W Style, and Eric R Dufresne. Direct measurement of strain-dependent solid surface stress. *Nature communications*, 8(1):1–6, 2017.
- [92] Rafael D Schulman, Miguel Trejo, Thomas Salez, Elie Raphaël, and Kari Dalnoki-Veress. Surface energy of strained amorphous solids. *Nature communications*, 9(1):1–6, 2018.
- [93] Jacco H Snoeijer, Etienne Rolley, and Bruno Andreotti. Paradox of contact angle selection on stretched soft solids. *Physical review letters*, 121(6):068003, 2018.
- [94] D Langevin. Rheology of adsorbed surfactant monolayers at fluid surfaces. *Annual review of fluid mechanics*, 46:47–65, 2014.
- [95] George L Gaines. Insoluble monolayers at liquid-gas interfaces. *New York: Interscience*, 1966.
- [96] Sven Reynaert, Carlton F Brooks, Paula Moldenaers, Jan Vermant, and Gerald G Fuller. Analysis of the magnetic rod interfacial stress rheometer. *Journal of Rheology*, 52(1):261–285, 2008.
- [97] Daniel K Schwartz, Charles M Knobler, and Robijn Bruinsma. Direct observation of langmuir monolayer flow through a channel. *Physical review letters*, 73(21):2841, 1994.
- [98] Reinhard Miller, Valentin B Fainerman, Jürgen Krägel, and Guiseppe Loglio. Surface rheology of adsorbed surfactants and proteins. *Current opinion in colloid & interface science*, 2(6):578–583, 1997.
- [99] Philipp Erni, Peter Fischer, Erich J Windhab, Victor Kusnezov, Heiko Stettin, and Jörg Läger. Stress-and strain-controlled measurements of interfacial shear viscosity and viscoelasticity at liquid/liquid and gas/liquid interfaces. *Review of scientific instruments*, 74(11):4916–4924, 2003.

- [100] Francisco Ortega, Hernán Ritacco, and Ramón G Rubio. Interfacial microrheology: particle tracking and related techniques. *Current Opinion in Colloid & Interface Science*, 15(4):237–245, 2010.
- [101] Joseph R Samaniuk and Jan Vermant. Micro and macrorheology at fluid–fluid interfaces. *Soft matter*, 10(36):7023–7033, 2014.
- [102] Myung Han Lee, Clayton P Lapointe, Daniel H Reich, Kathleen J Stebe, and Robert L Leheny. Interfacial hydrodynamic drag on nanowires embedded in thin oil films and protein layers. *Langmuir*, 25(14):7976–7982, 2009.
- [103] V Bergeron and D Langevin. Monolayer spreading of polydimethylsiloxane oil on surfactant solutions. *Physical review letters*, 76(17):3152, 1996.
- [104] A Yeung, T Dabros, and J Masliyah. Dissipative interfaces and departures from the young–laplace equation. *Langmuir*, 13(24):6597–6606, 1997.
- [105] ME Leser, S Acquistapace, A Cagna, AV Makievski, and R Miller. Limits of oscillation frequencies in drop and bubble shape tensiometry. *Colloids and Surfaces A: Physicochemical and Engineering Aspects*, 261(1-3):25–28, 2005.
- [106] Francesca Ravera, Giuseppe Loglio, and Volodymyr I Kovalchuk. Interfacial dilational rheology by oscillating bubble/drop methods. *Current Opinion in Colloid & Interface Science*, 15(4):217–228, 2010.
- [107] Anthony Yeung and Lichun Zhang. Shear effects in interfacial rheology and their implications on oscillating pendant drop experiments. *Langmuir*, 22(2):693–701, 2006.
- [108] Dominique Langevin et al. *Light scattering by liquid surfaces and complementary techniques*. M. Dekker, 1992.
- [109] John C Earnshaw. Surface light scattering: a methodological review. *Applied optics*, 36(30):7583–7592, 1997.
- [110] Reinhard Miller, James K Ferri, Aliyar Javadi, Jürgen Krägel, Nenad Mucic, and Rainer Wüstneck. Rheology of interfacial layers. *Colloid and Polymer Science*, 288(9):937–950, 2010.
- [111] Andrey Shmyrov, Aleksey Mizev, Anastasia Shmyrova, and Irina Mizeva. Capillary wave method: An alternative approach to wave excitation and to wave profile reconstruction. *Physics of Fluids*, 31(1):012101, 2019.
- [112] Francisco Monroy and Dominique Langevin. Direct experimental observation of the crossover from capillary to elastic surface waves on soft gels. *Physical review letters*, 81(15):3167, 1998.

- [113] Abdelhamid Maali, Rodolphe Boisgard, Hamza Chraïbi, Zaicheng Zhang, Hamid Kellay, and Aloïs Würger. Viscoelastic drag forces and crossover from no-slip to slip boundary conditions for flow near air-water interfaces. *Physical Review Letters*, 118(8):084501, 2017.
- [114] E. J. Hinch. *Perturbation Methods*. Cambridge Texts in Applied Mathematics. Cambridge University Press, 1991.
- [115] DC Bardos. Contact angle dependence of solid probe–liquid drop forces in afm measurements. *Surface science*, 517(1-3):157–176, 2002.
- [116] Baudouin Saintyves, Theo Jules, Thomas Salez, and L. Mahadevan. Self-sustained lift and low friction via soft lubrication. *Proceedings of the National Academy of Sciences*, 113(21):5847–5849, 2016.
- [117] Zaicheng Zhang, Vincent Bertin, Muhammad Arshad, Elie Raphaël, Thomas Salez, and Abdelhamid Maali. Direct measurement of the elasto-hydrodynamic lift force at the nanoscale. *Phys. Rev. Lett.*, 124:054502, 2020.
- [118] Yoshikiyo Moroi, Kinsi Motomura, and Ryohei Matuura. The critical micelle concentration of sodium dodecyl sulfate-bivalent metal dodecyl sulfate mixtures in aqueous solutions. *Journal of Colloid and Interface Science*, 46(1):111–117, 1974.
- [119] Elisabet Fuguet, Clara Ràfols, Martí Rosés, and Elisabeth Bosch. Critical micelle concentration of surfactants in aqueous buffered and unbuffered systems. *Analytica Chimica Acta*, 548(1-2):95–100, 2005.
- [120] Kedar Joshi and James F Gilchrist. Effect of added surfactant on convective assembly of monosized microspheres. *Applied Physics Letters*, 116(8):083702, 2020.
- [121] Ofer Manor, Ivan U Vakarelski, Geoffrey W Stevens, Franz Grieser, Raymond R Dagastine, and Derek YC Chan. Dynamic forces between bubbles and surfaces and hydrodynamic boundary conditions. *Langmuir*, 24(20):11533–11543, 2008.
- [122] Francis P Bretherton. The motion of rigid particles in a shear flow at low reynolds number. *Journal of Fluid Mechanics*, 14(2):284–304, 1962.
- [123] PGT Saffman. The lift on a small sphere in a slow shear flow. *Journal of fluid mechanics*, 22(2):385–400, 1965.
- [124] RG Cox and H Brenner. The lateral migration of solid particles in poiseuille flow—i theory. *Chemical Engineering Science*, 23(2):147–173, 1968.
- [125] RG Cox and SK Hsu. The lateral migration of solid particles in a laminar flow near a plane. *International Journal of Multiphase Flow*, 3(3):201–222, 1977.
- [126] Pradeep Cherukat and John B McLaughlin. The inertial lift on a rigid sphere in a linear shear. *Journal of Fluid Mechanics*, 263:1–18, 1994.

- [127] Nilanka IK Ekanayake, Joseph D Berry, Anthony D Stickland, David E Dunstan, Ineke L Muir, Steven K Dower, and Dalton JE Harvie. Lift and drag forces acting on a particle moving with zero slip in a linear shear flow near a wall. *Journal of Fluid Mechanics*, 904, 2020.
- [128] G Segre and A Silberberg. Radial particle displacements in poiseuille flow of suspensions. *Nature*, 189(4760):209–210, 1961.
- [129] Jian Zhou and Ian Papautsky. Fundamentals of inertial focusing in microchannels. *Lab on a Chip*, 13(6):1121–1132, 2013.
- [130] Thomas M Geislinger and Thomas Franke. Hydrodynamic lift of vesicles and red blood cells in flow—from fähræus & lindqvist to microfluidic cell sorting. *Advances in colloid and interface science*, 208:161–176, 2014.
- [131] Raymond G Cox and Howard Brenner. The slow motion of a sphere through a viscous fluid towards a plane surface—ii small gap widths, including inertial effects. *Chemical Engineering Science*, 22(12):1753–1777, 1967.
- [132] Jianyong Mo and Mark G Raizen. Highly resolved brownian motion in space and in time. *Annual Review of Fluid Mechanics*, 51:403–428, 2019.
- [133] Andrea Prosperetti. Viscous effects on small-amplitude surface waves. *The Physics of Fluids*, 19(2):195–203, 1976.
- [134] Bruno Issenmann, Régis Wunenburger, Hamza Chraïbi, Morgane Gandil, and Jean-Pierre Delville. Unsteady deformations of a free liquid surface caused by radiation pressure. *Journal of fluid mechanics*, 682:460–490, 2011.
- [135] Da Wei, Parviz G Dehnavi, Marie-Eve Aubin-Tam, and Daniel Tam. Measurements of the unsteady flow field around beating cilia. *Journal of Fluid Mechanics*, 915, 2021.
- [136] Howard Brenner. The slow motion of a sphere through a viscous fluid towards a plane surface. *Chemical engineering science*, 16(3-4):242–251, 1961.
- [137] Michael E O’Neill. A slow motion of viscous liquid caused by a slowly moving solid sphere. *Mathematika*, 11(1):67–74, 1964.
- [138] Constantine Pozrikidis et al. *Boundary integral and singularity methods for linearized viscous flow*. Cambridge university press, 1992.
- [139] Itzhak Fouxon and Alexander Leshansky. Fundamental solution of unsteady stokes equations and force on an oscillating sphere near a wall. *Physical Review E*, 98(6):063108, 2018.
- [140] BU Felderhof. Effect of the wall on the velocity autocorrelation function and long-time tail of brownian motion. *The Journal of Physical Chemistry B*, 109(45):21406–21412, 2005.

- [141] Akarsh Simha, Jianyong Mo, and Philip J Morrison. Unsteady stokes flow near boundaries: the point-particle approximation and the method of reflections. *Journal of Fluid Mechanics*, 841:883–924, 2018.
- [142] Alfred Barnard Basset. *A treatise on hydrodynamics: with numerous examples*, volume 2. Deighton, Bell and Company, 1888.
- [143] Clémence Devailly, Patrick Bouriat, Christophe Dicharry, Frédéric Risso, Thierry Ondarçuhu, and Philippe Tordjeman. Long-range hydrodynamic forces in liquid fm-afm. *Nanotechnology*, 31(45):455501, 2020.
- [144] Hassan Masoud and Howard A Stone. The reciprocal theorem in fluid dynamics and transport phenomena. *Journal of Fluid Mechanics*, 879, 2019.
- [145] Yansong Wang and Q. Jane Wang. *Stribeck Curves*, pages 3365–3370. Springer US, Boston, MA, 2013.
- [146] G Amontons. 1699. de la résistance causée dans les machines. *Mémoires de l'Académie Royale A*, pages 257–282.
- [147] Charles Augustin Coulomb. *Théorie des machines simples en ayant égard au frottement de leurs parties et à la roideur des cordages*. Bachelier, 1821.
- [148] Duncan Dowson. *History of tribology*. Addison-Wesley Longman Limited, 1978.
- [149] Kenneth Holmberg and Ali Erdemir. Global impact of friction on energy consumption, economy and environment. *Fme Trans*, 43(3):181–5, 2015.
- [150] Abdoulaye Fall, B Weber, M Pakpour, Nicolas Lenoir, N Shahidzadeh, J Fiscina, C Wagner, and Daniel Bonn. Sliding friction on wet and dry sand. *Physical review letters*, 112(17):175502, 2014.
- [151] Matthieu Auzanneau. *Or noir: la grande histoire du pétrole*. La découverte, 2021.
- [152] Duncan Dowson and Gordon Robert Higginson. *Elasto-hydrodynamic lubrication: international series on materials science and technology*. Elsevier, 2014.
- [153] Emily E Brodsky and Hiroo Kanamori. Elastohydrodynamic lubrication of faults. *Journal of Geophysical Research: Solid Earth*, 106(B8):16357–16374, 2001.
- [154] Charles S Campbell. Self-lubrication for long runout landslides. *The Journal of Geology*, 97(6):653–665, 1989.
- [155] James A Greenwood. Elastohydrodynamic lubrication. *Lubricants*, 8(5):51, 2020.
- [156] Malcolm B Jones, GR Fulford, Colin P Please, DLS McElwain, and Michael J Collins. Elastohydrodynamics of the eyelid wiper. *Bulletin of mathematical biology*, 70(2):323–343, 2008.

- [157] Van C Mow, Mark H Holmes, and W Michael Lai. Fluid transport and mechanical properties of articular cartilage: a review. *Journal of biomechanics*, 17(5):377–394, 1984.
- [158] Sabrina Jahn, Jasmine Seror, and Jacob Klein. Lubrication of articular cartilage. *Annual Review of Biomedical Engineering*, 18:235–258, 2016.
- [159] Jian Ping Gong. Friction and lubrication of hydrogels – its richness and complexity. *Soft matter*, 2(7):544–552, 2006.
- [160] K Sekimoto and L Leibler. A mechanism for shear thickening of polymer-bearing surfaces: elasto-hydrodynamic coupling. *EPL (Europhysics Letters)*, 23(2):113, 1993.
- [161] Nichole Moyle, Haibin Wu, Constantine Khripin, Florian Bremond, Chung-Yuen Hui, and Anand Jagota. Enhancement of elasto-hydrodynamic friction by elastic hysteresis in a periodic structure. *Soft matter*, 16(6):1627–1635, 2020.
- [162] Haibin Wu, Nichole Moyle, Anand Jagota, and Chung-Yuen Hui. Lubricated steady sliding of a rigid sphere on a soft elastic substrate: hydrodynamic friction in the Hertz limit. *Soft Matter*, 16(11):2760–2773, 2020.
- [163] Chung-Yuen Hui, Haibin Wu, Anand Jagota, and Constantine Khripin. Friction force during lubricated steady sliding of a rigid cylinder on a viscoelastic substrate. *Tribology Letters*, 69(2):1–17, 2021.
- [164] P Gondret, M Lance, and L Petit. Bouncing motion of spherical particles in fluids. *Physics of fluids*, 14(2):643–652, 2002.
- [165] Matthew Ryan Tan, Yumo Wang, and Joelle Frechette. Criterion for particle rebound during wet collisions on elastic coatings. *Physical Review Fluids*, 4(8):084305, 2019.
- [166] Farzaneh Kaveh, Javed Ally, Michael Kappl, and Hans-Jürgen Butt. Hydrodynamic force between a sphere and a soft, elastic surface. *Langmuir*, 30(39):11619–11624, 2014.
- [167] Yumo Wang, Ziyuan Feng, and Joelle Frechette. Dynamic adhesion due to fluid infusion. *Current Opinion in Colloid & Interface Science*, page 101397, 2020.
- [168] Steven P Meeker, Roger T Bonnecaze, and Michel Cloitre. Slip and flow in soft particle pastes. *Physical Review Letters*, 92(19):198302, 2004.
- [169] Xavier Grandchamp, Gwennou Coupier, Aparna Srivastav, Christophe Minetti, and Thomas Podgorski. Lift and down-gradient shear-induced diffusion in red blood cell suspensions. *Physical Review Letters*, 110(10):108101, 2013.

- [170] Manouk Abkarian, Colette Lartigue, and Annie Viallat. Tank treading and unbinding of deformable vesicles in shear flow: determination of the lift force. *Physical Review Letters*, 88(6):068103, 2002.
- [171] JM Skotheim and Lakshminarayanan Mahadevan. Soft lubrication. *Physical Review Letters*, 92(24):245509, 2004.
- [172] Thomas Salez and Lakshminarayanan Mahadevan. Elastohydrodynamics of a sliding, spinning and sedimenting cylinder near a soft wall. *Journal of Fluid Mechanics*, 779:181–196, 2015.
- [173] J Beaucourt, T Biben, and C Misbah. Optimal lift force on vesicles near a compressible substrate. *EPL (Europhysics Letters)*, 67(4):676, 2004.
- [174] JM Skotheim and L Mahadevan. Soft lubrication: The elastohydrodynamics of nonconforming and conforming contacts. *Physics of Fluids*, 17(9):092101, 2005.
- [175] Javier Urzay, Stefan G Llewellyn Smith, and Beverley J Glover. The elastohydrodynamic force on a sphere near a soft wall. *Physics of Fluids*, 19(10):103106, 2007.
- [176] Javier Urzay. Asymptotic theory of the elastohydrodynamic adhesion and gliding motion of a solid particle over soft and sticky substrates at low reynolds numbers. *Journal of fluid mechanics*, 653:391, 2010.
- [177] A.-S. Bouchet, C. Cazeneuve, N. Baghdadli, G. S. Luengo, and C. Drummond. Experimental study and modeling of boundary lubricant polyelectrolyte films. *Macromolecules*, 48:2244, 2015.
- [178] Heather S Davies, Delphine Débarre, Nouha El Amri, Claude Verdier, Ralf P Richter, and Lionel Bureau. Elastohydrodynamic lift at a soft wall. *Physical Review Letters*, 120(19):198001, 2018.
- [179] Bhargav Rallabandi, Naomi Oppenheimer, Matan Yah Ben Zion, and Howard A Stone. Membrane-induced hydroelastic migration of a particle surfing its own wave. *Nature Physics*, 14(12):1211–1215, 2018.
- [180] Pierre Vialar, Pascal Merzeau, Suzanne Giasson, and Carlos Drummond. Compliant surfaces under shear: Elastohydrodynamic lift force. *Langmuir*, 35(48):15605–15613, 2019.
- [181] Christophe Clanet. Sports ballistics. *Annual Review of Fluid Mechanics*, 47:455–478, 2015.
- [182] Martin H Essink, Anupam Pandey, Stefan Karpitschka, Cornelis H Venner, and Jacco H Snoeijer. Regimes of soft lubrication. *Journal of Fluid Mechanics*, 915, 2021.
- [183] Anupam Pandey, Stefan Karpitschka, Cornelis H Venner, and Jacco H Snoeijer. Lubrication of soft viscoelastic solids. *Journal of fluid mechanics*, 799:433–447, 2016.

- [184] Bhargav Rallabandi, Baudouin Saintyves, Theo Jules, Thomas Salez, Clarissa Schönecker, L Mahadevan, and Howard A Stone. Rotation of an immersed cylinder sliding near a thin elastic coating. *Physical Review Fluids*, 2(7):074102, 2017.
- [185] Baudouin Saintyves, Bhargav Rallabandi, Theo Jules, Jesse Ault, Thomas Salez, Clarissa Schönecker, Howard A Stone, and Lakshminarayana Mahadevan. Rotation of a submerged finite cylinder moving down a soft incline. *Soft matter*, 16(16):4000–4007, 2020.
- [186] Milton Abramowitz and Irene A Stegun. *Handbook of mathematical functions with formulas, graphs, and mathematical tables*, volume 55. US Government printing office, 1964.
- [187] ME O’Neill and K Stewartson. On the slow motion of a sphere parallel to a nearby plane wall. *Journal of Fluid Mechanics*, 27(4):705–724, 1967.
- [188] AJ Goldman, RG Cox, and H Brenner. Slow viscous motion of a sphere parallel to a plane wall – ii couette flow. *Chemical engineering science*, 22(4):653–660, 1967.
- [189] Mohamed Chaoui and François Feuillebois. Creeping flow around a sphere in a shear flow close to a wall. *Quarterly Journal of Mechanics and Applied Mathematics*, 56(3):381–410, 2003.
- [190] Abdallah Daddi-Moussa-Ider, Bhargav Rallabandi, Stephan Gekle, and Howard A Stone. Reciprocal theorem for the prediction of the normal force induced on a particle translating parallel to an elastic membrane. *Physical Review Fluids*, 3(8):084101, 2018.
- [191] John William Strutt. Vi. on the application of the principle of reciprocity to acoustics. *Proceedings of the Royal Society of London*, 25(171-178):118–122, 1877.
- [192] John William Strutt and John William Strutt Baron Rayleigh. *The theory of sound*, volume 1. Macmillan, 1877.
- [193] John R Carson. A generalization of the reciprocal theorem. *The Bell System Technical Journal*, 3(3):393–399, 1924.
- [194] Enrico Betti. Teoria della elasticita. *Il Nuovo Cimento (1869-1876)*, 7(1):158–180, 1872.
- [195] HA Lorentz. A general theorem concerning the motion of a viscous fluid and a few consequences derived from it. *Zittingsverlag Akad. Wet. Amsterdam*, 5:168–175, 1896.
- [196] Thomas GJ Chandler and Dominic Vella. Validity of winkler’s mattress model for thin elastomeric layers: beyond poisson’s ratio. *Proceedings of the Royal Society A*, 476(2242):20200551, 2020.

- [197] Arash Kargar-Estahbanati and Bhargav Rallabandi. Lift forces on three-dimensional elastic and viscoelastic lubricated contacts. *Physical Review Fluids*, 6(3):034003, 2021.
- [198] J Le Rouzic, P Delobelle, P Vairac, and B Cretin. Comparison of three different scales techniques for the dynamic mechanical characterization of two polymers (pdms and su8). *The European Physical Journal Applied Physics*, 48(1):11201, 2009.
- [199] SJ Weekley, SL Waters, and OE Jensen. Transient elastohydrodynamic drag on a particle moving near a deformable wall. *The Quarterly Journal of Mechanics and Applied Mathematics*, 59(2):277–300, 2006.
- [200] J. H. Snoeijer, J. Eggers, and C. H. Venner. Similarity theory of lubricated hertzian contacts. *Physics of Fluids*, 25(10):101705, 2013.
- [201] Heinrich Hertz. On the contact of elastic solids. *Z. Reine Angew. Mathematik*, 92:156–171, 1881.
- [202] Kenneth Langstreth Johnson and Kenneth Langstreth Johnson. *Contact mechanics*. Cambridge university press, 1987.
- [203] Cornelis Henricus Venner and Antonius Adrianus Lubrecht. *Multi-level methods in lubrication*. Elsevier, 2000.
- [204] Ralf Greve and Heinz Blatter. *Dynamics of ice sheets and glaciers*. Springer Science & Business Media, 2009.
- [205] Ross W Griffiths. The dynamics of lava flows. *Annual review of fluid mechanics*, 32(1):477–518, 2000.
- [206] Paul Stoodley, Karin Sauer, David Gwilym Davies, and J William Costerton. Biofilms as complex differentiated communities. *Annual Reviews in Microbiology*, 56(1):187–209, 2002.
- [207] JB Grotberg. Pulmonary flow and transport phenomena. *Annual Review of Fluid Mechanics*, 26(1):529–571, 1994.
- [208] W Shyy and, M Francois, HS Udaykumar, N N’dri and, and R Tran-Son-Tay. Moving boundaries in micro-scale biofluid dynamics. *Appl. Mech. Rev.*, 54(5):405–454, 2001.
- [209] Milton Ohring. *Materials science of thin films*. Elsevier, 2001.
- [210] Daniel Bonn, Jens Eggers, Joseph Indekeu, Jacques Meunier, and Etienne Rolley. Wetting and spreading. *Reviews of modern physics*, 81(2):739, 2009.
- [211] Alexander Oron, Stephen H Davis, and S George Bankoff. Long-scale evolution of thin liquid films. *Reviews of modern physics*, 69(3):931, 1997.

- [212] Richard V Craster and Omar K Matar. Dynamics and stability of thin liquid films. *Reviews of modern physics*, 81(3):1131, 2009.
- [213] Sebastian Jachalski, Dirk Peschka, Andreas Münch, and Barbara Wagner. Impact of interfacial slip on the stability of liquid two-layer polymer films. *Journal of Engineering Mathematics*, 86(1):9–29, 2014.
- [214] Thomas Salez, Joshua D McGraw, Sara L Cormier, Oliver Bäumchen, Kari Dalnoki-Veress, and Elie Raphaël. Numerical solutions of thin-film equations for polymer flows. *The European Physical Journal E*, 35(11):1–9, 2012.
- [215] Michael Rubinstein, Ralph H Colby, et al. *Polymer physics*, volume 23. Oxford university press New York, 2003.
- [216] Joshua D McGraw, Nicholas M Jago, and Kari Dalnoki-Veress. Capillary levelling as a probe of thin film polymer rheology. *Soft Matter*, 7(17):7832–7838, 2011.
- [217] Joshua D McGraw, Thomas Salez, Oliver Bäumchen, Elie Raphaël, and Kari Dalnoki-Veress. Self-similarity and energy dissipation in stepped polymer films. *Physical Review Letters*, 109(12):128303, 2012.
- [218] Grigory Isaakovich Barenblatt. *Scaling, self-similarity, and intermediate asymptotics: dimensional analysis and intermediate asymptotics*. Number 14. Cambridge University Press, 1996.
- [219] Oliver Bäumchen, Michael Benzaquen, Thomas Salez, Joshua D McGraw, Matilda Backholm, Paul Fowler, Elie Raphaël, and Kari Dalnoki-Veress. Relaxation and intermediate asymptotics of a rectangular trench in a viscous film. *Physical Review E*, 88(3):035001, 2013.
- [220] Matilda Backholm, Michael Benzaquen, Thomas Salez, Elie Raphaël, and Kari Dalnoki-Veress. Capillary levelling of a cylindrical hole in a viscous film. *Soft Matter*, 10(15):2550–2558, 2014.
- [221] Thomas Salez, Joshua D McGraw, Oliver Bäumchen, Kari Dalnoki-Veress, and Elie Raphaël. Capillary-driven flow induced by a stepped perturbation atop a viscous film. *Physics of Fluids*, 24(10):102111, 2012.
- [222] Michael Benzaquen, Paul Fowler, Laetitia Jubin, Thomas Salez, Kari Dalnoki-Veress, and Elie Raphaël. Approach to universal self-similar attractor for the levelling of thin liquid films. *Soft matter*, 10(43):8608–8614, 2014.
- [223] Mark Ilton, Miles MP Couchman, Cedric Gerbelot, Michael Benzaquen, Paul D Fowler, Howard A Stone, Elie Raphaël, Kari Dalnoki-Veress, and Thomas Salez. Capillary leveling of freestanding liquid nanofilms. *Physical review letters*, 117(16):167801, 2016.

- [224] Yu Chai, Thomas Salez, Joshua D McGraw, Michael Benzaquen, Kari Dalnoki-Veress, Elie Raphaël, and James A Forrest. A direct quantitative measure of surface mobility in a glassy polymer. *Science*, 343(6174):994–999, 2014.
- [225] Mark Ilton, Thomas Salez, Paul D Fowler, Marco Rivetti, Mohammed Aly, Michael Benzaquen, Joshua D McGraw, Elie Raphaël, Kari Dalnoki-Veress, and Oliver Bäumchen. Adsorption-induced slip inhibition for polymer melts on ideal substrates. *Nature communications*, 9(1):1–7, 2018.
- [226] Oliver Bäumchen, Renate Fetzer, and Karin Jacobs. Reduced interfacial entanglement density affects the boundary conditions of polymer flow. *Physical review letters*, 103(24):247801, 2009.
- [227] CLMH Navier. Mémoire sur les lois du mouvement des fluides. *Mémoires de l'Académie Royale des Sciences de l'Institut de France*, 6(1823):389–440, 1823.
- [228] Lydéric Bocquet and Elisabeth Charlaix. Nanofluidics, from bulk to interfaces. *Chemical Society Reviews*, 39(3):1073–1095, 2010.
- [229] PG De Gennes. Comptes rendus hebdomadaires des seances de l'academie des sciences serie b. *Sciences physiques*, 288:219, 1979.
- [230] Jean Baptiste Joseph baron Fourier. *Théorie analytique de la chaleur*. Chez Firmin Didot, père et fils, 1822.
- [231] Adolph Fick. V. on liquid diffusion. *The London, Edinburgh, and Dublin Philosophical Magazine and Journal of Science*, 10(63):30–39, 1855.
- [232] Albert Einstein. Über die von der molekularkinetischen theorie der wärme geforderte bewegung von in ruhenden flüssigkeiten suspendierten teilchen. *Annalen der Physik*, 322(8):549–560, 1905.
- [233] Marian Smoluchowski. *Essai d'une théorie cinétique du mouvement Brownien et des milieux troublés*. Acad. Litterarum Cracoviensis, 1906.
- [234] Paul Langevin. Sur la théorie du mouvement brownien. *Compt. Rendus*, 146:530–533, 1908.
- [235] Geoffrey Ingram Taylor. Dispersion of soluble matter in solvent flowing slowly through a tube. *Proceedings of the Royal Society of London. Series A. Mathematical and Physical Sciences*, 219(1137):186–203, 1953.
- [236] R Byron Bird, Warren E Stewart, and Edwin N Lightfoot. *Transport phenomena*, volume 1. John Wiley & Sons, 2006.
- [237] Henrik Bruus. *Theoretical microfluidics*, volume 18. Oxford university press Oxford, 2008.

- [238] AJ Roberts. The utility of an invariant manifold description of the evolution of a dynamical system. *SIAM journal on mathematical analysis*, 20(6):1447–1458, 1989.
- [239] GN Mercer and AJ Roberts. A centre manifold description of contaminant dispersion in channels with varying flow properties. *SIAM Journal on Applied Mathematics*, 50(6):1547–1565, 1990.
- [240] Sophie Marbach and Karen Alim. Active control of dispersion within a channel with flow and pulsating walls. *Physical Review Fluids*, 4(11):114202, 2019.
- [241] Margaret Beck, Osman Chaudhary, and C Eugene Wayne. Rigorous justification of taylor dispersion via center manifolds and hypocoercivity. *Archive for Rational Mechanics and Analysis*, 235(2):1105–1149, 2020.
- [242] Rutherford Aris. On the dispersion of a solute in a fluid flowing through a tube. *Proceedings of the Royal Society of London. Series A. Mathematical and Physical Sciences*, 235(1200):67–77, 1956.
- [243] NG Barton. On the method of moments for solute dispersion. *Journal of Fluid Mechanics*, 126:205–218, 1983.
- [244] Søren Vedel and Henrik Bruus. Transient taylor–aris dispersion for time-dependent flows in straight channels. *Journal of fluid mechanics*, 691:95–122, 2012.
- [245] Søren Vedel, Emil Hovad, and Henrik Bruus. Time-dependent taylor–aris dispersion of an initial point concentration. *Journal of fluid mechanics*, 752:107–122, 2014.
- [246] H. Brenner and D.A. Edwards. *Macrotransport Processes*, edited by Butterworth. Heinemann, 1993.
- [247] P. H. Haynes and J. Vanneste. Dispersion in the large-deviation regime. part 1: shear flows and periodic flows. *Journal of Fluid Mechanics*, 745:321–350, 2014.
- [248] Marcel Kahlen, Andreas Engel, and Christian Van den Broeck. Large deviations in taylor dispersion. *Physical Review E*, 95(1):012144, 2017.
- [249] Ch Van den Broeck. Taylor dispersion revisited. *Physica A: Statistical Mechanics and its Applications*, 168(2):677–696, 1990.
- [250] Thomas Guérin and David S Dean. Force-induced dispersion in heterogeneous media. *Physical review letters*, 115(2):020601, 2015.
- [251] T Guérin and David S Dean. Kubo formulas for dispersion in heterogeneous periodic nonequilibrium systems. *Physical Review E*, 92(6):062103, 2015.
- [252] Arthur Alexandre, Thomas Guérin, and David S Dean. Generalized taylor dispersion for translationally invariant microfluidic systems. *arXiv preprint arXiv:2105.06212*, 2021.

- [253] PC Chatwin and CM Allen. Mathematical models of dispersion in rivers and estuaries. *Annual Review of Fluid Mechanics*, 17(1):119–149, 1985.
- [254] Howard Brenner. Dispersion resulting from flow through spatially periodic porous media. *Philosophical Transactions of the Royal Society of London. Series A, Mathematical and Physical Sciences*, 297(1430):81–133, 1980.
- [255] Jean-Louis Auriault and PM Adler. Taylor dispersion in porous media: Analysis by multiple scale expansions. *Advances in Water Resources*, 18(4):217–226, 1995.
- [256] Howard A Stone, Abraham D Stroock, and Armand Ajdari. Engineering flows in small devices: microfluidics toward a lab-on-a-chip. *Annu. Rev. Fluid Mech.*, 36:381–411, 2004.
- [257] Patrick Tabeling. *Introduction to microfluidics*. OUP Oxford, 2005.
- [258] Jeffrey J. Fredberg. Augmented diffusion in the airways can support pulmonary gas exchange. *Journal of Applied Physiology*, 49(2):232–238, 1980.
- [259] J.B. Grotberg. Pulmonary flow and transport phenomena. *Annual Review of Fluid Mechanics*, 26(1):529–571, 1994.
- [260] Luca Salerno, Giulia Cardillo, and Carlo Camporeale. Aris-taylor dispersion in the subarachnoid space. *Physical Review Fluids*, 5(4), April 2020.
- [261] Derek Stein, Frank H.J. van der Heyden, Wiepke J.A. Koopmans, and Cees Dekker. Pressure-driven transport of confined dna polymers in fluidic channels. *Proceedings of the National Academy of Sciences*, 103(43):15853–15858, 2006.
- [262] R.N. Bearon and A.L. Hazel. The trapping in high-shear regions of slender bacteria undergoing chemotaxis in a channel. *Journal of Fluid Mechanics*, 771, 2015.
- [263] Amin Dehkharghani, Nicolas Waisbord, Jörn Dunkel, and Jeffrey S Guasto. Bacterial scattering in microfluidic crystal flows reveals giant active taylor–aris dispersion. *Proceedings of the National Academy of Sciences*, 116(23):11119–11124, 2019.
- [264] Sophie Marbach, Karen Alim, Natalie Andrew, Anne Pringle, and Michael P Brenner. Pruning to increase taylor dispersion in physarum polycephalum networks. *Physical Review Letters*, 117(17):178103, 2016.
- [265] P.C. Chatwin. The initial development of longitudinal dispersion in straight tubes. *Journal of Fluid Mechanics*, 80(1):33–48, 1977.
- [266] Francesco Gentile, Mauro Ferrari, and Paolo Decuzzi. The transport of nanoparticles in blood vessels: the effect of vessel permeability and blood rheology. *Annals of Biomedical Engineering*, 36(2):254–261, 2008.
- [267] Jifu Tan, Antony Thomas, and Yaling Liu. Influence of red blood cells on nanoparticle targeted delivery in microcirculation. *Soft Matter*, 8(6):1934–1946, 2012.

- [268] Thomas K. Nielsen, Ulrike Bösenberg, Rapee Gosalawit, Martin Dornheim, Yngve Cerenius, Flemming Besenbacher, and Torben R. Jensen. A reversible nanoconfined chemical reaction. *ACS Nano*, 4(7):3903–3908, June 2010.
- [269] Angela B. Grommet, Moran Feller, and Rafal Klajn. Chemical reactivity under nanoconfinement. *Nature Nanotechnology*, 15(4):256–271, April 2020.
- [270] Ioana Bena, Michel Droz, Kirsten Martens, and Zoltan Racz. Reaction–diffusion fronts with inhomogeneous initial conditions. *Journal of Physics: Condensed Matter*, 19(6):065103, 2007.
- [271] Melinda Tonks Hoffman, Janet Sheung, and Paul R. Selvin. Fluorescence imaging with one nanometer accuracy: in vitro and in vivo studies of molecular motors. In *Single Molecule Enzymology*, pages 33–56. Springer, 2011.
- [272] Zhenzhen Li, Loïc D’eramo, Choongyeop Lee, Fabrice Monti, Marc Yonger, Patrick Tabeling, Benjamin Chollet, Bruno Bresson, and Yvette Tran. Near-wall nanovelocimetry based on total internal reflection fluorescence with continuous tracking. *Journal of Fluid Mechanics*, 766:147–171, 2015.
- [273] Gabriel Guyard, Alexandre Vilquin, Nicolas Sanson, Stéphane Jouenne, Frédéric Restagno, and Joshua D. McGraw. Near-surface rheology and hydrodynamic boundary condition of semi-dilute polymer solutions. *Soft Matter*, 17:3765–3774, 2021.
- [274] B. Derjaguin. On the repulsive forces between charged colloid particles and on the theory of slow coagulation and stability of lyophobic sols. *Transactions of the Faraday Society*, 35:203–215, 1940.
- [275] Evert Johannes Willem Verwey. Theory of the stability of lyophobic colloids. *The Journal of Physical Chemistry*, 51(3):631–636, 1947.
- [276] Dennis C. Prieve. Measurement of colloidal forces with TIRM. *Advances in Colloid and Interface Science*, 82(1-3):93–125, 1999.
- [277] Xu Zheng, Fei Shi, and Zhanhua Silber-Li. Study on the statistical intensity distribution (SID) of fluorescent nanoparticles in TIRFM measurement. *Microfluidics and Nanofluidics*, 22(11):127, 2018.
- [278] Lawrence Korson, Walter Drost-Hansen, and Frank J. Millero. Viscosity of water at various temperatures. *The Journal of Physical Chemistry*, 73(1):34–39, January 1969.
- [279] A.J. Goldman, R.G. Cox, and H. Brenner. Slow viscous motion of a sphere parallel to a plane wall—ii couette flow. *Chemical Engineering Science*, 22(4):653–660, 1967.
- [280] Manuchehr Aminian, Francesca Bernardi, Roberto Camassa, Daniel M. Harris, and Richard M. McLaughlin. How boundaries shape chemical delivery in microfluidics. *Science*, 354(6317):1252–1256, 2016.

- [281] S. Jin, P. Huang, J. Park, J.Y. Yoo, and Kenneth S. Breuer. Near-surface velocimetry using evanescent wave illumination. *Experiments in Fluids*, 37(6):825–833, 2004.
- [282] Luc P. Faucheux and Albert J. Libchaber. Confined brownian motion. *Physical Review E*, 49(6):5158, 1994.
- [283] Peter Huang and Kenneth S. Breuer. Direct measurement of anisotropic near-wall hindered diffusion using total internal reflection velocimetry. *Physical Review E*, 76(4):046307, 2007.
- [284] Anthony Saugey, Laurent Joly, Christophe Ybert, Jean-Louis Barrat, and Lyderic Bocquet. Diffusion in pores and its dependence on boundary conditions. *Journal of Physics: Condensed Matter*, 17(49):S4075, 2005.
- [285] Maxime Lavaud, Thomas Salez, Yann Louyer, and Yacine Amarouchene. Stochastic inference of surface-induced effects using brownian motion. *Phys. Rev. Research*, 3:L032011, Jul 2021.
- [286] E. Taghizadeh, F.J. Valdés-Parada, and B.D. Wood. Preasymptotic taylor dispersion: evolution from the initial condition. *Journal of Fluid Mechanics*, 889, 2020.
- [287] T.G.M. Van de Ven. Diffusion of brownian particles in shear flow. *Journal of Colloid and Interface Science*, 62(2):352–355, 1977.
- [288] G.K. Batchelor. Mass transfer from a particle suspended in fluid with a steady linear ambient velocity distribution. *Journal of Fluid Mechanics*, 95(2):369–400, 1979.
- [289] R.T. Foister and T.G.M. Van De Ven. Diffusion of brownian particles in shear flows. *Journal of Fluid Mechanics*, 96(1):105–132, 1980.
- [290] C. Van den Broeck, J.M. Sancho, and M. San Miguel. Harmonically bound brownian motion in flowing fluids. *Physica A: Statistical Mechanics and its Applications*, 116(3):448–461, 1982.
- [291] Kunimasa Miyazaki and Dick Bedeaux. Brownian motion in a fluid in simple shear flow. *Physica A: Statistical Mechanics and its Applications*, 217(1-2):53–74, 1995.
- [292] Hiroshi Orihara and Yoshinori Takikawa. Brownian motion in shear flow: Direct observation of anomalous diffusion. *Physical Review E*, 84(6):061120, 2011.
- [293] Einar Orn Fridjonsson, Joseph D. Seymour, and Sarah L. Codd. Anomalous preasymptotic colloid transport by hydrodynamic dispersion in microfluidic capillary flow. *Physical Review E*, 90(1):010301, 2014.
- [294] Yoshinori Takikawa, Takahiro Nunokawa, Yuji Sasaki, Makoto Iwata, and Hiroshi Orihara. Three-dimensional observation of brownian particles under steady shear flow by stereo microscopy. *Physical Review E*, 100(2):022102, 2019.

- [295] Howard Brenner and Lawrence J Gaydos. The constrained brownian movement of spherical particles in cylindrical pores of comparable radius: Models of the diffusive and convective transport of solute molecules in membranes and porous media. *Journal of Colloid and Interface Science*, 58(2):312–356, 1977.
- [296] P. G. Saffman. On the effect of the molecular diffusivity in turbulent diffusion. *Journal of Fluid Mechanics*, 8(2):273–283, 1960.
- [297] Nicolaas Godfried Van Kampen. *Stochastic processes in physics and chemistry*, volume 1. Elsevier, 1992.
- [298] Zeev Schuss. *Brownian dynamics at boundaries and interfaces*. Springer, 2015.
- [299] Jacob N Israelachvili. *Intermolecular and surface forces*. Academic press, 2015.
- [300] Howard Brenner. *Interfacial transport processes and rheology*. Elsevier, 2013.
- [301] Aidan Rinehart, Uģis Lācis, Thomas Salez, and Shervin Bagheri. Lift induced by slip inhomogeneities in lubricated contacts. *Physical Review Fluids*, 5(8):082001, 2020.
- [302] RG Cox. Electroviscous forces on a charged particle suspended in a flowing liquid. *Journal of Fluid Mechanics*, 338:1–34, 1997.
- [303] Clemens Bechinger, Roberto Di Leonardo, Hartmut Löwen, Charles Reichhardt, Giorgio Volpe, and Giovanni Volpe. Active particles in complex and crowded environments. *Reviews of Modern Physics*, 88(4):045006, 2016.
- [304] Renaud Trouilloud, S Yu Tony, AE Hosoi, and Eric Lauga. Soft swimming: Exploiting deformable interfaces for low reynolds number locomotion. *Physical review letters*, 101(4):048102, 2008.
- [305] Thomas P Russell and Yu Chai. 50th anniversary perspective: putting the squeeze on polymers: a perspective on polymer thin films and interfaces. *Macromolecules*, 50(12):4597–4609, 2017.
- [306] JA Forrest, K Dalnoki-Veress, JR Stevens, and JR Dutcher. Effect of free surfaces on the glass transition temperature of thin polymer films. *Physical review letters*, 77(10):2002, 1996.
- [307] Günther Grün, Klaus Mecke, and Markus Rauscher. Thin-film flow influenced by thermal noise. *Journal of Statistical Physics*, 122(6):1261–1291, 2006.
- [308] LD Landau and EM Lifshitz. Fluid mechanics. translated from the russian by jb sykes and wh reid. *Course of Theoretical Physics*, 6, 1987.
- [309] Jean-Baptiste Salmon and Frédéric Doumenc. Buoyancy-driven dispersion in confined drying of liquid binary mixtures. *Physical Review Fluids*, 5(2):024201, 2020.

- [310] Olinka Ramirez-Soto and Stefan Karpitschka. Taylor dispersion governs the compositional evolution of marangoni-contracted droplets. *arXiv preprint arXiv:2102.08727*, 2021.
- [311] Paul B Bailey, William N Everitt, and Anton Zettl. The sleign2 sturm-liouville code. *ACM Trans. Math. Software*, 27(2):143–192, 2001.
- [312] Corinna C Maass, Carsten Krüger, Stephan Herminghaus, and Christian Bahr. Swimming droplets. *Annual Review of Condensed Matter Physics*, 7:171–193, 2016.
- [313] Ziane Izri, Marjolein N Van Der Linden, Sébastien Michelin, and Olivier Dauchot. Self-propulsion of pure water droplets by spontaneous marangoni-stress-driven motion. *Physical review letters*, 113(24):248302, 2014.